

JAN 5 1965

AIAA Journal

LOVELACE FOUNDATION
ADVANCEMENT OF RESEARCH AND
TECHNOLOGY IN THE DEPARTMENT
OF AERONAUTICS AND SPACE
DOCUMENT LIBRARY

VOLUME 2

DECEMBER 1964

NUMBER 12

Aerodynamic Aspects of the Magnetospheric Flow

R. H. LEVY, H. E. PETSCHKE, AND G. L. SISCOE

Avco-Everett Research Laboratory, Everett, Mass.

I. Introduction

It has been apparent for some time that the solar corona should be considered as extending well beyond the orbit of the earth. Diverse observations and interpretations that have contributed to our understanding of this and related phenomena include the scattering of sunlight, occultation of stars, behavior of comet tails, earth-sun phenomenological correlations, modulation of galactic cosmic rays, modulation of energetic particles of solar origin, and, more recently, and, alternatively, direct satellite observations. The over-all picture that has emerged is that the corona is heated at its base (probably by absorbing noise generated in lower turbulent levels of the solar wind) and expands freely into the solar system. This outward flow is often referred to as the solar wind. At the orbit of the earth the flow is supersonic, having a Mach number of 7-10. The solar wind consists almost entirely of ionized hydrogen.

The modulation of the forementioned cosmic rays is clear proof of the existence of a magnetic field in the solar wind; the strength of this field is on the order of 5γ (5×10^{-5} gauss). This is, of course, far less than the magnetic field near the surface of the earth which is about 0.5 gauss. Both these magnetic fields influence the motions of energetic cosmic rays, the former because of its greater extent; both fields also influence the motions of the less energetic but more numerous particles making up the solar wind. The latter particles, however, carry almost all the mass, momentum, and energy resident in the interplanetary gas. It is therefore more accurate to say that the over-all magnetic field configuration will be determined by the mechanics of these low-energy particles. The orbits of higher-energy particles will in turn be determined by the magnetic and electric fields resulting from this flow.

Two regions in the configuration resulting from the interaction of the solar wind with the earth's magnetic field have

R. H. Levy was educated at the Universities of Cambridge and Princeton, obtaining degrees in mathematics and aeronautical engineering. At Princeton, he was also holder of a Guggenheim Jet Propulsion Fellowship.

At Avco-Everett Research Laboratory, he has conducted research on a wide variety of topics including plasma physics, astrophysics, aerodynamics, magnetohydrodynamics, space flight (especially the protection of astronauts against radiation), and the applications of superconducting magnets. He is the author of many papers dealing with these fields.

Dr. Levy is an associate fellow of the AIAA and is a member of the American Physical Society, the American Geophysical Union, and the American Association for the Advancement of Science.

Harry E. Petschek received his Ph.D. in engineering physics from Cornell University in 1955. Following this he spent a year as an Instructor in the Physics Department at Princeton University. Since 1956 he has been a Principal Research Scientist at the Avco-Everett Research Laboratory where he has engaged in research in magnetohydrodynamics and plasma physics. He has published papers on radiation from plasmas, ionization rates, magnetohydrodynamic flows, plasma propulsion, and dissipation mechanisms in high temperature plasmas and their application to space plasmas.

In 1964 George L. Siscoe received the degree of Doctor of Philosophy in Physics from the Massachusetts Institute of Technology, where he was a Shell Fellow. He worked the summer of 1964 as an assistant scientist at the Avco-Everett Research Laboratory. He presently holds a research fellowship in the Department of Physics at the California Institute of Technology where he is continuing his studies in the field of space physics. He has made contributions to the literature in this field.

JAN 5 1965

RESEARCH AND DEVELOPMENT
AIAA Journal
DOCUMENT LIBRARY
VOLUME 2 NUMBER 12

DECEMBER 1964

**Reproduced From
Best Available Copy**

SURVEY PAPER

Aerodynamic Aspects of the Magnetospheric Flow.....R. H. Levy, H. E. Petschek, G. L. Siscoe 2065

CONTRIBUTED PAPERS

Small Magnetofluid-Dynamic Peristaltic Motions Inside an Annular Circular Cylindrical Induction Compressor...J. L. Neuringer and J. H. Turner 2076

Energy Transfer Processes in a Partially Ionized, Two-Temperature Gas.....D. M. Dix 2081

Hypersonic Magnetohydrodynamics with or without a Blunt Body...R. H. Levy, P. J. Gierasch, D. B. Henderson 2091

A Theoretical Investigation of MHD Channel Entrance Flows.....A. Maciulaitis and A. L. Loeffler Jr. 2100

Viscous Multicomponent-Multiphase Flow with Application to Axisymmetric Jets of Hydrogen.....R. Edelman and H. Rosenbaum 2104

Numerical Methods in Multidimensional Shocked Flows.....S. Z. Burstein 2111

Laminar Boundary Layer with Hydrogen Injection Including Multicomponent Diffusion.....P. A. Libby and M. Pierucci 2118

Confined Vortex Flows with Boundary-Layer Interaction.....M. L. Rosenzweig, W. S. Lewellen, D. H. Ross 2127

Cesium Neutral and Ion Emission from Carburized and Oxygenated Porous Tungsten...A. Y. Cho and H. Shelton 2135

Vortex Gas Accelerator.....S. A. Colgate 2138

Stability of Circumferentially Corrugated Sandwich Cylinders under Combined Loads.....E. H. Baker 2142

Influence of Boundary Conditions on the Modal Characteristics of Thin Cylindrical Shells.....K. Forsberg 2150

Approximate Laplace Transform Inversions in Viscoelastic Stress Analysis.....T. L. Cost 2157

Influence Coefficients of a Circular Cylindrical Shell with Rapidly Varying Parabolic Wall Thickness.....D. Bushnell and N. J. Hoff 2167

Influence of Work-Hardening on the Dynamic Stress-Strain Curves of 4340 Steel..B. M. Butcher and J. R. Canon 2174

Close Analogy between Radiative and Conductive Heat Flux in a Finite Slab.....M. A. Heaslet and B. Baldwin 2180

Interplanetary Trajectories in the Restricted Three-Body Problem.....L. M. Perko 2187

Solar Radio Emission as a Criterion for Solar Proton Event Warning.....J. D. Fletcher 2193

Mass and Magnetic Dipole Shielding against Electrons of the Artificial Radiation Belt.....A. Bhattacharjee and I. Michael 2198

Technical Notes and Technical Comments are listed on the back cover

A publication of the American Institute of Aeronautics and Astronautics Devoted to Aerospace Research and Development

20000915 036

AIAA JOURNAL

A Publication of the AMERICAN INSTITUTE OF AERONAUTICS AND ASTRONAUTICS Devoted to Aerospace Research and Development

EDITOR-IN-CHIEF

LEO STEG, General Electric Company

ASSOCIATE EDITORS (Terms expire in year indicated)

WALTER G. BERL, Applied Physics Laboratory (1964)
ARTHUR E. BRYSON JR., Harvard University (1965)
BERNARD BUDIANSKY, Harvard University (1966)
ALFRED M. FREUDENTHAL, Columbia University (1964)
FRANZ T. GEYLING, Bell Telephone Laboratories (1966)
ROBERT G. JAHN, Princeton University (1965)
IGOR JURKEVICH, General Electric Company (1964)
PAUL A. LIBBY, University of California at San Diego (1966)
EDWIN L. RESLER, Cornell University (1966)
ERALDUS SCALA, Cornell University (1966)

DIRECTOR OF PUBLICATIONS SERVICES

IRWIN HERSEY
MANAGING EDITOR,

SCIENTIFIC PUBLICATIONS

RUTH F. BRYANS
SENIOR EDITORIAL ASSISTANTS
NORMA HERRIN
CAROL RUBENSTEIN
EDITORIAL ASSISTANTS
DOLORES AMIR
VIRGINIA EDWARDS
SUSAN GRITZ
MILLICA JOVANOVIĆ
MAY LEAVENWORTH

Scope

This Journal is devoted to the advancement of astronautics and aeronautics through the dissemination of original papers disclosing new technical knowledge and exploratory developments based on new knowledge. The field of astronautics and aeronautics (also called the aerospace field) is understood here to embrace selected aspects of jet and rocket propulsion, space flight, atmospheric flight, hydronautics, combustion, fluid mechanics, astrodynamics, guidance, flight control, structures, physics of the atmosphere and space, etc. Papers will be sought also which review in an intensive manner the results of recent research or development along one of the lines defined above.

Acceptance of a submitted paper will depend on the results of rigorous technical review and on the judgment of the Editors as to the importance of the paper to the Journal's readers.

Papers devoted to vehicle design, missions, systems and components, performance testing, field installations and facilities, production methods, and engineering economic studies should be sent to the Institute's companion archive periodicals, *Journal of Aircraft* and *Journal of Spacecraft and Rockets*. Papers that interpret or review new research, engineering, program developments, and future trends in the fields of space flight, rocketry, and aeronautics which are written for a broad readership should be sent to the Institute's monthly magazine, *Astronautics & Aeronautics*.

Submission of Manuscripts

Submit manuscripts in triplicate (original plus two carbons) with three sets of illustrations and covering letter to the Managing Editor, AIAA Journal, 1290 Avenue of the Americas, New York, N. Y. 10019. See Information for Contributors on inside back cover.

Preprints of papers presented at AIAA meetings will be considered *automatically* for one of the AIAA publications. No formal submittal by the author will be necessary in the case of preprints, but the editors would naturally welcome a statement by the authors as to the publication he prefers.

Publication Charges

Author's institutions will be requested to pay a publication charge of \$40 per page, with a minimum of \$40 per Note or Comment which, if honored, entitles them to 100 free reprints. Instructions will be sent with galley proofs.

AMERICAN INSTITUTE OF AERONAUTICS AND ASTRONAUTICS

1290 Avenue of the Americas, New York, N. Y. 10019 Area Code 212 LT 1-4300

OFFICERS (Terms expire in January of year indicated)

President

COURTLAND D. PERKINS (1965)

Vice-Presidents

Publications: MARTIN SUMMERFIELD (1965)

Technical Activities: HAROLD T. LUSKIN (1965)

Section Affairs: CHARLES TILGNER JR. (1965)

Executive Secretary

JAMES J. HAFORD

Secretary

ROBERT R. DEXTER

Treasurer

R. DIXON SPEAS (1965)

Counsel

ALLAN D. EMIL

ANDREW G. HALEY

AIAA Journal is published monthly by the American Institute of Aeronautics and Astronautics, Inc. at 20th & Northampton Sts., Easton, Pa., U.S.A. Editorial offices: 1290 Avenue of the Americas, New York, N. Y. 10019. West Coast office: 7660 Beverly Blvd., Los Angeles 36, Calif. European office: 401 Avenue Louise, Brussels 5, Belgium. Price: Members, \$5.00 per year; Nonmembers, \$30.00 per year; Foreign, \$31.00 per year, \$5.00 per single copy. Second-class postage paid at Easton, Pa., with additional entry at New York, N. Y. Notice of change of address should be sent to the Secretary, AIAA, at least 30 days prior to publication. © Copyright 1964 by the American Institute of Aeronautics and Astronautics, Inc.

Aerodynamic Aspects of the Magnetospheric Flow

R. H. LEVY, H. E. PETSCHKE, AND G. L. SISCOE

Avco-Everett Research Laboratory, Everett, Mass.

I. Introduction

IT has been apparent for some time that the solar corona should be considered as extending well beyond the orbit of the earth. Diverse observations and interpretations that have contributed to our understanding of this and related phenomena include the scattering of sunlight, occultation of radio stars, behavior of comet tails, earth-sun phenomenological correlations, modulation of galactic cosmic rays, modulation of energetic particles of solar origin, and, more recently and definitively, direct satellite observations. The over-all picture one has is that the corona is heated at its base (probably by absorbing noise generated in lower turbulent levels of the sun) and expands freely into the solar system. This general outward flow is often referred to as the solar wind. Near the orbit of the earth the flow is supersonic, having a Mach number of 7-10. The solar wind consists almost entirely of fully ionized hydrogen.

The modulation of the forementioned cosmic rays is clear proof of the existence of a magnetic field in the solar wind; the strength of this field is on the order of 5γ (5×10^{-5} gauss). This is, of course, far less than the magnetic field near the surface of the earth which is about 0.5 gauss. Both these magnetic fields influence the motions of energetic cosmic rays, the former because of its greater extent; both fields also influence the motions of the less energetic but more numerous particles making up the solar wind. The latter particles, however, carry almost all the mass, momentum, and energy resident in the interplanetary gas. It is therefore more accurate to say that the over-all magnetic field configuration will be determined by the mechanics of these low-energy particles. The orbits of higher-energy particles will in turn be determined by the magnetic and electric fields resulting from this flow.

Two regions in the configuration resulting from the interaction of the solar wind with the earth's magnetic field have

R. H. Levy was educated at the Universities of Cambridge and Princeton, obtaining degrees in mathematics and aeronautical engineering. At Princeton, he was also holder of a Guggenheim Jet Propulsion Fellowship.

At Avco-Everett Research Laboratory, he has conducted research on a wide variety of topics including plasma physics, astrophysics, aerodynamics, magnetohydrodynamics, space flight (especially the protection of astronauts against radiation), and the applications of superconducting magnets. He is the author of many papers dealing with these fields.

Dr. Levy is an associate fellow of the AIAA and is a member of the American Physical Society, the American Geophysical Union, and the American Association for the Advancement of Science.

Harry E. Petschek received his Ph.D. in engineering physics from Cornell University in 1955. Following this he spent a year as an Instructor in the Physics Department at Princeton University. Since 1956 he has been a Principal Research Scientist at the Avco-Everett Research Laboratory where he has engaged in research in magnetohydrodynamics and plasma physics. He has published papers on radiation from plasmas, ionization rates, magnetohydrodynamic flows, plasma propulsion, and dissipation mechanisms in high temperature plasmas and their application to space plasmas.

In 1964 George L. Siscoe received the degree of Doctor of Philosophy in Physics from the Massachusetts Institute of Technology, where he was a Shell Fellow. He worked the summer of 1964 as an assistant scientist at the Avco-Everett Research Laboratory. He presently holds a research fellowship in the Department of Physics at the California Institute of Technology where he is continuing his studies in the field of space physics. He has made contributions to the literature in this field.

been recognized for some time. The magnetosphere boundary, which separates these regions, is defined as the boundary to which the solar-wind particles can penetrate before being stopped by the earth's field. Considerable attention has been directed to the analysis of the flow external to the magnetosphere and the determination of the shape of the boundary. On the other hand, ionospheric and auroral observations strongly suggest that a significant flow pattern also exists inside the magnetosphere. Dungey¹ has observed that the ionospheric current pattern is consistent with the one that would result if a significant fraction of the interplanetary magnetic field lines became reconnected to the magnetic field lines from the earth. The resulting component of magnetic field normal to the boundary provides a handle by which the solar wind can drag the magnetic field lines within the magnetosphere. Dungey¹ was therefore led to suggesting that a mechanism exists which gives rise to appreciable reconnection of the field lines at the magnetosphere boundary. Hines and Axford² have greatly extended the model of internal convection patterns within the magnetosphere. Although they do not specify the driving mechanism in detail, they suggest that it is provided by a shear stress at the magnetosphere boundary. More recently Petschek³ has analyzed the flow in the neighborhood of a boundary across which there is a sharp change in magnetic field direction and showed that the resulting rate of field cutting decreases only logarithmically with the magnetic Reynolds number. The logarithmic dependence implies a rapid rate of reconnection which fortunately is very insensitive to uncertainties in the effective conductivity of the plasma. As will be shown below, applying this result to the flow over the magnetosphere, we conclude that more than 10% of the magnetic field lines brought to the surface of the magnetosphere by the solar wind get broken and reconnected to the earth's polar field lines. This rapid rate of reconnection is in rough quantitative agreement with the amount required to drive the internal convection pattern. The combination of the analyses of the external, internal, and boundary region flows thus provides us with a general view of the over-all flow pattern. This description provides some insight into the extent to which phenomena occurring within the magnetosphere and in the auroral regions are related to the solar wind.

In Secs. III, IV, and V the three component regions will be reviewed, and in Sec. VI the results will be synthesized. Before proceeding with this program, we must, however, define what basic description of the plasma is appropriate. On the basis of the fact that the mean free path for particle scattering by binary collisions is large, many authors have attempted to describe the flow in terms of the individual particle trajectories. On the other hand, others have treated the fluid as a continuum and applied the magnetohydrodynamic equations. In Sec. II we will review the arguments that suggest that the continuum rather than the particle trajectory approach is more appropriate for the consideration of the basic flow.

The major objective of this paper is to describe the overall features of the flow of the solar wind over the magnetosphere. This description is undertaken with a view to synthesizing the experimental observations with theoretical considerations to provide an intelligible view of the whole. However, the multiplicity of relevant phenomena and the complicated character of many of the observations mean that any attempt at concise description must be strongly selective both in terms of the evidence brought out and theoretical interpretation. In the present paper, the authors have deliberately tried to give a coherent explanation for selected phenomena rather than an encyclopedic review of facts and theories concerning the magnetosphere.

II. Justification of Continuum Assumption

Although the conditions in the plasma composing the solar wind are known to fluctuate appreciably, the data from Mari-

ner⁴ have shown that the solar wind exists at all times. Commonly accepted typical conditions in the solar wind correspond to a magnetic field of the order of 5γ , a particle density of about 10 protons/cm³, flow velocities of the order of 500 km/sec, and thermal velocities of the ions of about $\frac{1}{10}$ the flow velocity. We may note that this corresponds to a supersonic flow since the flow velocity is about 10 times either the thermal velocity or the Alfvén speed. Other basic parameters that may be deduced from the foregoing plasma conditions are that the Debye length is of the order of 10 m, the ion gyroradius based on this magnetic field and the streaming velocity is of the order of 10^3 km, and the mean free path for Coulomb scattering based on the thermal velocity is of the order of one a.u.* and would be appreciably larger if based on the streaming velocity. The radius of the magnetosphere is about ten earth radii or roughly 10^6 km.

It is apparent that the mean free path for binary collisions is larger by several orders of magnitude than the entire magnetosphere. If we were dealing with the flow of an ionized gas, we would immediately conclude that a continuum approach was unjustified and that a free molecule approach should be used. In the case of a plasma, however, the situation is fundamentally different, since there are several mechanisms involving electric and magnetic fields which give rise to coherent phenomena in a plasma. For example, we cannot have appreciable differences between the electron and ion densities over distances larger than the Debye length, which is minute compared to the scale of the magnetosphere. A further example of coherence is the known existence in collision-free plasma of several linear wave propagation modes (plasma oscillations, whistlers, etc.). It is therefore clear that the orbits of individual particles are much more dependent on the orbits of other particles than they would be in the case of free molecule flow of an ionized gas. More specifically, it can be shown that in two special cases the isentropic continuum magnetohydrodynamic equations apply to a collision-free plasma. The first of these is the case in which the ion thermal velocities are small compared to either the flow velocity or the Alfvén speed (this is often referred to as the cold plasma case). This case will be discussed below. In the second case, finite temperatures are allowed, but we restrict ourselves to a two-dimensional flow in which the magnetic field is perpendicular to the plane of the flow. In this case it can be shown that the conservation of the magnetic moments of the individual particles gives rise to a pressure-density relation that is completely equivalent to the usual isentropic relation corresponding to a gas with two degrees of freedom.⁵ As a result, as long as flow properties change only by small amounts in a distance of the order of the gyroradius, detailed consideration of the particle orbits does in fact lead us to the isentropic continuum magnetohydrodynamic equations. Thus, in this particular case we are able to use a continuum treatment to describe even nonlinear effects. It follows almost immediately from this conclusion that a compression pulse will steepen to form a discontinuity or shock wave.⁶ Since the steepening analysis is valid for gradients small compared to the gyroradius, the steepening process will continue at least until thicknesses of the order of the ion gyroradius are reached. It also has been shown that a nonlinear pulse propagating along the magnetic field lines into a cold plasma will steepen to form a discontinuity.⁷ We are thus led to the conclusion that in at least these two special cases coherent effects in a collision-free plasma can lead to the familiar aerodynamic concept of the formation of shock waves and that these shock waves may indeed have a thickness that is small compared to the relevant flow dimensions for the magnetosphere. There have been several attempts to give theoretical descriptions of the structure of such collision-free shock waves.⁸⁻¹⁴ There is

* The a. u. (astronomical unit) is a unit of distance equal to the radius of the orbit of the earth, that is, 1.5×10^8 km.

considerable disagreement as to the mechanisms that are responsible for controlling the shock structure and even the order of magnitude of the shock thickness. However, none of these theories predicts shock thicknesses for strong shocks that are more than a few times the ion gyroradius. Thus, on the basis of any of them we would expect shock waves that are thin compared to the dimensions of the magnetosphere. A further feature to which we will return below and which all of these theories have in common is that, in the shock front itself and for some distance behind it, the flow is highly nonuniform and might be described as being turbulent.

Unfortunately, there is at present no clear-cut laboratory experimental evidence for the existence of collision-free shock waves. Some experiments that had been identified as exhibiting collision-free shocks^{13, 14} may be subject to other interpretations.^{15, 16} There are also no published results from satellite experiments which demonstrate clearly the existence of collision-free shock waves in the interplanetary medium. Very recent satellite experiments may answer this question unambiguously.† At the present time the best evidence for the existence of collision-free shock waves comes from terrestrial observations of the sudden commencement of magnetic storms. These are events in which a day or two after a solar flare almost all magnetic observatories register a sharp increase in magnetic field with a rise time of the order of 2 min. The rapid rise time of the disturbance as compared to the long travel time from the sun to earth clearly indicates coherent behavior of the plasma. However, if we calculate a velocity for the disturbance based on the time it takes to come from the sun, we find that 2 min is close to the time taken for the disturbance to pass the magnetosphere. Thus, even an infinitely thin shock wave would give rise to a terrestrial disturbance having a rise time of at least 2 min. Consequently, this observation does not allow us to set a lower limit to the thickness of the disturbance.

Thus, on theoretical grounds with some experimental backing, we would expect some phenomena characteristic of continuous flows, in particular the formation of shock waves, to exist even in a collision-free plasma. At this point, therefore, let us attempt to see what assumptions are required to arrive at the full set of continuum equations starting from the known equations that govern the individual particle motions. The individual particle motions can be described in terms of the Boltzmann equation neglecting binary collisions. We may now, with complete rigor, take the moments of the Boltzmann equation corresponding to the conservation of mass, momentum, and energy.¹⁸ The resulting equations are similar to the magnetohydrodynamic equations with the exception that the pressure and energy flux are tensors defined only in terms of moments over the distribution of particle velocities. Since, in order to define these tensors, we would have to analyze the particle orbits in detail, the procedure of taking moments is at first sight somewhat useless. If, however, we can find an assumption sufficient to define these moments over the particle distributions, then the moment equations would be of some value. This is particularly easy to do in the case of a plasma with zero temperature (i.e., zero thermal velocity). In this case, the distribution function becomes a delta function in velocities, i.e., at a particular point in space and time all of the particles have precisely the same velocity. It then is easy to take the moments of the distribution function, and the moment equations reduce to the continuum hydrodynamic equations for a zero temperature plasma. This particular case is of some interest. It can be shown, for example, that compression waves traveling

in arbitrary directions relative to the magnetic field into a zero temperature plasma, will steepen to form shock waves. We cannot, however, expect this case to apply in the flow over the magnetosphere where the presence of strong shock waves will give rise to high temperatures.

In ordinary hydrodynamics when the mean free path is small compared to the scale of the flow field, we are justified in assuming that the particle distributions are randomized by collisions and, therefore, that to zero order the particle distribution is isotropic. This assumption leads us to the isentropic continuum equations. First-order corrections in terms of the ratio of mean free path to scale length of the flow give rise to slight distortions of the distribution and result in the transport terms (viscosity and heat conduction) in the hydrodynamic equations. In the case of the flow over the magnetosphere, we will also make the assumption that the distance in which particle motions are randomized is small compared to the flow dimensions. This assumption, of course can not be justified in terms of scattering by binary collisions since the mean free path for this scattering is large compared to the magnetosphere. It may, however, be possible to justify it in terms of the observed turbulence that exists just outside the boundary of the magnetosphere. Measurements from Pioneer I indicated that the magnetic field changes by its own order of magnitude with characteristic frequencies in the neighborhood of 1 rad/sec.¹⁹ Appreciable fluctuations at higher frequencies also may be present, but these would have been beyond the frequency response of this particular experiment.

We note that this frequency is about half of the cyclotron frequency of the ions in the average magnetic field and that, as the magnetic field fluctuates, so does the cyclotron frequency. This suggests that the ion motions will be affected by the cyclotron resonance. Of course, the opposite effect in which the particle motions affect the field is also present. These remarks suggest that there is an effective randomizing time for the particles which corresponds very roughly to the angular frequency of the magnetic field turbulence and to the ion cyclotron frequency ~ 1 sec. Another way of putting this is to say that the randomizing distance or equivalent mean free path is the distance a particle travels in a cyclotron period, or what is the same thing, a Larmor radius. These distances amount to a few hundred kilometers and are indeed small compared to the dimensions of the magnetosphere flow. This should not be taken too seriously as a quantitative estimate of the effective dissipation length. It does, however, make plausible the assumption that the randomizing length is small compared to the flow dimensions, and, therefore, there is some justification in using continuum equations to describe the flow field. It should be pointed out that from this viewpoint the transport coefficients will depend critically on the effective dissipation length or mean free path and, therefore, that our knowledge of the effective value of these transport coefficients has considerable uncertainty. As we shall see later, certain features of the magnetosphere flow do depend in principle on the transport coefficients, but are nevertheless highly insensitive to their magnitudes. Thus, the results that we will describe will be appreciably more accurate than our knowledge of the transport coefficients.

Given the turbulence in the magnetic field, the calculation of detailed particle trajectories becomes effectively impossible. As a result, calculations based on the study of detailed trajectories have neglected the turbulence and have replaced the actual magnetic field by a smooth one. This assumes that the particles can negotiate the fluctuating field without appreciably modifying their orbits. Since several of the continuum features of a collision-free plasma could be derived without the assumption of turbulent scattering, it is probable that many of the features of the flow derived from these two view-points will be similar. However, it would seem that, in the cases where the results do not agree, the continuum assumption has a greater a priori probability of

† At the time this paper was written (December 1963), highly preliminary results from plasma probe measurements on IMP (Explorer XVIII), which had then been in orbit only one week, appeared to give evidence for a thin shock.¹⁷ Since then, a large amount of data obtained by this important satellite have been released.^{48, 49} These data are briefly described in the Appendix to this paper, written in August 1964.

being correct than the assumption that the turbulence in the plasma can be neglected.

We should point out that the continuum approach will not describe some of the features of the flow. In particular, the magnitude of the turbulent fluctuations will not be described, and we will consider only the average properties. Also, although we have said that the moments over the distribution function can be approximated as being almost symmetric, this should not be taken to imply that there is not a small fraction of the particles with, for example, very high energies as compared to the average particle energy. To obtain the turbulent amplitudes or the detailed particle distribution, more detailed analysis would be required. Thus, with the present analysis we limit ourselves to describing the gross properties of the flow field.

III. External Flow

The original suggestion that there should be a termination to the earth's magnetic field because of the surrounding plasma is due to Chapman and Ferraro.²⁰ They envisioned a stream of particles coming from the sun in the absence of an interplanetary magnetic field. As the particles impinge on the earth's field, they are deflected. The force required to reflect the entire stream of particles may be considered as resulting from the $j \times B$ force associated with the motion of the individual particles. Since the gyroradii of the particles are small, the region in which they turn and, therefore, the region in which the current exists is very narrow. Also, outside of this region there can be no magnetic field, otherwise the particles would be deflected there. This therefore, leads to a very abrupt termination of the earth's magnetic field.

The shape of the boundary can be determined by the condition that the force required to reflect the particles from the boundary is $2\rho u^2 \cos^2\theta$, where ρ is the density, u the stream velocity, and θ the angle between the stream direction and the normal to the boundary surface. This force must be equal to the magnetic force on the boundary which in turn is the magnetic pressure just inside the boundary $B^2/8\pi$. The problem of determining the shape of the boundary then reduces to the problem of solving for the magnetic field in the vacuum inside the cavity, with the boundary conditions that the earth's dipole field exists near the origin and that the shape of the cavity must be such as to satisfy the pressure condition as just stated. In the hypothetical two-dimensional case, this can be done precisely by conformal mapping techniques.^{21, 22} In three-dimensions, it is not as yet possible to obtain an analytical solution for the internal magnetic field, and therefore several approximations have been used to estimate the magnetic field just inside the boundary.²³⁻²⁵ The most common of these has been to assume that just inside the boundary the magnetic field has a value that is twice what the tangential component would have been for a pure dipole field.^{24, 26, 27} The general shape of the boundary, which is obtained in this manner, is that in the solar direction the boundary occurs at about 10 earth radii. Its radius of curvature in this region is slightly larger than its distance from the earth. As one goes around behind the earth, the cavity approaches a constant width. The cavity would close at a finite distance behind the earth if one allowed for some thermal motion in the freestream.

It should be noted that the details of the shape are relatively insensitive to variations in the calculation,²⁸ since the dipole magnetic field falls off as the cube of the radius and therefore the magnetic pressure as the sixth power. The distance to any point on the cavity therefore only changes with the sixth root of the changes in, for example, density of the stream. For this reason, if we look at the same problem from the continuum viewpoint, we will find very little difference in the shape of the cavity; however, the flow outside of the cavity will be appreciably altered. As long as the medium is assumed to have a high electrical conductivity, the flow will still

not be able to penetrate into the earth's field. As a result, the cavity can be represented as a blunt body in a hypersonic flow. In this case we expect a bow shock some distance ahead of the body or magnetosphere boundary.²⁹⁻³¹ The region between the shock and the body would then contain a high-temperature plasma as well as appreciable turbulence generated by the shock.

The fact that the shape of the magnetosphere boundary will not be altered significantly is seen most easily by noting that a rough approximation to the pressure distribution on a hypersonic body is the Newtonian distribution. The boundary condition at the surface is that the pressure just outside must equal the magnetic pressure inside. The Newtonian distribution is, apart from a factor of 2, identical to the pressure required to reflect the particles at the boundary. Therefore, the shape obtained from the free-particle picture is identical to the shape obtained from the Newtonian distribution if the freestream density is twice as high in the Newtonian case. Several refinements of the aerodynamics beyond the Newtonian distribution are, of course, possible, based on our presently more detailed knowledge of the hypersonic flow over blunt bodies.³² These would produce some quantitative changes in the shape, particularly away from the stagnation region. However, details some distance behind the earth are probably highly questionable. An unsteady wake could, for example, cause the downstream portion of the magnetosphere cavity to oscillate. Also, as will be discussed in Sec. VI, there is some reason to believe that field reconnection can appreciably affect the shape of the downstream portions of the cavity.

In our discussion thus far, we have neglected the effect of the interplanetary magnetic field on the aerodynamic calculation, except, of course, that we have made use of it to justify the continuum approach. This is a reasonable approximation in much of the flow. The dynamic pressure in the interplanetary plasma is so much larger than the magnetic pressure that behind a normal shock the gas pressure will be several times the magnetic pressure, and, therefore, it seems reasonable to neglect the magnetic pressure. There is, however, at least one exception to this which occurs in the neighborhood of the stagnation point. If we look at a tube of magnetic field lines which is moving toward the stagnation point, the plasma on this field tube can flow out along the field lines. The magnetic field can, however, only go around the body by moving sideways. For field lines close to the stagnation streamline, the plasma can escape more rapidly than the field lines. Thus, we may expect that the density would decrease as the stagnation point is approached. The decrease in plasma pressure would be balanced by an increase in the magnetic pressure. This conclusion may explain the observation that, in some cases, although the direction of the magnetic field changes abruptly at the magnetosphere boundary, its magnitude is almost the same on both sides.³³

In summary, the general shape of the magnetosphere boundary is a blunt body that extends considerably further behind the earth than it does toward the sun. The quantitative description is quite accurate near the stagnation point, but uncertainties grow as we move toward the region behind the earth. We would expect a bow shock at nearly the ordinary aerodynamic standoff distance ahead of the stagnation point.

Satellite experiments have confirmed the existence of a sharp magnetosphere boundary that occurs at approximately the expected location in the neighborhood of the stagnation point.³³ Behind the earth the boundary has also been observed.^{34, 35} Its position in this region seems to vary with time. It is not clear whether this is caused by variations in the strength and direction of the solar wind or by unsteadiness in the wake. In any event, observations of the magnetic field strength in this region are in conflict with the simple aerodynamic model. This point will be discussed in Sec. VI.

The region between the boundary and the shock has been shown to contain appreciable turbulence¹⁹ as was to some extent anticipated by collision free shock theories. As mentioned earlier, the shock wave itself may have been seen on very recent experiments.¹⁷

IV. Internal Motions

It was observed by Gold³⁶ that the resistance of the earth's atmosphere would permit motion within the magnetosphere. Since the earth is a good conductor, the magnetic field lines are solidly anchored at ground level. If there were direct contact with the conducting plasma in the magnetosphere, the base of the magnetosphere would have to move with the earth. However, with the insulation provided by the atmosphere, the field and, therefore, the base of the magnetosphere are free to slide over the top of the ionosphere. This situation is quite analogous to the case of a copper disk placed between the pole pieces of a magnet. If the disk rotates, it will become polarized and have a radial electric field within it. If no electrical connection is made to a stationary conductor, no current will flow, and there will be no deceleration of the angular velocity of the disk. The electric field within the copper would be such that $E + v \times B = 0$. This is just the condition that, in plasma language, is described as having the magnetic field lines within the copper moving with the copper. We thus have a situation in which the magnetic field in the copper disk (magnetosphere) moves relative to the magnetic field in the pole face (earth).

The motions within the magnetosphere are, however, severely restricted. Since the dipole field increases rapidly in magnitude as we move in from the boundary, we would expect the magnetic pressure to be large compared to the plasma pressures over most of the magnetosphere. As a result, the magnetic field must be very accurately force-free. This implies that in these regions the field will be very close to the dipole field. Motions that are allowed must, therefore, leave the field unchanged. Such motions occur if an entire magnetic field line interchanges its position with another line. Therefore, if the flow pattern is known on one plane intersecting the magnetosphere, the flow pattern of any other plane can be obtained by tracing the field lines to the second plane. We may also note that, since we have already satisfied momentum balance by the force-free condition, the determination of the flow pattern reduces principally to a kinematic problem. It also should be remembered that inside, but near the boundary as well as behind the earth where the field is weak, the foregoing restrictions do not apply since the plasma stresses can be appreciable.

Our knowledge of the flow of plasma within the magnetosphere is derived almost entirely from observations of the geophysical phenomena that this flow produces. There are two categories of geophysical phenomena which can be interpreted as resulting directly from plasma flow within the magnetosphere, namely, auroral motions and magnetic disturbances. The second of these is more completely understood because of the comparative ease of obtaining and reducing magnetic data. Also, since magnetic disturbance data may be represented by equivalent current systems flowing in the ionosphere,³⁷⁻³⁹ the conservation of current allows the entire northern ionosphere currents to be mapped using simultaneous observations at a relatively few observatories. However, in the case of the aurora, to obtain a complete picture of auroral phenomena at a given time would require enough observatories to see the entire northern sky. Therefore, magnetospheric motions have been inferred mostly from magnetic disturbance data, and these motions have been shown to be consistent with auroral observations. It is well known that the field of ionospheric measurements and auroral observations is characterized by a wealth of detail that is described in many more or less subjective ways. We

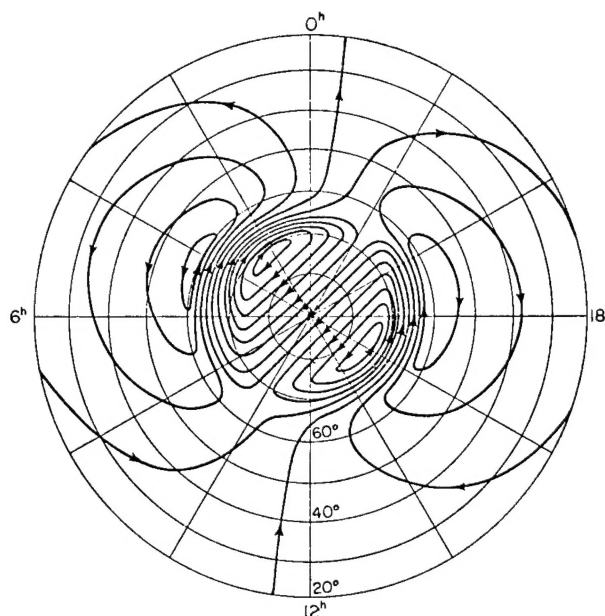


Fig. 1 Taken from Fukushima and Oguti.³⁹ Idealized ionospheric current system needed to produce the observed magnetic disturbance (*DS* component). 1.5×10^4 amp flows between adjacent streamlines.

shall, in this paper, give only the barest outline of this mass of observational data and its interpretation.

The observed disturbances of the geomagnetic field are assumed to be due to currents flowing in the ionosphere. These ionospheric current systems have been derived for a number of magnetically disturbed days, and a model idealized system⁴⁰ is shown in Fig. 1. The pattern of motion of field lines in the ionosphere is the same as the current pattern, with the direction of motion opposite to the direction of current. This relationship between the field line motions and the ionospheric currents derives from two properties of the ionosphere, namely, the dominance of the Hall conductivity and the immobility of ionospheric ions. Since $\omega\tau$ for the electrons is large, the electron motions are frozen to the magnetic field lines, $E + v_e \times B = 0$. The ions, on the other hand, are immobile because of frequent collisions with the neutrals. This implies that the ionospheric currents are primarily due to the motions of electrons. Combining these properties gives the approximate relation $J = -neV_B$, where J is the ionospheric current, n the electron density, and V_B the velocity of the magnetic field lines. One can now see the "typical" motion of magnetic field lines by again referring to Fig. 1. The field line motions in the plane of the ionosphere are along the current streamlines, but in a direction opposite to that indicated by the arrows. If the current densities and electron densities are known, then the magnitude of the field lines' velocities can also be determined.

There appear to be two separate, but related closed patterns of motion of the field lines. One is a polar pattern in which field lines move across the polar region in the antisolar direction and return in a lower latitude band. This pattern is tilted to the west of earth-sun line. The second pattern is at lower latitudes and is composed of two separate closed systems, one on the morning side and one on the evening side of the earth. Each of these two subsystems rotates in a sense opposite to the adjacent polar system.

Next, we look briefly at the extent to which these derived motions of the field lines are supported by auroral observations. The plasma in the magnetosphere is frozen to the magnetic field. Hence, field lines and plasma move together, and this motion will be reflected in the motion of associated visual or radio auroras in the ionosphere. Observations of the motion of auroras⁴¹ reveal that in the auroral zone (60°–

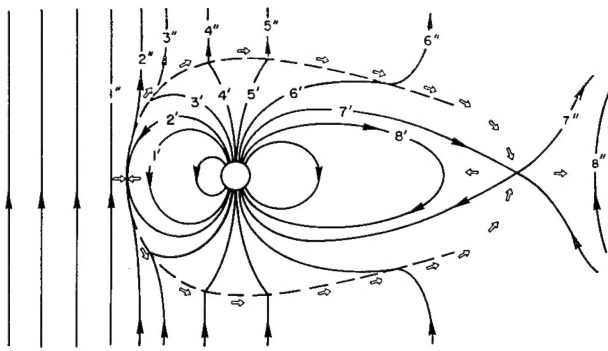


Fig. 2 Magnetic field configuration (heavy arrows) and plasma flow pattern (open arrows) allowing for some reconnection of field lines. Note that two neutral points are required since, for the whole flow field, the net rate at which interplanetary field lines become attached to dipole lines must be zero. Numbers indicate the motion of individual field lines with the motion progressing toward higher numbers. The figure is drawn in the plane determined by the earth-sun line and the earth's dipole axis. Details within the shock layer have not been shown.

70° geomagnetic latitude) auroras move to the west in the evening and to the east in the morning. At higher latitudes, the reverse situation occurs. This can be restated as: below approximately 70° geomagnetic latitude auroras move toward the sun, and above this latitude auroras move away from the sun. This is seen to agree qualitatively with the polar pattern deduced from magnetic disturbances. The crossover between eastward-moving auroras and westward-moving auroras in the auroral zone has been observed by Davis⁴² to occur at approximately local magnetic midnight. This is about 3 hr later than one would expect from the ionospheric current pattern. The difference might possibly be due to the earth's rotation, which produces an apparent westward motion of the auroras which is comparable in magnitude to the observed auroral velocities. However, this point is not clear. Motions corresponding to the subpolar pattern show up in studies by Davis⁴³ of large auroral loops opening to the west near midnight. Motions of irregularities along a loop are clockwise if viewed from the ground, although the loop as a whole is moving westward partly because of the earth's rotation. This clockwise motion of auroras indicates a counterclockwise directed current that corresponds to the subpolar system.

Several theoretical models have been constructed in which the high latitude currents and auroral motions are generated in some manner, directly or indirectly by the action of the solar wind on the geomagnetic field. In the model of Dungey,¹ the interplanetary magnetic field plays a dominant role. He considers a situation in which the interplanetary field has a generally southward orientation. It will then combine with the earth's field to produce a neutral point in the subsolar region and also one in the antisolar region. The resulting steady-state magnetic field and plasma flow configurations in the plane containing the earth's dipole and the solar-wind direction are shown in Fig. 2. The field lines are indicated by continuous lines with heavy arrow heads giving the sense. The plasma motion is indicated by the open arrows; these arrows also indicate the motion of the field lines since the field is frozen to the plasma. (This figure omits some flow and field discontinuities that are not relevant at this point.)

Since the situation is assumed to be steady, the diagram can be interpreted as being either the total field topology and flow morphology at a given time or a time sequence of the motion of an individual field line and a "particle" of plasma. This second interpretation is made explicit in the diagram by labeling the order of events with numbers increasing with time. The subsolar apex of the field line whose initial posi-

tion coincides with the line labeled 1' moves sunward until it reaches the subsolar neutral point where field line cutting occurs (which will be discussed in Sec. V). Here the internal field line connects to the external field line, which has moved to the neutral point from an initial position which coincides with the line labeled 1''. The field lines now coincide with the position of the lines labeled 2' and 2''. The lines indicated by 3 through 6 coincide with the positions reached at progressively later times by our two original field lines that now are joined and are being swept back by the solar wind. For a steady flow, the rate at which field lines become joined must equal the rate at which they become detached. Thus, eventually they must reach a position coinciding with line 7 (which intersects the antisolar neutral point) and separate. The internal field line then moves toward the earth 8', and the external field line is carried away by the solar wind 8''. In order to complete the cycle the field line must move from position 8' to position 1'. It is reasonable to suppose that this is accomplished by moving some distance towards the earth and then going around the earth.

The resulting motion of field lines in the ionosphere corresponding to the sequence 1-8 is seen to be across the poles and in an antisolar direction (assuming that the wind comes from a direction near the sun). This corresponds exactly to the solar-directed currents in the polar current system. As the field line returns from position 8 to position 1, its motion in the ionosphere must correspond to the lower latitude return band of the polar current system. The ability of this model to reproduce the general features of the polar current system is not critically dependent on the orientation of the interplanetary magnetic field. As long as some joining of field lines occurs, the field lines will be dragged in a generally antisolar direction across the poles and return at lower latitudes.

Hines and Axford² have greatly extended the description of the internal flow patterns in the magnetosphere. They observe that the correlations with observational data that they obtain are independent of the driving mechanism of the convection pattern. Although they list several possible mechanisms, including field reconnection, they tend to favor the existence of a shear stress at the magnetosphere boundary. More recently Axford⁴⁴ has observed that it would not be unreasonable for a transport of momentum across the boundary by waves to give the required shear stress. In addition to considering the convection pattern due to the drag of the magnetosphere boundary, they also consider the effects due to the rotation of the earth. Since the feet of the field lines move around with the earth, there will be some superposed rotational motion. In this manner they are able to account for some of the observed evening-morning asymmetries of high latitude geophysical phenomena such as auroral break-up, magnetic bays, and numerous ionospheric disturbances. The inclusion of the rotation also allows them to estimate the latitude at which the polar current pattern returns. They further postulate that the subpolar current system corresponds to a secondary convection zone driven by the primary convection zone, which in turn is driven by the solar wind.

This brief description does not do justice to the many details of the flow pattern and correlations with observations that Hines and Axford have succeeded in enumerating. We have, however, tried to emphasize that their model is based primarily on convection cells driven by an interaction with the solar wind. It is interesting to note that both they and Dungey felt that the evidence for such an interaction was strong enough to require them to postulate its existence even though no mechanism was known which required such an interaction. In Secs. V and VI of this paper we will observe that the rate at which field lines are reconnected at the boundary provides an interaction that is of the right order of magnitude to drive the primary convection cell. Thus, reconnection of field lines is probably the driving mechanism for the internal flow.

V. Boundary

Thus far in considering the external flow between the magnetosphere boundary and the shock wave we have been able to assume the plasma to have infinite conductivity. Within this approximation, the magnetosphere boundary would be an infinitely thin layer containing a current sheet which gives rise to the required change in magnetic field across it. If we now consider a finite, but high conductivity, this change in field will take place across a narrow but finite thickness. In this section we will briefly review an analysis³ of this boundary layer, paying particular attention to the role of the normal component of the magnetic field across the layer which gives rise to the coupling between the external and the internal flows.

Let us first notice that we expect an appreciable change in the direction of the magnetic field across this boundary. The external magnetic field will be forced against the boundary by the wind. It will, therefore, lie essentially in the plane of the boundary, but can have an arbitrary direction in this plane determined by its direction in the free-stream. The internal magnetic field will also lie essentially in the plane of the boundary, but will have its direction determined by the dipole axis of the earth. Since these two directions are unrelated, we would, in general, expect to have an appreciable change in the direction of the magnetic field as we cross the boundary. Furthermore, since the magnetic field in the interplanetary plasma is known to fluctuate considerably, we would expect to have different changes in direction at different times. The simplest case to analyze is the case in which the direction of the magnetic field changes by 180° , that is, the field direction in the interplanetary plasma and the magnetic field of the earth are antiparallel. We will consider only this case and assume that the result is not too angle-sensitive and therefore that the results will apply approximately to any case in which the angle is large.

A sketch of the flow and magnetic field configuration of the over-all flow, including some resolution of the boundary layer, is shown in Fig. 3. The field lines in the interplanetary plasma are carried toward the magnetosphere by the solar wind. As the field lines cross the shock, they will be somewhat distorted, but they will continue to move toward the magnetosphere boundary. The field lines will reach the boundary first in the neighborhood of the stagnation point. Since the magnetic field is of opposite sign on the two sides of the boundary, there must be a point within the boundary where the magnetic field is zero. At such a neutral point in the magnetic field it is possible to have magnetic field lines cross. The motion of the magnetic field lines toward the boundary corresponds to an electric field perpendicular to the plane of the paper. Since for a steady flow $\nabla \times E = 0$, this electric field cannot change across a thin boundary and is therefore the same on both sides of the boundary. However, since the magnetic fields are in opposite directions, they move in opposite directions on the two sides of the boundary. In other words, the magnetic fields on both sides of the boundary move toward the boundary. When these field lines move through the crossed configuration at the neutral point they can reconnect themselves and move out along the boundary. That is, the top half of the interplanetary field line becomes connected to a field line that goes to the North Pole of the earth while the other half of the interplanetary field line becomes connected to the portion of the earth's field line coming from the South Pole. This is most easily visualized on Fig. 3 by considering the successive field lines drawn as a time sequence in the history of an individual field line. (This particular feature is indicated more clearly in Fig. 2, although the details of the shock layer are not shown.) Now such reconnection of the field lines is only possible in a finite-conductivity medium. For an infinite-conductivity medium the condition $E + v \times B = 0$ applied at the neutral point would require zero electric field. Zero electric field in turn

would mean that the magnetic field lines approach the neutral point at zero velocity and, therefore, that no reconnection occurs. In the presence of finite conductivity this restriction does not apply since the electric field does not have to vanish when the magnetic field vanishes.

The foregoing discussion of the motion of the field lines was based, to some extent, on the two-dimensional picture. In the actual three-dimensional case, a field line does not have to continue to move toward the neutral point and be reconnected, but can move out of the plane of the paper and go around the magnetosphere. In fact, the infinite-conductivity treatment of the shock layer assumes that all of the field lines must go around the body. The number of field lines which will be reconnected rather than going around the body depends then upon the efficiency of the reconnection process.

The flow in the neighborhood of a neutral point has received considerable attention in the literature.⁴⁵⁻⁴⁷ In particular, Parker⁴⁷ has analyzed a steady-flow situation that is in some respects similar to the case of interest here. His model is based entirely on the diffusion of magnetic fields due to the finite electrical conductivity of the medium. The result obtained is quite close to the usual stagnation-point solution in ordinary aerodynamics, namely that the rate at which fluid flows into the boundary layer decreases as the square root of the appropriate Reynolds number. For the high electrical conductivity, which we expect in the interplanetary plasma, the rate at which the plasma and, therefore, magnetic field lines move into the boundary layer would, on this basis, be extremely small. This analysis, however, grossly underestimates the rate at which field lines can move toward the boundary and get reconnected.

In a magnetohydrodynamic fluid it is not immediately obvious that the boundary layer must spread only by diffusion processes. For example, we know that a shear discontinuity, which in the absence of a magnetic field would spread only because of viscosity, in the presence of a magnetic field will propagate along magnetic field lines as an Alfvén wave. Since the wave-propagation speed is independent of the conductivity of the medium, the wave will spread the information of the shear discontinuity much more rapidly into the fluid at high electrical conductivities than the diffusion process.

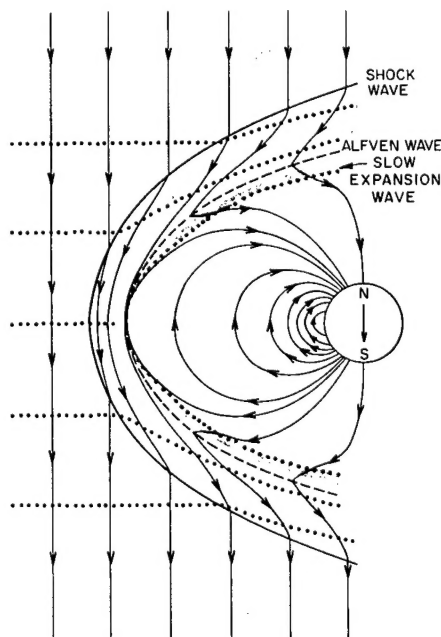


Fig. 3 Schematic drawing of magnetic field (solid lines) and plasma flow (dots) in the subsolar region. The flow is decelerated by the bow shock. The magnetosphere boundary is resolved into an Alfvén wave and a slow expansion fan.

ess. We may therefore anticipate that there may be wave processes associated with the boundary which would spread the boundary much more rapidly than diffusion.

In a dissipationless magnetohydrodynamic fluid there are three different wave modes that can propagate. Although the flow behind the bow shock must be subsonic relative to the fast propagation speed, this flow can still be supersonic relative to the intermediate (i.e., Alfvén) and slow propagation speeds. In such a case we might expect to find standing intermediate and slow waves somewhere in the flow behind the bow shock. Actually, the propagation speed of both the intermediate and the slow waves perpendicular to the magnetic field is zero. Therefore, precisely on the stagnation streamline we cannot have a standing wave at any flow velocity. However, if we go slightly away from the stagnation point along the boundary, the presence of field cutting at the stagnation point can give rise to a normal component of magnetic field (Fig. 3). Therefore, a short distance away from the stagnation point standing waves may exist. We may therefore look for a configuration in which the changes required across the boundary are accomplished by waves at some distance from the stagnation point, and diffusion is required only in the vicinity of the stagnation point. We might further expect that for very high conductivities the wave-propagation velocity can compete with the diffusion velocity for very small normal components of the magnetic field and therefore that the diffusion region can become very small. This reduction in the length of the diffusion region decreases its Reynolds number and therefore has the effect of allowing a much more rapid flow through the neutral point and hence an appreciably more rapid rate of field reconnection.

We must now ask whether it is possible to construct a set of waves which will take us from the external region, where there is a field of one sign and finite gas pressure, to the region behind the boundary, where the field is essentially of the opposite sign and where the gas pressure is zero. Such a set of waves can be found and are sketched in Fig. 3. The field reversal can be accomplished by an intermediate wave that has the property that the tangential component of magnetic field can be rotated through an arbitrary angle including 180° , although its magnitude does not change. The pressure and density of the plasma also do not change across such a wave. Behind the intermediate wave we are then left with a region in which the magnetic-field direction has already been reversed, but the gas pressure is still finite. We can now get from this condition to the zero pressure condition by means of a slow expansion fan in which the magnetic pressure increases to balance the decrease in plasma pressure. We may note that, as the fluid moves to the intermediate wave, the sharp bend in the magnetic field lines gives it a large acceleration. Thus, behind the intermediate wave the fluid is moving along the boundary at a speed roughly equal to the Alfvén speed. This rapid motion represents a significant mass flow away from the stagnation region even in a thin layer.

In terms of rather gross arguments of momentum and mass conservation, it was shown³ that such a wave region could be matched consistently to the diffusion region which is required in the neighborhood of the stagnation point. In fact, this matching can be done for a whole range of values of the velocity of the fluid approaching the stagnation point. As the velocity or the rate of field reconnection increases, the length of the diffusion region continually decreases. The existence of a range of values can be interpreted in terms of a low velocity flow over such a stagnation point. If the freestream flow velocity is within the range for which consistent solutions are allowed, then the stagnation streamline will not slow down as it approaches the stagnation point. The fluid coming in along this line can be pulled out fast enough by the acceleration across the intermediate wave. However, if the freestream velocity exceeds the maximum velocity allowed

for by the boundary, the presence of the body will begin to affect the freestream. The stagnation streamline will have a velocity that decreases toward the stagnation point. The boundary will be at the point where the flow velocity just matches the maximum allowed velocity into the boundary layer. In the flow that we are considering, the freestream velocity is very high; therefore, the rate at which flow goes into the boundary layer will be the maximum one allowed by the rate of field reconnection.

The maximum rate at which field lines can flow toward the neutral point and become reconnected is determined by the fact that, in the wave region as the flow velocity increases, the normal component of magnetic field must increase. This flux through the boundary removes field lines from the stagnation region, thus decreasing the magnetic field in that neighborhood. As this field decreases, the rate at which field lines diffuse to the neutral point decreases, and therefore the entire process is self-limiting. Estimating this limit as occurring when the magnetic field has been reduced by a factor of 2 the following relation was obtained for the maximum flow velocity through the neutral point:

$$u_{\max} = \frac{V_A}{\ln(8\pi\sigma u_{\max}^2 R V_A^{-1})} = \frac{V_A}{\ln[(2u_{\max}/V_A)(R/\delta)]}$$

where u_{\max} is the maximum flow velocity, V_A is the Alfvén speed based on the absolute magnitude of magnetic field and the density in the region slightly upstream of the stagnation point, σ is the effective electrical conductivity in electromagnetic units, R is a scale length of the flow field along the boundary which can be taken roughly as the radius of the magnetosphere, and δ is the thickness of the boundary in the diffusion region. The foregoing relation was estimated to be good to about a factor of 2 if the electrical conductivity is known.

The significant feature of this result is that the rate of field reconnection depends only logarithmically on the electrical conductivity. Thus, even if the electrical conductivity is very high, the rate of field reconnection will be appreciable. The logarithmic dependence is also extremely fortunate in that it is quite insensitive to the considerable uncertainty in the value of the effective conductivity in the turbulent medium which was indicated in Sec. II.

The foregoing equation was written also in terms of the thickness of the diffusion region since it is probably easier to estimate this thickness than it is to estimate the conductivity itself. In order to obtain a lower limit to the rate of field reconnection, we may assume that the boundary-layer thickness in the diffusion region cannot be any smaller than an electron gyroradius. If it were smaller than this and carried the required current, the electrons would have to move at a velocity higher than their thermal speeds just ahead of the boundary layer. Such a thickness would seem to be a lower limit to the possible thickness of the boundary. Taking the magnetosphere radius as 10^5 km and the electron gyroradius as 3 km, the velocity of reconnection becomes $\sim 0.1 V_A$. Probably a more reasonable value for the minimum thickness of the diffusion region would be the ion gyroradius, ~ 100 km. Although some satellite evidence suggests this order of magnitude of thickness, the interpretation is somewhat ambiguous because of possible motion of the boundary. Using 100 km for the thickness of the diffusion region, we obtain a reconnection velocity of $\sim 0.2 V_A$. We therefore conclude that the rate of field reconnection at the magnetosphere boundary is at least $0.1 V_A$ and is probably more like $0.2 V_A$.

From this rate of reconnection we may now estimate what fraction of the field lines that pass through the bow shock wave also pass through the reconnection region rather than going around the magnetosphere without being cut. For a freestream ratio of flow speed to Alfvén speed of 8, the flow velocity behind a normal shock is $1.1 V_A$. The fraction reconnected is roughly the ratio of the flow through the stag-

nation point (uB) to that through the shock. If we assume that neither the magnetic field strength nor the Alfvén speed change appreciably as we move from the shock toward the stagnation point, this would imply that the fraction reconnected is ~ 0.1 or 0.2 , depending upon the choice of δ . Actually, the variations in the density and the magnetic field strength mentioned in Sec. III are in such a direction that this is an underestimate of the fraction of the field lines which will become reconnected. The lower limit to the fraction reconnected is therefore 0.1 . There is, of course, an absolute upper limit of unity. As a result, the estimate of 0.2 , which corresponds to a more likely choice of δ , is fairly closely bracketed.

The estimate of 0.2 corresponds to a significant fraction of the incident field lines becoming reconnected to the earth's field lines. In fact (Sec. VI), it is sufficient to drive the internal convective pattern. However, most of the field lines still go around the magnetosphere. Therefore, analyses of the external flow which neglect field reconnection are not significantly disturbed at least in the stagnation region, but significant effects may occur toward the wake.

VI. Over-All Flow

The estimate made in the previous section of the rate of field reconnection leads to the possibility of quantitative evaluation of various couplings between the internal and external flows. In addition to the transfer of momentum due to the dragging of the field lines by the solar wind, the existence of a normal component of magnetic field allows the flow of some plasma and high energy particles across the boundary. In the present paper we will, however, restrict ourselves to the discussion of two features. First, we will show that the quantitative estimate of the fraction of field lines reconnected leads to the right order of magnitude of auroral velocities from which it follows that the reconnection rate is sufficient to drive the internal flow. Secondly, we will discuss the relation of field cutting to the predictions of the magnetosphere shape behind the earth and Explorer X measurements in this region.

As discussed in Sec. IV, the over-all flow patterns observed in the auroral regions are consistent with the picture of some reconnection of field lines. In order to claim that field reconnection is responsible for driving this internal flow, we must still show that it produces quantitatively the correct order of magnitude of flow. This can be done most directly by comparing the total flow rate of magnetic field lines. The flow rate of field lines within the polar convection pattern must equal the flow rate of magnetic field lines that intersect the magnetosphere boundary. The rate at which field lines are incident on the bow shock wave is the product of the interplanetary magnetic field, $\sim 5 \times 10^{-5}$ gauss, the flow velocity of the solar wind, ~ 500 km/sec, and the diameter of the magnetosphere which we will take as 20 earth radii, or about 10^5 km. From our estimate that one-fifth of these field lines become reconnected, the flux of field lines that are joined to the earth is about one-fifth of this product, or approximately 500 gauss-km²/sec (or 5×10^{12} Maxwells/sec). The flow rate in the ionosphere in the polar regions is the product of the local magnetic field strength, 0.6 gauss, the width of the region in which the flow is in one direction, which can be seen from Fig. 1 to be about 30° or 3×10^3 km, and auroral velocities that are typically between 0.1 and 0.5 km/sec.⁴¹ This gives a total flow rate of 200 to 1000 gauss-km²/sec. The estimated flow rate at the magnetosphere boundary is therefore in excellent agreement with the observed flow rates in the ionosphere. Thus, field reconnection

not only gives qualitatively the current pattern observed in the ionosphere, but also gives a quantitatively correct prediction of the total flow rate involved.

It has been suggested that the Explorer X measurements give direct evidence for the existence of a normal component of magnetic field at the boundary of the magnetosphere.^{34, 35} The orbit of this satellite had an apogee of about 40 earth radii in an antisolar direction. Data were recorded only during one outward pass. In this time the satellite apparently crossed the boundary of the magnetosphere several times most likely because of the motions of the boundary. At each transition the average magnetic field was observed to change both in direction and in magnitude corresponding to a transition between an internal and an external field. Plasma probe measurements also indicated regions in which there was and was not plasma, the boundary being consistent with the magnetic field indication. If a physical boundary is drawn at each transition consistent with the position of the satellite and a reasonable wind direction, then the measurements of the magnetic field direction indicate a substantial normal component of the field to the boundary. This argument has been criticized on the basis that the direction of the boundary may not be known with sufficient accuracy to make the measurement of the direction of the magnetic field relative to the boundary significant.³⁵

In addition to the foregoing argument, which may be open to some question, Explorer X provided other evidence that can be interpreted in terms of escaping field lines. The internal magnetic field strength near the boundary dropped appreciably more slowly than a dipole field as the satellite increased its distance from the earth. Thus, at 30 earth radii, the field strength was about 15γ . If the field lines did not escape and currents were restricted to the magnetosphere boundary, then the image dipole method could be used to estimate the strength of the internal field. This procedure would tend to give a reduction in the field strength at these distances from the earth as compared to the dipole field strength. Hence, the field strength at 30 earth radii should be less than the corresponding dipole field strength which is about 2γ . The observed field strength is therefore almost 10 times too large at this point. This increased field strength is consistent with the observation that the cavity appears to be conically expanding and therefore makes a larger angle with the wind direction than would be expected from the theoretical analyses. These data indicate that some stress must exist which drags the field lines with the wind and therefore increases the field strength in these regions. It is tempting to suggest that this stress is provided by the field lines that escape through the magnetosphere boundary. If this can be found to agree quantitatively it would indicate that the field reconnection can also give rise to significant changes in the shape of the magnetosphere.

Appendix: Early Results from the Satellite IMP

Since this report was prepared, a considerable amount of information received from the IMP satellite (Explorer XVIII) has become available. This satellite was launched into a highly eccentric orbit (apogee ~ 30 earth radii) on November 27, 1963. Since then it has monitored magnetic fields⁴⁸ and particle fluxes^{49, 50} through a large part of the magnetosphere. The results provide direct confirmation of several features of the magnetospheric flow which had been predicted, but which had not hitherto been observed. IMP has already proven to be a powerful tool for the study of the magnetosphere, and there can be no doubt that the analysis of all the information received will provide us with a greatly increased understanding of the charged particles and magnetic fields in the environs of the earth. Though all this analysis is still far from complete, the results published thus far have a considerable bearing on this report, and we are therefore pleased to adopt the suggestion of a reviewer and

† The flow rates derived from ionospheric currents are not as well determined as auroral velocities because of uncertainties in the electron density in the ionosphere. However, within these uncertainties, they agree.

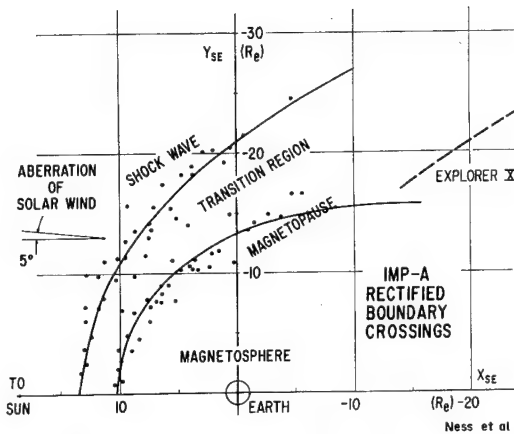


Fig. 4 This figure, reproduced from Ness, et al.,⁴⁸ shows the shape of the over-all flow in the magnetosphere as established by measurements of the magnetic field. The origin of the coordinate system used is the center of the earth. The X axis is the earth-sun line; the Y axis lies in the ecliptic plane, and the units on both axes are earth radii. The solid lines represent the positions of the shock wave and boundary as calculated theoretically by Spreiter and Jones³¹ and others. These calculations have been modified to allow for the diurnal change in the tilt of the earth's magnetic axis and the aberration effect due to the motion of the earth in orbit. The data represent the experimental points; since these were generally not in the plane of the ecliptic, each point was rectified by rotation in a meridian plane. Shown for comparison is the orbit of Explorer X,^{34, 35} similarly rectified.

include here a brief critical summary of the information presently available (August 1964).

In the first place, the existence of a clearly defined over-all flow pattern consisting of a shock wave, a transition region, and an interface (boundary) has been amply demonstrated. Both the shock and the interface are thin compared to their separation distance, thus substantiating the arguments given in Sec. II for the validity of the continuum analysis. The observed flow pattern is in excellent agreement with general predictions as to both its nature and its shape. The positions of the shock and boundary as determined by the magnetic data are shown in Fig. 4 (reproduced by kind permission of Ness, Searce, and Seek). The agreement with aerodynamic theory (that of Spreiter and Jones³¹ and others) is seen to be excellent, especially when it is recalled that the data shown was collected over a period of about 3 months during which time (in spite of a low level of solar activity) the velocity and density of the solar wind could hardly have remained perfectly constant.

The magnetic field and particle measurements demonstrate clearly the existence of a collisionless shock wave. Across this shock, the plasma flow changes abruptly from supersonic to subsonic as evidenced particularly by the directional resolution of the plasma probe.⁴⁹ Ahead of the shock the flow is highly directed, whereas behind the shock the flux is approximately isotropic. The magnetic field increases sharply across the shock and also changes direction. Figure 5 (also reproduced from Ness et al.)⁴⁸ shows the magnetic field strength and variance as measured on a single pass. The shock is clearly visible at about 22 earth radii. It is apparent that the field becomes markedly noisier behind the shock. This presumably corresponds to turbulence that was produced within the shock in order to accomplish the necessary dissipation.

At the present time the data have not been analyzed in sufficient detail to determine the actual shock thickness or to define clearly the nature of the turbulent dissipation process. Some indications exist, however, which suggest that the important scale length is the ion gyroradius as proposed in

Refs. 12-14, rather than the smaller scale lengths proposed in Refs. 8-10. In Fig. 5, although the magnitude of the field appears to rise abruptly in less than the time between adjacent plotted data points, the variance rises over a measurable distance ($\sim 10^3$ km) corresponding roughly to an ion gyroradius based on the velocity and magnetic field in the supersonic stream. In data from some other passes, the rise in magnitude of the magnetic field also occurs over a measurable distance of the same order of magnitude. Also, the observation of a variance in the field comparable to the average field based on an averaging procedure which did not include frequencies above the ion cyclotron frequency suggests that significant turbulence resides in the frequency range of the ion cyclotron frequency or below. Since these frequencies correspond to wavelengths of the order of the ion gyroradius or longer, the basic scale of the turbulence is probably in this range. Since the raw data contain an appreciably better frequency response that is represented by the averages that have been published thus far, we may anticipate that future analysis will provide a much clearer definition of the properties of collision free shock waves. One rather surprising observation is the apparent existence⁵⁰ of a thin (< 500 km) region containing electrons with energies greater than 30 keV. Although the possibility of heating electrons in a collision free shock and producing a uniform region of energetic electrons behind the shock had been previously discussed, the possibility of the existence of a narrow spike had not been anticipated.

The evidence of IMP on the question of field cutting and reconnection as discussed in this report is not yet clear. Di-

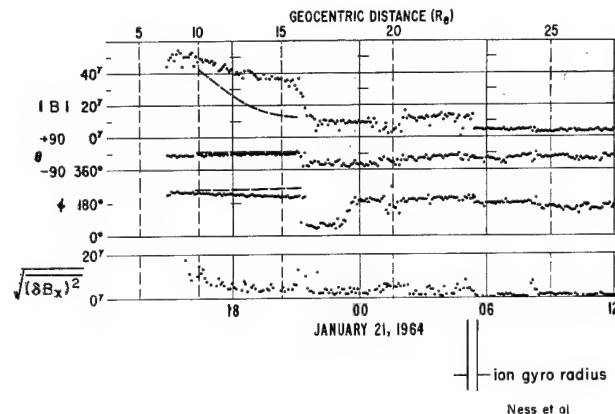


Fig. 5. These data, also from the report of Ness, et al.,⁴⁸ show the strength of the magnetic field and a measure of its noisiness as recorded by the satellite on an outbound pass. The angles θ and ϕ give the direction of the magnetic field. θ determines a latitude; $\theta = 0$ defines the ecliptic plane. ϕ determines a longitude, $\phi = 0$ is the direction towards the sun. The dashed lines represent an extrapolation of the earth's magnetic field. The compression of this field to higher values as the boundary is approached, and the rapid drop at the boundary (~ 16 earth radii) is clearly visible. Although these data could be interpreted as supporting our prediction that the field should change direction (Alfvén wave) ahead of the place where it increases in magnitude (slow expansion), the point is not very clear. Most of the other passes illustrated are even less clear, so that this question can not yet be regarded as settled. Ahead of the boundary, the field strength remains on the order of 10γ , with a noise level not much smaller, indicating considerable turbulence until (~ 22 earth radii) the satellite crosses the shock wave. After that, the instrument records the very steady interplanetary magnetic field of a few γ 's. The variance in this region is equivalent to the noise level of the instrument and the analytical procedure. The spike in the noise at ~ 24 earth radii appears on several passes and has been interpreted⁴⁸ as a precursor wave.

rect measurement of the normal component of the magnetic field at the boundary is probably difficult since the predicted value is only about 10% of the tangential component. However, if the wave pattern illustrated in Fig. 3 is indeed present, it should be the case that the field changes direction at one place (Alfvén wave) and changes strength (slow expansion) at another. The spatial separation between these two changes depends upon the distance along the boundary away from the neutral line at which the measurement is made. Since the position of the neutral line is not known, the expected separation is not clearly defined. The boundary that in Fig. 5 occurs at about 16 earth radii shows a change in both magnitude and direction; however, it does seem to show a small separation between them, but this is not entirely clear; other passes were even less clear. A small fraction of the boundary crossings observed by Cahill⁸ with Explorer XII did show such a separation, the majority, however, did not. A clearer resolution of this point must await a more careful analysis of the data.

References

- ¹ Dungey, J. W., "Interplanetary magnetic field and the auroral zones," *Phys. Rev. Letters* **6**, 47-48 (January 15, 1961).
- ² Axford, W. I. and Hines, C. O., "A unifying theory of high-latitude geophysical phenomena and geomagnetic storms," *Can. J. Phys.* **39**, 1433-1464 (1961).
- ³ Petschek, H. E., "Magnetic field annihilation," *AAS-NASA Symposium on the Physics of Solar Flares*, edited by W. N. Hess, NASA SP-50 (1964).
- ⁴ Neugebauer, M. and Snyder, C. W., "Preliminary results from Mariner-II solar plasma experiment," *Jet Propulsion Lab. Tech. Memo.* 33-111 (1962).
- ⁵ Chew, G. F., Goldberger, M. L., and Low, F. E., "The Boltzmann equation and the one-fluid hydromagnetic equations in the absence of particle collisions," *Proc. Roy. Soc. A* **236**, 112-118 (1956).
- ⁶ Petschek, H. E., "Aerodynamic dissipation," *Rev. Mod. Phys.* **30**, 966-974 (1958).
- ⁷ Montgomery, D., "Stability of large amplitude waves in the one dimensional plasma," *Phys. Fluids* **3**, 274-277 (1960).
- ⁸ Morawetz, C. S., "Magnetohydrodynamic shock structure without collisions," *Atomic Energy Commission Research Rept. (NYO-2885)*, New York Univ. (1960); also "Magnetohydrodynamic shock structure without collisions," *Phys. Fluids* **4**, 988-1006 (1961).
- ⁹ Gardner, C. S., Goertzel, H., Grad, H., Morawetz, C. S., Rose, M. H., and Rubin, H., "Hydromagnetic shock waves in high-temperature plasmas," *Second UN Intern. Conf. Peaceful Uses At. Energy* **31**, 230 (1958).
- ¹⁰ Parker, E. N., "Plasma dynamical determination of shock thickness in an ionized gas," *Astrophys. J.* **129**, 217-223 (1959).
- ¹¹ Davis, L., Lust, R., and Schluter, A., "The structure of hydromagnetic shock waves, I—Non linear hydromagnetic waves in a cold plasma," *Z. Naturforsch.* **13A**, 916-936 (1958).
- ¹² Auer, P. L., Hurwitz, H., Jr., and Kilb, R. W., "Low Mach number magnetic compression waves in a collision-free plasma," *Phys. Fluids* **4**, 1105-1121 (1961); also "Large-amplitude magnetic compression of a collision-free plasma. II. Development of a thermalized plasma," *Phys. Fluids* **5**, 298-316 (1962).
- ¹³ Fishman, F. J., Kantrowitz, A. R., and Petschek, H. E., "Magnetohydrodynamic shock wave in a collision-free plasma," *Rev. Mod. Phys.* **32**, 959-966 (1960).
- ¹⁴ Camac, M., Kantrowitz, A. R., Litvak, M. M., Patrick, R. M., and Petschek, H. E., "Shock waves in collision-free plasmas," *Nucl. Fusion Suppl.*, Part 2, 423-445 (1962).
- ¹⁵ Gerry, E. T., Kantrowitz, A. R., and Petschek, H. E., "Alternate explanation of MAST shock thickness measurements," *Bull. Am. Phys. Soc.* **8**, 158 (1963).
- ¹⁶ Gerry, E. T., Patrick, R. M., and Petschek, H. E., *Proceedings of the Sixth International Conference on Ionization Phenomena in Gases* (SERMA, Paris, 1963), pp. 389-396.
- ¹⁷ Lyon, E. F. and Bridge, H. S., private communication (November 1963).
- ¹⁸ Chapman, S. and Cowling, T. G., *The Mathematical Theory of Non-Uniform Gases* (Cambridge University Press, Cambridge, England, 1958).
- ¹⁹ Sonett, C. P., "The distant geomagnetic field. 2—Modulation of a spinning coil EMF by magnetic signals," *J. Geophys. Res.* **68**, 1229-1232 (1963).
- ²⁰ Chapman, S. and Ferraro, V. C. A., "Theory of magnetic storms," *Terrestrial Mag.* **36**, 77-97, 171-186 (1931); also **37**, 147-156, 421-429 (1932); also **38**, 79-96 (1933); also **45**, 245-268 (1940).
- ²¹ Zhigulyev, V. N. and Romishevski, E. A., "Concerning the interaction of currents flowing in a conducting medium with the earth's magnetic field," *Soviet Phys. Doklady (English transl.)* **4**, 859-862 (1960).
- ²² Hurley, J., "Interaction of a streaming plasma with the magnetic field of a two-dimensional dipole," *Phys. Fluids* **4**, 854-859 (1961).
- ²³ Ferraro, V. C. A., "An approximate method of estimating the size and shape of the stationary hollow carved out in a neutral ionized stream of corpuscles impinging on the geomagnetic field," *J. Geophys. Res.* **65**, 3951-3953 (1960).
- ²⁴ Beard, D. B., "The interaction of the terrestrial magnetic field with the solar corpuscular radiation," *J. Geophys. Res.* **65**, 3559-3568 (1960).
- ²⁵ Spreiter, J. R. and Briggs, B. R., "On the choice of conditions to apply at the boundary of the geomagnetic field in the steady-state Chapman Ferraro problem," *J. Geophys. Res.* **67**, 2983-2985 (1962).
- ²⁶ Beard, D. B., "The interaction of the terrestrial magnetic field with the solar corpuscular radiation. 2—Second-order approximation," *J. Geophys. Res.* **67**, 477-483 (1962).
- ²⁷ Davis, L. and Beard, D. B., "A correction to the approximate condition for locating the boundary between a geomagnetic field and a plasma," *J. Geophys. Res.* **67**, 4505-4507 (1962).
- ²⁸ Midgley, J. E. and Davis, L., "Calculation by a moment technique of the perturbation of the geomagnetic field by the solar wind," *J. Geophys. Res.* **68**, 5111-5123 (1963).
- ²⁹ Kellogg, P. J., "Flow of plasma around the earth," *J. Geophys. Res.* **67**, 3805-3811 (1962).
- ³⁰ Axford, W. I., "The interaction between the solar wind and the earth's magnetosphere," *J. Geophys. Res.* **67**, 3791-3796 (1962).
- ³¹ Spreiter, J. R. and Jones, W. P., "On the effect of a weak interplanetary magnetic field on the interaction between the solar wind and the geomagnetic field," *J. Geophys. Res.* **68**, 3555-3564 (1963).
- ³² Lees, L., "Interaction between the solar plasma wind and the geomagnetic cavity," *AIAA J.* **2**, 1576-1582 (1964).
- ³³ Cahill, L. J. and Amazeen, P. G., "The boundary of the geomagnetic field," *J. Geophys. Res.* **68**, 1835-1843 (1963).
- ³⁴ Bonetti, A., Bridge, H. S., Lazarus, A. J., Rossi, B., and Scherb, F., "Explorer X plasma measurements," *J. Geophys. Res.* **68**, 4017-4063 (1963).
- ³⁵ Heppner, J. P., Ness, N. F., Scarce, C. S., and Skillman, T. L., "Explorer X magnetic field measurements," *J. Geophys. Res.* **68**, 1-46 (1963).
- ³⁶ Gold, T., "Motions in the magnetosphere of the earth," *J. Geophys. Res.* **64**, 1219-1224 (1959).
- ³⁷ Chapman, S. and Bartels, J., *Geomagnetism* (Oxford University Press, Oxford, England, 1940).
- ³⁸ Vestine, E. H., Laporte, L., Lange, I., Scott, W. E., "The geomagnetic field; its description and analysis," *Carnegie Institute of Washington, Publ.* 580 (1947).
- ³⁹ Fukushima, N., "Polar magnetic storms and geomagnetic bays," *J. Fac. Sci. Univ. Tokyo, Sec. II VIII*, Part V (1953).
- ⁴⁰ Fukushima, N. and Oguti, T., "Polar magnetic storms and geomagnetic bays," *Rep. Ionosph. Res. Japan* **7**, 137-146 (1953).
- ⁴¹ Cole, K. D., "Motions of the aurora and radio-aurora and their relationships to ionospheric currents," *Planetary Space Sci.* **10**, 129-163 (1963).
- ⁴² Davis, T. N., "The morphology of the auroral displays of 1957-1958 2—Detail analyses of Alaska data and analyses of high-latitude data," *J. Geophys. Res.* **67**, 75-110 (1962).
- ⁴³ Davis, T. N., "The morphology of the polar aurora," *J. Geophys. Res.* **65**, 3497-3500 (1960).
- ⁴⁴ Axford, W. I., "Viscous interaction between the solar wind and the earth's magnetosphere," *Planetary Space Sci.* **12**, 45-53 (1964).

§ Based on a rough examination of data for a number of passes, examples of which appear in Ref. 33.

⁴⁵ Dungey, J. W., *Cosmic Electrodynamics* (Cambridge University Press, Cambridge, England, 1958).

⁴⁶ Sweet, P. A., "The neutral point theory of solar flares," *Proceedings of the International Astronomical Union Symposium No. 6 Electromagnetic Phenomena in Cosmical Physics* (Cambridge University Press, Cambridge, England, 1958); also "The production of high energy particles in solar flares," *Nuovo Cimento Suppl.* 8 X, 188-196 (1958).

⁴⁷ Parker, E. N., "The solar-flare phenomenon and the theory of reconnection and annihilation of magnetic fields," *Astrophys. J. Suppl.* 77 8, 177-211 (1963).

⁴⁸ Ness, N. F., Searce, C. S., and Seek, J. B., "Initial results of the IMP-1 magnetic field experiment," *J. Geophys. Res.* 69 3531-3571 (1964).

⁴⁹ Bridge, H., Egidi, A., Lazarus, A., and Lyon, E., "Preliminary results of plasma measurements on IMP-A," *Cospar Meeting, Florence, Italy* (May 1964); also NASA-CR-56294.

⁵⁰ Fan, C. Y., Gloeckler, G., and Simpson, J. A., "Evidence for > 30-keV electrons accelerated in the shock transition region beyond the earth's magnetospheric boundary," *Phys. Rev. Letters* 13, 149-153 (1964).

DECEMBER 1964

AIAA JOURNAL

VOL. 2, NO. 12

Small Magnetofluid-Dynamic Peristaltic Motions Inside an Annular Circular Cylindrical Induction Compressor

JOSEPH L. NEURINGER* AND JAMES H. TURNER†

Avco Corporation, Wilmington, Mass.

The small magnetofluid-dynamic peristaltic motions inside an annular circular cylindrical induction compressor are studied. The compressor consists of a circular cylindrical traveling wave tube of radius r_0 on which is impressed a purely sinusoidal current sheet of the form $nI \exp i(kz - \omega t)\hat{\theta}$, where nI is the number of ampere turns per unit length, k the wave number, and ω the circular frequency. Inside the tube, an annulus $r_0 \geq r \geq r_1$ is filled with a highly conducting fluid that is constrained at the ends not to move in the axial direction. The fluid to be pumped moves in an annulus $r_1 \geq r \geq r_2$ and is separated from the conducting fluid by an impermeable flexible diaphragm. The electromagnetically induced motions of these two inviscid and incompressible fluids, when the electromechanical coupling is weak, i.e., in the limit of small magnetic Reynolds number (based on wave speed and wavelength), are examined analytically. From the nature of the axial component of the body force induced in the constrained conducting fluid, it is shown that a time-averaged constant axial pressure gradient is induced which is transmitted to the pumped fluid by virtue of the mechanical coupling between them. If now, the induced, purely oscillatory, radial force component is sufficient to pinch and trap the pumped fluid, the ensuing motion of the latter would consist of trapped packets of fluid traveling in the wave direction with the wave speed of the diaphragm (equal to the speed of the traveling current sheet) against the pressure gradient induced in it.

I. Introduction

RECENTLY, a great deal of interest has been shown in the application of the principles of magnetofluid-dynamics to the compression and acceleration of poorly conducting liquids (e.g., sea water), with an eye toward its possible application to the propulsion of undersea craft.^{1, 2} To date, most of all of the schemes proposed involve the direct interaction of the magnetic and electric fields with the poor conductor. Since the electrical conductivity of sea water is approximately six orders of magnitude less than ordinary liquid metal conductors, such schemes are doomed to failure because the magnitudes of the induced currents are so small that tremendous field strengths are required to produce significant forces. However, this low conductivity limitation could be circumvented, for example, if a pumping scheme could be devised wherein the electromagnetic field, instead

of acting directly on the poor conductor, is made to act directly on an intermediate working fluid of large conductivity. If now, the working fluid and the fluid pumped are mechanically coupled, the large forces induced in the working fluid could conceivably be transmitted to the pumped fluid.

A possible scheme that utilizes the foregoing concept is shown schematically in Fig. 1. An annulus $r_0 \geq r \geq r_1$, inside a circular cylindrical tube of radius r_0 , is filled with a highly conducting fluid that is constrained at the ends not to move in the axial direction. The pumped fluid, moving in the annulus $r_2 \leq r \leq r_1$, is separated from the conducting fluid by a flexible impermeable diaphragm. Impressed on a transmission line, in the form of a coil wound around the cylinder, is a purely sinusoidal traveling current sheet of the form $nI \exp i(kz - \omega t)\hat{\theta}$, where nI is the amplitude of the number of ampere turns per unit length, k the wave number, ω the circular frequency, and $\omega/k = V$, the wave speed. If the relative speed between the fluid conductor and wave is different from zero, then from the circular symmetry; closed azimuthal currents will be induced in the conductor. These currents, when crossed with the radial and axial components of the traveling \mathbf{B} field associated with the traveling current sheet, produce axial and radial body forces, respectively. Since the conducting fluid is constrained at the ends not to move in the axial direction, the axial velocity of the fluid

Received December 26, 1963; corrected manuscript received August 13, 1964. This work was supported by the Power Branch, Office of Naval Research, under contract N(onr) 4047 FBM.

* Senior Consulting Scientist, Research and Advanced Development Division. Associate Fellow Member AIAA.

† Associate Scientist. Research and Advanced Development Division.

conductor averaged across its annulus per cycle is zero, so that an axial pressure gradient is induced in the conductor given by

$$\sigma V B_r^2 = \partial p / \partial z \quad (1)$$

where B_r is the radial component of the traveling \mathbf{B} field and p is the fluid pressure. This pressure gradient, which is never negative because of the quadratic dependence on the radial magnetic field component, is transmitted to the pumped fluid via the mechanical coupling between the fluids. If now the radial forces (which will be shown to be purely oscillatory) in the conductor are sufficient to pinch and trap the pumped fluid, the ensuing motion of the pumped fluid would consist of trapped packets of fluid traveling with the wave speed of the diaphragm (equal to the speed of the traveling current sheet) against the pressure gradient induced in it by virtue of the axial body forces induced in the conducting liquid. In effect, this peristaltic action could be compared to a series of compressors, each giving a finite pressure rise to the pumped fluid, each wavelength corresponding to a single compressor stage.

The twofold purpose of this paper is as follows: 1) to investigate analytically the nature of the electromechanically induced motions inside the compressor, both of the fluid conductor and the pumped fluid, when the electromechanical coupling is weak, i.e., in the limit of small magnetic Reynolds number (based on wave speed and wavelength), and 2) to examine, in this limiting case of small motions, under what conditions and to what extent the forementioned conjectured behavior of the compressor is predicted analytically.

II. Vector Potential and Induced Forces

In order to carry out the magnetofluid-mechanical calculation, we must first find the appropriate expressions for the induced forces in the fluid conductor. Let us assume that the pumped fluid has zero conductivity and free space permeability μ_0 , so that, as far as the electromagnetics is concerned, the region between $r_1 \geq r \geq 0$, where r_1 is the equilibrium position of the diaphragm, is considered a homogeneous vacuum. We denote this region as region 1. The annular region filled with conducting fluid $r_0 \geq r \geq r_1$ is denoted as region 2, and the region outside the tube $\infty \geq r \geq r_0$ as region 3. Starting with Maxwell's equations, neglecting the displacement current, introducing the vector potential, and following the derivation of Ref. 3, the following partial differential equations and boundary conditions are obtained for the corresponding azimuthal component of the vector potential³:

$$\frac{\partial^2 A_1}{\partial r^2} + \frac{1}{r} \frac{\partial A_1}{\partial r} - \frac{A_1}{r^2} + \frac{\partial^2 A_1}{\partial z^2} = 0 \quad r_1 \geq r \geq 0 \quad (2)$$

$$\frac{\partial^2 A_2}{\partial r^2} + \frac{1}{r} \frac{\partial A_2}{\partial r} - \frac{A_2}{r^2} + \frac{\partial^2 A_2}{\partial z^2} = \mu_0 \sigma_2 \frac{\partial A_2}{\partial t} \quad r_0 \geq r \geq r_1 \quad (3)$$

$$\frac{\partial^2 A_3}{\partial r^2} + \frac{1}{r} \frac{\partial A_3}{\partial r} - \frac{A_3}{r^2} + \frac{\partial^2 A_3}{\partial z^2} = 0 \quad \infty \geq r \geq r_0 \quad (4)$$

at $r = r_0$,

$$\partial A_2 / \partial z = \partial A_3 / \partial z \quad (5)$$

$$\frac{1}{r} \frac{\partial}{\partial r} (r A_2) - \frac{1}{r} \frac{\partial}{\partial r} (r A_3) = \mu_0 n I \exp i(kz - \omega t) \quad (6)$$

at $r = r_1$,

$$\partial A_1 / \partial z = \partial A_2 / \partial z \quad (7)$$

$$\frac{1}{r} \frac{\partial}{\partial r} (r A_2) - \frac{1}{r} \frac{\partial}{\partial r} (r A_1) = 0 \quad (8)$$

with the requirements that

$$A_1 \text{ be finite at } r = 0 \quad (9)$$

$$A_3 \rightarrow 0 \text{ as } r \rightarrow \infty \quad (10)$$

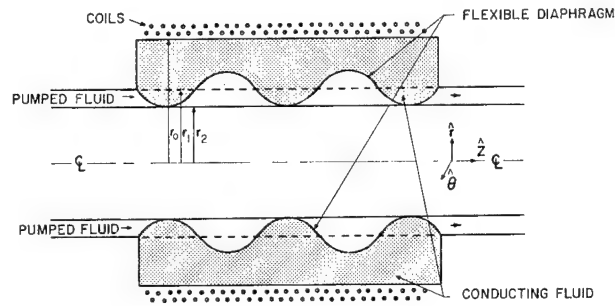


Fig. 1 Schematic diagram of peristaltic annular circular cylindrical induction compressor.

In Eq. (3), σ_2 represents the conductivity of the fluid conductor, and unlike the corresponding equation of Ref. 3, we have set the zero-order velocity of the constrained conducting fluid equal to zero.

The solution of the three region system (2-10) is given in Ref. 3. In particular, we obtain the following solution for the azimuthal component of the vector potential in region 2:

$$A_2(r, z, t) = R_e \left[\mu_0 n I \frac{M_2 K_1(kr_0) I_1(\alpha r) + M_4 K_1(kr_0) K_1(\alpha r)}{M_2 M_3 + M_4 M_5} \times \exp[i(kz - \omega t)] \right] \quad (11)$$

where

$$\begin{aligned} M_2 &= K_1(\alpha r_1) I_0(kr_1) - \alpha I_1(kr_1) K_0(\alpha r_1) \\ M_3 &= \alpha I_0(\alpha r_0) K_1(kr_0) - k I_1(\alpha r_0) K_0(kr_0) \\ M_4 &= \alpha I_1(kr_1) I_0(\alpha r_1) - I_1(\alpha r_1) I_0(kr_1) \\ M_5 &= \alpha K_0(\alpha r_0) K_1(kr_0) - k K_1(\alpha r_0) K_0(kr_0) \end{aligned} \quad (12)$$

In (11) and (12), I_0 and I_1 represent the modified Bessel functions of the first kind of order zero and one, respectively, whereas K_0 and K_1 represent the corresponding Bessel functions of the second kind. The symbol α is defined by

$$\alpha^2 = k^2(1 - i\beta) \quad (13)$$

where $\beta = \mu_0 \sigma_2 \omega / k^2$ and represents the fluid magnetic Reynolds number based on wave speed and wavelength. Expanding (11) about small β , and using the identity

$$I_0(kr_0) K_1(kr_0) - I_1(kr_0) K_0(kr_0) = -(1/kr_0)$$

we obtain, to the zeroth order in β ,

$$A_2(r, z, t) = -\mu_0 n I r_0 K_1(kr_0) I_1(kr) \cos(kz - \omega t) \quad (14)$$

From the definitions of the azimuthal component of the current density and radial and axial components of the magnetic field in terms of the vector potential,³ we have

$$\left. \begin{aligned} j_\theta &= -\sigma_2 (\partial A_2 / \partial t) = \\ &\quad \sigma_2 \omega \mu_0 n I r_0 K_1(kr_0) I_1(kr) \sin(kz - \omega t) \\ B_r &= -(\partial A_2 / \partial z) = \\ &\quad -k \mu_0 n I r_0 K_1(kr_0) I_1(kr) \sin(kz - \omega t) \\ B_z &= (1/r) (\partial / \partial r) (r A_2) = \\ &\quad -k \mu_0 n I r_0 K_1(kr_0) I_0(kr) \cos(kz - \omega t) \end{aligned} \right\} \quad (15)$$

Thus, the radial and axial components of the induced body force acting on the fluid conductor, to order β , are given by

$$F_r = (\mathbf{j} \times \mathbf{B})_r = j_\theta B_z = \frac{1}{2} \beta \mu_0 n^2 I^2 k^3 r_0^2 K_1^2(kr_0) I_1(kr) I_0(kr) \sin 2(kz - \omega t) \quad (16)$$

$$F_z = (\mathbf{j} \times \mathbf{B})_z = -j_\theta B_r = \frac{1}{2} \beta \mu_0 n^2 I^2 k^3 r_0^2 K_1^2(kr_0) I_1^2(kr) [1 - \cos 2(kz - \omega t)] \quad (17)$$

It is to be noted from (16) and (17) that the radial force component is purely sinusoidal, propagating at twice the frequency of the traveling current sheet, whereas the axial component (which is never negative) consists of the sum of a nonpropagating part plus a propagating component, at twice the input frequency, which is 90° out of phase with the radial vibration.

III. Fluid Flow Equations and Boundary Conditions

We treat the fluid flow problem under the following five assumptions: 1) the motion is axisymmetric, 2) both fluids are inviscid, 3) no azimuthal component of velocity (this is reasonable since the assumption that \mathbf{j} is purely azimuthal implies that no azimuthal forces are induced in the conducting fluid; thus if the conducting fluid has zero azimuthal velocity initially, it will have zero azimuthal velocity for all time thereafter), 4) both fluids are incompressible and, in order to avoid gravitational effects, are assumed to be of the same density ρ , and 5) the electromagnetic force in the poorly conducting pumped fluid is taken to be zero. Let the subscripts c and w refer to the fluid mechanical variables of the fluid conductor and the pumped fluid, respectively.

Letting $\mathbf{q}_c = \beta(v_c \hat{\mathbf{r}} + u_c \hat{\mathbf{z}})$ and $P_c = P_{0c} + \beta p_c$, where βv_c and βu_c are the perturbed radial and axial velocity components, respectively, P_{0c} the undisturbed pressure, and βp_c the perturbation pressure, the continuity and momentum equations, to order β , in the fluid conductor $r_0 \leq r \leq r_1$, are

$$\frac{\partial}{\partial r}(rv_c) + \frac{\partial}{\partial z}(ru_c) = 0 \quad (18)$$

$$\rho \frac{\partial v_c}{\partial t} = -\frac{\partial p_c}{\partial r} + \frac{1}{\beta} F_r \quad (19)$$

$$\rho \frac{\partial u_c}{\partial t} = -\frac{\partial p_c}{\partial z} + \frac{1}{\beta} F_z \quad (20)$$

where F_r and F_z are given by (16) and (17), respectively. Again, letting $\mathbf{q}_w = U_0 \hat{\mathbf{z}} + \beta(v_w \hat{\mathbf{r}} + u_w \hat{\mathbf{z}})$ and $P_w = P_{0w} + \beta p_w$, where U_0 is the unperturbed uniform axial velocity of the pumped fluid through its annulus $r_2 \leq r \leq r_1$, the continuity and momentum equations, to order β , in the pumped fluid are

$$\frac{\partial}{\partial r}(rv_w) + \frac{\partial}{\partial z}(ru_w) = 0 \quad (21)$$

$$\rho \left(\frac{\partial v_w}{\partial t} + U_0 \frac{\partial v_w}{\partial z} \right) = -\frac{\partial p_w}{\partial r} \quad (22)$$

$$\rho \left(\frac{\partial u_w}{\partial t} + U_0 \frac{\partial u_w}{\partial z} \right) = -\frac{\partial p_w}{\partial z} \quad (23)$$

The boundary conditions that the system (18–23) must satisfy are as follows. At the rigid walls $r = r_0$ and $r = r_2$, we require

$$v_c(r_0, z, t) = 0 \quad (24)$$

$$v_w(r_2, z, t) = 0 \quad (25)$$

The following considerations lead to the boundary conditions that must be satisfied at the equilibrium position of the diaphragm $r = r_1$. The diaphragm, representing a material surface, requires that the component of fluid velocity normal to the instantaneous position of the diaphragm surface in each of the fluid regions be equal to the velocity of the diaphragm in its normal direction. Since a small perturbation solution is being generated, we assume that the amplitude of the diaphragm is very small compared to its wavelength and that its instantaneous slope is of order β . In

this case, the fluid velocities normal to the diaphragm surface is given by v_c and v_w . Thus, we have the boundary condition

$$v_c(r_1, z, t) = v_w(r_1, z, t) \quad (26)$$

The second boundary condition requires that the total pressure (magnetic plus fluid mechanical) be continuous across the unstressed diaphragm. Since the magnetic field components are continuous across the diaphragm (no current sheet), the magnetic pressures are automatically equal. Hence, we require

$$P_{0c} = P_{0w} \quad p_c(r_1, z, t) = p_w(r_1, z, t) \quad (27)$$

One final boundary condition must be considered, i.e., that imposed by the ends of the device. We assume that at the ends of the device the conducting fluid is bounded by walls such that $u_c = 0$ at the ends. Away from the ends there is therefore allowed no time-average mass flow of conducting fluid across any position z . Mathematically,

$$\int_{r_1}^{r_0} \langle \rho u_c \rangle_t 2\pi r dr = 0 \quad (28)$$

We now seek a solution of the system (18–23) subject to the boundary conditions (24–28).

IV. Solution

A. Fluid Conductor Region

Consider the fluid conductor region first. Multiplying (19) and (20) by r , differentiating (19) with respect to r and (20) with respect to z , adding, and dividing by r , we obtain, using continuity (18),

$$0 = -\frac{1}{r} \frac{\partial}{\partial r} \left(r \frac{\partial p_c}{\partial r} \right) - \frac{\partial^2 p_c}{\partial z^2} + \frac{1}{\beta} \left\{ \frac{1}{r} \frac{\partial}{\partial r} (r F_r) + \frac{\partial F_z}{\partial z} \right\}$$

Using the definitions of F_r and F_z given by (16) and (17) and carrying out the differentiations indicated by the right-hand side, we obtain

$$\frac{1}{r} \frac{\partial}{\partial r} \left(r \frac{\partial p_c}{\partial r} \right) + \frac{\partial^2 p_c}{\partial z^2} = \frac{1}{2} \mu_0 n^2 I^2 k^2 r_0^2 K_1^2(kr_0) \times [I_1^2(kr) - I_0^2(kr)] \sin 2(kz - \omega t) \quad (29)$$

It is readily verified by direct substitution that

$$\bar{P}_c = \frac{1}{4} \mu_0 n^2 I^2 k^2 r_0^2 K_1^2(kr_0) I_0^2(kr) \sin 2(kz - \omega t)$$

is the particular integral of Eq. (29). We take as our general solution

$$p_c = \frac{1}{4} \mu_0 n^2 I^2 k^2 r_0^2 K_1^2(kr_0) I_0^2(kr) \sin 2(kz - \omega t) + [C_1 I_0(2kr) + C_2 K_0(2kr)] \sin 2(kz - \omega t) + (C_3 + C_4 \ln r) z + f_1(t) \quad (30)$$

where it is again easily verified that each of the terms in the second row satisfies the homogeneous equation and where the unknown function $f_1(t)$ and constants C_1 , C_2 , C_3 , and C_4 remain to be determined.

Substituting (16) and (30) into (19) yields

$$\rho (\partial v_c / \partial t) = -\mu_0 n^2 I^2 k^2 r_0^2 K_1^2(kr_0) I_1(kr) I_0(kr) \sin 2(kz - \omega t) - 2k [C_1 I_1(2kr) + C_2 K_1(2kr)] \sin 2(kz - \omega t) - C_4 z / r$$

Integrating yields

$$\rho v_c = -(1/2\omega) \mu_0 n^2 I^2 k^2 r_0^2 K_1^2(kr_0) I_1(kr) I_0(kr) \cos 2(kz - \omega t) - k/\omega [C_1 I_1(2kr) + C_2 K_1(2kr)] \cos 2(kz - \omega t) - C_4 z t / r$$

The boundary condition (24) requires $v_c(r_0, z, t) = 0$ for all z and t , hence $C_4 = 0$ and

$$C_1 I_1(2kr_0) + C_2 K_1(2kr_0) = -\frac{1}{2} \mu_0 n^2 I^2 k^2 r_0^2 K_1^2(kr_0) I_1(kr_0) I_0(kr_0) \quad (31)$$

Substituting (17) and (30) into (20) yields

$$\rho(\partial u_c / \partial t) = \frac{1}{2} \mu_0 n^2 I^2 k^3 r_0^2 K_1^2(kr_0) I_1^2(kr) - \frac{1}{2} \mu_0 n^2 I^2 k^3 r_0^2 K_1^2(kr_0) [I_1^2(kr) + I_0^2(kr)] \cos 2(kz - \omega t) - [C_1 I_0(2kr) + C_2 K_0(2kr)] 2k \cos 2(kz - \omega t) - C_3$$

Integrating yields

$$\rho u_c = \frac{1}{2} \mu_0 n^2 I^2 k^3 r_0^2 K_1^2(kr_0) I_1^2(kr) t + (1/4\omega) \mu_0 n^2 I^2 k^3 r_0^2 \times K_1^2(kr_0) [I_1^2(kr) + I_0^2(kr)] \sin 2(kz - \omega t) + k/\omega [C_1 I_0(2kr) + C_2 K_0(2kr)] \sin 2(kz - \omega t) - C_3 t \quad (32)$$

We have then, at this point, u_c given by (32), v_c and p_c given by

$$\rho v_c = -(1/2\omega) \mu_0 n^2 I^2 k^3 r_0^2 K_1^2(kr_0) I_1(kr) I_0(kr) \cos 2(kz - \omega t) - k/\omega [C_1 I_1(2kr) + C_2 K_1(2kr)] \cos 2(kz - \omega t) \quad (33)$$

$$p_c = \frac{1}{4} \mu_0 n^2 I^2 k^3 r_0^2 K_1^2(kr_0) I_0^2(kr) \sin 2(kz - \omega t) + [C_1 I_0(2kr) + C_2 K_0(2kr)] \sin 2(kz - \omega t) + C_3 z + f_1(t) \quad (34)$$

and the relation (31) coming from the boundary condition (24).

B. Pumped Fluid Region

Multiplying (22) and (23) by r , differentiating (22) with respect to r and (23) with respect to z , adding, and dividing by r , gives, using continuity (21),

$$\frac{1}{r} \frac{\partial}{\partial r} \left(r \frac{\partial p_w}{\partial r} \right) + \frac{\partial^2 p_w}{\partial z^2} = 0 \quad (35)$$

We take as general solution of (35)

$$p_w = [C_5 I_0(2kr) + C_6 K_0(2kr)] \sin 2(kz - \omega t) + (C_7 + C_8 \ln r) z + f_2(t) \quad (36)$$

Substituting (36) into (22) gives

$$\rho \left(\frac{\partial v_w}{\partial t} + U_0 \frac{\partial v_w}{\partial z} \right) = -2k [C_5 I_1(2kr) + C_6 K_1(2kr)] \sin 2(kz - \omega t) - C_8 \frac{z}{r}$$

Integrating yields

$$\rho v_w = \frac{-k}{(\omega - U_0 k)} [C_5 I_1(2kr) + C_6 K_1(2kr)] \times \cos 2(kz - \omega t) - \frac{C_8}{r} \frac{z^2}{2U_0}$$

The boundary condition (25), requiring $v_w(r_2, z, t) = 0$ for all z and t , gives $C_8 = 0$ and

$$C_5 I_1(2kr_2) + C_6 K_1(2kr_2) = 0 \quad (37)$$

Substituting (36) into (23) gives

$$\rho \left(\frac{\partial u_w}{\partial t} + U_0 \frac{\partial u_w}{\partial z} \right) = -2k [C_5 I_0(2kr) + C_6 K_0(2kr)] \sin 2(kz - \omega t) - C_7$$

Integrating yields

$$\rho u_w = \frac{k}{(\omega - U_0 k)} [C_5 I_0(2kr) + C_6 K_0(2kr)] \times \sin 2(kz - \omega t) - C_7 t \quad (38)$$

We have then, at this point, u_w given by (38), v_w and p_w given by

$$\rho v_w = \frac{-k}{(\omega - U_0 k)} [C_5 I_1(2kr) + C_6 K_1(2kr)] \times \cos 2(kz - \omega t) \quad (39)$$

$$p_w = [C_5 I_0(2kr) + C_6 K_0(2kr)] \sin 2(kz - \omega t) + C_7 z + f_2(t) \quad (40)$$

and the relation (37) coming from the boundary condition (25).

C. Solution (continued)

The boundary condition (26), using (33) and (39), gives

$$C_1 I_1(2kr_1) + C_2 K_1(2kr_1) - C_5 \frac{\omega}{(\omega - U_0 k)} I_1(2kr_1) - C_6 \frac{\omega}{(\omega - U_0 k)} K_1(2kr_1) = -\frac{1}{2} \mu_0 n^2 I^2 k^3 r_0^2 K_1^2(kr_0) I_1(kr_1) I_0(kr_1) \quad (41)$$

The boundary condition (27), using (34) and (40), gives

$$C_3 = C_7 \quad f_1(t) = f_2(t) \quad (42)$$

$$C_1 I_0(2kr_1) + C_2 K_0(2kr_1) - C_5 I_0(2kr_1) - C_6 K_0(2kr_1) = -\frac{1}{4} \mu_0 n^2 I^2 k^3 r_0^2 K_1^2(kr_0) I_0^2(kr_1) \quad (43)$$

Equations (31, 37, 41, and 43) form a system of four inhomogeneous linear algebraic equations for the four unknown constants C_1 , C_2 , C_5 , and C_6 . Inspection of the inhomogeneous terms shows that each of these constants is proportional to $\frac{1}{2} \mu_0 n^2 I^2 k^3 r_0^2 K_1^2(kr_0)$. Thus, let

$$C_1 = \frac{1}{2} \mu_0 n^2 I^2 k^3 r_0^2 K_1^2(kr_0) C_{IC}$$

$$C_2 = \frac{1}{2} \mu_0 n^2 I^2 k^3 r_0^2 K_1^2(kr_0) C_{KC}$$

$$C_5 = \frac{1}{2} \mu_0 n^2 I^2 k^3 r_0^2 K_1^2(kr_0) C_{IW}$$

$$C_6 = \frac{1}{2} \mu_0 n^2 I^2 k^3 r_0^2 K_1^2(kr_0) C_{KW}$$

Hence, from (32-34 and 38-40) we obtain

$$\rho u_c = \frac{1}{2} \mu_0 n^2 I^2 k^3 r_0^2 K_1^2(kr_0) I_1^2(kr) t - C_3 t + (1/2\omega) \mu_0 n^2 I^2 k^3 r_0^2 K_1^2(kr_0) \left\{ \frac{1}{2} [I_1^2(kr) + I_0^2(kr)] + C_{IC} I_0(2kr) + C_{KC} K_0(2kr) \right\} \sin 2(kz - \omega t) \quad (44)$$

$$\rho v_c = -(1/2\omega) \mu_0 n^2 I^2 k^3 r_0^2 K_1^2(kr_0) \{ I_1(kr) I_0(kr) + C_{IC} I_1(2kr) + C_{KC} K_1(2kr) \} \cos 2(kz - \omega t) \quad (45)$$

$$p_c = \frac{1}{2} \mu_0 n^2 I^2 k^3 r_0^2 K_1^2(kr_0) \left\{ \frac{1}{2} I_0^2(kr) + C_{IC} I_0(2kr) + C_{KC} K_0(2kr) \right\} \sin 2(kz - \omega t) + C_3 z + f_1(t) \quad (46)$$

$$\rho u_w = \frac{1}{2(\omega - U_0 k)} \mu_0 n^2 I^2 k^3 r_0^2 K_1^2(kr_0) \times \{ C_{IW} I_0(2kr) + C_{KW} K_0(2kr) \} \sin 2(kz - \omega t) - C_3 t \quad (47)$$

$$\rho v_w = -\frac{1}{2(\omega - U_0 k)} \mu_0 n^2 I^2 k^3 r_0^2 K_1^2(kr_0) \times \{ C_{IW} I_1(2kr) + C_{KW} K_1(2kr) \} \cos 2(kz - \omega t) \quad (48)$$

$$p_w = \frac{1}{2} \mu_0 n^2 I^2 k^3 r_0^2 K_1^2(kr_0) \{ C_{IW} I_0(2kr) + C_{KW} K_0(2kr) \} \sin 2(kz - \omega t) + C_3 z + f_1(t) \quad (49)$$

where we have still to evaluate C_3 and $f_1(t)$.

The constant C_3 is determined from the boundary condition (28). Substituting (44) into (28), and remembering that the average of the periodic term over a cycle is zero, we obtain

$$t \int_{r_1}^{r_0} \left\{ \frac{1}{2} \mu_0 n^2 I^2 k^3 r_0^2 K_1^2(kr_0) I_1^2(kr) - C_3 \right\} 2\pi r dr = 0$$

Thus,

$$C_3 \frac{1}{2} (r_0^2 - r_1^2) = \frac{1}{2} \mu_0 n^2 I^2 k^3 r_0^2 K_1^2(kr_0) \int_{r_1}^{r_0} r I_1^2(kr) dr = \frac{1}{2} \mu_0 n^2 I^2 k^3 r_0^2 K_1^2(kr_0) \left\{ \frac{1}{2} r^2 [I_1^2(kr) - I_0(kr) I_2(kr)] \right\}_{r_1}^{r_0}$$

or

$$C_3 = \frac{\mu_0 n^2 I^2 k^3 r_0^2 K_1^2(kr_0)}{2(r_0^2 - r_1^2)} \{ r_0^2 [I_1^2(kr_0) - I_0(kr_0) I_2(kr_0)] - r_1^2 [I_1^2(kr_1) - I_0(kr_1) I_2(kr_1)] \} \quad (50)$$

The unknown function $f_1(t)$ is afforded the same interpretation as is given to the integration function in the usual derivation of the nonsteady Bernoulli equation, that is, $f_1(t)$ is determined from the time dependence of the perturbed input pressure of the incoming fluid being pumped.

Finally, the motion of the diaphragm is obtained as follows. Let βr_d be the radial displacement of the diaphragm to order β , then

$$\partial r_d / \partial t = v_c(r_1, z, t)$$

Integrating (45) with respect to t , we obtain

$$r_d(z, t) = (1/4\omega^2\rho)\mu_0 n^2 I^2 k^3 r_0^2 K_1^2(kr_0) \cdot \{I_1(kr_1)I_0(kr_1) + C_{IC}I_1(2kr_1) + C_{KC}K_1(2kr_1)\} \sin 2(kz - \omega t) \quad (51)$$

V. Discussion

The resulting fluid mechanical motions inside the annular traveling wave peristaltic compressor, in the weak coupling limit, are given by Eqs. (44–49) with the motion of the tensionless diaphragm separating the two fluids given by Eq. (51). Apart from the particular radial dependence generated by the solution, the following behavior for the different fluid mechanical variables in each of the fluid regions is observed:

1) The axial velocity component in each region consists of the sum of a linear time-dependent term superimposed on a purely sinusoidal traveling component of the same wave speed but of twice the frequency of the input current sheet. The generation of the linear time-dependent term is due naturally to the existence of the nonperiodic part in the expression for the axial body force. The solution generated, then, is both a small time and small coupling solution and is invalid for large times. In any actual case, however, the magnitude of the axial velocity component cannot increase indefinitely with time, being limited eventually both by viscous effects and the fact that when the velocity reaches the wave speed coupling ceases, the electromagnetic force goes to zero, and the fluid coasts thereafter.

2) The radial velocity component in each region consists of a purely sinusoidal traveling component only, which is 90° out of phase with the corresponding periodic component of the axial velocity. It should be noted that the singularity $U_0 = \omega/k$ in Eqs. (47) and (48) is only apparent. Examination of the linear set of equations from which the constants C_{IW} and C_{KW} are derived shows that each constant is proportional to $(\omega - U_0 k)$.

3) As conjectured in the Introduction, the diaphragm motion is indeed characterized by the axial propagation of a

purely sinusoidal wave down the diaphragm whose speed is equal to that of the traveling current sheet but at twice the frequency, and whose amplitude (and therefore pinching and trapping ability) is proportional to $\mu_0(nI)^2$, i.e., the magnetic pressure associated with the current sheet.

4) The pressure in each region consists, apart from the integration functions $f_1(t) = f_2(t)$, of a purely sinusoidal traveling part plus a term linear in z . The existence, in the pumped fluid, of this latter term is the crux of the entire analysis and makes its appearance only when the axial motion in the conducting fluid is constrained. If the motion in the conductor were not constrained, this term would never appear and the device would behave like an accelerator rather than a pump. As an accelerator, the axial body force would simply go into developing a purely sinusoidal pressure gradient plus increasing the axial velocity of the working fluid. However, as conjectured in the Introduction, as a pump, the work that ordinarily would be done by the axial body force in accelerating the conducting fluid now goes into the work done in pumping the incoming fluid against the pressure gradient induced in it by virtue of the mechanical coupling between the two fluids. Further, one would imagine that the constant pressure gradient induced in the pumped fluid would be proportional to the time-averaged axial body force evaluated at r_1 , i.e., at the equilibrium position of the diaphragm. Examination of C_3 , however, shows that the pressure gradient is equal to the time-averaged axial body force averaged over the conductor annulus. Since the magnitude of the body force decreases inward from the coils, the analysis predicts a pumping force larger than suspected.

In conclusion, although one cannot, in general, predict the behavior of a nonlinear system from the periodic behavior of the corresponding linear one, still, it may well be that the compressor behavior, when the electromechanical coupling is strong, corresponds to some limit cycle situation whose gross features (apart from the linear time-dependent terms) are similar to these just obtained. In any case, the proof of the pudding lies in experimental verification.

References

- ¹ Way, S., "MHD submarine propulsion," Westinghouse Research Memo. 62-111-600-M1 (August 1962).
- ² Friauf, J. B., "MHD propulsion for submarines," Bureau of Ships Code 660 (February 28, 1963).
- ³ Neuringer, J. L., "Induced forces in annular magneto-fluid dynamic traveling wave devices," AIAA J. 2, 267-274 (1964).

Energy Transfer Processes in a Partially Ionized, Two-Temperature Gas

DONALD M. DIX*

Aerospace Corporation, El Segundo, Calif.

The elementary situation of convective energy transfer between parallel plates at different temperatures is analyzed for partially ionized, nonreacting, monatomic hydrogen wherein the electrons may be at a temperature different from that of the heavier species. The gas conditions considered are such that an ion sheath, less than a mean free path in spatial extent, forms on the fully catalytic colder surface. The numerical results obtained indicate that 1) the gross features of the continuum solution are rather insensitive to the models of sheath and transition regions employed; 2) the energy transfer between ions and electrons due to the electric field external to the sheath is appreciable, particularly in its effect of reducing electron temperature; 3) thermal nonequilibrium effects on total heat transfer are not as great as might be anticipated because of the energy transfer between species by electric fields and the contribution of diffusional processes; and 4) magnetic field effects on total heat transfer are less than the effect on electronic thermal conductivity would indicate and are further lessened by thermal nonequilibrium effects.

Nomenclature

A_w	= velocity ratio defining edge of transition region $v_{A, t}/v_{A, s}$
B	= magnetic induction
C_j	= mean thermal speed of species j
c_p	= specific heat at constant pressure
D_{jk}	= binary diffusion coefficient of mixture of species j and k
D_A	= ambipolar diffusion coefficient ($D_A = 2D_{in}$)
E	= electric intensity
e	= magnitude of electronic charge
f	= neutral fraction = $n_n/(n_i + n_n)$
F_w	= diffusion flux of ions
j	= current density
k	= Boltzmann's constant
k_j	= thermal conductivity of species j in the total mixture
L	= distance between plates
Le	= Lewis number, $\rho_r c_p D_\infty / k_\infty$
m	= particle mass
n	= particle number density
p	= total pressure of mixture
p_j	= partial pressure of species j
Q_0	= factor for variation of ion-neutral diffusion coefficient, defined by Eq. (28)
Q	= collision cross section
Sc	= Schmidt number, $\mu_\infty / \rho_r D_\infty$
T	= temperature
u, v, w	= mass velocity of mixture
u_A, v_A, w_A	= mass velocity of ions relative to the mixture
x, y, z	= Cartesian components
α	= current fraction, defined by Eq. (2)
β	= Hall parameter = $(\omega\tau)$
γ	= $e \phi_{sw} /kT_{e, s}$
γ_i	= $e \phi_{iw} /kT_{e, i}$
δ	= $[e\rho(1-f)/m_i]^2/\sigma$
δ_{en}	= energy exchange effectiveness, defined by Eq. (29)
ϵ_n	= negative ionization energy
λ_{jk}	= coefficient of collisional energy transfer from species k to species j
ρ	= mass density of mixture
σ	= electrical conductivity
ϕ_{jk}	= electrical potential between points j and k

Subscripts

c	= conduction
d	= diffusion
e	= electrons
g, h	= heavy particles
i	= ions
n	= neutral particles
r	= quantity used for normalization
s	= sheath edge
t	= edge of transition region
w	= cold surface
x, y, z	= Cartesian components
∞	= hot surface

I. Introduction

THE occurrence of an appreciable degree of ionization in a gas introduces some features quite different from those encountered in chemical dissociation primarily because of the presence of electrons. First, the extremely low mass of the electrons yields a species possessing a thermal conductivity that can be much greater than that of the other species present; second, the collisional energy-transfer processes between electrons and heavy particles are relatively slow, giving rise to the possible situation wherein the electrons may have a temperature much different from that of the heavy species, even though the energy-transfer processes are adequately described by continuum equations; third, the charged species are sensitive to electromagnetic fields, yielding a possible method of controlling the associated components of energy transfer and further yielding an additional mechanism for energy transfer between electrons and ions; fourth, when such a gas is in contact with a cold surface, a space charge sheath is formed which may appreciably affect the energy transfer to the surface. The physical situations in which these unique features of appreciably ionized gases are likely to manifest themselves are becoming more frequent, both in the laboratory and in practical applications. Therefore, it appears that investigations aimed toward obtaining a physical appreciation of these phenomena are appropriate; this view is supported by the recent appearance in the literature^{1, 2} of two investigations in the general problem area where the electrons present in a gas are not thermally equilibrated with the heavy particles.

Camac and Kemp¹ have formulated the shock tube end wall boundary-layer problem in appreciably ionized argon, at conditions where the Debye length is less than the ion-neutral

Received January 23, 1964; revision received July 13, 1964. The author expresses appreciation to Z. O. Bleviss and M. Kolpin for several beneficial suggestions regarding the preparation of the manuscript.

* Member of the Technical Staff, Plasma Research Laboratory, Laboratory Operations. Member AIAA.

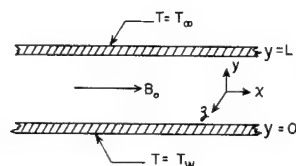


Fig. 1 Geometry of parallel-plate problem.

mean free path, and have obtained two numerical results; one for the limiting case of complete thermal equilibrium and the other for the limiting case of no collisional energy transfer between ions and electrons, both results being based upon the local similarity approximation. Although these results are closely related to a clearly physical situation, it is difficult to extract the roles of the various energy-transfer processes from only these results, and the interpretation is further complicated by the use of the local similarity approximation. For these reasons, the entirely different approach employed in the present investigation (described in the next paragraph), aimed specifically toward obtaining an understanding of the roles of the various energy-transfer processes, appears to have some merit, although the formulation of the basic equations and boundary conditions are closely related to that of Camac and Kemp. Chung and Mullen² have investigated thermal nonequilibrium effects in a stagnation-point boundary layer in a slightly ionized gas, with primary emphasis on electrical characteristics, rather than energy transfer. The major differences in the formulation of the basic equations and the cold surface boundary conditions utilized by Chung and Mullen and those to be employed here are that the former considers the sheath to be collision dominated and, in addition, incorporates the assumptions that the energy transfer between ions and electrons due to electric fields is negligible everywhere and that the diffusional velocities are proportional to gradients in mass fractions, rather than partial pressures. These latter assumptions are not justifiable in the general case.

As any detailed analysis of an appreciably ionized gas is necessarily complex, the situation considered here is the elementary one of a gas between parallel plates of different temperatures (to be described more fully in the succeeding section) for which results can be obtained without resorting to approximate techniques. The purpose of the investigation of this elementary situation is, in addition to presenting new computational results, to obtain a physical appreciation of the aforementioned features of ionized gases, which is not readily obtainable in previous work, in the belief that the results obtained can be used as a qualitative indication of the effects in more complicated flow situations (e.g., boundary layers) as well as a guide to permissible simplifications in these more complex problems. Specific emphasis is placed upon the effects on energy transfer to a cold surface, including the effects on the individual processes (thermal conduction and diffusional transport by both electrons and heavy particles) of the following phenomena: 1) the role of the space charge sheath (in which a continuum description is not strictly valid and which can be solved in only very crude ways) in determining the appropriate boundary conditions for the continuum equations: this follows closely the work of Camac and Kemp,¹ with some additional considerations of sheaths in which the ion temperature is not negligible, as well as sheaths in which the electron and ion flow processes are each considered adiabatic rather than spatially isothermal; 2) the presence of the transition region between the sheath and the region where the usual continuum equations are valid; 3) the contribution of the energy transfer between ions and

electrons due to the electric field external to the sheath; 4) thermal nonequilibrium between electrons and heavy particles; and, finally, 5) the effect of a magnetic field parallel to a cold surface.

II. Problem Formulation

2.1 Problem Definition

The physical situation considered here is that of partially ionized atomic hydrogen placed between two electrically conducting plates at different temperatures (see Fig. 1).[†] The steady-state solution is desired wherein all quantities are a function of the single spatial variable y only. It is further assumed that 1) there is no net mass transfer between the gas and the cold surface at $y = 0$, hence $v(0) = 0$; 2) the applied magnetic field is uniform and in the positive x direction; 3) the applied electric field vanishes in the x and z directions, hence $E_x = E_z = 0$; 4) the magnetic field due to currents existing in the gas is negligible (this can be shown to be the case at the conditions encountered here), hence, $B_z = B_y = 0$, $B_x = B_0$; 5) the total pressure gradient in the y direction is negligible [this is valid if $(\omega\tau)(\omega\tau) \ll 1$]. With these assumptions, the governing equations (Sec. 2.2) indicate that, if the magnetic field and a net current flow do not occur simultaneously, there is no net mass motion of the gas, and diffusion and current flow (if it exists) occur only in the direction normal to the plates. If the magnetic field and a net current flow normal to the plates exist simultaneously, then, in addition to diffusion normal to the plates, mass motion, current flow, and diffusion also occur in the z direction.

The conditions considered in the present investigation are such that near the cold surface, which is assumed fully catalytic to electron-ion recombination,[‡] the Debye length is less than a heavy particle mean free path. In this case, it is well known that the following three rather distinct regions exist near the surface (Fig. 2): 1) away from the wall, the gas is quasi-neutral, the ion diffusion velocity is small, and the behavior of the gas in this region is described by continuum equations; 2) near the wall (but not adjacent to it), the gas remains quasi-neutral, but the ion diffusion velocity is comparable to the ion sound velocity and the usual equations are not valid; this region will be referred to here as the "transition" region; and 3) adjacent to the wall, a space charge sheath, on the order of a Debye length in spatial extent, exists wherein the gas is no longer quasi-neutral (in all cases considered here, the sheath is composed of excess ions, yielding an electric field that acts to repel electrons). A major difficulty exists in connection with the latter two regions in that, to obtain precise solutions, it is necessary to solve the Boltzmann (or Vlasov, as appropriate) equation for each species, and at present this does not constitute a tractable problem. The approach employed here, in this regard, is to obtain crude solutions in these regions, which relate the species' temperatures and velocities at the edge of the transition region to the known properties of the cold surface. Combined with the observation that the spatial extent of these regions is negligible compared to the plate

[†] The hotter "plate" is actually best described as a control surface in this investigation in that the temperatures of the species and the mixture composition are prescribed here, thus permitting diffusion to occur across the surface and allowing a nontrivial steady-state solution to be obtained. Further, with this interpretation, the radiative properties of the hotter plate are then determined by the properties of the gas and the amount that exists above this surface.

[‡] It is assumed that only monatomic hydrogen is produced by recombination at the surface. This may be unrealistic for hydrogen since some of the diatomic species may be formed, depending upon the catalytic properties of the surface. However, the results to be obtained are qualitatively similar for any monatomic gas

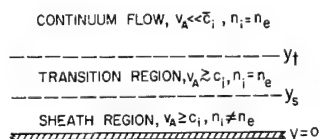


Fig. 2 Flow regimes near a cold surface.

separation, these solutions are employed to provide boundary conditions at $y = 0$ for the continuum equations in an attempt to determine the extremes of behavior to be expected and the resultant effects upon the solution to these equations. The continuum equations are presented in Sec. 2.2, and a detailed formulation of the boundary conditions is presented in Sec. 2.4.

To conclude the problem definition, the following assumptions are employed in the derivation of the continuum equations presented in the next section: 1) the mixture remains quasi-neutral; 2) the ratio of electron to ion mass is negligible compared to unity; 3) the diffusional velocity of each species is negligible compared to its thermal (or sonic) velocity; 4) the temperatures of ionic and neutral species are equal; 5) energy transfer due to radiation is negligible; and 6) there exists no gas-phase chemical reaction. The first three assumptions are rather common, and merit no additional comment. Because of the essentially equal masses of the heavier species, assumption 4 must be valid in continuum flow. The validity of the last two assumptions depends in detail upon the gas conditions, surface properties, and the particular geometrical configuration contemplated. For radiative transfer considerations, it can be shown by utilizing the work of Bates and Kingston¹³ that, for monatomic hydrogen at conditions of interest ($p \sim 0.1$ – 1.0 atm, $T \sim 15,000^\circ$ – $50,000^\circ$ K), the gas is transparent over the length in which appreciable thermal non-equilibrium is likely to occur; further, the emitted radiation from this depth is appreciably smaller than the convective energy transfer. For example, for hydrogen at $50,000^\circ$ K and 1 atm, the length over which appreciable thermal non-equilibrium exists is approximately 0.4 mm, and the ratio of the convected energy transfer through this depth to a cold surface to the emitted radiation is approximately 150. Thus, if a boundary-layer situation is visualized, a depth of gas of approximately 6 cm is required before the total emitted radiation is equal to the convective energy transfer across a boundary layer of 0.4 mm thickness. For heavier gases, the relative importance of radiation would probably be somewhat greater.

The amount of gas-phase reaction is, of course, determined by the ratio of the residence time of a particle between the plates, which is governed by the diffusion process, to a characteristic reaction time. Gas-phase reaction in the presence of thermal nonequilibrium is somewhat more complex than that at thermal equilibrium since, in addition to the importance of the recombination mechanisms at lower temperatures near thermal equilibrium, the ionization mechanisms are likely to become important at low gas temperatures if the electron temperature is sufficiently high. A more detailed discussion of this matter is beyond the scope of the present work; however, it can be stated that, as pressure and/or plate spacing are decreased, the relative importance of gas-phase reaction decreases, and it is probable that conditions do exist in which they are unimportant. It should be emphasized at this point that the primary purpose of this investigation is to examine the nature of two temperature effects alone on convective energy transfer. As will be seen, this exhibits several important effects even in the absence of other complicating phenomena. Thus, although the matters of radiative transfer and gas-phase reaction are certainly legitimate areas for further investigation, since both can contribute importantly to the energy transfer between electrons and heavy particles, it is believed by this writer that the present investigation is justified by the merits of revealing important effects as well as providing a helpful guide in the investigation of these other phenomena.

2.2 Governing Continuum Equations

Utilizing the previous assumptions, the continuum equations for the parallel plate configuration can be written as

follows. Conservation of mass[§] requires $v = 0$; conservation of ions requires, after integration with respect to y ,

$$\rho(1 - f)v_A = F_w = \text{const} \quad (1)$$

Conservation of current requires

$$j_y = j_w = \alpha \frac{e\rho(1 - f)}{m_i} v_A \quad (2)$$

which also serves to define the current fraction α . The z component of the momentum equation is the only nontrivial one:

$$(d/dy)[\mu_{in}(dw/dy)] = j_y B_0 \quad (3)$$

where μ_{in} is the viscosity of the heavy particle mixture (the viscosity due to electrons is negligible).

Since the primary case of interest here is the situation where the electron temperature is different from that of the heavy particles, two energy equations are required. For the heavy particles, one obtains

$$\frac{d}{dy} \left(-k_{in} \frac{dT_o}{dy} \right) = \frac{e\rho(1 - f)}{m_i} v_A E_y + \lambda_{ch}(T_e - T_o) \quad (4)$$

whereas the electron energy equation is

$$\frac{d}{dy} \left(-k_e \frac{dT_e}{dy} \right) = - \frac{e\rho(1 - f)}{m_i} v_A E_y + E_y j_y - \lambda_{ch}(T_e - T_o) + \frac{d}{dy} \left\{ \left[\rho(1 - f)v_A - \frac{m_i}{e} j_y \right] c_{pe} T_e \right\} \quad (5)$$

where each species is assumed to behave as a perfect gas. It is pointed out that, in addition to the usual terms, these equations contain a term representing energy transfer between light and heavy species due to collisional processes [$\lambda_{ch}(T_e - T_o)$] and a term representing energy transfer between charged species due to motion in an electric field (first term on the right side of both equations).

The generalized form of Ohm's law yields $j_x = 0$ and

$$j_y \frac{(1 + \beta_e^2)}{\sigma} = E_y + w B_0 + \frac{m_i}{e\rho(1 - f)} \frac{dp_e}{dy} \quad (6)$$

$$j_z = \beta_e j_y \quad (7)$$

Similarly, the diffusion equation yields $u_A = 0$ and

$$\frac{2(1 - f)p}{D_A[1 + (1 - f)(T_e/T_o)]} v_A - f j_z B_0 = - \frac{d}{dy} (p_i + p_e) \quad (8)$$

$$\frac{2(1 - f)p}{D_A[1 + (1 - f)(T_e/T_o)]} w_A = - f j_y B_0 \quad (9)$$

It is noted that the scalar electrical conductivity in (6) can be related to the binary diffusion coefficients[¶] by utilizing the diffusional relations presented by Hirschfelder, Curtiss, and Bird,⁴ suitably modified by the fact that the momentum transfer between electrons and heavier species is governed by the electron temperature when the temperatures are unequal, and further neglecting the effects of thermal diffusion and strong electric and magnetic fields on the velocity distribution functions. The latter assumptions are not wholly justifiable in the general case, but their use will not alter the character of the results for effects of magnetic

§ A more detailed development of the multidimensional form of the governing equations, consisting primarily of algebraic manipulation of the conservation relations for each species in which all terms are retained, can be found in Ref. 3; development of the present one-dimensional form can be found in Ref. 12. Unfortunately, space does not permit presentation of these developments here.

¶ The "binary" coefficients are here defined as the value of the diffusion coefficient in the binary mixture at the same number densities and temperatures as exist in the total mixture.

fields and electron temperature nonequilibrium on energy transfer (which is the purpose of the investigation), but will, of course, cause the quantitative results to be somewhat in error. These assumptions are further supported by the fact that, in the case treated here, the electronic Hall parameter, $\beta_e = (\omega\tau)_e$, is restricted to values less than six. The resulting relation is

$$\sigma^{-1} = \left(\frac{1}{n_e e}\right)^2 \left(\frac{f}{D_{en}} + \frac{1}{2D_{ie}}\right) \frac{p(1-f)}{(1-f + T_e/T_e)} \quad (10)$$

As has been previously noted by Kemp,⁵ the ion diffusion velocity is proportional to partial pressure gradients in (8) rather than the more common case of concentration gradients. Actually, the former is the more fundamental form, with the importance of the distinction lying in the fact that this form reduces to the common one involving concentration gradients (expressed in terms of mass fractions) only if the temperatures of all species are equal.

Equations (1-8), with the thermal equations of state for each species, form a set of eleven equations in the unknowns $T_e, T_g, v_A, f, \rho, j_y, j_z, w, E_y, p_i, p_e$ with (9) providing a determination of w_A (which will not be of interest here). To nondimensionalize these equations, it is first convenient to introduce the quantity $\delta = [ep(1-f)/m_i]^2/\sigma$ to replace the electrical conductivity and then to introduce the following normalization quantities: $L_r = L, \rho_r = 5p_\infty/2c_{pg}T_\infty, T_r = T_\infty, p_r = p_\infty, \mu_r = \mu_\infty, k_r = k_\infty, D_{Ar} = D_\infty, \delta_r = p_\infty/D_\infty, \lambda_r = k_\infty/L^2, E_r = kT_\infty/eL, B_r = B_0, v_{Ar} = v_A, \tau = D_\infty/L, w_r = E_r/B_r, F_{wr} = \rho_r v_{Ar} \tau$, and $j_{r\tau} = (e/m_i)\rho_r v_{Ar} \tau$. The subscript ∞ refers to conditions at the upper (hot) plate, and D_∞ is taken as the value of D_A at p_∞ and T_∞ , assuming only a trace of ionization. The dimensionless parameters $Le = \rho_r c_{pg} D_\infty / k_\infty, Sc = \mu_\infty / \rho_r D_\infty$, and $\psi = e^2 B_0^2 L^2 / m_i k T_\infty$ arise as a consequence of the normalization scheme. The preceding equations, in terms of the dimensionless variables, become (after some manipulation)**

$$\rho(1-f)v_A = F_w \quad (11)$$

$$\frac{d}{dy} \left(\mu_{in} \frac{dw}{dy} \right) = \frac{\psi}{Sc} \alpha F_w \quad (12)$$

$$\frac{d}{dy} \left(-k_{in} \frac{dT_g}{dy} \right) = \frac{2}{5} (Le) \left[\alpha \delta (1 + \beta_e^2) v_A^2 - F_w w - F_w v_A \frac{d}{dy} \left(\frac{T_e}{v_A} \right) \right] + \lambda_{eh} (T_e - T_g) \quad (13)$$

$$\frac{d}{dy} \left(-k_e \frac{dT_e}{dy} \right) = -\frac{2}{5} (Le) (1 - \alpha) \left[\alpha \delta (1 + \beta_e^2) v_A^2 - F_w w - F_w v_A \frac{d}{dy} \left(\frac{T_e}{v_A} \right) \right] - (Le) (1 - \alpha) F_w \frac{dT_e}{dy} - \lambda_{eh} (T_e - T_g) \quad (14)$$

$$v_A = \frac{D_A}{2\rho(1-f)T_g(1-\beta_e\theta)} \frac{dg}{dy} \quad (15)$$

$$E_y = \frac{\alpha\delta}{F_w} (1 + \beta_e^2) v_A^2 - w - v_A \frac{d}{dy} \left(\frac{T_e}{v_A} \right) \quad (16)$$

where

$$\rho = [T_g + (1-f)T_e]^{-1} \quad (17)$$

$$\theta = (eB_0 D_\infty / k T_\infty) \alpha D_{Af} / 2 T_g \quad (18)$$

$$g = f / [1 + (1-f)(T_e/T_g)] \quad (19)$$

In this form, Eqs. (12-15) represent a coupled set of four nonlinear differential equations in the variables (for example) T_e, T_g, w , and v_A .

** Hereafter, dimensional quantities will be denoted by a prime, unless otherwise specified.

2.3 Transport Properties††

To obtain the values of the various transport properties of the mixture, it is necessary to obtain the properties of the pure species‡‡ and then, in the case of viscosity and thermal conductivity, to compute the mixture properties by standard (although approximate) mixture rules. It should be remarked that experimental determination of these values is rather sparse and often nonexistent at the temperatures of interest, hence the following theoretical predictions are subject to error. Further, these theoretical predictions may not be the best available; however, it is believed that all significant qualitative trends are faithfully reproduced, which is adequate for the present purposes.

In this connection, it is pointed out that, although the properties are computed for partially ionized monatomic hydrogen (which is, in a sense, unrealistic because of the possible presence of H_2), these properties are qualitatively similar for any partially ionized monatomic gas, and hence some insight into the behavior of these other gases can be gained from the results for hydrogen. To elaborate somewhat on this remark, if it is desired to extrapolate the results obtained for hydrogen to some other gas, the features of the transport properties which must be accounted for are the change in characteristic magnitudes and the change in temperature-composition dependence.§§ Of these two features, the change in characteristic magnitudes can always be accounted for by an appropriate nondimensionalization scheme and hence causes no difficulty. If, however, the change in temperature-composition dependence of a particular property is markedly different in two gases, there exists no way to extrapolate the results from one gas to the other. Fortunately, this is not the case in the transport properties of hydrogen as computed here and the transport properties of the noble gases, since the relevant particle cross sections are not significantly different (with the single exception of the electron-neutral cross section, which does not play an important role at the gas conditions of interest). For example, if the thermal conductivities of the electronic component and the ion-neutral component and the ion-neutral diffusion coefficient as computed by Camac and Kemp⁴ for argon are multiplied by one, ten, and three, respectively, it is found that the results are very close to the corresponding properties as computed here for monatomic hydrogen, with no qualitative change in temperature-composition dependence. Thus, it is expected that the results obtained in the present investigation can be qualitatively applied to argon, provided that the change in characteristic magnitudes are accounted for by nondimensionalization. Accordingly, the following theoretical predictions are presented without further apology.

The transport properties of a mixture of equal numbers of ions and electrons have been computed by Braginskii,⁶ with the following results¶¶:

$$(\mu_i)_p = 0.246 \left(\frac{m_i}{k} \right) (k_i)_p = 0.18 \left(\frac{2kT_g}{e^2} \right)^2 \left(\frac{kT_g}{\pi} \right)^{1/2} \frac{m_i^{1/2}}{\ln \Lambda_i} \quad (20)$$

†† All quantities in this section are dimensional.

‡‡ As the transport properties of charged species are most readily available in terms of a fully ionized gas, the subsequent discussion considers a mixture of equal numbers of ions and electrons as a pure species.

§§ Any transport property q can be written as $q = q_r F(T_j, n_j)$, where q_r is the value of the transport property at some point in the flow. In the present terminology, q_r is referred to as the characteristic magnitude and F as the temperature-composition dependence.

¶¶ The notation employed is that a quantity enclosed in parentheses denotes a property of an individual species, the inner subscript referring to that species and the outer subscripts referring to the number of species present: i, e, n = ions, electrons, or neutrals, only, respectively; p = ions and electrons; no outer subscript indicates all species are present.

$$(k_e)_{\parallel} = 0.419k \left(\frac{2kT_e}{e^2} \right)^2 \left(\frac{kT_e}{\pi} \right)^{1/2} \frac{1}{m_i^{1/2} \ln \Lambda_e} \quad (21)$$

$$D_{ie} = 0.293 \frac{(kT_e)^{5/2}}{n_e m_e^{1/2} e^4 p_e \ln \Lambda_e} \quad (22)$$

$$\lambda_{ie} = 3m_e n_e k / m_i \tau_{ei} \quad (23)$$

where the subscript \parallel refers to the direction parallel to the magnetic field and

$$\ln \Lambda_{i,e} = (3/2e^3) (k^3 T_{e,e}^3 / \pi n_{i,e})^{1/2} \quad (24)$$

$$\tau_{ei} = 3m_e^{1/2} (kT_e)^{3/2} / 4(2\pi)^{1/2} e^4 n_e \ln \Lambda_e \quad (25)$$

Reasonable approximations of the results of Vanderslice, et al.⁷ for the viscosity and thermal conductivity of atomic hydrogen are

$$(\mu_n)_n = 1.03 \times 10^{-8} T_g \text{ (kg/m-sec)} \quad (26)$$

$$(k_n)_n = 3.20 \times 10^{-4} T_g \text{ (joules/m-sec-}^\circ\text{K)} \quad (27)$$

The value of the ion-neutral binary diffusion coefficient is obtained from the data of Brown⁸ for helium and from assuming that the coefficient varies as the inverse square root of the atomic mass, with the result

$$D_{in} = 7.60 \times 10^{-10} T_g^{1/2} / p_{in} Q_0 \text{ (m}^2\text{/sec)} \quad (28)$$

where p_{in} denotes the partial pressure (in atmospheres) of the ion-neutral mixture and $Q_0 = 1$. As this result is subject to considerable error, the factor Q_0 is included as a simple method for investigating possible changes in D_{in} .

For want of other data, the electron-neutral cross section is assumed to be $Q_{en} = 10^{-19} \text{ m}^2$, with the corresponding mean free time between collisions of $\tau_{en} = (n_n Q_{en} C_e)^{-1}$. The resulting energy exchange coefficient is

$$\lambda_{en} = \left(\frac{3}{2} k \right) \left(2 \frac{m_e}{m_n} \right) \left(\frac{n_e}{\tau_{en}} \right) \delta_{en} \quad (29)$$

where $\delta_{en} = 1$ is a good approximation for the effectiveness of a collision in transferring energy in monatomic gases. The electron-neutral diffusion coefficient is

$$D_{en} = 2.52 \times 10^{-6} T_e^{1/2} T_g / p_{in} \text{ (m}^2\text{/sec)} \quad (30)$$

where p_{in} is in atmospheres.

The properties of the total mixture can be computed from the properties of the pure species by standard mean free path considerations proposed by Fay⁹ and will not be discussed further here. The results are as follows: for the viscosity of the ion-neutral component,

$$\mu_{in} = (\mu_n)_n \left[1 + 1.35 \frac{(1-f)}{f} Q_0 \right]^{-1} + (\mu_i)_p \left[1 + (3.8 \times 10^{-8}) \left(\frac{f}{1-f} \right) \frac{Q_0 T_g^{3/2}}{\ln \Lambda_i} \right]^{-1} \quad (31)$$

for the thermal conductivity of the ion-neutral components,

$$k_{in} = (k_{in})_n \left[1 + 1.35 \left(\frac{1-f}{f} \right) Q_0 \right]^{-1} + (k_i)_p \left[1 + (3.8 \times 10^{-8}) \left(\frac{f}{1-f} \right) \frac{Q_0 T_g^{3/2}}{\ln \Lambda_i} \right]^{-1} \quad (32)$$

for the thermal conductivity of the electrons,

$$k_{\parallel} = (k_e)_{\parallel} \left[1 + (2.0 \times 10^{-10}) \left(\frac{f}{1-f} \right) \frac{T_e^2}{\ln \Lambda_e} \right]^{-1} \quad (33)$$

for the total energy exchange coefficient,

$$\lambda_{eh} = \lambda_{ei} + \lambda_{en} \quad (34)$$

and for the electronic Hall parameter,

$$(\omega\tau)_e = (3.92 \times 10^{-12}) \left(\frac{B}{p} \right) T_e^{5/2} \left(\frac{T_g}{T_e} \right) \times \frac{1 + (1-f)(T_e/T_g)}{(1-f)\ln \Lambda_e + (2.0 \times 10^{-10})fT_e^2} \quad (35)$$

where B is in webers per square meter, p in atmospheres, and T in degrees Kelvin. Finally, the thermal conductivity of the electrons transverse to the magnetic field (the only direction of interest here) is taken as

$$k_e = [1 + (\omega\tau)_e^2]^{-1} k_{e\parallel} \quad (36)$$

It should be mentioned that the ionic contributions to the thermal conductivity and viscosity, as well as the contributions of electron-neutral interaction to energy exchange and to the value of the Hall parameter, are essentially negligible at the conditions encountered in the present investigation.

2.4 Boundary Conditions

At the conditions of interest here, the most appropriate analysis of the sheath to date has been given by Schulz and Brown.¹⁰ Their analysis incorporates the assumptions that the electrons are isothermal in the sheath and that the directed energy of the ions is much greater than the thermal energy; solution of the continuity and momentum equations (in the absence of transport effects), in conjunction with Poisson's equation, yields the result that the ion diffusion velocity at the sheath edge must satisfy the inequality (in dimensional form)

$$v_{A,s}^2 \geq kT_{e,s} / m_i \quad (36a)$$

and the corresponding potential drop across the sheath satisfies

$$\gamma \equiv \frac{e|\phi_{sw}|}{kT_{e,s}} \leq \ln \left(\frac{C_e}{4|v_{A,s}|(1-\alpha)} \right) = \ln \frac{(m_i/2\pi m_e)^{1/2}}{(1-\alpha)} \quad (36b)$$

where α is the ratio of the net current flow to the wall to the ion current (the analysis being restricted to $|\alpha| \lesssim 1$). Some elementary extensions of this solution which indicate the effect of other plausible assumptions are as follows. First, if the ion thermal energy is not neglected and both electrons and ions are assumed isothermal in the sheath, the corresponding results are

$$v_{A,s}^2 \geq (k/m_i)(T_{e,s} + T_{i,s}) \quad (37a)$$

$$\gamma \equiv \frac{e|\phi_{sw}|}{kT_{e,s}} \leq \ln \frac{(m_i/2\pi m_e)^{1/2}}{(1-\alpha)(1 + T_{i,s}/T_{e,s})^{1/2}} \quad (37b)$$

Similarly, if both electrons and ions are assumed to be adiabatic in the sheath, the results become

$$v_{A,s}^2 \geq \frac{5}{3} (k/m_i)(T_{e,s} + T_{i,s}) \quad (38a)$$

$$\gamma \equiv \frac{e|\phi_{sw}|}{kT_{e,s}} \leq \ln \frac{(3m_i/10\pi m_e)^{1/2}}{(1-\alpha)(1 + T_{i,s}/T_{e,s})^{1/2}} \quad (38b)$$

At the sheath edge then, the appropriate boundary conditions on the ion temperature and ion diffusion velocity are that $T_g = T_w$ (since the ions are in thermal equilibrium with the neutrals) and $v_A = v_{A,s}^*$ respectively. The boundary condition relevant to the electron temperature is obtained by calculating the energy flux across the sheath edge carried by the electrons

$$q_{ew}' = \rho_{i,s} v_{A,s} (1-\alpha)(2+\gamma) \left(\frac{3}{2} c_{pe} T_{e,s} \right) \quad (39)$$

which is the result of Jukes¹¹ quoted by Camac and Kemp¹ and may be obtained by assuming the electron velocity dis-

* The equalities in the sheath relations are assumed to hold.¹⁰

tribution to be Maxwellian at the sheath edge and computing the energy flux carried toward the wall by electrons possessing sufficient energy to penetrate the sheath potential. It should be pointed out that, although only a very small fraction of the electrons incident on the sheath edge succeeds in penetrating it, this small fraction originates in the high energy portion of the Maxwellian distribution and hence carries a significant amount of energy. Further, the energy flux by electrons across the sheath edge does not represent the energy flux by electrons to the wall, since most of this energy is transferred to the ions in the sheath (via electric fields).

The problem remains to relate the quantities T_e , T_o , and v_A at the edge of the transition region to relevant properties at the sheath edge. In the work of Camac and Kemp,¹ the transition region was neglected, so that the boundary conditions for the continuum equations became $T_o = T_o, s = T_w$, $v_A = v_A, s$ and

$$[-k_e(dT_e/dy) + \rho_i v_A(1 - \alpha)c_{p0}T_{e, s}]_s = [\rho_i v_A(1 - \alpha)(2 + \gamma)(\frac{2}{3}c_{p0}T_e)]_s \quad (40)$$

where v_A, s and γ were given by Eqs. (36). Boundary conditions of this type will also be considered here. In addition, it is proposed that the transition region is of very small spatial extent and therefore may be treated in a way analogous to the sheath treatment. The edge of the transition region will be defined by the relation $v_{A, t}/v_{A, s} = A_w$; that is, the ion diffusion velocity at the transition edge is some fraction of the velocity at the sheath edge. Then the continuity, momentum, and energy equations for ions and electrons in the transition region (where $n_i = n_e$ and transport effects are again neglected) may be solved with the same assumptions as led to Eqs. (36-38), respectively, to yield for the potential difference across both the sheath and transition region:

$$\gamma_1 \equiv \frac{e|\phi_{tw}|}{kT_{e, t}} \leq \ln \frac{(m_i/2\pi m_e)^{1/2}}{(1 - \alpha)} + \frac{1}{2}(1 - A_w^2) \quad (41)$$

for the cold ion, isothermal electron case;

$$\gamma_1 \leq \ln \frac{(m_i/2\pi m_e)^{1/2}}{(1 - \alpha)(1 + T_{o, t}/T_{e, t})^{1/2}} + \frac{1}{2}(1 - A_w^2) \quad (42)$$

for the isothermal ion and electron case[†]; and

$$\gamma_1 \leq \frac{3}{4} \left(1 + \frac{A_w^2}{4 - A_w^2}\right) \ln \frac{(3m_i/10\pi m_e)^{1/2}}{(1 - \alpha)(1 + T_{o, t}/T_{e, t})^{1/2}} + \frac{5(1 - A_w^2)}{2(4 - A_w^2)} \quad (43)$$

for the adiabatic electron and ion case. The boundary conditions at the edge of the transition region become then $T_{o, t} = T_w$ (the ions are still assumed to be in thermal equilibrium with the neutrals, and the transition region is assumed sufficiently small so that the temperature is essentially the wall temperature), $v_{A, t} = A_w v_{A, s}$, and the energy balance for electrons yields a relation identical to (40) with γ replaced by γ_1 , if (41) or (42) apply, whereas if (43) applies, γ in (40) should be replaced by

$$\gamma_2 = \frac{1 - A_w^2}{2(4 - A_w^2)} + \frac{3}{4} \left(1 + \frac{A_w^2}{4 - A_w^2}\right) \ln \frac{(3m_i/10\pi m_e)^{1/2}}{(1 - \alpha)(1 + T_{o, t}/T_{e, t})^{1/2}} \quad (44)$$

In dimensionless form, (40) becomes, at $y \approx 0$,

$$k_e(dT_e/dy) = F_w(Le)(1 - \alpha)(0.2 - 0.4\gamma_i)T_e$$

[†] It is mentioned that the results for the isothermal assumption are basically inconsistent, since collisional and transport effects were neglected in the equations of motion; hence there exists no mechanism to maintain isothermality.

The heat transfer to the cold surface is given by (in dimensionless form)

$$q_w = q_{ei} + q_{di} + q_{ce} + q_{de} + q_{is}$$

where the transfer by conduction due to ions and neutrals is

$$q_{ei} = [k_{in}(dT_o/dy)]_{y=0}$$

the transfer by diffusion of recombination energy is

$$q_{di} = -F_w(Le)(-\epsilon_n)$$

the transfer by conduction in the electrons is

$$q_{ce} = [k_e(dT_e/dy)]_{y=0}$$

the transfer by diffusion of electron thermal energy is

$$q_{de} = -F_w(Le)(1 - \alpha)(T_e)_{y=0}$$

and the energy transfer due to the gain of energy by the ex-cursions in crossing the sheath is

$$q_{si} = -0.4F_w(Le)\alpha\gamma_i(T_e)_{y=0}$$

The dimensional heat-transfer q_w' is related to the dimensionless quantity by $q_w = q_w' L / k_{\infty} T_{\infty}$. To complete the problem formulation, the boundary conditions at the upper surface are (in dimensionless form) at $y = 1$: $T_e = T_o = 1$, $f = f_{\infty}$, and $dw/dy = 0$, and, in addition, at the cold surface, $w = 0$. The fluid motion (which occurs only in the presence of net current flow and a magnetic field) is assumed to be unimpeded at the upper surface.

It is rather evident from the form of the equations and the transport properties that numerical solutions are indicated. Such solutions have been obtained, although with some difficulty; space does not permit discussion of the numerical technique involved.

III. Results and Discussion[‡]

3.1 Discussion of Numerical Results[§]

3.1.1 Sheath-transition region model and energy transfer by electric fields

The effect of incorporating a transition region near the cold surface on temperature profiles and total heat transfer is shown in Fig. 3 for the case $\lambda_{\infty} \equiv (\lambda_{eh})_{\infty} = 0.140$ and $T_{\infty} = 50,000^\circ\text{K}$. The cold ion, isothermal electron sheath model [Eqs. (36a, 36b, and 41)] has been employed. In one case (curve 2, $A_w = 1.0$) the transition region has been neglected, and the continuum equations are assumed to be valid to the sheath edge, whereas in the other case (curve 4, $A_w = 0.25$) the transition region begins when the ion drift velocity is 25% of that at the sheath edge. The differences in the two results are attributable to the fact that the transition region model employed yields less energy transfer between electrons and ions by electric fields than if the continuum equations are assumed valid to the sheath edge. It is observed that the differences are small, and it therefore may be concluded that the solution is not greatly affected by the transition region. This conclusion is further supported by the observation that the boundary condition on electron temperature diminishes in importance as thermal equilibrium is approached, and hence the effect of the transition region will diminish at higher values of λ_{∞} . Of course, if the value of the ion drift velocity at the transition region edge is assumed

[‡] A more detailed presentation of the results of this investigation, including some useful analytical solutions, can be found in Ref. 12.

[§] Unless otherwise specified, the following values of the parameters are employed in the numerical computations: $p = 1$ atm, $L = 10^{-3}$ m, $T_w = 500^\circ\text{K}$, $Q_0 = 2$, $\beta_{\infty} = 0$, $\alpha = 0$. Variations in $\lambda_{\infty} \equiv (\lambda_{eh})_{\infty}$ are for parametric purposes primarily; physically, they may be construed as variations in L .

successively smaller, a point will eventually be reached where the mole fraction of ions existing at the transition region edge will be substantial compared to the mole fraction existing at the upper surface. This indicates that the spatial extent of the transition region so defined is not negligible. The resultant effect is to decrease the flux of ions toward the wall, thereby decreasing heat transfer. For example, the results of a calculation with $A_w = 0.05$, when compared with those for $A_w = 0.25$, yielded a decrease in ion flux of 14%, a decrease in heat transfer of 11%, and an increase in electron wall temperature of 13%.

The influence of the models of the sheath-transition region proposed in Sect. 2.4 have been investigated by comparing the results of the cold ion, isothermal electron model calculation at $T_\infty = 50,000^\circ\text{K}$, $\lambda_\infty = 0.140$, and $A_w = 0.5$ with the results of calculations at the same conditions for the completely isothermal model [Eqs. (37a, 37b, and 42)] and the adiabatic model [Eqs. (38a, 38b, 43, and 44)]. The resulting variations in heat transfer and electron wall temperature effected by these models were not great (maximum variations of 0.7 and 7.4%, respectively). It is concluded that the solution is not greatly affected by the sheath-transition region model employed. In all subsequent calculations, except for those discussed in the next paragraph, the isothermal sheath model is employed with $A_w = 0.5$.

In Fig. 3, the curves labeled 1 and 3 have been computed identically to curves 2 and 4, respectively, with the exception that energy transfer between ions and electrons by electric fields is neglected in the region external to the sheath-transition region. It is observed that this energy-transfer mechanism has an appreciable effect on the electron temperature profile and the total heat transfer to the wall. It should be noted that the major part of this electric field energy transfer occurs near the cold surface where E_y is large; this accounts for the decreased effect when a transition region is included. This observation indicates that a useful approximation in more complex problems may be to assume a value of A_w as low as is consistent with neglecting the spatial extent of the transition region and then neglect the electric field energy transfer external to the sheath. This is affirmed by the previously discussed calculation for $A_w = 0.05$ wherein the difference in total heat transfer resulting from neglecting this energy transfer was 3.6%; the fact that this value of A_w is somewhat too low to neglect the spatial extent of the transition region is of little consequence in this regard.

The preceding remarks are qualitatively applicable to different gas conditions or other noble gases. The quantitative effects are modified by the fact that, in situations where the nonequilibrium contribution of electrons to energy transfer is relatively greater, the differences resulting from

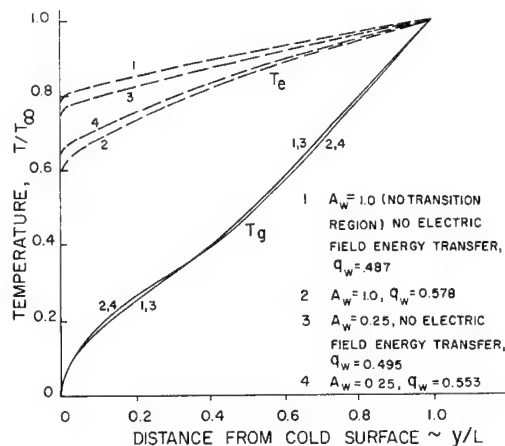


Fig. 3 Sheath-transition region and electric field energy transfer effects on temperature profiles; $T_\infty = 50,000^\circ\text{K}$, $\lambda_\infty = 0.140$, cold ion sheath model.

the use of the various sheath-transition region models will be somewhat more pronounced.

3.1.2 Thermal nonequilibrium effects on property profiles and energy transfer

The parameter that best characterizes the degree of thermal nonequilibrium is $\lambda_\infty \equiv (\lambda_{eh})_\infty L^2 / (k_e')_\infty$. It represents the ratio of the collisional energy-transfer rate between electrons and heavy particles to the energy-transfer rate by thermal conduction in electrons. If this ratio is small, the electrons are essentially thermally uncoupled, whereas if this ratio is large, thermal equilibrium prevails. The chief virtue of this parameter, as the results will show, is that the value required for virtually complete nonequilibrium is insensitive to the relative magnitudes of k_e , k_{in} , and D_A ; hence, the value is not sensitive to gas conditions.

Because of the dependence of the transport properties on temperature and composition, it is necessary to appreciate the effects of thermal nonequilibrium on the temperature and composition profiles before the effects on heat transfer can be fully understood. These effects of thermal nonequilibrium, characterized by λ_∞ , on the temperature and composition profiles are shown in Fig. 4. The most important effect portrayed in this figure is the change in the heavy particle temperature profile as λ_∞ varies. This change in temperature profile is largely due to the change in temperature and composition dependence of the effective thermal conductivity. For example, at $\lambda_\infty = 0$, the heavy particle thermal conductivity determines T_g , and since $k_{in} \sim fT_g/[f + (1 - f)Q_0]$ exhibits a maximum, the slope of the heavy particle temperature profile exhibits a minimum. This is clearly evident in Fig. 4. On the other hand, at $\lambda_\infty = \infty$, the electron thermal conductivity is significant in determining T_g , and since $k_e \sim T_e^{3/2}$, this tends to yield a temperature profile with a continually decreasing slope; this is also evident in Fig. 4. The net result of this effect is to decrease the

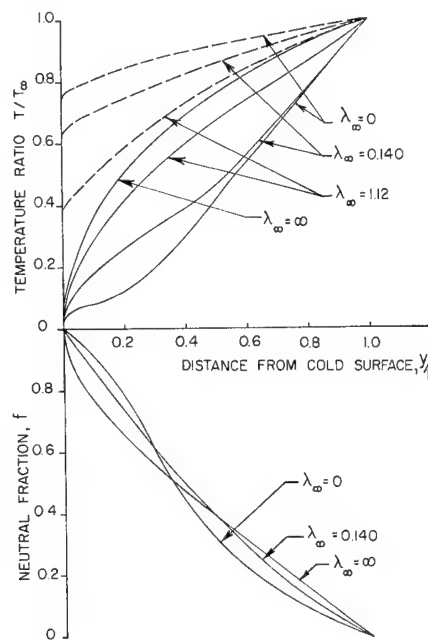


Fig. 4 Thermal nonequilibrium effects on temperature and composition profiles; $T_\infty = 50,000^\circ\text{K}$.

¶ The parameter λ_∞ employed in the figures is actually $(\lambda_{eh})_\infty L^2 / (k_e' + k_{in}')_\infty$. This differs from the parameter λ_∞ discussed in the text by the factor $(k_e' + k_{in}')_\infty / (k_e')_\infty$; however, for all cases considered here, this factor is 1.04, and hence the difference in the two parameters is not significant.

heavy particle temperature everywhere as thermal nonequilibrium becomes more pronounced. As will be seen, since both k_{in} and D_A are functions of T_θ , this change plays an important role in determining the magnitude of thermal nonequilibrium effects on total heat transfer.

Two additional features evident in Fig. 4 are worthy of note. First, the electron temperature is not constant between the plates when $\lambda_\infty = 0$. This is, of course, due to the energy transfer by electric fields between electrons and ions. As mentioned in Sec. 3.1.1, a minor portion of this energy transfer occurs external to the sheath-transition region, whereas the major portion occurs in this region (evidenced by the boundary condition on electron temperature). Second, the region of thermal nonequilibrium is not well confined near the cold surface at higher values of λ_∞ . This is due to the strong temperature dependences of the collisional energy coupling and the thermal conductivities. It is remarked in passing that calculations performed for $Q_0 = 1$, resulting in a factor of 2 increase in D_A , indicate that the influence of thermal nonequilibrium on the temperature profiles in Fig. 4 is not qualitatively altered. The major effect of the increase in D_A is a decrease in electron wall temperature in the nonequilibrium situation due to increased electric field energy transfer between electrons and ions. Finally, it is noted that the effects exhibited in Fig. 4 are not expected to be altered in the noble gases because of the previously mentioned similarity in temperature-composition dependence of the transport properties.

The most important effects of thermal nonequilibrium on diffusional processes, as indicated in Fig. 5, are twofold. First, the heat transfer due to recombination at the cold surface (q_{di}) is essentially a constant fraction of the total heat transfer, regardless of the degree of nonequilibrium. This reflects the fact that $q_{di} \sim D_A \sim T_\theta$. As observed in the preceding discussion, T_θ decreases as λ_∞ decreases; hence

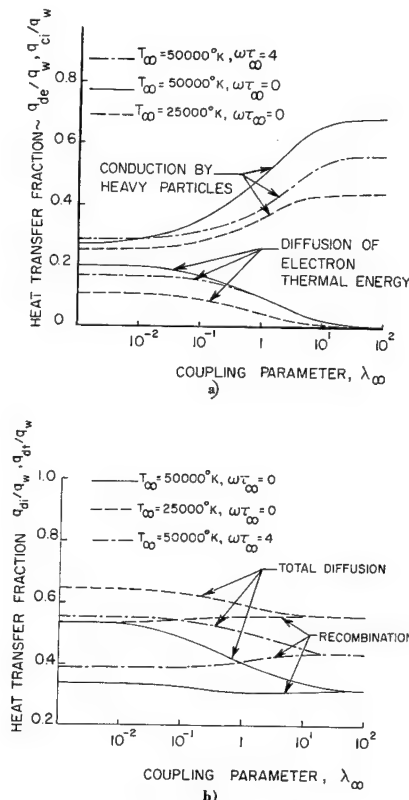


Fig. 5 Thermal nonequilibrium effects on heat transfer due to various sources. (The heat transfer due to electronic conduction is indistinguishable from that due to diffusion of electron thermal energy.)

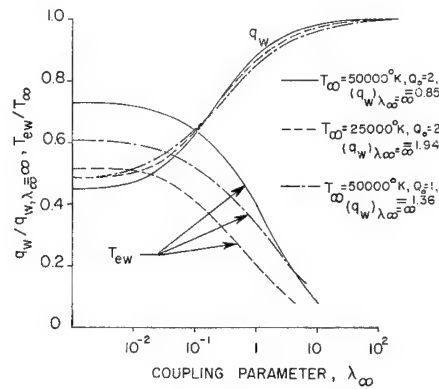


Fig. 6 Thermal nonequilibrium effects on total heat transfer and electron temperature.

q_{di} does likewise. Second, the heat transfer due to the diffusion of electron thermal energy (q_{de}), as well as the related heat conduction, becomes an appreciable part of the total heat transfer as complete nonequilibrium is approached. It should be noted however, that the total heat transfer decreases as $\lambda_\infty \rightarrow 0$, as shown in Fig. 6. This indicates that the tendency for diffusion to increase the electronic contribution to heat transfer in the nonequilibrium condition is not sufficient to overcome the factors tending to decrease this heat transfer. These factors are of course the loss of the electronic contribution to conduction in the equilibrium condition, the decrease in recombinational heat transfer, and finally, the decrease in heavy particle conduction as complete nonequilibrium is approached. This last effect is again due to the decrease in T_θ as λ_∞ decreases, since $q_{ci} \sim k_{in} \sim T_\theta$.

The relative roles of the conduction and diffusion processes in both electrons and heavy particles in the presence of thermal nonequilibrium effects can be more fully appreciated by examining the results for two different upper surface temperatures. These results are also shown in Figs. 5 and 6. Because of the temperature dependences of the transport properties ($k_e \sim T_e^{5/2}$, $k_{in} \sim T_\theta$, $\rho D_A \sim T_\theta$), it is to be expected that the electronic contribution to heat transfer will be relatively less at a lower temperature level, while the contribution of recombination will be relatively greater. The lesser contribution of the electrons at lower temperatures is evidenced in Fig. 5 by both the decreased fraction of the total heat transfer, which is directly attributable to the electronic component, and the decreased effect of nonequilibrium on the heat transfer due to heavy particle conduction. The greater contribution of recombination to the total heat transfer at the lower temperature is also evident in Fig. 5. Superficially, it might be expected that thermal nonequilibrium effects on total heat transfer would be considerably less at lower temperatures because of the decreased contribution of electrons. Figure 6 indicates, however, that nonequilibrium effects are only slightly less at $T_\infty = 25,000^\circ\text{K}$ than at $T_\infty = 50,000^\circ\text{K}$. This is of course due to the increased importance of recombinational heat transfer at the lower temperature and the fact that the appreciable effect of nonequilibrium on this quantity is not very sensitive to these temperature levels. It is also worthy of note that the fractional change in total heat transfer from equilibrium to complete nonequilibrium is only slightly less when the diffusion coefficient is doubled (Fig. 6); again, this is primarily because of the insensitivity to nonequilibrium effects of the fraction of the total heat transfer due to recombination.

However, at temperature levels where the gas at the hot surface is no longer fully ionized, the recombinational energy transfer becomes much less sensitive to nonequilibrium effects. This is due to the fact that the variation of $k_{in}(T_\theta, f)$ is such that the nonequilibrium heavy particle temperature differs much less from the equilibrium profile than at higher tem-

peratures. Hence, it is expected that, at these conditions, the total heat transfer is much less sensitive to nonequilibrium effects. This has been verified by a computation at $T_\infty = 15,000^\circ\text{K}$ where $f_\infty = 0.45$, which yielded a decrease in total heat transfer from equilibrium to complete nonequilibrium of only 7.7%. This result is in qualitative agreement with the result obtained by Camac and Kemp¹ in argon.

Finally, it should be noted in Fig. 6 that the values of λ_∞ , which are indicative of transition from thermal nonequilibrium to equilibrium, are not sensitive to temperature level or the magnitude of the ion-neutral diffusion coefficient. Specifically, the value of λ_∞ required for a change in total heat transfer (from nonequilibrium toward equilibrium) of 90% of the total change is in the range 2.8–4.4, whereas the value for a similar change of 10% is in the range 0.02–0.03, with the higher value occurring at the lower temperature. It is also remarked that calculations indicate that the presence of a magnetic field, which significantly alters the relative importance of the electronic thermal conductivity, does not have a significant effect on the transitional values of λ_∞ .

The preceding discussion allows two general conclusions with regard to thermal nonequilibrium effect on total heat transfer in gases other than hydrogen. First, for gases in which the electronic contribution to the thermal conductivity is greater relative to the heavy particle contribution and the contribution from diffusional processes, thermal nonequilibrium will have a greater effect in reducing heat transfer. Generally, in any heavier gas at the same temperature and ionization level as hydrogen, the relative electronic contribution will be greater. This is confirmed in the specific case of argon by the brief discussion of transport properties given in Sec. 2.3. The second general conclusion is that the values of λ_∞ indicative of transition from thermal equilibrium to nonequilibrium are not appreciably different for other gases. Both of these conclusions of course presuppose that the temperature-composition dependences of k_{in} and D_A in other gases are similar to those in hydrogen, and, hence, these conclusions are limited to the noble gases.

Before terminating this discussion of thermal nonequilibrium effects on energy transfer, it should be pointed out that another possible approximation to the chemical state of the gas, not treated here, is that where the ion and electron densities are in chemical equilibrium with the neutrals at the electron temperature. This approximation may be valid at sufficiently high temperatures, and, for the present cases, would yield a fully ionized gas everywhere, except for a thin layer near the cold wall, for electron temperatures above $25,000^\circ\text{K}$. In this case, diffusional processes and thermal conduction by neutrals would play a very minor role in determining the total energy transfer, and thermal nonequilibrium would have a considerably more drastic effect in reducing heat transfer.

3.1.3 Magnetic field effects on heat transfer

In the absence of a net current passing between the plates, it is evident from the governing equations and transport properties that the sole effect of a magnetic field is to decrease the electronic thermal conductivity. It is to be expected then that the magnetic field will decrease the total heat transfer in both equilibrium and nonequilibrium situations; this is clearly evident in the numerical results shown in Fig. 7. These results also indicate that nonequilibrium effects on total heat transfer are less in the presence of a magnetic field; this merely reflects the fact that the effects of thermal equilibrium on heat transfer decrease when the electronic contributions decrease. Further, the previous discussion of thermal nonequilibrium effects on heat transfer has indicated that the electronic contributions are greater at equilibrium than at nonequilibrium. In the presence of a magnetic field, this fact is evidenced in Fig. 5 by the increased fraction

of the total heat transfer due to recombination at equilibrium relative to that at nonequilibrium. Hence, it is expected that the effect of the magnetic field in decreasing heat transfer would be less as the amount of thermal nonequilibrium increases; this feature is also evident in Fig. 7.

It is of interest to compare the numerical results of Fig. 7 with the effect of the magnetic field on heat transfer if electronic and ionic heat conduction were the only processes of importance. This has been accomplished by means of analytical solutions for the case of a fully ionized gas in thermal equilibrium, in which no neutrals are present and diffusion vanishes. Such a situation could be envisioned if the cold surface were noncatalytic to recombination. Assuming that $k_e \sim T_e^{5/2}$, $k_i \sim T_e^{5/2}$, and $(\omega\tau)_e \sim T_e^n$, the governing equations can readily be solved for $n = 0, 1.75$, and 2.33 . These results are shown in Fig. 7 for $k_e/k_i = 25$, which is the value appropriate for fully ionized hydrogen. Comparison of the results for $n = 0$ and $n = 2.33$ shows the considerable effect of the temperature dependence of $(\omega\tau)_e$ in reducing the effects of the magnetic field on heat transfer. Since the actual dependence of $(\omega\tau)_e$ is essentially $T_e^{5/2}$, this effect should be slightly more pronounced in the actual case than the two curves indicate. The differences between the analytical result for $n = 2.33$ and the actual numerical results indicate the importance of the other energy-transfer mechanisms, notably diffusion and heavy particle conduction, in determining the total heat transfer.

The point deserving emphasis in this discussion is that the large effect of the magnetic field in reducing the electronic thermal conductivity at the hot surface does not have a correspondingly large influence on total heat transfer; this is, of course, partly due to sources of heat transfer other than electronic conduction and partly due to the strong temperature dependence of $(\omega\tau)_e$. This observation must be tempered by the fact that, for other gases where the contribution of the electronic thermal conductivity to the total heat transfer is a greater fraction than in hydrogen, the effect of the magnetic field will be correspondingly greater.

3.1.4 Effect of net current on electrical characteristics

The effect of passing a net current between the plates on various potential differences and on the electron wall temperature is shown in Fig. 8 for the complete nonequilibrium conditions ($\lambda_\infty = 0$). It should be noted that the current consists of an excess ion flux to the cold surface, which tends to repel more electrons as it is made more negative with

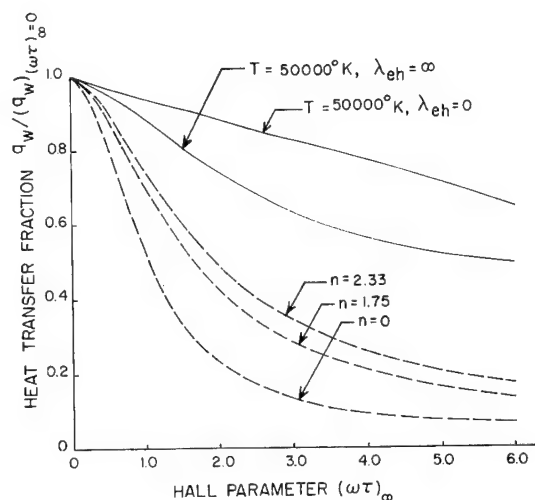


Fig. 7 Magnetic field effects on heat transfer. Broken lines are analytical results for a fully ionized gas (noncatalytic wall) assuming $(\omega\tau)_e \sim T_e^n$ and $r = k_e/k_{in} = 25$.

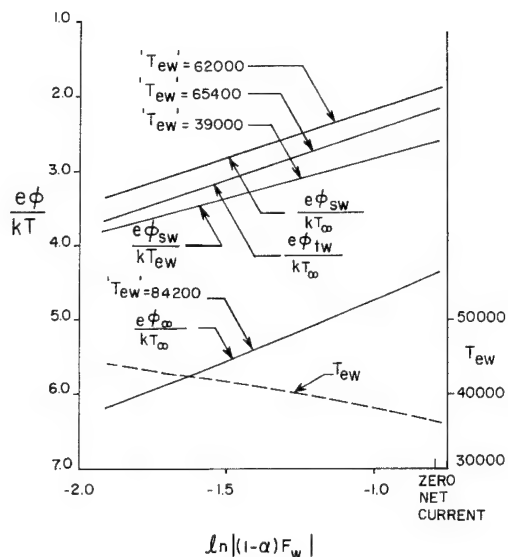


Fig. 8 Effect of net current on various potential differences; $T_\infty = 50,000^\circ\text{K}$.

respect to the hot wall, thus accounting for the increase in T_{ew} as the current increases. By conventional Langmuir probe theory, in which both the electron temperature at the sheath edge and the total ion flux to the cold surface are assumed to be unaffected by the net current, the slopes of the curves labeled $e\phi_{sw}/kT_\infty$ and $e\phi_{sw}/kT_{ew}$ in Fig. 8 should be equal to T_{ew}/T_∞ and unity, respectively. This allows the values for T_{ew} , indicated on each curve, to be deduced from these slopes (evaluated at the point of zero net current). The fact that the temperature deduced from $e\phi_{sw}/kT_{ew}$ is not equal to that of the electrons at the sheath edge indicates that the ion flux is not independent of net current (the ion flux increases by 6.7% as the current increases over the range shown in Fig. 8). The temperature deduced from $e\phi_{sw}/kT_\infty$ ($62,000^\circ\text{K}$) differs drastically from the actual value at the sheath edge ($36,000^\circ\text{K}$) which is somewhat surprising in view of the rather modest change in T_{ew} with j . The rather obvious significance of this discussion is that interpretation of a conventional Langmuir probe characteristic in terms of the electron temperature at these conditions is highly unreliable, unless the voltage is varied at a rate that allows insufficient time for the electron temperature at the sheath edge to change.

3.2 Conclusions

The major conclusions that can be drawn from the present investigation are:

1) The gross features of the continuum solution are relatively insensitive to the sheath-transition region model

employed. The energy transfer between electrons and ions by electric fields external to the sheath-transition region is sensitive to the ion diffusion velocity at the edge of the transition region and, in general, may not be neglected.

2) The ratio $(\lambda_E')_\infty = \lambda_\infty' L^2 / (k_e')_\infty$ is a valid indicator of thermal nonequilibrium effects. In the cases studied, $(\lambda_E')_\infty \lesssim 0.02$ resulted in essentially no collisional energy transfer between electrons and heavy particles, whereas $(\lambda_E')_\infty \gtrsim 4.0$ resulted in virtual thermal equilibrium.

3) Thermal nonequilibrium effects on total heat transfer are strongly influenced by the relative importance of electronic heat conduction to the other heat-transfer mechanisms and, in addition, by the temperature and composition dependences of the heavy particle thermal conductivity and the ion-neutral diffusion coefficient.

4) Magnetic field effects on total heat transfer are much less than the effect on the electron thermal conductivity; departures from thermal equilibrium result in further decreased magnetic field effects.

5) A simple interpretation of the conventional Langmuir probe characteristic in terms of electron temperature at the sheath edge is not possible.

References

- Camac, M. and Kemp, N. H., "A multitemperature boundary layer," AIAA Preprint 63-460 (August 1963).
- Chung, P. M. and J. F. Mullen, "Nonequilibrium electron temperature effects in weakly ionized stagnation boundary layers," Aerospace Corp. Rept. TDR-169(3230-12)TN-7 (May 20, 1963).
- Dix, D. M., "The governing macroscopic equations of partially ionized gases," Aerospace Corp. Rept. TDR-169(2230-04)TN-2 (July 25, 1962).
- Hirschfelder, J., Curtiss, C. F., and Bird, R. B., *Molecular Theory of Gases and Liquids* (John Wiley & Sons, Inc., New York, 1954).
- Kemp, N. H., "A multi-temperature boundary layer," presentation to Aerospace Corp. (October 1963).
- Braginskii, S. I., "Transport phenomena in a completely ionized plasma," Soviet Phys.-JETP 6(33), 358-369 (1958).
- Vanderslice, J. T., Weissman, S., Mason, E. A., and Fallon, R. J., "High temperature transport properties of dissociating hydrogen," Phys. Fluids 5, 155-164 (1962).
- Brown, S. C., *Basic Data of Plasma Physics* (The Technology Press, Cambridge, Mass., 1959), p. 90.
- Fay, J. A., "Hypersonic heat transfer in the air laminar boundary layer," Avco-Everett Research Lab., AMP 71 (March 1962).
- Schulz, G. J. and Brown, S. C., "Microwave study of positive ion collection by probes," Phys. Rev. 98, 1642-49 (1955).
- Jukes, J., "Heat transfer from highly ionized argon produced by shock waves," Thesis, Graduate School of Aeronautical Engineering, Cornell Univ. (June 1956).
- Dix, D. M., "Energy transfer processes in a partially ionized two-temperature gas," Aerospace Corp. TR ATN-64(9232)-1 (1964).
- Bates, D. R. and Kingston, A. E., "Properties of a decaying plasma," Planetary Space Sci. 11, 1-22 (1963).

Hypersonic Magnetohydrodynamics with or without a Blunt Body

R. H. LEVY,* P. J. GIERASCH,† AND D. B. HENDERSON‡

Avco-Everett Research Laboratory, Everett, Mass.

We consider the hypersonic flow of a cold gas past an axially symmetric body containing a magnetic dipole with its axis oriented parallel to the flow. The magnetic moment of the dipole and the size of the body are of arbitrary proportions. A uniform scalar conductivity σ is turned on by the shock, and the magnetic Reynolds number is low. We introduce an interaction parameter $S = \epsilon \sigma B_0^2 r_c / \rho_\infty u_\infty$, where $\epsilon (\ll 1)$ is the reciprocal compression ratio across a strong shock, B_0 is the magnetic field strength at the shock, r_c is the shock radius of curvature, and ρ_∞ and u_∞ are the density and velocity in the freestream. When $S \ll \epsilon^{1/2}$, the flow is quasi-aerodynamic. Certain discrepancies existing in the literature on the flow in this regime are reconciled. When $S \gg \epsilon^{1/2}$, a thin layer somewhat akin to a shock layer is formed behind the shock, but this whole layer is separated from the body by an extensive region of low Mach number flow. When $S \approx 1.6$, the entire flow field can be supported by the magnet, i.e., without the hot gas touching the body. Assuming a large compression ratio across the shock, a simple analysis can be performed. Calculations covering various representative cases are exhibited; the validity and significance of these calculations are discussed.

Nomenclature

$x, y, r, \theta,$	
$R, \phi, n, s,$	
\bar{r}, \bar{n}, ξ	= various coordinates
u, v	= velocity components
p	= pressure
ρ	= density
B	= magnetic field
B_r, B_θ, B_s, B_n	= various magnetic field components
j	= current density
σ	= conductivity
ψ	= stream function
S	= interaction parameter
ϵ	= limiting shock compression ratio
$r_c, r_s, r_b, \Delta, \delta$	= various distances
κ	= curvature
k	= reference pressure gradient
η	= magnetic field line parameter
I, M, P	= integral quantities
t	= dummy variable
G, h, f_1, f_2	= auxiliary functions

Subscripts

0	= reference quantity
∞	= freestream value
M	= matching
L	= deceleration layer

I. Introduction

WE consider the interaction between a hypersonic flow and a fixed magnetic field under conditions for which the magnetic Reynolds number is negligibly low. Such flows can be regarded as entirely aerodynamic in structure, although differing from traditional types of aerodynamic flows in that the applied forces act through a volume rather than at surfaces. In addition to assuming that the magnetic Reynolds number will be small, we shall suppose that the con-

ductivity of our gas will be "turned on" by a strong bow shock wave. This assumption corresponds to the conditions encountered in hypersonic flight in planetary atmospheres. We shall see later on that it will be legitimate to consider this conductivity as a constant over an interesting part of the flow field. Now these general conditions have formed the basis of quite a few studies. We can distinguish two groups of such studies, namely, those in which the flow is considered to be primarily aerodynamic and is modified by the magnetic field, and those in which the flow is dominated by the magnetic interaction and the presence of a body is of secondary importance. We shall be concerned with both categories, but will emphasize in particular those flows in which forces exerted at solid surfaces play a negligible role. However, it will be useful to review briefly both categories of studies in order to establish a perspective.

A group of papers by Kemp,¹ Bush,² and Lykoudis³ deals with the modification by a magnetic field of the hypersonic flow of gas over a body. The points of difference between these papers are largely in the choice of method, the actual problem being similar in all cases. Although not explicitly stated in all the papers, the general idea is that the magnetic forces are less than those exerted at the surface of the body. Bush, however, does suggest the possibility of the opposite extreme. The results of all these papers are given in terms of calculated modifications of the aerodynamic flow. Thus, the effect of the magnetic field is to reduce the stagnation-point velocity gradient, to increase the shock standoff distance, and therefore to reduce the convective stagnation-point heat transfer. The drag is largely unaffected.

A different approach is given in a paper of Levy and Petschek.⁴ Here, a rather special two-dimensional problem is studied with a view to describing a flow in which the body is entirely absent. The results of such a study clearly cannot be stated with reference to any standard aerodynamic flow. Rather, such parameters as the location of the shock are given in terms, for instance, of the current flowing in the magnet. An important feature of this type of flow is the existence of an inner boundary to the flow behind which the gas density is very low. If the body that houses the magnet is inside this inner zone, it is essentially not in contact with the flow at all, and the convective heat transfer to it should be very small.

In the present paper, we attempt to combine features of both the foregoing problems. The geometry we study is

Received February 14, 1964; revision received June 17, 1964. This research was supported by Headquarters, NASA, under Contract No. NAS w-748. The authors wish to express appreciation to H. E. Petschek for helpful suggestions during the course of this work.

* Principal Research Scientist. Associate Fellow Member AIAA.

† Assistant Scientist.

‡ Assistant Engineer.

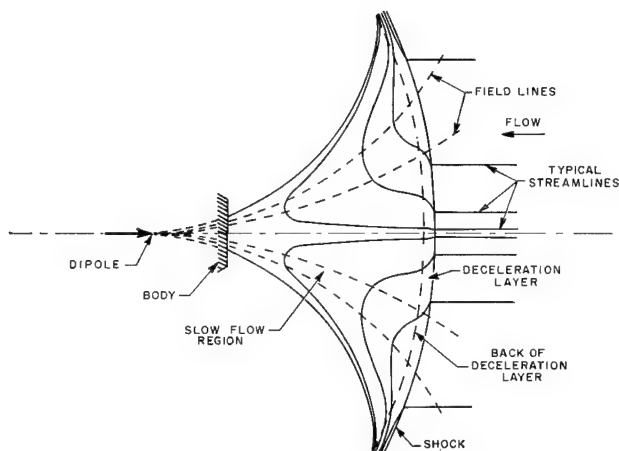


Fig. 1 Illustration of the principal features of the flow to be expected when $S \approx 1$. The conductivity is zero ahead of the shock.

the physically realistic geometry of the first group of papers, but we use the methods of Levy and Petschek and concentrate strongly on the case in which the body plays a negligible role in the flow. In the course of the work, certain discrepancies existing in the first group of papers are resolved, and the flow corresponding to the limit discussed by Bush is extensively described. In subsequent sections, we will analyze the flow in greater detail and discuss particularly the limiting cases in which the flow is principally supported by either the magnetic field or the body. In the last section, we will draw some general conclusions from our study and also describe some of the physical limitations on the validity of our analysis.

The entire analysis described in this paper has been extended to the corresponding two-dimensional problems by Levy et al.⁵; this reference also treats the subject matter of this paper at greater length.

II. Description and Analysis of the Flow

The general features of the flow to be treated are illustrated in Fig. 1, and the coordinate systems and other dimensions used in the analysis are shown in Fig. 2. A strong shock is formed in the gas ahead of the object; behind this shock the gas is weakly conducting. We neglect heat conduction and

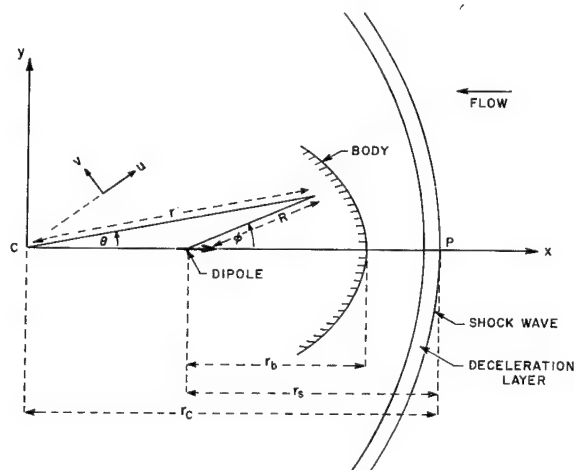


Fig. 2 Illustration of the coordinate systems used in the text. C is the center of curvature of the deceleration layer at the point P . The components (u, v) of the velocity are polar and are referred to the coordinate system (r, θ) with origin at C .

viscosity since the viscous Reynolds number is high; when there is no body in the flow there will not even be a thin viscous boundary layer. The current flow (in the absence of Hall effect) is in the azimuthal direction, and it follows that $\mathbf{j} \cdot \mathbf{E} = 0$. Thus, in our case, each streamline is isolated energetically and therefore has a constant total enthalpy. It follows that the total enthalpy is constant throughout the flow and equal, since the flow is hypersonic, to $\frac{1}{2}u_\infty^2$. In the region where the Mach number is low (behind the normal part of the shock, for example), the static enthalpy will be approximately constant. We shall assume that the properties of the gas are such that the electrical conductivity may be treated as constant when the enthalpy is constant, even though the gas may undergo a considerable expansion. This assumption will allow us to take the conductivity as constant through a large part of the flow. We also assume that the gas conditions are such that the Hall effect may be neglected; in the last section we shall estimate limits to the validity of this assumption.

The statement that the gas is weakly conducting behind the shock is to be taken to mean that the magnetic Reynolds number is low. The general features of flows at low magnetic Reynolds numbers have been outlined elsewhere.^{6,7} In order to have a substantial exchange of momentum between the field and the flow, the product of the magnetic Reynolds number and the ratio of magnetic to dynamic pressures must be of order unity. We call this product the interaction parameter and denote it by S . Throughout this paper, we will use an interaction parameter defined by $S = \epsilon B_0^2 r_c / \rho_\infty u_\infty$, where $\epsilon \ll 1$ is the reciprocal compression ratio across the shock, σ the conductivity behind the shock, B_0 the field strength at the normal point of the shock, and r_c the radius of curvature of the shock.

The geometrical configuration shown in Fig. 1 is generically the same as that treated by Bush et al. The body is taken to be axially symmetric but need not be spherical. The magnetic field is that due to a dipole whose axis coincides with the axis of the body and with the flow direction. The location of the dipole is, within the limitations of symmetry, arbitrary, except that it is supposed not to be right at the stagnation point of the body. Also, we do not make any a priori assumption about the shape or the location of the shock.

We define the deceleration layer (Fig. 1) as the region just behind the shock for which the velocity component parallel to the shock is larger than the component normal to the shock. (The deceleration layer reduces when there is no magnetic interaction to the aerodynamic shock layer. The reason for this choice of terminology will become apparent later on.) Although this definition breaks down near the place where the shock is normal, it can be extended in a consistent manner to the stagnation streamline by using the gradient of the velocity component parallel to the shock, multiplied by the radius of curvature of the shock. The important thing to notice is that, because of the requirement of continuity, the deceleration layer as defined is thin. In fact, since the ratio of the velocity components perpendicular and parallel to the shock is on the order of ϵ , the continuity equation tells us that the thickness of the layer is approximately ϵr_c , where r_c is the radius of curvature of the shock. Since $\epsilon \ll 1$, we introduce in the deceleration layer the expanded coordinate \tilde{r} defined by $\tilde{r} = \epsilon^{-1}(1 - r/r_c)$, so that $\tilde{r} = 0$ at the shock and is of order unity at the back of the layer.

We commence our detailed analysis of the flow problem in that part of the deceleration layer which is close to the place where the shock is normal. We nondimensionalize all the flow quantities in accordance with the general picture of the flow anticipated in the deceleration layer. Thus, the pressure is nondimensionalized with the freestream dynamic pressure, $\rho_\infty u_\infty^2$, the density with the density behind a strong shock, ρ_∞ / ϵ , all distances with r_c , the velocity components in the radial and tangential directions with ϵu_∞ and u_∞ , and

the magnetic field with B_0 . In the deceleration layer we shall neglect $1/r$ compared with $\partial/\partial r = (-1/\epsilon r)(\partial/\partial \bar{r})$. We also neglect the change in the field components across the layer.

The energy equation, as has already been explained, has for an integral the condition of constant total enthalpy throughout the flow. We shall suppose the gas to be so close to perfect that the enthalpy may be taken to be proportional to p/ρ . Then, with the nondimensionalization just described, the energy equation reduces to

$$p = \rho(1 - v^2) \quad (2.1)$$

with the neglect of terms of order ϵ^2 . v , B_θ , and j are odd functions of θ , and all other quantities are even functions of θ . Hence, on the stagnation streamline $\theta = 0$,

$$p = \rho \quad (2.2)$$

The equation of continuity reduces, on the stagnation streamline, to

$$d(\rho u)/d\bar{r} = 2\rho \partial v/\partial \theta \quad (2.3)$$

The quantities appearing in (2.2) and (2.3) are regarded as functions of \bar{r} only. This method gives the appearance of treating the stagnation streamline by itself, but is, in fact, no different in principle from the methods common in aerodynamics⁸ involving expansions in powers of θ . On the stagnation streamline the current (nondimensionalized with $\sigma u_\infty B_0$) is given by

$$\partial j/\partial \theta = \epsilon u \partial B_\theta/\partial \theta - B_\theta \partial v/\partial \theta \quad (2.4)$$

This is the appropriate form of Ohm's law. We shall assume that $\partial B_\theta/\partial \theta \ll \epsilon^{-1} B_r$. This condition implies only that the dipole is not located right at the back of the deceleration layer. A result of this assumption is that we may take the current in the deceleration layer to be given on the stagnation streamline by

$$\partial j/\partial \theta = -\partial v/\partial \theta \quad (2.5)$$

The radial momentum equation reduces in the deceleration layer to

$$\rho v^2 + dp/d\bar{r} + SB_\theta v = 0 \quad (2.6)$$

On the stagnation streamline, this gives

$$dp/d\bar{r} = 0 \text{ and therefore } p = 1 \quad (2.7)$$

Thus, to this approximation, the pressure on the stagnation streamline is constant. From (2.2) we immediately deduce, also for the stagnation streamline, that the density is constant, or $\rho = 1$. Applying this to the continuity equation as written for the stagnation streamline (2.3) gives

$$du/d\bar{r} = 2 \partial v/\partial \theta \quad (2.8)$$

We shall use (2.6) to deduce the pressure gradient at the back of the deceleration layer when we have found a suitable profile for v . We therefore differentiate it twice with respect to θ and set $\theta = 0$ to find (since $\rho = 1$)

$$d(\partial^2 p/\partial \theta^2)/d\bar{r} = -2(\partial v/\partial \theta)^2 - 2S(\partial B_\theta/\partial \theta)(\partial v/\partial \theta) \quad (2.9)$$

We shall return to this equation in due course. The tangential momentum equation in the deceleration layer reduces on the stagnation streamline (after differentiation with respect to θ) to

$$-u d(\partial v/\partial \theta)/d\bar{r} + (\partial v/\partial \theta)^2 + \epsilon \partial^2 p/\partial \theta^2 + S \partial v/\partial \theta = 0 \quad (2.10)$$

We can neglect the pressure gradient in this equation as long as we do not integrate beyond the point where the other terms become comparable to the pressure gradient. Thus,

$$-u d(\partial v/\partial \theta)/d\bar{r} + (\partial v/\partial \theta)^2 + S \partial v/\partial \theta = 0 \quad (2.11)$$

This must be solved, together with (2.8). The boundary conditions at the shock are $u = -1$, $\partial v/\partial \theta = 1$. The solution may be written implicitly as

$$\begin{aligned} \bar{r} &= \{[1 - (-u)^{1/2}]/(1 + S)\} - \\ &\quad [S/(1 + S)^2] \ln[(-u)^{1/2}(1 + S) - S] \quad (2.12) \\ \bar{r} &= [(1 - \partial v/\partial \theta) - S \ln \partial v/\partial \theta](1 + S)^{-2} \end{aligned}$$

These equations show the principal features of the behavior of the flow in the deceleration layer. The inward radial velocity tends to the limit $S^2/(1 + S)^2$, whereas the tangential velocity decreases without limit as we approach the back of the layer. In order to find the back of the deceleration layer, we use the profile of (2.12) in (2.10) and see at what point the equation is no longer a balance between two terms both larger than the pressure gradient term. Substitution shows that we must distinguish two cases:

1) If S is small, (2.10) can be considered as a balance between the two convective terms. This is the aerodynamic limit. At a distance $\bar{r} \approx 1$, $\partial v/\partial \theta \approx \epsilon^{1/2}$, and the pressure gradient becomes important. At this point $-u \approx \epsilon$.

2) If S is large, (2.10) can be considered as a balance between the first of the two convective terms and the magnetic term. This is the magnetohydrodynamic limit. At a distance $\bar{r} = S(1 + S)^{-2} \ln(S/\epsilon)$, $S(\partial v/\partial \theta) = \epsilon$, and the pressure gradient becomes important. At this point $-u = S^2(1 + S)^{-2}$.

This leads to an interesting situation; apart from extremely small values of the interaction parameter, the transverse component of the velocity at some distance back from the shock may fall to low values before we reach the body (the body is where the radial velocity vanishes). By our definition, the place where the two components are comparable in magnitude is the back of the deceleration layer. Thus, in the magnetohydrodynamic case, there may be an outflow from the back of the deceleration layer. There is, therefore, an additional flow region behind the deceleration layer which will have to be studied in order to complete the solution to the whole flow problem. In view of the fact that in this region both velocity components are of order ϵu_∞ , we call it the "slow flow region" (see Fig. 1). Since the Mach number is very low, the convection of momentum in it will be negligible compared to the pressure gradients and the magnetohydrodynamic forces. The balance of these last two, therefore, determines the nature of the flow. Two additional remarks concerning the slow flow region are important. First, since the velocity components in both directions are comparable, the equation of continuity shows that the dimensions of the slow flow region are roughly comparable in all directions. Secondly, since there is no magnetohydrodynamic force along the field lines, the pressure is a given constant for each field line.

Now, in order to solve the flow in the slow flow region, we must know, from study of the deceleration layer, the pressure on each field line and the flow velocity across the boundary between the regions. We have shown how to calculate the latter, and it remains to determine the pressure at the back of the layer. This is done using (2.9). Now $\partial^2 p/\partial \theta^2 = -2$ at the shock, $\bar{r} = 0$, since $p \sim \cos^2 \theta$. Therefore, integrating (2.9) and evaluating it at the back of the deceleration layer where $\partial v/\partial \theta$ is small, we find

$$k = -\frac{\partial^2 p}{\partial \theta^2} \bigg|_{\theta=0} = 2 + \frac{2/3}{(1 + S)^2} + \frac{S[1 + (\partial B_\theta/\partial \theta)]}{(1 + S)^2} + \frac{2S^2(\partial B_\theta/\partial \theta)}{(1 + S)^2} \quad (2.13)$$

The first of these terms represents the pressure gradient at the shock, the second is the centrifugal effect, and the last two are the magnetohydrodynamic effect. For the dipole, as shown in Fig. 2,

$$\partial B_\theta/\partial \theta|_{\text{stag. pt.}} = (3 - 2r_s)/2r_s \quad (2.14)$$

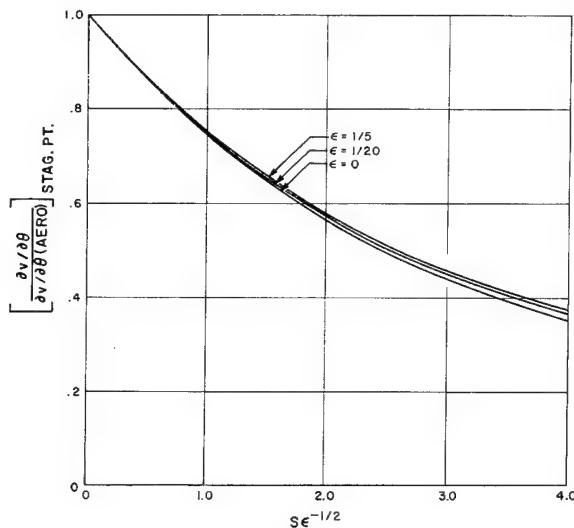


Fig. 3 Illustration of the reduction in the stagnation-point velocity gradient effected by introducing a magnetic field. The calculation is reasonable only as far as $S\epsilon^{-1/2} \approx 1$.

If the dipole happens to be right at the center of curvature of the shock, $r_s = 1$. We see that the centrifugal effect is always weakened by the presence of a magnetic field and that the magnetohydrodynamic effect can be of either sign, depending on whether the field lines in the deceleration layer appear to diverge from a point ahead of or behind the center of curvature of the deceleration layer. These remarks explain the difference in the sign of the change in the body pressure gradient in the work of Kemp and Bush. Kemp has a pole at the center of curvature of the deceleration layer. The only effect on the pressure is, then, that the centrifugal effect is reduced. As a result, the pressure at the body is higher than in the aerodynamic case, and the stagnation-point pressure gradient is reduced. Bush, on the other hand, has a dipole at the center of curvature of the shock layer. Thus, the magnetic force is outward, the pressure on the body is reduced, and the stagnation-point pressure gradient is increased.

In order to find the remaining details of the deceleration layer near $\theta = 0$, we substitute k for the pressure gradient in (2.10). This will not affect the solution near the front of the layer (where $-\partial p^2/\partial \theta^2 = -2$ not k) but is important at the back, where $\partial^2 p/\partial \theta^2$ is equal to k . Equation (2.10) becomes

$$-u d(\partial v/\partial \theta)/d\bar{r} + (\partial v/\partial \theta)^2 + S \partial v/\partial \theta - k\epsilon = 0 \quad (2.15)$$

Equations (2.8) and (2.15) have been integrated by Lykoudis³ on the assumption that $k = \frac{8}{3}$, its aerodynamic value, obtained from (2.13) by setting $S = 0$. We have repeated the integration using (2.15) as appropriate. The stagnation-point velocity gradient ratio is plotted in Fig. 3. The standoff distance is plotted in Fig. 4. The differences from Lykoudis' calculation are small when $S\epsilon^{-1/2}$ is small. The line on Fig. 3 marked $\epsilon = 0$ corresponds exactly to Lykoudis' calculation in the sense that if $\epsilon = 0$, but $S\epsilon^{-1/2}$ is finite, S must be zero and hence k takes its aerodynamic value. Also shown in Fig. 4 are the thicknesses of the deceleration layer, defined as the region where $1 \geq -u \geq S^2(1+S)^{-2}$. The difference between these two lengths is the incipient slow flow region. All the lengths in Fig. 4 are normalized with respect to the aerodynamic standoff distance, $\epsilon[1 + (8\epsilon/3)^{1/2}]^{-1}$. It can be seen that, with increasing $S\epsilon^{-1/2}$, the deceleration layer thickness does not change very much, whereas the total standoff distance grows rapidly. This merely confirms our previous discussion in which, for large $S\epsilon^{-1/2}$ we divided the flow into a thin deceleration layer and a fat slow flow region. Figure 4, therefore, illustrates

the incipient growth of the slow flow region. It cannot, however, be used, as Lykoudis has used it, to determine the distance between the body and the shock when $S\epsilon^{-1/2} > \text{about } 1$. The reasons for this are that the assumptions that went into (2.15) from which the numbers appearing in Fig. 4 were calculated are violated as follows in the region $-u < S^2(1+S)^{-2}$.

1) The tangential velocity is reduced to the same order of magnitude as the radial velocity, so that, referring to (2.4), the current is no longer given by (2.5).

2) The fact that the velocity components are equal in order of magnitude implies that the scale of the problem is no longer compressed. Thus, the flow now extends over regions comparable in size in all directions with the body, and the pressure gradient can no longer be treated as constant.

3) The deceleration layer can no longer be assumed concentric with the body and the dipole.

To conclude this part of the work, we point out that the type of analysis used here, in the magnetohydrodynamic as in the aerodynamic case, gives the standoff distance of the shock in terms of the shock radius of curvature, but does not give the radius of curvature of the body. To establish the body radius of curvature, we must consider the flow at greater distances from the stagnation streamline.

We next turn to the study of the slow flow region, which intervenes between the deceleration layer and the body and in which both velocity components are of order ϵu_∞ . Since this velocity is strongly subsonic, the enthalpy is effectively constant and from (2.1),

$$p = \rho \quad (2.16)$$

although these quantities will vary considerably through the region. We note that this isenthalpic motion may involve a considerable rise in the entropy. Since the flow is subsonic, we may neglect the convection of momentum and consider the flow to be governed by the remains of the momentum equation:

$$\nabla p = S \mathbf{j} \times \mathbf{B} \quad (2.17)$$

The neglect of the inertia term in (2.17) will result in infinite velocities; these should be interpreted as sonic. The equation of continuity is

$$\nabla \cdot \rho \mathbf{u} = 0 \quad (2.18)$$

These equations may be considered to have been nondimensionalized just as before, with two exceptions. Both components of velocity are now nondimensionalized with respect to ϵu_∞ , and distances are referred simply to r_c . The current now involves contributions from both velocity components. We shall find it convenient to work in the polar coordinates (R, ϕ) fixed at the dipole and define the radial and tangential velocity components in these coordinates by means of a stream function ψ , nondimensionalized with respect to $\rho_\infty u_\infty r_c$. The components are

$$-\frac{1}{\rho R \sin \phi} \frac{\partial}{\partial \phi} (\psi \sin \phi) \quad \frac{1}{\rho R} \frac{\partial}{\partial R} (\psi R) \quad (2.19)$$

Note that this stream function is defined like a vector potential, that is to say, the mass flow vector is represented as the curl of a vector of magnitude ψ pointing in the azimuthal direction. Thus, the streamlines are represented not by $\psi = \text{const}$, but by $R \sin \phi \psi = \text{const}$. The choice of definition is arbitrary, but the distinction must be remembered when plotting streamlines. We multiply (2.17) by $p = \rho$ and find

$$\frac{1}{2} \nabla p^2 = S(\rho \mathbf{v} \times \mathbf{B}) \times \mathbf{B} \quad (2.20)$$

When we substitute from (2.19) in (2.20), we find two linear equations [the components of (2.20)] for the two unknowns p^2 and ψ . The field components are

$$\mathbf{B} = (r_s/R)^3 \cos \phi \quad \frac{1}{2}(r_s/R)^3 \sin \phi \quad (2.21)$$

Resolution of (2.20) along the magnetic field gives the result that p is a function only of

$$\eta = r_s^2 R^{-1} \sin^2 \phi \quad (2.22)$$

so that the pressure has a constant value on any field line. Resolution of (2.20) across the field lines and use of the knowledge that $p = p(\eta)$ lead to

$$-\sin \phi \frac{dp^2}{d\eta} = S \left(\frac{r_s}{R} \right)^4 \left[\frac{\cos \phi}{R} \frac{\partial}{\partial R} (R\psi) + \frac{1}{2R} \frac{\partial}{\partial \phi} (\psi \sin \phi) \right] \quad (2.23)$$

In view of the fact that $dp^2/d\eta$, like p , is a function of η alone, we can find solutions of (2.23) of the form

$$\psi = -(1/S)(dp^2/d\eta)G(R, \phi) \quad (2.24)$$

G satisfies the equation

$$\left(\frac{r_s}{R} \right)^4 \left[\frac{\cos \phi}{R} \frac{\partial}{\partial R} (GR) + \frac{1}{2R} \frac{\partial}{\partial \phi} (G \sin \phi) \right] = \sin \phi \quad (2.25)$$

A particular solution of this equation is

$$G = \left(\frac{2R^5}{r_s^4} \right) \sin^{-13} \phi \int_0^\phi \sin^{13} t dt \quad (2.26)$$

In addition, any function $(R \sin \phi)^{-1} h(\eta)$ satisfies the homogeneous part of (2.25) so that the general solution of the problem is

$$\psi = -\frac{1}{S} \frac{dp^2}{d\eta} \frac{1}{R r_s^4 \sin \phi} \left[\frac{2R^6}{\sin^{12} \phi} \int_0^\phi \sin^{13} t dt + \eta h(\eta) \right] \quad (2.27)$$

This equation tells us everything we need to know about the slow flow region. We notice in particular that ψ vanishes on three separate lines: first, on the stagnation streamline since (by symmetry) $dp/d\eta$ vanishes; second, on the body where the quantity in brackets vanishes. Since $h(\eta)$ is arbitrary, any body can be described. Finally, ψ vanishes on the two symmetrically placed field lines for which p vanishes.

We find some relationships among S , r_s , and r_b by using the results just obtained. At the back of the deceleration layer the pressure is given for small values of θ (and therefore for small η) by

$$p \approx 1 - \frac{1}{2} k r_s \eta \quad (2.28)$$

from (2.13) and the definition of η (2.22). Since, in the slow flow region, p is a function of η alone, (2.28) is valid for any r between the shock and the body. Next, we specialize the general solution for the stream function in the slow flow region (2.27) to the stagnation streamline. This gives us

$$\psi \approx (r\theta k / S r_s^3) \{ (R^4/7) + [h(0)r_s^2/R^3] \} \quad (2.29)$$

From this relation, we can find the flow near $\theta = 0$ all the way from the shock to the body. In particular, at the shock we can calculate the radial velocity

$$u \approx (-1/\rho r_s \phi) \partial(\psi\phi)/\partial\phi \approx (-1/\theta) \partial(\psi\theta)/\partial\theta |_{\theta=0; r=1} \quad (2.30)$$

However, this radial velocity has already been calculated in (2.12). It is just the residual radial velocity at the back of the deceleration layer. Thus, we find the important matching condition

$$[S/(1+S)]^2 = (2k/Sr_s^3) \{ (r_s^4/7) + [h(0)/r_s] \} \quad (2.31)$$

To find $h(0)$, we recall that the body is given when $\psi = 0$ as a result of the vanishing of the last bracket in (2.29). Using this to eliminate $h(0)$ from (2.31) gives

$$21S^3 - [18S^2 + (24r_s + 9)S + 16r_s] \times [1 - (r_b/r_s)^7] = 0 \quad (2.32)$$

This is the sought after relation between S , r_s , and r_b . From it we can make a number of deductions, the most important of which is the following: In a given flight situation (i.e., ρ_∞ , u_∞ , and ϵ given, as well as the magnetic moment of the dipole and its location relative to the body), (2.32) does not give unique values for the quantities appearing in it. We recall that r_b and r_s are nondimensionalized with respect to r_c , and that r_c is also the length appearing in the definition of S . Suppose some value of r_c is given; then from the geometry we can calculate r_b . However, S is proportional to B_0^2 , which in turn is proportional to the inverse sixth power of r_s . But this procedure will be valid for any r_c , and there is no way of knowing which is correct.

We measure the standoff distance by means of a non-dimensional distance $\Delta = (r_s/r_b) - 1$. Equation (2.32) gives, in terms of S and r_s ,

$$\Delta = [1 - 21S^3 \{ 18S^2 + (24r_s + 9)S + 16r_s \}^{-1}]^{1/7} - 1 \quad (2.33)$$

The standoff distances calculated in this way are not directly comparable to the aerodynamic standoff distance, for the aerodynamic standoff distance is a quantity of order ϵ , whereas Δ in (2.33) is of order unity. This is a result of the slow flow region having comparable dimensions parallel and perpendicular to the flow. These remarks also explain why, if we put $S = 0$ in (2.33), we recover $\Delta = 0$.

There are values of S and r_s such that $\Delta \rightarrow \infty$. They satisfy the relation

$$21S^3 - 18S^2 - (24r_s + 9)S - 16r_s = 0 \quad (2.34)$$

These values are of particular interest to us. They do not correspond to an infinite distance from the shock to the dipole, but rather to a zero distance between the body and the dipole $r_b = 0$. Thus, they correspond to what we refer to as the fully magnetohydrodynamic case. The region on the body in contact with the flow shrinks to a point, and the entire drag generated by the flow field is felt by the magnet.

We can compare our analytical calculations (for $\epsilon \ll 1$) up to this point with Bush's numerical calculations for $\epsilon = \frac{1}{11}$, which assume the dipole is at the center of curvature of the shock, by setting $r_s = 1$ in (2.33). When the interaction parameters are modified to allow for differences in notation, the agreement is quite good. In particular, for the axisymmetric case, Bush finds $\Delta = \infty$ for $S \approx 1.53$. This compares with our value $\Delta = \infty$ for $S = 1.90$ from (2.34) with

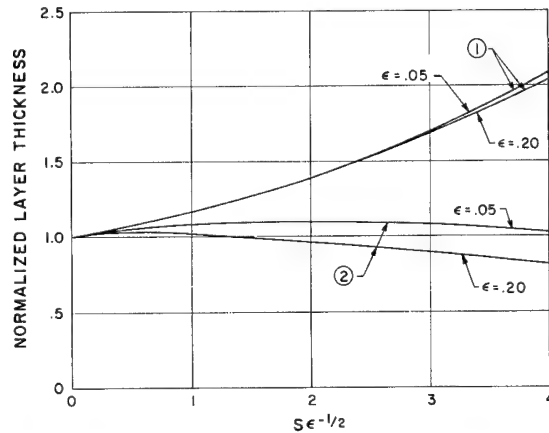


Fig. 4 Illustration of the increase in the shock standoff distance effected by introducing a magnetic field. The calculation is reasonable only as far as $S\epsilon^{-1/2} \approx 1$. The lines marked 1 represent the entire standoff distance. The lines marked 2 give the thickness of the deceleration layer defined as extending from the shock to the place where $-u = S^2(1+S)^{-2}$. These lengths are normalized with respect to the aerodynamic shock-layer thickness.

$r_s = 1$. The difference can probably be attributed to finite ϵ effects.

The picture we now have of the flow for $S \gg \epsilon^{1/2}$ is as follows. The deceleration layer is no longer in contact with the body, but is separated from it by the slow flow region. There is no longer any justification for assuming that the layer is concentric with the body, or, for that matter, with the dipole. Whatever the geometry, the type of flow we expect is illustrated schematically in Fig. 1. The pressure at the back of the deceleration layer is reduced by the combined action of the centrifugal and magnetic forces. At the same time, the component of velocity parallel to the deceleration layer at the back of the layer rises as we proceed away from the stagnation streamline; the gradient of this velocity component at the stagnation streamline is $\epsilon u_\infty r_c^{-1}$, but it will subsequently grow more rapidly when the angle between the field and the deceleration layer becomes small. At some point, it will reach sonic velocity $\epsilon^{1/2} u_\infty$. At this point, the flow in the "slow flow region" can no longer be slow. On the other hand, flow that entered the slow flow region near the axis can be expected to escape at higher speed in the general direction of the magnetic field. The analysis of this flow is beset with a number of difficulties. Thus, as the velocity rises, the temperature and hence the conductivity will fall; furthermore, the density will also be lower away from the stagnation streamline; at some point nonequilibrium, Hall and ion-slip effects must all become important. Two methods are available at this stage. The first, used by Bush (and others), is to introduce the ad hoc assumption that the dipole is at the center of curvature of the shock wave. No justification of this assumption seems possible, but it does lead to a definite problem that can be solved without discussing the tricky matter of the nature of the flow near the sonic points. The second alternative is to construct a satisfactory model of the flow out to the sonic point. In this paper we have adopted the second alternative; we shall see, however, that in order to construct this flow we are obliged to make assumptions about gas properties that are not too well justified in practice. An important result of our analysis will be a reasonable degree of agreement between our results and those of Bush. Since the results are obtained by different methods, it is felt that each lends support to the other.

We now have a solution for the slow flow region valid everywhere behind the deceleration layer and a solution for the deceleration layer near the stagnation streamline. To complete the construction of a model valid to the sonic point

we need to study the deceleration layer away from the stagnation streamline. The results we need, in order to match a possible shock configuration to the slow flow region, are the pressure and the normal velocity at the back of the layer. In the absence of analytical solutions we have to resort to approximate methods. Since we do not know a priori the shape of the layer, we must introduce an arbitrary system of coordinates fixed in the layer. This system is shown in Fig. 5. n and s are coordinates perpendicular and parallel to the layer. The position of the layer itself is referred to Cartesian coordinates fixed at the center of curvature of the normal part of the layer. Thus, it is given parametrically in terms of the arc length s by $x = x_L(s)$, $y = y_L(s)$; the subscript referring to the layer. Using (as before) r_c as the unit of length, x_L and y_L are given for small s by

$$x_L = 1 - \frac{1}{2}s^2 \dots \quad y_L = s - \frac{1}{6}s^3 \dots \quad (2.35)$$

u and v are the components of velocity in the n and s directions. Since the thickness of the layer is on the order of ϵr_c , we introduce a coordinate \tilde{n} such that $\tilde{n} = 0$ is at the shock and $\partial/\partial \tilde{n} = (-1/\epsilon) \partial/\partial n$. The continuity equation is

$$\partial(\rho u)/\partial \tilde{n} - (1/y_L) \partial(\rho v y_L)/\partial s = 0 \quad (2.36)$$

where u and v are nondimensionalized with respect to ϵu_∞ and u_∞ , respectively. The current is effectively given by

$$j = -v B_n \quad (2.37)$$

where B_n is the component of the magnetic field normal to the layer. This expression is valid until B_n is comparable with ϵB_s , where B_s is the component of the magnetic field parallel to the layer. At this point, as we will see, the current no longer affects the dynamics of the layer appreciably and can therefore be neglected. B_s and B_n may be regarded as functions of s only. The normal momentum equation becomes

$$\kappa \rho v^2 + \partial p / \partial \tilde{n} + S v B_n B_s = 0 \quad (2.38)$$

κ , the curvature of the layer, is a function only of s and is given in terms of the derivatives of x_L and y_L . The s momentum equation is

$$\rho u \partial v / \partial \tilde{n} - \rho v \partial v / \partial s - S v B_n^2 = 0 \quad (2.39)$$

Finally, the energy equation is just the same as (2.1). At the shock, $\tilde{n} = 0$, we have the following boundary conditions (dot indicates d/ds):

$$\rho = 1 \quad p = \dot{y}_L^2 \quad u = -\dot{y}_L \quad v = -\dot{x}_L \quad (2.40)$$

As indicated earlier, we lack general solutions to these equations. Consequently, we resort to a momentum integral method somewhat analogous to that used in boundary-layer theory.⁹ We introduce the quantities

$$\begin{aligned} I(s) &= \int v d\tilde{n} & M(s) &= \int \rho v d\tilde{n} \\ P(s) &= \int \rho v^2 d\tilde{n} \end{aligned} \quad (2.41)$$

These quantities measure, respectively, the current, mass flux, and momentum flux in the deceleration layer. The integrals are carried from the shock $\tilde{n} = 0$ to the effective back of the layer. On integrating (2.38) across the layer, we find

$$\kappa P + p_M - \dot{y}^2 + S B_n B_s I = 0 \quad (2.42)$$

where $p_M(s)$ is the pressure at the back of the deceleration layer. The subscript indicates that we will use this quantity to match with our solution for the flow in the slow flow region. Integrating (2.39) through the layer and making use of the continuity equation (2.36) leads to

$$[\rho u v] - (1/y_L) \int \partial(\rho v^2 y_L) / \partial s d\tilde{n} - S B_n^2 I = 0 \quad (2.43)$$

We can evaluate $\rho u v$ at the shock using (2.40). At the back

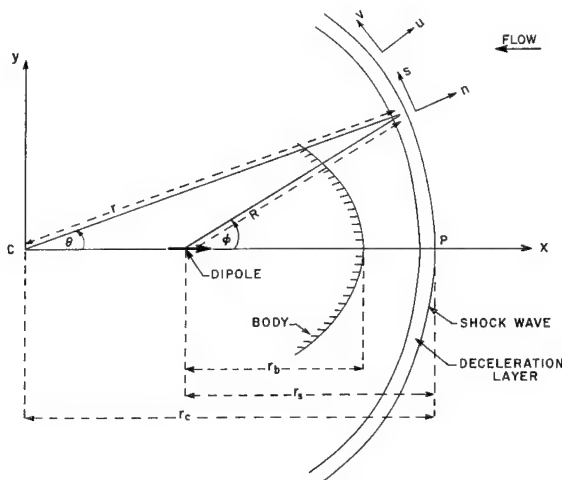


Fig. 5 Illustration of the coordinate system used in the analysis of the deceleration layer away from the stagnation line. C is the center of curvature of the deceleration layer at the point P . The components (u , v) of the velocity are, respectively, in the n and s directions. In the text, the length r_c is taken to be unity.

of the layer it is effectively zero since v is reduced to the order of ϵ at that point. Thus,

$$\dot{x}_L \dot{y}_L + (1/y_L) d(P y_L)/ds + S B_n^2 I = 0 \quad (2.44)$$

Rather than evaluate the normal component of velocity at the back of the layer, it is convenient to introduce a stream function appropriate to the layer defined by

$$\rho u = -(1/y_L) \partial(\psi y_L)/\partial s \quad \rho v = -\partial\psi/\partial \tilde{n} \quad (2.45)$$

Noting that $\psi = \frac{1}{2} y_L$ at the shock, integration of the second equation (2.45) gives

$$M = \frac{1}{2} y_L - \psi_M \quad (2.46)$$

where ψ_M is the stream function at the back of the shock layer. ψ_M and p_M are the two quantities we use to relate the deceleration layer to the slow flow region.

An interesting observation to make on (2.42) and (2.44) is that, if $S = 0$, corresponding to the aerodynamic case, we can eliminate P directly and find the Busemann relation¹⁰ for the pressure in Newtonian shock layers. When the magnetic interaction is present, no such simple result is available to us. We now have to assume profiles for v and ρ through the layer in terms of a shape parameter $\delta(s)$ of some kind, so that I , M , and P can all be expressed as functions of $\delta(s)$. The problem can then be shown⁵ to reduce to a system of five ordinary differential equations for the six unknowns, x_L , y_L , κ , δ , ψ_M , and p_M . To complete the set, we need to introduce one further relation, and this is the slow flow solution (2.27). Along the deceleration layer we have

$$d\eta/ds = (2R/r_s) B_n \sin\phi \quad (2.47)$$

so that (2.27) becomes

$$\psi_M = -\frac{p_M}{S B_n} \frac{dp_M}{ds} \left[\frac{2R^4}{r_s^3} \int_0^\phi \frac{\sin^{13} t dt}{\sin^{14} \phi} + \frac{h(\eta)}{r_s R^3} \right] \quad (2.48)$$

The equations just described can be used to solve two fundamentally different problems. The first of these, which we call the direct problem (by analogy to a somewhat similar aerodynamic problem), is that in which the body shape and the dipole location relative to the body are given. It is required to find the shape of the shock wave and the deceleration layer. The second problem, which we call the inverse problem, is that in which the shape of the shock wave and deceleration layer are given and also the location of the dipole relative to the shock wave. It is required to find the body shape. We shall give numerical results for both these types of problems subsequently, but before proceeding to these calculations we must consider again our model of the flow in the region away from the stagnation streamline. We have seen how to calculate along the deceleration layer, and we have seen how to join to the deceleration layer a consistent slow flow region. How far can we take this process?

As we proceed along the deceleration layer, p_M falls. Where it reaches zero, the deceleration layer is fully supported by the centrifugal and $j \times B$ forces. Clearly, this point is a natural limit to the validity of our calculation. Another such limit can be found by considering the component of magnetic field normal to the deceleration layer. In all reasonable configurations this field component must drop and will eventually reach zero. We assume that these two points (i.e., the points where p_M and B_n vanish) coincide.

In justification of this model, suppose first that p_M reaches zero while B_n is finite. Equation (2.48) shows that at this point $\psi_M = 0$, that is, the stagnation streamline reaches the deceleration layer at this point. This implies that all the slow flow region is exhausted by being forced back into the deceleration layer. By the definition of the deceleration layer this implies that the slow flow is accelerated at least to sonic velocity in some region near the back of the deceleration layer. But the $j \times B$ force would oppose this acceleration,

and therefore, if it exists, it must be due to the pressure gradient. But previously, we saw that, as long as $S\epsilon^{-1/2} \gg 1$, the $j \times B$ force is always greater than the pressure gradient. The argument given there is directly applicable to our case as long as B_n remains of order unity. If B_n is of order $\epsilon^{1/4}$, however, the effective interaction parameter makes $S\epsilon^{-1/2} \sim 1$, in which case the pressure gradient does become important. But, on our assumption that $\epsilon^{1/4}$ is small, this implies that B_n is small, which is contrary to our hypothesis. Thus we reject situations in which p_M goes to zero before B_n . The weakest link in the foregoing argument is the assumption $\epsilon^{1/4} \ll 1$. We shall discuss the implications of finite ϵ in Sec. III.

Returning to our model, suppose on the other hand that B_n goes to zero before p_M . From (2.48) we see that, if ψ_M is to remain finite (which is physically essential), either dp_M/ds must vanish or the quantity in brackets must vanish. If dp_M/ds vanishes for finite p_M , p_M goes through a minimum and starts to increase again. This seems to be unrealistic. The quantity in brackets, on the other hand, vanishes at the body and cannot vanish twice on the same field line.

We are, therefore, led (by reductio ad absurdum) to suppose that p_M and B_n vanish simultaneously and that ψ_M is finite at that point. What are the consequences of this model? The numerical answers to this question will be given, but it will be useful to anticipate certain results. At the point where p_M and B_n vanish, the slow flow velocity becomes infinite. This infinity must be regarded as meaning sonic. However, formally speaking, the area required to pass a finite mass at infinite velocity is zero, provided the density is not zero, a condition that is certainly fulfilled for isothermal flow that expands by a factor $e^{1/2}$ in going from stagnation to sonic conditions. Therefore, all the slow flow gas must be immediately behind the point where p_M and B_n go to zero, and the field line through this point delimits the flow in the sense that it must coincide with $\psi = 0$. This point, which has practical importance, will be reviewed in Sec. III in the light of a more realistic view of the gas properties.

We consider now the choice of profiles to be used in calculating I , M , and P . We introduce the following quantities: $\delta(s)$ is an effective thickness of the deceleration layer. ξ , defined by $\xi = \tilde{n}/\delta$, varies from zero at the shock to unity at the back of the layer. We let

$$v/(-\dot{x}_L) = f_1(\xi) \quad \rho = f_2(\xi) \quad (2.49)$$

Thus, at the shock we have $f_1(0) = f_2(0) = 1$. At the back of the deceleration layer, v is of order ϵ and thus may be taken to be zero, that is, $f_1(1) = 0$, and from the energy equation (2.44), $f_2(1) = p_M$. These boundary conditions suffice to define linear profiles:

$$f_1(\xi) = 1 - \xi \quad (2.50)$$

$$f_2(\xi) = 1 - (1 - p_M)\xi \quad (2.51)$$

With these profiles we readily calculate

$$I(s) = -\dot{x}_L \delta \int_0^1 f_1(\xi) d\xi = -\frac{1}{2} \dot{x}_L \delta \quad (2.52)$$

$$M(s) = -\dot{x}_L \delta \int_0^1 f_1 f_2 d\xi = -\frac{1}{6} \dot{x}_L \delta (2 + p_M) \quad (2.53)$$

$$P(s) = \dot{x}_L^2 \delta \int_0^1 f_1^2 f_2 d\xi = \frac{1}{12} \dot{x}_L^2 \delta (3 + p_M) \quad (2.54)$$

Before we can use these for integration, we must examine their behavior for small s . Since the linear profiles do not agree with the exponential profiles calculated in the deceleration layer analysis, we may expect that the starting conditions developed previously will have to be modified. It can be shown⁵ that use of these profiles requires us to replace (2.34) with

$$21S^2 - (32r_s + 18S)[1 - (r_b/r_s)^7] = 0 \quad (2.55)$$

and that this introduces no substantial errors.

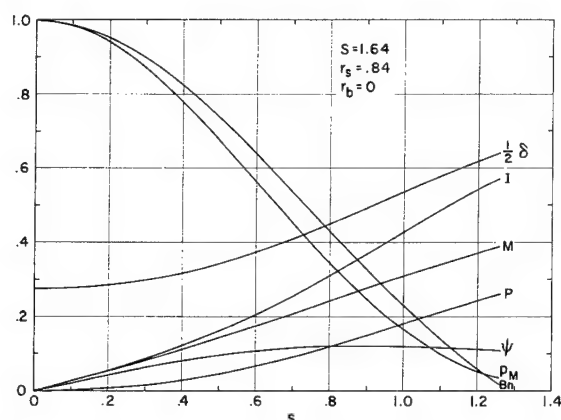


Fig. 6 Variation of the significant quantities relevant to the deceleration layer for the fully magnetohydrodynamic case. The abscissa represents arc length. p_M and B_n vanish at the same place to a sufficient degree of accuracy.

We chose problems characteristic of both the inverse and the direct case for detailed numerical treatment. The inverse problem, finding the shapes of the bodies that go with circular deceleration layers, is treated by Levy et al.⁵ and will not be given in detail here. A noteworthy result of this calculation is that, as far as the calculation went, a circular deceleration layer always corresponds to a value of r_s close to 0.7. It is not easy to see why r_s should be as insensitive as it is over this range, but an explanation along the following lines seems reasonable: If $r_s = 1$, $B_n = 0$ at $\theta = \phi = \pi/2$. With centrifugal forces, the deceleration layer can never reach $\theta = \pi/2$ with $p_M > 0$. Therefore, we always expect $r_s < 1$. On the other hand, if B_n is to vanish (i.e., layer and field become parallel) at an angle like one radian, r_s cannot be too small. A second feature to notice is the effect of the seventh power in (2.55). The range of interaction parameters for which r_b/r_s is substantially less than unity is very small. This situation has an important practical consequence. For in some physical situation we could imagine the quantity $\sigma/\rho_\infty u_\infty$ changing by many orders of magnitude. The significance of the seventh power in (2.55) is then that the change from quasi-aerodynamic to fully magnetohydrodynamic flow takes place when $\sigma/\rho_\infty u_\infty$ varies only by a factor of 2 or so. Put another way, the fully magnetohydrodynamic case is either "on" or "off" in any physical situation.

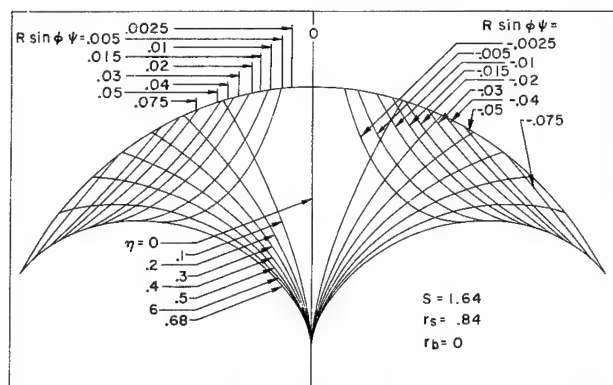


Fig. 7 Representation of the streamlines for the fully magnetohydrodynamic flow. Equal masses flow between the streamlines shown. Note the displacement of the streamlines in the deceleration layer. The magnetic field lines are also shown. The center of curvature of the shock is at the bottom of the figure.

We turn now to a direct problem, finding the deceleration layer that goes with no body. In this case the geometry is initially unknown. With $r_b = 0$, (2.55) is a relation between S and r_s ; it is a question of finding which pair of values S and r_s , satisfying (2.55), leads [using $h(\eta) \equiv 0$] to a deceleration layer for which p_M and B_n vanish simultaneously. The result of the calculation was $S = 1.64$, $r_s = 0.84$. The variation of the properties along the deceleration layer are shown in terms of arc length in Fig. 6, and the slow flow region and over-all geometry are shown in Fig. 7. The resultant shock shape is, as can be seen, nearly circular. The limiting streamline is the field line $\eta = 0.68$. The most important number to emerge from this analysis is the value $S = 1.6$, for this is the largest possible value of S ; any further increase in, say, the conductivity or magnetic moment of the coil, results only in a larger standoff distance, the value of S being unchanged. Figure 7 should probably be disregarded beyond about $\eta = 0.5$, on which field line the pressure and density are about 0.25. Beyond this field line, Fig. 7 predicts a substantial rise in velocity (coming together of the streamlines) indicating that the low Mach number approximation is no longer valid.

III. Discussion and Conclusions

The principal result of the foregoing analysis is that when

$$S = \epsilon \sigma u_\infty r_s B_0^2 / \rho_\infty u_\infty^2 \approx 1.6 \quad (3.1)$$

a flow pattern is set up in which the forces acting on the flow are almost entirely magnetic in origin. Forces exerted at solid surfaces are important only over a negligible area around the stagnation point. The demonstration that this type of flow can exist even at low magnetic Reynolds number was one of our principal objectives. On the other hand, the result (3.1) was not achieved without making a number of assumptions, nearly all of which need closer examination if we are to make a more accurate assessment of the physical conditions to which (3.1) should apply. In this section we shall discuss some of these physical conditions and also mention briefly the situation as regards experimental (laboratory) verification of the theoretical work in this area.

We commence with a discussion of the effects of finite (as opposed to vanishingly small) ϵ . In practical situations ϵ may be as small as 0.05, in which case $\epsilon^{1/4}$ is about 0.5. This obviously casts a shadow on those parts of the flow picture dependent on $\epsilon^{1/4}$ being small, notably the joining of the deceleration layer to the slow flow region near the sonic points. We feel, however, that the effect of finite ϵ will be one in which things get "smeared out" rather than fundamentally changed. Most notably, for finite ϵ , the slow flow will require a considerable area to be passed out at sonic speed parallel to the magnetic field. However, the distinction between the deceleration layer and the slow flow region is also less distinct for larger ϵ , so that it seems fair to describe the net effect as one "blurring" a picture whose sharp outlines are useful for descriptive and mathematical purposes, but not physically realistic.

We turn next to consideration of the Hall effect. When $\omega\tau$ is not small, the electric current is reduced in magnitude and does not flow in the direction of the applied electric field. However, cases can arise in which the angle between the current and the electric field remains small, and the magnitude of the current stays the same even though $\omega\tau$ grows to values in excess of unity. Just such a case arose in the paper of Levy and Petschek.⁴ Here the Hall currents (roughly the component of the electric current perpendicular to the electric field) were restricted to flow in a long narrow region of aspect ratio ϵ . This inhibited them to the extent that no important effect was noted until $\omega\tau$ grew to values in excess of ϵ^{-1} . This case does not occur in the present geometry; the Hall currents would flow, in this case, throughout the slow flow region. For this reason, the result (3.1)

can be expected to hold only for values of $\omega\tau$ less than unity. Toward the edge of the slow flow region $\omega\tau$ will rise considerably because of the decrease in the gas density. Thus the Hall effect will limit the sharpness of the boundary to the slow flow region. A similar effect is ion slip, which occurs when the density is so low that the neutrals can leak past the ions. The presence of ion slip would result in some small heat transfer to those parts of the surface of the body which the ideal theory shows to be not in contact with the hot gas.

A further physical limitation is that of chemical nonequilibrium. At sufficiently low density there may not be time for the ionization processes in the gas to reach equilibrium. Thus Boyer¹¹ claims that nonequilibrium effects make the attainment of substantial interaction parameters in hypersonic wind-tunnel facilities problematical for unseeded air. For the flight case, it is probably fair to say that, where nonequilibrium effects are important, the density must be so low as to preclude useful dynamic effects. However, it is difficult to generalize on this subject, and we must usually be content with calculating the magnitude of likely effects in any given case.

A final limitation on the physical realizability of the flows discussed in this paper arises from the following considerations. The gas ahead of the strong shock is supposed to be cold and un-ionized, a condition that is certainly met in the planetary entry case. However, the magnetic field of the coil extends substantially beyond the shock, and the cold gas therefore "sees" an effective electric field. The question arises as to whether this electric field is sufficient to break down the gas. This question is quite involved and is discussed at the end of the paper by Levy and Petschek.⁴ On the one hand, arguments can be given to show that breakdown could not occur for velocities less than about 5×10^6 cm/sec, i.e., about five times satellite velocity. On the other hand, unanswered questions remain having to do with the possibility of substantial photo ionization in the gas ahead of the shock.

This comment about photo ionization introduces the subject of radiant heat transfer. It has been shown, for instance, by Goulard¹² and Romig¹³ that the magnetohydrodynamic interaction can sometimes increase the radiant heat transfer to a body while decreasing the convective heat transfer, the flow conditions remaining fixed. This effect is due to the increased volume of hot radiating gas that is a consequence of the increase in the standoff distance. Since in this paper we deal only with the dynamics of the flow, and since under ordinary conditions radiation does not affect the dynamics of this type of flow, we shall not pursue this subject here. It does seem worth pointing out however, that, for a fixed object, re-entry may take place at a higher altitude because of dynamic effects. Thus, the radiant heat transfer to a body could be reduced by causing it to decelerate at a higher altitude.

We conclude by reviewing the status of quantitative experiment in the field of low magnetic Reynolds number hypersonic flows. Early work in the field by Bush and Ziemer¹⁴ appeared to give good results, but a recent article by Cloupeau¹⁵ appears to throw some doubt on the quantitative interpretation of results achieved in electromagnetic shock tubes of the type used by Bush and Ziemer. Work on this subject has also been reported by Wilkinson¹⁶ and Ericson et al.,¹⁷ although neither of these studies appears to have given very good results. We understand that a

description by Locke, Petschek, and Rose¹⁸ of experimental work performed by them with the object of verifying the existence of fully magnetohydrodynamically supported hypersonic flows (as predicted by Levy and Petschek⁴) is forthcoming. Preliminary results indicate that such flows can be supported with negligible physical contact between the hot gas and solid surfaces.

References

- ¹ Kemp, N. H., "On hypersonic stagnation point flow with a magnetic field," *J. Aeronaut. Sci.* **25**, 405-407 (1958); also Freeman, N. C., "On the flow past a sphere at hypersonic speed; with a magnetic field," *J. Aerospace Sci.* **26**, 670-672 (1959) also Kemp, N. H., "Author's reply," *J. Aerospace Sci.* **26**, 672 (1959).
- ² Bush, W. B., "Magnetohydrodynamic-hypersonic flow past a blunt nose," *J. Aerospace Sci.* **25**, 685-690 (1958); also Bush, W. B., "A note on magnetohydrodynamic-hypersonic flow past a blunt body," *J. Aerospace Sci.* **26**, 536 (1959).
- ³ Lykoudis, P. S., "The Newtonian approximation in magnetic hypersonic stagnation-point flow," *J. Aerospace Sci.* **28**, 541-546 (1961).
- ⁴ Levy, R. H. and Petschek, H. E., "Magnetohydrodynamically supported hypersonic shock layer," *Phys. Fluids* **6**, 946-961 (1963).
- ⁵ Levy, R. H., Gierasch, P. J., and Henderson, D. B., "Hypersonic magnetohydrodynamics with or without a blunt body," Avco-Everett Research Lab. Research Rept. 173 (January 1964).
- ⁶ Kemp, N. H. and Petschek, H. E., "Two-dimensional incompressible magnetohydrodynamic flow across an elliptical solenoid," *J. Fluid Mech.* **4**, 553 (1958).
- ⁷ Hains, F. D., Yoler, Y. A., and Ehlers, E., "Axially symmetric hydromagnetic channel flow," *Dynamics of Conducting Gases*, edited by A. B. Cambel and J. B. Fenn (Northwestern University Press, Evanston, Ill., 1959), pp. 86-103.
- ⁸ Li, T. Y. and Geiger, R. E., "Stagnation point of a blunt body in hypersonic flow," *J. Aeronaut. Sci.* **24**, 25 (1957).
- ⁹ Pohlhausen, K., "Zur näherungsweise Integration der Differentialgleichung der laminaren Reibungsschicht," *Z. Angew. Math. Mech.* **1**, 252 (1921).
- ¹⁰ Busemann, A., "Flüssigkeits-und-Gasbewegung," *Handwörterbuch der Naturwissenschaften* (VEB Gustav Fischer, Verlag, Jena, 1933), 2nd ed., Vol. IV, pp. 244-279.
- ¹¹ Boyer, D. W., "Ionization nonequilibrium effects on the magnetogasdynamic interaction in the stagnation region of an axisymmetric blunt body," Cornell Aeronautical Lab. Rept. AG-1547-Y-1 (June 1963).
- ¹² Goulard, R., "An optimum magnetic field for stagnation heat transfer reduction at hypersonic velocities," *ARS J.* **29**, 604 (1959).
- ¹³ Romig, M. F., "The influence of electric and magnetic fields on heat transfer to electrically conducting fluids," *Advances in Heat Transfer* (Academic Press, New York, 1964), Vol. 1.
- ¹⁴ Bush, W. B. and Ziemer, R. W., "Magnetic field effects on bow shock stand-off distance," *Phys. Rev. Letters* **1**, 58 (1958).
- ¹⁵ Cloupeau, M., "Interpretation of luminous phenomena observed in electromagnetic shock tubes," *Phys. Fluids* **6**, 679-688 (1963).
- ¹⁶ Wilkinson, J. B., "Magnetohydrodynamic effects on stagnation-point heat transfer from partially ionized nonequilibrium gases in supersonic flow," AeroChem TP-43, AeroChem Research Lab., Inc., Princeton, N. J. (March 1962).
- ¹⁷ Ericson, W. B., Maciulaitis, A., Spagnolo, R. A., Loeffler, A. L., Scheuing, R. A., Hopkins, H. B., "An investigation of magnetohydrodynamic flight control," Grumman Aircraft Engineering Corp., Bethpage, N. Y. (May 1962).
- ¹⁸ Locke, E. V., Petschek, H. E., and Rose, P. H., "Experiments with magnetohydrodynamically-supported shock layers," Avco-Everett Research Lab., Research Rept. 191 (August 1964); also *Phys. Fluids* (to be published).

§ We are indebted to a reviewer for this reference.

A Theoretical Investigation of MHD Channel Entrance Flows

A. MACIULAITIS* AND A. L. LOEFFLER JR.†

Grimman Aircraft Engineering Corporation, Bethpage, N. Y.

A momentum-integral boundary-layer analysis is made of the entrance MHD flow of an incompressible electrically conducting fluid in a two-dimensional constant area channel. It is assumed that a uniform magnetic field perpendicular to the insulated channel walls exists in the channel. An electric field, perpendicular to both the magnetic field and mean flow, is permitted. The magnetic Reynolds number is assumed small. Closed-form solutions are obtained for both the laminar and turbulent cases. Variation of the freestream velocity in the flow direction is fully accounted for. Two cases are considered: the uniform velocity entry case, and the situation where the velocity profile at the channel entry plane is nonmagnetically fully developed. Agreement between the present work and more exact numerical solutions for a few particular flow cases is excellent. Increasing the Hartmann number is shown to reduce entrance lengths appreciably, except in the very low Hartmann number range. Flows with nonmagnetically fully developed entry profiles, in general, require much larger entrance lengths than flows with a uniform entry profile.

Nomenclature

a	= half-height of channel
B	= magnetic induction
C	= const(= 0.0456)
E	= electric field
f	= friction factor ($\equiv 8\tau_w/\rho U_m^2$)
j	= electric current density
M	= Hartmann number [$\equiv (\sigma/\mu)^{1/2}Ba$]
p	= static pressure
Re	= Reynolds number ($\equiv 4aU_m\rho/\mu$)
U, V	= velocities in x and y directions, respectively
W	= half-width of channel
x, y, z	= coordinates (see Fig. 1)
δ	= boundary-layer thickness
δ^*	= displacement thickness
ρ	= fluid density
σ	= fluid electric conductivity
θ	= momentum thickness
μ	= fluid viscosity
τ_w	= wall shear stress

Subscripts

FD	= fully developed
∞	= freestream
w	= wall
m	= mean

Introduction

A BETTER knowledge of the velocity fields, boundary-layer development, and friction factors in the entrance region of MHD channels is of interest both to the curious fluid dynamicist and the practical designer. In order to avoid the added difficulties that are present in the solution of the problem of a channel with an arbitrary, finite aspect ratio, this investigation, as most that preceded it, is addressed to the special case of an infinite aspect ratio channel, i.e., the flow between two parallel plates. It can be expected that the solutions to this problem will be applicable to high aspect ratio channels and will possibly indicate trends even when the ratio is low. In his analysis of the laminar flow case, Shercliff¹ linearized the problem by the Rayleigh approximation and obtained solutions for the deviation of the

local from the ultimate, or Hartmann, velocity profile in terms of an orthogonal series. In some special cases, the leading terms of the series were evaluated. Shohet² and Dix³ have independently obtained numerical solutions to the laminar flow situation when the velocity across the channel entrance is uniform. Also, for uniform entrance velocity, Moffatt⁴ has obtained closed-form laminar and turbulent solutions, with the further restriction that the freestream velocity be constant. Moffatt used the momentum integral method with assumed similar velocity profiles across the boundary layers. In the present investigation, Moffatt's method has been extended to include variation of the freestream velocity in the flow direction, thereby satisfying overall conservation of mass for a constant area channel. Two cases are treated: the uniform entry velocity case and the heretofore unsolved situation of a nonmagnetically fully developed velocity profile at the channel entry plane.

Problem and Solutions

The geometric configuration of the problem to be solved is shown in Fig. 1. The channel is assumed to have a sufficiently high aspect ratio and negligible three-dimensional effects for the problem to be considered two dimensional. For $x \geq 0$, the flow is in the presence of uniform, mutually perpendicular, magnetic and electric fields, whereas for $x < 0$, the fields are zero. Fluid density, viscosity, and electrical conductivity are assumed to be constant for simplicity. Hall effects and induced magnetic fields are assumed to be small enough to be neglected.

With the usual boundary-layer assumptions, the integral method leads to the balance of forces and momentum fluxes:

$$\tau_w + \delta \frac{\partial p}{\partial x} - \int_0^\delta jB dy = U_\infty \frac{\partial}{\partial x} \int_0^\delta \rho U dy - \frac{\partial}{\partial x} \int_0^\delta \rho U^2 dy \quad (1)$$

The freestream momentum equation

$$\frac{dp}{dx} = -\rho U_\infty \frac{dU_\infty}{dx} + j_\infty B \quad (2)$$

and Ohm's law

$$j = \sigma(E - UB) \quad (3)$$

provide the means for expressing the pressure gradient and the Lorentz force in terms of velocities and the magnetic

Received March 9, 1964; revision received June 15, 1964.

* Research Engineer, Research Department. Member AIAA.

† Head of MHD and Plasma Physics Group, Research Department.

Table 1 Summary of solutions

Type of flow → Entry velocity profile	Laminar	Turbulent
Uniform	$\frac{x}{aRe} = \frac{3}{20(2M^2 - \frac{3}{2} - \frac{3}{2}M^2)} \left\{ -\left(\frac{16}{3} + M^2\right) \ln\left(1 - \frac{\delta}{3a}\right) - \frac{(1 - \frac{3}{2}M^2)\delta/a}{1 - (\delta/3a)} \right\} - \left(\frac{6}{6}\right)^{1/2} + \frac{M(\delta/a)}{M(\delta/a)} \ln\left[1 - \left(\frac{M^2}{6}\right)\frac{\delta^2/a^2}{2}\right] \quad (A)$	$\frac{x}{aRe} = \frac{23}{576} \frac{(\delta/a)^{3/4}}{0.06448Re^{3/4} - M^2(\delta/a)^{5/4}} - \frac{7}{45M^2} \ln\left[1 - \frac{M^2(\delta/a)^{5/4}}{0.06448Re^{3/4}}\right] \quad (C)$
Nonmagnetically fully developed	$\frac{x}{aRe} = \frac{3}{20(2M^2 - \frac{3}{2} - \frac{3}{2}M^2)} \left\{ -\left(\frac{16}{3} + M^2\right) \ln\frac{1 - (\delta/3a)}{3} - \frac{3[(\delta/a)^{1/2} + (\delta/a)M][(6)^{1/2} - M]}{[(6)^{1/2} - (\delta/a)M][(6)^{1/2} + M]} + \frac{(11M^2 + \frac{14}{3})}{2(6)^{1/2}M} - \frac{(11M^2 + \frac{14}{3})}{2(6)^{1/2}M} \ln\frac{1 - (M^2/6)(\delta^2/a^2)}{1 - (M^2/6)} \right\} \quad (B)$	$\frac{x}{aRe} = \frac{23}{576} [(\delta/a) - 1] \left\{ \frac{(\delta/a)^{5/4}}{0.06448Re^{3/4} - M^2(\delta/a)^{5/4}} + \frac{1}{0.06448Re^{3/4} - M^2} \right\} - \frac{7}{45M^2} \ln \frac{0.06448Re^{3/4} - M^2(\delta/a)^{5/4}}{0.06448Re^{3/4} - M^2} \quad (D)$

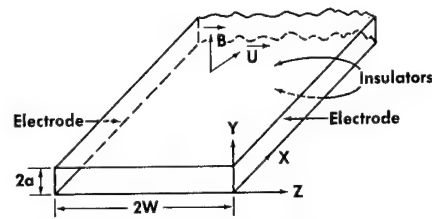


Fig. 1 Geometric configuration of the problem.

field. The resulting equation for the shear stress τ_w is then given by

$$\tau_w = \delta B^2 U_\infty \sigma \left[1 - \int_0^1 \frac{U}{U_\infty} d\left(\frac{y}{\delta}\right) \right] + \delta^* \rho U_\infty \frac{dU_\infty}{dx} + \frac{d}{dx} (\rho U_\infty^2 \theta) \quad (4)$$

wherein θ and δ^* are the momentum and displacement thicknesses, respectively.

For the laminar flow case, one can substitute $\mu(\partial U/\partial y)_w$ for the shear, which is evaluated from the assumed velocity profile, whereas for the turbulent flow, Blasius' friction law is applicable. In order to solve the equations for the boundary-layer thickness, it is assumed that in the laminar case the velocity profile consists of a parabolic variation

$$U/U_\infty = 1 - [(y/\delta) - 1]^2$$

across the boundary layer and a uniform core velocity. In the turbulent case, a one-seventh power velocity distribution in the boundary layer is assumed. The core velocity is allowed to vary in the x direction in order to satisfy the conservation of mass equation applied across the entire channel cross section. The boundary conditions at $x = 0$ are: $\delta = a$ for the nonmagnetically fully developed entry, and $\delta = 0$ for the uniform entry velocity.

With the stated assumptions, and after lengthy but simple integrations, algebraic manipulations, and nondimensionalizing, the solutions for the laminar and turbulent cases can be written in tabular form (Table 1). Whereas Eqs. (A) and (B) represent closed-form solutions in the strict sense of the word, in deriving Eqs. (C) and (D), several unmanageable integrals were encountered, and it was necessary to assume that $\delta/8a \ll 1$ and use the approximation

$$\int_{(\delta/a)_1}^{(\delta/a)_2} \frac{(\delta/a)^{5/4} d(\delta/a)}{(C/Re^{1/4}) - (M^2/Re)(\delta/a)^{5/4}} \approx \frac{1}{2} \left[\left(\frac{\delta}{a}\right)_2 - \left(\frac{\delta}{a}\right)_1 \right] \left[\frac{(\delta/a)_2^{5/4}}{(C/Re^{1/4}) - (M^2/Re)(\delta/a)_2^{5/4}} + \frac{(\delta/a)_1^{5/4}}{(C/Re^{1/4}) - (M^2/Re)(\delta/a)_1^{5/4}} \right]$$

In the laminar case, it should be noted that the nondimensional length parameter x/aRe , familiar from Schlichting's⁵ nonmagnetic solution, is a function of δ/a and the Hartmann number M only. The Hartmann number can be viewed as a measure of the magnetic interaction. In the turbulent case, x/aRe depends also on the Reynolds number. For the assumed flow model, the boundary-layer development and the velocity profiles are independent of the electric field if the Hartmann and Reynolds numbers are specified.

Some specific examples of the laminar solution are shown in Fig. 2, which plots the variation of δ/a with the length parameter for two Hartmann numbers, 10 and 100, for both entrance situations. The effect of the magnetic field on the entrance flow is graphically illustrated. For the nonmagnetically fully developed entrance profile at $x = 0$, the boundary layers are assumed to join at the channel center. Proceeding into the channel, a core flow develops, and the boundary layers spread apart and diminish to an asymptotic value.

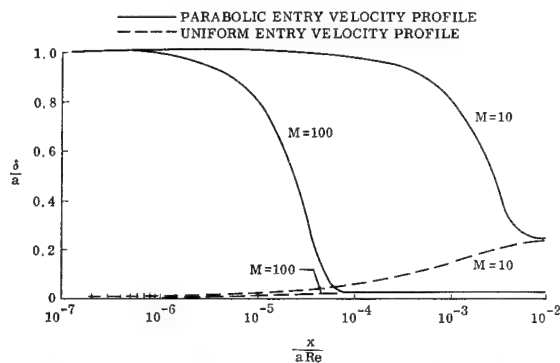


Fig. 2 Development of laminar MHD boundary layers in the channel entrance region.

For the uniform velocity entry, the boundary layer grows from zero until it attains the same asymptotic value.

The variation of the entrance length with Hartmann number is presented in Fig. 3. The entrance length is defined here as the distance required for the friction factor to come within 10% of the final, fully developed value. Generally, the results demonstrate a decrease in the entrance length with increasing Hartmann number. The curves for the nonmagnetically fully developed entrance condition show an increase in entrance length with increasing Hartmann number for low Hartmann numbers; this is consistent with the fact that the entrance length for this condition must go to zero for $M = 0$. It is interesting that the curves for the uniform velocity entrance condition must also show such a reverse trend for sufficiently low M , since the entrance lengths for nonmagnetic ($M = 0$) flow can be shown to be less than the maximum entrance length values exhibited by the curves of Fig. 3. It was impossible to use our integral technique for M values less than those yielding $\delta/a = 1$ for

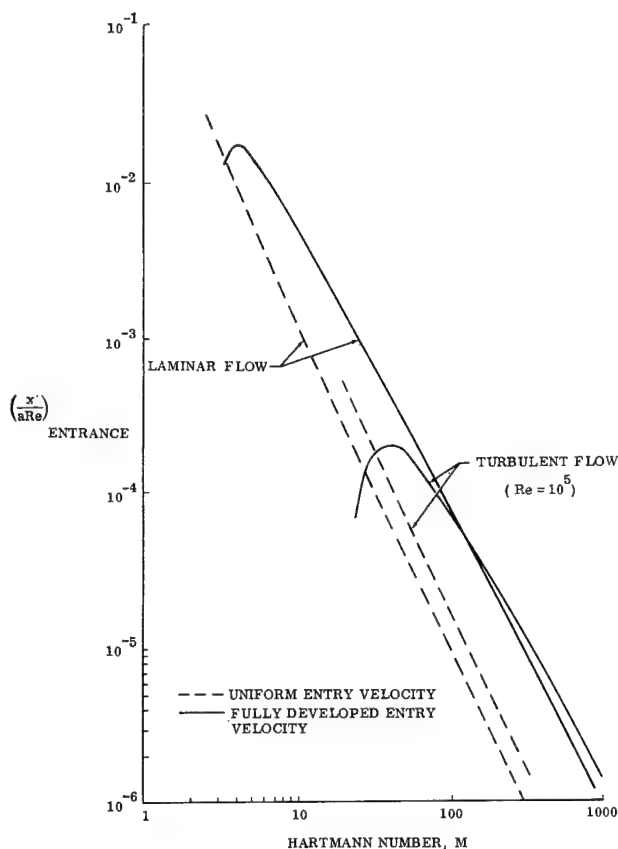


Fig. 3 MHD entrance lengths.

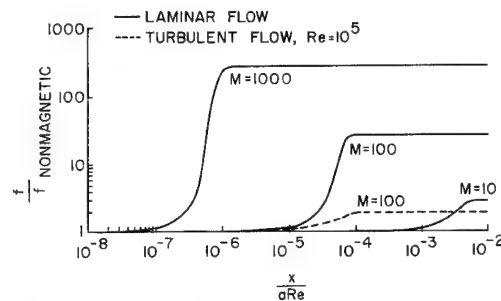


Fig. 4 Friction factor development in the channel entrance region for nonmagnetically fully developed entry velocity profiles.

fully developed flow.† For laminar flow, this minimum value of M was about 2.45; for the turbulent case it depended on Re and was about 19 for an Re of 10^5 .

In Fig. 3, the turbulent entrance lengths generally exceed those for laminar flow. This fact is in contrast to what one would expect, since for nonmagnetic flow the reverse is true. However, over much of the Hartmann number range of Fig. 3, the entrance lengths for both laminar and turbulent flow are so small as to be almost negligible. Furthermore, the possibility of transition from turbulent to laminar flow at higher Hartmann numbers (above 110 for $Re = 10^5$ according to Ref. 6) has not been taken into consideration.

Shercliff had defined the entrance length as the distance over which the predominant term in the series, representing the deviation of the local velocity from the Hartmann profile, decreased by $1/e$. Obviously, this differs significantly from the definition used in Fig. 3. To establish a more compatible basis for comparison, the entrance length could be defined as the distance required for δ/a to reach 99% of its ultimate, fully developed value. The authors found that for the laminar flow, with uniform entrance velocity,§ such entrance lengths were within 20% of those computed by Shercliff.

The influence of the Hartmann number on the friction factor development is illustrated in Fig. 4, which contains results for the nonmagnetically fully developed entry case. For laminar flow, the increase over the nonmagnetic friction factors can amount to several orders of magnitude. For the turbulent flow, for which only one curve is shown, the increase is much smaller. The trend with Hartmann number, though not shown in Fig. 4, is similar to that for laminar flow.

Discussion

The validity of the solutions presented is contingent upon the accuracy of the assumptions made. It is important,

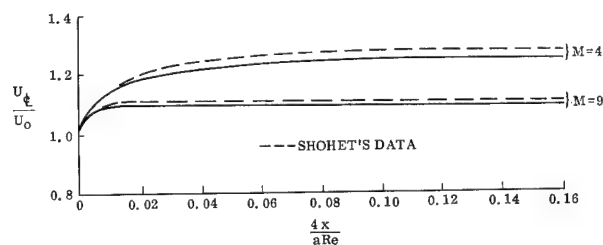


Fig. 5 Comparison of channel centerline velocities with Shohet's results (laminar flow, uniform inlet velocities U_0).

† It is possible to bypass this limitation in the case of uniform entrance velocity if the entrance length is redefined as the length to the position at which $\delta/a = 1$.

§ Shercliff did not work out the solution for the nonmagnetically fully developed entry case.

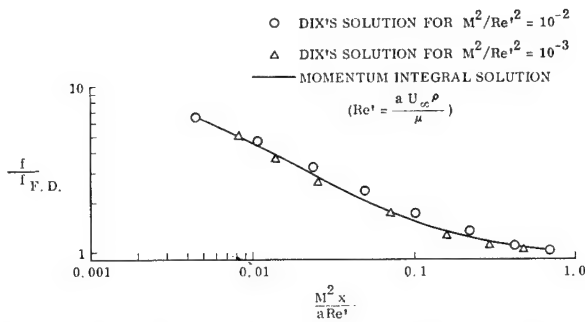


Fig. 6 Comparison of skin friction with the numerical solution of Dix (laminar flow, uniform entry velocity).

therefore, to examine these carefully. It is felt that boundary-layer assumptions would be reasonably valid up to those Hartmann numbers for which the entrance lengths are of the same order of magnitude as the asymptotic boundary-layer thickness. For larger Hartmann numbers, it would be probably inaccurate to assume that $\partial p / \partial y \ll \partial p / \partial x$ or that $V \ll U$.

There are neither experimental measurements nor exact numerical solutions of the nonmagnetically fully developed entry problem. Therefore, the support for the assumed velocity profiles can only come, by inference, from comparisons with numerical solutions to the related problem with uniform entry velocity.¹¹ For the laminar case, Shohet and Dix have independently obtained such solutions.

As seen in Fig. 5, the comparison of the development of core velocities with Shohet's numerical solution shows reasonably good agreement. The agreement would improve for higher Hartmann numbers. This comparison is, of course, for the uniform entry velocity case.

Comparison of friction factors with those of Dix's doctoral thesis (Fig. 6) shows an embarrassingly good agreement. The ordinate in this plot is the ratio of the local friction factor to the friction factor of the fully developed flow. Data shown are again for the case of uniform entry velocity.

It is well known that the effect of the magnetic field is to flatten the velocity profile. Comparison of the laminar velocity profiles for very large x , as obtained in the present work, shows a reasonably good agreement with Hartmann's profiles. At the channel entry, the parabolic profile for the laminar case is, of course, an exact representation of the fully developed nonmagnetic profile.

For the turbulent case, only the friction factors corresponding to x larger than the entrance length can be compared to existing data, namely, Murgatroyd's⁶ test results. That the agreement is quite satisfactory is shown in Fig. 7 where the friction factors corresponding to three Reynolds numbers have been graphed. They were computed from

$$f_{FD} = 0.446 \frac{(M/Re)^{0.4}}{\{1 - [0.0139/(M/Re)^{1.6} Re]\}^{7/4}} \quad (5)$$

¹¹ The comparison with Shercliff's approximate solution was discussed in the preceding section.

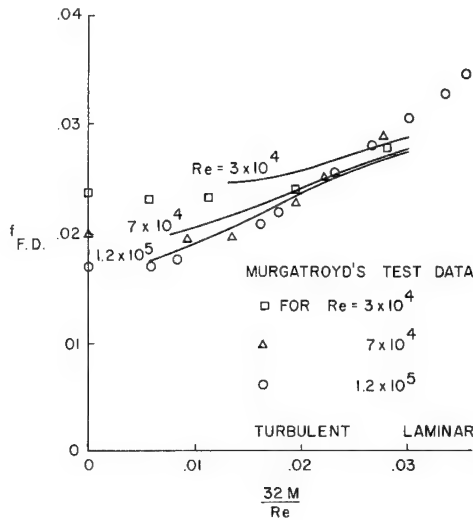


Fig. 7 Comparison of theoretical fully developed turbulent friction factors with Murgatroyd's data.

It is important to be cognizant of the restricted range of applicability for the turbulent results of the present work. The lower limits of $32M/Re$ on the theoretical curves in Fig. 7 are given by that Hartmann number for which $\delta/a = 1$ as $x \rightarrow \infty$. The upper limit is set by $32M/Re \approx 0.030$ above which Murgatroyd's data indicate that the flow becomes laminar.

It is worth noting from Fig. 7 that the turbulent, fully developed friction factor is a function not only of M/Re but also of Re itself, which is in agreement with Murgatroyd. The Reynolds number dependence, lower limit on M/Re and the much closer general agreement with test results constitute, in the authors' opinion, a substantial improvement over Moffatt's correlation.

In view of the foregoing comparisons, it is felt that the assumptions made are at least partially substantiated, and the results presented are close to reality.

References

- ¹ Shercliff, J. A., "Entry of conducting and nonconducting fluids in pipes," *Proc. Cambridge Phil. Soc.* **52**, 573-583 (1956).
- ² Shohet, J. L., "Velocity and temperature profiles for laminar MHD flow in the entrance region of channels," Ph.D. Thesis, Carnegie Institute of Technology (September 1961).
- ³ Dix, D. M., "The MHD flow past a nonconducting flat plate in the presence of a transverse magnetic field," Doctoral Thesis, Massachusetts Institute of Technology (1961); also TR 397.
- ⁴ Moffatt, W. C., "Boundary layer effects in magnetohydrodynamic flows," Massachusetts Institute of Technology Magnetogasdynamics Lab. Rept. 61-4 (May 1961).
- ⁵ Schlichting, H., *Boundary Layer Theory* (Pergamon Press, New York, 1955), 1st English ed., Chap. IX, p. 147.
- ⁶ Murgatroyd, W., "Experiments on magneto-hydrodynamic channel flow," *Phil. Mag.* **44**, 1348 (1953).

Viscous Multicomponent-Multiphase Flow with Application to Axisymmetric Jets of Hydrogen

RAYMOND EDELMAN* AND HAROLD ROSENBAUM†

General Applied Science Laboratories, Inc., Westbury, N.Y.

A model is established for the continuum flow of a multicomponent system of gases and their condensed phases. The general conservation equations governing the behavior of the gases and condensed phases are derived. Viscosity heat conductivity, diffusion, and production of species by chemical reactions are included in the development. Nonequilibrium phenomena associated with the presence of condensed phases are discussed. To illustrate some of the features of the viscous two-phase flow problem, a study is made on a chemically frozen, fully expanded axisymmetric jet. In particular, low-temperature hydrogen is injected into a parallel high-velocity air stream, and the resulting two-phase composition and diffusive spreading characteristics are determined.

Nomenclature

f	= force of interaction between gas and condensed phases
H	= stagnation energy
h	= static enthalpy
h_D	= mass-transfer coefficient
\mathbf{j}_{ri}	= diffusional mass flux
k	= thermal conductivity
L	= heat of phase change
L_ℓ	= Lewis number, $(\rho DC_p/k)$
N_{pc}	= droplet number concentration
P_r	= Prandtl number, $(C_p \mu/k)$
p	= pressure
Q	= heat-transfer interaction between gas and condensed phases
q	= heat flux by conduction
R	= gas constant
Re	= Reynolds number, $(\rho v r/\mu)$
r	= radial coordinate
T	= temperature
U	= nondimensional streamwise velocity component
u	= internal energy
V	= velocity
W	= molecular weight
\dot{W}_c	= production of gas by chemical reaction
X_{pi}	= mass concentration of the i th condensed species in the condensed phases
x	= streamwise coordinate
Y_{ri}	= mass concentration of the i th gaseous species in the gas phase
β_i	= mass concentration of i th species in the mixture
δ	= density
μ	= viscosity
ξ	= transformed x coordinate defined by Eq. (33)
π	= stress tensor
ρ	= mass concentration in mixture
$\dot{\sigma}_v, \dot{\sigma}_l$	= unilateral evaporation and condensation rate, respectively
$\dot{\sigma}_v - \dot{\sigma}_l$	= production of gas by evaporation
Ψ	= stream function defined by Eq. (41)

Subscripts

e	= freestream
g	= gas mixture
i	= i th species
j	= jet
m	= total mixture
p	= particle
v	= component in the gas phase

I. Introduction

THE dumping of combustibles overboard from stages of boost vehicles creates several problems of potential importance. The combustion, surface heating, and induced pressure forces acting on the missile surface are possible consequences of the dumping process. The problem is quite complex owing to the combined effects of finite-rate chemistry and jet boundary-layer interaction with the external flow. In general, the existing literature contains combustion studies limited to gas-phase configurations. However, when cryogenic hydrogen is the fuel under consideration, it becomes necessary to consider the possibility of two-phase flow. In fact, a typical state in the hydrogen fuel tank consists of saturated liquid hydrogen at approximately 20°K ($p \cong 1$ atm). Thus, at high altitudes, say of the order of 100,000 ft, it is possible to expand the hydrogen into the solid-vapor region. Furthermore, if the expansion is nearly isentropic, from 40 to 80% of the hydrogen can be in the solid phase (where $T \cong 10^\circ\text{K}$), depending on whether vapor or liquid is bled from the tank. It is clear, therefore, that the subsequent mixing with the surrounding air can lead to condensation of the air. In general then, we can expect the flow field to be comprised of the components of air and hydrogen each occurring in two phases.

The problem of accounting for the effects due to the presence of condensed species can be divided into two parts: 1) development of the conservation equations for the flow field and 2) determination of constitutive relations for the transfer of mass, momentum, and energy between the phases. The first part involves the description of the conservation of mass, momentum, and energy for the gas-phase and the condensed-phase systems. The second part involves the description of the dynamic and thermodynamic interactions between the gas- and condensed-phase systems. In general, this involves the description of velocity differences between the phases (dynamic nonequilibrium), temperature differences (thermal nonequilibrium), and mass transfer between the phases (nonequilibrium phase changes).

The purpose of the present report is to provide a model from which a system of governing equations may be deduced

Presented as Preprint 63-5017 at the AIAA Heterogeneous Combustion Conference, Palm Beach, Fla., December 11-13, 1963; revision received August 28, 1964. This research was carried out under Contract No. NAS8-2686 with NASA George C. Marshall Flight Center, of Huntsville, Ala. The authors gratefully acknowledge the usefulness of discussions with Simon Slutsky of General Applied Science Laboratories, Inc., Vito Agosta of the Polytechnic Institute of Brooklyn, and Andrew Pouring of Yale University, as well as the numerical calculations carried out by David Soll and the IBM 7090 program written by Jay Hoffman.

* Senior Scientist. Member AIAA.

† Senior Scientist. Associate Member AIAA.

and to indicate constitutive relations that may be used to account for the interaction phenomena. Finally, the results of the analysis are applied to special cases that are of present interest.

II. Analysis

In establishing a model for the present complex flow system, it becomes necessary to make certain assumptions. These assumptions are, in general, made in regard to the nature of the condensed-phase system. The basic assumptions are discussed below.

1) The condensed phase is in the form of a cloud of solid or liquid particles. This assumption is more of a statement of fact evidenced by launch experience and wind-tunnel studies relating to condensation of various gases.¹

2) Droplet-droplet interaction is negligible. That is, the condensed phase is assumed to form a dilute suspension in the gas phase.

3) The volume occupied by the condensed phase is negligible. This is merely a statement of the fact that the mass density of a condensed species is much greater than the mass density of its vapor.

4) Random motion of the particles of condensed phase is assumed negligible. That is, pressure, temperature, and transport properties associated with random motion are considered negligible compared with those of the gas phase. The validity of this assumption rests on the condition that the particle size be larger than that of the molecules in the gas phase.

5) Thermal radiation is neglected. The low temperatures with which we are concerned implies that thermal radiation will be negligible.

6) Each droplet has a uniform temperature at any instant. That is, conduction (and convection within the droplet in the case of liquid droplets) is negligible. In general, droplet sizes will be small enough to render this assumption valid.

7) We shall assume that the state of the vapor at the droplet surface corresponds to the droplet temperature and velocity. This assumption is made in order to provide a means of systematically accounting for the condensed-phase gas-phase interactions.

8) Surface energy, gravity, and electric charge effects are neglected.

In general, the approach will be to develop a system of governing equations which will describe the behavior of the gas-phase globally and the condensed species individually. This permits the gases to be treated as a multicomponent diffusing system with chemical reactions, a method previously developed for gaseous systems (see, e.g., Ref. 2). On the other hand, the condensed species are treated individually so that the mass, momentum, and thermal interactions can be handled in terms of the best available information for flow about particles under the conditions that prevail in the present investigation.

In accordance with assumption 7, each droplet may be thought to have a film of vapor surrounding it. Within this film, velocity and temperature are brought from the gas-phase values to the values at the droplet surface. Since the film is vapor, it is associated with the gas phase but is considered to contain negligible mass. This implies that the instantaneous flow of mass, momentum, and energy from the particles is equal to the instantaneous gain of mass, momentum, and energy by the gas phase. Thus, the film is the source of irreversible entropy production due to the nonequilibrium transfer of mass, momentum, and energy between the phases. It must be noted that the mass transfer, which is due to evaporation and condensation, has an associated momentum and energy transfer. These are in addition to the momentum and energy transfers due to velocity and temperature differences, respectively. Let us consider this point in more detail. In the first place, assumption 2

implies that the influence of the condensed phase on the flow field may be constructed in terms of the interactions associated with a single particle and its surroundings, multiplied by a local number density of droplets in the elemental volume of mixture. This permits the use of available information for the interaction of single droplets in an infinite fluid. Further, the introduction of the local number density "smears" out the actual discrete nature of droplet system. The result of this is to predict a local as well as an over-all average effect of the droplets on the flow field. We consider first the mass, momentum, and energy transfers associated with the evaporation and condensation process.

Mass Transfer

The process of evaporation is composed of a simultaneous, unilateral evaporation rate $\dot{\sigma}_v$ and a unilateral condensation rate $\dot{\sigma}_l$. The net of the two unilateral rates is the evaporation rate \dot{W}_v^F :

$$\dot{W}_v^F = \dot{\sigma}_v - \dot{\sigma}_l \quad (1)$$

Clearly, if this difference is negative we have condensation and if it is zero there is, in effect, no phase change.

Momentum

The droplet loses momentum at a rate equal to $\dot{\sigma}_v \mathbf{V}_p$ and simultaneously gains momentum at a rate equal to $\dot{\sigma}_l \mathbf{V}_p$. This is in accordance with the condition that, at the interface, the vapor and droplet have the same velocity \mathbf{V}_p . Thus, the net loss of droplet momentum is given by

$$\mathbf{V}_p(\dot{\sigma}_v - \dot{\sigma}_l) = \mathbf{V}_p \dot{W}_v^F \quad (2)$$

Energy

The droplet energy loss associated with the unilateral evaporation rate is composed of condensed-phase enthalpy, kinetic energy, and the heat of vaporization. The gain of droplet energy associated with the unilateral condensation rate is composed of the vapor enthalpy and kinetic energy evaluated at the interface state. Thus, the net loss of droplet energy is given by

$$\dot{\sigma}_v \left(h_p + L + \frac{\mathbf{V}_p \cdot \mathbf{V}_p}{2} \right) - \dot{\sigma}_l \left(h_{v_{T_p}} + \frac{\mathbf{V}_p \cdot \mathbf{V}_p}{2} \right) = \dot{W}_v^F \left(h_p + L + \frac{\mathbf{V}_p \cdot \mathbf{V}_p}{2} \right) \quad (3)$$

Note that the droplet gives up the heat of vaporization and gains the heat of condensation where

$$h_{v_{T_p}} = h_p + L \quad (4)$$

In addition, the interface moves in accordance with the rate of evaporation of the droplet. This results in a work transfer given by

$$P_p / \delta_l \dot{W}_v^F \quad (5)$$

where

$$\begin{aligned} P_p &\equiv \text{interface pressure} \\ \delta_l &\equiv \text{droplet density} \\ \dot{W}_v^F / \delta_l &\equiv \text{rate of increase in gas-phase volume due to droplet evaporation} \end{aligned}$$

Since, in general $L \gg P_p / \delta_l$, the energy associated with Eq. (5) is negligible compared with that given by Eq. (3).

It has been pointed out that, in addition to mass, momentum, and energy transfers associated with evaporation, there exist dynamic and thermal interactions by virtue of the velocity and temperature nonequilibrium between the phases, respectively. These are discussed, in order, in the following.

Drag Force

The drag force constitutes a momentum interchange between the phases. We shall assume that this force is purely a viscous phenomenon and depends only on the velocity difference, i.e.,

$$\mathbf{f}_p = \mathbf{f}_p(\mathbf{V}_g - \mathbf{V}_p) \quad (6)$$

Additional forces exist, but can be shown to be, in general, of higher order.⁴

Thermal Interaction

This thermal interaction, which is dependent on the temperature difference between the phases, is merely a statement of convective heat transfer. This precludes the existence of radiation heat transfer in accordance with assumption 5. This convective heat transfer is expressed by

$$\dot{Q}_p = \dot{Q}_p(T_v - T_p) \quad (7)$$

Conservation Equations

In consideration of the preceding discussion, we can write down the conservation equations in a systematic manner. In order to maintain generality, we consider i gaseous species and i condensed species, i.e., each component can exist in each phase, and we consider each condensed species individually. Application of the fundamental laws for the conservation of mass, momentum, and energy leads to the following system of governing equations for steady, two-phase flows.

Continuity of Mass: Mixture

$$\nabla \cdot (\rho_g \mathbf{V}_g + \sum_i \rho_{pi} \mathbf{V}_{pi}) = 0 \quad (8)$$

i th Condensed Phase

$$\nabla \cdot \rho_{pi} \mathbf{V}_{pi} = \nabla \cdot \rho_p \mathbf{V}_p X_{pi} = \dot{W}_{pi}^F = -\dot{W}_{vi}^F \quad (9)$$

i th Gas Phase

$$\nabla \cdot \rho_g \mathbf{V}_g Y_{vi} = \dot{W}_{vi}^F + \dot{W}_{vi}^c - \nabla \cdot \mathbf{j}_{vi} \quad (10)$$

Momentum: Mixture

$$\nabla \cdot (\rho_g \mathbf{V}_g \mathbf{V}_g + \sum_i \rho_{pi} \mathbf{V}_{pi} \mathbf{V}_{pi}) = \nabla \cdot \boldsymbol{\pi}_g \quad (11a)$$

or

$$\rho_g \mathbf{V}_g \cdot \nabla \mathbf{V}_g + \sum_i \rho_{pi} \mathbf{V}_{pi} \cdot \nabla \mathbf{V}_{pi} = \nabla \cdot \boldsymbol{\pi}_g + \sum_i \dot{W}_{vi}^F (\mathbf{V}_{pi} - \mathbf{V}_g) \quad (11b)$$

i th Condensed Phase

$$\rho_{pi} \mathbf{V}_{pi} \cdot \nabla \mathbf{V}_{pi} = \mathbf{f}_{pi} \quad (12)$$

Energy: Mixture

$$\nabla \cdot \left[\rho_g \left(h_g + \frac{\mathbf{V}_g \cdot \mathbf{V}_g}{2} \right) \mathbf{V}_g + \sum_i \rho_{pi} \left(h_{pi} + \frac{\mathbf{V}_{pi} \cdot \mathbf{V}_{pi}}{2} \right) \mathbf{V}_{pi} \right] = -\nabla \cdot \mathbf{q}_g + \nabla \cdot (\boldsymbol{\tau}_g \cdot \mathbf{V}_g) - \sum_i \nabla \cdot \mathbf{j}_{vi} h_{vi} \quad (13a)$$

or

$$\rho_g \mathbf{V}_g \cdot \nabla \left(h_g + \frac{\mathbf{V}_g \cdot \mathbf{V}_g}{2} \right) + \sum_i \rho_{pi} \mathbf{V}_{pi} \cdot \nabla \left(h_{pi} + \frac{\mathbf{V}_{pi} \cdot \mathbf{V}_{pi}}{2} \right) = -\nabla \cdot \mathbf{q}_g + \nabla \cdot (\boldsymbol{\tau}_g \cdot \mathbf{V}_g) - \sum_i \nabla \cdot \mathbf{j}_{vi} h_{vi} + \sum_i \dot{W}_{vi}^F \left[\left(h_{pi} + \frac{\mathbf{V}_{pi} \cdot \mathbf{V}_{pi}}{2} \right) - \left(h_g + \frac{\mathbf{V}_g \cdot \mathbf{V}_g}{2} \right) \right] \quad (13b)$$

i th Condensed Phase

$$\rho_{pi} \mathbf{V}_{pi} \cdot \nabla h_{pi} = \dot{Q}_{pi} - \dot{W}_{vi}^F L_i \quad (14)$$

In the preceding system of equations, certain variables have been introduced for convenience. These are defined by the following relations:

$$\rho_g = \sum_i \rho_{vi} \quad (15)$$

$$\rho_g \mathbf{V}_g = \sum_i \rho_{vi} \mathbf{V}_{vi} \quad (16)$$

where \mathbf{V}_{vi} is the velocity of the i th gas-phase component. Furthermore, the diffusional mass flux is defined by

$$\mathbf{j}_{vi} = \rho_{vi}(\mathbf{V}_{vi} - \mathbf{V}_g) \quad (17)$$

The gas-phase mass fractions are defined by

$$Y_{vi} = \rho_{vi}/\rho_g \quad (18)$$

where

$$\sum_i Y_{vi} = 1 \quad (19)$$

Similarly, for the condensed phase, we define the condensed-phase mass fractions given by

$$X_{pi} = \rho_{pi}/\rho_p \quad (20)$$

where

$$\rho_p = \sum_i \rho_{pi} \quad (21)$$

and

$$\sum_i X_{pi} = 1 \quad (22)$$

A similar set of governing equations for multiphase flow, found in Ref. 3, were developed from a statistical viewpoint. The relations (8-10, 11a or 11b, 12, 13a or 13b, and 14) constitute seven partial differential equations for the nine unknowns:

$$\begin{array}{ccc} \rho_g & h_g & \rho_{pi} \\ \mathbf{V}_g & p_g & \mathbf{V}_{pi} \\ Y_{vi} & h_{vi} & h_{pi} \end{array}$$

The additional relations are supplied by equations of state

$$p_g = p_g(\rho_g, T_g, Y_{vi}) \quad (23)$$

$$h_g = \sum_i Y_{vi} h_{vi}(T_g) \quad (24)$$

$$u_{pi} \cong h_{pi}(T_{pi}) \quad (25)$$

We note that this discussion assumes knowledge of the dependence of \mathbf{q}_g , $\boldsymbol{\tau}_g$, and \mathbf{j}_{vi} on the preceding variables. A discussion of this, and a more detailed derivation of the governing equations, may be found in Ref. 5.

III. Application to Chemically Frozen Axisymmetric Jet in Phase Equilibrium

The inherent complexity of the general problem expressed by Eqs. (8-14) is due to the effect of viscosity on the global scale. The resulting equations are of the Navier-Stokes-type for which no general solution technique exists. There are, however, illustrative and practical problems that are governed by reduced forms of the general equations which retain the basic features of viscous two-phase flows.

In order to establish limits regarding the presence of a condensed phase, we consider the flow to be in equilibrium. The existence of temperature and velocity equilibrium is an assumption based on the condition that the condensed phase is in the form of a cloud of small droplets. If the droplets are small, then the heat convection and drag force are large, and the resulting temperature and velocity lags will be small. Thus, the presence of small particles is an inherent condition

in the equilibrium assumption. Surface tension effects are also neglected. The surface tension plays the governing role in determining the degree of supersaturation which occurs prior to condensation. This effect is primarily limited to the nucleation process where the nucleus size is of molecular dimensions.⁶ This effect on the nonequilibrium condensation decreases exponentially with the inverse of the droplet radius. A fully axisymmetric jet of low-temperature hydrogen discharging into a high-velocity air stream is considered. In the absence of severe streamwise velocity and temperature gradients, which is characteristic of the present mixing process, the assumption regarding equilibrium condensation of air appears to be a reasonable approximation for the major portion of the flow field.

The phase equilibrium of hydrogen requires that the condensed fraction flash to vapor on entering the atmosphere. This equilibrium requirement is perhaps the limiting assumption in the present example particularly at the higher condensed-phase concentrations (up to 0.45 in present calculations).

In any case, effects of the preceding assumptions on the flow field decrease as the mass fraction of condensed phase decreases. Thus, we consider the present calculations as a guide to the more complex physical phenomena actually occurring, and interpret the results as quantitatively accurate for a small mass fraction of condensed phase and qualitatively descriptive for other configurations.

Governing Equations

In accordance with the previous discussion, the governing equations (8-14) reduce to the following system for the axisymmetric jet, Fig. 1, with gas-phase Prandtl and Lewis numbers all equal to unity. Furthermore, the jet is assumed fully expanded to the local air pressure. The behavior of the flow downstream of the jet exit plane is then governed only by viscous phenomena, and the equations are reduced to a boundary-layer system. These equations are taken to be identical in form for both laminar and turbulent flow, with mean turbulent quantities replacing their laminar counterparts.

Continuity: Global

$$\frac{\partial \rho_m u r}{\partial x} + \frac{\partial \rho_m v r}{\partial r} = 0 \quad (26)$$

Species

$$\rho_m u \frac{\partial \beta_i}{\partial x} + \rho_m v \frac{\partial \beta_i}{\partial r} = \frac{1}{r} \frac{\partial}{\partial r} r K \frac{\partial \beta_i}{\partial r} \quad (27)$$

Momentum

$$\rho_m u \frac{\partial u}{\partial x} + \rho_m v \frac{\partial u}{\partial r} = \frac{1}{r} \frac{\partial}{\partial r} r K \frac{\partial u}{\partial r} \quad (28)$$

Energy

$$\rho_m u \frac{\partial H_m}{\partial x} + \rho_m v \frac{\partial H_m}{\partial r} + \frac{1}{r} \frac{\partial}{\partial r} r K \frac{\partial H_m}{\partial r} \quad (29)$$

The appropriate boundary and initial conditions for a jet of radius a are for

$$\begin{aligned} x = 0 \quad 0 \leq r < a \quad u = u_i \quad v = 0 \\ H_m = H_i \quad \beta_{O_2} = \beta_{N_2} = 0 \quad \beta_{H_2} = 1 \end{aligned}$$

for

$$\begin{aligned} x = 0 \quad r > a \quad u = u_e \quad v = 0 \\ H_m = H_e \quad \beta_{O_2} = \beta_{O_{2e}} \quad \beta_{N_2} = \beta_{N_{2e}} \quad \beta_{H_2} = 0 \\ x \geq 0 \end{aligned}$$

$$\lim_{r \rightarrow \infty} H = H_e \quad u = u_e \quad v = 0$$

$$\beta_{O_2} = \beta_{O_{2e}} \quad \beta_{N_2} = \beta_{N_{2e}} \quad \beta_{H_2} = 0$$

with the regularity condition applied along the jet centerline. For laminar flow we have $K = \mu_0$, and for turbulent flow we have $K = (\rho \epsilon)_m$, where ϵ is the eddy viscosity coefficient.

In virtue of the unity Prandtl and Lewis numbers, similarity in the equations for β_i , u , and H_m exists. Further, since the boundary conditions are similar, the system admits Crocco relations for H_m and the β_i 's, i.e., H_m and β_i are linearly dependent on the velocity u . Thus, the problem reduces to that of determining the solution for the velocity distribution. This, together with equations of state, and appropriate phase equilibrium relations, fully determines the problem.

The solution for u is more readily handled in a corresponding incompressible plane. Following Ref. 9, we introduce the following stream function:

$$\rho_m u r = \rho_e u_e \Psi \Psi_r \quad (30)$$

$$-\rho_m v r = \rho_e u_e \Psi \Psi_z$$

Introducing Von Mises' transformation, i.e., $x, r \rightarrow \Psi$ where

$$r^2 = \int_0^\Psi \frac{2 \rho_e u_e}{\rho_m u} \Psi' d\Psi' \quad (31)$$

and applying a modified Oseen approximation in the form

$$\mu g \rho_m r^2 u / \rho_e^2 u_e^2 \Psi^2 \cong f(x) \quad (32)$$

where the additional transformation

$$\xi = \int_0^x \frac{f(x')}{\Psi'} dx' \quad (33)$$

is introduced, the momentum equation becomes

$$\frac{\partial U}{\partial \xi} = \frac{\Psi_j}{\Psi} \frac{\partial}{\partial \Psi} \left[\Psi \frac{\partial U}{\partial \Psi} \right] \quad (34)$$

where

$$\Psi_j = a \left(\frac{\rho_i u_i}{\rho_e u_e} \right)^{1/2} \quad U = \frac{u}{u_e} \quad (35)$$

Following Libby,⁷ for laminar flow, the approximation function $f(x)$ is evaluated along the jet centerline yielding the inverse transformation

$$\frac{x}{\Psi_j} = \int_0^\xi \frac{\rho_e u_e}{(\mu_0) C_L} d\xi' \quad (36)$$

For turbulent flow studies, a variety of eddy viscosity models are available for particular applications. The most widely used model is that due to Prandtl¹⁸ and is the one used here to indicate the turbulent behavior of the present system. Applying the model, the approximation function becomes

$$f(x)_t = (n r_{1/2} / u_e) (u_e - u_{CL}) \quad (37)$$

where $r_{1/2}$ is the "half radius" defined by

$$(u)_r^{1/2} = \frac{1}{2} (u_e + u_{CL}) \quad (38)$$

and n is the Prandtl mixing length constant.

The inverse transformation then becomes

$$\frac{x_t}{\Psi_j} = \int_0^\xi \frac{1}{f(x)_t} d\xi' \quad (39)$$

The initial and boundary conditions on the momentum equation become

$$\begin{aligned} U(0, \Psi) &= U_i & 0 < \Psi < \Psi_j \\ &= 1 & \Psi > \Psi_j \end{aligned}$$

and

$$\lim_{\Psi \rightarrow \infty} U(\xi, \Psi) \rightarrow 1$$

Table 1 Numerical parameters

Altitude, km	60	40	20
P_e , atm	0.000252	0.00298	0.0545
T_e , °K	254	261	216
u_e , fps	7330	4990	2420
H_e , cal/g	658	340	117
H_j , cal/g	175	175	175
u_j , fps	2785	2460	1880

With the regularity condition applied along the jet centerline $\Psi = 0$.

The solution of the momentum equation is given by the offset circular probability function P :

$$P = \frac{1 - U}{1 - U_j} = \frac{\Psi_j}{2\xi} \int_0^1 \exp\left[-\frac{(\Psi/\Psi_j)^2}{4\xi/\Psi_j}\right] \Gamma d\Psi' \quad (40)$$

$$\Gamma = I_0 \Psi' \left(\frac{\Psi}{\Psi_j}\right) \left(\frac{2\xi}{\Psi_j}\right)^{-1}$$

which has been tabulated in Ref. 9.

In order to perform the inverse transformations to the physical plane [Eqs. (31 and 36 or 39)], the thermodynamic properties must be determined. The stagnation enthalpy is given by

$$H_m = \frac{H_e(U - U_j) + H_j(1 - U)}{1 - U_j} = \frac{u^2}{2} + h_m \quad (41)$$

and the total species concentrations are given by

$$\begin{aligned} \beta_{O_2} &= \beta_{O_{2e}}[(U - U_j)/(1 - U_j)] \\ \beta_{N_2} &= \beta_{N_{2e}}[(U - U_j)/(1 - U_j)] \\ \beta_{H_2} &= [(1 - U)/(1 - U_j)] \end{aligned} \quad (42)$$

The equation of state is given by

$$P = P_e = \rho_m \left\{ \frac{\beta_{O_{2g}}}{W_{O_2}} + \frac{\beta_{N_{2g}}}{W_{N_2}} + \frac{\beta_{H_{2g}}}{W_{H_2}} \right\} RT \quad (43)$$

where

$$\begin{aligned} P_{O_{2g}} &= \rho_m \frac{\beta_{O_{2g}}}{W_{O_2}} RT \\ P_{N_{2g}} &= \rho_m \frac{\beta_{N_{2g}}}{W_{N_2}} RT \\ P_{H_{2g}} &= \rho_m \frac{\beta_{H_{2g}}}{W_{H_2}} RT \end{aligned} \quad (44)$$

The stagnation enthalpy is given by

$$\begin{aligned} H_m &= \frac{u^2}{2} + \beta_{O_2} \left[h_{O_{2g}} - \frac{\beta_{O_2} - \beta_{O_{2g}}}{\beta_{O_2}} I_{O_2} \right] + \\ &\quad \beta_{N_2} \left[h_{N_{2g}} - \frac{\beta_{N_2} - \beta_{N_{2g}}}{\beta_{N_2}} L_{N_2} \right] + \\ &\quad \beta_{H_2} \left[h_{H_{2g}} - \frac{\beta_{H_2} - \beta_{H_{2g}}}{\beta_{H_2}} L_{H_2} \right] \end{aligned} \quad (45)$$

where

$$h_{ig} = h_{ig}(T) \quad (46)$$

and

$$L_i = L_i(T) \quad (47)$$

The equilibrium conditions used in the present calculation will be an approximation to the results presented in Sec. IV of Ref. 5. We shall consider the partial pressure of a species in two phases to be equal to the saturation pressure corresponding to the existing temperature. This is exact when only one of the species condensed. However, the error is small in virtue of the steep slope of the vapor-pressure curves. That is, the range of temperature over which two phases of

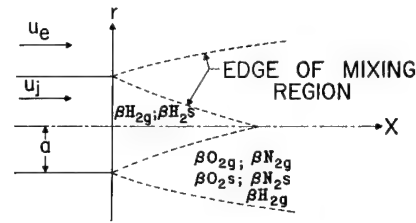


Fig. 1 Schematic of flow region.

each species exist in comparable proportions is extremely narrow. This, coupled with the close similarity between oxygen and nitrogen, justifies the assumption.

Further details of the numerical procedure are given in Ref. 5 where calculations were carried out for the data given in Table 1. Additional quantities, which were taken as constants in the calculations, are $\beta_{O_2e} = 0.232$, $\beta_{N_2e} = 0.768$, $L_{O_2} \cong 65$ cal/g, and $L_{N_2} \cong 57$ cal/g. For the thermodynamic property, $T_e = 20.0^\circ\text{K}$ saturated and $a = 1$ in. Thermodynamic properties used in the calculations are given in Refs. 11 and 12.

IV. Discussion

The description of the phenomena resulting from the dumping of cryogenic hydrogen into the atmosphere requires a departure from the usual one-dimensional pipe flow models found in the literature for treating two-phase flows. The class of problems of interest depends on mixing for their description and therefore requires a multidimensional analysis. Since the present problem involves the mixing into air of cryogenic hydrogen with a normal boiling point substantially lower than the air, we will, in general, encounter small condensed-phase mass fractions. Thus, in such a mixing

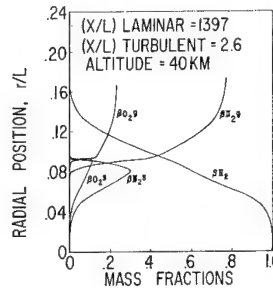


Fig. 2 Radial distributions of condensed-phase and gas-phase mass fractions.

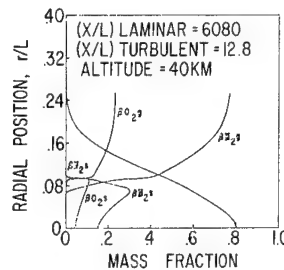


Fig. 3 Radial distributions of condensed-phase and gas-phase mass fractions.

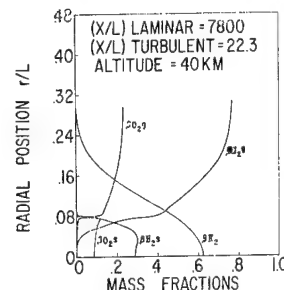


Fig. 4 Radial distributions of condensed-phase and gas-phase mass fractions.

process, the condensed phase will form a dilute suspension in the gas phase. In the present work a model is developed for treating the flow of a dilute suspension of condensing and evaporating components. Velocity and temperature lags between the phases are accounted for in terms of appropriate momentum and energy interaction parameters. Evaporation and condensation is accounted for in terms of appropriate mass transfer and the associated momentum and energy transfer parameters. In addition to these interphase transfers, we have gas-phase viscosity, thermal conductivity, and diffusion of the gas-phase components. The description of the interphase transport phenomena poses a substantial problem in itself. There is a general lack of fundamental constitutive relations to account for the simultaneous occurrence of the previously discussed interphase rate processes. This is particularly true of the nucleation and condensation processes at the low temperatures of current interest. In any case, this area requires much additional work. Thus, it is necessary to adopt a semiempirical approach that, in general, will be qualitatively valid and in certain limiting cases will provide quantitatively valid results.

In the present numerical example, the boundary conditions are such that the flow will be chemically frozen. This removes the added complication of rate chemistry and permits this preliminary analysis to focus on multiphase effects. In particular, the analysis and numerical results for a diffusion controlled axisymmetric jet are presented. Fig-

Fig. 5 Radial distribution of velocity and temperature.

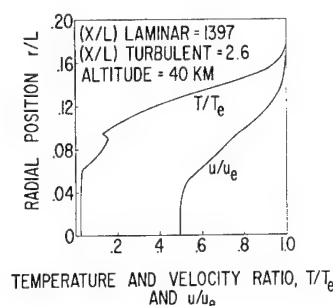


Fig. 6 Radial distribution of velocity and temperature.

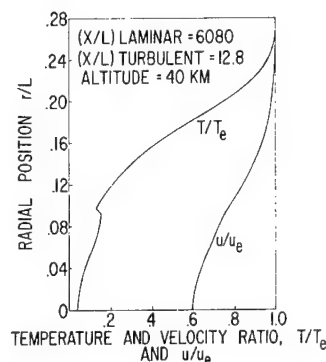


Fig. 7 Radial distribution of velocity and temperature.

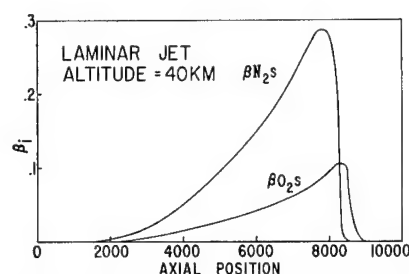
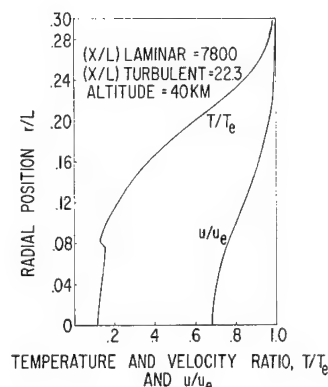


Fig. 8 Axial distribution of condensed-phase mass fraction.

ures 1-9 show the jet geometry and the distributions of the pertinent variables, respectively. Figure 1 is a schematic representation of the axisymmetric jet showing the inner cone composed essentially of undisturbed two-phase hydrogen. In crossing the cone boundary, the hydrogen flashes to vapor in accordance with the equilibrium assumption. The remaining figures show the radial and axial distributions of mixture mass fractions of condensed-phase and gas-phase components. In addition, temperature and velocity distributions are presented. These results are presented for the altitude of 40 km. Calculations at the altitudes of 20 and 60 km have been made. However, there are some general features characteristic of all altitude determinations. We note that the air is completely condensed until certain radial points corresponding to specific axial positions are attained (Figs. 2-4). At these points, there is a rapid space-wise transition from solid to vapor accompanied by a plateau on an actual decrease in temperature. The rapid phase change is due to the large rate of increase in saturation pressure with temperature. Thus, a point is reached where the local pressure and mixture concentrations cannot support the condensed phase. The energy required for the evaporation is derived from the gas phase and consequently inhibits a temperature increase in this transition zone (Figs. 5-7). A feature of considerable interest is the streamwise extent within which two phases exist. The two limiting cases of laminar and fully developed turbulent flows have been treated and provided the maximum and minimum "two-phase lengths," respectively. The long lengths in the laminar flow are attributed to the low viscosities associated with the low temperatures (Figs. 8 and 9). The turbulent model used in the present case provides an eddy viscosity based strictly on dynamic quantities, i.e., on the velocity difference between the axis and freestream. This could account for the large $\sim \frac{1000}{T}$ ratio for the laminar to turbulent two-phase lengths on the axis. We expect ratios of the order of $\frac{100}{T}$. In any case, the actual two-phase lengths depend on the degree to which turbulence has developed. Thus, we can only estimate that for the present problem two-phase lengths on the order of hundreds of feet can be expected.

Regarding effects on ignition and combustion of hydrogen, we note that two-phase flow does not exist above $T \approx 50^\circ\text{K}$.

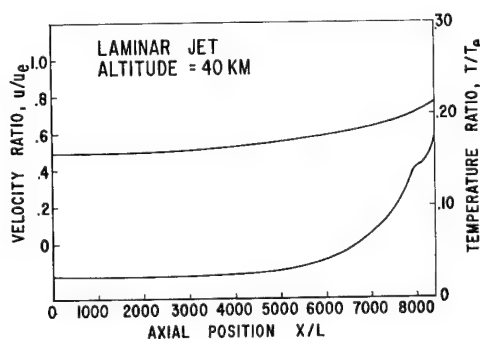


Fig. 9 Axial distribution of velocity and temperature.

At temperatures of this magnitude, we cannot expect any chemical activity. This implies that even for appropriate (high temperature) freestream conditions, the existence of two-phase flow provides an additional ignition time delay factor. That is, before ignition occurs, re-evaporation must take place where temperature rises are inhibited.

It has been pointed out that the equilibrium assumption applied to the hydrogen is perhaps the limiting assumption in the present jet problem. In order to assess this assumption, a "partial equilibrium" analysis has been carried out.¹³ In particular, two-phase hydrogen is injected into an air stream where it is assumed that the air condenses in equilibrium, whereas the condensed hydrogen particles are allowed to evaporate according to an appropriate rate law. The results of this analysis show that, for initial particle sizes ranging from 1 to 10 μ , the evaporation time ranges from 10^{-5} to 10^{-3} sec. Thus, these results indicate that the flashing assumption for the hydrogen is reasonable. It must be kept in mind, however, that the quantitative accuracy of the rate calculations depends upon the transport coefficients used in the rate equations.

References

- ¹ Wegener, P. P. and Mack, L. M., "Condensation in supersonic and hypersonic wind tunnels," *Advances in Applied Mechanics* (Academic Press Inc., New York, 1958), p. 307-447.
- ² Hirschfelder, J. O., Curtiss, C. F., and Bird, R. B., *Molecular Theory of Gases and Liquids* (John Wiley and Sons, Inc., New York, 1954).
- ³ Williams, F. A., "Detonations in dilute sprays," *ARS Progress in Astronautics and Rocketry: Detonation and Two-Phase Flow*, edited by S. S. Penner and F. A. Williams (Academic Press, New York, 1962), Vol. 6, pp. 99-114.
- ⁴ Edelman, R. B., "The flow of dilute suspension of solids in a laminar gas boundary layer," Doctoral Thesis, Yale Univ. (1962).
- ⁵ Edelman, R. and Rosenbaum, H., "Generalized viscous multicomponent-multiphase flow with application to laminar and turbulent jets of hydrogen," AIAA Preprint 63-507 (December 1963).
- ⁶ Frenkel, J., *Kinetic Theory of Liquids* (Dover Publications, Inc., New York, 1955), Chap. 7.
- ⁷ Libby, P. A., "Theoretical analysis of turbulent mixing of reactive gases with application to supersonic combustion of hydrogen," *ARS J.* **32**, 388-396 (1962).
- ⁸ Prandtl, L., "Bemerkungen zur Theorie der Freien Turbulenz," *Z. Angew. Math. Mech.* **22**, 241 (1942).
- ⁹ Kleinstein, G., "An approximate solution for the axisymmetric jet of a laminar compressible fluid," *Quar. Appl. Math.* **20**, 49-54 (April 1962).
- ¹⁰ Masters, J. I., "Some applications in physics of the P. function," *J. Chem. Phys.* **23**, 1865-1874 (1955).
- ¹¹ *Tables of Thermodynamic Properties of Gases* (National Bureau of Standards, Washington, D. C., 1955), Circular 564.
- ¹² Mullins, J. C., Ziegler, W. T., and Kirk, B. S., "The thermodynamic properties of oxygen from 20° to 100°K," Georgia Institute of Technology, TR-2, National Bureau of Standards, MR-8 (March 1, 1962).
- ¹³ Edelman, R. B. and Rosenbaum, H., "Finite rate evaporation of cryogenic hydrogen in two-phase air," General Applied Science Labs. TR 367 (September 1963).

Numerical Methods in Multidimensional Shocked Flows

SAMUEL Z. BURSTEIN*

Courant Institute of Mathematical Sciences, New York, N. Y.

Numerical methods are described for the calculation of two-dimensional time-dependent inviscid flows that contain shocks. Methods are employed which do not consider the shock as in interior moving boundary. The conservation equations describing such flows are differenced by the Lax-Wendroff method. These procedures allow the computed shock-wave transition to be given over two to three mesh widths while accurately giving the proper jump conditions across the discontinuity. Several additional methods are tested and compared. Numerical results are given for oblique and Mach reflections in air. Comparison with the exact solution for ordinary reflection is good. The Mach reflection calculation agrees with experimental photographic data obtained from wind-tunnel tests.

Introduction

MULTIDIMENSIONAL time-dependent inviscid flows provide a formidable task for computation. The problem is made more difficult by the spontaneous appearance of discontinuities in the fluid. As a result, the partial differential equations, usually written in characteristic form, cannot be integrated over the entire region of space. Instead, one applies the integral form of the differential equations at the discontinuities while continuing to use the differential equations in the remaining regions. Such methods, although conceptually simple, prove lengthy and cumbersome in practice. The purpose of this paper is to introduce the reader to new methods useful in the solution of such problems.

Until most recently, the equations of motion were written in Eulerian or Lagrangian form and then differenced for use in computations. Peter Lax¹⁻⁴ suggested that the partial differential equations be written in conservation or divergence free form, and then from these equations the difference equations should be generated. In this paper, this method is tested together with several additional numerical techniques. Although these methods have been applied to flows that are physically steady in time, in general they may be applied to time-dependent problems. The test cases of ordinary oblique shock reflection and Mach reflection were generated as time-dependent problems. This allows the partial differential equations to remain hyperbolic even when the flow is of a mixed type containing subsonic as well as supersonic regions. The solution to these steady problems is obtained asymptotically as $t \rightarrow \infty$.

Differential Equations

The mass, momentum, and energy of a fluid contained in a volume region of space will undergo a time rate of change that depends on the flux of such quantities into the space. The inviscid equations of fluid motion may be written so as to fulfill this conservation law

Presented as Preprint 64-2 at the AIAA Aerospace Sciences Meeting, New York, January 20-22, 1964; revision received August 3, 1964. The work presented in this paper is supported by the Atomic Energy Commission Computing and Applied Mathematics Center, Courant Institute of Mathematical Sciences, New York University, under Contract AT(30-1)-1480 with the U. S. Atomic Energy Commission. The author would like to thank Robert Richtmyer for stimulation given⁵ as well as Herbert Keller and John Gary for their helpful discussions. Appreciation and thanks is given to Peter Lax for his many ideas, all of which made this paper possible.

* Associate Research Scientist. Member AIAA.

$$\begin{aligned}\rho_{,t} &= -m_{,x} - n_{,y} \\ m_{,t} &= -\left(p + \frac{m^2}{\rho}\right)_{,x} - \left(\frac{mn}{\rho}\right)_{,y} \\ n_{,t} &= -\left(\frac{nm}{\rho}\right)_{,x} - \left(p + \frac{n^2}{\rho}\right)_{,y} \\ E_{,t} &= -\left[\frac{m}{\rho}(p + E)\right]_{,x} - \left[\frac{n}{\rho}(p + E)\right]_{,y}\end{aligned}\quad (1)$$

These equations are said to be in divergence free form. Here ρ is the mass per unit volume, the density, and $m = \rho u$ and $n = \rho v$ is the momenta per unit volume in the x and y directions. If e is the specific internal energy and u and v are the velocity components corresponding to their respective momenta, then $E = \rho[e + \frac{1}{2}(u^2 + v^2)]$ is the total energy per unit volume. The subscripts following the comma denote partial differentiation. The pressure p , the fifth dependent variable, may be expressed in terms of the other quantities through the equation of state $p = P(\rho, e)$. If γ is the ratio of specific heats, the functional P can be given by the ideal gas law:

$$p = \rho(\gamma - 1)e = (\gamma - 1)\{E - \frac{1}{2}[(m^2 + n^2)/\rho]\}$$

Equation (1) can now be written completely in terms of the conservation variables ρ , m , n , and E . These equations may be written in a more easily handled form. If a vector quantity w has the four components,

$$w = \begin{pmatrix} \rho \\ m \\ n \\ E \end{pmatrix}$$

the conservation law can be expressed as

$$w_{,t} = f_{,x} + g_{,y} \quad (2)$$

The vectors f and g are just functions of w and are given by

$$(w) = \begin{bmatrix} -m \\ \frac{\gamma - 3}{2} \frac{m^2}{\rho} - (\gamma - 1)E + \frac{\gamma - 1}{2} \frac{n^2}{\rho} \\ -\frac{mn}{\rho} \\ -\gamma \frac{Em}{\rho} - \frac{\gamma - 1}{2} \frac{m^3 + mn^2}{\rho^2} \end{bmatrix}$$

$$g(w) = \begin{bmatrix} -n \\ -\frac{nm}{\rho} \\ \frac{\gamma - 3}{2} \frac{n^2}{\rho} - (\gamma - 1)E + \frac{\gamma - 1}{2} \frac{m^2}{\rho} \\ -\gamma \frac{En}{\rho} - \frac{\gamma - 1}{2} \frac{n^3 + nm^2}{\rho^2} \end{bmatrix}$$

Because of the nonlinearity of Eq. (2), smooth solutions, in general, will not exist for all time. If we admit discontinuities in the solution, then the solution of Eq. (2) is a weak solution.^{2, 3} A classical solution to a fluid dynamic problem consists of the description of w up to a time when shocks first appear in the domain of interest. A weak solution is a solution that may be continued so as to predict the shocked region for all subsequent times. This is possible since the Rankine-Hugoniot shock conditions, which express conservation of mass, momentum, and energy, are contained in a weak solution. Most important, the weak solutions obtained from a given set of equations is determined by the form in which the equations are written. If new variables z are introduced as nonlinear functions of w such that a conservation law can be written for z , the weak solutions obtained from Eq. (2), say w' , can be transformed by these nonlinear functions into a solution z' . In general, z' will not be a weak solution of its own conservation equations.

As a consequence of the theory of weak solutions, the shock is not considered an interior boundary but is a part of the solution,⁶ and as such differs from the usual treatment of flows that contain such discontinuities. Usually the shock wave, which is considered as an interior boundary, is located by intersecting characteristics of the same family. At this point, the conditions needed to match the flow on either side are the Rankine-Hugoniot equations.⁷ The use of the characteristic equations may then be continued in the smooth part of the flow. The basic difference equations corresponding to Eq. (2) will now be given.

Lax-Wendroff Difference Equations

The Lax-Wendroff method^{3, 4} is based on the Taylor expansion of the vector function $w(x, y, t + \Delta t)$ so as to include the second-order term $\frac{1}{2}\Delta t^2 w_{,tt}$. It is this term that, when added to the "intuitive" difference analog of Eq. (2), i.e.,

$$w(x, y, t + \Delta t) = w(x, y, t) + [f_x(t) + g_y(t)]\Delta t \quad (3)$$

produces a stable difference approximation. It is a well-known fact that difference equation (3) is unconditionally unstable. However, the central difference approximation could be replaced by a forward or backward difference resulting in a difference scheme that is conditionally stable, but only accurate to $O(\Delta t^2)$. The notation f_x denotes the centered difference quotient that approximates the derivative $f_{,x}$ within an error that is $O(\Delta x^3)$. This second-order term also increases the order of the accuracy since the truncation error becomes $O(\Delta t^3)$. Lax and Wendroff observed that the form of this added second-order term may be established by the differential equation itself, i.e.,

$$\begin{aligned} \frac{1}{2}\Delta t^2 w_{,tt} &= \frac{1}{2}\Delta t^2 (f_{,x} + g_{,y})_{,t} = \frac{1}{2}\Delta t^2 (f_{,tx} + g_{,ty}) \\ &= \frac{1}{2}\Delta t^2 [(Aw_{,t})_{,x} + (Bw_{,t})_{,y}] \\ &= \frac{1}{2}\Delta t^2 \{ [A(f_{,x} + g_{,y})]_{,x} + [B(f_{,x} + g_{,y})]_{,y} \} \end{aligned} \quad (4)$$

Here we have used A and B to represent the Jacobians of $f(w)$ and $g(w)$ with respect to w . Taking centered differences of (4) and adding the result to (3) yields

$$w(x, y, t + \Delta t) = w(x, y, t) + (f_x + g_y)\Delta t + \{ [A(f_x + g_y)]_x + [B(f_x + g_y)]_y \} (\Delta t^2/2) + O(\Delta t^3) \quad (5)$$

Since this difference scheme is conditionally stable, a linear analysis⁴ allows the computation of the linear stability limit. The time increment Δt and space increments Δx and Δy are related to the flow Mach number $M = (u^2 + v^2)^{1/2}/c$ (c being the local sound speed) by

$$\frac{\Delta t}{\Delta x} \leq \frac{(M+1)^{-1}}{c(8)^{1/2}} \quad \frac{\Delta t}{\Delta y} \leq \frac{(M+1)^{-1}}{c(8)^{1/2}} \quad (5a)$$

Lax and Wendroff modified Eq. (5) by adding an additional term that is $O(\Delta t^4)$. The term is

$$-\frac{1}{8}\Delta t^4 (A^2 + B^2) w_{,xxyy} \quad (6)$$

For this difference scheme, a linear analysis⁴ gives, for the restriction on the time step,

$$\Delta t/\Delta \leq (2\lambda)^{1/2} \quad \lambda = \text{eigenvalue}_{\max} \{A^2 + B^2\}, \Delta x = \Delta y = \Delta \quad (6a)$$

The allowable time step given by Eq. (6a) is greater than that given by Eq. (5a). The large amount of additional computing time required at each mesh point for the evaluation of Eq. (6) is a drawback for this method. All computations carried out in this paper were obtained with difference scheme (5) unless otherwise noted. Although there is no unique way of differencing Eq. (5), the conservation form of differencing will be shown.

A Third Difference Scheme of Second-Order Accuracy

The amplification matrix⁹ associated with a given differencing scheme is defined by the relation $V(t + \Delta t) = HV(t)$. Here V is a vector function, which, when operated on by H (the amplification matrix), is mapped into a later time. Repeated applications of H results in V being known at increasing intervals of time, $t + 2\Delta t$, $t + 3\Delta t$, etc. The amplification matrix G_1 and G_1' of the Lax-Wendroff difference schemes can be given after a Fourier transformation [allow $\xi \approx \sin \xi$ and $\xi^2 \approx 2(1 - \cos \xi)$] by

$$G_1(\xi, \eta) = I + i(\xi A + \eta B) - \frac{1}{2}(\xi A + \eta B)^2 + O(\xi^3) \quad (7)$$

$$G_1'(\xi, \eta) = G_1(\xi, \eta) - \frac{1}{8}(A^2 + B^2)\xi^2\eta^2 \quad (8)$$

Equation (7) can also be obtained by expanding the amplification matrix of exact solutions of Eq. (2), $e^{i(\xi A + \eta B)}$ for small values of the wave numbers ξ and η . In order to generate additional difference schemes (possibly with less stringent stability requirements), one may try to find an approximation to the exact amplification matrix. The approximation should differ from G_1 only in third- or higher-order terms so as to preserve the second-order accuracy of the scheme. This idea was suggested by G. Strang. It is not difficult to show that

$$e^{i(\xi A + \eta B)} = \frac{e^{i\xi A} e^{i\eta B} + e^{i\eta B} e^{i\xi A}}{2} + O(\xi^3) \quad (9)$$

Rewrite the right-hand side of Eq. (9) by expanding each of the matrices in a Taylor series and collect terms. Define the result by G_2 , a new amplification matrix:

$$\begin{aligned} G_2 &= I + i(\xi A + \eta B) - \frac{1}{2}(\xi A + \eta B)^2 + K \\ K &= \frac{A^2 B^2 + B^2 A^2}{8} \eta^2 \xi^2 - \\ &\quad i \left(\frac{AB^2 + B^2 A}{4} \xi \eta^2 + \frac{A^2 B + B A^2}{4} \eta \xi^2 \right) \end{aligned} \quad (10)$$

Equations (10) and (7) differ only by terms which are $O(\xi^3)$. Clearly the difference scheme associated with Eq. (10) is

also second-order accurate. The additional terms are difference analogs of the differential operators

$$\frac{\Delta t^3}{4} \left\{ (AB^2 + B^2A) \frac{\partial^3}{\partial x \partial y^2} + (A^2B + BA^2) \frac{\partial^3}{\partial x^2 \partial y} \right\} + \frac{\Delta t^4}{8} (A^2B^2 + B^2A^2) \frac{\partial^4}{\partial x^2 \partial y^2} \quad (10a)$$

and will be referred to as a triple viscosity, a stabilizing term. The value of these additional terms lies in the fact that the amplification matrix G_2 may be written in the separated and more easily handled form

$$G_2(\xi, \eta) = [M(\xi)N(\eta) + N(\eta)M(\xi)]/2 \quad (11)$$

The abbreviations $M(\xi) \equiv e^{i\xi A}$ and $N(\eta) \equiv e^{i\eta B}$ have been used. It is a well-known fact of hyperbolic equations that A and B are real. Friedrichs has shown that A and B can be symmetrized. Then $M = M^T = M^*$, i.e., M is equal to its transposed complex conjugate M^* as a result of the following relations:

$$M = I + iA\xi - (A^2\xi^2/2) + O(\xi^3)$$

$$M^* = I - iA^T\xi - (A^2)^T(\xi^2/2) + O(\xi^3)$$

$$M^* = I - iA\xi - (A^2\xi^2/2) + O(\xi^3)$$

Hence M is Hermitian and also $MM^* = I = M^*M$, i.e., the matrices denoted by M (and N) are unitary. A unitary transformation corresponds to a generalized rotation which leaves all vectors unaltered in length.

Using Eq. (11), the inner product (G_2q, q) (q being an arbitrary unit vector) may be formed:

$$2[G_2(\xi, \eta)q, q] = \{[M(\xi)N(\eta) + N(\eta)M(\xi)]q, q\}$$

The unitary property states $[M(\xi)q, q] \leq 1$ and a similar statement can be made for $N(\eta)$. Hence, the amplification matrix, Eq. (11), satisfies the inequality $[G_2(\xi, \eta)q, q] \leq 1$. According to Lax's new stability theorem,⁴ this implies that the absolute value of all integer powers of G_2 are bounded and the difference equations are stable if the time and space increments satisfy the eigenvalue inequalities

$$|\lambda_{\max}(A)|\Delta t/\Delta x \leq 1 \quad |\lambda_{\max}(B)|\Delta t/\Delta x \leq 1$$

This is the famous Courant-Friedrichs-Lewy condition.⁸

It is clear that the three additional terms represented by K in Eq. (10) act as stabilizers so as to allow the maximum possible time step for these explicit methods. The price one pays is the increase in computation time per net point because of the large number of matrix multiplications.

A Fourth Difference Scheme Using Pseudoviscosity

The idea of introducing an artificial viscosity into shock calculations is attributed to Von Neumann and Richtmyer.⁶ They wanted to produce a smooth transition across the shock in all the dependent variables when using the partial differential equations of motion everywhere in the flow field. The idea is to introduce an additional viscous pressure term ϕ wherever the pressure term p appears, i.e., the substitution $p + \phi \rightarrow p$. In vector notation, Eq. (2) becomes

$$w_{,t} = (f + r)_{,x} + (g + s)_{,y} \quad (12)$$

The new vectors are defined by

$$r = \begin{pmatrix} 0 \\ -\phi \\ 0 \\ -(m/\rho)\phi \end{pmatrix} \quad s = \begin{pmatrix} 0 \\ 0 \\ -\phi \\ -(n/\rho)\phi \end{pmatrix} \quad (13)$$

The value of these vectors should be small when away from sharp compressions and should attain maximum values in

the shock region. ϕ should have a nonzero contribution when the shocked flow is locally one-dimensional and should be invariant under a rotation of coordinates. A simple form for the viscosity is

$$\phi = \beta^2 \rho [(\partial u / \partial x) + (\partial v / \partial y)]^2$$

This form reduces to the Richtmyer viscosity in one dimension.⁹ The constant β has the dimension of length and is proportional to Δx or Δy , and so ϕ has the dimensions of pressure. ϕ is also restricted when the fluid is undergoing a local expansion, i.e.,

$$\phi = \beta^2 \rho \left[\left(\frac{m}{\rho} \right)_{,x} + \left(\frac{n}{\rho} \right)_{,y} \right]^2 \begin{cases} \text{if } \left(\frac{m}{\rho} \right)_{,x} < 0, \left(\frac{n}{\rho} \right)_{,y} < 0 \\ \text{if } \left(\frac{n}{\rho} \right)_{,y} \geq 0, \left(\frac{m}{\rho} \right)_{,x} < 0 \\ \text{if } \left(\frac{m}{\rho} \right)_{,x} \geq 0, \left(\frac{n}{\rho} \right)_{,y} < 0 \\ \text{if } \left(\frac{m}{\rho} \right)_{,x} \geq 0, \left(\frac{n}{\rho} \right)_{,y} \geq 0 \end{cases} \quad (14)$$

As a result of the dissipation terms, Eq. (12) is no longer a first-order quasilinear partial differential equation. Based on previous experience⁹ with the one-dimensional form of these higher-order equations, it is expected that the allowable time increment for stability of the difference analog to Eq. (12) will be appreciably smaller than required for the previous difference schemes.

During computations, β^2 was chosen small enough so that the shock transition would be as sharp as possible, but large enough so that oscillations would be damped. A value of $\beta^2 = 1.9$ seemed to be a good compromise. This value falls within the range obtained by Richtmyer for the one-dimensional case. Since β is proportional to Δx it is possible to neglect the presence of $r_{,x}$ and $s_{,y}$ in the term $w_{,t}$. $\Delta t^2/2$ since third-order quantities are neglected. The proposed difference scheme is then

$$w_{i,j}(\Delta t) = \Psi_{i,j}(0) + [r_{i+1/2,j}(0) - r_{i-1/2,j}(0)]\Delta t/\Delta + (s_{i,j+1/2}(0) - s_{i,j-1/2}(0))\Delta t/\Delta \quad (15)$$

subject to the constraints imposed by Eq. (14), where the terms given on the right-hand side of Eq. (16) are represented by $\Psi_{i,j}(0)$.

Interior and Boundary Net Points

Usually the computations performed with the four difference methods were carried out on a square spatial mesh. The one exception was for the flow field of Ref. 12. Here a rectangular array of points were used ($\Delta x = \frac{7}{6}\Delta y$). If one is given initial data at each mesh point (x_i, y_j) at time $t = 0$, i.e., $\rho(x_i, y_j, 0)$, $m(x_i, y_j, 0)$, $n(x_i, y_j, 0)$, and $E(x_i, y_j, 0)$ then the fundamental difference equation for the evaluation of $w(x_i, y_j, t + \Delta t)$ is

$$w_{i,j}(t + \Delta t) = w_{i,j}(t) + \frac{\Delta t}{2\Delta} [f_{i+1,j}(t) - f_{i-1,j}(t)] + \frac{\Delta t}{2\Delta} [g_{i,j+1}(t) - g_{i,j-1}(t)] + \sum_{l=1}^4 (-1)^{l-1} C_l(t) \frac{\Delta t^2}{2\Delta^2} \quad (16)$$

Here equal net spacing $\Delta x = \Delta y = \Delta$ is used and the subscripts (i, j) correspond to the net point with coordinates (x_i, y_j) . The vectors C_l are evaluated at $(i + \frac{1}{2}, j)$, $(i - \frac{1}{2}, j)$, $(i, j + \frac{1}{2})$ and $(i, j - \frac{1}{2})$, respectively, i.e.,

$$\begin{aligned} C_1 &= A_{i+1/2,j} \{ (f_{i+1,j} - f_{i,j}) + \frac{1}{2}(g_{i,j+1} - g_{i,j-1} + g_{i+1,j+1} - g_{i+1,j-1}) \} \\ C_2 &= T_{-1}^{(x)} C_1 \\ C_3 &= B_{i,j+1/2} \{ \frac{1}{2}(f_{i+1,j} - f_{i-1,j} + f_{i+1,j+1} - f_{i-1,j+1}) + (g_{i,j+1} - g_{i,j-1}) \} \\ C_4 &= T_{-1}^{(y)} C_3 \end{aligned} \quad (17)$$

Table 1 Results of numerical stability tests

Method	Experimental stability value
1. Eq. (16)	≤ 0.86 CFL
2. Eq. (16) + Eq. (6)	≤ 0.86 CFL
3. Eq. (9)	≤ 0.8 CFL
4. Eq. (15)	≤ 0.1 CFL

$T_{\theta}^{(x)}$, $T_{\theta}^{(y)}$ are translation operators that shift the index of the expressions for C_1 and C_3 from i to $i + \theta$ and j to $j + \theta$, respectively. The coefficient matrices are taken to be $A_{i+1/2, j} = \frac{1}{2}(A_{i+1, j} + A_{i, j})$, etc. It is to be noted that once computation is completed at point (x_i, y_j) , if computational sequencing is by points on rows (columns), $C_1 \rightarrow C_2$ for point (x_{i+1}, y_j) [$C_3 \rightarrow C_4$ for point (x_i, y_{j+1})]. Hence, except for regions of the flow near the boundary, these vectors are alternately added to and subtracted from the flow canceling in pairs in the interior region. This result follows as a consequence of conservation differencing and insures the conservation of the mass, momentum, and energy in the interior region.

The same difference equations may be used for mesh points on the boundary of the fluid region. Walls or obstructions in the flow field are represented by a string of net points and are treated as regular interior net points. This may be accomplished if the conservation variables are defined on a virtual line of net points constructed within the solid boundary. These points obtain their values via a reflection principle that images the flow properties near the boundary according to simple rules. The virtual points are only used to generate approximations to partial derivatives for the points defining the boundary. If the boundary is parallel to the x axis ($y = y_i$), as is the upper boundary in this paper, the reflection rule is

$$\begin{aligned} \rho_{i, j+1} &= \rho_{i, j-1} & m_{i, j+1} &= m_{i, j-1} \\ n_{i, j+1} &= -n_{i, j-1} & E_{i, j+1} &= E_{i, j-1} \end{aligned}$$

For a boundary parallel to the y axis ($x = x_i$), the rules for the density and total energy are the same, but $m_{i+1, j} = -m_{i-1, j}$ and $n_{i+1, j} = n_{i-1, j}$.

For boundaries that are not parallel to either coordinate axis but make some angle α with the horizontal, the construction is somewhat more complicated. Here quadratic interpolation and evaluation of derivatives of the conservation variables with unequal spacing is necessary. For this computation¹⁰ instabilities may occur whenever two points come much closer than a characteristic length equal to $c\Delta t$.^{7, 11}

The inflow boundary is prescribed as a known constant state. The conditions describing the outflow boundary is more complicated, since centered differences in the x directions cannot be evaluated in the usual manner. Rather than compute the x direction by centered formulas, left-sided differences are used at this boundary. Wherever Eqs. (16) and (17) contain x differences, extrapolated approximations are used.¹⁰

Shock Relations

The general form of the integral or jump conditions may be obtained from the differential equations (2). If the left-hand side is integrated over a volume region of space while the left-hand side is integrated over the surface defining this region, the result

$$s[w_i] = [F_i \cdot n] \quad (18)$$

is the Rankine-Hugoniot relations valid for a shock contained in the volume region of space. Here n is the unit normal vector to the discontinuity; F_i represents the vector (f_i, g_i) , and s is the normal speed of the discontinuity. $[\lambda]$ indicates

the jump in λ . Every weak solution must satisfy these jump conditions across a line of discontinuity. This fact was used to test the two-dimensional numerical method as far as its ability to reproduce one-dimensional shocks. When a stationary one-dimensional shock solution is given as the initial condition, the difference equations were identically satisfied for all times t . The Rankine-Hugoniot conditions, in this case ($s = 0$), is

$$[f] = 0 \quad (18a)$$

i.e., $f_+ = f_-$. The two-dimensional equations reduce to

$$w(x, t + \Delta t) = w(x, t) + f^- \Delta t + (Af_x)_2(\Delta t^2/2)$$

Since the shock connects two constant states, the centered second derivative vanishes. Across, the shock equation (18a) is satisfied so that at the shock a centered difference in f (numerically equal to $[f]$) vanishes.

Equations (18), after much algebraic manipulation, may be written in the form of a cubic polynomial for the local tangent of the shock angle σ , i.e.,

$$\tan^3 \sigma + c_2 \tan^2 \sigma + c_1 \tan \sigma + c_0 = 0 \quad (19)$$

The coefficients are given by

$$c_2 = 2(1 - M^2)/\{\tan \alpha [2 + (\gamma - 1)M^2]\}$$

$$c_1 = [2 + (\gamma + 1)M^2]/[2 + (\gamma - 1)M^2]$$

$$c_0 = 2/\{\tan \alpha [2 + (\gamma - 1)M^2]\}$$

The flow makes an angle α with the horizontal, and the Mach number is M . Since $M > 1$, Descartes' rule of signs allows no more than two positive roots and one negative root. The positive roots correspond to the strong and weak compression shocks, the choice of the solution being dictated

Table 2 Comparison of the four difference methods^a

Eq. (5)	Eqs. (5) and (6)	Eq. (9)	Eq. (15)	
1.000	1.000	1.000	1.000	exact density 1.0
1.000	1.000	1.000	1.000	
1.000	1.000	1.000	1.000	
1.000	1.000	1.000	1.000	
1.000	1.000	1.000	1.000	
1.000	1.000	1.000	1.000	
1.000	1.000	1.000	1.000	
0.999	1.000	1.000	1.000	
1.000	1.000	1.000	1.000	
1.001	1.001	1.000	1.000	
1.000	1.001	1.000	0.999	exact shock position exact density 2.277
0.998	0.999	1.000	0.999	
0.998	0.998	0.999	1.002	
1.003	1.000	0.997	1.000	
1.007	1.005	1.011	1.000	
0.996	0.993	0.988	0.987	
0.982	0.970	0.986	0.991	
0.964	0.948	0.957	1.068	
0.962	0.975	0.995	1.239	
1.246	1.283	1.199	1.499	
2.072	2.035	2.097	1.796	
2.509	2.479	2.678	2.042	
2.319	2.356	2.248	2.214	
2.296	2.308	2.265	2.323	
2.327	2.320	2.338	2.342	
2.318	2.314	2.319	2.306	
2.319	2.317	2.306	2.246	
2.337	2.331	2.347	2.216	
2.334	2.330	2.366	2.220	
2.341	2.337	2.369	2.212	

^a The density is shown at the upper boundary for the case of oblique reflection, $M_\infty = (u^2 + v^2)^{1/2}/c = 2$.

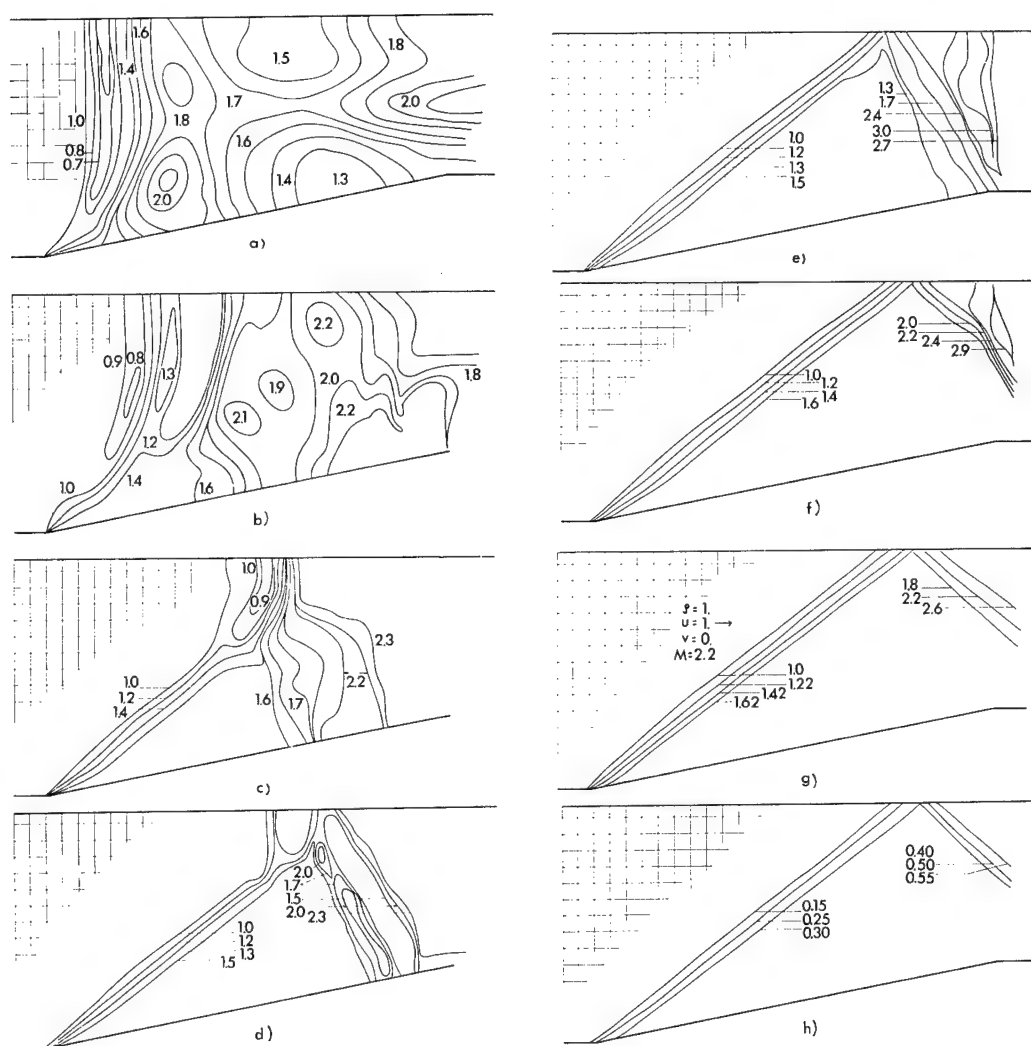


Fig. 1 Approach of the density field to the asymptotic solution for ordinary reflection when $M_{\infty} = 2.2$ ($\gamma = 1.4$). Figures 1a-1g correspond to the following time multiples of Δt : a) 70; b) 140; c) 210; d) 350; e) 420; f) 560; g) 700 ($\Delta t/\Delta = 0.233$). Figure 1h is the pressure field corresponding to 1g. Over-all average density ratio = 2.33, exact = 2.34.

by the boundary condition on the pressure downstream of the shock. An expansion shock corresponds to the negative root, but this leads to a contradiction of the second law of thermodynamics.

Equation (19) together with Eqs. (18) define the flow field for the exact solution of regular oblique shock reflection. Comparison can then be made between exact theory and the solutions generated as a result of the numerical methods. Positive roots are not obtained from Eq. (19) for all values of the parameters M and α . For some range of these parameters, complex roots occur which correspond to the case of Mach reflection. For this case, the flow pattern cannot be predicted exactly and, as a result, the numerical methods must be compared with either approximate theories or experimental evidence.

Initial Conditions

The four difference schemes (16, 16 and 6, 9, and 15) were tested on the problem of ordinary shock reflection. The steady-state solution is such that the flow is everywhere supersonic and irrotational. A constriction or wedge of angle α appears in the channel. In this region, an incident shock changes the flow direction through the angle α so that it is parallel to the wedge. A secondary or reflecting shock from the upper wall changes the flow direction by an equal amount so that it is again parallel to the upper wall. Since

these conditions represent an exact solution, it was felt that a comparison of the difference solution of this steady flow problem with the exact solution would be a good measure of the computing methods. Considering the problem as being time-dependent allowed the flow to approach the steady-state shock reflection solution when arbitrary initial data were prescribed. In this way, one could also ascertain the rate of convergence of the method. An incident shock, acting as a strong perturbation on the flow, was set normal to the inflow ($\sigma = \pi/2$) at the toe of the wedge ($x = 0$) whose angle $\alpha = \tan^{-1}(1/3)$. The jump conditions across this shock were made to differ from those predicted by the Hugoniot conditions, i.e., if w_{∞} is the inflow condition, w_1 is not connected to w_{∞} through Eq. (18). In addition, the reflected shock was completely eliminated in the initialization. Then the initial conditions prescribed were

$$\left. \begin{aligned} -\infty < x \leq 0 \\ 0 \leq y \leq y_{wall} \end{aligned} \right\} w = w_{\infty}$$

$$\left. \begin{aligned} \infty > x > 0 \\ y_{wedge} \leq y \leq y_{wall} \end{aligned} \right\} w = w_1 \quad (20)$$

For the case of Mach reflection considered in Ref. 12, the initial condition prescribed was that of impulsive flow, i.e., $w(x, y, 0) = w_0$ everywhere. All other cases of Mach reflection used the same conditions as given by Eqs. (20).

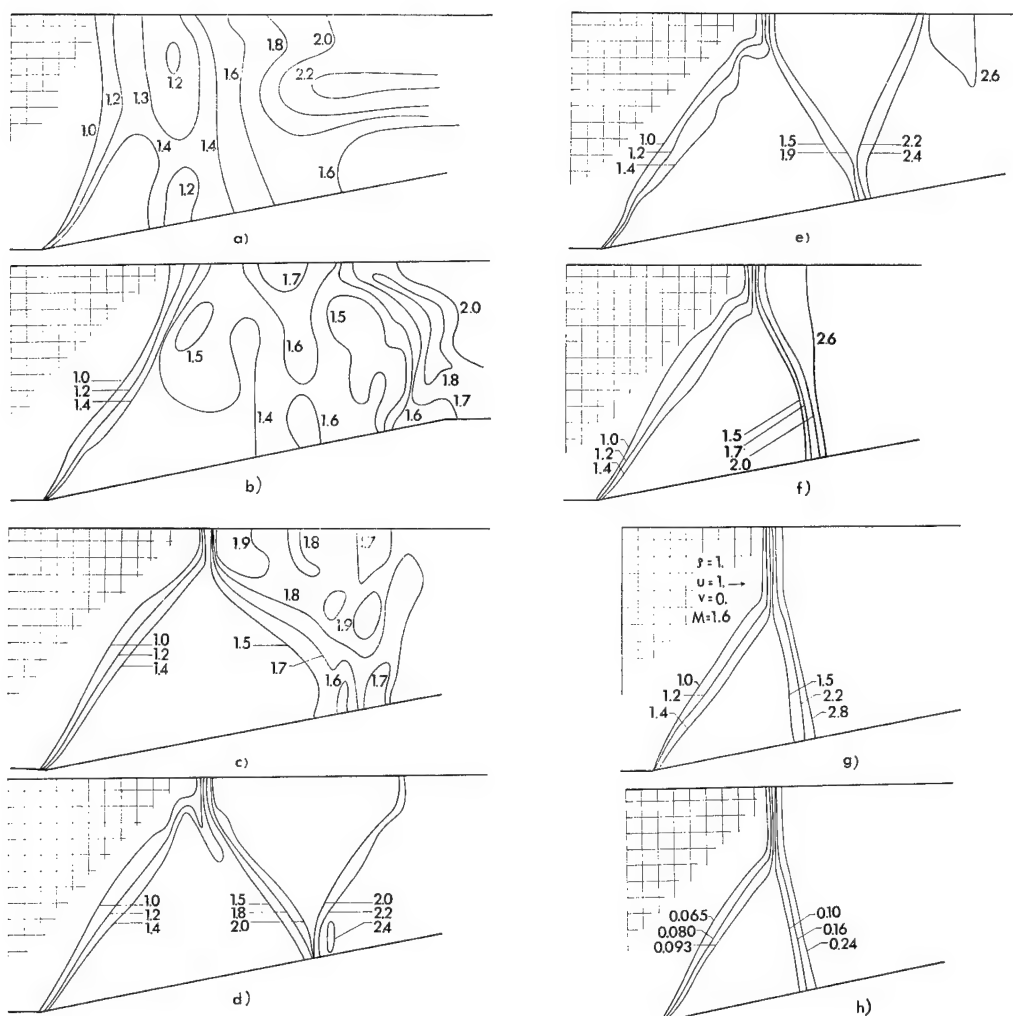


Fig. 2 Approach of the density field to the asymptotic solution for Mach reflection when $M_{\infty} = 1.6$ ($\gamma = 1.2$). Figures 2a-2g correspond to the following time multiples of Δt : a) 70; b) 140; c) 210; d) 350; e) 420; f) 560; g) 700 ($\Delta t/\Delta = 0.229$). Figure 2h is the pressure field corresponding to 2g.

Tests of Stability and Numerical Results

The Courant-Friedrichs-Lewy (CFL) stability condition $\Delta t/\Delta \leq 1/(|u| + c) \equiv \text{CFL}$ where $|u| = (u^2 + v^2)^{1/2}$ was used as a measure of the stability of the difference methods. The difference scheme associated with the triple viscosity should exhibit stability for this value of the time increment. Table 1 gives the empirically obtained values of stability. Method 3 requires a lower value of the time increment compared with the theoretical value. This is probably because the matrices A and B vary quite rapidly in the shocked region, contradicting the assumption of linearization. In addition, the effect of the boundaries and their treatment does not appear in the analysis. Method 2 allows, in practice, a time interval greater than that predicted by Eq. (6a) by a factor of approximately 2. It is clear that the reason for this lies in the stability proof,⁴ which makes use of inequality estimates that lead to conservative results.

A comparison of the four methods is shown in Table 2. Notice the spread of the shock at the reflection point on the

upper boundary and the resultant decrease in oscillations near the shock position for the method involving Eq. (15). The first three methods seem to give essentially the same result. Since Eq. (16) results in the fastest computation, it was used to give all the following results.

This numerical scheme was tested for various values of the Mach number at the inflow boundary, viz., $1.3 \leq M_{\infty} \leq 3.2$. Exact solutions are compared to the numerical results in Table 3. For the wedge angle used, the flow followed one of two solutions, which are distinct and depend quite strongly on the value of the Mach number. For $M_{\infty} \leq 1.87$, Mach reflection occurred, whereas for larger values of the Mach number, the asymptotic solution was that of ordinary shock reflection. The methods used were able to predict quite sharply this limiting value of the Mach number. Figure 1 gives the characteristic appearance of the time-dependent solution for values of $M_{\infty} > 1.87$, whereas Fig. 2 shows the time-dependent Mach reflection solution for $M_{\infty} = 1.6$ and $\gamma = 1.2$.

These Mach reflection calculations were not compared with experimental data, but the behavior seems to be qualitatively correct. Instead, an additional calculation was performed in which the boundary conditions closely approximated the experimental wind tunnel of Ref. 12. Here $\alpha = \tan^{-1}(3/7)$ whereas the spatial mesh was defined by unequal mesh intervals, i.e., $\Delta x = \frac{7}{6}\Delta y$. Quantitative comparison is given at the bottom of Table 4. Here the shock angles are defined by

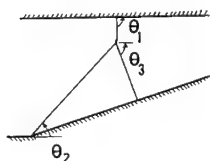


Fig. 3 Geometry of Mach reflection.

Table 3 Results of oblique reflection ($\gamma = 1.4$)

M_∞	Wedge angle	Incident shock, deg		Reflected shock, deg	
		Computed	Exact	Computed	Exact
2.0	$\tan^{-1}(\frac{1}{5})$	40.2	40.8	45.8	54.0
2.2	$\tan^{-1}(\frac{1}{5})$	37.2	37.2	47.0	46.6
3.0	$\tan^{-1}(\frac{1}{5})$	27.3	28.6	not computed	33.8

Fig. 3. The Mach stem and incident shock angles agree quite well. The reflected shock in the experiment interacted with an expansion fan, and so the agreement here cannot be as good.

A steady-state solution for values of $M_\infty \leq 1.4$, $\alpha = \tan^{-1}(\frac{1}{5})$ could not be obtained. The reason seems to be associated with a combination of factors. The rapidly shrinking triangular region under the triple point combined with the technique of computing derivatives at the surface of the wedge leads to inaccuracies. The reflection method that is used on the wedge is a second-order scheme and hence will be inaccurate when there are large variations in the flow properties, i.e., when many shocks are present in a small region. In addition, for these low values of Mach number, the long Mach shock implies that the flow is basically subsonic in the downstream region, a fact that allows disturbances (which might be generated numerically by the extrapolating procedure) to propagate upstream from that boundary.

In addition, the slipline emerging from the triple point could not be numerically resolved in these calculations. This was probably due to the weakness of the shocks in this study, i.e., the strength of the slipline depends upon the difference of entropy across this discontinuity. The entropy production from a weak shock, however, behaves as the cube of the shock strength.

References

- ¹ Lax, P. D., "Hyperbolic systems of conservation laws II," *Commun. Pure Appl. Math.* **10**, 537-566 (1957).
- ² Lax, P. D., "Weak solutions of nonlinear hyperbolic equa-

Table 4 Mach reflection ($\gamma = 1.4$)

M_∞	Wedge angle	Mach stem θ_1 , deg	Incident shock θ_2 , deg	Reflected shock θ_3 , deg
1.85	$\tan^{-1}(\frac{1}{5})$	90.0	46.2	66-80
1.7	$\tan^{-1}(\frac{1}{5})$	90.0	48.7	61-73
1.6	$\tan^{-1}(\frac{1}{5})$	90.0	54.6	65.3
1.5	$\tan^{-1}(\frac{1}{5})$	90.0	59.0	70.2
1.6 ($\gamma = 1.2$)	$\tan^{-1}(\frac{1}{5})$	90.0	52.3	72.4
3.075	$\tan^{-1}(\frac{1}{5})$	90.0	41.0	35.5
$\Delta x = \frac{7}{6} \Delta y$				
Experimental ¹²		Experimental ¹²		
3.15	$\approx 23^\circ$	40.5-42.5° $\approx 43.5^\circ$		

tions and their numerical computation," *Commun. Pure Appl. Math.* **7**, 159-193 (1954).

³ Lax, P. D. and Wendroff, B., "Systems of conservation laws," *Commun. Pure Appl. Math.* **13**, 217-237 (1960).

⁴ Lax, P. D. and Wendroff, B., "Difference schemes with high order of accuracy for solving hyperbolic equations," NYO Rept. 9759, Courant Institute of Mathematical Sciences, New York Univ. (July 1962).

⁵ Richtmyer, R. D., "Proposed fluid dynamics research," unpublished memo., Courant Institute of Mathematical Sciences, New York Univ. (September 28, 1960).

⁶ Von Neumann, J. and Richtmyer, R. D., "A method for the numerical calculation of hydrodynamical shocks," *J. Appl. Phys.* **21**, 232-237 (1950).

⁷ Richtmyer, R. D., "Progress report on the Mach reflection calculation," NYO 9764, Courant Institute of Mathematical Sciences, New York Univ. (September 1961).

⁸ Courant, R., Friedrichs, K. O., and Lewy, H., "Über die Partiellen Differenzengleichungen der Mathematischen Physik," *Math. Ann.* **100**, 32 (1928).

⁹ Richtmyer, R. D., *Difference Methods for Initial-Value Problems* (Interscience Publishers, Inc., New York, 1957), Chap. IV.

¹⁰ Burstein, Samuel Z., "Numerical calculations of multi-dimensional shocked flows," NYO 10,433, Courant Institute of Mathematical Sciences, New York Univ. (November 1963).

¹¹ Gary, J., private communication (1963).

¹² Gross, R. A. and Chinitz, W., "A study of supersonic combustion," *J. Aerospace Sci.* **27**, 517-524 (1960).

Laminar Boundary Layer with Hydrogen Injection Including Multicomponent Diffusion

PAUL A. LIBBY* AND MAURO PIERUCCI†
Polytechnic Institute of Brooklyn, Freeport, N. Y.

A laminar flow, which is simple from the fluid mechanical and chemical points of view, but which involves multicomponent diffusion and relatively accurate transport properties is considered. Thus a similar boundary layer with hydrogen injection and with chemical behavior idealized according to the flame sheet model is treated. On the basis of several numerical examples, it is found that the present analysis predicts a boundary-layer behavior that is significantly different from that given by analyses with simple transport; e.g., the velocity profiles with hydrogen injection resemble suction profiles because of the reduction in the $\rho\mu$ product. Accordingly, the accuracy of existing analyses involving species with a spectrum of molecular weights and employing the assumption of simple transport properties would appear doubtful.

Nomenclature

c_p	= coefficient of specific heat at constant pressure
C	= ratio of $\rho\mu$ products, $\rho\mu/\rho_e\mu_e$
$C_{v,i}/R_0$	= normalized molal specific heat of species i
\mathcal{D}_{ij}	= binary diffusion coefficient
f	= modified stream function
G	= shear function, Cf''
h	= static enthalpy
\bar{h}	= normalized static enthalpy, $h/h_{s,e}$
h_s	= stagnation enthalpy
j_i	= diffusional mass flux, $\rho_i V_i$
\bar{j}_i	= normalized diffusional mass flux, $j_i(2\bar{s})^{1/2}/\rho_e\mu_e u_e r^i$
L	= total number of elements present
\bar{m}	= compressibility parameter, $u_e^2/2h_{s,e}$
N	= total number of species present
N_h	= heat-transfer coefficient, cf. Eq. (48)
p	= pressure
q	= energy flux
r	= cylindrical radius
R	= energy flux function, cf. Eq. (20)
\bar{s}	= transformed streamwise coordinate
T	= temperature
u	= streamwise velocity component
v	= normal velocity component
V_i	= diffusional velocity
\dot{w}_i	= volumetric mass rate of creation
W	= molecular weight
x	= streamwise coordinate
y	= normal coordinate
Y_i	= species mass fraction
\bar{Y}_j	= element mass fraction
η	= transformed normal coordinate
λ	= coefficient of thermal conductivity
μ	= coefficient of viscosity
μ_{ij}	= number of atoms of element j in a molecule of species i
ξ	= velocity ratio, f'
ρ	= mass density
σ	= Prandtl number, molecular diameter
ψ	= stream function

Subscripts

e	= value in external stream
f	= value at the flame sheet
i	= species, inner $0 \leq \eta \leq \eta_f$
j	= element
w	= value at wall or surface
0	= outer, $\eta_f \leq \eta$
1, 2, 3, 4	= O_2 , H_2 , H_2O , N_2 , respectively

Introduction

IN the recent advances in laminar boundary-layer theory applied to chemically reacting flows, it has been customary to employ two groups of simplifying assumptions. One group pertains to the chemical behavior of the flow; in particular, one of the two limiting cases of either equilibrium chemistry or zero gas phase reaction is treated. The other group of assumptions pertains to the transport processes. It has frequently been assumed that the product of mass density and viscosity is constant, either that the Lewis number associated with the diffusion coefficient of each of the species is unity or that a single diffusion coefficient exists, and that thermal diffusion is negligible. When these assumptions are employed, great simplifications occur, and many of the solutions available from previous analyses of nonreacting boundary layers can be applied to reacting flows. The power of these assumptions has been illustrated, for example, by the work in Refs. 1-5.

The complete description of the laminar boundary layer with both groups of assumptions curtailed, i.e., with more accurate representations for the transport processes and with finite rate chemistry considered, is becoming more tractable by finite difference methods and large scale computation. However, it is the purpose of this report to present a study of a particular flow in which the description of the transport processes will be reasonably accurate but in which the chemical behavior will still be highly idealized. In particular, there will be treated the similar flow associated with the injection of hydrogen through a porous surface with a uniform, external stream of air. The static pressure will be assumed sufficiently high and the temperature conditions to be such that equilibrium chemical behavior as approximated by the flame sheet model prevails. A single product from the oxidation of the hydrogen, namely water, will be assumed. Accordingly, four species O_2 , H_2 , H_2O , and N_2 will exist in the boundary layer; since the molecular weights of these four may be considered in three widely different groups, namely O_2 and N_2 , H_2O , and H_2 , an accurate description of the diffusive behavior of the mixture does not allow a single

Received February 20, 1964; revision received June 26, 1964. This research was supported in part by the U. S. Air Force, Office of Aerospace Research, Aerospace Research Laboratories, under Contract No. AF 33(616)-7661, Project No. 7064, Task No. 7064-01, "Research on Hypersonic Flow Phenomena," and is partially supported by the Ballistic Systems Division. Andrew Boreske Jr. is the contract monitor.

* Professor of Aerospace Engineering; now Professor of Aerospace Engineering, University of California at San Diego, La Jolla, Calif. Associate Fellow Member AIAA.

† NASA Trainee. Student Member AIAA.

diffusion coefficient to be introduced, i.e., multicomponent diffusion must be considered. Thus there will not be employed the usual binary mixture approximation, which is generally applied even when more than two species are present, provided the species may be grouped into two sets of roughly constant molecular weight in each. Indeed, the principal motivation for this study resides in the treatment of a laminar boundary layer in which the diffusional fluxes are explicitly retained in the describing equations. Such a treatment would appear to have applicability to a variety of boundary layers involving complex gas mixtures, e.g., ionized gases and products of sublimation.[‡] A second motivation resides in the quantitative assessment of the effect of reasonably accurate descriptions of the transport properties on the predictions of the technically interesting gross quantities such as skin friction and heat transfer. It has long been realized that flows involving gas mixtures with a spectrum of molecular weights can have significantly different behavior from that predicted by analyses based on simplified transport properties; however, there has been relatively little work devoted to a quantitative assessment of the errors involved.

The boundary layer that results from the injection of hydrogen into an air stream has been treated in the past under the assumptions of simplified chemical and transport behavior. Eckert et al.^{6,7} considered nonreacting hydrogen injection with accurate transport properties under a variety of flow conditions. Hartnett and Eckert⁸ presented an analysis of the boundary layer with hydrogen injection but with constant density, with equilibrium chemistry as idealized by the flame sheet model, and with simple transport properties. Eschenroeder⁹ carried out a similar analysis but for compressible flow and for the case wherein mixtures of oxygen and hydrogen are injected at the wall. Cohen et al.² have treated inter alia hydrogen injection under the assumptions of simple transport properties and of a chemical model based on two temperatures, one for dissociation and one for recombination. Finally, Libby and Economos¹⁰ proposed a model for chemical reaction within a boundary layer involving contiguous regions of frozen and equilibrium flow and applied the model to the injection of oxygen-hydrogen mixtures with simple transport properties.

In the following section, the basic conservation equations involving general diffusional velocities are first transformed to similar form. The model of the chemistry of hydrogen oxidation is then discussed in order that specific boundary conditions and explicit relations for the diffusional velocities can be developed. The approximations attendant with the molecular model employed in the transport properties are then discussed. In the next section, the basic equations are put in a form convenient for numerical treatment. Finally, the results of several numerical examples are compared with those given by the usual simplified treatments and are shown to be considerably changed by consideration of multicomponent diffusion.[§]

Analysis

In this section, the equations for a laminar boundary layer of the similar type with four species and multicomponent diffusion are presented and put in a form suitable for numerical analysis. The basic conservation equations are discussed first. In this general discussion, the gas mixture will be assumed to consist of N species involving L elements.

[‡] There have been published recently some results of large scale computations of the air system with the diffusional fluxes retained in the equations, but the main emphasis of these studies has been the computed results and not the methodology of analysis.

[§] The authors are pleased to acknowledge the assistance of Leo Rute in the early stages of this study.

Conservation Equations in the Physical Variables

Consider a laminar boundary layer on a surface with a uniform external stream. Within the boundary-layer approximation, only the components of the diffusional velocities normal to the surface, i.e., in the y direction, need be considered. Accordingly, the following equations apply[¶]:

x -Wise Momentum

$$\rho u u_x + \rho v u_y = (\mu u_y)_y \quad (1)$$

Global Continuity

$$(\rho u r^i)_x + r^i(\rho v)_y = 0 \quad (2)$$

Species Continuity

$$\rho u (Y_i)_x + \rho v (Y_i)_y = -(j_i)_y + \dot{w}_i \quad i = 1, 2, \dots, N \quad (3)$$

Energy

$$\rho u (h_s)_x + \rho v (h_s)_y = -(q)_y + (\mu u u_y)_y \quad (4)$$

In Eqs. (3) and (4), there appear the diffusional mass flux of species i denoted by j_i and the energy transport q , which involves inter alia j_i according to the equation

$$q = -\lambda T_y + \sum_{i=1}^N j_i h_i \quad (5)$$

If Eq. (5) is substituted into Eq. (4), and if there is considered the definition of h_s , namely,

$$h_s = \left(\frac{u^2}{2}\right) + \sum_{i=1}^N Y_i h_i \quad (6)$$

then there is obtained

$$\rho u (h_s)_x + \rho v (h_s)_y = \left[\left(\frac{\lambda}{c_p}\right) \left\{ (h_s)_y - \sum_{i=1}^N h_i \left[(Y_i)_y + \left(\frac{c_p}{\lambda}\right) j_i \right] \right\} - [\mu(\sigma^{-1} - 1) u u_y] \right]_y \quad (7)$$

It will be convenient for later developments to consider element conservation; the species creation terms are related according to the equations

$$\sum_{i=1}^N \frac{\mu_{ij} \dot{w}_i}{W_i} = 0 \quad j = 1, 2, \dots, L \quad (8)$$

These suggest the introduction of element mass fractions**

$$\tilde{Y}_j = \sum_{i=1}^N \frac{\mu_{ij} W_j Y_i}{W_i} \quad j = 1, 2, \dots, L \quad (9)$$

The conservation equations for elements can be obtained from Eqs. (3) multiplied by $\mu_{ij} W_j / W_i$ and summed over i ; there are obtained the equations

$$\rho u (\tilde{Y}_j)_x + \rho v (\tilde{Y}_j)_y = - \left(\sum_{i=1}^N \frac{\mu_{ij} W_j j_i}{W_i} \right)_y \quad j = 1, \dots, L \quad (10)$$

which involve no creation terms.^{††}

[¶] These equations may be deduced from the general equations for reacting gas flows given, e.g., in Refs. 11 (pp. 514-610) and 12, provided the usual arguments concerning thin layers and normal gradients are applied.

** The concept of element mass fractions is apparently due to Zeldovitch¹³ and has been widely applied in boundary-layer theory (cf., e.g., Ref. 5).

^{††} As will be seen below, Eqs. (10) are especially useful in the flame sheet model. It is also noted that if, and only if, a single diffusion coefficient exists so that $j_i = -D(Y_i)_y$ does the equation for element conservation take on the usual convection-diffusion form.

Transformation to Similar Form

Assume now that the boundary and initial conditions and the chemical behavior are such that similar flow exists, i.e., that all flow and gas parameters are functions of η alone where

$$\eta \equiv \rho_e u_e r^i (2\tilde{s})^{-1/2} \int_0^y \left(\frac{\rho}{\rho_e} \right) dy \quad (11)$$

In addition, introduce in the customary way a stream function:

$$\psi = (2\tilde{s})^{1/2} f(\eta) \quad (12)$$

Then Eqs. (1, 3, 7, and 10) become

$$(Cf'')' + f'' = 0 \quad (1a)$$

$$fY_i' - (\tilde{j}_i)' + (2\tilde{s}\tilde{w}_i/\rho_e\mu_e u_e r^{2i}) = 0 \quad i = 1, 2, \dots, N \quad (3a)$$

$$\left[\left(\frac{C}{\sigma} \right) g' \right]' + fg' - 2\tilde{m}[C(\sigma^{-1} - 1)f'f'']' - \left[\sum_{i=1}^N \tilde{j}_i \tilde{h}_i \right]' - \left[\left(\frac{C}{\sigma} \right) \sum_{i=1}^N \tilde{h}_i Y_i' \right]' = 0 \quad (7a)$$

$$f\tilde{Y}_j' - \sum_{i=1}^N \frac{\mu_{ij}W_{ij}\tilde{j}_i'}{W_i} = 0 \quad j = 1, 2, \dots, L \quad (10a)$$

where $(\)' \equiv \partial/\partial\eta \equiv d/d\eta$ and where $\tilde{j}_i \equiv (2\tilde{s})^{1/2}(\tilde{j}_i/\rho_e\mu_e u_e r^i) = \tilde{j}_i(\eta)$.

These equations for similar flow are in rather general form and must be supplemented by statements of the boundary conditions, by descriptions of the transport properties implicit in C and σ , and by relations yielding the diffusional fluxes in the form \tilde{j}_i . However, it is more convenient to choose a chemical system and to specialize these equations for that system before proceeding with these statements.

A Model for the Hydrogen-Air Reaction

For the purpose of the present study, it will be sufficient to consider the case of hydrogen injection into an air stream with nitrogen treated as inert, with water as the only product, and with equilibrium chemical behavior as approximated by the flame sheet model assumed to prevail. Thus $N = 4$, $L = 3$. The flame sheet model assumes that there exists a value of $\eta = \eta_f$ such that for $0 < \eta < \eta_f$ no oxygen exists in molecular form and for $\eta > \eta_f$ no hydrogen exists in molecular form; water is formed at the surface $\eta = \eta_f$ and diffuses in both directions, i.e., toward the wall and toward the external stream.

According to this model, the complete solution for the boundary-layer properties in terms of η must be considered to consist of two solutions, one for $0 \leq \eta \leq \eta_f$ and another for $\eta \geq \eta_f$. At $\eta = \eta_f$, the bulk velocities u and v , the state properties ρ and T , the species mass fractions Y_i , and the element mass fractions \tilde{Y}_i must be continuous. However, the gradients of temperature and composition are related to q' , \tilde{j}_i , Y_i' , and \tilde{Y}_i' , and these are discontinuous across the surface defined by $\eta = \eta_f$. This can be seen more clearly by integrating Eqs. (1a, 3a, 7a, and 10a) across the line $\eta = \eta_f$, i.e., from $\eta = \eta_f - \epsilon$ to $\eta = \eta_f + \epsilon$. If f and f' are continuous, then since C is continuous, Eq. (1a) yields

$$Cf''|_{\pm} = 0 \quad \text{or} \quad f''|_{\pm} = 0 \quad (13a)$$

where $(\)_{\pm}$ implies

$$\lim_{\epsilon \rightarrow 0} (\) \Big|_{\eta_f \pm \epsilon}$$

On the contrary, Eq. (3a) yields, with Y_i continuous,

$$\tilde{j}_i|_{\pm} = F \int_{-\infty}^{+\infty} \tilde{s}\tilde{w}_i d\eta \quad (13b)$$

where F is a continuous function of η evaluated at η_f ; now in the flame sheet model, $\tilde{w}_i(\eta_f) \rightarrow \infty$, and the integral is non-zero in the limit as $\epsilon \rightarrow 0$ so that

$$\tilde{j}_i|_{\pm} \neq 0$$

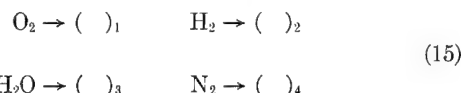
for i corresponding to active species, i.e., to oxygen, hydrogen, and water. Accordingly, Eq. (7a) yields

$$q' \Big|_{-}^{+} = \sum_{i=1}^N h_{i,f} \left[\left(\frac{\sigma}{C} \right) \tilde{j}_i - Y_i' \right] \Big|_{-}^{+} \quad (13c)$$

There appears to be no a priori reason why the right-hand side of Eq. (13c) should be zero, so that discontinuities in q' at $\eta = \eta_f$ must be expected.^{††} Finally, Eq. (10a) yields restrictions on the \tilde{j}_i 's, namely,

$$\sum_{i=1}^N \left(\frac{\mu_{ij}W_{ij}\tilde{j}_i}{W_i} \right) \Big|_{-}^{+} = 0 \quad (14)$$

It will be convenient in the further development of the analysis to use the following notation for the four species:



Thus, the three element mass fractions are

$$\tilde{Y}_1 \equiv Y_1 + (W_1/2W_3)Y_3 \quad (9a)$$

$$\tilde{Y}_2 \equiv Y_2 + (W_2/W_3)Y_3 \quad (9b)$$

$$\tilde{Y}_4 \equiv Y_4 \quad (9c)$$

If the distributions of the element mass fractions are found as functions of η for the two ranges of η , then the composition is completely known by virtue of the supplemental relations

$$\begin{aligned} Y_1 &= 0 & 0 < \eta < \eta_f \\ Y_2 &= 0 & \eta > \eta_f \end{aligned} \quad (16)$$

Note that

$$\sum_{i=1,2,4} \tilde{Y}_i \equiv 1$$

so that only two element mass fractions must be considered explicitly, the third being obtained from this identity. In this study, $\tilde{Y}_4 \equiv Y_4$ will be so determined since it tends to be relatively large. Similarly $\tilde{j}_4 = -(\tilde{j}_1 + \tilde{j}_2 + \tilde{j}_3)$, so that in each region only two diffusional flux parameters must be considered explicitly. Thus, it will be sufficient to consider explicitly only the two conservation equations for the element mass fractions, i.e., Eqs. (10a), with the "jump" condition of Eq. (14).§§

In view of Eqs. (16), it is convenient to write the species mass fractions in the two regions in terms of the element mass fractions as follows:

For $0 \leq \eta \leq \eta_f$

$$Y_1 = 0 \quad Y_2 = \tilde{Y}_2 - (2W_2/W_1)\tilde{Y}_1 \quad (17)$$

$$Y_3 = (2W_3/W_1)\tilde{Y}_1 \quad Y_4 = \tilde{Y}_4 = 1 - \tilde{Y}_1 - \tilde{Y}_2$$

For $\eta > \eta_f$

$$Y_1 = \tilde{Y}_1 - (W_1/2W_2)\tilde{Y}_2 \quad Y_2 = 0 \quad (18)$$

$$Y_3 = (W_3/W_2)\tilde{Y}_2 \quad Y_4 = \tilde{Y}_4 = 1 - \tilde{Y}_1 - \tilde{Y}_2$$

†† This is in contrast to the usual treatments of the flame sheet model with simplified transport properties wherein $q'|_{\pm} = 0$ because the right side is zero identically.

§§ The point of view to be taken with respect to Eq. (13b) is that the right-hand side takes on whatever value required to obtain the "jump" in \tilde{j}_i .

Clearly, Eqs. (17) and (18) can be differentiated with respect to η to yield the derivatives Y_i' , $i = 1, 2, 3, 4$ in terms of the derivatives \tilde{Y}_i' , $i = 1, 2$.

Corresponding to Eqs. (16) are the following relations pertinent to the diffusional mass fluxes:

$$\bar{j}_1 = 0 \quad 0 < \eta < \eta_f \quad (19)$$

$$\bar{j}_2 = 0 \quad \eta > \eta_f$$

With these conditions the restrictions on the \bar{j}_i 's at the flame sheet given by Eq. (14) become as follows:

$$(\bar{j}_1)^+ = (W_1/2W_3)[(\bar{j}_3)^- - (\bar{j}_3)^+] \quad (14a)$$

$$(\bar{j}_2)^- = (W_2/W_3)[(\bar{j}_3)^+ - (\bar{j}_3)^-]$$

Final Differential Equations

It is now convenient to anticipate the numerical analysis and thus to present the final equations for momentum, energy, and element conservation for each region in terms of first-order differential equations. In order to avoid differentiation of transport properties, it is convenient to introduce the following new variables:

$$\begin{aligned} G &\equiv Cf'' & \xi &\equiv f' \\ R_i &\equiv (C/\sigma)g' - 2\tilde{m}C(\sigma^{-1} - 1)f'f'' - \bar{h}_2\{\bar{j}_2 + (C/\sigma)[\tilde{Y}_2' - (2W_2/W_1)\tilde{Y}_1']\} - \\ &\quad \bar{h}_3\{\bar{j}_3 + (C/\sigma)(2W_3/W_1)\tilde{Y}_1'\} + \\ &\quad \bar{h}_4\{\bar{j}_2 + \bar{j}_3 + (C/\sigma)(\tilde{Y}_1' + \tilde{Y}_2')\} \\ R_0 &\equiv (C/\sigma)g' - 2\tilde{m}C(\sigma^{-1} - 1)f'f'' - \\ &\quad \bar{h}_1\{\bar{j}_1 + (C/\sigma)[\tilde{Y}_1' - (W_1/2W_2)\tilde{Y}_2']\} - \\ &\quad \bar{h}_3\{\bar{j}_3 + (C/\sigma)(W_3/W_2)\tilde{Y}_2'\} + \\ &\quad \bar{h}_4\{\bar{j}_1 + \bar{j}_3 + (C/\sigma)(\tilde{Y}_1' + \tilde{Y}_2')\} \end{aligned} \quad (20)$$

If Eqs. (20) are substituted into Eqs. (1a) and (7a), and if Eqs. (10a) are considered in view of the model and notation employed here, the following equations are obtained:

For all η

$$G' = -\xi G/C \quad (21)$$

$$\xi' = G/C \quad (22)$$

For $0 \leq \eta \leq \eta_f$

$$R_i' = -fg' \quad (23)$$

$$\begin{aligned} g' &= (\sigma/C)(R_i + 2\tilde{m}\xi G(\sigma^{-1} - 1) + \\ &\quad \bar{h}_2\{\bar{j}_2 + (C/\sigma)[\tilde{Y}_2' - (2W_2/W_1)\tilde{Y}_1']\} + \\ &\quad \bar{h}_3\{\bar{j}_3 + (C/\sigma)(2W_3/W_1)\tilde{Y}_1'\} - \\ &\quad \bar{h}_4\{\bar{j}_2 + \bar{j}_3 + (C/\sigma)(\tilde{Y}_1' + \tilde{Y}_2')\}) \end{aligned} \quad (24)$$

For $\eta_f \leq \eta$

$$R_0' = -fg' \quad (25)$$

$$\begin{aligned} g' &= (\sigma/C)(R_0 + 2\tilde{m}\xi G(\sigma^{-1} - 1) + \\ &\quad \bar{h}_1\{\bar{j}_1 + (C/\sigma)[\tilde{Y}_1' - (W_1/2W_2)\tilde{Y}_2']\} + \\ &\quad \bar{h}_3\{\bar{j}_3 + (C/\sigma)(W_3/W_2)\tilde{Y}_2'\} - \\ &\quad \bar{h}_4\{\bar{j}_1 + \bar{j}_3 + (C/\sigma)(\tilde{Y}_1' + \tilde{Y}_2')\}) \end{aligned} \quad (26)$$

For $0 \leq \eta \leq \eta_f$

$$\bar{j}_3' = f(2W_3/W_1)\tilde{Y}_1' \quad (27)$$

$$\bar{j}_2' = f[\tilde{Y}_2' - (2W_2/W_1)\tilde{Y}_1'] \quad (28)$$

For $\eta_f < \eta$

$$\bar{j}_1' = f[\tilde{Y}_1' - (W_1/2W_2)\tilde{Y}_2'] \quad (29)$$

$$\bar{j}_3' = f(W_3/W_2)\tilde{Y}_2' \quad (30)$$

It will be shown below that the differential quantities \tilde{Y}_i' can be expressed in terms of finite quantities; thus the right-hand sides of Eqs. (23-30) involve only finite quantities, and the preceding equations are in the form suitable for integration by standard numerical techniques.

Boundary Conditions at the Wall

With the final conservation equations available consider next the boundary conditions at the wall. The conditions on f are easily specified; from Eqs. (13a) and (13b) and the transformation equations $(x, y) \rightarrow (s, \eta)$ with $f_w' = 0$, there is obtained for the bulk mass flux $(\rho v)_w$ the usual relation

$$(\rho v)_w = \rho_e u_e [\mu_e r^i / (2s)^{1/2}] (-f_w) \quad (31)$$

Note from Eq. (31) the well-known distribution of mass flux at the surface required for similar flows, i.e., $(\rho v)_w \sim x^{-1/2}$ for $(-f_w)$ to be constant. Thus the boundary conditions on f are, at $\eta = 0$,

$$f = f_w = \text{const} \quad f' = 0 \quad (32)$$

The boundary condition on g at $\eta = 0$ is here specified only indirectly; it seems most reasonable for comparison purposes to fix the wall temperature T_w ; thus the wall enthalpy ratio g_w is determined once the composition at the surface is known. Note that here a heat balance at the wall is not imposed, since it is assumed that either an arbitrary coolant temperature or a cooling mechanism exists so that the prescribed T_w prevails.

It will be assumed that pure hydrogen is injected; thus the bulk velocity of water and nitrogen must vanish at $\eta = 0$. Note that according to the flame sheet model employed herein, there is no oxygen in the inner layer $0 \leq \eta \leq \eta_f$ so that no explicit relation concerning oxygen flux at the wall is required. Now by definition of the diffusional velocities there are obtained

$$v_{3w} = v_w + V_{3w} = 0 \quad v_{4w} = v_w + V_{4w} = 0 \quad (33)$$

so that some rearrangement, using the definitions of \bar{j}_i and the Eqs. (17) and (31), yields the following convenient expressions for the diffusion fluxes:

$$\bar{j}_{2,w} = (-f_w)[1 - \tilde{Y}_2 + (2W_2/W_1)\tilde{Y}_1]_w \quad (34)$$

$$\bar{j}_{3,w} = (-f_w)[-(2W_3/W_1)\tilde{Y}_1]_w$$

Equations (34) thus relate the wall values of the diffusional parameters \bar{j}_i and of the concentrations \tilde{Y}_i .

Boundary Conditions at Infinity

The conditions to be imposed for large η are those that make the solutions compatible with the external flow. Thus, as $\eta \rightarrow \infty$,

$$f' = 1 \quad g = 1 \quad \tilde{Y}_1 = \tilde{Y}_{1,e} \quad (35)$$

$$\tilde{Y}_2 = 0 \quad \tilde{Y}_4 = Y_{4,e} = 1 - \tilde{Y}_{1,e}$$

Diffusional Fluxes

In the boundary layer under consideration, the diffusional flux parameters \bar{j}_i will depend on concentration gradients and on thermal gradients. In the present study, the effect of thermal diffusion will be neglected; however, at the flame sheet, severe temperature gradients will occur so that some effect of thermal diffusion may prevail even though the thermal diffusion coefficients are generally small.¹¹

Here the diffusional velocities are related explicitly to the concentration gradients by the binary diffusion coefficients.

¹¹ According to the method of solution employed here, the inclusion of this effect should not be difficult.

Accordingly, the \bar{y}_i parameters will depend on gradients of the concentrations of all species. The appropriate equations can be derived as follows: On each side of the flame sheet, only three species are present; thus, consider explicitly the inner region $0 \leq \eta < \eta_f$. After either Ref. 11 (p. 516) or Ref. 12 (p. 244) the diffusional velocities V_i , $i = 2, 3, 4$ are related in matrix form to $(Y_i)_y$ according to

$$V_i = \sum_j C_{ij}(Y_j)_y \quad (36)$$

in contrast to the usual Fick's law $V_i \sim (Y_i)_y$. In Eq. (36), the C_{ij} coefficients are functions of the binary diffusion coefficients, of the concentrations, and of molecular weights. Now Eq. (36) can be put in a form convenient for the present study. Some rearrangement with the use of Eqs. (17), of the definitions \bar{y}_i , and of the explicit expressions for the C_{ij} matrix elements leads to the following equations for $0 \leq \eta \leq \eta_f$:

$$(\mu/\mathcal{D}_{14}\rho)C^{-1} \begin{vmatrix} a_{11}' & a_{21}' \\ a_{12}' & a_{22}' \end{vmatrix} \begin{vmatrix} \bar{y}_2 \\ \bar{y}_3 \end{vmatrix} = \begin{vmatrix} b_{11}' & b_{21}' \\ b_{12}' & b_{22}' \end{vmatrix} \begin{vmatrix} \bar{Y}_1' \\ \bar{Y}_2' \end{vmatrix} \quad (37)$$

where

$$a_{11}' = \bar{Y}_1[(2W_4\mathcal{D}_{14}/W_1\mathcal{D}_{23}) - (2W_2\mathcal{D}_{14}/W_1\mathcal{D}_{24}) - (\mathcal{D}_{14}/\mathcal{D}_{24}) + (\mathcal{D}_{14}/\mathcal{D}_{34})]$$

$$a_{21}' = \bar{Y}_1[(2W_2W_4\mathcal{D}_{14}/W_1W_3\mathcal{D}_{23}) - (2W_2\mathcal{D}_{14}/W_1\mathcal{D}_{24})] + \bar{Y}_2[(\mathcal{D}_{14}/\mathcal{D}_{24}) - (W_4\mathcal{D}_{14}/W_3\mathcal{D}_{23})]$$

$$a_{12}' = \bar{Y}_1[(2W_3\mathcal{D}_{14}/W_1\mathcal{D}_{34}) - (2W_3W_4\mathcal{D}_{14}/W_1W_2\mathcal{D}_{23})]$$

$$a_{22}' = \bar{Y}_1[(2W_3\mathcal{D}_{14}/W_1\mathcal{D}_{34}) - (\mathcal{D}_{14}/\mathcal{D}_{34}) - (2W_4\mathcal{D}_{14}/W_1\mathcal{D}_{23})] + \bar{Y}_2[(W_4\mathcal{D}_{14}/W_2\mathcal{D}_{23}) - (\mathcal{D}_{14}/\mathcal{D}_{24}) + (\mathcal{D}_{14}/\mathcal{D}_{34})]$$

$$b_{11}' = \bar{Y}_2[(2W_4/W_1) - (2W_2/W_1) - 1] + (2W_2/W_1)$$

$$b_{21}' = \bar{Y}_1[1 - (2W_4/W_1) + (2W_2/W_1)] - 1$$

$$b_{12}' = \bar{Y}_2[(2W_3/W_1) - (2W_3W_4/W_1W_2)] - (2W_3/W_1)$$

$$b_{22}' = \bar{Y}_1[(2W_3W_4/W_1W_2) - (2W_3/W_1)]$$

Now it is interesting to note that if $(\mu/\mathcal{D}_{14}\rho) \equiv C \equiv 1$ and if $\mathcal{D}_{14}/\mathcal{D}_{ij} \equiv 1$ for all i, j , then Eqs. (37) yield

$$(W_1/2W_3)\bar{y}_3 = -\bar{Y}_1' \quad (37a)$$

$$\bar{y}_2 + (W_2/W_3)\bar{y}_3 = -\bar{Y}_2' \quad (37b)$$

so that Eqs. (27) and (28) become the usual element conservation equations applicable for the simplified transport properties related to $C = 1$, $Le_i = 1$ for all i . It is also of interest to note that the multiplying factor on the left-hand side of Eq. (37) is a Schmidt number based on \mathcal{D}_{14} divided by C .

In a similar fashion, the diffusion flux parameters in the region $\eta \geq \eta_f$ are given by the equations*

$$(\mu/\rho\mathcal{D}_{14})C^{-1} \begin{vmatrix} a_{11}'' & a_{21}'' \\ a_{12}'' & a_{22}'' \end{vmatrix} \begin{vmatrix} \bar{y}_1 \\ \bar{y}_3 \end{vmatrix} = \begin{vmatrix} b_{11}'' & b_{21}'' \\ b_{12}'' & b_{22}'' \end{vmatrix} \begin{vmatrix} \bar{Y}_1' \\ \bar{Y}_2' \end{vmatrix} \quad (38)$$

where

$$a_{11}'' = \bar{Y}_2[(W_4\mathcal{D}_{14}/W_2\mathcal{D}_{13}) - (W_1/2W_2) - 1] + 1$$

$$a_{21}'' = \bar{Y}_1[1 - (\mathcal{D}_{14}W_4/\mathcal{D}_{13}W_3)] + \bar{Y}_2[(W_1W_4\mathcal{D}_{14}/2W_2W_3\mathcal{D}_{13}) - (W_1/2W_2)]$$

$$a_{12}'' = \bar{Y}_2[(W_3\mathcal{D}_{14}/W_2\mathcal{D}_{34}) - (W_3W_4\mathcal{D}_{14}/W_1W_2\mathcal{D}_{31})]$$

$$a_{22}'' = \bar{Y}_1[(W_4\mathcal{D}_{14}/W_1\mathcal{D}_{31}) - (\mathcal{D}_{14}/\mathcal{D}_{31})] + \bar{Y}_2[(W_3\mathcal{D}_{14}/W_2\mathcal{D}_{34}) - (W_4\mathcal{D}_{14}/2W_2\mathcal{D}_{31}) - (\mathcal{D}_{14}/\mathcal{D}_{34})] + (\mathcal{D}_{14}/\mathcal{D}_{34})$$

$$b_{11}'' = \bar{Y}_2[1 - (W_4/W_2) + (W_1/2W_2)] - 1$$

$$b_{21}'' = \bar{Y}_1[(W_4/W_2) - 1 - (W_1/2W_2)] + W_1/2W_2$$

$$b_{12}'' = \bar{Y}_2[(W_3W_4/W_1W_2) - (W_3/W_2)]$$

$$b_{22}'' = \bar{Y}_1[(W_3/W_2) - (W_3W_4/W_1W_2)] - W_3/W_2$$

Again it is noted that, if $\mu/\rho\mathcal{D}_{14} \equiv C \equiv 1$ and if $\mathcal{D}_{14}/\mathcal{D}_{ij} \equiv 1$ for all i and j , then Eqs. (38) give

$$\bar{y}_1 + (W_1/2W_3)\bar{y}_3 = -\bar{Y}_1' \quad (38a)$$

$$(W_2/W_3)\bar{y}_3 = -\bar{Y}_2' \quad (38b)$$

so that Eqs. (29) and (30) reduce to the usual element conservation equations valid in both regions, i.e., for all η .

It is now noted, as indicated previously, that Eqs. (37) and (38) can be solved in each region for \bar{Y}_i' , $i = 1, 2$ in terms of finite quantities, and thus Eqs. (23-30) can be put in the standard form for numerical integration.

Molecular Model and the Transport Properties

The final differential equations, the boundary conditions, and the diffusion flux relations presented previously must be supplemented by equations describing the transport properties of the gas mixture. For the present study, it is considered sufficient to employ a rigid-sphere model for computing the coefficients of viscosity and of thermal conductivity and the binary diffusion coefficients. More accurate molecular models would lead to temperature variations of these coefficients somewhat different from those given by the rigid sphere model but are not considered to result in essential changes. Accordingly, it is assumed herein that (cf. Ref. 11, p. 14)

$$\mu_i = 2.67(10^{-6})(W_iT)^{1/2}\sigma_i^{-2} \text{ g/cm-sec}$$

$$\lambda_i = (\frac{15}{4})(R_0\mu_i/W_i)[(\frac{4}{15})(C_{v,i}/R_0) + (\frac{3}{2})] \text{ cal/cm-sec}^\circ\text{K} \quad (39)$$

$$\mathcal{D}_{ij} = 2.63(10^{-3})[T^3(W_i + W_j)/2W_iW_j]^{1/2}p^{-1}\sigma_{ij}^{-2} \text{ cm}^2/\text{sec}$$

where σ_i is the molecular diameter in angstroms, $\sigma_{ij} \equiv (\sigma_i + \sigma_j)/2$, where T is in degrees Kelvin, and where p is in atmospheres. In the description of the coefficient of thermal conductivity, constant values of $C_{v,i}/R_0$ representative of the values for temperatures of 2000°K have been assumed according to following:

	i	$C_{v,i}/R_0$
O ₂	1	9.0
H ₂	2	8.2
H ₂ O	3	12.0
N ₂	4	8.6

The following molecular diameters have been employed here:

	i	$\sigma_i, \text{\AA}$	Ref. 11
O ₂	1	3.541	p. 1111
H ₂	2	2.915	p. 1110
H ₂ O	3	2.824	p. 599
N ₂	4	3.749	p. 1111

As a consequence of these approximations to the molecular properties, the quotients of the binary diffusion coefficients, $\mathcal{D}_{14}/\mathcal{D}_{ij}$, are constants varying from roughly 0.2 to 0.7, and the ratios μ_i/μ_e , which arise in the expressions for the transport parameter C when the mixture viscosity rule is

* Note that in the outer region the binary approximation should be quite satisfactory since no H₂ is present. It has not, however, been applied here.

considered, become constants times $(T/T_e)^{1/2}$. Similarly, it is found convenient to treat the Prandtl number as a value normalized with respect to the Prandtl number in the external stream; thus the quotients λ_i/λ_e arise and become constants times $(T/T_e)^{1/2}$.

The mixture coefficients of viscosity and conductivity, i.e., μ and λ are computed according to the mixture rules, which are due to Fay¹⁴ and which are similar to those used previously. Thus

$$\mu = \sum_{i=1}^N \frac{(Y_i/W_i) \mu_i}{\sum_{k=1}^N \left(\frac{Y_k}{W_k}\right) G_{ik}} \quad (42)$$

$$\lambda = \sum_{i=1}^N \frac{(Y_i/W_i) \lambda_i}{\sum_{k=1}^N \left(\frac{Y_k}{W_k}\right) G_{ik}} \quad (43)$$

where

$$G_{ik} = 1 \quad i = k$$

$$= 1.2(\sigma_{ik}/\sigma_{ii})^2(2m_{ik}/m_i)^{1/2} \quad i \neq k$$

$$m_{ik}/m_i = W_k/(W_k + W_i)$$

Enthalpy-Temperature Relations and Their Implications

It is considered sufficiently accurate for present purposes to assume a linear relation between the species enthalpies and the temperature. Thus

$$h_i = \bar{\Delta}_i + \bar{c}_{p,i} T \quad (44)$$

where the following values of $\bar{\Delta}_i$ and $\bar{c}_{p,i}$ have been assumed†:

	<i>i</i>	$\bar{\Delta}_i$, cal/g	$\bar{c}_{p,i}$, cal/g-°K
O ₂	1	-124	0.283
H ₂	2	-1876	4.10
H ₂ O	3	-3562	0.656
N ₂	4	-127	0.303

As a consequence of the approximation attendant with Eq. (44), the temperature can be expressed explicitly in terms of the prime dependent variables in each region. In general there is obtained in terms of the species mass fraction

$$\theta \equiv \frac{T}{T_e} = \frac{\sum_{i=1}^N (Y_{i,e} \bar{c}_{p,i}) \left[g - \tilde{m} f'^2 - \sum_{i=1}^N \left(\frac{Y_i \bar{\Delta}_i}{h_{s,e}} \right) \right]}{\sum_{i=1}^N Y_i \bar{c}_{p,i} \left[1 - \tilde{m} - \sum_{i=1}^N \left(\frac{Y_{i,e} \bar{\Delta}_i}{h_{s,e}} \right) \right]} \quad (46)$$

When Eq. (46) is applied at the wall, it provides the expression for g_w in terms of T_w and $Y_{i,w}$.

Heat Transfer to the Wall

A result of interest from the present analysis is the heat transfer to the wall given by

$$q_w \equiv (\lambda T_w)_w - \left(\sum_{i=1}^N \rho_i V_i h_i \right)_w \quad (47)$$

Equation (47) can be rewritten in a form more convenient for the present purposes and for the variables considered here, i.e.,

$$N_h \equiv \left[\frac{q_w (2s)^{1/2}}{\rho_e \mu_e u_e r^{1/2} h_{s,e}} \right] = \left\{ \left(\frac{C}{\sigma} \right) g' - \sum_{i=1}^N \left[\left(\frac{C}{\sigma} \right) Y_i' + \bar{j}_i \right] \bar{h}_i \right\}_w \quad (48)$$

† These are the same as those used in Ref. 10 provided the slightly different form of Eq. (44) is considered.

For rates of injection sufficiently high so that the flame sheet model applies, the right-hand side of Eq. (48) results in

$$N_h = R_{i,w} \quad (49)$$

For zero injection, the equations for the outer region apply at the wall, and

$$N_h = R_{0,w} \quad (49a)$$

Numerical Analysis and Results

The only difficulty associated with obtaining numerical solutions to the describing equations by standard integration techniques pertains to the two-point boundary conditions. If the integration is started at the wall, $\eta = 0$, it is necessary to estimate four quantities, e.g., f_w'' , g_w' , $\bar{Y}_{i,w}$, $i = 1, 2$ such that as $\eta \rightarrow \infty$, the conditions given by Eqs. (35) are satisfied. Thus a solution vector in a four-space is sought; there is employed here the usual trial and error technique of establishing errors, computing influence coefficients, and then computing new estimates described, e.g., in Ref. 15. However, a difficulty associated with this technique for the present problem arises because of the restrictions which pertain to $T > 0$ and $0 \leq \bar{Y}_i \leq 1$, $i = 1, 2, 4$, and whose violation generally hampers the integration.

It was found that, unless reasonably accurate estimates of the wall quantities were used, these restrictions were not respected, and the trial and error procedure failed.† Indeed, as will be seen below, it was not possible to find solutions for injection rates exceeding those corresponding to $-f_w \simeq 0.1$; these are generally considered relatively low, but according to the present analysis are sufficient to cause significant changes in boundary-layer properties. These difficulties may indicate "blowoff" as defined by either $G_w = 0$ or by $\bar{Y}_{2,w} = 1$ at surprisingly low values of f_w .

The numerical analysis was carried out on a RECOMP III computer at PIBAL employing a Kutta-Runge-Gill integration routine. Values of $\bar{Y}_{i,w}$, $i = 1, 2$, of G_w , and of $R_{i,w}$ were assumed or computed from a previous calculation. The integration was carried forward until the location of the flame sheet where $\bar{Y}_1 = (W_1/2W_2) \bar{Y}_2$, i.e., where $Y_2 = 0$. The set of equations valid for $\eta > \eta_f$, and the initial conditions therefor determined from the requirements of continuity of G , ξ , and g and from Eqs. (14a) were then picked up and the integration continued. When the assumed wall parameters were close to the correct, i.e., the solution values, it was found, as might be expected, that the value of θ for large η provided a sensitive indicator which could be used to obtain the final corrections. The step-size in η , used in the integration, was reduced as a solution was approached with a final value of 0.1, except in the neighborhood of the flame sheet, where values as small as 0.02 were found necessary. The integration was carried out to a value of η between 4.5 and 6 depending upon the injection rate. A solution was considered to have been obtained when the value of θ at the extreme value of η was unity within $\pm 2\%$; this resulted in satisfaction of the infinity conditions on g , f' , and \bar{Y}_i , $i = 1, 4$ within 0.1%.

Flow Parameters and Injection Rates

Two sets of flow conditions have been assumed for the numerical examples, one being considered representative of conditions in hypersonic flight and the other in hypersonic wind tunnels; they are taken from Ref. 10 and have the values listed in Table 1.

For each set of flow conditions, a calculation was carried out for zero injection by applying the equations for the outer region throughout the layer. The solutions in this case

† The existence of the flame sheet appears to preclude use of iteration procedures that were employed, e.g., in Ref. 16, and that would probably eliminate the difficulties associated with the restrictions on T and \bar{Y}_i .

Table 1

	M_e , approx	\bar{m}	$h_{s, e}$, cal/g	T_e , °K	T_w , °K
I	11.8	0.968	4444	900	900
II	3.8	0.810	750	900	900

correspond to an air boundary layer with reasonably accurate transport properties. Three other values of $(-f_w)$ were assumed; namely, 0.03, 0.0707, 0.106. The latter two values correspond to solutions provided by Emmons and Leigh.¹⁷ Note that there is a minimum injection rate for which the flame sheet model of chemical behavior prevails (cf. Ref. 10); the lowest positive value of $(-f_w)$ chosen here exceeded this minimum rate.

Results in Terms of Profiles

The results of the numerical analysis are summarized in Table 2 in terms of the wall values permitting integration of a solution to be started; the results are discussed below in terms of the profiles of velocity, of stagnation enthalpy, of species mass fractions, and of temperature and in terms of the variation of wall properties with injection rate. The variation of transport properties is indicated in terms of the variation with injection rate of those properties evaluated at the wall; the severe departures from the values employed in approximate calculations are thereby emphasized.

The velocity profiles for the four rates of injection considered in each set of flow conditions are shown in Figs. 1 and 2. Also shown for comparison are representative profiles for $C \equiv 1$. It will be noted immediately that the effect of injection is opposite to that expected from previous analyses based on simple transport, namely, that the thickness of the boundary layer defined in terms of a velocity ratio close to unity is decreased by injection. It will be seen in Table 2 and also shown below that this behavior is due to the severe reduction in the $\rho\mu$ product associated with the addition of hydrogen and that the shear related to Cf'' is indeed reduced by injection.

The profiles of stagnation enthalpy are shown in Figs. 3 and 4, those of the concentrations of oxygen and hydrogen in Fig. 5, those of the concentrations of water in Fig. 6, and those of the temperature ratio θ in Figs. 7 and 8. In each case there is shown for comparison purposes the corresponding profiles as given by simple transport with $-f_w = 0.106$. Again it will be noted that significant changes in wall concentrations and profiles are associated with more accurate descriptions of transport properties. Of particular interest is the shift towards the wall of the flame sheet.

Results in Terms of Wall Values

In Fig. 9 there is shown the variation with $(-f_w)$ of the wall parameters f_w'' and G_w , and of the heat transfer characterized by N_h . It will be noted immediately that, in accord with the discussion of Figs. 1 and 2, the wall shear characterized by G_w decreases with increasing $(-f_w)$, indeed at a faster rate than that given by simplified transport, while f_w'' increases rapidly. Thus the behavior of the velocity

profile is accounted for by a severe reduction in C with increasing injection, a reduction that overwhelms the decrease in G . Also to be noted is the significant difference in skin friction as characterized by G_w between the predictions of analyses with $C \equiv 1$ and with accurate transport. Similar errors in heat transfer in terms of N_h are also found.

An indication of the reason for the significant alterations in boundary-layer properties as predicted by the present

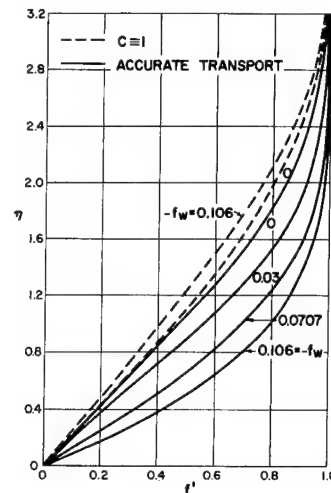
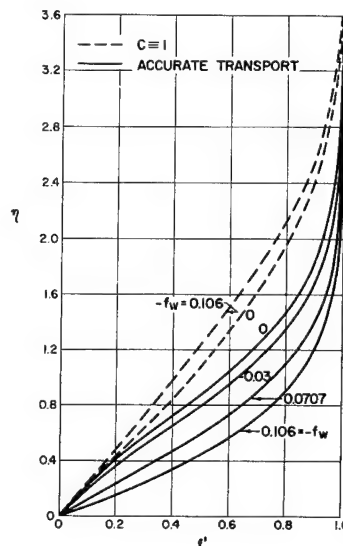
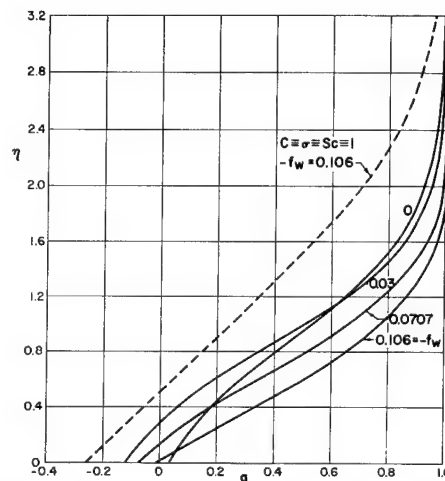
Fig. 1 Velocity profiles, $M_e \sim 11.8$.Fig. 2 Velocity profiles, $M_e \sim 3.8$.Fig. 3 Stagnation enthalpy profiles, $M_e \sim 11.8$.

Table 2 Summary of wall values

Case	$-f_w$	$\bar{Y}_{1, w}$	$Y_{2, w}$	G_w	$R_{h, w}$
I	0	0.232	0	0.349	0.367 ^a
	0.03	0.212	0.0573	0.293	0.365
	0.0707	0.214	0.182	0.209	0.269
	0.106	0.186	0.378	0.139	0.183
II	0	0.232	0	0.437	0.375 ^a
	0.03	0.210	0.0507	0.341	0.671
	0.0707	0.216	0.157	0.244	0.450
	0.106	0.196	0.330	0.165	0.263

^a Should be denoted $R_{0, w}$ since, with no injection, R_0 applies for all η .

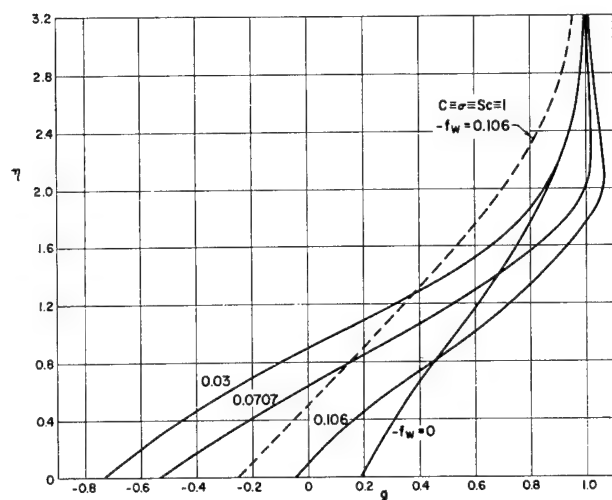
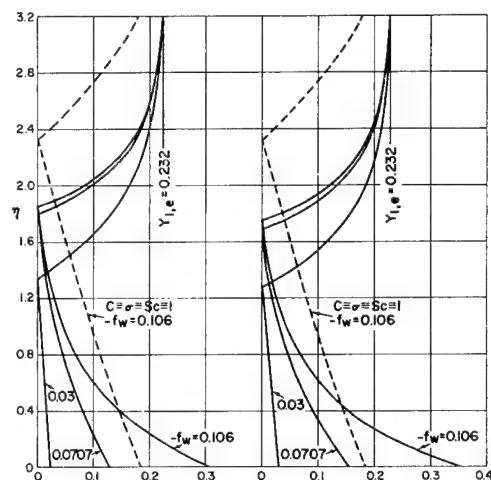
Fig. 4 Stagnation enthalpy profiles, $M_e \sim 3.8$.

Fig. 5 Hydrogen and oxygen profiles.

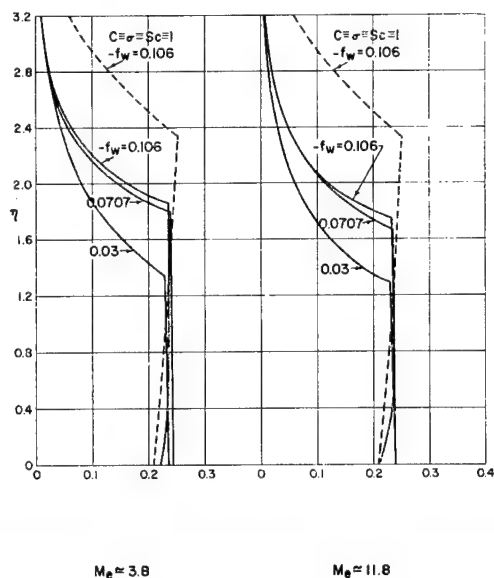


Fig. 6 Profiles of water concentration.

analysis is shown in Fig. 10, wherein the variations of C_w and of $(\mu/\rho\mathcal{D}_{14})_w C_w^{-1}$ with $(-f_w)$ are shown. It will be noted that these parameters differ by an order of magnitude from unity, the value frequently assumed therefor. The mixture Prandtl number at the wall is found to be from 0.45 to 0.54 for $-f_w \geq 0.03$, and therefore its variation does not appear to play as important a role as the other transport parameters.

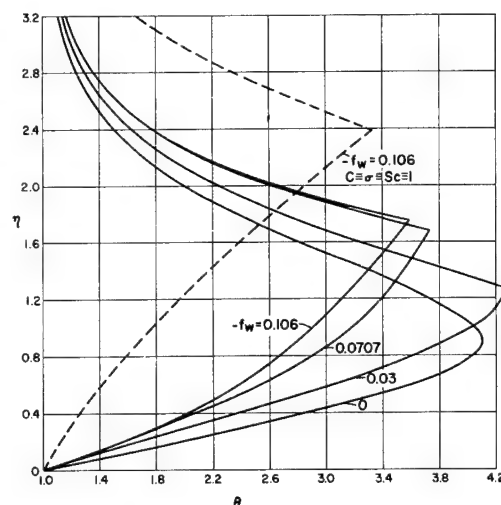
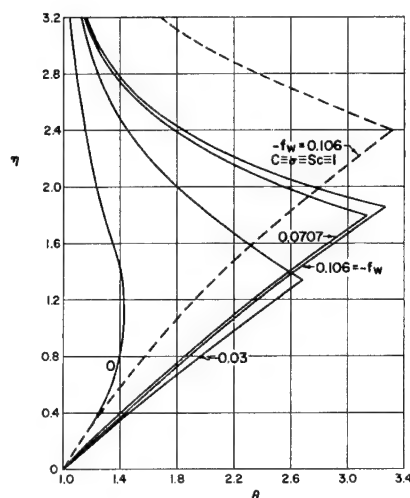
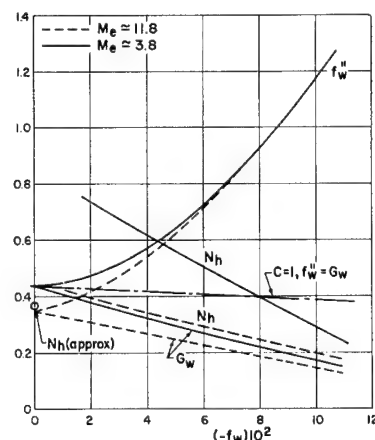
Fig. 7 Profiles of temperature ratio, $M_e \sim 11.8$.Fig. 8 Profiles of temperature ratio, $M_e \sim 3.8$.

Fig. 9 Variation of flow variables at the wall with injection rate (unless indicated results are for accurate transport).

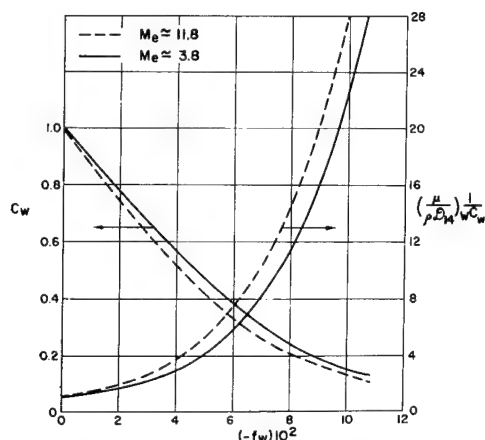


Fig. 10 Variation of transport properties at the wall with injection rate.

Concluding Remarks

An analysis has been carried out of a reacting laminar boundary layer that is relatively simple in all respects except for its transport properties. In particular, the similar flow that results from the injection of hydrogen and that is characterized by a flame sheet has been treated. Multi-component diffusion and reasonably accurate transport properties have been considered.

Several numerical examples are presented and show significant effects of the transport properties on boundary-layer behavior. The most dramatic effect appears to be that the velocity profiles with injection resemble those usually attributed to suction; the reason for this is the severe reduction in the values of the $\rho\mu$ product due to the presence of hydrogen. Relatively large alterations in predicted skin friction and heat transfer are found.

The implication of these results seems to be that in laminar flows involving gases with a spectrum of molecular weights the predictions of analyses based on simple transport properties may be in serious error.

Appendix: Solution for the Case of Simplified Transport

For completeness and for ready reference, the solution for the flame sheet model of hydrogen injection with simplified transport properties is presented here. The analysis has been given in a somewhat different manner in Ref. 9. Make the following approximation:

$$C \cong 1 \quad \sigma \cong 1 \quad \mathcal{D}_{ij}/\mathcal{D}_{ij} \cong 1 \quad \mu/\mathcal{D}_{14}\rho \cong 1 \quad (\text{A1})$$

Then the equations in the two regions $0 \leq \eta \leq \eta_f$ and $\eta > \eta_f$ become identical and are

$$f''' + ff'' = 0 \quad (\text{A2})$$

$$f\tilde{Y}_i' + \tilde{Y}_i'' = 0 \quad i = 1, 2 \quad (\text{A3})$$

$$g'' + fg' = 0 \quad (\text{A4})$$

subject, as may be seen from Eqs. (23) and (24), to the boundary conditions at $\eta = 0$

$$\begin{aligned} f &= f_w & f' &= 0 \\ \tilde{Y}_1' &= (-f_w)\tilde{Y}_1 \end{aligned} \quad (\text{A5})$$

$$\tilde{Y}_2' = -(-f_w)(1 - \tilde{Y}_2)$$

$$g = g_w$$

and at $\eta \rightarrow \infty$

$$= f' = 1 \quad \tilde{Y}_1 = \tilde{Y}_{1,\infty} \quad \tilde{Y}_2 = 0 \quad g = 1 \quad (\text{A6})$$

The solution of Eq. (A2) subject to the boundary conditions on f in Eqs. (A5) and (A6) has been provided by Emmons and Leigh^{17,8} so that $f(\eta)$ can be assumed to be given with f_w as a parameter. The solutions for \tilde{Y}_i , $i = 1, 2$ and for g are readily obtained in terms of f' so that the complete solution with f_w as the sole parameter is given by

$$\begin{aligned} g &= g_w + (1 - g_w)f' \\ \tilde{Y}_1 &= \{Y_{1e}/[f_w''/(-f_w) + 1]\}\{f' + [f_w''/(-f_w)]\} \\ \tilde{Y}_2 &= (1 - f')/\{[f_w''/(-f_w)] + 1\} \\ \tilde{Y}_4 &= 1 - \tilde{Y}_1 - \tilde{Y}_2 \end{aligned} \quad (\text{A7})$$

where the wall condition specified in terms of temperature g_w is computed from Eq. (46).

References

- Emmons, H. W., "The film combustion of liquid fuel," *Z. Angew. Math. Mech.* **36**, Heft 1/2, 60-71 (January-February 1956).
- Cohen, C. B., Bromberg, R., and Lipkin, R. P., "Boundary layers with chemical reactions due to mass addition," *Jet Propulsion* **28**, 659-668 (1958).
- Marble, F. and Adamson, T. C., Jr., "Ignition and combustion in a laminar mixing zone," *Jet Propulsion* **24**, 85-94 (1954).
- Dooley, D. A., "Ignition in the laminar boundary layer of a heated plate," *Proceedings of the 1957 Heat Transfer and Fluid Mechanics Institute* (Stanford University Press, Stanford, Calif., 1957), pp. 321-342.
- Lees, L., "Convective heat transfer with mass addition and chemical reactions," *Combustion and Propulsion Third AGARD Colloquium* (Pergamon Press, New York, 1958), pp. 451-498.
- Eckert, E. R. C., Schneider, P. J., Hayday, A. A., and Larson, R. M., "Mass-transfer cooling of a laminar boundary layer by injection of a light-weight foreign gas," *Jet Propulsion* **28**, 11, 34-39 (1958).
- Eckert, E. R. G., Hayday, A. A., and Minkowycz, W. J., "Heat transfer, temperature recovery, and skin friction on a flat plate with hydrogen release into a laminar boundary layer," *Intern. J. Heat Mass Transfer* **4**, 17-29 (1961).
- Hartnett, J. P. and Eckert, E. R. G., "Mass transfer cooling with combustion in a laminar boundary layer," *Proceedings of the Heat Transfer and Fluid Mechanics Institute* (Stanford University Press, Stanford, Calif., 1958), pp. 65-68.
- Eschenroeder, A. Q., "Combustion in the boundary layer on a porous surface," *J. Aerospace Sci.* **27**, 901-906 (1960).
- Libby, P. A. and Economos, C., "A flame zone model for chemical reaction in a laminar boundary layer with application to the injection of hydrogen-oxygen mixtures," *Intern. J. Heat Mass Transfer* **6**, 113-128 (1963); also Polytechnic Institute of Brooklyn PIBAL Rept. 722, ARL 199 (October 1961).
- Hirschfelder, J. O., Curtiss, C. F., and Bird, R. B., *Molecular Theory of Gases and Liquids* (John Wiley and Sons, Inc., New York, 1954).
- Penner, S. S., *Chemistry Problems in Jet Propulsion* (Pergamon Press, New York, 1957).
- Zeldovich, Y. B., "On the theory of combustion of initially unmixed systems," *Zh. Tekh. Fiz.* **19**, 1199-1210 (1944); also transl. as NACA TM 1296 (June 1950).
- Fay, J. A., "Hypersonic heat transfer in air laminar boundary layer," AGARD Specialists Conference, Brussels, Belgium (1962); also Avco-Everett Research Lab. Rept. AMP-71 (1962).
- Cohen, C. B. and Reshotko, E., "Similar solutions for the compressible laminar boundary layer with heat transfer and pressure gradient," NASA Rept. 1293 (1956).
- Janowitz, G. S. and Libby, P. A., "The effect of variable transport properties on a dissociated boundary layer with surface reaction," Polytechnic Institute of Brooklyn, PIBAL Rept. 804 (October 1963); also *Intern. J. Heat Mass Transfer* (to be published).
- Emmons, H. W. and Leigh, D. C., "Tabulation of the Blasius function with blowing and suction," Aeronautical Research Council Rept. 15, p. 996 (June 1953).

§ The critical parameter f_w'' as a function of f_w has been presented in terms of the present variables in Ref. 10.

Confined Vortex Flows with Boundary-Layer Interaction

M. L. ROSENZWEIG,* W. S. LEWELLEN,† AND D. H. ROSS‡
Aerospace Corporation, Los Angeles, Calif.

Axisymmetric flow of an incompressible fluid in a right-cylindrical vortex tube bounded by planar end walls is considered. The mutual interaction of the primary vortex flow field and the end-wall boundary layers is studied by relating the stream function and circulation in these regions. An interaction parameter is defined which determines the magnitude of the influence of the boundary layers on the circulation and mass-flow distributions in the primary flow. These distributions are obtained numerically, primarily as functions of the interaction parameter and the Reynolds number based on the radial flow. Experimental results are interpreted in the light of this theory, and it is concluded that substantial turbulence levels (though somewhat less than estimates made without consideration of boundary-layer effects) must be assumed to explain the experimental results.

Nomenclature

A	= boundary-layer interaction parameter defined in Eq. (17)
c	= coefficient of friction
F	= dimensionless part of the stream function that is independent of z
f	= dimensionless part of the stream function that is linear with z
l	= length of the vortex chamber
p	= pressure
Q	= volume flow per unit length, wr
Q_{BL}	= volume flow in the end-wall boundary layer
Re_r	= radial Reynolds number = $\rho ur/\mu$
Re_r^*	= "effective" turbulent radial Reynolds number
Re_t	= tangential Reynolds number = $\rho vr/\mu$
r	= radial coordinate
u	= radial velocity, positive outward
v	= tangential velocity
w	= axial velocity
z	= axial coordinate
α	= velocity-profile shape parameter in the boundary layer
Γ	= circulation, vr
δ	= end-wall boundary-layer thickness
ϵ	= dimensionless parameter defined in Eq. (5)
η	= dimensionless radial coordinate squared
μ	= viscosity
ν	= kinematic viscosity
ξ	= dimensionless axial coordinate
ρ	= density
ψ	= stream function defined in Eq. (7)

Subscripts

0	= value at outer edge of the vortex tube
e	= value at the edge of the exhaust hole
m	= minimum value

I. Introduction

VORTEX tubes of one form or another have been of interest to fluid dynamicists for some time. Applications such as the Ranque-Hilsch tube, cyclone separator, and, more recently, the MHD vortex power generator¹ and gaseous-core nuclear rocket² have provided the stimulus for re-

search in this field. Analytical and experimental investigations of confined vortex flows have been numerous. The theoretical treatments have concerned with the main body of rotating fluid and, for the most part, have been restricted to one-dimensional flow models (i.e., tangential and radial velocities being functions of radius only). Donaldson³ examined the full Navier-Stokes equations under these assumptions and found a family of exact solutions. These exact solutions are not readily applicable to the flow in an actual vortex tube, however, because of their inability to satisfy boundary conditions imposed by the end walls and exhaust-hole geometry. Others^{4, 5} have developed approximate theories in which the radial distributions of axial velocity are specified (rather arbitrarily) in order to satisfy conditions imposed by the exhaust ports. A notable exception is a study by Anderson⁶ in which the laminar end-wall boundary-layer interaction problem was first treated.

Lewellen⁷ has reviewed these studies and has clarified the mathematical foundation of the approximate solutions. In particular, he has shown that under certain circumstances (which are usually met experimentally) the one-dimensional hypothesis can yield a valid first approximation to the solution. In regions where this is the case, the axial velocity distribution is determined to the same degree of exactness by its boundary values. In an actual vortex tube, these are determined by the boundary layers on the end walls and by the location and geometry of the exit port (or ports), as just mentioned. Solutions based on arbitrarily specified axial velocity distributions have been reasonably successful in predicting the qualitative behavior of the measured tangential velocity distributions, numerical discrepancies being attributed usually to turbulence in the flow field.^{4, 8, 9}

The boundary layers that are formed on the end walls of the vortex chamber have been studied previously without regard to their effect on the primary vortex flow that drives them. Boundary-layer growth on a finite disk under the influence of a vortex-like outer flow has been studied originally by Taylor¹⁰ and more recently by Mack,¹¹ King,¹² Weber,¹³ Rott,¹⁴ and others. These studies, in which the external velocity distributions were specified functions of the radial coordinate, have demonstrated that such boundary layers are capable of transporting large quantities of fluid radially inward. This radial flow is coupled through the continuity equation to an axial flow, so that in fact it is the boundary-layer flow that determines, for the most part, the axial velocity distribution in a vortex tube.

For a fixed total flow through the tube, diversion of fluid into the boundary layers reduces the radial flow through the main body of the vortex and tends to weaken the vortex strength or circulation. In an actual vortex tube (such as pictured in Fig. 1), however, the boundary layers must at

Received February 26, 1964; revision received July 27, 1964. The authors wish to acknowledge the contributions of Jack Macki and Irene Wong of the Aerospace Corporation Computation and Data Processing Center for the programing and computation of data used in this paper.

* Staff Scientist, Laboratories Division. Member AIAA.

† Head, Fluid Dynamics Section, Laboratories Division. Member AIAA.

‡ Member of the Technical Staff, Laboratories Division. Member AIAA.

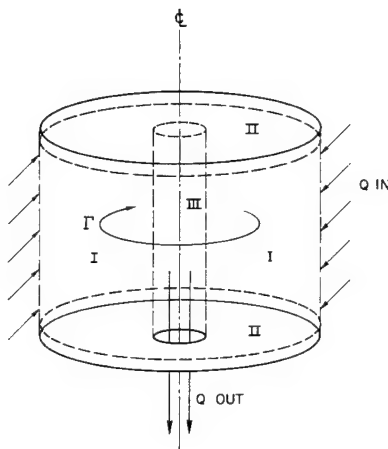


Fig. 1 Vortex tube geometry showing division of flow into the three regions described in the paper.

some point discharge their contents. If this process is accomplished in such a way as to return the boundary-layer fluid to the main flow before it has lost much of its angular momentum and before it is passed axially out of the tube, then (as is described in this paper) it is possible to maintain a near-constant circulation distribution in the vortex.

Mass flow may be caused to leave the boundary layer for two reasons. First, the boundary-layer theory itself indicates mass ejection when the external circulation distribution decreases with decreasing radius.¹² Second, certain discontinuities in the wall geometry, such as a circular step or the sharp edge of an exhaust orifice (i.e., regions where boundary-layer theory is not locally applicable), can also induce mass ejection. Experimental evidence of such boundary-layer mass ejection is plentiful¹⁵⁻¹⁷; typical examples are shown in Figs. 2 and 3 using a water vortex with dye injection. Figure 2 shows boundary-layer mass ejection in the vicinity of the exhaust-hole radius, resulting, most likely, from both

mechanisms. Figure 3 illustrates the effect of a circular step in the end wall at approximately midradius. Mass ejection is again observed.

The full three-dimensional flow pattern in a vortex tube is thus the result of a complicated interaction between the primary vortex flow and the end-wall boundary layers. The purpose of the present paper is to study this interaction theoretically in order to demonstrate the unusual mutual influences exerted by the primary and secondary flows in right-cylindrical vortex tubes of the type illustrated in Fig. 1. The results are compared with experiments, and, as a corollary, certain observations are made concerning turbulence levels in confined vortex flows.

II. Description of Flow Model

An incompressible, constant viscosity fluid is assumed. For the purposes of the analysis the flow is considered divisible into three regions, as indicated in Fig. 1. It will be assumed that the ratio of volume flow to circulation is small so that in region I, the primary flow region, the tangential velocity is a function of radius only. Region II consists of the boundary layers on both top and bottom end walls, in which axial velocity gradients and therefore axial viscous stresses become significant. Region III, bounded by an imaginary cylinder of radius equal to that of the exhaust hole, includes the flow in the vicinity of the axis of the tube where both tangential and radial velocities vanish.

Appropriate solutions are employed in each of these regions, and a consistent flow picture is obtained by application of suitable matching conditions. The solution of Lewellen,⁷ which determines the circulation distribution in terms of the stream function, is used in regions I and III. This solution becomes exact in the limit of large circulation and requires that the stream function be specified at the periphery of the applicable regions. The approximate boundary-layer solution of Rott¹⁴ is used along the end walls, up to the edge of region III, to provide a second relationship between the stream function and circulation in the primary flow, thereby establishing the interaction. The

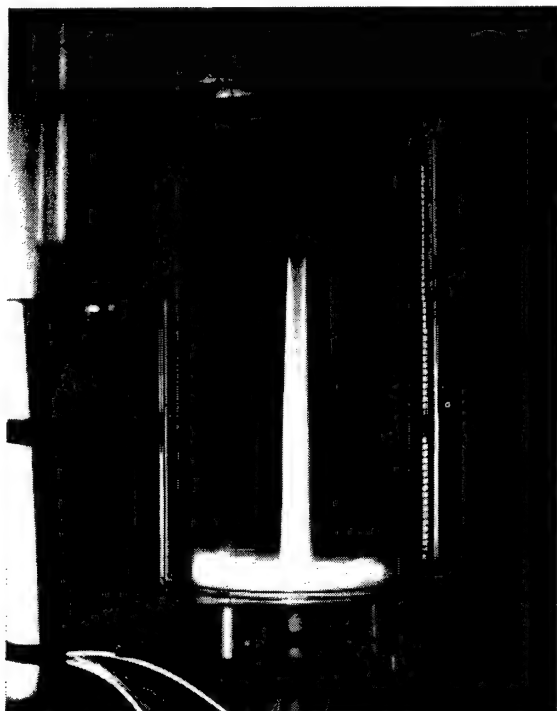


Fig. 2 Vortex flow visualization picture with dye injected into the boundary layer showing mass ejection in vicinity of exhaust radius.

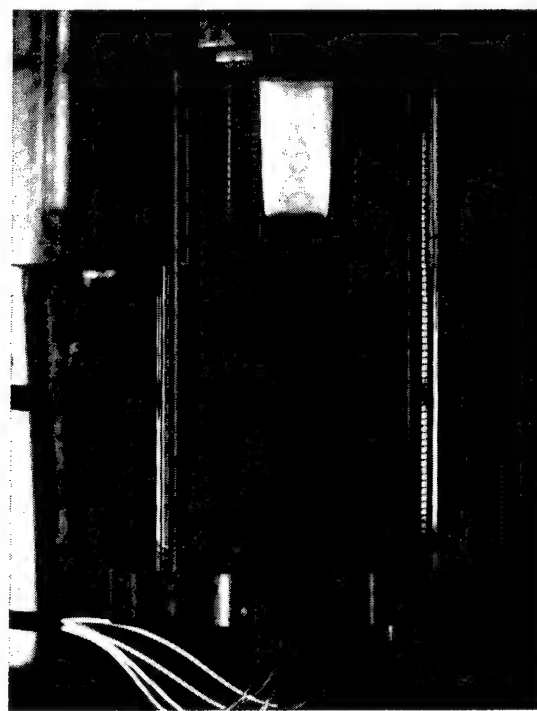


Fig. 3 Vortex flow visualization picture with dye injected into the boundary layer with a stepped-down end wall showing mass ejection in neighborhood of step.

mathematical framework is completed with the specification of the stream function in region III. Provision is included to allow the consideration of boundary-layer mass ejection due to the exhaust-hole discontinuity. Since little of a quantitative nature is known about this process at the present time, this phenomenon is treated parametrically. The fraction ζ of boundary-layer mass flow at the radius of the exhaust, which is returned to the main flow before leaving the tube, is introduced into the computational program and allowed to vary from zero to one. The complete set of equations is solved iteratively using a digital computer for a range of the governing parameters.

Before proceeding with the analysis, several comments are in order. First, the division of the flow into regions as indicated is not equivalent to the usual division of flows into a viscous boundary layer and an inviscid outer flow. In the present problem, the entire flow field is considered viscous; however, in the boundary layers, the axial velocity gradients predominate, whereas in regions I and III only the radial gradients are considered.

Second, the details of the flow in region III are oversimplified as a result of insufficient knowledge. Recirculation of fluid originating downstream of the exhaust hole, which frequently occurs along the axis of the vortex tube, has been neglected. This can be justified only by the belief that such a phenomenon does not strongly influence the velocity distributions in regions I and II.

Finally, a real and possibly important phenomenon is not considered at all in this paper, i.e., the boundary layer on the cylindrical-containing walls and the details of the jet-mixing region if the vortex is driven by tangential fluid injection, as is commonly the case. These effects may influence the end-wall boundary-layer growth and will certainly make the determination of the peripheral circulation difficult in an actual experiment. For the present purposes, however, it is assumed that the outer cylinder is rotating and porous so that such questions may be avoided.

III. Derivation of the Interaction Equations

Consider a cylindrical coordinate system, r, θ, z , with associated velocity components u, v, w . The continuity and Navier-Stokes equations in these coordinates for an incompressible fluid with constant viscosity are

$$\frac{\partial(ru)}{\partial r} + \frac{\partial(rw)}{\partial z} = 0 \quad (1)$$

$$u \frac{\partial u}{\partial r} + w \frac{\partial u}{\partial z} - \frac{v^2}{r} = -\frac{1}{\rho} \frac{\partial p}{\partial r} + \nu \left(\frac{\partial^2 u}{\partial r^2} + \frac{1}{r} \frac{\partial u}{\partial r} - \frac{u}{r^2} + \frac{\partial^2 u}{\partial z^2} \right) \quad (2)$$

$$u \frac{\partial v}{\partial r} + w \frac{\partial v}{\partial z} + \frac{uv}{r} = \nu \left(\frac{\partial^2 v}{\partial r^2} + \frac{1}{r} \frac{\partial v}{\partial r} - \frac{v}{r^2} + \frac{\partial^2 v}{\partial z^2} \right) \quad (3)$$

$$u \frac{\partial w}{\partial r} + w \frac{\partial w}{\partial z} = -\frac{1}{\rho} \frac{\partial p}{\partial z} + \nu \left(\frac{\partial^2 w}{\partial r^2} + \frac{1}{r} \frac{\partial w}{\partial r} + \frac{\partial^2 w}{\partial z^2} \right) \quad (4)$$

where the $\partial/\partial t$ and $\partial/\partial \theta$ terms have been eliminated by assuming that the flow is steady and axisymmetric.

The axisymmetric stream function ψ is defined so that Eq. (1) is everywhere satisfied:

$$u = \frac{1}{r} \frac{\partial \psi}{\partial z} \quad w = -\frac{1}{r} \frac{\partial \psi}{\partial r} \quad (5)$$

In addition, the dimensionless coordinates $\eta = (r/r_0)^2$ and $\xi = z/l$ and the quantities $Q = ur$ and $\Gamma = v$ are introduced.

Lewellen⁷ showed that $\partial Q/\partial \xi$ was of order ϵ , where

$$\epsilon = (\psi_0/\Gamma_0 r_0)^2 \quad (6)$$

Therefore, in regions where the ratio of stream function to circulation is small, Γ may be considered independent of z , to order ϵ . Further, examination of Eq. (3) shows that, when v is independent of z , the radial velocity u must also be independent of z (unless $\Gamma = \text{const}$). In this case, Eq. (3) reduces to an ordinary, linear differential equation for Γ in terms of u and v :

$$r^2 \frac{d}{dr} \left(\frac{1}{r} \frac{d\Gamma}{dr} \right) - \frac{ur}{v} \frac{d\Gamma}{dr} = 0 \quad (7)$$

The most general form of ψ , consistent with the condition that u be independent of z , is

$$\psi = Q_0 l [\xi f(\eta) + F(\eta)] \quad (8)$$

so that

$$u = \frac{Q_0}{r} f \quad w = -\frac{2Q_0 l}{r_0^2} \left(\frac{z}{l} f' + F' \right)$$

Lewellen⁷ has further shown that, since the equation that determines ψ is of order ϵ , to this order then the functions f and F remain to be determined by the boundary conditions.

In terms of f, η , and the radial Reynolds number $Re_r = Q_0/\nu$, Eq. (7) may be rewritten:

$$2\eta f'' - Re_r f \Gamma' = 0 \quad (9)$$

The functions ψ and Γ as defined by Eqs. (8) and (9) were shown by Lewellen⁷ to be the zeroth-order terms in a series expansion solution of Eqs. (1-4), in powers of ϵ .

If the axial and tangential velocities are of the same order in region III, then in this region the ϵ expansion given in Ref. 7 is not strictly valid. This question is quite complicated but is treated in detail in Ref. 18 where it is shown that it is still possible to carry out a consistent expansion in u/v , which almost always remains a small parameter. In such an expansion, the leading term in Γ is still a function of r only and may be determined by an equation similar to Eq. (9), which depends on the boundary values of ψ :

$$2\eta \Gamma'' - Re_r f \Gamma' = -4Re_r \frac{\eta F'}{\Gamma} \left[F''' f - F' f'' - \frac{2}{Re_r} (2F'''' + \eta F''''') \right] \left(\frac{w}{v} \right)^2 \quad (10)$$

If precise values of ψ could be obtained on the boundaries of region III, then Eq. (10) would yield an accurate description of Γ even for $(w/v)_e$ of order one. However, for the idealized stream function that will be used in this study, the right-hand side of Eq. (10) is identically zero and the equation reduces to Eq. (9).

Applying the boundary conditions $\Gamma = 0$ at $\eta = 0$ and $\Gamma = \Gamma_0$ at $\eta = 1$, Eq. (9) may be integrated to give

$$\frac{\Gamma}{\Gamma_0} = c_1 \int_0^\eta \exp \left[\frac{Re_r}{2} \int_0^\eta \frac{f(\eta)}{\eta} d\eta \right] d\eta \quad (11)$$

where

$$c_1 = \left\{ \int_0^1 \exp \left[\frac{Re_r}{2} \int_0^\eta \frac{f(\eta)}{\eta} d\eta \right] d\eta \right\}^{-1}$$

Thus, with a given value of the radial Reynolds number and the radial distribution of f , the circulation distribution is uniquely determined.

It should be noted at this point that only f enters in the determination of Γ . That is, only that portion of the axial flow which is coupled to the radial flow through the continuity relationship plays a role.

The f distribution, or equivalently the distribution of radial velocity through regions I and III, will be determined by consideration of the end-wall boundary-layer flow. Since it is assumed that the boundary-layer mass flow grows from

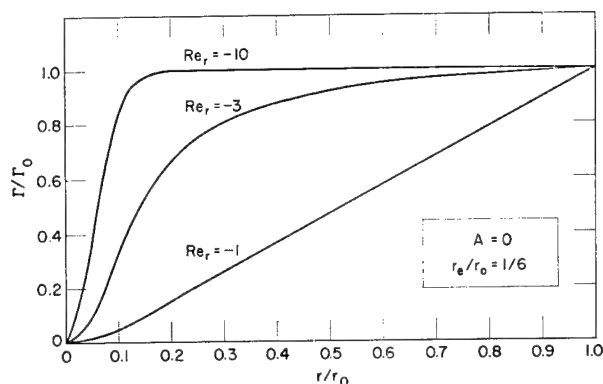


Fig. 4 Circulation distributions as a function of radius for $A = 0$.

zero at r_0 , any increase (or decrease) in the radial flow in the boundary layers must result in a corresponding decrease (or increase) in the radial flow through the primary vortex region. Thus (in region I),

$$f = 1 - (2Q_{BL}/Q_0) \quad (12)$$

where

$$Q_{BL} = \int_0^\delta r u dz$$

There have been several analyses of the end-wall boundary-layer region.¹¹⁻¹⁴ For the present study, the results of the turbulent analysis of Rott¹⁴ will be used. This is chosen because, at the tangential Reynolds numbers ordinarily encountered in vortex tubes, the boundary layers are most likely turbulent, and although Rott's analysis yields the simplest expression for the mass flow in the boundary layer, the results agree quite favorably with those of other, more complicated approaches. Assuming that the turbulent shear components are proportional to the squares of the respective velocity components and that the coefficient of friction so defined is constant, Rott, using a momentum-integral approximation, expressed the volume flow in the boundary layer in terms of the Γ distribution of the external flow as follows:

$$Q_{BL} = -\alpha c \Gamma^{\alpha-1} \int_0^x \Gamma^{2-\alpha} dx \quad (13)$$

where $x = r_0 - r$, α is a velocity-profile shape parameter, and c is the coefficient of friction. Following Rott, the values

$$\alpha = 5 \quad c = 0.027 (Re_t)^{-1/5} \quad (14)$$

will be used for this study.

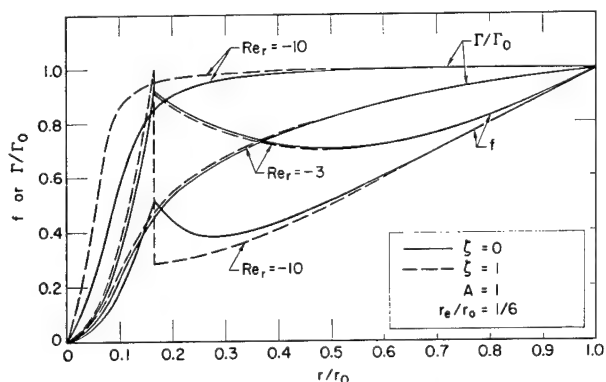


Fig. 5 Circulation and stream function distributions as a function of radius for $A = 1$.

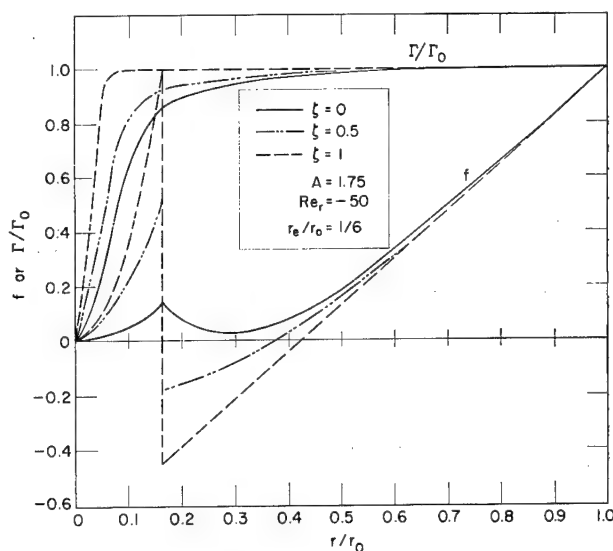


Fig. 6 Circulation and stream function distributions as a function of radius for $A = 1.75$ and $Re_x = -50$.

The specification of f in region III is not quite so straightforward. As mentioned previously, the discontinuity at the edge of the exit hole (assumed here to be a sharp-edged orifice) produces local mass ejection from the boundary layer. The fraction of the boundary-layer mass flow that is ejected and ultimately finds its way back into the primary flow is as yet undetermined. Furthermore, the questions of recirculatory flow along the axis and the validity of the boundary-layer analysis near the axis contribute to the difficulty of specifying f in detail in region III. Fortunately, as far as the calculation of the circulation is concerned, only the integral of f appears in Eq. (11). Thus, Γ should be insensitive to the details of the axial velocity distribution (as long as v is independent of z).

It will be assumed then that a certain fraction ζ of the boundary-layer volume flow at r , (the radius of the exit hole) is ejected and returned to the primary flow to be redistributed into radial flow uniformly over the length of the tube. The representation of this boundary-layer mass ejection by a discontinuous change in f is, of course, an idealization of the actual phenomena illustrated in Figs. 2 and 3. The quantity ζ will be considered parametrically in the computations, and its effect on the Γ and f distributions will be assessed. In addition, inside the radius of the ex-

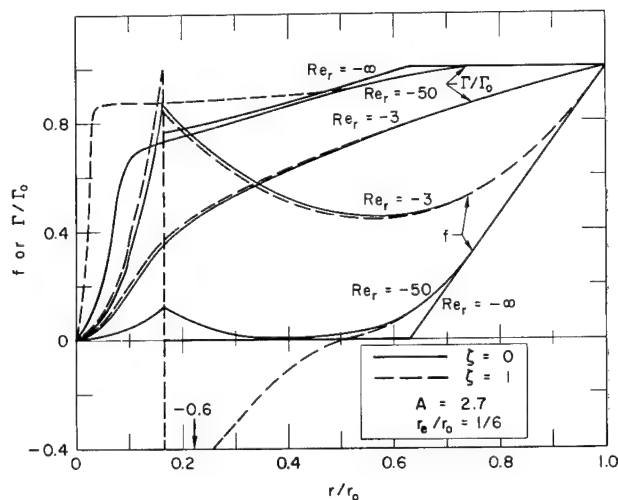


Fig. 7 Circulation and stream function distributions as a function of radius for $A = 2.7$.

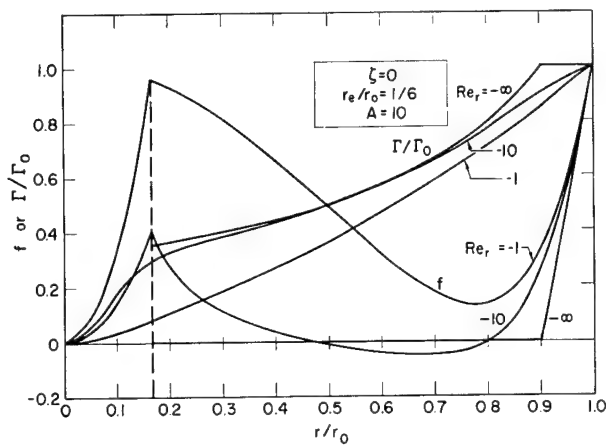


Fig. 8 Circulation and stream function distributions as a function of radius for $A = 10$.

haust, the simplest possible assumption will be made, namely, that the radial velocity falls to zero at $r = 0$ linearly with r . Under these conditions,

$$f = \left[1 - (1 - \zeta) \frac{2Q_{BL}(r_e)}{Q_0 l} \right] \frac{r^2}{r_e^2} \quad (15)$$

when $r \leq r_e$.

Considering Eqs. (12-15), f may be written as

$$f = 1 - A \left[\frac{\Gamma(\eta)}{\Gamma_0} \right]^4 \int_{\eta}^1 \left[\frac{\Gamma_0}{\Gamma(\eta)} \right]^3 \frac{d\eta}{2(\eta)^{1/2}} \quad 1 \geq \eta > \eta_e \quad (16)$$

$$f = \frac{\eta}{\eta_e} \left\{ 1 - (1 - \zeta) A \left[\frac{\Gamma(\eta_e)}{\Gamma_0} \right]^4 \int_{\eta_e}^1 \left[\frac{\Gamma_0}{\Gamma(\eta)} \right]^3 \frac{d\eta}{2(\eta)^{1/2}} \right\} \quad 0 \leq \eta \leq \eta_e$$

where

$$A = - \frac{0.27}{(Re_r)^{1/5}} \left(\frac{\Gamma_0 r_0}{Q_0 l} \right) = \frac{2rc}{\epsilon^{1/2}} \quad (17)$$

Equations (11) and (16) determine f and Γ as functions of the radius and the parameters Re_r , A , r_e/r_0 , and ζ . These equations have been solved iteratively using a digital computer for ranges of the governing parameters, and the results are presented and discussed in the next section.

IV. Discussion of Results

The quantity A characterizes the boundary-layer interaction since it is a measure of the fraction of the total mass flow that passes through the boundary layer. If Γ were constant and equal to Γ_0 for all r , then it can be seen from Eqs. (13, 14, and 17) that A would be equal to the fraction of the total mass flow in the boundary layers at $r = 0$. Also, from Eq. (17) it is seen that $A \sim 1/\epsilon^{1/2}$, so that small values of ϵ ordinarily correspond to large values of the boundary-layer interaction parameter. Thus, it is precisely in the regime where Γ is independent of z that the end-wall boundary-layers will play a significant role in the determination of the radial Γ distribution.

An interesting exception occurs in the limit of A going to zero as a result of frictionless, or suitably rotating, end walls (i.e., not because ϵ becomes large). In this case, the present problem becomes identical with that considered by Einstein and Li.⁵ This solution is shown in Fig. 4 for three values of the radial Reynolds number and $r_e/r_0 = \frac{1}{6}$.

Another interesting limiting case, which may be solved analytically, occurs when $Re_r \rightarrow -\infty$. This case has been

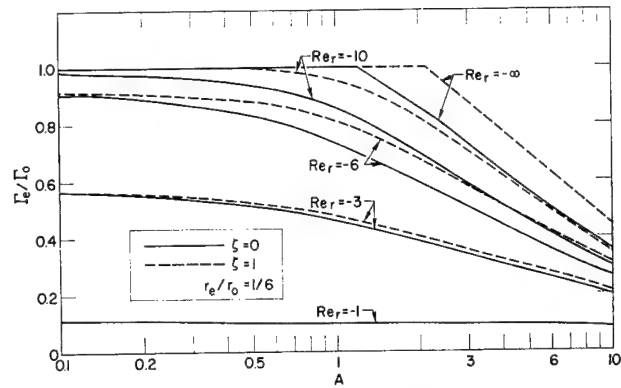


Fig. 9 Circulation at the edge of the exhaust hole as a function of A for constant Re_r .

solved in the Appendix. In this limit, the circulation distribution remains constant for $A < 0(1)$. For $A > 0(1)$, the circulation remains constant with decreasing radius from r_0 until all of the flow reaches the end-wall boundary layers. Between this radius and the edge of the exhaust, the total radial flow remains in the boundary layers, and the circulation distribution is that required to drive this boundary-layer flow.

Results of the digital computer solutions for Γ and f distributions corresponding to various combinations of the governing parameters are shown in Figs. 5-8. All of these results were obtained for a constant value of $r_e/r_0 = \frac{1}{6}$. The successive figures correspond to increasing values of A . Values of radial Reynolds number have been chosen so that results representative of the distributions obtainable are presented. In most of these figures, curves are plotted only for $\zeta = 0$ and $\zeta = 1$, since results for intermediate values may be easily inferred from those presented. In Fig. 6, the curve for $\zeta = 0.5$ is also presented, indicating a rather uniform variation of the distributions with ζ between the extremes of zero and one. Results of the analytical solution of the Appendix for $Re_r = -\infty$ are included in Figs. 7 and 8.

The curves illustrate that when $A \leq 1$ the effect of the boundary-layer interaction is relatively small. The same is true when $|Re_r|$ is small regardless of the value of A . In both of these areas, of course, the influence of ζ is also small. For slightly larger values of A , the boundary-layer interaction begins to exert a considerable influence, especially at the higher values of $|Re_r|$. The effect of ζ also becomes

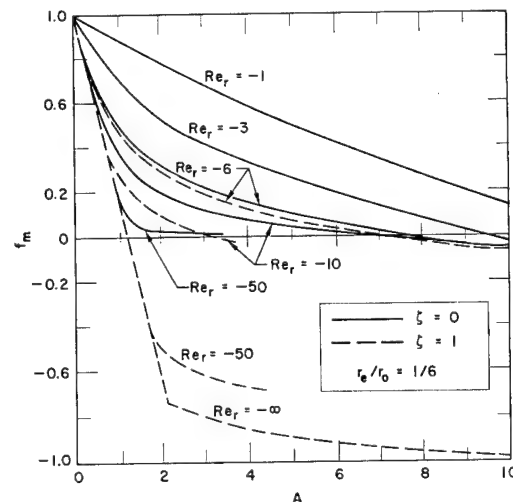


Fig. 10 Minimum mass flow in the primary flow region as a function of A for constant Re_r .

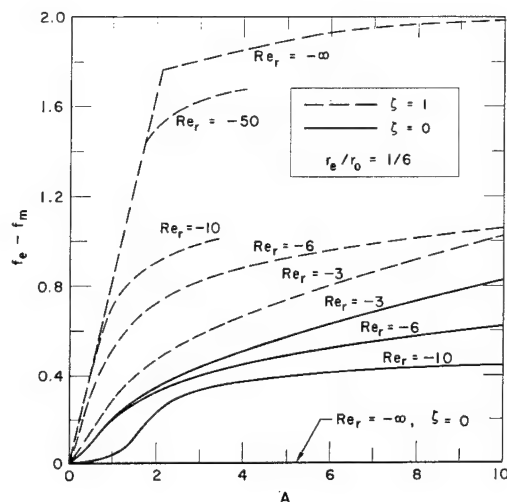


Fig. 11 Amount of fluid returned by the boundary layers to the primary flow as a function of A for constant Re_r .

more pronounced here. A value of $\zeta = 1$ causes the circulation distribution to stay closer to a constant and results in increases of Γ_e/Γ_0 of up to 20%. Its influence on the mass-flow distribution is more profound (as seen in Figs. 6 and 7), resulting in negative values of f , which implies that the boundary-layer mass flow is locally greater than the total through-flow so that radial outflow must exist in the primary-flow region. It is interesting to note that, in spite of this excess mass flow in the boundary layers, the Γ distribution remains essentially constant.

At still larger values of the interaction parameter, the Γ distribution decreases faster (see Fig. 8), and the theoretical results for infinite Reynolds number are approximated closely by those for more moderate Reynolds numbers.

In order to characterize the effect of the interaction in a simple way, the value of Γ_e/Γ_0 is plotted in Fig. 9 as functions of A and Re_r for $r_e/r_0 = \frac{1}{6}$. This curve also illustrates the influence of ζ . It is seen that, for $\zeta = 0$, values of Γ_e/Γ_0 begin to depart from one when $A > 1.2$, even for infinite Reynolds number. For $\zeta = 1$, this departure is delayed until $A > 2.2$.

The mass-flow distributions are characterized by the minimum value of f (designated f_m) and the amount of fluid that is returned by the boundary layers to the primary flow ($f_e - f_m$). These distributions are plotted in Figs. 10 and 11.

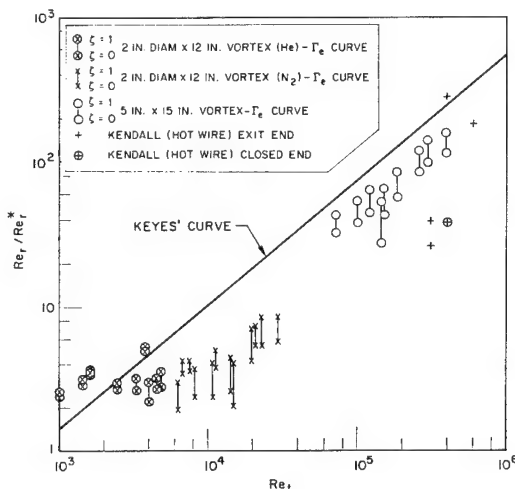


Fig. 12 The ratio of laminar radial Reynolds number to effective turbulent radial Reynolds number as a function of tangential Reynolds number.

Negative values of f_m indicate reverse flow regions in the primary flow.

In order to assess the influence of r_e on the Γ and f distributions, solutions were obtained for values of r_e/r_0 other than $\frac{1}{6}$. These results are contained in Ref. 19.

The effects of compressibility are also treated in Ref. 19 by consideration of an isothermal flow. It is concluded that the present results are accurate for most practical applications.[§]

V. Comparison with Experiment and Comments Regarding Turbulence

It has been traditional to compare experimental results and theory by matching the measured circulation distributions (deduced from static pressure measurements) with the analytical predictions. In all cases, it has been found that circulation profiles could be matched only when the measured laminar radial Reynolds number was much higher than its theoretical counterpart. As mentioned in the Introduction, previous investigations of vortex flow in tubes were based on one-dimensional flow models (equivalent to setting $A = 0$ in the present theory) and tended to ascribe discrepancies between measured and theoretically computed circulation profiles to the presence of turbulence in the flow field. It was assumed that the turbulence produced a large "eddy viscosity" that in turn resulted in a reduced radial Reynolds number. The ratio of the theoretically deduced "effective" radial Reynolds number to the actual radial Reynolds number based on a laminar viscosity was used as a measure of the turbulence level in the tube. Thus, Keyes,⁸ for example, was able to arrive at a correlation between apparent turbulence level and the tangential peripheral Reynolds number of the flow.

Subsequently, Kendall¹⁶ and others pointed out the significance of the end-wall boundary-layer interaction and suggested that the reduction in Γ distribution, which had been attributed to turbulence, may indeed be explainable largely or wholly by the three-dimensional boundary-layer interaction. It was argued that diversion of flow into the boundary layers reduced the radial Reynolds number in the primary flow, thus accounting for the reduced values of Γ/Γ_0 .

As the present study shows, however, when Γ/Γ_0 begins to depart from one, the boundary-layer growth slows down and finally reverses, resulting in fluid being returned to the primary flow. Since only a fraction of the fluid's angular momentum is lost in the boundary layer (on the average), mass ejection from the boundary layer tends to support the angular momentum distribution, retarding its further decline. Finite values of ζ contribute further to this trend, resulting, as has been seen, in the requirement that A be greater than 1.2 for $\zeta = 0$ (or 2.2 if $\zeta = 1$) before any significant degradation of the Γ profile occurs because of the boundary-layer interaction.

In order to determine whether three-dimensionality can indeed explain all or part of the experimentally observed velocity distributions, some new experiments were conducted, using two different vortex chambers. Somewhat modified versions of the apparatus described by Rosenzweig²⁰ and by Grabowsky and Rosenzweig²¹ were used. The vortex tubes were similar to those employed by Keyes, having rows of discrete jets injecting tangentially at the periphery and a central exhaust hole at one end. One tube was 2-in. i.d. \times 12 in. long and was operated in a low-density (low Reynolds number) regime with either nitrogen or helium as the working fluid. The other tube was 5-in. i.d. \times 15 in. long and was operated with nitrogen only. Mass-flow measurements and radial pressure distributions were taken. The latter were used to infer tangential velocity distributions. It was pos-

[§] An independent analysis by Anderson²² has treated the compressibility effects in more detail but with similar conclusions.

sible, therefore, to calculate A , Γ_e , and the laminar radial and tangential Reynolds numbers from the measured quantities.

In comparing the normalized values of Γ_e with those predicted by the present theory for the same values of A and Re_r , it was found that the experimental values were consistently lower, the discrepancy being larger for higher tangential Reynolds numbers. Thus, the trends indicated by the one-dimensional analyses were still present.

Assuming that the theory adequately represents the three-dimensional interaction, it must be concluded that end-wall boundary-layer effects alone cannot explain the relatively weak vortices observed in experiments. In the authors' opinion it is most probable that the discrepancy is due to the presence of turbulence in the experimental flow field.

If it is assumed that the effects of turbulence can be treated theoretically by the introduction of a spatially constant turbulent "eddy viscosity" and suitably time-averaged velocity components (as is traditional in turbulent analyses), then the present theory remains valid if the radial Reynolds number is replaced by an "effective" Reynolds number based on the eddy viscosity. This hypothesis is certainly a questionable one for the present flow configuration because of the strong radial gradients and the likelihood that the turbulent fluctuations are highly anisotropic. Nevertheless, because of its simplicity, it has been used in the one-dimensional analyses and will be pursued further here for comparison.

The experiments just described were used in conjunction with the theory to infer a value of effective radial Reynolds number (Re_r^*). Results are shown in Fig. 12 as a ratio of actual to "effective" radial Reynolds number vs tangential Reynolds number based on tube radius. A spread is indicated for each test point, the upper bound corresponding to $\zeta = 1$ and the lower to $\zeta = 0$. Also shown are several actual measurements of turbulence intensity made by Kendall¹⁶ using a hot-wire anemometer and Keyes' least-squares line, which was fitted to data reduced using the one-dimensional hypothesis.⁸ Values of A in the present experiments varied from 0.6 to 1.5, and Re_r ranged from 12 to several thousand. Calculations indicate that values of A of order one were also representative of Keyes' experiments. The comparison shown in Fig. 12 indicates that early estimates of turbulence levels in jet-driven vortices, even though based on one-dimensional flow models, are not far from those arrived at after consideration of three-dimensional effects.

VI. Conclusions

The equations governing the interaction between the primary flow and end-wall boundary layers in a vortex tube have been presented and solved iteratively on a digital computer. The controlling parameters include a boundary-layer interaction parameter A representing a measure of the mass fraction diverted to the boundary layers, the radial Reynolds number, and a parameter ζ representing the boundary-layer mass ejection occurring as a result of the geometrical discontinuity existing at the exhaust-hole radius. Circulation and mass-flow distributions are presented, illustrating the variety of results obtainable in the different flow regimes. Over-all results are characterized by the values of Γ_e/Γ_0 , the circulation ratio at the exhaust radius, and f_m , the minimum mass flow in the primary flow region.

The results show that, if $A < 1$, the effect of the boundary layer interaction on the circulation distribution is small. The same is true if $|Re_r|$ is of order one, regardless of A . As A increases, the effect is more pronounced, the interaction producing a reduced Γ_e/Γ_0 and f_m . A variation of ζ from zero to one produces a maximum increase of approximately 20% in Γ_e/Γ_0 , but can have a profound effect on f_m , causing negative values (i.e., reverse flow) to occur in some instances. It has been shown that in some cases it is possible to have an

excess of flow in the boundary layer (i.e., $f_m < 0$) while Γ/Γ_0 remains close to unity.

The theoretical results have been compared with experiments by matching experimental and theoretical circulation profiles and thereby determining a ratio of actual (laminar) to "effective" radial Reynolds number. By comparison with previous results, it has been concluded that turbulence levels in jet-driven vortex flows are not appreciably less than those based on one-dimensional model assumptions.

Appendix: Analytic Solution for Infinite Reynolds Number

An analytic solution to Eqs. (11) and (16) is possible in the limit of $Re_r \rightarrow -\infty$. From Eq. (9) it is seen that, in order to have a finite value of f in this limit, either an infinity or a zero in Γ' is required. Conversely, any Γ distribution is possible when $f = 0$, since the product $Re_r f$ is then indeterminate. Therefore, it is evident that in this limit Γ will remain constant at large radii until all of the flow reaches the end-wall boundary layers, i.e., until $f = 0$. Proceeding inward from this point, all the flow will remain in the boundary layers, and the circulation will distribute itself in just such a way as to keep $f = 0$. This distribution may be found by writing Eq. (13) in differential form

$$(d/dr)Q_{BL}\Gamma - \alpha Q_{BL}(d\Gamma/dr) = \alpha c\Gamma^2 \quad (A1)$$

For $Q_{BL} = \text{const}$, this reduces to

$$\frac{1}{\Gamma^2} \frac{d\Gamma}{dr} = \frac{\alpha c}{Q_{BL}(1 - \alpha)} \quad (A2)$$

Equation (A2) integrates to

$$\frac{\Gamma_0}{\Gamma} = \frac{A}{(1 - \alpha)(1 - f)} \frac{r}{r_0} + c_2 \quad (A3)$$

in terms of previously defined dimensionless parameters. The constant c_2 is evaluated by the condition that $\Gamma/\Gamma_0 = 1$ at $r = \hat{r}$, the radius at which f first reaches zero. For $r > \hat{r}$, from Eqs. (12) and (13)

$$f = 1 - A[1 - (r/r_0)] \quad (A4)$$

Therefore,

$$\hat{r}/r_0 = 1 - 1/A \quad (A5)$$

From Eq. (A5) and the condition that $\Gamma/\Gamma_0 = 1$, $f = 0$ at $\hat{r} = \hat{r}$, Eq. (A3) reduces to

$$\frac{\Gamma}{\Gamma_0} = \frac{\alpha - 1}{\alpha - 2 + A[1 - (r/r_0)]} \quad r < \hat{r} \quad (A6)$$

For $\zeta = 0$, the solution for the Γ distribution in the limit of $Re_r \rightarrow -\infty$ is $\Gamma = \Gamma_0$ for $r > \hat{r}$ and is given by Eq. (A6) for $r_e < r < \hat{r}$. Inside the exhaust radius it is undetermined.

The solution for $\zeta \neq 0$ is slightly different. At the radius of the exhaust, flow is forced out of the boundary layer so that $f > 0$ when $r < r_e$. Thus Γ' must be zero here from Eq. (9). Furthermore, differentiation of Eq. (11) indicates that Γ' must remain zero for $r > r_e$ until

$$\int_0^{\eta_f} \frac{f}{\eta} d\eta \leq 0 \quad (A7)$$

This in turn requires f to be negative in some region outside the radius of the exhaust. Thus, for $\zeta \neq 0$, Eq. (A6) applies only to $r > r^*$, with r^* defined so that

$$\int_0^{\eta^*} \frac{f}{\eta} d\eta = 0 \quad (A8)$$

To complete Eq. (A8), f is given by

$$f = (\eta/\eta_e)[1 + (1 - \zeta)(f_e - 1)] \quad \eta < \eta_e \quad (A9)$$

$$f = A(\Gamma_e/\Gamma_0)[\eta^{1/2} - (\eta^*)^{1/2}] \quad \eta_e < \eta < \eta^*$$

Equations (A8) and (A9) yield an algebraic equation relating Γ_e and η^* :

$$1 - (1 - \zeta) \left\{ 1 - A \frac{\Gamma_e}{\Gamma_0} [\eta^{1/2} - (\eta^*)^{1/2}] \right\} = A \frac{\Gamma_e}{\Gamma_0} \times \left\{ (\eta^*)^{1/2} \ln \frac{\eta^*}{\eta_e} - 2[(\eta^*)^{1/2} - (\eta_e)^{1/2}] \right\} \quad (A10)$$

A second equation relating Γ_e and η^* is obtained from Eq. (A6), which is valid at η^* :

$$\frac{\Gamma_e}{\Gamma_0} = \frac{\alpha - 1}{\alpha - 2 + A[1 - (\eta^*)^{1/2}]} \quad (A11)$$

Equations (A10) and (A11) must be solved simultaneously to obtain Γ_e and η^* . Results for Γ_e/Γ_0 are included in Fig. 9.

References

- ¹ Lewellen, W. S. and Grabowsky, W. R., "Nuclear space power systems using magnetohydrodynamic vortices," *ARS J.* **32**, 693-700 (1962).
- ² Kerrebrock, J. L. and Meghreblian, R. V., "Vortex containment for the gaseous fission rocket," *J. Aerospace Sci.* **28**, 710-724 (1961).
- ³ Donaldson, C. duP. and Sullivan, R. D., "Behavior of solutions of the Navier-Stokes equations for a complete class of viscous vortices," *Proceedings of the Heat Transfer and Fluid Mechanics Institute* (Stanford University Press, Stanford, Calif., 1960), pp. 16-30.
- ⁴ Deissler, R. G. and Perlmutter, M., "An analysis of the energy separation in laminar and turbulent compressible vortex flows," *Proceedings of the Heat Transfer and Fluid Mechanics Institute* (Stanford University Press, Stanford, Calif., 1958), pp. 40-53.
- ⁵ Einstein, H. A. and Li, H., "Steady vortex flow in a real fluid," *Proceedings of the Heat Transfer and Fluid Mechanics Institute* (Stanford University Press, Stanford, Calif., 1951), pp. 33-43.
- ⁶ Anderson, O., "Theoretical solutions for the secondary flow on the end wall of a vortex tube," UAC Research Labs. Rept. R-2494-1, United Aircraft Corp. (November 1961).
- ⁷ Lewellen, W. S., "A solution for three-dimensional vortex flows with strong circulation," *J. Fluid Mech.* **14**, 420-432 (1962).
- ⁸ Keyes, J. J., Jr., "An experimental study of flow and separation in vortex tubes with application to gaseous fission heating," *ARS J.* **9**, 1204-1210 (1961).
- ⁹ Ragsdale, R. G., "NASA research on the hydrodynamics of the gaseous vortex reactor," NASA TN-D-288 (June 1960).
- ¹⁰ Taylor, G. I., "The boundary layer in the converging nozzle of a swirl atomizer," *Quart. J. Mech. Appl. Math.* **3**, 129-139 (1950).
- ¹¹ Mack, L. M., "Laminar boundary layer on a disk of finite radius in a rotating flow, Part I," *Jet Propulsion Lab. Rept. TR-32-224* (May 1962).
- ¹² King, W. S., "Momentum integral solutions for the laminar boundary layer on a finite disk in a rotating flow," *Aerospace Corp. Rept. ATN-63(9227)-3* (June 1963).
- ¹³ Weber, H. E., "Boundary layer inside a conical surface due to swirl," *J. Appl. Mech.* **23**, 587-592 (1956).
- ¹⁴ Rott, N., "Turbulent boundary layer development on the end walls of a vortex chamber," *Aerospace Corp. Rept. ATN-62(9202)-1* (July 1962).
- ¹⁵ Rosenzweig, M. L., Ross, D. H., and Lewellen, W. S., "On secondary flows in jet-driven vortex tubes," *J. Aerospace Sci.* **29**, 1142 (1962).
- ¹⁶ Kendall, J. M., Jr., "Experimental study of a compressible viscous vortex," *Jet Propulsion Lab. Rept. TR-32-290* (June 1962).
- ¹⁷ Ross, D. H., "An experimental study of secondary flow in jet-driven vortex chambers," *Aerospace Corp. Rept. ATN-64(9227)-1* (January 1964).
- ¹⁸ Lewellen, W. S., "Three-dimensional viscous vortices in incompressible flow," Ph.D. Dissertation, Univ. of California at Los Angeles (1964).
- ¹⁹ Rosenzweig, M. L., Lewellen, W. S., and Ross, D. H., "Confined vortex flows with boundary-layer interaction," *Aerospace Corp. Rept. ATN-64(9227)-2* (February 1964).
- ²⁰ Rosenzweig, M. L., "Summary of research in the field of advanced nuclear propulsion, semiannual technical report," *Aerospace Corp. Rept. TDR-930(2210-14)-TR-1* (March 1962).
- ²¹ Grabowsky, W. R. and Rosenzweig, M. L., "Advanced propulsion, semiannual technical note," *Aerospace Corp. Rept. ATN-63(9227)-2* (April 1963).
- ²² Anderson, O., "Theoretical effect of Mach number and temperature gradient on primary and secondary flows in a jet-driven vortex," UAC Research Labs. Rept. RTD-TDR-63-1098, United Aircraft Corp. (November 1963).

Cesium Neutral and Ion Emission from Carburized and Oxygenated Porous Tungsten

A. Y. CHO* AND H. SHELTON†

TRW Space Technology Laboratories, Redondo Beach, Calif.

Experimental data on the temperature dependence of the ion, electron, and neutral emitting properties of clean, carbided, and oxygenated porous tungsten indicate that 1) W_2C has a higher work function (~ 4.85 v) than does clean tungsten, it adsorbs cesium less tightly at ion operating temperature than does clean tungsten, and therefore it emits fewer neutral cesium atoms and possesses a lower critical temperature than does clean tungsten; 2) oxygenated tungsten has a higher work function (~ 5.0 v) than does clean tungsten, it adsorbs cesium more tightly than does clean tungsten, and therefore it emits fewer neutrals and possesses a higher critical temperature than does clean tungsten. The clean tungsten is produced by exposure to oxygen to remove carbon, long-time high-temperature cesium ion operation, and sputtering in high vacuum free of oxygen and hydrocarbons. The carbided surface is produced by cracking hydrocarbon vapors (C_2H_2 , CH_4 , C_2H_4 , etc.) and stabilizing by high-temperature operation. X rays show the surface to be W_2C , and an increase in thermal emissivity is noted. Oxygenated tungsten is produced by exposing to oxygen partial pressures of from 1×10^{-8} to 1×10^{-5} torr. The experimentally observed effects of other impurities (calcium, silicon, and boron) are also discussed.

Introduction

IN the use of hot porous tungsten to produce cesium ions for electrical propulsion, the degree of tungsten purity is of extreme importance. Materials affect the tungsten performance mainly altering the work-function, the cesium binding energy, and the emissivity. The materials that raise the work-function lower the ratio of neutral emission to ion emission. Materials that lower the work function increase the neutral emission, often above the ion emission. If the binding energy is increased, the critical temperature necessary to evaporate a given current density of ions will increase. If the binding energy is decreased, the critical temperature will be lower.

Tungsten can be brought to a very high degree of purity simply by raising its temperature, causing foreign materials to diffuse to the surface and evaporate. In the case of practical ion emitters, however, the practical difficulties of heating large areas, the temperature limitations imposed by the brazes, and deleterious effects of further sintering interfere with the use of this method. The experimenter may, therefore, often be working with other than clean tungsten.

This paper describes experiments on porous tungsten emitters in which special measures were taken to control surface conditions. Ultrahigh vacuum was maintained, emitters were designed to allow prolonged heating to $2000^\circ K$, capability for surface sputtering was provided, and controlled amounts of impurities could be introduced.

Results are presented showing that oxygen decreases neutrals but increases critical temperature. Carbon decreases neutrals and decreases the critical temperature, but raises emissivity. Calcium increases neutrals and increases critical temperature. These observations result from careful repeated study of each of these materials deposited on tungsten that had first been cleaned by high-temperature operation in high vacuum followed by sputtering.

Experimental Procedures

The measurements were made on 1-in.-diam porous tungsten disks manufactured by Semicon of California. The ions are focused and accelerated by two fine grids of tungsten wires. These grids can be heated to $2600^\circ K$ so as to keep the surface clean. Electron currents from the accelerating grid to the source during ion emission and from the focusing grid during electron emission are thus eliminated. When maintained hot and at a positive potential, the grids also can be used to sputter the tungsten source, since a fraction of the cesium from the source will be intercepted, surface-ionized, and accelerated back to the source.

A hot-ribbon neutral sensor off to one side of the ion beam "sees" the surface of the porous tungsten through the fine set of grid wires. Although the neutral detector measures propellant utilization as modified by the accelerating structure rather than the desired true neutral fraction, in this case, because of the small amount of neutral scattering by the fine grids, the two are essentially the same.

The vacuum obtained by a Welch "turbomolecular" pump is oxygen-free and hydrocarbon-free, as monitored by a mass spectrometer mounted in the system. A large copper surface at liquid nitrogen temperature surrounds the ion source, cools the neutral detector, and condenses cesium and water vapor. The total pressure when operating is a few times 10^{-8} torr and is mostly untrapped cesium.

A clean tungsten surface is obtained by first heating in oxygen to remove carbon, operating for hours at a relatively high ($5\text{--}10$ ma/cm²) cesium ion current density at $2000^\circ K$, and then sputtering. Such a surface can then operate clean for many minutes. During this time a leak of oxygen producing a pressure of 1×10^{-8} torr will detectably alter the surface condition. Because the measurements were made on thoroughly cleaned porous tungsten at relatively low ion current density where the pore distribution has little effect, these data are believed to be valid for all clean porous tungsten regardless of manufacturer.

The carbided surface is produced by cracking hydrocarbon vapors (C_2H_2 , CH_4 , C_2F_4 , etc.) and stabilizing by high-temperature operation. The short exposure time (minutes) and the low pressure (a few times 10^{-6} torr) results in a very thin

Presented as Preprint 64-11 at the AIAA Aerospace Sciences Meeting, New York, January 20-22, 1964; revision received August 6, 1964. This work was supported by Contract No. NAS3-2524 through the NASA Lewis Research Center.

* Member of Technical Staff. Associate Member AIAA.

† Member of Technical Staff. Member of AIAA.

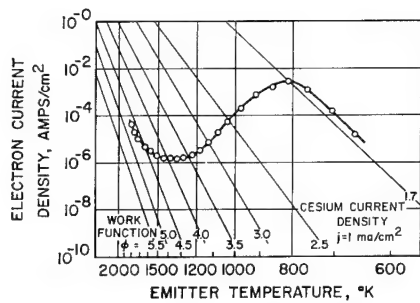


Fig. 1 Electron emission S-shaped curve for clean porous tungsten ionizer.

coating of W_2C a few microns thick. It has been identified by x rays. This surface can be cleaned up by long (at high T) exposure to oxygen. It is noteworthy that oxygen at any pressure up to 10^{-5} torr or more has no effect on the electronic properties of this surface for considerable periods of exposure. This effect and the cleanup of carbon is attributed to the rapid formation and evaporation of CO.

The qualitative features of an oxygenated surface have been gathered over a long period of time on many different samples of porous tungsten. The quantitative effect depends on the degree of oxygenation, cesium ion current density, trace impurities, and the past history of the surface. The carbided surface, on the other hand, exhibits the same quantitative characteristics time and time again on different sources carbided in different manners. This surface is also much less sensitive to traces of poisoning contaminants. The truly clean tungsten surface is harder to achieve and maintain; after the tungsten is essentially clean, the remnant surface contaminants such as oxygen can be sputtered off.

Experimental Results

Clean Tungsten

In Fig. 1 is plotted the electron current density from clean porous tungsten fed with cesium. The feed rate was such as to produce 1 mA/cm^2 ion current density if the voltages were reversed. Plotted lightly in the background are constant work-function lines based on the Richardson equation $j = 120 T^2 \exp(-e\Phi/kT)$ amp/ cm^2 . When the experimental points lie parallel to these lines, the surface is maintaining a constant work-function. The value of the work-function of any point can be interpolated from its position on the experimental curve relative to the lines of constant Φ . We can see in this instance that, at high temperature, cesium coverage is essentially zero, and we find the work-function of this clean porous tungsten to be 4.7 v. At lower temperatures, the cesium sticks; this lowers the work-function, and causes the electron emission to increase. The temperature at which the electron current crosses the 3.7 v line (1300°K in Fig. 1) is approximately the critical temperature for ion emission.

Under different surface conditions, the S-shaped curve may depart from the constant work-function line at higher tem-

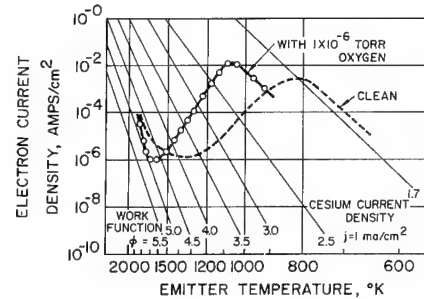


Fig. 3 Electron emission S-shaped curve for oxygenated porous tungsten ionizer.

peratures, the minimum electron emission may occur at a higher temperature, and the rising portion of the curve on the low-temperature side of the minimum may have a greater slope. The critical temperature then will be higher. The portion of the curve to the right of the critical temperature relates to the adherence of large cesium coverages and has no bearing on ion production.

In Fig. 2 we see the percentage fraction of neutral cesium emitted from the same surface during ion operation at high voltages. At the right, the temperature is below critical, and the neutrals are nearly 100%. The critical temperature is indeed 1300°K. Constant work-function lines are shown, based on the Saha-Langmuir equation, which predicts that the fraction of the total cesium emitted as neutrals will be

$$\alpha = (1 + \frac{1}{2} \exp(\Phi - V_i)/kT)^{-1}$$

where the cesium ionization potential V_i is 3.9 v. (A report¹ by Teem and co-workers shows that, when a patchy surface is involved, it is the electron work-function as we measure it with $A = 120$ which should be used in this equation to predict neutrals.) At high temperatures the cesium coverage is very low, and the work-function is that of clean tungsten. The resulting neutral fraction and its temperature dependence agree reasonably well with the work-function found from the S curve.

Oxygenated Tungsten

Figure 3 shows the S-shaped curve for oxygenated tungsten. The dotted curve for clean tungsten is included for comparison. For the higher temperatures to the left, we see a high work-function decreasing toward the value for clean tungsten. The abrupt steep rise as the temperature is decreased indicates that the cesium has a high binding energy and that a high critical temperature will result. Although oxygenated tungsten in vacuum results in a larger low-temperature maximum,² the continuous maintenance of an oxygen pressure in this case suppresses the electron emission at low temperature. In Fig. 4 we see that the critical temperature is increased and that the neutrals are lower, relative to clean tungsten. The broad flat minimum region indicates the adherence of a sizable cesium coverage to quite high temperatures, again indicating a high binding energy.

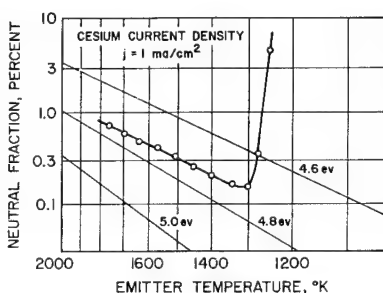


Fig. 2 Cesium neutral fraction vs temperature for clean porous tungsten ionizer.

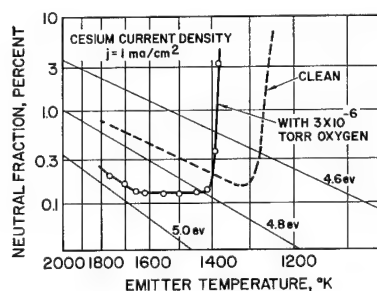


Fig. 4 Cesium neutral fraction vs temperature for oxygenated porous tungsten ionizer.

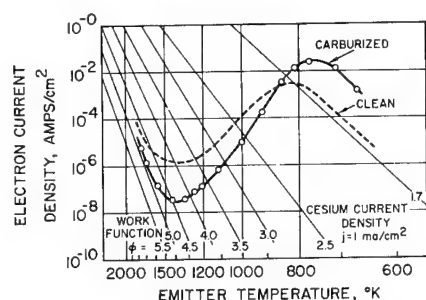


Fig. 5 Electron emission S-shaped curve for carburized porous tungsten ionizer.

Carburized Tungsten

In Fig. 5 the S-shaped curve for carburized tungsten is shown. The work-function is about 4.85 v. Also as evidenced by the low valley, the binding energy is lowered, predicting a lower critical temperature (1210°K). It is of interest to note that the binding energy for large cesium coverages is increased, giving a larger low-temperature peak emission. This characteristic is in close analogy to the effect of W_2C on electron emission from barium-impregnated porous tungsten. At high temperatures, W_2C is used to suppress electron emission by allowing the barium to evaporate. At low temperatures, electron emission is enhanced from W_2C areas.³

Figure 6 shows the neutral fraction vs temperature for carburized tungsten. We see that the critical temperature is lower, that the neutrals are lower, and that the strong temperature dependence as governed by the Saha-Langmuir equation is evidenced.

The improved ion emitter properties of carburized tungsten are offset by its higher thermal emissivity, which is approximately 0.4. Also a continuous high rate of carbon deposition will eventually form the nonequilibrium WC phase on the surface which has a lower work function⁴ and will degrade the ion emitting properties.

Calcium, Fluorine, and Other Contaminants

Calcium was studied and found to be a bad poison; it appeared both to lower the work-function, thereby producing high neutral emission, and to hold the cesium tightly, producing a high critical temperature. High-temperature operation was necessary in order to lower the calcium concentration on the surface by evaporation. A high pseudocritical temperature existed where the diffusion rate to the surface matched the evaporation. This temperature was often above 1700°K.

Fluorine acts like oxygen. It raises the critical temperature and lowers the neutrals. Silicon and boron were found to have little effect on ion and neutral emission, although they raised the tungsten work-function slightly.

The presented data have all been at the relatively low current density of 1 ma/cm² in order to illustrate graphically the basic effect of work-function and binding energy. The in-

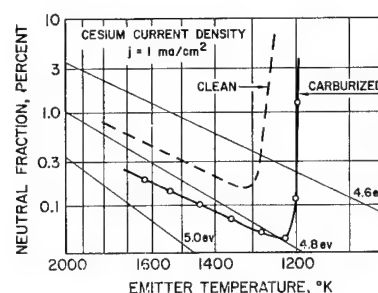


Fig. 6 Cesium neutral fraction vs temperature for carburized porous tungsten ionizer.

crease of neutrals with current density because of insufficiently fine pore distribution is barely seen here. As pointed out by the work of Hussman,⁵ the neutrals increase at higher ion current densities, badly so with a coarse-grain porous tungsten and less so with a fine-grain porous tungsten. Also, the critical temperature is less well defined at high ion current densities with a large range of temperatures where an increase in temperature decreases the neutrals. High current densities up to 16 ma/cm² on many different porous tungsten samples have been studied by the authors, and the different characteristics of high-current-density ion emission and the data presented here are not contradictory and are due to the pore distribution.

Conclusion

An oxygenated tungsten surface is identifiable from its S-shaped curve by its high bare work-function and high cesium coverage at ion operating temperatures and from its ion emission by the high critical temperature and the small constant percentage value of neutrals at higher temperatures. A carburized surface is identifiable from its S-shaped curve by its stable 4.85 v work-function insensitive to oxygen and the deep minimum, and from its ion emission by the low critical temperature and the rapid rise of neutrals at higher temperatures. Clean tungsten is identifiable by its known work-function and its extreme sensitivity to small amounts of oxygen.

References

- ¹ Teem, J. M. and Taylor, L. H., "Ionizer development and surface physics studies," Electro-Optical Systems Rept. 1660/1-IR-1, p. 16 (December 1962).
- ² Langmuir, I. and Kingdon, K. H., "Thermionic effects caused by vapours of alkali metals," Proc. Roy. Soc. London **A107**, 75 (1925).
- ³ Levi, R., private communication (1963); also Levi, R. and Rittner, E. S., "Role of carburization in the suppression of emission from barium-activated tungsten and molybdenum surfaces," J. Appl. Phys. **33**, 2336 (1962).
- ⁴ Baker, J. B. and Gaines, G. B., "Evaluation of electron emission behavior for detecting carbon in tungsten and rhenium," Battelle Memorial Institute Rept. BMI-1649 (September 1963).
- ⁵ Hussman, O., "A comparison of the contact ionization of cesium on tungsten with that of molybdenum, tantalum, and rhenium surfaces," AIAA J. **1**, 2607 (1963).

Vortex Gas Accelerator

STIRLING A. COLGATE*

University of California, Livermore, Calif.

The exhaust velocity of a propellant gas from an isothermal cavity can be significantly increased by a factor of approximately 1.7 above that corresponding to the usual isentropic expansion by utilizing multiple reheat by blackbody radiation from the walls during expansion. In order to reduce the necessary volume and the frictional drag with the walls during this reheat and expansion process, the gas is wrapped up in a rotational flow pattern in which angular momentum per unit mass is constant along all streamlines. As a consequence, the expansion in the nozzle corresponds to the conversion of rotational to linear momentum, rather than the usual thermal to linear. In order to absorb the radiant energy from the walls, the gas must have a sufficient optical opacity (achieved by a small contaminant addition to hydrogen) such that the gas in the cavity is approximately one radiation mean free path thick.

ROTATIONAL gas flow can be used to enhance the exhaust velocity from a constant-temperature source provided radiation-transport heating can be made greater than the vortex flow frictional decay time. In simplest terms, a partially isothermal expansion of the working fluid can be achieved as opposed to the usual adiabatic expansion. The additional enthalpy supplied to the fluid during isothermal expansion results in a higher specific impulse for rocket applications. Since this enthalpy must be added to the fluid by radiation flow, the opacity, density, frictional decay rate, and radiation intensity become the determining quantities.

There are two general forms of rotational gas flow: one is at constant angular velocity (frequently referred to as "wheel rotation") and describes the lowest order state of a gas in equilibrium inside a rotating cylinder; the second form occurs at constant angular momentum per unit mass and, to exist, requires that the rate of angular momentum supplied to the flow pattern must be large compared to the frictional drag, both with the walls and internally. The state of constant angular momentum, therefore, exists either transiently or as the result of a continuous flow of injected angular momentum and partially degraded exhaust.

In this paper we are primarily concerned with the second form of rotational gas flow in which the gas is injected tangentially at the periphery of a cylindrical cavity and expands radially toward the axis. The gas leaves the cavity by axial flow through a hole of smaller radius at one end of the cavity (Fig. 1). Both axial and radial velocities are considered as small perturbations to the primary flow, which is circular. The energy transferred in the isothermal expansion from the state of the gas at the outer wall to that at the smaller radius of exhaust is stored in kinetic energy of rotational velocity. This rotational velocity can then be converted to axial velocity in a standard nozzle (Appendix A).

It is useful to describe the density and/or pressure distribution of the wheel rotation flow in order to gain a qualitative understanding of the flow pattern near injection. In particular, one would wish to substantiate the possibility of injecting the gas tangentially at the periphery, in a thin layer, at near-constant angular momentum and pressure equilibrium with the surrounding gas. The subsequent radial and rotational flow is assumed to occur at constant

angular momentum. The conditions required for this to occur will be discussed.

Imagine a hot cylindrical cavity (e.g., a reactor at temperature T) and a working gas injected tangentially at a velocity u_0 . To the extent that the gas flow pattern can be approximated by a rigidly rotating body with a boundary layer in shear between the gas and the stationary cylindrical wall, then

$$dp/dr = r\Omega^2\rho \quad (1)$$

where

Ω = angular frequency

p = pressure

ρ = density

However, $p = \rho kT/m$, and letting $\rho(0)$ = density at the axis, we obtain

$$\rho(0) \exp(\Omega^2 r^2 m / 2kT) \quad (2)$$

Defining

$$M = \left(\frac{u_0^2}{2kT/m} \right)^{1/2}$$

then

$$\rho = \rho(0) \exp[M^2(r^2/r_0^2 - 1)] \quad (3)$$

If we now assume for the injected gas $M^2 \gg 1$, so that the mass is concentrated in a relatively thin layer of constant angular momentum, and then ask for the distribution as this gas is heated and forced toward the axis conserving angular momentum; and if we assume sufficient radiation transport to maintain constant temperature, then the velocity distribution becomes

$$m\Omega r^2 = \text{const, or } \Omega r = u = u_0 r_0 / r \quad (4)$$

Radial equilibrium from Eq. (1) demands that

$$dp/dr = r\Omega^2\rho = \rho u_0^2 r_0^2 / r^3$$

or

$$\frac{dp}{\rho} = \frac{u_0^2}{kT/m} \frac{dr}{r^3}$$

Letting ρ_0 and p_0 be the density and pressure at the wall, then (see Fig. 2)

$$\rho = \rho_0 \exp M^2(1 - r_0^2/r^2) \quad (5a)$$

$$p = p_0 \exp M^2(1 - r_0^2/r^2) \quad (5b)$$

Received March 10, 1964; revision received August 17, 1964. This work was performed under the auspices of the U. S. Atomic Energy Commission. I am indebted to James Hadley and Harry Reynolds for many useful discussions and encouragement.

* Physicist, Lawrence Radiation Laboratory.

In the injection nozzle, M may be large in order that the injected gas has uniform angular momentum, but after entering the cavity the gas is soon reheated by radiation. If one assumes that the injected gas expands rapidly and adiabatically in a small nozzle from a reservoir at temperature T and is then reheated "slowly" in the cavity to the same temperature T by radiation flow, then one obtains $M = [1/(\gamma - 1)]^{1/2}$. The gas is then assumed to leave the vortex by axial flow from the cavity at the radius r . The density distribution of Eqs. (5) implies a large expansion ratio during the transport from r_0 to r , and it is this isothermal expansion that gives rise to the enhanced gas velocity $u_0 r_0/r$.

The rate at which energy must be supplied to the gas during this expansion is determined primarily by the mass flow, and the minimum mass flow rate in turn is determined by the viscous drag. The energy removed by drag must be smaller than the energy supplied by radiation; otherwise, the enhanced exhaust velocity cannot be achieved. The drag occurs both at the outer wall and the end walls; the internal shear flow should be laminar because the shear flow is irrotational at constant angular momentum. In addition, the density and pressure distribution of Eqs. (5) is stable against small adiabatic radial deformations. This condition is

$$-\frac{1}{\gamma} \frac{1}{p} \frac{dp}{dr} < -\frac{1}{\rho} \frac{dp}{dr} \quad (6)$$

which expresses the fact that, for stability, a small cell of gas transported radially outward adiabatically and in pressure equilibrium with its surrounding gas must have lower density than its surrounding gas. By inspection, the distribution of Eqs. (5) satisfies the inequality (6) provided only that the specific heat ratio $\gamma > 1$, which, indeed, is always the case. The restoring force implied by Eq. (6) is compared to the velocity shear stress in Appendix B and shown to give stability. Consequently, the internal flow should be laminar. The drag, therefore, takes place at the outer walls, and the internal flow can be considered frictionless.

The drag on the outer wall will be determined by turbulent flow and is given by

$$\tau = c_f \rho u^2 \text{ dynes/cm}^2 \quad (7)$$

where c_f is the coefficient of turbulent skin friction, which for large Reynolds number is of the order $\frac{1}{500}$.

The drag at the end wall is determined by the thickness of the Eckman layer. If this layer is less than 100 mean free paths thick (Reynolds number of 100), then the laminar shear stress becomes the drag. If the layer is thicker than 100 mean free paths, then presumably the layer will be turbulent, and Eq. (7) gives the drag. The Eckman layer is the depth of penetration of a diffusion wave (e.g., viscous shear wave) within the traversal time of sound over a distance corresponding to the local logarithmic density gradient (i.e., scale height of the exponential atmosphere). This description of the thickness of the boundary layer has been confirmed by Greenspan and Howard¹ in a linearized theory of rotational flow, but it appears physically as the result of the "buoyancy" of the nonrotating gas "rising" in the centrifugal gravitational field of the rotating gas. Since the diffusion coefficient can be expressed in terms of mean free paths and sound speed, the Eckman layer thickness becomes

$$\delta = (Dh/c)^{1/2} \quad (8)$$

where

$$D = \text{diffusion coefficient} = \frac{1}{3} \lambda c$$

$$\lambda = \text{mean free path}$$

$$h = \text{scale height of density distribution} = (dp/\rho dr)^{-1}$$

$$c = \text{sound speed}$$

Then

$$\delta/\lambda = [\frac{1}{3}(h/\lambda)]^{1/2} = \text{Reynolds number of the Eckman layer} \quad (9)$$

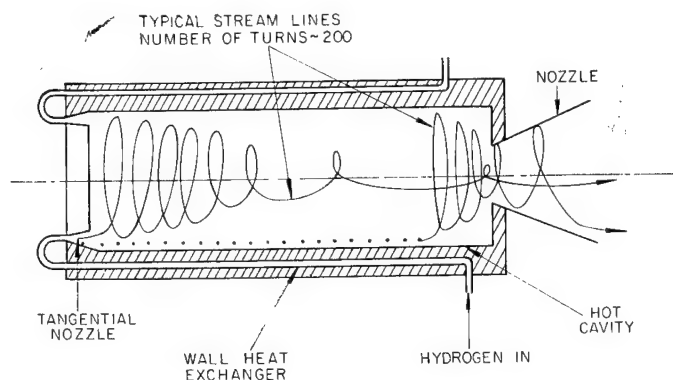


Fig. 1 Vortex gas accelerators.

and the shear stress becomes

$$\tau = \nu \rho u / \delta \text{ dynes/cm}^2 \text{ for } \delta/\lambda \leq 100 \quad (10)$$

where ν is the kinematic viscosity, and $\nu = \frac{1}{3} \lambda c' / c' = \text{sound speed within the layer}$.

If $u \geq c$, where c is measured in the unperturbed gas, then locally within the layer $c' \approx u$, and Eq. (10) becomes

$$\tau \approx (\rho u^2/3)(\delta/\lambda) \quad (11)$$

which approaches Eq. (7) for $\delta/\lambda \approx 100$.

The radiation-flow heating required to insure an isothermal angular-momentum-conserving expansion in the presence of these frictional losses can be divided into two parts, namely, 1) the heat flow required for an isothermal expansion for a mass flow rate determined by the outer wall angular momentum loss and 2) heat flow required for the end wall loss.

The end wall drag, assuming an Eckman layer thickness $\delta/\lambda \geq 100$, becomes

$$\begin{aligned} \tau_{\text{end}} &= \int_{r_0}^r c_f \rho u^2 2\pi r dr \\ &= 2\pi c_f \rho_0 u_0^2 r_0^2 \int_{r_0}^r \left(\frac{1}{r}\right) \exp\left[M^2\left(1 - \frac{r_0^2}{r^2}\right)\right] dr \quad (12) \end{aligned}$$

For $(Mr_0/r)^2 \gg 1$,

$$\tau_{\text{end}} \approx (\pi/2) r_0^2 c_f \rho_0 u_0^2 / M^2 \quad (13)$$

The total cylindrical outer wall drag for a length L becomes

$$\tau_{\text{out}} = 2\pi r_0 L c_f \rho_0 u_0^2 \quad (14)$$

so that, provided the cylinder is long compared to the radius ($L \gg r_0/4M^2$), the end wall drag can be neglected. Then the radial mass flow rate per unit length must give rise to an angular momentum flow greater than the outer wall drag.

If the minimum radial mass flow per unit length is given as

$$\beta = 2\pi r \dot{r} \rho \text{ g/cm-sec} \quad \dot{r} = dr/dt \quad (15)$$

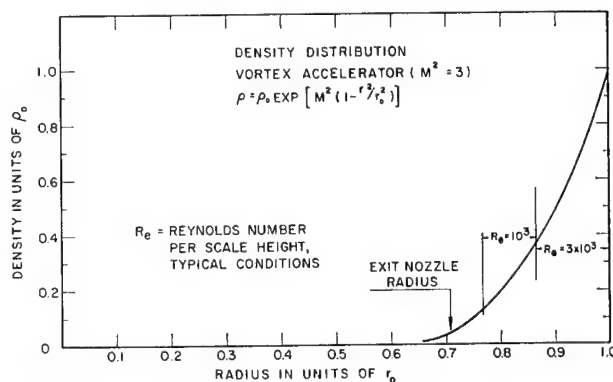


Fig. 2 Density distribution for the vortex accelerator.

Then equating drag to momentum flow at $r = r_0$ gives

$$2\pi r_0 c_f \rho_0 u_0^2 = 2\pi \dot{r} \rho_0 u_0 r_0 \quad (16)$$

and at $r = r_0$, $\dot{r} = c_f u_0$; but by Eq. (15), β is a constant, and so

$$\dot{r} = c_f r_0 u_0 \rho_0 / r \rho \quad (17)$$

The heating rate per gram corresponds to the pressure times volume work on the surrounding gas:

$$W(r) = \frac{d}{dt} \left[\int_{v_0}^v p dv \right] = \frac{d}{dt} \left[p_0 v_0 \ln \frac{v}{v_0} \right] = \frac{\rho_0 v_0}{\rho} \frac{d\rho}{dt} \quad (18)$$

By Eq. (5) and by observing that after reheat the kinetic energy of injection must be equal to the internal energy, then

$$\begin{aligned} W(r) &= \dot{r} \frac{u_0^2}{2} (\gamma - 1) \frac{2r_0^2 M^2}{r^3} \exp \left[M^2 \left(1 - \frac{r_0^2}{r^2} \right) \right] \\ &= c_f u_0^3 \frac{r_0^3}{r^4} \exp \left[M^2 \left(\frac{r_0^2}{r^2} - 1 \right) \right] \text{ ergs/g-sec} \end{aligned} \quad (19)$$

For an isothermal, blackbody cavity, the opacity ($\mu \text{ cm}^2/\text{g}$) required at temperature T is determined by

$$c_l a T^4 \mu = W(r)$$

where

$$\begin{aligned} c_l &= \text{velocity of light} \\ a &= \text{Boltzmann constant} \end{aligned}$$

or

$$\mu = c_f r_0^3 u_0^3 \exp \{ M^2 [(r_0^2/r^2) - 1] \} / c_l a T^4 r^4 \text{ cm}^2/\text{g} \quad (20)$$

Assume hydrogen in a cylindrical cavity reactor with $r_0 = 20 \text{ cm}$, $r = 14 \text{ cm}$, $T = 2800^\circ \text{K}$, $M^2 = 3$, $u_0 = 8 \times 10^5 \text{ cm/sec}$, and $c_f = 0.002$. Then

$$\mu \geq 3 \times 10^5 \text{ cm}^2/\text{g}$$

This corresponds to a minimum cross section of 10^{-18} cm^2 /molecule of hydrogen and can be compared to an optical cross section of the halogen gases of the order $3 \times 10^{-17} \text{ cm}^2$ and opaque carbon macromolecules of $\sim 10^{-14} \text{ cm}^2$. It would therefore appear feasible to meet the opacity requirements by the addition of a small percentage impurity.

The opacity might also be achieved by a carbon suspension. A carbon particle of radius $R \ll \lambda$ has a drag coefficient D for suspension in a velocity field \dot{r} of

$$D = \pi R^2 \rho c \dot{r} \text{ dynes} \quad (21)$$

which for suspension must be in equilibrium with the centrifugal force, giving

$$\pi R^2 \rho c \dot{r} = \frac{4}{3} \pi R^3 \rho_p (u^2/r) \quad (22)$$

where

$$\begin{aligned} \rho_p &= \text{density of particle} \\ c &= \text{local sound speed} \approx u_0 \end{aligned}$$

From Eq. (22) we have

$$R = \frac{3}{4} (\rho_0/\rho_p) c_f (r^2/r_0) \quad (23)$$

For the conditions

$$\begin{aligned} \rho_p &= 1 & \rho_0 &= 1.6 \times 10^{-6} \text{ g/cm}^3 \\ c_f &= 0.002 & r_0 &= 20 \text{ cm} & r &= 14 \text{ cm} \end{aligned}$$

then $R = 2 \times 10^{-8} \text{ cm}$, corresponding to molecules comprised of a few atoms.

Separation

The small critical size of the carbon molecule for suspension in the radial velocity suggests the partial separation of

heavy element additions. The critical hydrogen density for suspension of a uranium atom becomes, from Eq. (22),

$$\rho = (M/\sigma)(r_0/r^2 c_f) \quad (24)$$

For the assumptions $\sigma = 10^{-15} \text{ cm}^2$, $r_0 = 20$, $r = 14$, and $c_f = \frac{1}{500}$,

$$\rho_0 = 2 \times 10^{-5} \text{ g/cm}^3$$

This is a higher density than that required for radiative power balance at $T = 2940^\circ \text{K}$ and so might permit a modestly higher wall temperature by the partial return of sublimated wall material.

Axial Velocity

The axial velocity required within the cavity at the exhaust radius r must be sufficient to maintain an axial mass flow equal to the radial mass flow. Assuming an exhaust area A , the axial velocity becomes

$$2\pi r_0 \dot{r} \rho L = \dot{z} A \rho$$

Therefore,

$$\dot{z} = 2\pi c_f u_0 r_0^2 L / A r \exp [M^2 (1 - r_0^2/r^2)] \quad (25)$$

For the idealized flow, the effective area becomes

$$A = \pi [r^2 - (r - h)^2] \quad (26)$$

where h , the scale height of the density distribution, is given by

$$h = [(1/\rho)(d\rho/dr)]^{-1} = r^3/2M^2 r_0^2 \quad (27)$$

However, the nonuniformity of the initial angular momentum distribution is unlikely to result in a scale height as small as is implied by Eq. (27). A more realistic lower limit to h is of the order $h \approx r/2$, giving

$$\dot{z} \approx \frac{8c_f u_0 r_0^2 L}{3r^3 \exp [M^2 (1 - r_0^2/r^2)]} \quad (28)$$

The limiting axial flow occurs when $\dot{z} \approx u$. Therefore, we have

$$L = \frac{3r^2 \exp [M^2 (1 - r_0^2/r_2)]}{r_0 8c_f} \quad (29)$$

For $r_0/r = 2^{1/2}$, $c_f = \frac{1}{500}$, and $M^2 = 3$,

$$L \approx 5r_0 \quad (30)$$

Energy Flow

The total energy that has been transferred to the gas can be divided into three parts:

1) The first part is the initial enthalpy corresponding to the convective heating of the gas at rest in a heat exchanger external to the cavity. The expansion of this heated gas ($RT_0 \text{ ergs/g}$) in the injection nozzle gives rise to the kinetic energy $u_0^2/2 \text{ ergs/g}$ at a lower temperature ($T_1 \ll T_0$).

2) The second part is the reheat of this gas at constant pressure p_0 from the injection nozzle exit temperature T_1 to the cavity temperature T_0 . This corresponds to an internal energy $R(T_0 - T_1) \text{ ergs/g}$ in addition to a work term

$$\int_{v_1}^{v_0} p_0 dv = (\gamma - 1) R(T_0 - T_1) \quad (31)$$

resulting in a total energy increase $\gamma R(T_0 - T_1)$. This reheat of the injected gas occurs in violation of the usual gas dynamic concept that the stagnation temperature must always be less than or equal to the reservoir temperature. In this case, however, the boundary layer is thin compared to a radiation mean free path ($\sim 5\%$), so that, despite the

higher local gas temperatures in the boundary layer, heat can still flow from the opaque wall through the hot boundary layer to the larger mass of cold gas in the freestream.

3) The third part is the work performed in the isothermal expansion as the gas flows from r_0 to r . This work is

$$p_0 v_0 \ln(v_2/v_0) = (\gamma - 1)RT_0 \ln(v_2/v_0)$$

giving a final total transfer of energy to the gas of

$$\Delta W = RT_0 \left\{ 1 + \gamma \left(1 - \frac{T_1}{T_0} \right) + (\gamma - 1) \left[M^2 \left(\frac{r_0^2}{r^2} - 1 \right) \right] \right\} \quad (32)$$

Considering the limitations in the L/r_0 ratio for a useful reactor, the low value of γ (≈ 1.35) for hydrogen at a feasible wall temperature, and a reasonable injection nozzle design, the over-all energy transfer becomes $\Delta W \approx 3 RT_0$, or an increase of specific impulse by $3^{1/2}$ above the standard nozzle.

Thrust

The thrust of such an engine is limited by the energy transfer rate from the wall. The latter, of course, is determined by the blackbody radiation from the wall for the rotational flow heating.

If T_c is the radiation temperature in the cavity, and T_w is the radiation temperature of the wall, then by Eq. (32) and assuming the reheat after injection occurs by radiation,

$$(c_1/4) a(T_w^4 - T_c^4) = 3\dot{r}_0 \rho_0 (u_0^2/2) \text{ ergs/cm}^2\text{-sec} \quad (33)$$

$$= 3(c_f u_0^3 \rho_0)/2$$

Assuming $T_w = 2940^\circ\text{K}$, $T_c = 2500^\circ\text{K}$, $r_0/r = 2^{1/2}$, $\gamma = 1.35$, $c_f = \frac{1}{5.60}$, and $M^2 = 3$, then

$$u_0 = 8 \times 10^5 \text{ cm/sec}$$

$$\rho_0 = 1.4 \times 10^{-6} \text{ g/cm}^3$$

$$p_0 = 0.14 \text{ atm}$$

The specific impulse becomes

$$\mathcal{L} = (3)^{1/2} u_0 \times 10^{-3} = 1400 \text{ sec} \quad (34)$$

The thrust becomes

$$T = 2\pi r_0 L \dot{r}_0 \rho_0 u_0 (3)^{1/2} \text{ dynes} \quad (35)$$

but, from Eq. (17), $\dot{r}_0 = c_f u_0$, so that

$$T = 2\pi L r_0 \rho_0 c_f u_0^2 (3)^{1/2} \text{ dynes} \quad (36)$$

For the preceding conditions

$$T = 10^5 r_0^2 \text{ dynes}$$

For a mean reactor density $\bar{\rho} = \frac{1}{3} \text{ g/cm}^3$, the maximum r_0 for 1-g acceleration is determined by

$$g \bar{\rho} \pi r_0^2 L = T \quad (37)$$

or, for the preceding example,

$$r_0 = 20 \text{ cm}$$

$$L = 100 \text{ cm}$$

Therefore, a reactor built of such nested cylinders with an over-all diameter of 320 cm and 100 cm long would operate at $2.85 \times 10^8 \text{ w}$ with a total thrust of $4 \times 10^3 \text{ kg}$.

Radiation Transfer

In the calculation of required opacity [Eq. (20)] and of the heating rate [Eq. (33)] there existed the tacit assumption

that the rotating gas was less than a radiation mean free path thick. If there were many mean free paths, then the radiation diffusion equation

$$\rho Q = \bar{\nabla} \cdot \left(\frac{\lambda c}{3} \bar{\nabla} a T^4 \right) \quad Q = \frac{\text{energy}}{\text{g-sec}} \quad (38)$$

would have to be used, and, in general, the radiation heat flow would be degraded by a factor roughly inversely proportional to the number of mean free paths. Since this number will be shown to be of the order unity, the diffusion equation becomes a poor approximation, and the isothermal cavity radiation temperature of Eq. (33) is a better approximation.

The optical thickness of the cavity in mean free paths is

$$n = \int_{r_0}^r \rho \mu dr = \mu \int_{r_0}^r \rho dr \quad (39)$$

From Eq. (5), and performing the integration for $r_0/r = 2^{1/2}$ and $M^2 = 3$,

$$n = 0.12 \rho_0 r_0 \mu \quad (40)$$

Using Eqs. (20) and (33) for μ , one obtains

$$n = \frac{0.12 \rho_0 r_0 c_f r_0^3 u_0^3 \exp[M^2(r_0^2/r^2 - 1)]}{M^2 c_1 a r^4 [T_c^4/(T_w^4 - T_c^4)](4/c_1 a)(3 c_f u_0^3 \rho_0/2)} \quad (41)$$

Letting

$$T_c^4/(T_w^4 - T_c^4) = f$$

then

$$n = \frac{0.01}{f} \left(\frac{r_0}{r} \right)^4 \exp \left[M^2 \left(\frac{r_0^2}{r^2} - 1 \right) \right] \quad (42)$$

For the conditions shown for Eq. (33), $f = 1$, and $r_0/r = 2^{1/2}$; then $n = 0.8$ mean free paths, confirming the isothermal cavity approximation.

In conclusion, it has been demonstrated that a significant improvement in specific impulse (1.7) can be achieved for a nuclear reactor hydrogen rocket system by utilizing a rotational flow pattern and radiation heat transfer.

Appendix A

The wall drag in the nozzle is assumed small [Eq. (7)], since the linear path of contact in the nozzle is small. As a consequence, angular momentum is conserved. Therefore, during radial expansion of the rotational flow in the nozzle, the tangential velocity $u = u_0(r_0/r)$ is reduced. Conservation of energy demands that this appear as energy of axial flow (exhaust velocity). The axial acceleration is the resultant force from the radial centrifugal stress acting on the inclined nozzle wall.

Appendix B

Turbulence

The condition [Eq. (6)] for the stability of a gravitationa atmosphere is necessary and sufficient for wheel rotation flow, i.e., no velocity shear. However, the question that arises is at what value of γ will the velocity shear implied by Eq. (4) be stabilized by the restoring force of Eq. (6)? A linear analysis certainly results in a necessary condition, but because of the damping of viscosity, the largest scale turbulence determines the stability condition. The largest meaningful radial perturbation, turble size, becomes the scale height of the density distribution, because any larger turble will necessarily be degraded by the very large changes in specific volume. Using Eq. (4) for the velocity distribution, the velocity shear energy available in one scale height h becomes

$$\frac{\Delta w^2}{2} = \frac{u_0^2}{2} \left(\frac{r_0}{r} - \frac{r_0}{r-h} \right)^2 \quad (B1)$$

Using h from Eq. (27), the energy in shear becomes

$$\frac{\Delta w^2}{2} = \frac{u_0^2}{8M^2} \frac{(r/Mr_0)^2}{[1 - 1/2(r/Mr_0)^2]^2} \quad (\text{B2})$$

On the other hand, the energy associated with the adiabatic restoring force of Eq. (6) is

$$\Delta w/w = \Delta T/T = \gamma - 1 \quad (\text{B3})$$

where w is the internal energy, and Δw is the change in w for e -fold expansion. However, from the injection conditions,

$$w = u_0^2/2$$

so that

$$\frac{(\Delta w)^2/2}{w} = \frac{(r/Mr_0)^2}{4M^2(\gamma - 1)[1 - 1/2(r/Mr_0)^2]^2} \quad (\text{B4})$$

For $M^2 = 3$,

$$\frac{(\Delta w)^2/2}{w} = 0.11$$

so that the energy available in velocity shear is small compared to the adiabatic work of perturbation. As a consequence, turbulence should be suppressed everywhere. Equation (B4) is essentially the Richardson² number and predicts turbulence close to the value unity.

References

- ¹ Greenspan, H. P. and Howard, L. N., "On the time-dependent motion of a rotating fluid," *J. Fluid Mech.* **17**, 385-404 (1963).
- ² Richardson, L. F., "The supply of energy from and to atmospheric eddies," *Proc. Roy. Soc. (London)* **A97**, 354 (1920).

DECEMBER 1964

AIAA JOURNAL

VOL. 2, NO. 12

Stability of Circumferentially Corrugated Sandwich Cylinders under Combined Loads

EDWARD H. BAKER*

North American Aviation, Inc., Downey, Calif.

Theoretical buckling coefficients are obtained for the general instability of simply-supported, corrugated-core, circular sandwich cylinders under combined loads with the corrugations oriented in the circumferential direction. The differential equations of equilibrium which are used to obtain the buckling equations are derived from the small deflection equations of Stein and Meyers which include the effect of deformation due to transverse shear. Approximate solutions to the differential equations are obtained by Galerkin's method. The resulting Galerkin equations are solved for the critical buckling coefficients with the aid of a digital computer. Curves that predict the critical buckling load are presented for axial compression, external lateral pressure, and torsion. In addition, curves are given for the combined loads of axial compression and external lateral pressure, torsion and internal or external lateral pressure, and axial compression and torsion.

Nomenclature

- a, b, c, d = Fourier coefficients
 A_c = cross-sectional area of core in the xz plane per inch of width, in.
 A = $2t$, cross-sectional area of the facing sheets per inch of width, in.
 E_c = $E_c I_c$, flexural rigidity per inch of width of the core in the direction of the corrugations, in.-lb
 D = $E t h^2 / 2(1 - \mu^2)$, flexural stiffness per inch of width of equal thickness isotropic facing sheets about the centroidal axis of the sandwich, in.-lb
 D_x, D_y = beam flexural stiffnesses per inch of width of orthotropic plate in axial and circumferential directions, respectively, in.-lb
 D_{xy} = twisting stiffness per inch of width and inch of length of orthotropic plate in xy plane, in.-lb
 E_c = Young's modulus of elasticity for core material, psi
 E = Young's modulus of elasticity for facing material, psi

- E_x, E_y = extensional stiffnesses of orthotropic plate in axial and circumferential directions, respectively, lb/in.
 G_c = core shear modulus in plane perpendicular to corrugations, psi
 G_{xy} = shear stiffness of orthotropic sandwich in xy plane, lb/in.
 h = distance between middle surfaces of facing sheets, in.
 I_c = moment of inertia per inch of width of the corrugations about the neutral axis of the sandwich composite, in.³
 J = $U L^2 / \pi^2 D$ sandwich cylinder stiffness parameter
 K = buckling coefficient
 L = length of cylinder, in.
 m, s = integers, number of half-waves in the axial direction
 n = integer, number of half-waves in the circumferential direction
 N_c = force in the axial direction per inch of width acting on the middle plane of the sandwich, lb/in.
 N_p = force in the circumferential direction per inch of width acting on the middle plane of the sandwich, lb/in.
 N_s = shear force per inch of width acting in the middle plane of the sandwich, lb/in.
 p = pressure acting on the cylinder in a directional normal to the plane of the sandwich, psi
 Q_x = intensity of transverse force per inch of width acting on cross sections parallel to yz plane, lb/in.
 r = radius of cylinder, in.

Received September 27, 1963; revision received July 31, 1964. Part of this paper is based on research completed at the University of California at Los Angeles in partial satisfaction of the requirements for the degree of Master of Science. The author is indebted to S. E. Cain for preparation of the IBM digital computer programs.

* Senior Research Engineer, Applied Mechanics Group, Space and Information Systems Division. Member AIAA.

- t = thickness of each facing sheet of the sandwich, in.
 t_c = core depth, in.
 t_0 = thickness of the corrugated core sheet, in.
 U = G_{xy} , elastic core shear stiffness per inch of width in plane perpendicular to corrugations, lb/in.
 w = total displacement in z direction
 x, y, z = Cartesian coordinates
 Z = $L^2/rh(1 - \mu^2)^{1/2}$
 β = $L/2\pi r$, cylinder aspect ratio
 μ_x, μ_y = Poisson's ratios associated with bending in x and y directions, respectively
 μ'_x, μ'_y = Poisson's ratios associated with extension in x and y directions, respectively
 μ = Poisson's ratio for the facing sheet material
 μ_c = Poisson's ratio for the core material

Introduction

THE solution for the general instability of corrugated-core circular sandwich cylinders with the core oriented in the circumferential direction is performed in a manner similar to the solution by Batdorf^{1,2} for the general instability of homogeneous isotropic thin-walled cylinders. In the solution presented and in Batdorf's solution, a differential equation obtained from small deflection theory is solved by Galerkin's³ method. Batdorf's solution of Donnell's⁴ differential equation for homogeneous isotropic circular cylinders is not valid for corrugated sandwich plate because of the low shear stiffness of the sandwich in the plane perpendicular to the corrugations. In the present report, the differential equations are obtained from the small-deflection theory for curved orthotropic sandwich plates by Stein and Mayers.⁵ The elastic constants for corrugated-core sandwich were derived from the basic corrugated sandwich geometry and material properties by Libove and Hubka.⁶ Stein and Mayers⁷ solved for the general instability of sandwich cylin-

ders with longitudinally corrugated core loaded under axial compression in a similar manner. Reference 8 solved for the general instability of longitudinally corrugated core sandwich cylinders loaded under combined loads. The present report takes into consideration axial compression, lateral internal and external pressure, and torsion on circumferentially corrugated cylinders.

The basic element of the idealized corrugated-core sandwich and the coordinate system are shown in Fig. 1. The element consists of relatively thin isotropic facings that have negligible flexural rigidities about their own centroidal axes and a highly orthotropic core, for which shear distortions are assumed to be admissible only in the x, z plane. Furthermore, the bending rigidity of the core is assumed to be negligible in the x direction. The facings are of equal thickness and are made of the same material. Both the facings and the core are assumed to be elastic. The length and radius of the cylinder are assumed to be large compared with the over-all thickness of the sandwich.

In general, for a corrugated core sandwich, the core shear modulus is many times greater in the plane along the corrugations than it is perpendicular to the corrugations, and the preceding assumption regarding the shear distortion appears to be realistic for many such configurations.

Derivation of Buckling Equations

Figure 1 shows the nomenclature for the sandwich cylinder. The shear stiffness in the yz plane is assumed to be infinite; therefore, the governing differential equations are given by Eqs. (7) and (14) of Ref. 5. The in-plane unit forces in the axial and circumferential directions (N_x and N_y , respectively) are defined as positive in tension in Ref. 5. If N_x and N_y are defined as positive in compression, the differential equations from Ref. 5 may be written as

$$\begin{aligned}
 L_D w + \frac{G_{xy}}{r^2} L_E^{-1} \frac{\partial^4 w}{\partial x^4} + \\
 \left(N_x \frac{\partial^2 w}{\partial x^2} + N_y \frac{\partial^2 w}{\partial y^2} + 2N_{xy} \frac{\partial^2 w}{\partial x \partial y} \right) - \\
 \frac{1}{U} \left[\frac{D_x}{1 - \mu_x \mu_y} \frac{\partial^3 Q_x}{\partial x^3} + \left(\frac{\mu_x D_y}{1 - \mu_x \mu_y} + D_{xy} \right) \frac{\partial^3 Q_x}{\partial x \partial y^2} \right] = 0 \quad (1) \\
 Q_x + \frac{D_x}{1 - \mu_x \mu_y} \left(\frac{\partial^3 w}{\partial x^3} - \frac{1}{U} \frac{\partial^2 Q_x}{\partial x^2} + \mu_y \frac{\partial^3 w}{\partial x \partial y^2} \right) + \\
 \frac{1}{2} D_{xy} \left(2 \frac{\partial^3 w}{\partial x \partial y^2} - \frac{1}{U} \frac{\partial^2 Q_x}{\partial y^2} \right) = 0 \quad (2)
 \end{aligned}$$

where

$$\begin{aligned}
 L_D = \frac{D_x}{1 - \mu_x \mu_y} \frac{\partial^4}{\partial x^4} + \\
 \left(\frac{\mu_y D_x}{1 - \mu_x \mu_y} + 2D_{xy} + \frac{\mu_x D_y}{1 - \mu_x \mu_y} \right) \frac{\partial^4}{\partial x^2 \partial y^2} + \frac{D_y}{1 - \mu_x \mu_y} \frac{\partial^4}{\partial y^4} \\
 L_E = \frac{G_{xy}}{E_y} \frac{\partial^4}{\partial x^4} + \left(1 - \mu'_x \frac{G_{xy}}{E_x} - \mu'_y \frac{G_{xy}}{E_y} \right) \frac{\partial^4}{\partial x^2 \partial y^2} + \frac{G_{xy}}{E_x} \frac{\partial^4}{\partial y^4} \\
 L_E^{-1} [L_E(w)] = L_E [L_E^{-1}(w)] = w
 \end{aligned}$$

For simply supported edges, the boundary conditions are

$$w = 0 \quad \frac{\partial^2 w}{\partial x^2} - \frac{1}{D_{Qx}} \frac{\partial Q_x}{\partial x} + \mu_y \frac{\partial^2 w}{\partial y^2} = 0 \quad \text{at } x = 0, L$$

These conditions are satisfied by the assumed orthogonal deflection function

$$w = \sin \frac{ny}{2r} \sum_{s=1}^{\infty} a_s \sin \frac{s\pi x}{L} + \cos \frac{ny}{2r} \sum_{s=1}^{\infty} b_s \sin \frac{s\pi x}{L} \quad (3)$$

$$Q_x = \sin \frac{ny}{2r} \sum_{s=1}^{\infty} c_s \cos \frac{s\pi x}{L} + \cos \frac{ny}{2r} \sum_{s=1}^{\infty} d_s \cos \frac{s\pi x}{L} \quad (4)$$

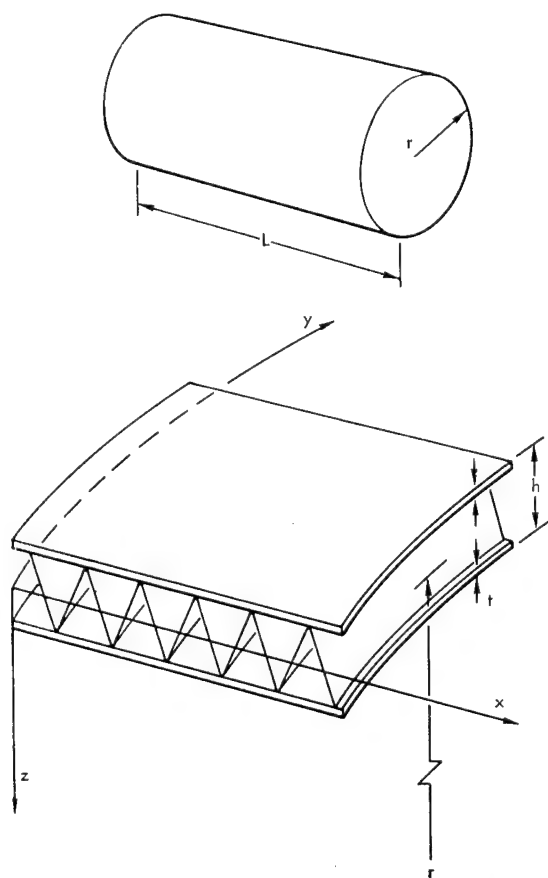


Fig. 1 Circumferentially corrugated sandwich cylinder.

where n is restricted to even positive integers equal to or greater than 4, and s is restricted to positive integers equal to or greater than 1.

The solution to Eqs. (1) and (2) is obtained by use of Galerkin's method as described in Ref. 3. The Galerkin equations are

$$\int_0^{2\pi r} \int_0^L R_1(Q_z, w) V_1 dx dy = 0 \quad (5a)$$

$$\int_0^{2\pi r} \int_0^L R_1(Q_z, w) V_2 dx dy = 0 \quad (5b)$$

$$\int_0^{2\pi r} \int_0^L R_2(Q_z, w) V_3 dx dy = 0 \quad (5c)$$

$$\int_0^{2\pi r} \int_0^L R_2(Q_z, w) V_4 dx dy = 0 \quad (5d)$$

where

$$V_1 = \sin \frac{ny}{2r} \sin \frac{m\pi x}{L} \quad V_2 = \cos \frac{ny}{2r} \sin \frac{m\pi x}{L}$$

$$V_3 = \cos \frac{ny}{2r} \cos \frac{m\pi x}{L} \quad V_4 = \sin \frac{ny}{2r} \cos \frac{m\pi x}{L}$$

The expression for $R_1(Q_z, w)$ is obtained by substituting Eqs. (3) and (4) into Eq. (1) and that for $R_2(Q_z, w)$ is obtained by substituting Eqs. (3) and (4) into Eq. (2).

After the proper substitution and integration have been performed on Eqs. (5a) and (5d), Eq. (5d) is solved for c_m , which is substituted in Eq. (5a). The following equation results:

$$\left\{ \frac{D_x}{1 - \mu_x \mu_y} \frac{\pi^4 m^4}{L^4} + \left(\frac{\mu_y D_x}{1 - \mu_x \mu_y} + 2D_{xy} + \frac{\mu_x D_y}{1 - \mu_x \mu_y} \right) \left(\frac{n}{2r} \right)^2 \left(\frac{\pi m}{L} \right)^2 + \frac{D_y}{1 - \mu_x \mu_y} \left(\frac{n}{2r} \right)^4 + \right. \\ \left. \frac{G_{xy}}{E_y} \frac{\pi^4 m^4}{L^4} + \left(1 - \mu_x' \frac{G_{xy}}{E_x} - \mu_y' \frac{G_{xy}}{E_y} \right) \frac{n^2 \pi^2 m^2}{4r^2 L^2} + \frac{G_{xy}}{E_x} \left(\frac{n}{2r} \right)^4 - \left[\frac{D_x}{U(1 - \mu_x \mu_y)} \left(\frac{\pi m}{L} \right)^3 + \frac{1}{U} \left(\frac{n}{2r} \right)^2 \frac{\pi m}{L} \left(\frac{\mu_x D_y}{1 - \mu_x \mu_y} + D_{xy} \right) \right] \times \right. \\ \left. \left[\frac{(\pi m/L)^3 D_x + \frac{D_x \mu_y}{1 - \mu_x \mu_y} \left(\frac{n}{2r} \right)^2 \frac{\pi m}{L} + D_{xy} \left(\frac{n}{2r} \right)^2 \frac{\pi m}{L}}{1 + \frac{D_x (\pi m/L)^2}{(1 - \mu_x \mu_y)U} + \frac{D_{xy}}{2U} \left(\frac{n}{2r} \right)^2} \right] - N_c \left(\frac{\pi m}{L} \right)^2 - N_p \left(\frac{n}{2r} \right)^2 \right\} a_m - N_s \frac{4n}{rL} \sum_{s=1}^{\infty} \frac{ms}{m^2 - s^2} b_s = 0 \quad (6)$$

where $m \pm s = \text{odd integers}$.

In a similar manner, after the proper substitution and integration have been performed on Eqs. (5b) and (5c), Eq. (5c) is solved for d_m , which is substituted into Eq. (5b). The following equation results after substitution and simplification:

$$\left\{ \frac{D_x}{1 - \mu_x \mu_y} \frac{\pi^4 m^4}{L^4} + \left(\frac{\mu_y D_x}{1 - \mu_x \mu_y} + 2D_{xy} + \frac{\mu_x D_y}{1 - \mu_x \mu_y} \right) \left(\frac{n}{2r} \right)^2 \left(\frac{\pi m}{L} \right)^2 + \frac{D_y}{1 - \mu_x \mu_y} \left(\frac{n}{2r} \right)^4 + \right. \\ \left. \frac{G_{xy}}{E_y} \frac{\pi^4 m^4}{L^4} + \left(1 - \mu_x' \frac{G_{xy}}{E_x} - \mu_y' \frac{G_{xy}}{E_y} \right) \frac{n^2 \pi^2 m^2}{4r^2 L^2} + \frac{G_{xy}}{E_x} \left(\frac{n}{2r} \right)^4 - \left[\frac{D_x}{U(1 - \mu_x \mu_y)} \left(\frac{\pi m}{L} \right)^3 + \frac{1}{U} \left(\frac{n}{2r} \right)^2 \frac{\pi m}{L} \left(\frac{\mu_x D_y}{1 - \mu_x \mu_y} + D_{xy} \right) \right] \times \right. \\ \left. \left[\frac{(\pi m/L)^3 D_x + \frac{D_x \mu_y}{1 - \mu_x \mu_y} \left(\frac{n}{2r} \right)^2 \frac{\pi m}{L} + D_{xy} \left(\frac{n}{2r} \right)^2 \frac{\pi m}{L}}{1 + \frac{D_x (\pi m/L)^2}{(1 - \mu_x \mu_y)U} + \frac{D_{xy}}{2U} \left(\frac{n}{2r} \right)^2} \right] - N_c \left(\frac{\pi m}{L} \right)^2 - N_p \left(\frac{n}{2r} \right)^2 \right\} b_m + N_s \frac{4n}{rL} \sum_{s=1}^{\infty} \frac{ms}{m^2 - s^2} a_s = 0 \quad (7)$$

where $m \pm s = \text{odd integers}$.

Formulas for the physical constants μ_x , μ_y , μ_x' , μ_y' , D_x , D_y , D_{xy} , E_x , E_y , and G_{xy} are obtained from Ref. 6 and substituted into Eqs. (6) and (7). The resulting equations may be simplified by introducing the following geometric and material parameters:

$$\beta = \frac{L}{2\pi r} \quad Z = \frac{L^2}{rh} (1 - \mu^2)^{1/2} \quad J = \frac{UL^2}{\pi^2 D}$$

$$D = \frac{Eth^2}{2(1 - \mu^2)} \quad D_c = E_c I_c \quad \delta_1 = \frac{1}{1 + (E_c A_c / EA)}$$

$$\delta_2 = \frac{1 + \mu}{1 + [(1 + \mu)/(1 + \mu_c)](t_0/A_c)^2 E_c A_c / EA} - \frac{\mu EA}{EA + E_c A_c}$$

$$\delta_3 = 1 - \mu^2 \frac{1}{1 + (EA/E_c A_c)} \quad K_p = \frac{N_p L^2}{\pi^2 D} = \frac{prL^2}{\pi^2 D}$$

$$K_c = \frac{N_c L^2}{\pi^2 D} \quad K_s = \frac{N_s L^2}{\pi^2 D}$$

With the introduction of these parameters, Eqs. (6) and (7) are simplified to the following form:

$$Aa_m - K_s \frac{8\beta n}{\pi m^2} \sum_{s=1}^{\infty} b_s \frac{ms}{m^2 - s^2} = 0 \quad (8)$$

$$Ab_m + K_s \frac{8\beta n}{\pi m^2} \sum_{s=1}^{\infty} a_s \frac{ms}{m^2 - s^2} = 0 \quad (9)$$

where $m \pm s = \text{odd integers}$ and

$$A = \frac{D_c}{D} \frac{n^4 \beta^4}{m^2} + \frac{[m^2 + n^2 \beta^2]^2 [2J + n^2 \beta^2 (1 - \mu)]}{[2J + n^2 \beta^2 (1 - \mu) + 2m^2] m^2} + \frac{4Z^2 m^2}{\pi^4 [\delta_1 m^4 + 2\delta_2 n^2 \beta^2 m^2 + \delta_3 \beta^4 n^4]} - K_c - K_p \frac{\beta^2 n^2}{m^2}$$

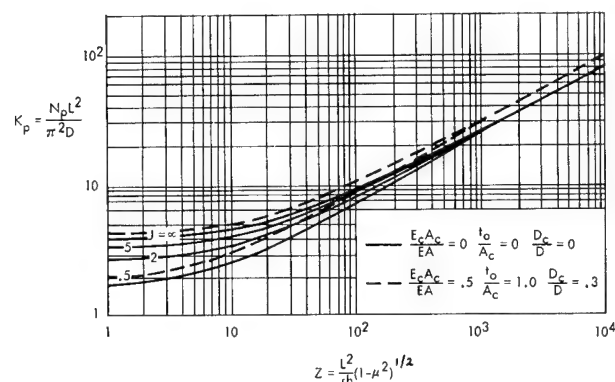


Fig. 2 Buckling coefficients for external lateral pressure.

The critical buckling coefficients K_p , K_c , and K_s can be obtained from Eqs. (8) and (9) for a given set of geometric and material parameters.

Mathematical Solutions for Buckling Coefficients

The buckling coefficients for circumferentially corrugated circular sandwich cylinders may be obtained from Eqs. (8) and (9) for given sets of parameters. In these solutions, m is restricted to positive integers and n is restricted to even positive integers equal to or greater than 4.

Solution for K_p ; K_c and $K_s = 0$

Any of the equations represented in Eqs. (8) and (9) may be used to solve for K_p , if K_s is equal to zero, because the equations are independent for this case.

If K_c and K_s are 0, close inspection of the equation reveals that, if m is restricted to positive integers, K_p will be a minimum for $m = 1$ and the equation can be written in the form

$$K_p = \frac{n^2 \beta^2 D_c}{D} + \frac{[1 + n^2 \beta^2]^2 [2J + n^2 \beta^2 (1 - \mu)]}{[2J + n^2 \beta^2 (1 - \mu) + 2] n^2 \beta^2} + \frac{4Z^2}{\pi^4 [\delta_1 + 2\delta_2 n^2 \beta^2 + \delta_3 \beta^4 n^4] n^2 \beta^2} \quad (10)$$

A digital computer program was coded to solve Eq. (10) for various values of n until the minimum value of K_p was found for the chosen parameters. A plot of K_p as a function of Z is shown in Fig. 2 for various values of J .

Solution for K_c ; K_p Known: $K_s = 0$

Any of the equations represented by Eqs. (8) and (9) may be used to solve for K_c if K_s is equal to zero, because each of the equations is independent. If K_s is equal to zero, Eq. (8) or (9) may be written in the form

$$K_c = \frac{D_c}{D} \frac{n^4 \beta^4}{m^2} + \frac{[m^2 + n^2 \beta^2]^2 [2J + n^2 \beta^2 (1 - \mu)]}{[2J + n^2 \beta^2 (1 - \mu) + 2m^2] m^2} + \frac{4Z^2 m^2}{\pi^4 [\delta_1 m^4 + 2\delta_2 n^2 \beta^2 m^2 + \delta_3 \beta^4 n^4]} - K_p \beta^2 \frac{n^2}{m^2} \quad (11)$$

A digital computer program was coded to solve Eq. (11) for various combinations of m and n until the minimum value of K_c was found for the chosen geometric and material parameters and for a specified value of K_p . Figure 3 is a plot of K_c as a function of Z for the special case of $K_p = 0$. Figures 4 and 5 are plots of K_c as a function of K_p for values of Z of 10 and 10³.

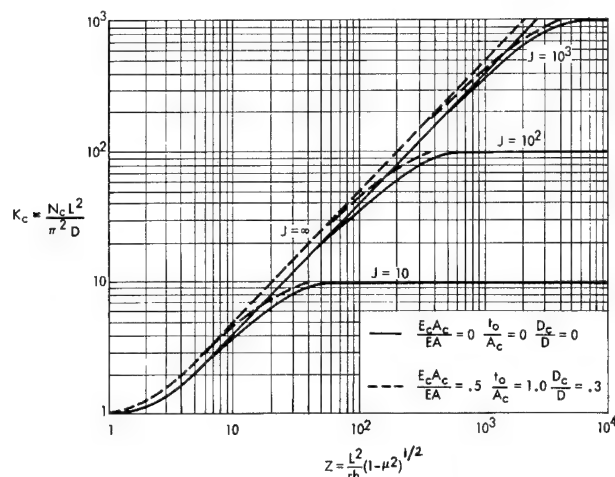


Fig. 3 Buckling coefficients for axial compression.

Solution for K_s ; K_p and K_c Known

Each of the equations represented by Eq. (8) may be expressed in the form

$$Aa_m - \lambda^{-1} Bb_s = 0 \quad (12)$$

Each of the equations represented by Eq. (9) may be expressed in the form

$$Ab_m + \lambda^{-1} Ba_s = 0 \quad (13)$$

where $m \pm s = \text{odd integers}$, and

$$B = \frac{8\beta n}{\pi m^2} \sum_s \frac{sm}{m^2 - s^2} \quad \lambda^{-1} = K_s$$

In matrix form, these equations become

$$\lambda \{a\} = [G_1] \{b\} \quad (14)$$

$$\lambda \{b\} = -[G_1] \{a\} \quad (15)$$

where λ is a scalar, and

$$[G_1] = [A]^{-1} [B]$$

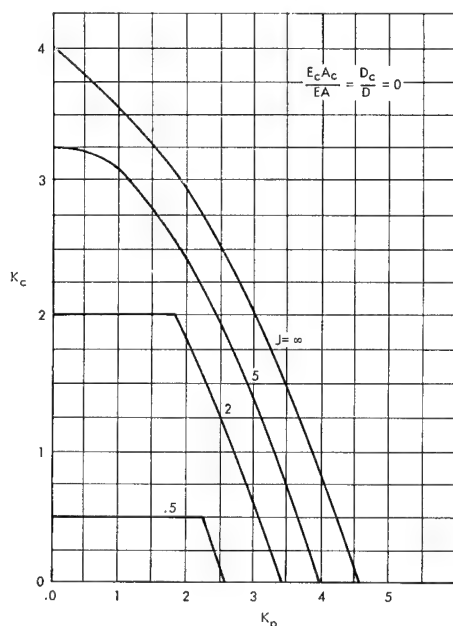


Fig. 4 Buckling coefficients for combined lateral pressure and axial compression for $Z = 10^3$.

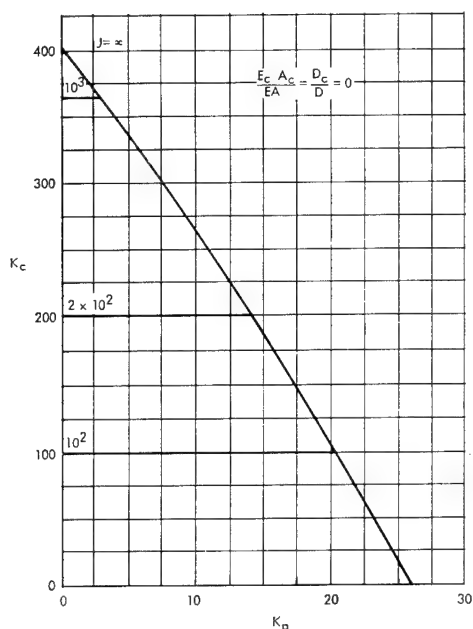


Fig. 5 Buckling coefficients for combined lateral pressure and axial compression for $Z = 10^3$.

The solution for λ by matrix iteration is complicated by the fact that the cylinder will buckle at a load level that is independent of the direction of the applied shear. Therefore, the buckling coefficients and corresponding eigenvalues occur in pairs that are equal in magnitude but opposite in sign. Solving Eq. (15) for the column matrix on the left-hand side and substituting into Eq. (14) results in the following equations:

$$\lambda^2 \{a\} = [G_2] \{a\}$$

where

$$[G_2] = [G_1] [-G_1]$$

The matrix G_2 can be formed either from Eq. (12) or (13). An 8×8 matrix was formed and iterated using a computer program to obtain the eigenvalue λ^2 . The iteration continued until the scalar λ^2 remained constant to six significant figures. The buckling coefficient K_s is the square root reciprocal of the eigenvalue λ^2 :

$$K_s = (1/\lambda^2)^{1/2}$$

The matrix G_1 , used to form the 8×8 G_2 matrix, was of the following form:

$$[G_1] = \begin{matrix} & \begin{matrix} s = 1 & s = 2 & s = 3 & s = 4 & s = 5 & s = 6 & s = 7 & s = 8 \end{matrix} \\ \begin{matrix} m = 1 \\ m = 2 \\ m = 3 \\ m = 4 \\ m = 5 \\ m = 6 \\ m = 7 \\ m = 8 \end{matrix} & \left[\begin{array}{cccccccc} 0 & \frac{B_{12}}{A_1} & 0 & \frac{B_{14}}{A_1} & 0 & \frac{B_{16}}{A_1} & 0 & \frac{B_{18}}{A_1} \\ \frac{B_{21}}{A_2} & 0 & \frac{B_{23}}{A_2} & 0 & \frac{B_{25}}{A_2} & 0 & \frac{B_{27}}{A_2} & 0 \\ 0 & \frac{B_{32}}{A_3} & & & & & & \\ \frac{B_{41}}{A_4} & 0 & & & & & & \\ 0 & \frac{B_{52}}{A_5} & & & & & & \\ \frac{B_{61}}{A_6} & 0 & & & & & & \\ 0 & \frac{B_{72}}{A_7} & & & & & & \\ \frac{B_{81}}{A_8} & 0 & & & & & & \end{array} \right] \end{matrix}$$

etc.

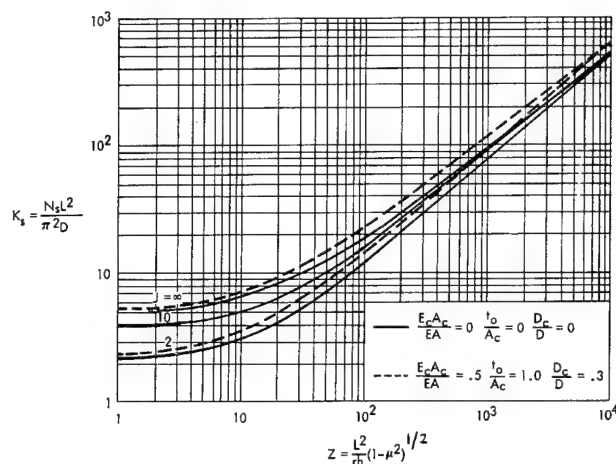


Fig. 6 Buckling coefficients for torsion.

where A_i is the value of A for $m = i$, $i = 1, 8$, and

$$B_{ms} = (8\beta n / \pi m^2) s m / (m^2 - s^2)$$

The parameter n is a constant for a particular G_1 matrix.

By the proper interchanging of rows and columns, the same value of K_s could have been obtained by iterating a 4×4 matrix instead of an 8×8 .

For a given set of numerical values of the sandwich parameters, buckling coefficients are obtained for single values of n until the minimum value of the buckling coefficients is found. Figure 6 is a plot of K_s as a function of Z for the special case of K_c and K_p equal to 0. Figures 7 and 8 are plots of K_s as a function of K_c for values of Z equal to 10 and 10^3 . Figures 9 and 10 are plots of K_p as a function of K_s for values of Z equal to 10 and 10^3 .

Comparison with Other Solutions

Cylinders

The method of solution used for the corrugated sandwich cylinders is the same as that used for homogeneous isotropic cylinders in Refs. 1 and 2. Therefore, if the parameters for a sandwich, which is the equivalent of a homogeneous sheet, are substituted into the sandwich cylinder stability equations, the resulting equations should be the same as the equations presented in Refs. 1 and 2.

A sandwich with $U = \infty$, $D_c/D = 0$, $E_c A_c / EA = 0$, and $t = h$ is the equivalent of homogeneous sheet. For the case

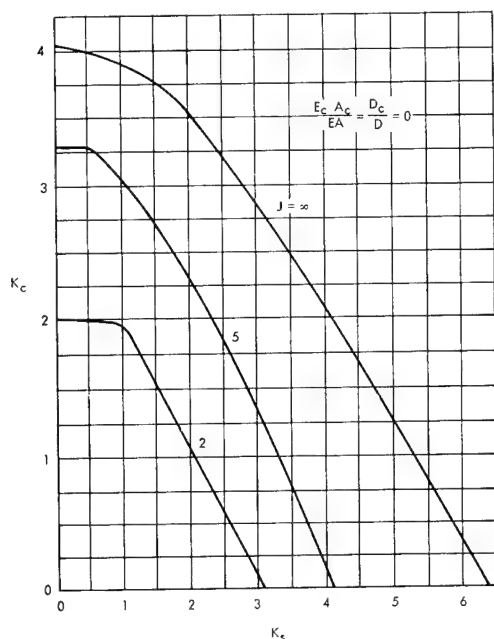


Fig. 7 Buckling coefficients for combined axial compression and torsion for $Z = 10$.

of $t = h$, the moment of inertia of the facing sheets about their own centroid cannot be neglected so that I is equal to $2/3 t^3$. With this correction, the equation becomes

$$\left[\frac{(m^2 + \beta_0^2)^2}{m^2} + \frac{12Z_0 m^2}{\pi^4 (m^2 + \beta_0^2)^2} - K_c - K_p \frac{\beta_0^2}{m^2} \right] a_m - K_s \frac{8\beta_0}{\pi m^2} \sum_s b_s \frac{ms}{m^2 - s^2} = 0 \quad (16)$$

where

$$\beta_0 = nL/2\pi r, Z_0 = (L^2/rt_H)(1 - \mu^2)^{1/2}, t_H = 2t$$

This equation is the same as the equations given in Refs. 1 and 2 for cylinders of homogeneous isotropic sheet.

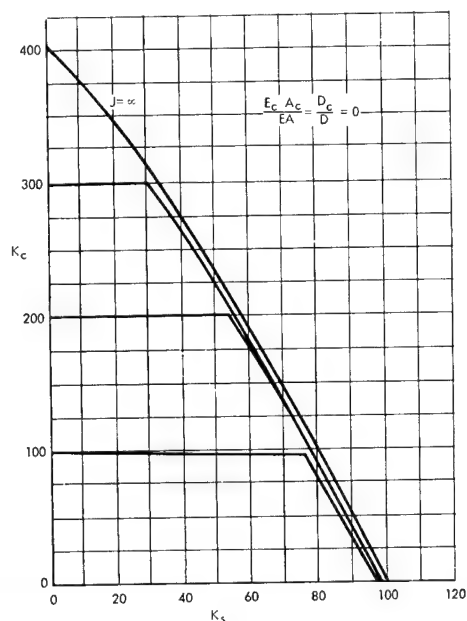


Fig. 8 Buckling coefficients for combined axial compression and torsion for $Z = 10^3$.

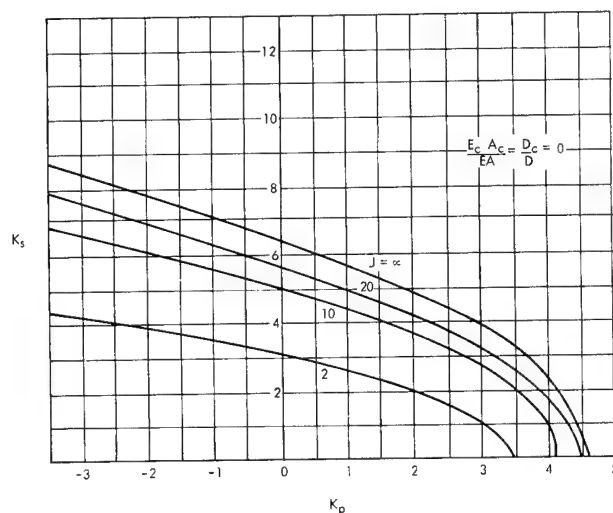


Fig. 9 Buckling coefficients for combined lateral pressure and torsion for $Z = 10$.

Comparison with Results for Flat Plates

As the value of Z for a cylinder becomes very small, the radius of the cylinder becomes very large, and the cylinder behaves like an infinitely wide plate. Therefore, at very low values of Z , the buckling coefficients of cylinders should be the same as the buckling coefficients either for a geometrically similar infinitely wide or infinitely long flat plate that is loaded in the same manner with the core oriented properly.

The buckling coefficients for the pure load case of shear at $Z = 1$ were compared with the appropriate buckling coefficients given in Ref. 9 for flat corrugated sandwich plates with aspect ratios of approximately 3. The buckling coefficients for the flat plates were a maximum of 15% higher than the buckling coefficients for cylinders with $Z = 1$, with most variations 5% or less. The buckling coefficients probably would be much closer if the length-to-width ratio of the plate were larger.

For the case of axial compression of a cylinder with a very large radius, Eq. (11) becomes

$$K_c = m^2/[1 + (m^2/J)]$$

K_c is a minimum for $m = 1$,

$$K_c = 1/[1 + (1/J)] \quad (17)$$

The buckling of a column with shear deformations included is presented in Ref. 10. It is valid for an infinitely wide

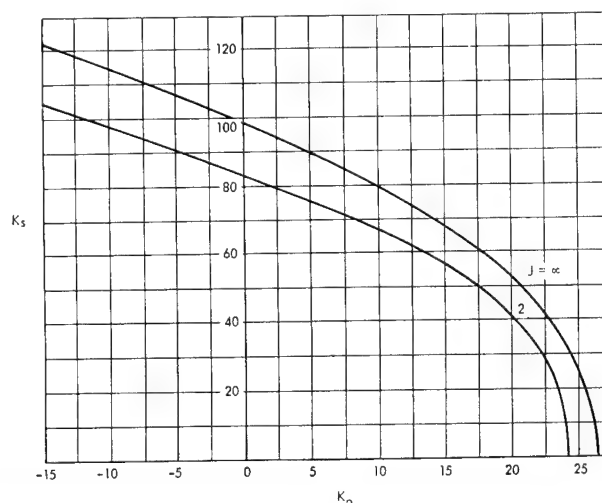


Fig. 10 Buckling coefficients for combined lateral pressure and torsion for $Z = 10^3$.

Table 1 Effect of L/r on K_p ; $J = \infty$, $D_c/D = 0$, $E_c A_c/EA = 0$

L/r	Z	1	5	10	5×10	10^2	5×10^2	10^3	5×10^3	10^4	5×10^4	10^5
0.1	n	64	68	76	120	146
	K_p	4.011	4.211	4.606	7.225	9.440
0.5	n	12	14	16	24	30	44	54	80	96
	K_p	4.021	4.211	4.606	7.225	9.478	19.11	26.39	57.25	80.35
1.0	n	6	6	8	12	14	22	26	40	48	72	86
	K_p	4.021	4.318	4.606	7.225	9.494	19.11	26.49	57.25	80.35	178.0	251.1
10.0	n	4	6	8	8
	K_p	57.25	98.35	187.7	259.6

plate if the moment of inertia of the column is replaced by the flexural rigidity of the plate. The critical buckling load presented in Ref. 10 would then agree with Eq. (17) if D_c/D were small in comparison to unity.

Upper Bound Axial Compression

If the value of m is set equal to infinity in Eq. (14) and $K_p = 0$, the resulting expression is

$$K_c = J + (n^2 \beta^2 / 2)(1 - \mu)$$

If the loading case is axial compression and $(mr/L)^2$ is very large in comparison to l , the theory that has been presented is valid for small values of n . The value of K_c is a minimum for the expression given previously if $n = 0$. Therefore, $K_c = J$ or $N_c = U = G_{tc}$.

This places an upper bound on the buckling coefficient of a circumferentially corrugated sandwich cylinder which is subjected to axial compression. This can be seen in Fig. 3. The buckling curve for a finite value of J increases with increased Z until it approaches a value of K_c which is equal to the value of J . At this point the curve becomes asymptotic to the value $K_c = J$.

When the critical load per inch equals the shear rigidity, the mode of failure is called crimping because the wavelength of the buckle is extremely short. This upper bound has been derived in all stability investigations that analyze sandwich plates and shells subjected to compressive forces in the direction of the sandwich that has finite shear rigidity. This upper bound can be seen in the stability curves for flat sandwich plates with either isotropic or corrugated core as well as the stability curves for sandwich cylinders with isotropic core. In addition, this upper bound was arrived at in a large deflection theory of sandwich cylinders subjected to axial compression.¹¹ Therefore, it is believed that curves presented for axial compression of circumferentially corrugated sandwich cylinders subjected to axial compression are valid in the range of $K_c = J$.

Effect of Geometric and Material Parameters

Stiffness Ratios

The parameters $E_c A_c/EA$, t_0/A_c , and D_c/D were investigated to determine their effect on the buckling coefficients. It can be seen from Eqs. (10) and (11) that, if any of these three parameters are increased while the remaining parameters are kept constant, the buckling coefficient is also increased. However, the effect on the critical buckling coefficient of varying $E_c A_c/EA$, t_0/A_c , and D_c/D through their practical range is small. This insensitivity to changes in the stiffness ratios is indicated in Figs. 2, 3, and 6 in which the solid curves are the buckling coefficients for cylinders with $E_c A_c/EA = 0$, $t_0/A_c = 0$, and $D_c/D = 0$, and the dashed lines are the buckling curves for $E_c A_c/EA = 0.5$, $t_0/A_c = 1.0$, and $D_c/D = 0.3$. The latter values of these parameters are believed to be about as high as can be achieved in practical applications, provided the sandwich material remains in the elastic range. It can be seen that the maximum differences between the dashed and solid curves are only about 20%. Therefore,

the solid curves can be used as a conservative close approximation to the critical buckling coefficient.

Effect of L/r on the Buckling Coefficients

If the value of L/r is varied in the buckling equation and all of the other parameters are kept constant, the critical buckling coefficient will also vary slightly. This variation is caused mainly by the fact that n is restricted to even integer values. If n could vary freely, the critical buckling coefficients for a given value of Z would be independent of the L/r ratio. If n is restricted to even integer values, cylinders with higher values of L/r often have slightly higher buckling coefficients.

The effect of L/r on the buckling coefficient is shown in Table 1 for the case of external pressure with $J = \infty$. It can be seen that the effect is small except for $L/r = 10$. Because the effect of L/r on the critical buckling coefficient was small, curves were not presented for the various values of L/r . The curves given were obtained with L/r values which resulted in critical values of n large enough so that the buckling coefficients would be very close to the absolute minimum of the equation. Therefore, the curves generally will be on the conservative side.

Conclusion

The theory and curves presented in the previous sections have been compared against existing theoretical results for the case of $Z = 1$ and $J = \infty$ as well as for the case of axial compression with relatively low shear modulus. The comparison at these extremes showed close agreement, and it is believed that the buckling curves presented in this report are valid within the limitations of small-deflection theory. For the cases of cylinders subjected to external pressure and/or torsion, small-deflection theory appears to be an adequate tool for predicting the buckling phenomena. This can be seen from Ref. 1, which derives the buckling curves for monocoque cylinders in a manner similar to method presented herein and compares the results with test data. For the case of external pressure or torsion, the agreement between theory and tests was quite good, and it is believed that test data of circumferentially corrugated sandwich cylinders subjected to external pressure, torsion, or combinations of the two will be in reasonable agreement with the theory that has been presented.

The buckling phenomena of homogeneous isotropic cylinders subjected to axial compression have not been well represented by small-deflection theory. Therefore, the results that have been presented for circumferentially corrugated sandwich cylinders under axial compression may predict buckling loads that are too high. However, for the limiting case in which shear distortion becomes predominant, the large-deflection theory presented in Ref. 10 predicts the same critical load as presented in Fig. 3 ($N_c = G_{tc}$), and the test results in Ref. 10 agree well with the theory for sandwich cylinders with relatively low shear stiffness. The accuracy of small-deflection theory for predicting the critical axial compression buckling load of a sandwich cylinder with rela-

tively high transverse shear rigidity can only be determined by an extensive series of tests.

The orientation of the core is an important design consideration for a corrugated core sandwich cylinder. The direction to orient the core is dependent upon the loading condition. Through the use of Figs. 2-10 and Ref. 8, the most efficient core orientation may be chosen for corrugated core sandwich cylinders.

If U is a set equal to infinity, Eqs. (7) and (8) are the small-deflection buckling equations for an orthotropic cylinder including the effects of Poisson's ratio. Equations (7) and (8) may then be used to determine the general instability under combined loads of a stiffened cylinder with relatively close stiffeners that are orientated in any direction by using the elastic constants presented in Ref. 12.

References

- ¹ Batdorf, S. B., "A simplified method for elastic stability analysis for thin cylindrical shells," NACA Rept. 874 (1947).
- ² Batdorf, S. B., Stein, M., and Schilderout, M., "Critical stress of thin walled cylinders in torsion," NACA TN 1344, (June 1947).
- ³ Wang, C., *Applied Elasticity* (McGraw-Hill Book Co., Inc., New York, 1953).
- ⁴ Donnell, L. H., "Stability of thin walled tubes under torsion," NACA Rept. 479 (1933).
- ⁵ Stein, M. and Mayers, J., "A small deflection theory for curved sandwich plates," NACA TN 2017 (February 1950).
- ⁶ Libove, C. and Hubka, R., "Elastic constants for corrugated core sandwich plates," NACA TN 2289 (February 1951).
- ⁷ Stein, M. and Mayers, J., "Compressive buckling of simply supported curved plates and cylinders of sandwich construction," NACA TN 2601 (January 1952).
- ⁸ Harris, L. A. and Baker, E. H., "Elastic stability of simply supported corrugated core sandwich cylinders," NASA TN D-1510.
- ⁹ Harris, L. A. and Auelmann, R. R., "Stability of flat simply supported corrugated core sandwich plates under combined loads," *J. Aerospace Sci.* **27**, 525-34 (July 1960).
- ¹⁰ Timoshenko, S. and Gere, J., *Theory of Elastic Stability* (McGraw-Hill Book Co., Inc., New York, 1961), 2nd ed.
- ¹¹ March, H. W. and Kuenzi, E. W., "Buckling of cylinders of sandwich construction in axial compression," Forest Products Lab. Rept. 1830 (December 1957).
- ¹² Dow, N., Libove, C., and Hubka, R., "Formulas for the elastic constants of plates with integral waffle-like stiffening," NACA RM L53E13a (August 1953).

Influence of Boundary Conditions on the Modal Characteristics of Thin Cylindrical Shells

KEVIN FORSBERG*

Lockheed Missiles and Space Company, Palo Alto, Calif.

The modal characteristics of thin cylindrical shells have previously been determined only for three sets of boundary conditions. In the present analysis, all sixteen sets of homogeneous boundary conditions have been examined at each end of the shell (each set contains four conditions). The equations of motion developed by Flügge for thin, circular cylindrical shells are used. The general solution to these equations can easily be written down. One can select a circumferential nodal pattern, eight boundary conditions, and a length of shell, and then iterate numerically to find the frequency of vibration that will meet these conditions. The advantage of this approach is that one can obtain a solution to the basic equations for any boundary conditions desired. Results indicate that, contrary to the rather common assumption, the condition placed on the longitudinal displacement u in many cases is more influential than restrictions on the slope $\partial w/\partial x$ or moment M_x . It has been found that even for long cylinders (length to radius ratio of 40 or more) the minimum natural frequency may differ by more than 50% depending upon whether $u = 0$ or the longitudinal stress resultant $N_x = 0$ at both ends.

Nomenclature

a	= radius of cylinder
h	= thickness of cylinder wall
k	= $h^2/12a^2$
l	= length of shell
m	= number of axial half-waves
n	= number of circumferential waves
u	= longitudinal displacement
v	= tangential displacement
w	= radial displacement
x	= dimensionless axial coordinate, ξ/a
E	= Young's modulus of elasticity
$M_x, M_{x\varphi},$ $N_x, N_{x\varphi},$	= stress resultants, see Fig. 1
Q_x	= $Q_x + \partial M_{x\varphi}/\partial \varphi$
S_x	= $N_x - M_{x\varphi}/a$
T_x	= $\rho a^2(1 - \nu^2)/E$
γ^2	= Poisson's ratio
ν	= axial coordinate
ξ	= mass density of shell material
ρ	= circumferential coordinate
φ	= circular frequency
ω	= lowest extensional frequency of a ring in plane
ω_0	strain, $= 1/\gamma$
$(\cdot)'$	= $\partial(\dots)/\partial x$
$(\cdot)_\varphi$	= $\partial(\dots)/\partial \varphi$

Introduction

THE determination of the modal characteristics for vibrations of thin cylindrical shells is a problem of great technical interest. However, in spite of the great number of papers devoted to this topic,¹ only three sets of boundary conditions (i.e., one set for a force-free end and two other sets loosely called "freely supported" end and "clamped" end) have been considered in the literature. Additionally there appears to be no discussion of how the modal char-

acteristics are altered when longitudinal displacement is prevented at the ends.

The primary contribution of this paper is the presentation of results obtained from an exact solution of the basic differential equations of motion. The method, which was outlined by Flügge in 1934, requires numerical evaluation of an eighth-order determinant to find its eigenvalues, and this is certainly the reason this approach was not feasible before the advent of a high-speed digital computer. Although the method requires numerical computation, the results are exact in the same sense that the numerical solution to the transcendental frequency equation for a beam yields an exact solution.

This study is identical in approach with the recently published work of Sobel² on the closely related area of stability of cylindrical shells. The results of these two independent studies lead to the same conclusions regarding the importance of the various boundary conditions.

The major purpose of the present report is to determine the ranges of the length-to-radius ratio l/a and radius-to-thickness ratio a/h for which a change in the boundary conditions will appreciably alter the modal characteristics. The modal behavior of a simply supported shell without axial constraint is used as the reference for comparison. This investigation will be directed into three areas: 1) the effect of the various boundary conditions on the frequency envelope (10 cases are considered here); 2) a study of a portion of the over-all frequency pattern for one value of a/h and for two sets of boundary conditions; and 3) a brief study of the modal stress resultants for several cases.

This study will be presented in two parts. The second part, which is in preparation, will consider the cases for which $n = 0$ and $n = 1$. Also in the second part a brief investigation will be made of shells having one or both ends entirely force free (all values of n will be considered). A comparison with experimental data will be made for a cylinder having force-free ends.

The Flügge equations used in the present analysis are based on the usual assumptions of linear thin shell theory, i.e., that the shell is thin (usually considered to mean $a/h > 10$), of constant wall thickness, and of a linear, homogeneous, isotropic material. The results apply only for small deflections and, since the effects of shear distortion and rotatory inertia of the shell wall have been neglected, the results apply only when the half-wave length of the mode shape is

Presented as Preprint 64-77 at the AIAA Aerospace Sciences Meeting, New York, January 20-22, 1964; revision received July 27, 1964. This work was partially sponsored by the Lockheed Independent Research Program. The author would like to express his appreciation to C. W. Coale for the helpful advice given during the writing of this paper.

* Research Specialist, Aerospace Sciences Laboratory. Member AIAA.

more than ten times the shell wall thickness ($l/ma > 10 h/a$, $\pi/n > 10 h/a$), where m and $2n$ are the number of axial and circumferential half-waves.

Method of Solution

The present analysis is based on the following equations of motion developed by Flügge³ for free vibrations of thin, circular cylindrical shells (see Fig. 1):

$$\left. \begin{aligned} u'' + \frac{1-\nu}{2}(1+k)u'' + \frac{1+\nu}{2}v'' - kw''' + \frac{1-\nu}{2}kw''' + \nu w' - \gamma^2 \frac{\partial^2 u}{\partial t^2} &= 0 \\ \frac{1+\nu}{2}u'' + v'' + \frac{1-\nu}{2}(1+3k)v'' - \frac{3-\nu}{2}kw''' + w' - \gamma^2 \frac{\partial^2 v}{\partial t^2} &= 0 \\ -ku''' + \frac{1-\nu}{2}ku''' + \nu u' - \frac{3-\nu}{2}kv''' + v' + w + k[w^{IV} + 2w''' + w'' + 2w' + w] + \gamma^2 \frac{\partial^2 w}{\partial t^2} &= 0 \end{aligned} \right\} \quad (1)$$

where

$$\begin{aligned} (\quad)' &= \partial(\quad)/\partial x & (\quad)' &= \partial(\quad)/\partial \phi \\ \gamma^2 &= \rho a^2(1-\nu^2)/E & k &= h^2/12a^2 \end{aligned}$$

For a complete cylinder, the general solution for modal vibration can easily be written in the following form:

$$\begin{aligned} u &= \left(\sum_{n=0}^{\infty} \sum_{s=1}^8 \alpha_{sn} A_{sn} e^{\lambda_{sn} x} \cos n \phi \right) e^{i\omega t} \\ v &= \left(\sum_{n=0}^{\infty} \sum_{s=1}^8 \beta_{sn} A_{sn} e^{\lambda_{sn} x} \sin n \phi \right) e^{i\omega t} \\ w &= \left(\sum_{n=0}^{\infty} \sum_{s=1}^8 A_{sn} e^{\lambda_{sn} x} \cos n \phi \right) e^{i\omega t} \end{aligned} \quad (2)$$

The arbitrary constants A_{sn} will be evaluated by considering the boundary conditions at each end of the shell. Any of the boundary conditions can be a general function of the circumferential coordinate ϕ and can be expressed by a Fourier series in ϕ . Thus, in the general case of nonuniform boundary conditions, the frequency of modal vibration ω will depend upon all of the harmonics n . For the special cases in which the boundary conditions depend on only one harmonic, or when the boundary conditions are homogeneous, the modal frequency will be a function of a single value of n , and the summation over n in Eq. (2) can be discarded. Only this latter case will be considered in the present paper. Thus the index n will be dropped.

Substitution of these expressions into the homogeneous differential equations leads to an eighth-order algebraic equation for λ_s :

$$\lambda_s^8 + g_{s6}\lambda_s^6 + g_{s4}\lambda_s^4 + g_{s2}\lambda_s^2 + g_{s0} = 0 \quad (3)$$

where

$$g_{sk} = g_{sk}(h/a, \nu, n, \omega)$$

The preceding solution is readily obtainable from Ref. 3. In contrast to the associated statics problem for which the roots of Eq. (3) are, in general, all complex, it can be shown that the solution for the vibration problem will usually have the form

$$\lambda = \pm a, \pm ib, \pm(c \pm id)$$

where a, b, c, d are real quantities. For a finite shell, there

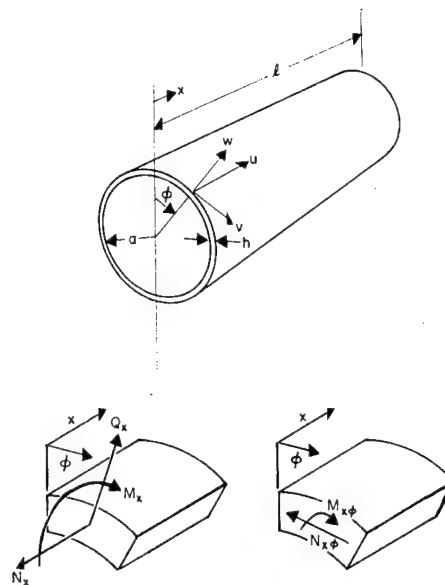


Fig. 1 Coordinate system and shell element.

will always be at least two roots of the form $(\pm ib)$. This leads to a solution of the form

$$w = \{C_1 e^{ax} + C_2 e^{-ax} + C_3 \cos bx + C_4 \sin bx + e^{cx}(C_5 \cos dx + C_6 \sin dx) + e^{-cx}(C_7 \cos dx + C_8 \sin dx)\} \cos n \phi e^{i\omega t} \quad (4)$$

with similar expressions for u and v . Note that Eq. (4) has been rewritten so that the complex constants A_s have been replaced by real constants C_s . The expressions for u and v involve combinations of the constants C_s and the real and imaginary parts of α_s or β_s . It should be noted that the parameters α_s and β_s depend on $\lambda_s, h/a, \nu, n$, and ω . When the solutions to Eq. (3) are obtained, α_s and β_s can be evaluated.

Once the boundary conditions are specified (four at each end of the shell), the problem is entirely determined. The detailed statement of these conditions leads directly to eight equations for the eight unknown constants C_s . These equations involve the four quantities a, b, c , and d . Since the boundary conditions are homogeneous, the determinant D of these equations must be zero for a nontrivial solution.

It does not appear feasible to seek analytic expressions for the quantities a, b, c , and d . Thus, at this point in the analysis, a numerical evaluation of the solution is introduced. We now select a given shell (i.e., fix $h/a, l/a, \nu$), an assumed number of circumferential waves n , and a specific set of boundary conditions at each end. Starting from some initial estimate for the frequency ω , we can iterate to find the values of ω which will make the determinant D go to zero. We can cover the entire range of problems of interest by varying the initial input to the determinant, i.e., by varying $h/a, l/a, \nu, n$, or the boundary conditions.

No assumptions or simplifications beyond those underlying Eqs. (1) have been introduced in the numerical evaluation, and the solution can be obtained with any desired degree of accuracy. In the present instance, the frequency was determined to six significant figures. Such accuracy, required only for intermediate computations, is necessary in order to obtain accurate values for the mode shapes and corresponding modal stress resultants. The final result is only meaningful for three or four significant figures of course. The number of iterations required for convergence is greatly reduced if good initial estimates are available. The solutions developed by Arnold and Warburton^{4,5} are excellent for this purpose. It should be noted that, for any given modal pattern (fixed number of axial half-waves m and cir-

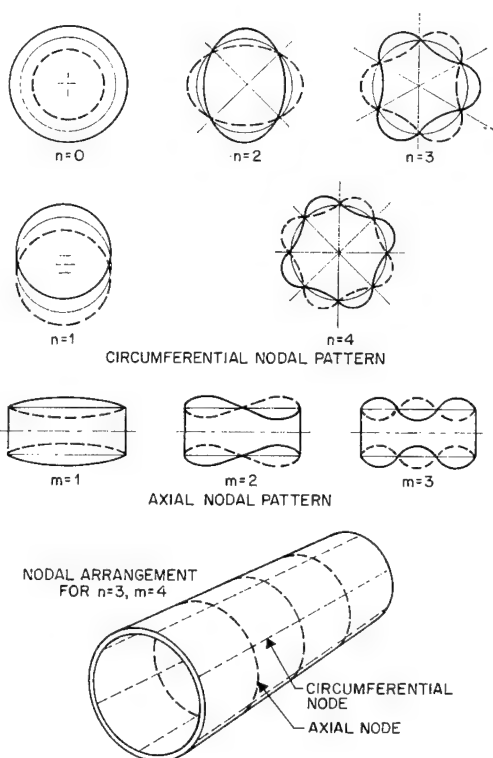


Fig. 2 Nodal patterns.

cumferential waves n), there are three frequencies, corresponding to different amplitude ratios in u , v , and w .⁴ If longitudinal and tangential inertia terms are omitted, there will be only one value of ω for each pair of m and n . For $n \geq 1$, this eigenvalue is an approximation to the lowest of the three frequencies just mentioned. In the present approach, the number of axial half-waves m cannot be specified conveniently in advance, and thus one must take care to determine the mode shape as well as the frequency in each instance, since there are an infinite number of eigenvalues for any fixed set of values of n , a/h , l/a , and ν . Although it is possible for two mode shapes to have identical natural frequencies, this can occur only if they have different values of n . For a given number of circumferential waves, the frequency increases monotonically as the number of axial waves increases. However, for long shells the frequencies for $m = 1, 2, 3, \dots$, are very closely spaced; the longer the shell the closer are the frequencies of adjacent axial modes.

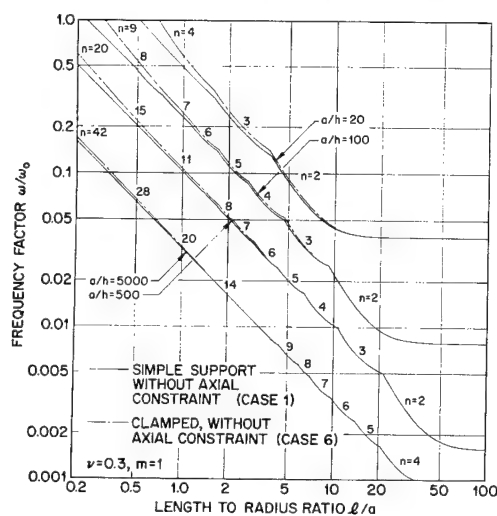


Fig. 3 Frequency envelope, cases 1 and 6.

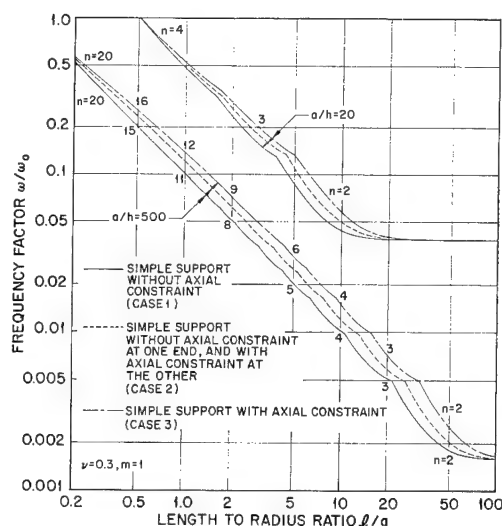


Fig. 4 Frequency envelope, cases 1-3.

Finally it should be pointed out that, for mode shapes in which $n \geq 2$, if one starts from a zero frequency, the minimum nonzero eigenvalue obtained will be that of an infinite cylinder (or a ring in a state of plane strain). This value is independent of the axial wavelength (and hence independent of the boundary conditions) and represents the asymptotic value for a given n , a/h , and ν as $l/a \rightarrow \infty$. It does not, in general, represent a solution for a finite shell. The numerical computation was done on an IBM 7094 computer.

Boundary Conditions

There are 16 possible sets of homogeneous boundary conditions which can be specified independently at each end of the shell. These consist of all combinations of the following:

$$w = 0 \text{ or } S_x = Q_x + (1/a) \partial M_{x\varphi} / \partial \varphi = 0 \quad (5a)$$

$$\partial w / \partial x = 0 \text{ or } M_x = 0 \quad (5b)$$

$$u = 0 \text{ or } N_x = 0 \quad (5c)$$

$$v = 0 \text{ or } T_x = N_{x\varphi} - (1/a) M_{x\varphi} = 0 \quad (5d)$$

(For a discussion of the origin of the force boundary conditions indicated in Eqs. (5a) and (5d), see Ref. 3, p. 233.) For completeness, all 16 sets of conditions were studied in the course of the present investigation for shells having the same boundary conditions at both ends. Free ends (cases with $S_x = 0$) will be discussed in a subsequent paper. Additionally, selected combinations of one set at one end and a different set at the other were examined.

The significant findings of this study can be summarized by discussing the ten cases indicated in Table 1. Certain symbols used therein are defined in Fig. 1. The exact solution for case 1 has been discussed in detail by Arnold and Warburton.⁴ It is included here for comparison. Arnold and Warburton also presented an approximate solution⁵ for case 7. A comparison of their results with the present analysis is given below.

Discussion of Results

Frequency Envelope for $n \geq 2$

The general character of the various mode shapes is indicated in Fig. 2. Modes for which $n < 2$ have a somewhat different behavior from those having $n \geq 2$ and will be treated at a later date.

For any fixed values of n and m , there are three natural frequencies corresponding to three mode shapes (having different u, v, w amplitude ratios). The asymptotic values of these frequencies for long axial wavelengths are:

Flexural Vibrations of a Ring ($w_{\max} = nv_{\max}, u = 0$)

$$(\omega_1/\omega_0)^2 = (h^2/12a^2)n^2(n^2 - 1)^2/(n^2 + 1)$$

Axial Shear Vibration ($w = v = 0$)

$$(\omega_2/\omega_0)^2 = (1 - \nu)n^2/2$$

Extensional Vibrations of Ring ($v_{\max} = nw_{\max}, u = 0$)

$$(\omega_3/\omega_0)^2 = n^2 + 1$$

In general, two of these three frequencies are several orders of magnitude higher than the minimum value and hence are not usually of immediate interest.

These higher frequencies will arise only if all three inertia terms are retained in Eqs. (1). Although these higher frequencies are not to be studied here, all three inertia terms have been retained in developing the results presented herein. One approach for determining the region of influence of the various boundary conditions on the modal behavior of cylindrical shells consists of looking at the minimum natural frequency (which is the envelope of the frequency curves drawn for constant values of n). The value of n varies from point to point as indicated on the curves shown in Figs. 3-7. Moreover, for a given shell of fixed length, changing the boundary conditions may alter the value of n associated with the mini-

Table 1 List of boundary conditions used in present analysis

Case no.	Description	Boundary conditions	
		$x = 0$	$x = l/a$
1	Simple support without axial constraint (called "freely supported" in Ref. 3)	$w = 0$ $v = 0$ $M_x = 0$ $N_x = 0$	$w = 0$ $v = 0$ $M_x = 0$ $N_x = 0$
2	Simple support without axial constraint at one end, with axial constraint at other	$w = 0$ $v = 0$ $M_x = 0$ $N_x = 0$	$w = 0$ $v = 0$ $M_x = 0$ $u = 0$
3	Simple support with axial constraint	$w = 0$ $u = 0$ $v = 0$ $M_x = 0$	$w = 0$ $u = 0$ $v = 0$ $M_x = 0$
4	Simple support, no tangential constraint (similar to case 1, with $v \neq 0$)	$w = 0$ $M_x = 0$ $N_x = 0$ $T_x = 0$	$w = 0$ $M_x = 0$ $N_x = 0$ $T_x = 0$
5	Simple support, axial constraint but no tangential constraint (similar to case 3, with $v \neq 0$)	$w = 0$ $u = 0$ $M_x = 0$ $T_x = 0$	$w = 0$ $u = 0$ $M_x = 0$ $T_x = 0$
6	Clamped end, without axial constraint	$w = 0$ $w' = 0$ $v = 0$ $N_x = 0$	$w = 0$ $w' = 0$ $v = 0$ $N_x = 0$
7	Clamped end, with axial constraint (called "fixed end" in Ref. 4)	$w = 0$ $w' = 0$ $u = 0$ $v = 0$	$w = 0$ $w' = 0$ $u = 0$ $v = 0$
8	Clamped end, no tangential constraint (similar to case 6, but with $v \neq 0$)	$w = 0$ $w' = 0$ $N_x = 0$ $T_x = 0$	$w = 0$ $w' = 0$ $N_x = 0$ $T_x = 0$
9	Clamped end, with axial constraint but no tangential constraint (similar to case 7, but with $v \neq 0$)	$w = 0$ $w' = 0$ $u = 0$ $T_x = 0$	$w = 0$ $w' = 0$ $u = 0$ $T_x = 0$
10	Simple support without axial constraint at one end, clamped with axial constraint at the other end	$w = 0$ $v = 0$ $M_x = 0$ $N_x = 0$	$w = 0$ $v = 0$ $w' = 0$ $u = 0$

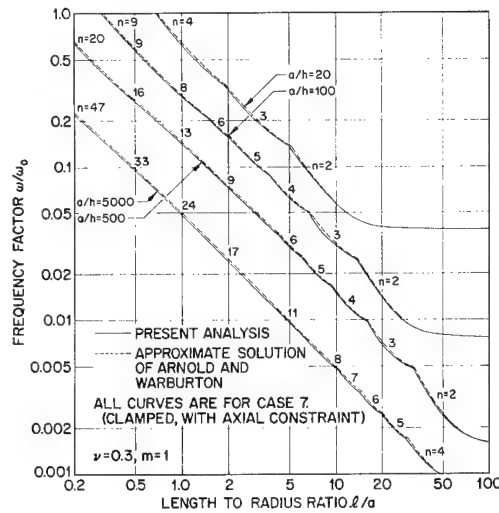


Fig. 5 Frequency envelope, case 7 and Arnold and Warburton's approximate solution.

um frequency. Since the minimum frequency always occurs for a mode having one axial half-wave ($m = 1$), Figs. 3-7 are all drawn for $m = 1$.

One should keep in mind the fact that, for long shells, the minimum frequency will occur for $n = 1$. The values of l/a for which this change takes place depend upon a/h . For $a/h = 20$, the crossover occurs for $l/a = 12$ to 18; for $a/h = 5000$, the change occurs for $l/a > 100$.

The effect of clamping ($\partial w/\partial x = 0$) is illustrated in Fig. 3, in which the minimum frequency for a simply supported shell without axial constraint is compared with that of a clamped shell without axial constraint. Clearly, the effect of clamping rapidly diminishes as the length increases. The magnitude of the increase in minimum frequency due to clamping is quite small for all but very short shells ($l/a < 1$).

The influence of axial constraint ($u = 0$) is illustrated in Fig. 4. Here the minimum frequency for a simply supported shell without axial constraint is compared with that of a simply supported shell with axial constraint at one or both ends. In direct contrast to the previous case, the effect of axial constraint is significant even for very long shells and for all values of a/h . Note that the minimum frequency for case 3 is about 40 to 60% higher than in that of case 1 through-

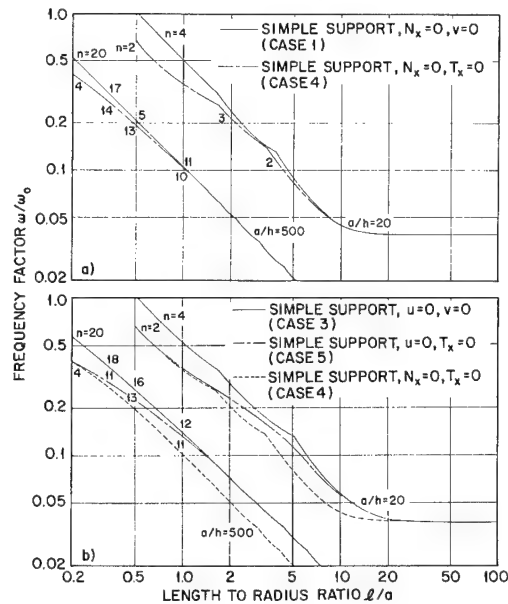


Fig. 6 Frequency envelope, cases 1 and 3-5.

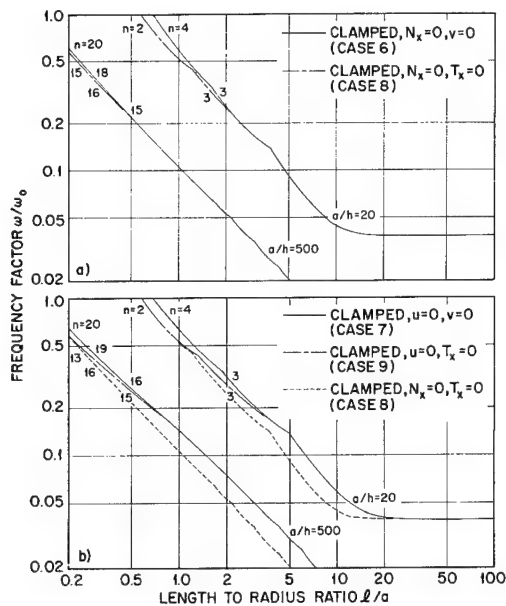
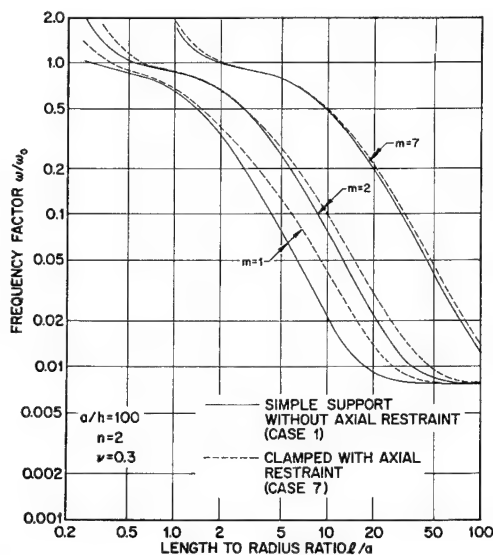
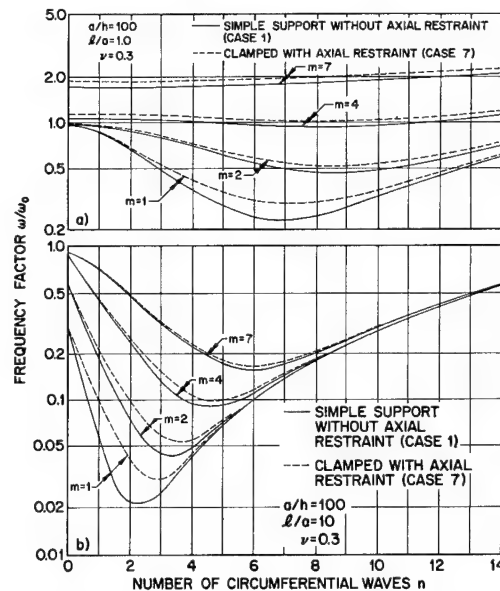


Fig. 7 Frequency envelope, cases 6-9.

out most of the region of interest. This difference may be even greater for certain modes (see Fig. 8). The physical reason for the difference in the influence of $u = 0$ as compared with $\partial w / \partial x = 0$ perhaps can best be understood by examining the modal stress resultants. This will be done in another section. Although the curves on Fig. 4 have been drawn for $m = 1$, the frequencies for modes having one axial node ($m = 2$), for a simply supported shell with axial constraint (case 3), can be determined directly from the intermediate curve (case 2) on Fig. 4. It can be shown that a shell of length $2l/a$, boundary conditions of case 3, and with $m = 2$, has the same modal behavior as a similar shell of length l/a , with $m = 1$ and boundary conditions of case 2. Further study indicates that, no matter what homogeneous boundary conditions are enforced at the ends of the shell, as m increases, the modal characteristics gradually approach those of a simply supported shell without axial constraint (case 1). This trend can be seen (for case 7) in Figs. 8-10.

Arnold and Warburton⁵ used the Rayleigh-Ritz procedure to obtain an approximate solution for what they called a shell

Fig. 8 Frequency distribution for $n = 2$, $m \geq 1$.Fig. 9 Frequency distribution for $l/a = 1$ and $l/a = 10$.

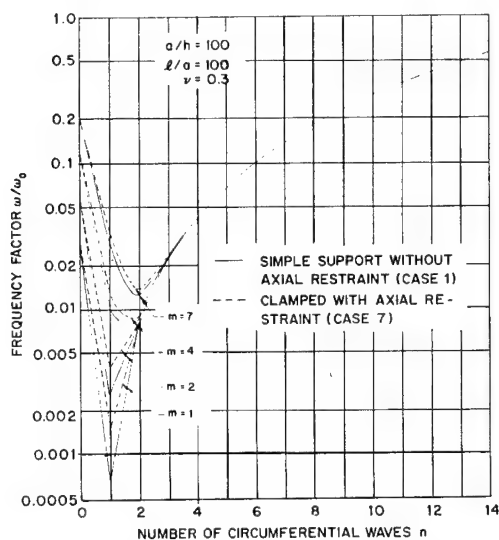
with "fixed ends." This is a shell clamped, with axial constraint, at both ends (case 7). Although they took only a one-term approximation to the mode shape, their solution for the frequency agrees very closely with the results of the present analysis (see Fig. 5), theirs being a maximum of 5% higher. For most cases, the results agree within 2%. As is to be expected, however, the modal stress resultants as predicted by their solutions are quite seriously in error. Arnold and Warburton's paper is misleading, however, in so far as it implies that the primary change from the "freely supported" case (studied earlier by them⁴) was the addition of clamping. The effect of elastic moment restraint which they considered must actually be quite small.

In all of the preceding cases, we have assumed that the tangential displacement v is zero. If this requirement is relaxed, with all other parameters remaining the same, the frequency will be lower (see Figs. 6 and 7). The greatest change in the frequency due to relaxing the condition $v = 0$ occurs for $n = 1$. It is important to note at this point that for this boundary condition the minimum frequency may occur for $n = 1$ even for short shells.

Over-All Frequency Pattern

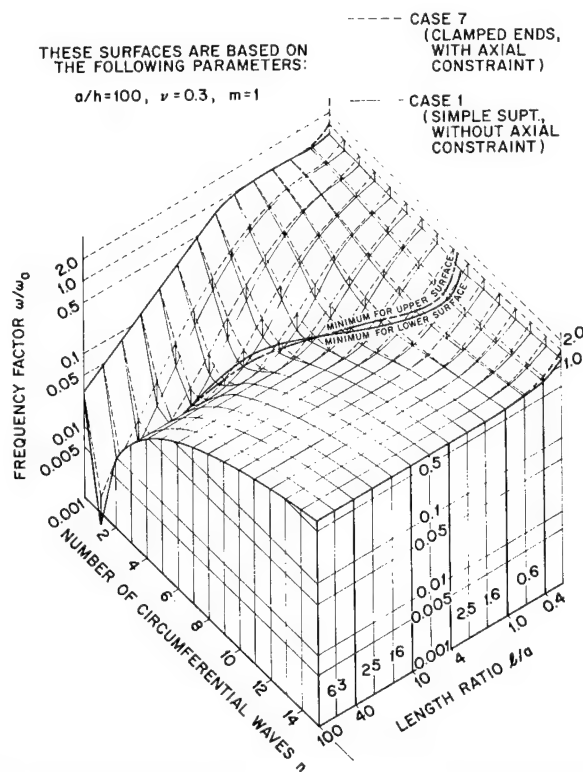
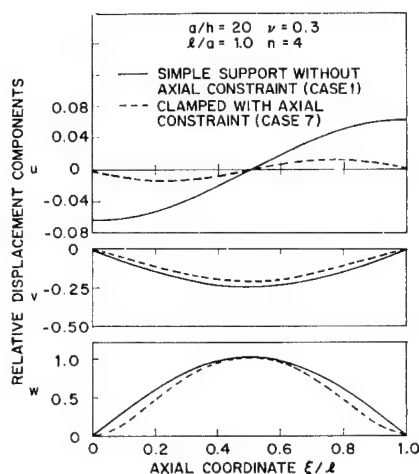
It is not practical to try to compare on a two-dimensional plot the influence of different boundary conditions on the over-all frequency distribution. This was the reason for discussing only the frequency envelope in the preceding figures. In order to understand how these figures relate to the over-all pattern, one case will be studied in more depth. Figure 11 is a three-dimensional plot of the frequency as a function of n and l/a , for a specific shell ($a/h = 100$, $\nu = 0.3$), and for one axial half-wave. Two different sets of boundary conditions are shown: simple support without axial constraint (case 1) and clamped with axial constraint (case 7). Note that the scale for l/a is reversed from the sense used in preceding figures. The minimum curves shown in Fig. 11 are the type of curves plotted in Figs. 3-7.

The difference between the surface for case 1 and the surface for case 7, for $l/a < 1$, is primarily due to the effect of moment restraint. For $l/a > 1$, the difference is due to the effect of axial restraint. The frequencies associated with the various values of n for a fixed l/a are very close in magnitude for short shells, as evidenced by the nearly horizontal grid lines in the n direction. For long shells, the influence of the boundary conditions extends over a much narrower band of circumferential waves.

Fig. 10 Frequency distribution for $l/a = 100$.

To further illustrate these points, a cross section of Fig. 11 has been drawn for three different values of l/a (i.e., 1, 10, 100). Figure 9a is the cross section for $l/a = 1$. (Only the $m = 1$ curve appears in Fig. 11.) Note that the value of n for which the minimum frequency occurs depends upon the half-wavelength l/ma . Note also that, for $m = 1$, there are nine values of n which have frequencies less than the minimum value for $m = 2$. For $l/a = 10$ (Fig. 9b), there are three values. Figure 10 shows a change in character of the ordered frequencies. The minimum frequency occurs for $n = 1$, and there are no other values of n which have frequencies less than that for $n = 1$ and $m = 3$. For $n = 2$, there are 10 values of m which have corresponding frequencies that are less than the minimum value for $n = 3$.

The detailed behavior of the higher modes for the entire range of l/a is illustrated in Fig. 8 for $n = 2$. These curves

Fig. 11 Over-all frequency pattern for $a/h = 100$.Fig. 12 Mode shape for $a/h = 20$, $l/a = 1$, $n = 4$.

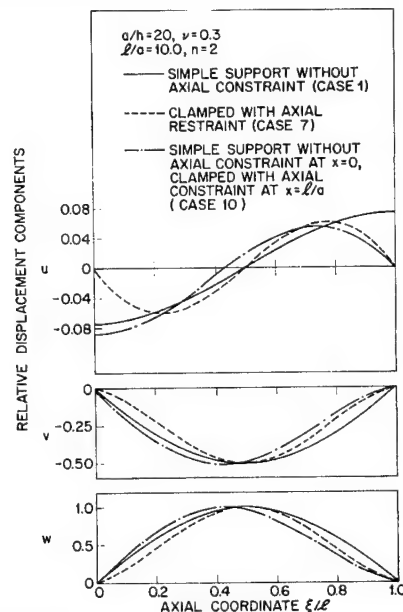
are typical of those obtained for any value of n . The diminishing influence of the boundary conditions on higher values of n is clearly seen here. Note also that, for $m = 1$ and $5 < l/a < 15$, the frequency for case 7 is almost 100% higher than for case 1. In this same region, the difference in minimum frequencies is about 50%.

Modal Stress Resultants

A study of selected stress resultants that arise during modal vibration is essential for full understanding of the influence of the various boundary conditions on the modal behavior of thin shells. The results shown in Figs. 12-16 are all for $a/h = 20$. For thinner shells, the moment distribution is not influenced nearly as much by the various boundary conditions and, in fact, is very close to that for a simply supported shell in all cases. The axial force distribution, on the other hand, is essentially independent of a/h .

There is no unique basis for comparing the magnitude of the various stress resultants for different conditions. For our purpose here, the maximum radial deflection has been taken as the normalizing factor. The important items to compare from case to case are not so much the magnitudes of the stress resultants, but rather their distributions.

In Figs. 14 and 15, distributions of both the axial force N_x and the axial moment M_x are compared for two sets of bound-

Fig. 13 Mode shape for $a/h = 20$, $l/a = 10$, $n = 2$.

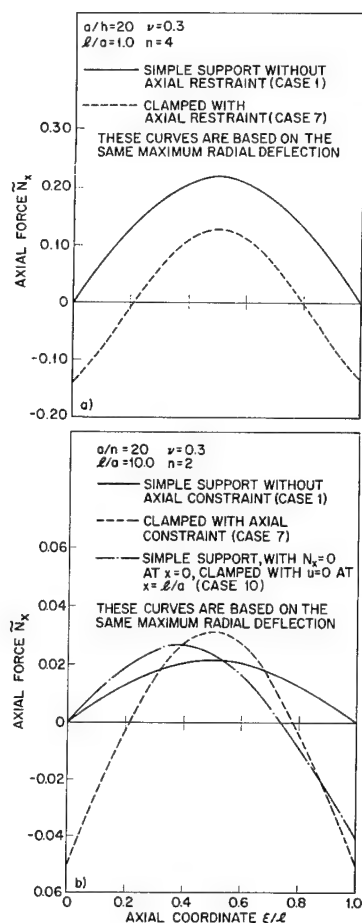


Fig. 14 Distribution of axial force during modal vibration.

any conditions, cases 1 and 7. From these figures, we can see that the region in which the moment is affected decreases as the shell gets longer. Furthermore, a study of other values of a/h shows that, as the shell becomes thinner, the boundary conditions have less and less influence on the

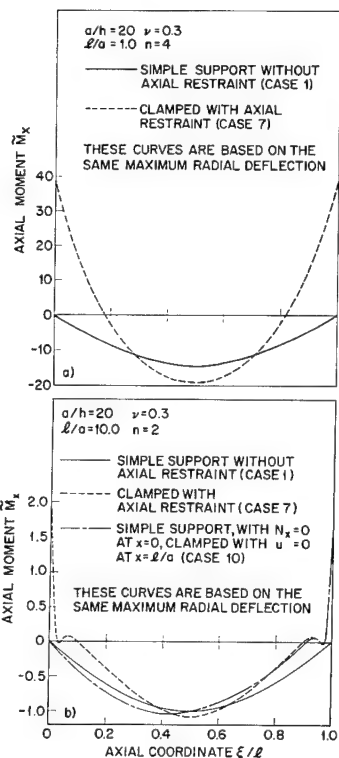


Fig. 15 Distribution of axial moment during modal vibration.

moment distribution. The influence of the condition $\partial w / \partial x = 0$ is generally localized, and this underlies the frequency distribution shown in Fig. 3. The shape of the axial force distribution shown in Fig. 14, on the other hand, could apply to any shell. It is apparent that the boundary condition $u = 0$ always has a strong influence on the axial force distribution, and this contributes to an understanding of the significant increase in the frequency shown in Fig. 4.

Figure 16 rather clearly demonstrates the increasing localization of the effects of the boundary conditions as the number of axial waves increases. This is in accord with the trend already noted in Figs. 8-10.

The difference in behavior of N_x and M_x for the various boundary conditions is similar to the static response of a thin cylindrical shell to various types of edge loading. It has been shown⁶ that, for cylindrical shells, certain types of edge loading produce significant stresses only in a very localized boundary zone, whereas other types of loading will propagate far into the interior of the shell.

Conclusions

The present approach provides a powerful tool for examining a wide variety of boundary conditions and their influence on the modal behavior of cylindrical shells. Since no approximations have been introduced beyond those underlying Flügge's equations, the mode shapes, modal accelerations, and modal stress resultants can be computed quite accurately. The results of this study clearly indicate that care must be taken in any approximate analysis to use appropriate boundary conditions.

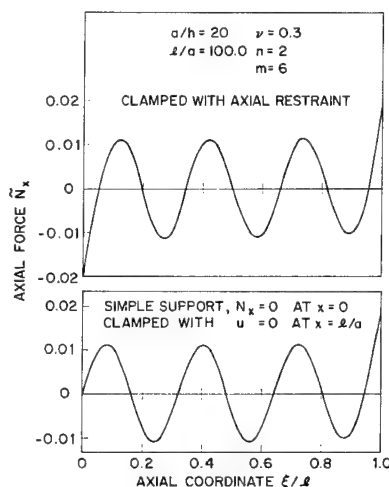


Fig. 16 Distribution of axial force during modal vibration when $m = 6$.

One important question, not studied here, is what constitutes reasonable boundary conditions in actual practice. Although this question is not answered, it is clear that the out of plane stiffness of end rings is far more important, in general, than the resistance of a ring to rotation of its cross section. Furthermore, it is to be noted that a stiff end ring will provide axial restraint for $n \geq 2$, even if the ends of the shell can move axially or rotate as a plane. This indicates that what constitutes axial restraint for $n \geq 2$ may not necessarily be considered axial restraint for $n = 0$ or $n = 1$.

References

- Gros, C. G. and Forsberg, K., "Vibrations of thin shells: a partially annotated bibliography," Lockheed Missiles and Space Co., SB 63-43 (1963).
- Sobel, L., "Effects of boundary conditions on the stability of cylinders subject to lateral and axial pressures," AIAA J. 2, 1437-1440 (1964).

³ Flügge, W., *Stresses in Shells* (Springer-Verlag, Berlin, 1960), Chap. 5, pp. 219 and 233.

⁴ Arnold, R. N. and Warburton, G. B., "Flexural vibrations of the walls of thin cylindrical shells having freely supported ends," *Proc. Roy. Soc. (London)* **A197**, 238-256 (1949).

⁵ Arnold, R. N. and Warburton, G. B., "The flexural vibrations of thin cylinders," *Inst. Mech. Engrs. (London), Proc. Automobile Div.* **167**, 62-80 (1953).

⁶ Steele, C. R., "Shells with edge loads of rapid variation," *Lockheed Missiles and Space Co., TR 6-90-63-84* (1963).

Approximate Laplace Transform Inversions in Viscoelastic Stress Analysis

THOMAS L. COST*

Rohm & Haas Company, Huntsville, Ala

An investigation was made of approximate methods for inverting Laplace transforms that occur in viscoelastic stress analysis when use is made of the elastic-viscoelastic analogy. Alfrey's and ter Haar's methods and Schapery's direct method were examined and shown to be special cases of a general inversion formula due to Widder. Schapery's least squares method and several techniques based on orthogonal function theory were also examined. Viscoelastic solutions to two problems involving deformations and stresses in solid propellant rocket motors under axial and transverse acceleration loads were obtained by use of several of the methods discussed. The problems were typical of the type where the associated elastic solution is known only numerically. The use of the orthogonal polynomial methods is explained in detail, and their limitations discussed. From the investigation described, it was concluded that Schapery's direct method and ter Haar's method generally give good results when applicable. Widder's general inversion formula, which includes Alfrey's method as a special case, is not useable for the type problems of interest here. Although the orthogonal polynomial methods possess characteristics that make them especially suited to the type problems considered, their use appears limited by severe computational difficulties. Schapery's least squares method gives good results to most problems of interest.

Introduction

THE elastic-viscoelastic analogy has been the method most commonly used for obtaining stress distributions and displacements in linear viscoelastic bodies. The analogy has been derived using both a separation of variables technique and an integral transform method. Alfrey¹ was the first to formulate the analogy using the separation of variables technique, whereas Read² was first to derive the analogy using Fourier integral transforms. Lee³ subsequently showed that the analogy could also be derived by use of the Laplace transform. Further developments and extensions have been concisely summarized by Hilton.⁴ In the remarks that follow, the elastic-viscoelastic analogy discussed will be the form derived by Lee.³

The elastic-viscoelastic analogy can be shown to exist by operating on the field equations, constitutive equations, and boundary conditions of a linear viscoelastic body with the Laplace transform with respect to time. This operation reduces derivatives and integrals with respect to time to algebraic expressions of the transform parameter. The equations that result after this operation are analogous to the field equations, constitutive equations, and boundary conditions that govern the behavior of an elastic body of the same geometry as the viscoelastic body. If the solution to

this associated elastic problem can be obtained, the solution to the time dependent viscoelastic problem can be obtained by operating upon the stresses and displacements of the associated elastic problem with an inverse Laplace transform. Thus, the results of the theory of elasticity can be used to obtain solutions to viscoelastic problems.

There are three general classes of problems where an exact form of the elastic-viscoelastic analogy does not apply. The first class consists of problems with moving boundaries where the motion is due to some external source and is entirely different from the usual infinitesimal deformations due to load, temperature, etc. The second class consists of problems where the type of boundary condition at a boundary point changes with time, i.e., a stress boundary condition at a point at one instant of time changes to a displacement boundary condition at another instant of time and vice versa. The third class consists of problems where the compressible material properties are time dependent. If the material properties are time dependent, the differential equations have variable coefficients or the integral equations are not of the convolution type. Thus, the constitutive equations do not reduce to algebraic expressions when operated on with the Laplace (or Fourier) transform.

Although these limitations are serious and exclude from consideration many problems of interest in viscoelastic stress analysis of solid propellant rocket motors, there are still many problems that fall within the realm of application of the analogy which are of interest. Until recently, viscoelastic solutions to problems in which the associated elastic problem was obtained by some numerical technique have been unobtainable by this method because of the difficulty of taking the inverse Laplace transform of functions that are known

Presented as Preprint 64-132 at the AIAA Solid Propellant Rocket Conference, Palo Alto, Calif., January 29-31, 1964; revision received August 4, 1964. This work was conducted for the Army Ordnance Corps under contract number DA-01-021-ORD-11878(Z).

* Intermediate Scientist, Applied Mechanics Group, Engineering Research Section, Redstone Arsenal Research Division.

only numerically, i.e., functions known only at discrete points in the body and only for discrete values of the material constants. Also, there exist many problems that possess associated elastic solutions that are algebraically too complicated to be readily inverted by formal inversion methods.

In this paper, several methods for accomplishing the approximate Laplace transform inversion of a function known only numerically for discrete values of the transform parameter will be discussed. Since an algebraically complicated associated elastic solution can be reduced to a solution known only at discrete points and for discrete values of the material constants, only the numerically known solution will be discussed.

Numerical Transformed Viscoelastic Solution

At this point it appears beneficial to outline the procedure for obtaining transformed viscoelastic solutions from associated elastic solutions obtained by some numerical process.

When the transformed viscoelastic solution or associated elastic solution can be expressed analytically, the moduli of the associated elastic problem are functions of the transform parameter. The form of these equivalent moduli depends on the transformed viscoelastic moduli. The boundary conditions of the associated problem also depend on the transform parameter. Laplace transform inversion of the associated elastic problem yields the viscoelastic solution directly.

When the associated elastic solution is not available in analytical form suitable for formal inversion, numerical values of the transformed viscoelastic solution must be obtained which correspond to certain discrete values of the transform parameter. If the time variation of the viscoelastic moduli of the particular material of interest is known, it is possible to express the equivalent moduli of the material in terms of the Laplace transform of the viscoelastic moduli. Since the equivalent moduli and the transformed boundary conditions can be evaluated for particular values of the transform parameter, the associated elastic solution can be evaluated for particular values of the transform parameter. The transformed viscoelastic solution (associated elastic solution) then can be found for all real values of the transform parameter. Now, if a method of inverting the solution for discrete values of the transform parameter is available, the viscoelastic solution to the problem can be obtained.

To further illustrate this procedure, consider the problem of finding the axial displacements in a finite-length, hollow, circular, linear viscoelastic cylinder bonded to a rigid case on the outer boundary of the cylinder and on one end and subjected to an axial acceleration loading. Application of the elastic-viscoelastic analogy involves the Laplace transform inversion of the solution of an associated elastic problem which consists of an elastic cylinder of the same shape subjected to boundary and loading conditions that are equal

to the transformed viscoelastic conditions. Inversion of such a solution would then yield the solution to the viscoelastic problem.

No closed form solution for this associated elastic problem has yet appeared in the literature, although a numerical solution has been obtained by Parr.⁵ This solution utilized an iterative process to solve a system of finite-difference equations to determine stress functions at a network of discrete points in the body. The stresses, strains, and displacements were evaluated from the stress functions by finite-difference forms of various analytical relations.

The axial displacement w at any point in the elastic problem could be expressed as

$$w = (b\delta g/E)f[(l/2b), (a/b), \nu] \quad (1)$$

where

- b = outer radius of propellant
- a = inner radius of propellant
- l = length of propellant grain
- δ = density of propellant
- g = axial acceleration
- E = tensile modulus
- ν = Poisson's ratio

Only three input parameters were required for the solution, the radius ratio a/b , the length-to-diameter ratio $l/2b$, and Poisson's ratio ν . The transformed viscoelastic solution is then obtained from Eq. (1) by replacing the elastic constants E and ν by the equivalent viscoelastic constants $E^*(p)$ and $\nu^*(p)$ and replacing the acceleration g by the transform of the acceleration in the viscoelastic problem $\bar{g}(p)$. The transformed viscoelastic displacement at a point is then given by

$$\bar{w}(p) = \frac{b\delta\bar{g}(p)}{E^*(p)} f\left(\frac{l}{2b}, \frac{a}{b}, \nu^*(p)\right) \quad (2)$$

$E^*(p)$ and $\nu^*(p)$, the equivalent moduli, are defined as

$$\begin{aligned} E^*(p) &= p\bar{E}^*(p) \\ \nu^*(p) &= p\bar{\nu}^*(p) \end{aligned} \quad (3)$$

where $\bar{E}^*(p)$ and $\bar{\nu}^*(p)$ are the Laplace transforms of the time-dependent relaxation modulus in uniaxial extension $E^*(t)$ and the viscoelastic Poisson's ratio $\nu^*(t)$ determined from a uniaxial tensile test, respectively.

The procedure for obtaining the transformed viscoelastic displacement $\bar{w}(p)$ at various values of p is as follows. First, compute values of $\bar{g}(p)$, $E^*(p)$, and $\nu^*(p)$ which correspond to a particular value of p , e.g., $p = p_0$. Second, the numerical procedure for obtaining the elastic solution w , as stated in Eq. (1), is then used with $\nu = \nu^*(p_0)$, $E = E^*(p_0)$, and $g = \bar{g}(p_0)$ (also values of a , b , l , and δ). This operation is equivalent to the procedure for evaluating Eq. (2). $\bar{w}(p_0)$ is therefore obtained by evaluating the elastic solution for w . Repeating this procedure with $p = p_i$, $i = 1, 2, 3, \dots$, gives values of the transformed function for various values of p_i . Thus, to obtain the viscoelastic solution, the values of the $\bar{w}(p_i)$, $i = 1, 2, 3, \dots$, must be used to obtain the inverse function $w(t)$. Several techniques for accomplishing such an inversion approximately will be discussed in the following section.

Approximate Laplace Transform Inversion Methods

General Theory

Before beginning a discussion of the approximate inversion methods, certain elementary aspects of Laplace transform theory will be reviewed here for terminology and completeness.[†]

[†] For a comprehensive treatment of Laplace transform theory, see one of the standard treatise on the subject such as Widder.⁶

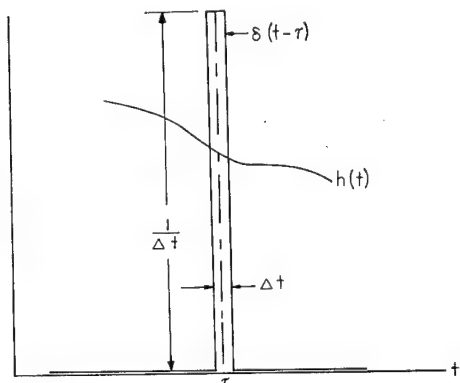


Fig. 1 Illustration of sifting property of Dirac delta function.

The Laplace transform $\bar{f}(p)$ of a function $f(t)$ is commonly indicated by $L\{f(t)\}$ and defined as

$$L\{f(t)\} = \bar{f}(p) = \int_0^{\infty} f(t)e^{-pt}dt \quad (4)$$

where p is the transform parameter and $\bar{f}(p)$ is a function of p different from, but related to $f(t)$. In order for the Laplace transform of a function to exist, it is sufficient that the function be sectionally continuous in every finite interval in the range $t \geq 0$ and that the function be of exponential order as $t \rightarrow \infty$. The parameter p , in general, is a complex variable.

If the transformed function $\bar{f}(p)$ is analytic and of order p^{-c} in a half-plane $\text{Re}(p) \geq \alpha$, where c is a constant greater than zero, then the inverse Laplace transform gives the original function $f(t)$, termed the "indicial function," in terms of a complex integral as

$$L^{-1}\{\bar{f}(p)\} = f(t) = \frac{1}{2\pi i} \lim_{\beta \rightarrow \infty} \int_{\alpha-i\beta}^{\alpha+i\beta} \bar{f}(p)e^{pt}dp \quad (5)$$

Here $L^{-1}\{f(p)\}$ is used to indicate the inverse Laplace transform of $f(t)$. Although this inversion integral, which is an integral in the complex plane along a line parallel to the imaginary axis, can be written in terms of a real infinite integral, the evaluation is more difficult than evaluation of the complex integral. Hence, the complex form is usually used in conjunction with certain auxiliary line integrals and the theory of residues. In any case, the inversion can be quite difficult and tedious for complicated forms of the transformed function $\bar{f}(p)$. If the function $\bar{f}(p)$ is known only numerically for discrete values of p , some approximate inversion scheme must be used.

The need for inverting Laplace transforms has been experienced in many fields, and, as a result, approximate inversion methods have been developed in connection with several distinct subjects. A unified treatment of the most promising approximate inversion methods is presented in the following sections.

Inversion Methods Based on Widder's General Inversion Formula

Widder⁶ has suggested use of a general inversion formula first proposed by Post.⁷ The general inversion formula represents the general case of a set of inversion methods that have recently been considered, namely, the methods of Alfrey,¹ ter Haar,⁸ and Schapery.⁹

Widder's general inversion formula

Widder's general inversion formula is based on the sifting property of the Dirac delta function. This property is best stated by the formula

$$\int_0^{\infty} h(t)\delta(t-\tau)dt = h(\tau) \quad \tau > 0 \quad (6)$$

where

$$\delta(t-\tau) = \begin{cases} 0 & t \neq \tau \\ \lim_{\Delta t \rightarrow 0} 1/\Delta t & t = \tau \end{cases}$$

A graphical interpretation of the sifting property of the delta function is shown in Fig. 1. From the figure it can be seen that $h(t)$ is essentially constant in the region where the impulse function is large ($t = \tau$), and the product $h(t)\delta(t-\tau)$ is zero elsewhere. The integral in Eq. (6) is accordingly equal to $h(t)|_{t=\tau}$ times the area below the $\delta(t-\tau)$ curve. Since, by definition, the area is unity, i.e.,

$$\int_0^{\infty} \delta(t-\tau)dt \equiv 1 \quad \tau > 0 \quad (7)$$

the result expressed in Eq. (6) becomes apparent.

To obtain the Laplace transform in a form in which this relation may be used, the definition integral is differentiated

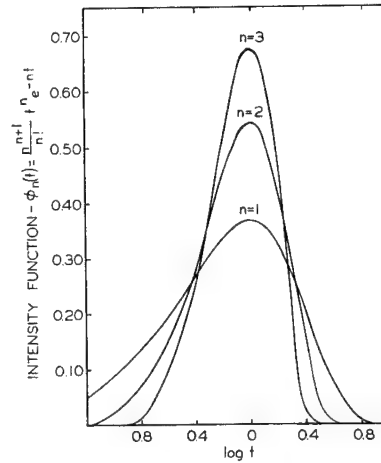


Fig. 2 Intensity functions arising in Widder's general inversion formula.

under the sign of integration n times with respect to the transform parameter p . This operation gives

$$\frac{d^n \bar{f}(p)}{dp^n} = (-1)^n \int_0^{\infty} f(t) [t^n e^{-pt}] dt \quad (8)$$

With a slight modification, this integral can be converted into a sifting integral as in Eq. (6). The function in brackets resembles a delta function and can be approximated by such a function after the normalization requirements stated in Eq. (7) are satisfied. Since the integral

$$\int_0^{\infty} t^n e^{-pt} dt = \frac{n!}{p^{n+1}} \quad (9)$$

is not unity, the function in brackets, hereafter called the intensity function, must be multiplied by $p^{n+1}/n!$ before being replaced by the delta function. Then,

$$(p^{n+1}/n!) t^n e^{-pt} \approx \delta(t - t_0) \quad (10)$$

where t_0 is any specified time at which the δ function is not zero. The function on the left has a maximum at $t = n/p$, and if the delta function is assumed to be located at this point, Eq. (10) becomes

$$\delta[t - (n/p)] \approx (p^{n+1}/n!) t^n e^{-pt} \quad (11)$$

The family of functions represented by successively higher values of n is shown in Fig. 2 where the location of the maximum point of the functions has been chosen to be at $t_0 = 1$ or $n/p = 1$. It can be seen from Fig. 2 that increasing the value of n increases the accuracy of the approximation stated in Eq. (11), and with the use of Stirling's formula it can be shown that

$$\lim_{n \rightarrow \infty} (p^{n+1}/n!) t^n e^{-pt} = \delta[t - (n/p)]$$

If Eq. (11) is substituted into Eq. (8), there results the sifting integral

$$(-1)^n \frac{p^{n+1}}{n!} \frac{d^n}{dp^n} \bar{f}(p) \approx \int_0^{\infty} f(t) \delta\left(t - \frac{n}{p}\right) dt \quad (12)$$

Applying the properties of the sifting integral [see Eq. (6)] to Eq. (12) yields the relation

$$(-1)^n \frac{p^{n+1}}{n!} \frac{d^n}{dp^n} \bar{f}(p) \approx f(t)|_{t=n/p} \quad (13)$$

Equation (13) can be written in a slightly different form to give the general inversion formula as proposed by Widder. This relation is

$$f(t) = \lim_{n \rightarrow \infty} \left[\frac{(-1)^n p^{n+1}}{n!} \frac{d^n}{dp^n} \bar{f}(p) \right]_{p=n/t} \quad (14)$$

where the limit has been applied to indicate that the accuracy of the approximation increases with n because of the stronger resemblance of the intensity function to the delta function for higher values of n .

Alfrey's approximation

Alfrey's approximation is

$$f(t) \approx \left[-p^2 \frac{d\bar{f}(p)}{dp} \right]_{p=1/t} \quad (15)$$

By inspection of Eq. (14), it can be seen that Alfrey's approximation is exactly the first-order approximation of Widder's general inversion formula, i.e., Widder's formula when $n = 1$. Hence, the assumptions and limitations of Alfrey's inversion method are a special case of those of Widder's method.

ter Haar's approximation

ter Haar⁸ proposed a method for approximate inversion of the Laplace transform which did not involve knowing any derivatives of the transformed function. ter Haar's approximation is

$$f(t) \approx [p\bar{f}(p)]_{p=1/t} \quad (16)$$

To arrive at this relation, a slightly different approach was used by ter Haar. Instead of differentiating the definition integral, as was done previously, ter Haar simply multiplied and divided the integrand of this integral by t . Performing this operation on Eq. (4) results in the expression

$$\bar{f}(p) = \int_0^\infty \frac{f(t)}{t} [te^{-pt}] dt \quad (17)$$

As was pointed out by ter Haar, the function in brackets resembles a delta function and therefore may be approximated by the function

$$te^{-pt} \approx [\delta(t - t_0)/p^2] \quad (18)$$

where the factor p^2 has been introduced for normalization purposes. Making this substitution in Eq. (17) yields

$$p^2\bar{f}(p) \approx \int_0^\infty \frac{f(t)}{t} \delta(t - t_0) dt \quad (19)$$

It can be seen by comparing Eqs. (18) and (10) that the intensity function of ter Haar, which is assumed to be approximated by a delta function, is the same as that of Widder when $n = 1$. Thus, the nature of ter Haar's approximation is the same as that of Widder when $n = 1$, although the indicial functions in Eqs. (19) and (12) differ by a factor of $1/t$. This difference results in somewhat different approximations.

Applying the sifting integral properties to Eq. (19) gives

$$p^2\bar{f}(p) \approx [f(t)/t]_{t=t_0} \quad (20)$$

Assuming the delta function location t_0 to be at the point where the intensity function is a maximum ($t = 1/p$) allows Eq. (20) to be rewritten in the form of Eq. (16), which is ter Haar's approximation.

Schapery's direct method of approximation

Schapery's direct method⁹ of approximate inversion gives the same result as ter Haar's except that the location of the delta function is chosen differently which results in a different relation between p and t . To obtain Schapery's formula, the delta function is located at the centroid of the intensity function in the $\log t$ scale which is the point where $pt \approx 0.5$. The final form of Schapery's direct method of approximation is

$$f(t) = [p\bar{f}(p)]_{p=0.5/t} \quad (21)$$

Schapery points out that the method is mainly limited to problems where $p\bar{f}(p)$ is essentially a linear function of $\log p$.

Method Based on Principle of Least Squares

This method was first proposed by Schapery.⁹ Schapery concludes from his studies of irreversible thermodynamics that the class of problems to which the elastic-viscoelastic analogy may be applied has time-dependent solutions of the form

$$f(t) = C_1 + C_2 t + \theta(t) \quad (22)$$

where C_1 and C_2 are constants and $\theta(t)$ is the transient component of the solution defined as

$$\theta(t) = \int_0^\infty H(\tau) e^{-t/\tau} d\tau \quad (23)$$

The function $H(\tau)$, referred to as a spectral function, may consist either entirely or partly of Dirac delta functions. As Schapery⁹ points out, if $H(\tau)$ is the sum of a series of delta functions such as

$$H(\tau) = \sum_{i=1}^m h_i(\tau - \tau_i) \quad (24)$$

then the transient component of the response function is

$$\theta(t) = \sum_{i=1}^m h_i e^{-t/\tau_i} \quad (25)$$

The form of Eq. (25) suggests that $\theta(t)$ may be expressed approximately as

$$\theta(t) \approx \theta^*(t) = \sum_{i=1}^m g_i e^{-t/\alpha_i} \quad (26)$$

where the α_i and g_i are constants to be determined by minimizing the mean square error between $\theta(t)$ and $\theta^*(t)$. This mean square error is, by definition,

$$E^2 = \int_0^\infty [\theta(t) - \theta^*(t)]^2 dt \quad (27)$$

By prescribing the α_i , the g_i may be determined by minimizing E^2 with respect to g_i . This minimization process results in the expression

$$\frac{\partial E^2}{\partial g_i} = \int_0^\infty 2[\theta(t) - \theta^*(t)] e^{-t/\alpha_i} dt = 0 \quad (i = 1, 2, \dots, m) \quad (28)$$

or, equivalently,

$$\int_0^\infty \theta(t) e^{-t/\alpha_i} dt = \int_0^\infty \theta^*(t) e^{-t/\alpha_i} dt \quad (i = 1, 2, \dots, m) \quad (29)$$

Equation (29) essentially means that, for the mean square error of the approximation to be a minimum, the Laplace transform of the approximation must equal the Laplace transform of the exact function at least at the m points $p = 1/\alpha_i$, $i = 1, 2, \dots, m$. Therefore, m relations are available relating the Laplace transforms of $\theta(t)$ and $\theta^*(t)$, each evaluated at $p = 1/\alpha_i$, i.e.,

$$\bar{\theta}(p)|_{p=1/\alpha_i} = \bar{\theta}^*(p)|_{p=1/\alpha_i} \quad (i = 1, 2, \dots, m) \quad (30)$$

Since $\theta(t)$ was assumed to be of the form indicated in Eq. (26), Eq. (30) reduces to the series of equations:

$$\bar{\theta}(p)|_{p=1/\alpha_i} = \sum_{j=1}^m \frac{g_j}{[(1/\alpha_i) + (1/\alpha_j)]} \quad (i = 1, 2, \dots, m) \quad (31)$$

which may be used to evaluate the g_i in terms of the values of the transformed function $\bar{\theta}(p)$ at the points $p_i = 1/\alpha_i$. Thus, the transient component of the solution of $\theta(t)$ may be determined and the constants C_1 and C_2 determined from given initial and boundary conditions.

Papoulis' Legendre Polynomial Inversion Method

Expansion of the desired time-dependent indicial function $f(t)$ into a series of orthogonal polynomials in real time as a means of approximate inversion has received the attention of two investigators, Papoulis¹⁰ and Lanczos.¹¹ The methods are based on the idea that the form of the transformed polynomials is known and the coefficients of the polynomials are calculable in terms of values of the transformed function at equidistant points along the real axis. The method, as described by Papoulis,¹⁰ which uses Legendre polynomials for the orthogonal set is presented in the following section.

As described by Papoulis,¹⁰ the definition integral [Eq. (4)] may be transformed according to the relation

$$e^{-\gamma t} = x \quad \gamma > 0 \quad (32)$$

where γ is a scaling factor that remains constant throughout any particular expansion; γ will be discussed in more detail later after it becomes clear what purpose it serves. The function $f(t)$ in Eq. (4) becomes

$$f(t) = f[-(1/\gamma) \ln x] \equiv \hat{f}(x) \quad (33)$$

Making these substitutions, Eq. (4) becomes

$$\gamma \bar{f}(p) = \int_0^1 x^{(p/\gamma)-1} \hat{f}(x) dx \quad (34)$$

By expressing p in terms of γ as

$$p = (2k + 1)\gamma \quad (35)$$

Eq. (34) takes the form

$$\gamma \bar{f}(2k\gamma + \gamma) = \int_0^1 x^{2k} \hat{f}(x) dx \quad (36)$$

Therefore, if the value of $\bar{f}(p)$ is known at the point $p = (2k\gamma + \gamma)$, this is equivalent to knowing the $2k$ th moment of the function $\hat{f}(x)$ in the interval $(0, 1)$.

The Legendre polynomials $P_n(x)$ form a complete orthogonal set in the interval $(-1, 1)$ and by extending the definition of $\hat{f}(x)$ in the interval $(-1, 1)$ by defining $\hat{f}(x)$ to be an even function, i.e.,

$$\hat{f}(x) = \hat{f}(-x) \quad (37)$$

the function $\hat{f}(x)$ can be expanded into a series of even Legendre polynomials. Such an expansion gives

$$\hat{f}(x) = \sum_{j=0}^{\infty} C_j P_{2j}(x) \quad (38)$$

The major task remaining is to evaluate the C_j . It is known¹⁰ that the series expansion of a function is uniquely determined by its moments that are known quantities as seen from Eq. (36). Using the fact that $P_{2j}(e^{-\gamma t})$ is an even polynomial in $e^{-\gamma t}$ of degree $2j$, Papoulis shows that the transform of $P_{2j}(e^{-\gamma t})$ is of the form

$$\bar{P}_{2j}(p) = \frac{[p - \gamma][p - 3\gamma] \dots [p - (2j - 1)\gamma]}{p[p + 2\gamma] \dots [p + 2j\gamma]} \quad (39)$$

Therefore, taking the Laplace transform of both sides of Eq. (38) gives

$$\bar{f}(p) = \frac{C_0}{p} + \sum_{j=1}^{\infty} \frac{[p - \gamma] \dots [p - (2j - 1)\gamma]}{p \dots [p + 2j\gamma]} C_j \quad (40)$$

Replacing p first by γ then $3\gamma, 5\gamma, \dots, (2j + 1)\gamma, \dots$ in Eq. (40) gives the following system of equations to evaluate the C_j :

$$\begin{aligned} \gamma \bar{f}(\gamma) &= C_0 & \gamma \bar{f}(3\gamma) &= \frac{1}{3} C_0 + \frac{2}{15} C_1 \\ \gamma \bar{f}(2j\gamma + \gamma) &= \frac{C_0}{2j + 1} + \frac{2j C_1}{[2j + 1][2j + 3]} + \dots + \\ &\quad \frac{2j[2j - 2] \dots 2C_j}{[2j + 1][2j + 3] \dots [4j + 1]} \end{aligned} \quad (41)$$

Thus, using Eqs. (41) to evaluate the C_j in terms of the known values of $\bar{f}(p)$ determines the expansion defined in Eq. (38), which in terms of real time is

$$f(t) = \sum_{j=0}^{\infty} C_j P_{2j}(e^{-\gamma t}) \quad (42)$$

As seen from Eq. (42), the scaling factor γ enters the final expression as a factor of the exponent of e . The function e^{-x} varies over the interval $(-2 < \log x < 1)$ but is essentially constant elsewhere. If a function $f(t)$ varies over an interval greater than $(-2 < \log \gamma t < 1)$, then functions of the form $e^{-\gamma t}$ cannot adequately describe its variation over the total range of variation. Thus, γ must assume multiple values depending on the interval of time of interest and different expansions must be obtained for each choice of γ .

Thus, the inversion of the Laplace transform can be accomplished by expanding the desired indicial function $f(t)$ in terms of an infinite convergent series of orthogonal functions whose coefficients are calculable in terms of equidistant values of the Laplace transform along the real axis.

Lanczos method,¹¹ which utilizes Legendre polynomials, differs in theory only slightly from the method described by Papoulis. Instead of using the exact form of the polynomials used by Papoulis, Lanczos uses a slightly modified form for the polynomials, which are orthogonal on the interval $(0, 1)$. Lanczos has refined the method of application to the point that computational efforts are minimized, and the coefficients C_j are determined in a slightly different form than in Papoulis' method. The nature of the results of the two methods are very similar.

The basic idea of the orthogonal polynomial approximations has also been extended by Papoulis and Lanczos to include Chebycheff and Laguerre polynomials. For a comprehensive description of these methods, see Ref. 12.

Numerical Examples

The methods of approximate inversion of the Laplace transform just presented vary considerably in regard to the assumptions and mathematical techniques used in their derivation. Also, application of the methods is considerably different. In order to illustrate the use of and clarify the restrictions on the various methods, solutions to two problems are presented which are of interest in solid propellant structural integrity analysis. The problems are typical of the type where the solution is unobtainable by formal Laplace transform inversion methods. The solutions presented here are intended only to indicate the method of application and nature of the results of the various methods and not necessarily to indicate the accuracy obtainable with any method.

The first problem is that of finding the circumferential stress σ_θ at a point on the inner boundary of an infinite-length, hollow, circular cylinder of linear viscoelastic material. The cylinder is bonded to an elastic case and is lying in a horizontal position loaded by its own weight. The cylinder is assumed supported by a concentrated load as illustrated in Fig. 3.

The second problem involves the determination of the axial displacement at a point on the inner boundary of a finite-length, hollow, circular cylinder of linear viscoelastic material bonded to a rigid case and subjected to an axial acceleration load as shown in Fig. 4.

In solving both problems, realistic material property data were used. The actual material behavior is idealized but is typical of many solid propellant materials. It is characterized by the tensile relaxation modulus $E^*(t)$ shown in Fig. 5 and is seen to have relaxation processes occurring over several decades of logarithmic time. The collocation method¹³ for fitting a series of exponentials to measured data was used to obtain an analytical expression for the tensile relaxation

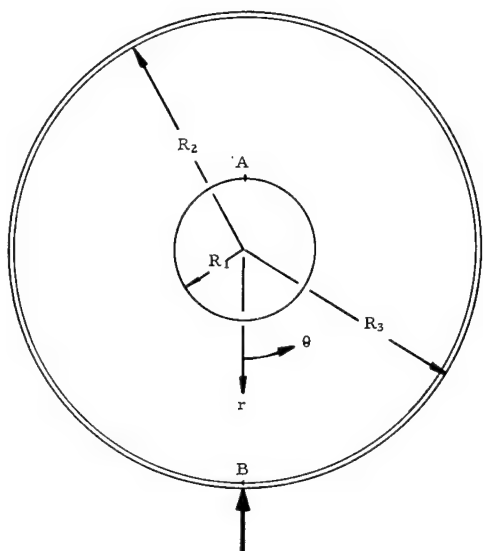


Fig. 3 Infinite-length cylinder under transverse acceleration load supported by point load at B .

modulus. The resulting expression for $E^*(t)$ used to obtain the curve in Fig. 5 is

$$E^*(t) = 600 - 1945.298e^{-500t} + 16334.19e^{-50t} + 21670.066e^{-5t} + 16951.871e^{-0.5t} + 6425.041e^{-0.05t} \quad (43)$$

where the units of $E^*(t)$ and t are pounds per square inch and minutes, respectively.

The material was assumed to be elastic in isotropic tension and the time dependent Poisson's ratio¹⁴ is thus expressible as

$$\nu^*(t) = \frac{1}{2} - [E^*(t)/6K] \quad (44)$$

where the bulk modulus K was assumed to have the value of 500,000 psi.

Problem I: Transverse Acceleration of Infinite-Length Cylinder

A viscoelastic solution has been obtained by Lianis¹⁵ to the problem of transverse slump of a solid propellant rocket grain bonded to a rigid case, but, as yet, no solution has appeared in the literature to the problem of a solid propellant rocket grain, assumed to be viscoelastic, bonded to an elastic case. From the results of the elastic solution of Gillis,¹⁶ the affect of the flexible case is considerable and would also be significant for a viscoelastic analysis.

The elastic solution obtained by Gillis¹⁶ was used to obtain the viscoelastic solution to the problem of transverse acceleration. Gillis solved the problem of an infinite-length, hollow, circular, elastic cylinder bonded to an elastic case. The

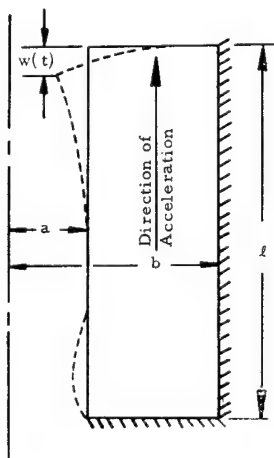


Fig. 4 Finite-length cylinder under axial acceleration load.

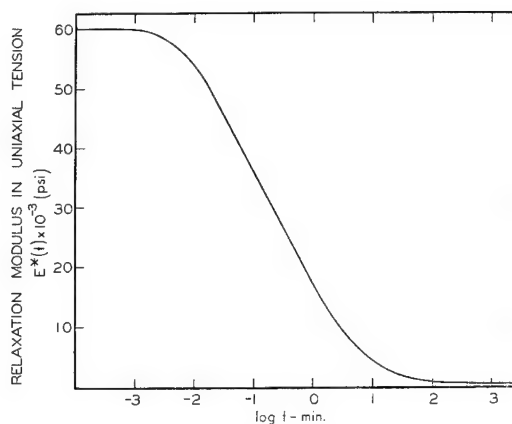


Fig. 5 Viscoelastic moduli used in numerical examples.

method of solution involved application of Muskhelishvili's complex variable method for solving problems with circular boundaries. Each concentric cylinder, i.e., the case and the grain, was considered separately. The unknown interface stresses were represented as infinite complex Fourier series with unknown coefficients. These coefficients were later evaluated by equating the normal and shearing stresses and the displacements at the interface.

The solution resulting from this technique was in the form of an infinite series whose coefficients were algebraically complicated functions of the elastic material properties; hence, formal Laplace transform inversion of such a form was impractical. Therefore, the approximate Laplace transform inversion methods described herein are particularly well suited for this problem.

The geometry of the problem considered is as shown in Fig. 3, and the following numerical values were used for the various descriptive parameters; $R_1/R_2 = 0.25$, $R_3/R_2 = 1.005$, $\rho/\delta = 4.733$, $\nu_e = 0.3$, and $G_e = 30.0 \times 10^6$ psi, where ρ is the weight density of case, δ the weight density of propellant, ν_e the Poisson's ratio of elastic case, and G_e the modulus of elasticity of case in shear.

The dimensionless circumferential elastic stress σ_θ at point A (Fig. 3) is a function of Poisson's ratio and the elastic tensile modulus. Application of the elastic-viscoelastic analogy to this function in the manner described earlier yields the following expression for the transformed viscoelastic stress:

$$\frac{\bar{\sigma}_\theta(p)}{\delta_0 R_2} = \frac{1}{p} f(\nu^\#, E^\#) \quad (45)$$

The gravitational acceleration has been assumed to be a constant applied at time $t = 0$ so that $\bar{\delta}(p) = \delta_0/p$ and $\bar{p}(p) = \rho_0/p$.

The equivalent modulus $G^\#(p)$ is expressible in terms of the equivalent moduli $\nu^\#(p)$ and $E^\#(p)$ as

$$G^\#(p) = \frac{E^\#(p)}{2[1 + \nu^\#(p)]} \quad (46)$$

Repeated computation of $[\bar{\sigma}_\theta(p)/\delta_0 R_2]$ with $\nu = \nu^\#(p)$ and $E = E^\#(p)$ then allows the transformed quantity to be determined numerically for various values of p .

The transformed viscoelastic solution will now be inverted by two of the methods discussed earlier.

Schapery's direct method

Application of Schapery's direct method of inversion is straightforward and needs no elaboration regarding its use. Equation (21) can be readily applied to this problem to give the direct method approximation as

$$\frac{\sigma_\theta(t)}{\delta_0 R_2} = \left[\frac{p \bar{\sigma}_\theta(p)}{\delta_0 R_2} \right]_{p=0.5/t} \quad (47)$$

It is seen that the time-dependent function $\sigma_\theta(t)$ is thus numerically equal to the transformed function $p\bar{\sigma}_\theta(p)$ when $p = 0.5/t$. Values of $p\bar{\sigma}_\theta(p)$ were computed for various p values in the manner described earlier maintaining as much accuracy as possible on an IBM 7090 computer. The results from these computations are shown in Fig. 6 on the appropriate curve.

Papoulis' Legendre polynomial approximation

Of the methods discussed in this paper, the methods based upon properties of orthogonal polynomials appear to be the least known. Therefore, more detail will be included in application of these methods than would normally be needed. The inversions performed here are intended only to indicate the method of application and the nature of the results obtained and not necessarily to indicate the best accuracy obtainable with these methods.

The first decision to be made is how many terms should be included in the expansion and what values the scaling factor γ should assume. In order to cover a span of time of several decades, a very large number of terms would have to be included in the series expansion for the time-dependent function, Eq. (42). An alternative to including a large number of terms in the series is to develop several expansions all with a smaller number of terms but which apply in different intervals of time. This is accomplished by considering expansions with different values of the scaling factor γ used in each expansion.

Previous results have shown^{12, 17} that, although Schapery's direct method may be in error a significant amount at any instant of time, the method, if applicable, still indicates the general behavior of the time-dependent function. Thus, Schapery's direct method can be used as a guide in determining what intervals of time are of greatest interest when deciding what values of the scaling factor γ are to be used. For the problem under consideration, observation of the results of the direct method (Fig. 6) indicates that the time interval of greatest interest is between $\log t = -3$ and $\log t = +3$, since the time-dependent function is essentially constant elsewhere.

The choice of the scaling factor γ also depends upon the number of terms considered in the series expansions. For minimum computation effort, it was decided to include only the first six terms in the series expansion. The resulting expression for the time-dependent function then becomes an expression of the form

$$f(t) = \sum_{i=0}^5 A_i e^{-2i\gamma t} \quad (48)$$

where the A_i are constants to be determined. Observation of the time dependence of these exponentials indicates that the series will be applicable, at most, over an interval of about two decades of logarithmic time. These limits on the interval of applicability are

$$-2.0 \leq \log \gamma t \leq 0$$

or

$$-[2.0 + \log \gamma] \leq \log t \leq -[\log \gamma] \quad (49)$$

Thus, by varying γ it is seen that the intervals of time over which the expansions are applicable are changed, and γ should be selected accordingly. From considerations of this type, it was determined that, for the problem under consideration, expansions would be made with $\gamma = 2.0$, $\gamma = 0.1$, and $\gamma = 0.01$.

Normal application of this Legendre polynomial inversion method involves solving Eqs. (41) for the C_j which, in this case, are evaluated in terms of $[p\bar{\sigma}_\theta(p)/\delta_0 R_2]$, where p assumes the successive values γ , 3γ , 5γ , 7γ , 9γ , and 11γ . Substitution of these C_j into Eq. (42) then gives the desired time-

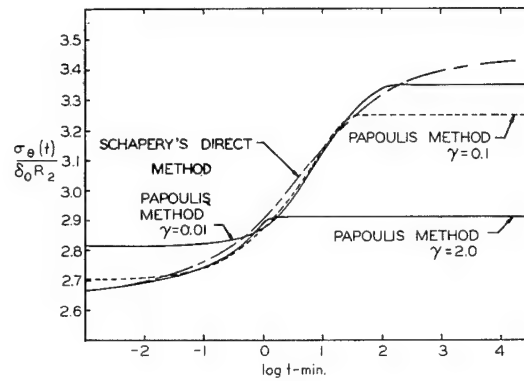


Fig. 6 Circumferential stress in infinite-length cylinder subjected to transverse acceleration load.

dependent expression. For convenience in applying the inversion method, it can be easily programed for performance on a high-speed computer. This was done, and the resulting time-dependent solution was obtained as a function of the values of the transformed function. Expressions for the time-dependent function, where up to six terms have been included in the expansion, are included in the Appendix for reference purposes. Here, it is only necessary to say that application of the method yielded the expression

$$[\sigma_\theta(t)/\delta_0 R_2] = A_0 + A_1 e^{-2\gamma t} + A_2 e^{-4\gamma t} + A_3 e^{-6\gamma t} + A_4 e^{-8\gamma t} + A_5 e^{-10\gamma t} \quad (50)$$

where the A_i are given for the various γ values in Table 1.

These equations are shown graphically in Fig. 6 along with the results of Schapery's direct method.

Problem II: Axial Slump of Finite-Length Cylinder

The geometry of the problem under consideration here is shown in Fig. 4, and the descriptive parameters for this problem take the numerical values $a/b = 0.2$ and $l/2b = 2.0$. The problem was discussed earlier in this paper in detail in regard to the method of obtaining the transformed viscoelastic solution from associated elastic solutions obtained by some numerical technique. Equation (2) gives the expression for the transformed viscoelastic displacement in terms of the equivalent moduli and boundary conditions. Assuming the acceleration $g(t)$ to be a step function of magnitude g_0 applied at time $t = 0$ allows Eq. (2) to become

$$\frac{\bar{w}(p)}{b\delta g_0} = \frac{f[(l/2b), (a/b), \nu^*(p)]}{E^*(p)} \quad (51)$$

This expression was used to compute $[\bar{w}(p)/b\delta g_0]$ at various p values and will now be inverted by ter Haar's approximate inversion formula and Papoulis' Legendre polynomial inversion method.

In problem I, all of the values for the transformed functions were computed by use of a digital computer. Since this involves calculating the associated elastic solution for each p value of interest, it can sometimes require large amounts of computer time. In order to determine if the

Table 1 Coefficients for Legendre polynomial series expansion for circumferential stress in infinite-length cylinder

	$\gamma = 2.0$	$\gamma = 0.1$	$\gamma = 0.01$
A_0	+2.9101288	+3.2446153	+3.3485413
A_1	-1.1336263	-1.5955523	-0.1508337
A_2	+4.9700432	+7.0635583	+1.3693328
A_3	-11.220680	-17.294206	-6.7259964
A_4	+11.587841	+19.018909	+10.444514
A_5	-4.514669	-7.7341720	-5.4694445

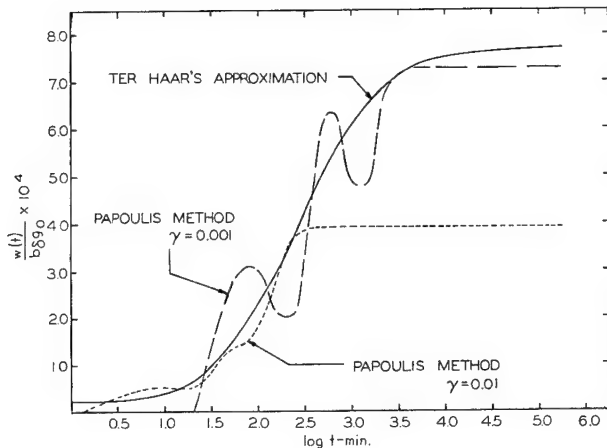


Fig. 7 Maximum vertical deflection of finite-length cylinder under axial acceleration.

associated elastic solution could be calculated for only a few values of p and the results interpolated to obtain the results for any p value of interest, the data for the values of the transformed displacement were obtained from a graph plotted from only a few exact values of the transformed displacement.

ter Haar's approximation

ter Haar's approximation was used to indicate that the method is the same as Schapery's direct method except that the results are shifted an amount equal to $\log 2$ parallel to the $\log t$ scale. Application of Eq. (16) gives the time-dependent vertical displacement at the location shown in Fig. 4 as

$$\frac{w(t)}{b\delta g_0} = \left[\frac{p\bar{w}(p)}{b\delta g_0} \right]_{p=1/t} \quad (52)$$

The results from Eq. (52) are shown graphically in Fig. 7.

Papoulis' Legendre polynomial inversion method

Expansions for $[w(t)/b\delta g_0]$ were obtained for scaling factor values of $\gamma = 0.001$ and $\gamma = 0.01$ again mainly to indicate the nature of the results. The computer program mentioned previously was used, and the results are expressions of the type

$$[w(t)/b\delta g_0] = A_0 + A_1 e^{-2\gamma t} + A_2 e^{-4\gamma t} + A_3 e^{-6\gamma t} + A_4 e^{-8\gamma t} + A_5 e^{-10\gamma t} \quad (53)$$

where the A_i assumes the values shown in Table 2. The results from these calculations are shown in Fig. 7.

Discussion

Widder's General Inversion Formula

Widder's method, which includes Alfrey's method as a special case, can be applied to problems having discrete elastic solutions but with doubtful accuracy. Application of these methods involves obtaining derivatives of successively

Table 2 Coefficients for Legendre polynomial series expansion for axial slump of a finite-length cylinder

	$\gamma = 0.01$	$\gamma = 0.001$
A_0	+0.00039179618	+0.00672576811
A_1	-0.002994930	-0.0063681163
A_2	+0.014314120	+0.051678120
A_3	-0.032746425	-0.15256234
A_4	+0.033910939	+0.18186449
A_5	-0.012904986	-0.75686391

higher orders. Because of the nature of the problem being considered, these derivatives must be obtained by numerical differentiation techniques. In order to examine the practicality of obtaining accurately the derivatives of a function by using various numerical differentiation techniques, several functions whose derivatives were known exactly were examined.¹² The functions examined were relatively well behaved and of exponential and decaying periodic forms. Derivatives up to the third order were obtained with the use of differentiation formulas that involved using three, five, and seven data points to obtain each derivative. It was found that derivatives of functions obtained near the ends of the interval under consideration were not reliable. Third-order derivatives were obtainable within the interval using central difference formulas with results falling within engineering accuracy. However, if the behavior of the function is not clear, the process of obtaining derivatives numerically does not give results having sufficient accuracy to warrant their use. This is due to the influence of the increment size between data points and the formula to be used in obtaining the derivative, i.e., 3, 5, or 7 point formulas. In general, attempting to obtain these derivatives numerically is a questionable procedure and should be avoided if possible. Thus, the applicability of Alfrey's and Widder's methods to problems of this type appears limited.

Schapery's Direct Method and ter Haar's Method

The direct method of Schapery and the method of ter Haar, being the same except for the relation between p and t , can be considered as one. This method obviously possesses a simplicity that is highly desirable. The method can be applied directly by simply multiplying the value of the transformed function by p and evaluating the result at $p = a/t$. Application of the method introduces no error except that inherent in the method itself. It appears that of the methods considered in this paper, the methods of ter Haar and Schapery are easiest to apply for all problems.

Unfortunately, the methods are not applicable except when the function $p\bar{f}(p)$ is practically a linear function of $\log p$. If the functions vary rapidly with time, the methods can give some extremely poor results.¹² For many problems in solid propellant structural integrity analysis, the behavior of the time-dependent function is such that the method is applicable. This allows a determination of an approximate solution very conveniently. However, at any instant of time the answer may be in error, and there is no way to estimate the error involved. If care is exercised in applying the method only to applicable problems, good results can generally be obtained.

Schapery's Least-Squares Method

Schapery's least-squares method has been examined in detail elsewhere^{9, 18} and hence was not used to obtain the solution to a specific problem in this paper. The extension suggested by Schapery⁹ to obtain better results to the problem of approximately inverting the function $[p\bar{R}(p)/E_0]$ considered by Muki and Sternberg¹⁴ was made with satisfactory results. Eight terms were included in the time-dependent expression. The results are shown in Fig. 8 along with Schapery's direct method approximation, ter Haar's approximation, and the finite-difference solution of Lee and Rogers.¹⁹

The method is well founded mathematically, and the scheme for collocating the transformed curve gives good results.

Orthogonal Polynomial Inversion Methods

The Papoulis' and Lanczos' methods are essentially the same, and their limitations will be discussed together.

The methods appear to be ideally suited to the inversion of functions known only at discrete real values of the transform parameter p . Fitting the transformed series expansion to

the transformed function in the p plane at certain prescribed points allows the coefficients of the expansion to be determined very readily. Unfortunately, the majority of functions of interest in solid propellant structural integrity analysis vary very slowly with time so that the coefficients depend to a large extent on small differences between very large numbers. This leads to computational difficulties and requires the original data, i.e., values of the transformed function, to be known extremely accurately.

Examples of the type of error encountered are shown in Fig. 7 where it will be recalled that the values of the transformed function were obtained by reading values from a graph. From inspection of Fig. 7, it can be seen that the expansions oscillate about some mean value. The magnitude of the oscillation is dependent upon the magnitude of the error involved in the computation.

Illustration of the good approximations that can be made are seen in Fig. 6 where the curves for the various expansions are generally very smooth over their range of application. For $\gamma = 2.0$, the range of application, according to the criterion discussed earlier, i.e., $-2 < \log t < 0$, is $-2.301 < \log t < -0.301$. It can be seen that the expansion with $\gamma = 2.0$ accurately describes a curve in its range of application. It differs somewhat from the direct method approximation; however, it is not known which of the curves is in error.

Similarly, the expansions for $\gamma = 0.1$ and $\gamma = 0.01$ which apply over the intervals $-1 < \log t < +1$ and $0 < \log t < +2$, respectively, accurately describe the time-dependent function. In regions where the interval of application of two expansions overlap, the expansions seem to agree fairly closely. It can be seen that, by fairing in a curve through the expansion solutions for $\gamma = 2.0$, $\gamma = 0.1$, and $\gamma = 0.01$ in their appropriate intervals of applicability, the actual time-dependent behavior of the function may be determined. Presumably, better approximations could be obtained by including more terms in the series expansions.

The magnitude of the coefficients of the Legendre polynomials limits the number of terms which can be considered in the series solution suggested by Papoulis. Since only the even Legendre polynomials are used, the order of the polynomials used is almost double the number of terms considered, e.g., a six-term expansion involves the use of a tenth-order polynomial. Since the magnitude of the coefficients of the Legendre polynomials increase very rapidly and small differences between very large numbers are significant as discussed earlier, there exists a practical limit to the number of terms that can be considered with the current capacities of high-speed computers. For the results presented in this paper, the Legendre polynomial expansions were obtained using double-precision computational schemes. Single precision routines were not of sufficient accuracy to give meaningful results.

In order to investigate the effect of slight error in the values of the transformed function which are used as data for the orthogonal expansion, an analysis was made for a series of exponentials of the form

$$f(t) = \sum_{i=0}^5 e^{-2it} \quad (54)$$

Operating on this function with the Laplace transform with respect to time gives

$$\bar{f}(p) = \sum_{i=0}^5 \left(\frac{1}{p + 2i} \right) \quad (55)$$

Values of this function were computed for p values of 1, 3, 5, 7, and 9 and the results used as input data for obtaining an orthogonal function expansion using Papoulis' Legendre polynomial inversion method. The results of this computation are shown in Fig. 9 as a solid line.

To examine the effect of error, the data point corresponding to $p = 7$ was changed from the correct value of 3.8310344

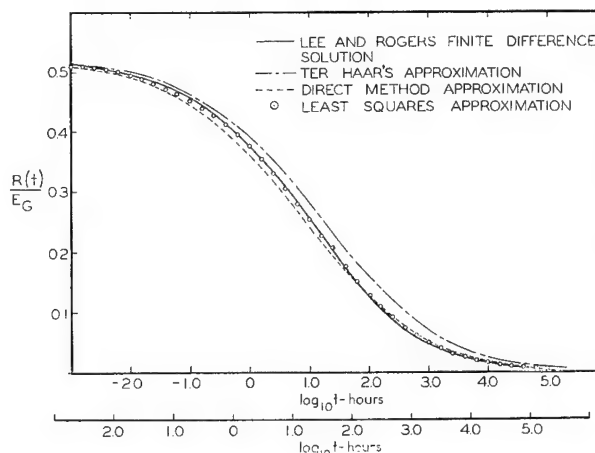


Fig. 8 Direct method, ter Haar's method, and eight term least-squares approximations for $R(t)/E_G$.

to 3.8348653, an error of 0.1%. The expansion was made in the same manner as before with the result shown by the dashed curve in Fig. 9. It can be seen that the method is extremely sensitive to errors in the original data, i.e., errors in values of the transformed function.

Conclusions

From the investigation conducted and results presented, several general conclusions can be drawn concerning the Laplace transform inversion methods discussed here.

In regard to Schapery's direct method and ter Haar's method, it appears that these methods, when applicable, will give a good description of the behavior of the time-dependent function. It is possible that the methods will give slight errors in magnitude at any instant of time. Also, the difference between the transform parameter p and time t is different for the two methods that result in the curves being slightly shifted from each other in the $\log t$ scale. Although Schapery's method for evaluating the relation between these parameters is more sophisticated than ter Haar's, ter Haar's method sometimes gives more accurate results.¹² In general, these methods provide a very quick and easy method for approximately inverting Laplace transforms, provided the functions are nearly linear in $\log t$. Large errors can occur if not.¹²

The methods of Widder which involve derivatives of successively higher orders appear to be of very limited use for approximately inverting functions known only numerically. The error involved with the use of numerical derivatives is sometimes great and hence makes the use of such methods highly questionable. If the method is applied to

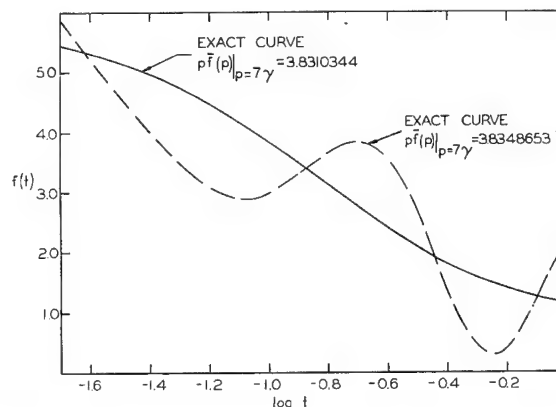


Fig. 9 Illustration of error sensitivity of Papoulis method.

Table 3 Coefficients of D_j in Eq. (A3) used in determining expression for Legendre polynomial series expansion

	D_0	D_1	D_2	D_3	D_4	D_5
B_0	1	0	0	0	0	0
B_1	-2.5	2.5	0	0	0	0
B_2	3.375	-11.25	7.875	0	0	0
B_3	-4.0625	28.4375	-51.1875	26.8125	0	0
B_4	4.6484375	-55.78125	184.078125	-227.90625	94.960903	0
B_5	-5.1679688	+99.746094	-164.22656	1055.7422	-997.08984	344.44922

problems with complicated algebraic analytical solutions where the derivatives of the transformed function can be determined exactly, then the methods give good approximations.

The collocation method or least-squares method of Schapery appears to offer a very good method for inverting functions of interest in viscoelastic stress analysis of solid propellant rocket grains. Of all the methods considered, the least-squares method seems to possess the greatest potential.

The orthogonal polynomial inversion methods are mathematically well founded and appear to possess many desirable features. The main disadvantage of the method is the extreme sensitivity to error in the original data. If this disadvantage could be overcome, the methods could be used to refine an answer to any degree of accuracy desired. In their present form, however, use of the methods appears limited.

By using a combination of the methods described in this paper, reliable results can be obtained to the problem of approximately inverting functions known only numerically for discrete values of the transform parameter. If accuracy of the magnitude being demanded in the representation of viscoelastic material property data is desired, only the orthogonal polynomial methods and Schapery's least-squares method possess the potential for accomplishing the inversion with this accuracy. The orthogonal polynomial methods appear limited by their sensitivity to error, but if this could be overcome, the results could be refined to any degree of accuracy desired.

Appendix: Simplified Form of Legendre Polynomial Inversion Method

The method of approximate Laplace transform inversion based upon properties of Legendre polynomials and described by Papoulis has been further simplified for the case of a six-term expansion. The simplification was made with the intention of programing the method for operation on a digital computer. Included in this Appendix is an expression for the time-dependent function in terms of values of the function $p\bar{f}(p)$, where $\bar{f}(p)$ is the Laplace transform of the time-dependent function of interest $f(t)$. The expression is presented in such a manner that errors due to rounding off are kept to a minimum. The expression for $f(t)$ is

$$f(t) = \left[B_0 - \frac{B_1}{2} + \frac{3}{8} B_2 - \frac{5}{16} B_3 + \frac{35}{128} B_4 - \frac{81}{256} B_5 \right] + \frac{3}{2} \left[B_1 - \frac{5}{2} B_2 + \frac{35}{8} B_3 + \frac{85}{16} B_4 + \frac{935}{128} B_5 \right] e^{-2\gamma t} + \frac{35}{8} \left[B_2 - \frac{9}{2} B_3 + \frac{99}{8} B_4 - \frac{429}{16} B_5 \right] e^{-4\gamma t} + \frac{231}{16} \left[B_3 - \frac{13}{2} B_4 + \frac{195}{8} B_5 \right] e^{-6\gamma t} + \frac{6435}{128} \left[B_4 - \frac{17}{2} B_5 \right] e^{-8\gamma t} + \frac{46189}{256} B_5 e^{-10\gamma t} \quad (A1)$$

where the B_i are given in terms of the values of $p\bar{f}(p)$ in Table 3. The D_i referred to in the table correspond to data points and are defined as

$$D_i = p\bar{f}(p)|_{p=[2i+1]\gamma} \quad (i = 0, 1, \dots, 5) \quad (A2)$$

The values given in the table are the coefficients α_{ij} of the D_i where the B_i are expressed as

$$B_i = \sum_{j=0}^5 \alpha_{ij} D_j \quad (A3)$$

Equation (A1) was programed for the IBM 7090 digital computer and the program used to obtain the polynomial expansion results included in this paper. Equation (A1) may be used with less than six terms by simply neglecting the B_i , which correspond to the terms to be neglected.

References

- Alfrey, T., "Non-homogeneous stress in viscoelastic media," *Quart. Appl. Math.* **2**, 113-119 (1944).
- Read, W. T., "Stress analysis for compressible viscoelastic materials," *J. Appl. Phys.* **21**, 671-674 (1950).
- Lee, E. H., "Stress analysis in viscoelastic bodies," *J. Appl. Mech.* **13**, 183-190 (1955).
- Hilton, H. H., "An introduction to viscoelastic analysis," Univ. of Illinois, Dept. of Aeronautical Astronautical Engineering TR AAE 62-1 (1962).
- Parr, C. H., "Deformations and stresses in case-bonded solid propellant grains of finite-length by numerical methods," Rohm & Haas Co., *Quart. Progr. Rept. on Engineering Research*, Rept. P-61-17 (June 1962).
- Widder, D. V., *The Laplace Transform* (Princeton University Press, Princeton, N. J., 1946).
- Post, E. L., "Generalized differentiation," *Trans. Am. Math. Soc.* **32**, 723-781 (1930).
- ter Haar, D., "An easy approximate method of determining the relaxation spectrum of a viscoelastic material," *J. Polymer Sci.* **6**, 247 (1951).
- Schapery, R. A., "Approximate methods of transform inversion for viscoelastic stress analysis," *Proceedings of the Fourth U. S. National Congress of Applied Mechanics* (1961), pp. 1075-1085.
- Papoulis, A., "A new method of inversion of the Laplace transform," *Quart. Appl. Math.* **14**, 405-414 (1957).
- Lanczos, C., *Applied Analysis* (Prentice Hall, Inc., Englewood Cliffs, N. J., 1961), pp. 280-299.
- Cost, T. L., "Approximate Laplace transform inversion techniques in viscoelastic stress analysis," Rohm & Haas Co., *Quart. Progr. Rept. on Engineering Research*, Rept. P-63-13 (July 1963).
- Schapery, R. A., "Two simple approximate methods of Laplace transform inversion for viscoelastic stress analysis," Graduate Aeronautical Labs. California Institute of Technology Rept. SM 61-23 (1961).
- Muki, R. and Sternberg, E., "On transient thermal stresses in viscoelastic materials with temperature dependent properties," *J. Appl. Mech.* **28**, 193-207 (1961).
- Lianis, G., "Stresses and strains in solid propellants during storage," *ARS J.* **32**, 688-692 (1962).
- Gillis, G. F., "Elastic stresses and displacements induced in solid propellant rocket motors by transverse gravity forces," Rohm & Haas Co., *Quart. Progr. Rept. on Engineering Research*, Rept. P-62-13 (July 1962).
- Sackman, J. L., "Steady creep of a nonhomogeneous beam," *J. Aerospace Sci.* **28**, 1015 (1962).
- Cost, T. L., "Approximate Laplace transform inversions in solid propellant structural integrity analysis," Addendum to Bull. of Second Ann. Meeting of ICRPG Working Group on Mechanical Behavior, CPIA Publ. 27-A, 127 (1964).
- Lee, E. H. and Rogers, T. G., "Solution of viscoelastic stress analysis problems using measured creep or relaxation functions," *J. Appl. Mech.* **30**, 127-133 (1963).

Influence Coefficients of a Circular Cylindrical Shell with Rapidly Varying Parabolic Wall Thickness

DAVID BUSHNELL*

Lockheed Missiles and Space Company, Sunnyvale, Calif.

AND

NICHOLAS J. HOFF†

Stanford University, Stanford, Calif.

A closed-form solution is given of the differential equation defining the axisymmetric deformations of a circular cylindrical shell with parabolically varying wall thickness, and the 16 influence coefficients connecting the deformations and the stress resultants acting in the end sections of a shell of finite length are presented in tabular form. A numerical example shows that the maximal stresses calculated with the aid of these influence coefficients can in some cases differ significantly from those obtained when the stress analysis is carried out in the usual manner, that is, with the aid of the influence coefficients of the shell of uniform wall thickness.

1. Introduction

A COMMON structure in the missile industry is the circular cylindrical shell whose wall thickness is constant. This shell supports the various loads imposed upon it principally by means of membrane stresses that are constant through the wall thickness. However, in many structural applications, it is necessary to join the cylinder to a shell of unequal radius of curvature or to a rigid bulkhead. Within a distance or boundary layer whose length from the juncture is of order

$$l = (ah_0)^{1/2} \quad (1.1)$$

where a is the radius and h_0 is the thickness of the shell, significant bending stresses and local variations of the membrane stresses arise; these are usually called discontinuity stresses. To strengthen the structure in this region, the wall thickness is often increased locally. The effect of this strengthening is generally not taken into account in the analysis of the stresses, because influence coefficients for finite-length circular cylindrical shells with rapidly varying wall thickness have not been calculated and tabulated. The purpose of the present paper is to help eliminate this inconsistency from the analysis through the development of a closed-form solution of the governing equation for shells with parabolically varying wall thickness and the tabulation of influence coefficients of cylindrical shells whose wall thickness varies considerably within the characteristic length (1.1).

Various authors have considered rotationally symmetric shells with variable wall thickness. Timoshenko¹ and Flügge² investigated a dome loaded by its own weight. They calculated the shape of the meridian such that the membrane stresses are constant everywhere and showed that for such a dome the thickness of the wall varies exponentially. De Silva and Naghdi³ examined a class of shells of revolution whose wall thickness varies in such a

way that the two governing differential equations of the problem (moment equilibrium and compatibility) can be combined into a single second-order complex differential equation and solved by a method of asymptotic integration. Honegger⁴ solved the problem of a conical shell with linearly varying wall thickness.

Many papers have been written on the circular cylindrical shell with variable wall thickness. Reissner and Sladd⁵ determined the upper and lower bounds of the influence coefficients of shells with arbitrarily varying thickness by application of the minimal principles of elasticity. They investigated the special case of a semi-infinite cylinder with exponentially varying thickness. C. R. Steele,⁶ in some unpublished calculations, found the exact solution of the equation of equilibrium of such a shell and showed that the exact values of the influence coefficients are about midway between the upper and lower bounds. Meissner⁷ analyzed a cylindrical shell whose wall thickness varies linearly, and Timoshenko¹ and Flügge² computed the discontinuity stresses in such shells where the thickness varies slowly enough that the effect of moments and transverse shear forces applied at one end is not felt at the other end. Federhofer⁸ considered the case of parabolically varying wall thickness and solved the problem of a liquid-filled tank whose upper boundary is free and whose lower boundary is clamped. The wall thickness varies along the entire length of the tank. He also calculated stresses and displacements in such a tank loaded axisymmetrically along its lower boundary by a moment or a shear force. However, he did not develop closed-form expressions for the influence coefficients, as is done here.

Esslinger⁹ derived influence coefficients for a finite-length cylindrical shell of constant thickness. These quantities are rederived herein in a different form that allows them to be easily compared to the influence coefficients of a cylindrical shell with parabolically varying wall thickness.

Sladd¹⁰ derived influence coefficients for circular cylindrical shells with linearly varying wall thickness.

In this paper, the influence coefficients of a finite circular cylindrical shell whose wall thickness varies rapidly and quadratically are obtained in closed form, and these influence coefficients are employed to find the discontinuity stresses in a cylindrical shell thickened only in the boundary region near the clamped edge at the bottom.

Received March 9, 1964; revision received June 19, 1964.

The work here presented is part of a thesis submitted to Stanford University in partial fulfillment of the requirements for the Ph.D. degree.

* Graduate Study Engineer/Scientist.

† Head, Department of Aeronautics and Astronautics. Fellow Member AIAA.

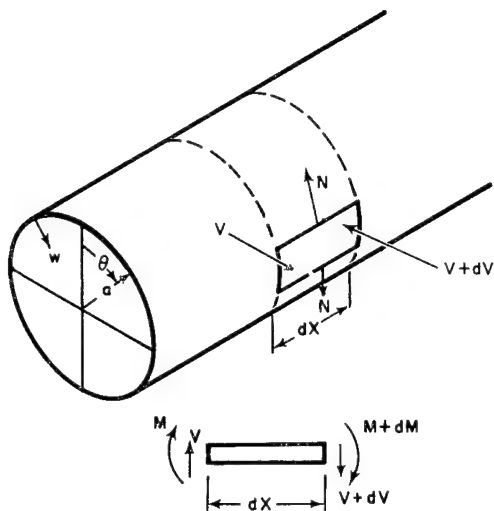


Fig. 1 Sign convention.

2. Differential Equation of Equilibrium and Solution

The equation of equilibrium of a circular cylindrical shell that deforms symmetrically to its axis is given by Timoshenko¹ as

$$\frac{d^2}{dx^2} \left(D \frac{d^2 w}{dx^2} \right) + \frac{Eh}{a^2} w = 0 \quad (2.1)$$

where D is the flexural rigidity

$$D = Eh^3/12(1 - \nu^2) \quad (2.2)$$

The sign convention for the stress and displacement quantities is shown in Fig. 1. The following nondimensional quantities will be introduced in this equation:

$$H = h/h_0 \quad \xi = x/x_1 \quad \delta = w/a \quad (2.3)$$

Here h_0 is the thickness of the shell at $x = x_1$, that is, at $\xi = 1$ (see Fig. 2).

The thickness of the shell is assumed to vary parabolically:

$$H = b\xi^2 \quad (2.4)$$

Since $h = h_0$ at $x = x_1$, the constant b must be equal to unity. Substitution from Eqs. (2.3) and (2.4) into Eq. (2.1) gives

$$(\xi^5 \delta'')'' + 4c^4 \xi^2 \delta = 0 \quad (2.5)$$

where

$$\begin{aligned} ()' &\equiv d()/d\xi & c &\equiv \tau x_1/a \\ \tau &\equiv [3(1 - \nu^2)(a/h_0)^2]^{1/4} \end{aligned} \quad (2.6)$$

The solution of Eq. (2.5) has the form

$$\delta = \xi^p \quad (2.7)$$

which yields the characteristic equation

$$p(p-1)(p+3)(p+4) + 4c^4 = 0 \quad (2.8)$$

Substitution of the new variable

$$q = p + \frac{3}{2} \quad (2.9)$$

leads to

$$(q^2 - \frac{9}{4})(q^2 - \frac{25}{4}) + 4c^4 = 0 \quad (2.10)$$

The four solutions of Eq. (2.10) are

$$q = \pm \alpha \pm i\beta \quad (2.11)$$

where

$$\alpha = \left[\frac{(15^2 + 8^2 c^4)^{1/2} + 17}{8} \right]^{1/2} \quad (2.12)$$

$$\beta = \left[\frac{(15^2 + 8^2 c^4)^{1/2} - 17}{8} \right]^{1/2} \quad (2.13)$$

If c is greater than unity, the quantities α and β are both real. If c is equal to unity, β is equal to zero, and the characteristic equation (2.10) has only two distinct roots. If c is less than unity, β is imaginary, and Eq. (2.10) has four distinct real roots. If $c \neq 1$ the roots of Eq. (2.8) are

$$p_j = -\frac{3}{2} \pm \alpha \pm i\beta \quad (2.14)$$

and the general solution of Eq. (2.5) becomes

$$\delta = \sum_{j=1}^4 A_j^* \xi^{p_j} \quad (2.15)$$

Equation (2.15) has four arbitrary constants A_j^* . These are determined from boundary conditions at x_1 and x_2 (see Fig. 2). The unique solution of Eq. (2.5) corresponding to particular boundary conditions is found more easily if Eq. (2.15) is written in the form

$$\delta = \xi^{-3/2} [A \sin \theta \sinh \phi + B \sin \theta \cosh \phi + C \cos \theta \sinh \phi + D \cos \theta \cosh \phi] \quad (2.16)$$

where

$$\theta \equiv \beta \log \xi \quad \phi \equiv \alpha \log \xi \quad (2.16a)$$

If $c = 1$, the general solution of Eq. (2.5) is

$$\delta = \xi^{-3/2} [A_1 \xi^{\sqrt{17}/2} + A_2 \xi^{-\sqrt{17}/2} + A_3 (\log \xi) \xi^{\sqrt{17}/2} + A_4 (\log \xi) \xi^{-\sqrt{17}/2}] \quad (2.17)$$

The influence coefficients will be calculated assuming that $c \neq 1$. The values for $c = 1$ may be obtained from these by allowing β to approach zero in Eqs. (3.22) to (3.31).

3. Calculation of Influence Coefficients

The moment distribution in the segment x_1 to x_2 can be calculated by substituting Eq. (2.16) in the expression

$$M = -\frac{D_0 a}{x_1^2} \xi^5 \delta'' \quad (3.1)$$

and the shear distribution can be calculated from

$$V = \frac{1}{x_1} (M)' = -\frac{D_0 a}{x_1^3} (\xi^5 \delta'')' \quad (3.2)$$

where

$$D_0 = \frac{Eh_0^3}{12(1 - \nu^2)} \quad (3.3)$$

Differentiation of Eq. (2.16) and substitution into Eq. (3.1) and Eq. (3.2) gives

$$M = (-D_0 a/x_1^2) \xi^{5/2} [A' \sin \theta \sinh \phi + B' \sin \theta \cosh \phi + C' \cos \theta \sinh \phi + D' \cos \theta \cosh \phi] \quad (3.4)$$

$$V = (-D_0 a/x_1^3) \xi^{3/2} [(\alpha B' - \beta C') \sin \theta \sinh \phi + (\alpha A' - \beta D') \sin \theta \cosh \phi + (\beta A' + \alpha D') \cos \theta \sinh \phi + (\beta B' + \alpha C') \cos \theta \cosh \phi] + \frac{5}{2} M / \xi x_1 \quad (3.5)$$

The integration constants A' , B' , C' , and D' are linear combinations of A , B , C , and D . The boundary conditions at $x = x_1$, that is at $\xi = 1$, yield

$$D' = -(x_1^2/D_0 a) M_1 \quad (3.6)$$

$$\beta B' + \alpha C' = -\frac{x_1^3}{D_0 a} \left(V_1 - \frac{5}{2} \frac{M_1}{x_1} \right) \quad (3.7)$$

The boundary conditions at $x = x_2$, that is at $\xi = x_2/x_1$, give

$$A' \sin \theta_2 \sinh \phi_2 + B' \sin \theta_2 \cosh \phi_2 + C' \cos \theta_2 \sinh \phi_2 + D' \cos \theta_2 \cosh \phi_2 = -\frac{a}{D_0} \left(\frac{x_1}{a} \right)^2 \left(\frac{x_1}{x_2} \right)^{5/2} M_2 \quad (3.8)$$

$$\begin{aligned} & (\alpha B' - \beta C') \sin \theta_2 \sinh \phi_2 + (\alpha A' - \beta D') \sin \theta_2 \cosh \phi_2 + \\ & (\beta A' + \alpha D') \cos \theta_2 \sinh \phi_2 + (\beta B' + \alpha C') \cos \theta_2 \cosh \phi_2 = \\ & -\frac{a^2}{D_0} \left(\frac{x_1}{a} \right)^3 \left(\frac{x_1}{x_2} \right)^{3/2} \left(V_2 - \frac{5}{2} \frac{M_2}{x_2} \right) \end{aligned} \quad (3.9)$$

where

$$\theta_2 \equiv \beta \log(x_2/x_1) \quad \phi_2 \equiv \alpha \log(x_2/x_1) \quad (3.10)$$

The four equations, i.e., Eqs. (3.6-3.9), can be solved for A', B', C', D' :

$$\begin{aligned} A' = \frac{a}{D_0} \left(\frac{x_1}{a} \right)^2 \frac{1}{\Delta} \left\{ M_1 \left[-\alpha \beta (\sin^2 \theta_2 + \sinh^2 \phi_2) + \right. \right. \\ \left. \left. \frac{5}{2} \beta \sinh \phi_2 \cosh \phi_2 - \frac{5}{2} \alpha \sin \theta_2 \cos \theta_2 \right] + \right. \\ \left. V_1 x_1 [-\beta \sinh \phi_2 \cosh \phi_2 + \alpha \sin \theta_2 \cos \theta_2] + \right. \\ \left. M_2 \left(\frac{x_1}{x_2} \right)^{5/2} \left[(\alpha^2 + \beta^2) \sin \theta_2 \sinh \phi_2 + \frac{5}{2} \alpha \sin \theta_2 \cosh \phi_2 - \right. \right. \\ \left. \left. \frac{5}{2} \beta \cos \theta_2 \sinh \phi_2 \right] + V_2 x_1 \left(\frac{x_1}{x_2} \right)^{3/2} [-\alpha \sin \theta_2 \cosh \phi_2 + \right. \\ \left. \left. \beta \cos \theta_2 \sinh \phi_2] \right\} \end{aligned} \quad (3.11)$$

$$\begin{aligned} B' = \frac{a}{D_0} \left(\frac{x_1}{a} \right)^2 \frac{1}{\Delta} \left\{ M_1 \left[\alpha^2 \sin \theta_2 \cos \theta_2 + \alpha \beta \sinh \phi_2 \cosh \phi_2 - \right. \right. \\ \left. \left. \frac{5}{2} \beta \sinh^2 \phi_2 \right] + V_1 x_1 [\beta \sinh^2 \phi_2] + \right. \\ \left. M_2 \left(\frac{x_1}{x_2} \right)^{5/2} \left[-\alpha^2 \sin \theta_2 \cosh \phi_2 - \alpha \beta \cos \theta_2 \sinh \phi_2 - \right. \right. \\ \left. \left. \frac{5}{2} \alpha \sin \theta_2 \sinh \phi_2 \right] + V_2 x_1 \left(\frac{x_1}{x_2} \right)^{3/2} [\alpha \sin \theta_2 \sinh \phi_2] \right\} \end{aligned} \quad (3.12)$$

$$C' = \frac{1}{\alpha} \left[-\frac{a^2}{D_0} \left(\frac{x_1}{a} \right)^3 \left(V_1 - \frac{5}{2} \frac{M_1}{x_1} \right) - \beta B' \right] \quad (3.13)$$

$$D' = -(a/D_0)(x_1/a)^2 M_1 \quad (3.6')$$

where

$$\Delta \equiv \alpha^2 \sin^2 \theta_2 - \beta^2 \sinh^2 \phi_2 \quad (3.14)$$

The original constants, A, B, C , and D , in Eq. (2.16) can be written in terms of A', B', C', D' in the following manner:

$$A = (1/b)(4A' + 2\alpha B' - 2\beta C' - \alpha \beta D') \quad (3.15)$$

$$B = (1/b)(2\alpha A' + 4B' - \alpha \beta C' - 2\beta D') \quad (3.16)$$

$$C = (1/b)(2\beta A' + \alpha \beta B' + 4C' + 2\alpha D') \quad (3.17)$$

$$D = (1/b)(\alpha \beta A' + 2\beta B' + 2\alpha C' + 4D') \quad (3.18)$$

where

$$b = 2(\beta^2 + 4)(4 - \alpha^2) \quad (3.19)$$

The 16 influence coefficients for displacements and rotations at x_1 and x_2 are found by substituting the expressions derived for A, B, C, D in Eq. (2.16) and its derivatives evaluated at

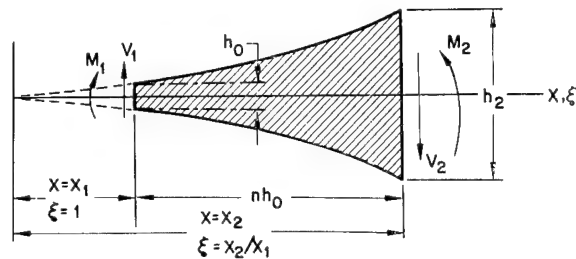


Fig. 2 Longitudinal section through wall with boundary moments and shear forces.

$\xi = 1$ and $\xi = x_2/x_1$. These displacements and rotations can be written as

$$\begin{Bmatrix} w_1 \\ \chi_1 \\ w_2 \\ \chi_2 \end{Bmatrix} = \begin{Bmatrix} C_{11} & C_{12} & C_{13} & C_{14} \\ C_{21} & C_{22} & C_{23} & C_{24} \\ C_{31} & C_{32} & C_{33} & C_{34} \\ C_{41} & C_{42} & C_{43} & C_{44} \end{Bmatrix} \begin{Bmatrix} V_1 \\ M_1 \\ V_2 \\ M_2 \end{Bmatrix} \quad (3.20)$$

where

$$\chi_1 = \frac{dw}{dx} \Big|_{x_1} \quad \chi_2 = \frac{dw}{dx} \Big|_{x_2} \quad (3.21)$$

It is found that

$$C_{11} = \frac{a^3}{D_0 \tau^3} \frac{c^3}{b \Delta} \left\{ -2\alpha^2 \sin^2 \theta_2 + 2\beta^2 \sinh^2 \phi_2 + \alpha^2 \beta \sin \theta_2 \cos \theta_2 - \alpha \beta^2 \sinh \phi_2 \cosh \phi_2 \right\} \quad (3.22)$$

$$\begin{aligned} C_{12} = -C_{21} = \frac{a^2}{D_0 \tau^2} \frac{c^2}{b \Delta} \left\{ \alpha^2 (1 - \beta^2) \sin^2 \theta_2 - \right. \\ \left. \beta^2 (1 + \alpha^2) \sinh^2 \phi_2 + \frac{5}{2} \alpha \beta^2 \sinh \phi_2 \cosh \phi_2 - \right. \\ \left. \frac{5}{2} \alpha^2 \beta \sin \theta_2 \cos \theta_2 \right\} \end{aligned} \quad (3.23)$$

$$C_{13} = -C_{31} = \frac{a^3}{D_0 \tau^3} \left(\frac{x_1}{x_2} \right)^{3/2} \frac{c^3}{b \Delta} \left\{ \alpha \beta [\beta \cos \theta_2 \sinh \phi_2 - \alpha \sin \theta_2 \cosh \phi_2] \right\} \quad (3.24)$$

$$C_{14} = C_{41} = \frac{a^2}{D_0 \tau^2} \left(\frac{x_1}{x_2} \right)^{5/2} \frac{c^2}{b \Delta} \alpha \beta \left\{ (\alpha^2 + \beta^2) \sin \theta_2 \sinh \phi_2 - \frac{5}{2} \beta \cos \theta_2 \sinh \phi_2 + \frac{5}{2} \alpha \sin \theta_2 \cosh \phi_2 \right\} \quad (3.25)$$

$$\begin{aligned} C_{22} = \frac{a}{D_0 \tau} \frac{c}{b \Delta} \alpha \beta \left\{ -5\alpha \beta (\sin^2 \theta_2 + \sinh^2 \phi_2) + \right. \\ \left. \beta \left(\alpha^2 + \beta^2 + \frac{25}{4} \right) \sinh \phi_2 \cosh \phi_2 + \right. \\ \left. \alpha \left(\alpha^2 + \beta^2 - \frac{25}{4} \right) \sin \theta_2 \cos \theta_2 \right\} \end{aligned} \quad (3.26)$$

$$\begin{aligned} C_{23} = C_{32} = \frac{a^2}{D_0 \tau^2} \left(\frac{x_1}{x_2} \right)^{3/2} \frac{c^2}{b \Delta} \alpha \beta \left\{ (\alpha^2 + \beta^2) \sin \theta_2 \sinh \phi_2 + \right. \\ \left. \frac{5}{2} \beta \cos \theta_2 \sinh \phi_2 - \frac{5}{2} \alpha \sin \theta_2 \cosh \phi_2 \right\} \end{aligned} \quad (3.27)$$

$$\begin{aligned} C_{24} = -C_{42} = \frac{a}{D_0 \tau} \left(\frac{x_1}{x_2} \right)^{5/2} \frac{c}{b \Delta} \alpha \beta \times \\ \left\{ -\beta \left(\alpha^2 + \beta^2 + \frac{25}{4} \right) \cos \theta_2 \sinh \phi_2 - \right. \\ \left. \alpha \left(\alpha^2 + \beta^2 - \frac{25}{4} \right) \sin \theta_2 \cosh \phi_2 \right\} \end{aligned} \quad (3.28)$$

Table 1 Influence coefficients for constant-thickness wall

$\tau L/a$	$-C_{11}^*$	$-C_{12}^*$	$-C_{13}^*$	C_{14}^*	C_{22}^*	$-C_{24}^*$
0.15	6.667	66.668	3.333	66.666	888.946	888.871
0.20	5.000	37.502	2.500	37.499	375.075	374.975
0.25	4.000	24.003	2.000	23.998	192.093	191.968
0.30	3.334	16.671	1.666	16.664	111.223	111.073
0.40	2.501	9.383	1.250	9.370	47.024	46.824
0.50	2.001	6.013	0.999	5.992	24.186	23.936
0.60	1.669	4.186	0.832	4.156	14.112	13.812
0.80	1.255	2.377	0.621	2.324	6.156	5.757
1.00	1.009	1.552	0.493	1.469	3.370	2.873
2.00	0.569	0.567	0.200	0.268	1.076	0.155
4.00	0.500	0.501	-0.002	-0.028	1.002	-0.052
10.00	0.500	0.500	0.000	0.000	1.000	0.000
>20.00	0.500	0.500	0.000	0.000	1.000	0.000

$$C_{33} = \frac{a^3}{D_0 \tau^3} \left(\frac{x_1}{x_2} \right)^3 \frac{c^3}{b \Delta} \{ -2\alpha^2 \sin^2 \theta_2 + 2\beta^2 \sinh^2 \phi_2 - \alpha^2 \beta \sin \theta_2 \cos \theta_2 + \alpha \beta^2 \sinh \phi_2 \cosh \phi_2 \} \quad (3.29)$$

$$C_{34} = -C_{43} = \frac{a^2}{D_0 \tau^2} \left(\frac{x_1}{x_2} \right)^4 \frac{c^2}{b \Delta} \left\{ \alpha^2 (1 - \beta^2) \sin^2 \theta_2 - \beta^2 (1 + \alpha^2) \sinh^2 \phi_2 - \frac{5}{2} \alpha \beta^2 \sinh \phi_2 \cosh \phi_2 + \frac{5}{2} \alpha^2 \beta \sin \theta_2 \cos \theta_2 \right\} \quad (3.30)$$

$$C_{44} = \frac{a}{D_0 \tau} \left(\frac{x_1}{x_2} \right)^5 \frac{c}{b \Delta} \alpha \beta \left\{ -5\alpha \beta (\sin^2 \theta_2 + \sinh^2 \phi_2) - \beta \left(\alpha^2 + \beta^2 + \frac{25}{4} \right) \sinh \phi_2 \cosh \phi_2 - \alpha \left(\alpha^2 + \beta^2 - \frac{25}{4} \right) \sin \theta_2 \cos \theta_2 \right\} \quad (3.31)$$

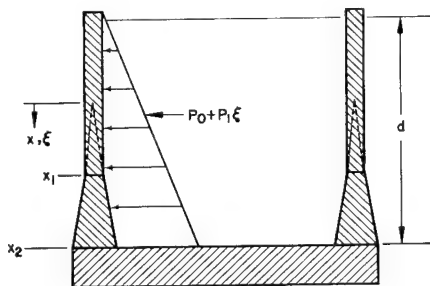
The quantities c , τ , D_0 , α , β , b , Δ , θ , and ϕ are given by Eqs. (2.6, 3.3, 2.12, 2.13, 3.19, 3.14, and 3.10), respectively. The influence coefficients for $c < 1$ are found by replacing β everywhere by $i\beta$. If β is allowed to approach zero, the influence coefficients for the case $c = 1$ result.

4. Influence Coefficients for Constant Wall Thickness

Expressions (3.22–3.31) are complicated indeed, and their derivation is rather tedious. They may be partially checked by comparing them with the influence coefficients for a finite-length cylindrical shell of constant thickness. These quantities can be derived from the solution of Eq. (2.1), where the coefficients D and Eh/a^2 are now constant. The general solution is

$$w = C_1 \sin(\tau x/a) \sinh(\tau x/a) + C_2 \sin(\tau x/a) \cosh(\tau x/a) + C_3 \cos(\tau x/a) \sinh(\tau x/a) + C_4 \cos(\tau x/a) \cosh(\tau x/a) \quad (4.1)$$

where τ is given by Eq. (2.6). The four constants of integration are evaluated as before in terms of the edge shear forces

**Fig. 3 Longitudinal section through cylindrical fuel tank attached to a rigid bulkhead.**

and moments, and the influence coefficients are defined as in Eqs. (3.20). The length of the shell is L . The 16 influence coefficients are

$$C_{11}' = \frac{a^3}{D_0 \tau^3} \frac{1}{2\Delta'} \left(\cosh \frac{\tau L}{a} \sinh \frac{\tau L}{a} - \sin \frac{\tau L}{a} \cos \frac{\tau L}{a} \right) = -C_{33}' \quad (4.2)$$

$$C_{12}' = \frac{a^2}{D_0 \tau^2} \frac{1}{2\Delta'} \left(\sinh^2 \frac{\tau L}{a} + \sin^2 \frac{\tau L}{a} \right) = -C_{21}' = C_{34}' = -C_{43}' \quad (4.3)$$

$$C_{13}' = \frac{a^3}{D_0 \tau^3} \frac{1}{2\Delta'} \left(\sin \frac{\tau L}{a} \cosh \frac{\tau L}{a} - \cos \frac{\tau L}{a} \sinh \frac{\tau L}{a} \right) = -C_{31}' \quad (4.4)$$

$$C_{14}' = \frac{a^2}{D_0 \tau^2} \frac{1}{\Delta'} \left(-\sin \frac{\tau L}{a} \sinh \frac{\tau L}{a} \right) = C_{41}' = C_{24}' = C_{32}' \quad (4.5)$$

$$C_{22}' = \frac{a}{D_0 \tau} \frac{1}{\Delta'} \left(-\cos \frac{\tau L}{a} \sin \frac{\tau L}{a} - \cosh \frac{\tau L}{a} \sinh \frac{\tau L}{a} \right) = -C_{44}' \quad (4.6)$$

$$C_{24}' = \frac{a}{D_0 \tau} \frac{1}{\Delta'} \left(\sin \frac{\tau L}{a} \cosh \frac{\tau L}{a} + \cos \frac{\tau L}{a} \sinh \frac{\tau L}{a} \right) = -C_{42}' \quad (4.7)$$

where

$$\Delta' \equiv \sin^2 \frac{\tau L}{a} - \sinh^2 \frac{\tau L}{a} \quad (4.8)$$

5. Influence Coefficients for Slowly Varying Wall Thickness

Equations (3.22–3.31) may be compared with Eqs. (4.2–4.7) for a shell whose wall thickness varies slowly. Let

$$h/h_0 = 1 \quad \text{at } x = x_1 \quad (5.1a)$$

$$h/h_0 = 1 + \epsilon \quad \text{at } x = x_2 \quad (5.1b)$$

$$x_2 - x_1 = L \quad (5.1c)$$

where ϵ is an arbitrarily small number. If

$$h/h_0 = \xi^2 \quad (2.4')$$

then from Eqs. (5.1a–5.1c),

$$x_2/x_1 = 1 + \frac{1}{2}\epsilon \quad (5.2)$$

and

$$\frac{x_1}{a} = \frac{2(L/a)}{\epsilon} (1 + O(\epsilon) + \dots) \quad (5.3)$$

From Eqs. (2.6, 2.12, and 2.13) it is seen that for small ϵ

$$\alpha = \beta = c = \frac{2\tau(L/a)}{\epsilon} (1 + O(\epsilon) + \dots) \gg 1 \quad (5.4)$$

The quantities (3.10) become

$$\theta_2 = \phi_2 = \frac{2\tau(L/a)}{\epsilon} (1 + O(\epsilon) + \dots) \log \left(1 + \frac{1}{2}\epsilon + \dots \right) = \tau L/a (1 + O(\epsilon) + \dots) \quad (5.5)$$

If Eqs. (5.3–5.5) are substituted into Eqs. (3.22–3.31) and ϵ is allowed to approach zero, the influence coefficients of a shell with parabolic thickness variation approach those for constant thickness [Eqs. (4.2–4.7)].

Dimensionless forms of the influence coefficients for constant thickness are listed in Table 1. They are functions of one parameter $\tau L/a$. Dimensionless forms of the C_{ij} for

parabolic thickness variation are listed in Table 2. They are functions of two parameters, h_2/h_0 and c . The quantity h_2/h_0 is the ratio of the thicknesses at x_2 and x_1 , respectively, and c is given by (2.6). In both tables, the C_{ij} can be expressed in terms of the dimensionless quantities C_{ij}^* by the following formulas:

$$C_{ij} = C_{ij}^*(a^3/D_0\tau^3) \text{ when } i \text{ and } j \text{ are odd}$$

$$C_{ij} = C_{ij}^*(a^2/D_0\tau^2) \text{ when one subscript is odd and the}$$

$$\text{other is even} \quad (5.6)$$

$$C_{ij} = C_{ij}^*(a/D_0\tau) \text{ when } i \text{ and } j \text{ are even}$$

Table 2 covers all cases of practical interest. If the thickness varies parabolically from h_0 to h_2 within the characteristic length $(ah_0)^{1/2}$, the parameter c satisfies the inequality

$$c \leq \frac{[3(1-\nu^2)]^{1/4}}{(h_2/h_0)^{1/2} - 1} \quad (5.7)$$

For the cases tabulated, the maximum value of c with the constraint (5.7) is $c = 3.14$ (Poisson's ratio = 0.3). If c is greater than the right-hand side of Eq. (5.7), the thickness variation is relatively slow, and the influence coefficients approach the appropriate values for a semi-infinite shell of constant thickness. If c is very small and h_2/h_0 is fairly large, the Kirchhoff-Love hypothesis (plane sections remain plane) may not be valid, thereby invalidating the governing equation (2.1). In this regard, the influence coefficients listed under $h_2/h_0 = 4$, $c = 0.15$ can be used only for very thin shells. For example, suppose $h_2/h_0 = 4$, $c = 0.15$, and a/h_0

= 100. Substitution of these numbers into Eqs. (2.4) and (2.6) with simple algebraic manipulations leads to

$$x_2 - x_1 = 1.16h_0 \quad (5.8)$$

Equation (5.8) states that in a distance approximately equal to the initial thickness of the shell, the wall thickness is quadrupled. Equation (2.1) is obviously not valid for such a rapid variation. On the other hand, if $a/h_0 = 2500$,

$$x_2 - x_1 = 29h_0 \quad (5.9)$$

The thickness quadruples over a distance of 29 times the initial thickness and the Kirchhoff-Love hypothesis is, therefore, realistic.

6. Discontinuity Stresses in a Cylindrical Fuel Tank

In a large fuel tank for a missile, discontinuity stresses at a juncture may design the thickness of the wall there. Considerable weight can be saved if the wall is thickened locally in such a way that a minimum amount of material added reduces the discontinuity stresses below some design level. The quantities n and h_2 (see Fig. 2) should be established for a shell of given a/h_0 such that the weight and stress requirements are satisfied. In the following analysis, the discontinuity stresses in a cylindrical fuel tank that is attached to a rigid bulkhead are calculated. Figure 3 shows such a tank filled with liquid to a depth d . The portion of the shell $x < x_1$ is of constant thickness and is assumed to be long compared to the characteristic length $(ah_0)^{1/2}$. It is joined at

Table 2 Influence coefficients for varying thickness

h_2/h_0	c	$-C_{11}^*$	$-C_{12}^*$	$-C_{13}^*$	C_{14}^*	C_{22}^*	C_{23}^*	$-C_{24}^*$	C_{33}^*	$-C_{34}^*$	$-C_{44}^*$
2	0.15	13.229	303.417	5.623	303.417	8773.120	241.674	8773.102	9.393	241.674	8773.110
	0.20	9.920	170.644	4.216	170.643	3700.554	135.919	3700.530	7.044	135.919	3700.540
	0.25	7.935	109.192	3.372	109.192	1894.356	86.972	1894.326	5.634	86.972	1894.338
	0.30	6.613	75.831	2.810	75.830	1096.319	60.399	1096.284	4.695	60.399	1096.298
	0.40	4.959	42.653	2.108	42.652	462.515	33.973	462.468	3.521	33.973	462.486
	0.50	3.967	27.299	1.686	27.297	236.836	21.742	236.777	2.817	21.743	236.800
	0.60	3.306	18.958	1.405	18.956	137.089	15.098	137.018	2.347	15.100	137.046
	0.80	2.480	10.666	1.054	10.662	57.889	8.492	57.795	1.761	8.494	57.832
	1.00	1.984	6.830	0.843	6.823	29.696	5.434	29.580	1.409	5.437	29.627
	2.00	0.995	1.727	0.420	1.699	3.900	1.352	3.664	0.705	1.366	3.757
	4.00	0.520	0.509	0.200	0.398	0.858	0.313	0.393	0.361	0.368	0.575
	6.00	0.404	0.361	0.109	0.133	0.704	0.098	0.047	0.261	0.209	0.297
	10.00	0.406	0.390	0.012	-0.005	0.790	-0.013	-0.033	0.214	0.161	0.230
	20.00	0.451	0.441	-0.000	0.000	0.885	0.001	0.001	0.195	0.142	0.201
	50.00	0.480	0.476	-0.000	0.000	0.952	-0.000	0.000	0.184	0.131	0.186
3	0.15	6.511	82.485	2.547	82.485	1279.206	57.980	1279.182	3.820	57.980	1279.188
	0.20	4.882	46.390	1.910	46.390	539.593	32.608	539.563	2.864	32.608	539.569
	0.25	3.905	29.685	1.527	29.684	276.242	20.865	276.204	2.291	20.866	276.212
	0.30	3.254	20.616	1.273	20.614	159.888	14.490	159.842	1.909	14.490	159.853
	0.40	2.441	11.597	0.955	11.595	67.487	8.150	67.426	1.432	8.151	67.440
	0.50	1.953	7.424	0.764	7.420	34.593	5.216	34.517	1.146	5.217	34.534
	0.60	1.627	5.158	0.636	5.152	20.062	3.621	19.970	0.955	3.623	19.991
	0.80	1.221	2.906	0.477	2.897	8.538	2.036	8.416	0.716	2.039	8.444
	1.00	0.978	1.867	0.381	1.852	4.452	1.301	4.299	0.573	1.306	4.334
	2.00	0.500	0.510	0.187	0.452	0.811	0.315	0.508	0.289	0.334	0.576
	4.00	0.325	0.282	0.070	0.077	0.581	0.046	0.015	0.159	0.111	0.135
	6.00	0.349	0.329	0.014	0.002	0.682	-0.008	-0.020	0.131	0.084	0.100
	10.00	0.405	0.389	-0.002	-0.002	0.787	-0.002	0.000	0.117	0.071	0.083
	20.00	0.451	0.441	0.000	0.000	0.885	-0.000	0.000	0.106	0.063	0.073
	50.00	0.480	0.476	0.000	0.000	0.952	0.000	0.000	0.100	0.058	0.067
4	0.15	4.263	38.961	1.581	38.961	427.827	25.210	427.801	2.200	25.210	427.805
	0.20	3.197	21.912	1.186	21.912	180.480	14.178	180.447	1.650	14.178	180.452
	0.25	2.557	14.022	0.946	14.021	92.412	9.072	92.370	1.320	9.072	92.376
	0.30	2.131	9.739	0.790	9.737	53.505	6.300	53.454	1.100	6.301	53.462
	0.40	1.598	5.479	0.593	5.476	22.614	3.543	22.546	0.825	3.544	22.557
	0.50	1.279	3.509	0.474	3.504	11.624	2.267	11.540	0.660	2.269	11.553
	0.60	1.066	2.440	0.395	2.433	6.775	1.574	6.674	0.550	1.576	6.689
	0.80	0.800	1.380	0.296	1.367	2.943	0.884	2.808	0.413	0.887	2.829
	1.00	0.642	0.893	0.236	0.873	1.598	0.564	1.430	0.330	0.569	1.455
	2.00	0.341	0.284	0.113	0.206	0.487	0.130	0.154	0.168	0.149	0.204
	4.00	0.292	0.266	0.029	0.020	0.573	0.004	-0.011	0.099	0.059	0.063
	6.00	0.348	0.330	-0.001	-0.004	0.680	-0.008	-0.007	0.085	0.047	0.049
	10.00	0.405	0.389	0.000	0.000	0.787	0.000	0.000	0.076	0.040	0.041
	20.00	0.451	0.441	0.000	0.000	0.885	0.000	0.000	0.069	0.035	0.036
	50.00	0.480	0.476	0.000	0.000	0.952	0.000	0.000	0.060	0.030	0.031

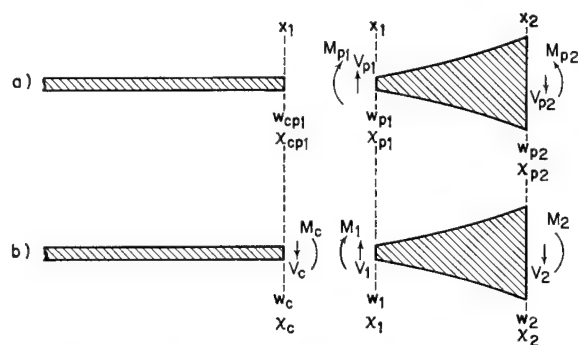


Fig. 4 a) Exploded longitudinal section through cylindrical tank showing moments and shear forces corresponding to particular solutions and b) additional moments and shear forces needed for compatibility at x_1 and x_2 .

$x = x_1$ to a short shell of parabolic thickness variation. The governing equation in the region $x_1 < x \leq x_2$ is

$$(\xi^2 \delta''')'' + 4c^4 \xi^2 \delta = 4c^4 (a/h_0) (1/E) (P_0 + P_1 \xi) \quad (6.1)$$

and in the region $x < x_1$ is

$$\delta_c'''' + 4c^4 \delta_c = 4c^4 (a/h_0) (1/E) (P_0 + P_1 \xi) \quad (6.2)$$

where

$$P_0 \equiv \gamma(x_2 - d) \quad P_1 \equiv -\gamma x_1 \quad (6.3)$$

The constant γ is the specific gravity of the liquid. The subscript c denotes constant thickness. The pressure is positive inward. The particular solutions of Eq. (6.1) and (6.2) are easily found to be, respectively,

$$\delta_p = \frac{c^4}{3 + c^4} \frac{a}{h_0} \frac{1}{E} (P_0 \xi^{-2} + P_1 \xi^{-1}) \quad (6.4)$$

$$\delta_{cp} = \frac{a}{h_0} \frac{1}{E} (P_0 + P_1 \xi) \quad (6.5)$$

The moment and shear distributions corresponding to the particular solutions of Eq. (6.1) and (6.2) are

$$M_p = -\frac{D_0 a}{x_1^2} \frac{c^4}{3 + c^4} \frac{a}{h_0} \frac{1}{E} (6P_0 \xi^2 + 2P_1 \xi^3) \quad (6.6)$$

$$V_p = \frac{-D_0 a}{x_1^3} \frac{c^4}{3 + c^4} \frac{a}{h_0} \frac{1}{E} (12P_0 \xi + 6P_1 \xi^2) \quad (6.7)$$

$$M_{cp} = 0 \quad (6.8)$$

$$V_{cp} = 0 \quad (6.9)$$

The particular solutions (6.4) and (6.5) and the corresponding moment and shear force (6.6) and (6.7) are shown in Fig. 4a. The displacement w is defined by Eq. (2.3). It is evident that the displacements, rotations, moments, and shears (6.4-6.9) are not compatible at x_1 , and that the boundary conditions $w = \chi = 0$ at x_2 are not satisfied. Figure

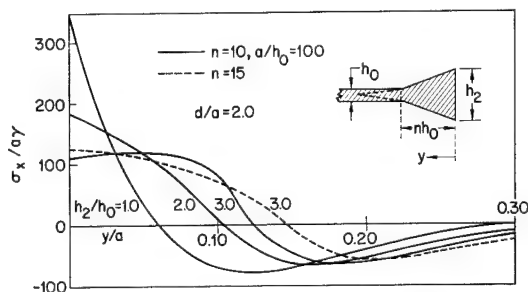


Fig. 5 Axial stress reduction due to thickening of the wall.

4b shows the moments and shears that must be introduced at x_1 and x_2 in order to satisfy all conditions. Geometric compatibility at x_1 demands that

$$c_{ep1} + w_c = w_{p1} + w_1 \quad (6.10)$$

$$\chi_{cp1} + \chi_c = \chi_{p1} + \chi_1 \quad (6.11)$$

Physical compatibility at x_1 demands that

$$M_c = M_{p1} + M_1 \quad (6.12)$$

$$V_c = V_{p1} + V_1 \quad (6.13)$$

The clamped edge condition at x_2 requires that

$$w_{p2} + w_2 = 0 \quad (6.14)$$

$$\chi_{p2} + \chi_2 = 0 \quad (6.15)$$

The deformation quantities w_1, χ_1, w_2 , and χ_2 are expressed in terms of M_1, V_1, M_2 , and V_2 by Eqs. (3.20), and w_c and χ_c are expressed in terms of M_c and V_c through the equations

$$\begin{Bmatrix} w_c \\ \chi_c \end{Bmatrix} = [\kappa_{ij}] \begin{Bmatrix} V_c \\ M_c \end{Bmatrix} \quad (6.16)$$

The κ_{ij} are the influence coefficients for a semi-infinite cylindrical shell with constant wall thickness:

$$\begin{aligned} \kappa_{11} &= \frac{1}{2} \frac{a^3}{D_0 \tau^3} & \kappa_{12} &= -\kappa_{21} = -\frac{1}{2} \frac{a^2}{D_0 \tau^2} \\ \kappa_{22} &= -\frac{a}{D_0 \tau} \end{aligned} \quad (6.17)$$

Now M_c, V_c, M_1, V_1, M_2 , and V_2 can be determined from the relations (6.10) to (6.15). The moment distribution in the region $x_1 < x < x_2$ due to M_1, V_1, M_2 , and V_2 is found with the help of Eqs. (3.6-3.9) and Eq. (3.4). The hoop stress distribution is calculated from

$$N = -Eh\delta = -Eh_0 \xi^2 \delta \quad (6.18)$$

where δ is given by Eq. (2.16). The resultant moment and hoop stress distributions in $x_1 < x < x_2$ are the sums of the distributions due to M_1, V_1, M_2 , and V_2 and those due to δ_p .

The moment and hoop stress distributions in the constant thickness region ($x < x_1$) are obtained from formulas in Timoshenko⁸ once M_c and V_c are known. The stresses at the outer fiber of the shell are computed from the moment and hoop resultants by means of

$$\sigma_x|_{-h/2} = 6M/h^2 \quad (6.19)$$

$$\sigma_\theta|_{-h/2} = N/h - \nu 6M/h^2 \quad (6.20)$$

Figures 5 and 6 demonstrate the effect of edge thickening on the discontinuity stresses (6.19) and (6.20). For various degrees of edge thickening, the axial and circumferential stress parameters $\sigma_x/a\gamma$ and $\sigma_\theta/a\gamma$ are plotted vs the non-dimensional distance from the edge y/a . These stresses are compared with the stresses generated in a similar shell

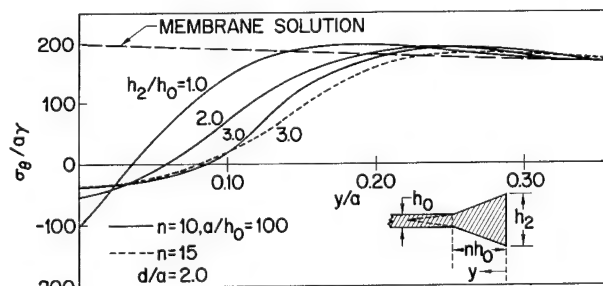


Fig. 6 Circumferential stress reduction due to thickening of the wall.

of constant thickness (lines labeled $h_2/h_0 = 1.0$). The depth of the liquid is equal to the diameter of the shell. For the case $a/h_0 = 100$, $n = 10$, and $h_2/h_0 = 3$, the maximum $\sigma_z/a\gamma$ is reduced from 350 to 120 (Fig. 5). This is indeed a significant reduction and demonstrates clearly that the influence coefficients given by Eqs. (3.22-3.31) must be used to obtain an accurate estimate of the maximum stress. The maximum $\sigma_\theta/a\gamma$ is reduced from 197 to 188 (Fig. 6). The effect of the thickening on $\sigma_{\theta \max}$ is small because the hoop stress builds up to its maximum away from edge where the shell thickness is constant.

In all the cases plotted, the maximum stress for the shells with the thickened edges is slightly higher than the membrane hoop stress due to the hydrostatic pressure.

References

- ¹ Timoshenko, S. P. and Woinowsky-Krieger, S., *Theory of Plates & Shells* (McGraw-Hill Book Co., Inc., New York, 1959), 2nd ed., Chap. 14, p. 442; Chap. 15, pp. 466-488.
- ² Flügge, W., *Stresses in Shells* (Springer-Verlag, Berlin, 1960), Chap. 2, p. 47; Chap. 5, p. 287.
- ³ DeSilva, C. N. and Naghdi, P. M., "Asymptotic solutions of a class of elastic shells of revolution with variable thickness," *Quart. Appl. Math.* **15**, 169-182 (1957).
- ⁴ Honegger, E., "Festigkeitsberechnung von Kegelschalen mit linear veränderlicher Wandstärke," *Diss. Luzern* (1919).
- ⁵ Reissner, E. and Sledd, M. B., "Bounds on influence coefficients for circular cylindrical shells," *J. Math. Phys.* **36**, 1-19 (1957).
- ⁶ Steele, C. R., unpublished calculations on cylindrical shells with exponentially varying wall thickness, Lockheed Missiles and Space Co., Palo Alto, Calif. (1964).
- ⁷ Meissner, E., "Beanspruchung und Formänderung zylindrischer Gefässe mit linear veränderlicher Wandstärke," *Vjschr. Naturforsch. Ges. Zurich* **62**, 153 (1917).
- ⁸ Federhofer, K., "Berechnung des kreiszylindrischen Flüssigkeitsbehälters mit quadratisch veränderlicher Wandstärke," *Öster. Ingr.-Arch* **6**, 43 (1951).
- ⁹ Esslinger, M., *Statische Berechnung von Kesselböden* (Springer-Verlag, Berlin, 1952), p. 45.
- ¹⁰ Sledd, M. B., "Influence coefficients for circular cylindrical shells with linearly varying wall thickness," Air Force Office of Scientific Research AFOSR TN-57-106, Armed Services Technical Information Agency Doc. 126491.

Influence of Work-Hardening on the Dynamic Stress-Strain Curves of 4340 Steel

BARRY M. BUTCHER* AND JACK R. CANON†
Sandia Corporation, Albuquerque, N. Mex.

The experimentally determined one-dimensional strain dynamic stress-strain curve of Rc54 hardness 4340 steel is shown to be in agreement with the uniaxial strain curve calculated from quasi-static properties. Strain-rate independent elastic-plastic theory including work-hardening was employed in the calculation. The agreement between theory and experiment shows that the stress-strain curve of fully hardened 4340 obtained at low strain rate, which indicates appreciable work-hardening, can be used to predict dynamic behavior. In contrast, the experimental data for Rc15- and Rc32-4340 steel showed strain-rate sensitivity. When these data are analyzed by the same procedure used for the fully hardened steel, a different stress-strain path is obtained for each peak stress level investigated. The results suggest that the observed large increase in flow stress with increase in strain rate is not limited to stress levels around the yield point but persists as long as the strain rate is high.

Introduction

THE determination of Hugoniot equations of state from shock-wave measurements has been reported by many investigators.¹⁻¹⁰ Many of these studies have utilized high explosives to produce shock waves with stresses in excess of 100 kbars.† Under these conditions, material rigidity contributes a relatively small amount to the observed stress, so that a strict hydrodynamic model of behavior has been applied with success to the compressive part of the loading cycle. Even at these stress levels, however, rigidity must be considered during unloading to accurately describe the attenuation of a stress pulse as it moves through the material.^{11, 12}

At stress levels of the same order of magnitude as the yield stress of the material, the effect of rigidity contributes significantly to all parts of the dynamic stress-strain curve. Fowles⁸ has analyzed the dynamic behavior of 2024 aluminum, in the precipitation hardened and annealed conditions, in this stress range by simple elastic-plastic theory. His results show that, within his experimental error, the plastic part of the experimentally determined dynamic stress-strain curve is offset from the hydrostat by $\frac{2}{3}Y_0$, where Y_0 is the static yield strength of the material. Similar results have been obtained for 6061-T6 aluminum by Lundergan and Herrmann.⁹ Work-hardening is not observed in either investigation because the flow stress Y of these alloys does not increase markedly with increase in strain; consequently, the experimentally determined stress-strain curves nearly parallel the hydrostats. In contrast, if a material exhibits pronounced work-hardening at small strains, the increase in flow stress Y must be reflected as an increasingly large offset of $\frac{2}{3}Y$ from the hydrostat for increasing strain.

This paper describes the experimental determination of the dynamic stress-strain curve of fully hardened 4340 steel, which exhibits considerable work-hardening in the strain range investigated. The curve is compared with the experimentally determined dynamic stress-strain curves of two softer conditions of 4340 steel which exhibit negligible work-hardening. A comparison is also made between the experi-

mentally determined dynamic stress-strain curves and dynamic curves predicted from the quasi-static properties of 4340. Of particular interest is the accuracy with which the plastic portion of the dynamic curve can be predicted from the results of a quasi-static (strain rates 10 to 10^{-3} in./in./sec) one-dimensional compressive stress test.

The possibility of a correlation between static and dynamic behavior assumes that the increase in flow stress with increased strain rate may be neglected (is of the order of the experimental error), or that the state of stress in the material is measured under the condition of low strain rate. Recent precise measurements by Barker, Lundergan, and Herrmann¹³ show that strain-rate effects do exist in 6061-T6 aluminum, a material that previously was thought to be "strain-rate independent." These effects were previously undetected because of the error in the measurement of dynamic response and the method of analysis of the resulting data. This suggests that, for many applications in which a state of one-dimensional strain exists, the precision of the work may not warrant inclusion of strain-rate effects.

Experimental Method and Analysis

The experimental work of this investigation concerned the generation of peak stresses from 10 to 55 kbar in 4340 steel of varying hardnesses. The steel was loaded symmetrically by impacting a flat target plate of uniform thickness with a flat projectile of the same material. Details of the air gun used to accelerate the projectiles to impact velocity are described elsewhere.⁹ The stress range corresponds to projectile velocities of 100 to 1000 fps.

The 4340 steel was originally in the form of $6\frac{1}{2}$ -in.-diam bar stock. This was cut into $\frac{1}{2}$ -in.-thick plates, some of which were reduced to 4 in. in diameter for use as projectile face plates. All plates were then heat treated according to the procedures of Table 1.

After heat treatment several $1\frac{1}{2}$ -in. by $\frac{1}{2}$ -in.-diam uniaxial compression specimens were ground to shape for quasi-static stress-strain determinations. The results of these tests are shown in Fig. 1. The remaining plates were then parallel ground and lapped flat enough to assure contact of all points of the impact surface within 0.01 μ sec. The flatness tolerance is therefore directly related to the proposed projectile velocity and ranges from 12×10^{-6} -in. deviation from plane over a 4-in.-diam area for a projectile velocity of 100 fps to ten times that for 1000 fps. The flatness was determined by an optical flat using a monochromatic light source.

Received February 28, 1964; revision received July 6, 1964. This work was supported by the U. S. Atomic Energy Commission.

* Staff Member.

† Staff Member; now Graduate Student, University of Illinois.

‡ 1 kbar = 14,504 psi; compressive stress and strain are taken as positive.

The projectile velocity, tilt, and free surface motion (see Fig. 2) were determined in the plate impact experiments. Tilt is defined as the angle between the face of the projectile and the impact surface of the target just prior to impact. If a perfect impact is not achieved, points on the free surface of the target opposite to points of first contact of impact begin to move first. A corresponding "tilt" in the free surface motion then occurs. Data obtained from different regions of the free surface must then be corrected for this effect before analysis is possible. The tilt in these experiments was always less than 0.05° . All observations of free surface motion were made prior to the arrival of the effects caused by the finite lateral geometry of the projectile, so that a state of one-dimensional strain existed with the principal stress parallel (σ_x) and perpendicular (σ_y, σ_z) to the direction of wave propagation ($\epsilon_y = \epsilon_z = 0$), and from symmetry $\sigma_y = \sigma_z$.

The instrumentation went through three states of refinement during the course of the investigation. The first procedure utilized a circumferential array of eight pins protruding at various lengths from the impact surface to measure tilt and projectile velocity. Electrical contact of these with the moving projectile were observed on an oscilloscope, and the motion of the projectile was deduced from the recorded trace. Similarly, an array of pins set various distances from the free surface were used to determine the distance-time history of the free surface by electrical contact time recordings. The pin settings were not close enough, however, to define the transition between the portions of the free surface motion due to the elastic and plastic parts of the incident wave; consequently, the data points defined two straight lines within experimental error. The first straight line segment was extrapolated to zero to get the arrival time of the elastic wave, and its intersection with the second line segment was taken as the arrival of the plastic wave. This information, the slope of the first line segment, and the projectile velocity measurement permitted calculation of the peak stress and strain in the material from the Hugoniot relations.³

The second measurement technique retained the eight pin array for the projectile velocity and tilt determinations. The innovation was a slant wire resistor for monitoring the free surface motion. This is a fine high-resistance wire, with a voltage across it, which is placed at a small angle to the free surface and progressively shorted out during the motion of the surface. The angle is small enough to assure that the velocity of the closeout point on the wire is supersonic so that the propagation of disturbances along the wire into portions that have not yet closed out does not occur. The change in voltage across the wire is recorded during closeout as a function of time and is then reduced to a distance-time history and corrected for tilt.

The present technique¹⁴ uses the slant wire to observe the free surface motion. A schematic of the experimental setup is shown in Fig. 2. The projectile velocity is measured to $\pm 0.3\%$ by determining the closure times of two adjacent pins of different lengths which project from the impact surface. The tilt is determined by four electrically isolated pins that are mounted in the target so that their tips are flush with the impact surface. This greatly increases the accuracy of their positioning and permits the use of very fast sweep speeds to record the closeout times. From this in-

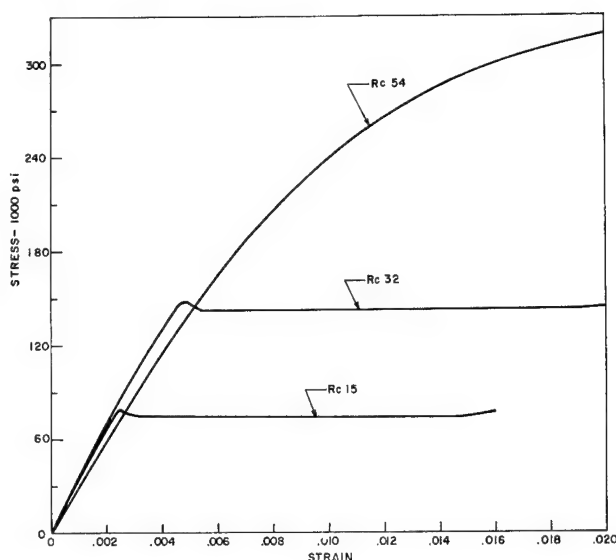


Fig. 1 Quasi-static stress-strain curves (one-dimensional stress) for 4340 steel.

formation, the angle between the projectile face and the target surface at impact may be calculated. The slant wire data are then corrected accordingly.

In the experiments in which the slant wires were used, three wires were mounted on each target. The final free surface displacement trace used for the analysis was a composite of the traces from all three wires. This was divided into as many straight line segments as necessary to give a good approximation of the curve. In most cases, four line segments were sufficient. An approximate dynamic stress-strain curve was then calculated^{15, 16} by estimating the shock velocities from the segment intersections (these define the time of arrival of each incremental stress pulse) and the material velocity changes from the slopes of adjacent segments. The approximation that the particle velocity change Δu is one-half the change in free surface velocity is generally made. The change in stress associated with each segment was then estimated as

$$\Delta \sigma_x = \rho_0 U_s \Delta u$$

where ρ_0 was taken as the initial density to facilitate calculation. The slope of the stress-strain curve associated with this increment was approximated by

$$\Delta \sigma_x / \Delta \epsilon_x = \rho_0 U_s^2$$

Starting with the first shock velocity-particle velocity pair, then, the complete dynamic stress-strain curve was constructed on the assumption of strain-rate independence. For some engineering calculations at low-stress levels this result is sufficient.

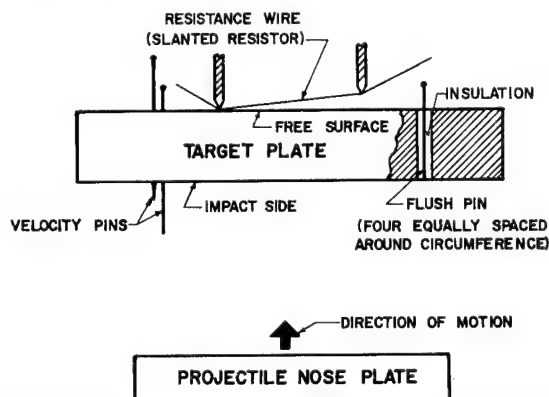


Fig. 2 Schematic diagram of the target instrumentation.

Table 1 Specimen heat-treatment procedures

Hardness	Heat treatment
Rc15	Packed in cast-iron chips, heated to 1450°F, and furnace cooled
Rc32	Heated in a salt bath to 1525°F, oil quenched, and reheated to 1050°F for 2 hr
Rc54	Heated in a salt bath to 1525°F and oil quenched

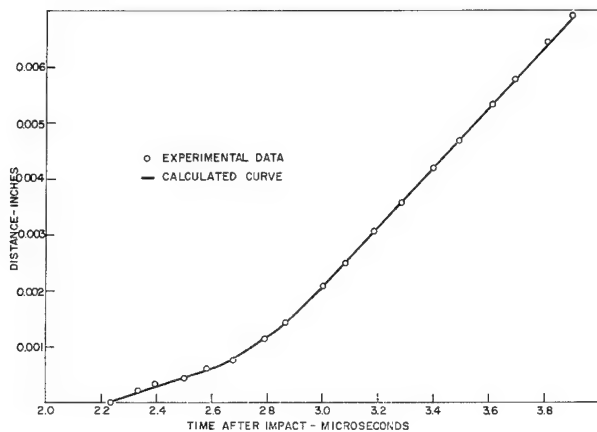


Fig. 3 Free surface distance-time plot for shot 26.

A refinement of this calculation is necessary, however, if the fine details of the dynamic stress-strain curve are to be deduced. The principle objections to the foregoing procedure are that change in density has not been considered, the particle velocity has been approximated, and the unloading by elastic rarefaction waves of the plastic part of the stress wave interacting with the free surface has been neglected. The latter occurs because of the faster propagation velocity of an elastic wave. The elastic wave reaches the free surface first and is reflected as a rarefaction wave moving back into the target. When this pulse meets oncoming plastic waves, the interaction is the same as the transmission and reflection of pulses at a boundary between two slightly dissimilar materials since the densities on each side of the interface are different. Consequently each interaction will have an effect on the free surface motion as the products of these interactions reach the free surface.

In principle, all these calculational refinements may be done by hand, but in practice, this is prohibitively tedious. Instead, the forementioned stress-strain curve estimate was used as the input to a computer program in which the method of characteristics and elastic-plastic strain-rate-independent theory were used to calculate the theoretical free surface motion.¹⁷ A 1604 CDC computer was used. The program determined all shock interactions with free surfaces and other shock waves and subsequently gave a complete stress-strain history for any desired point in the target or projectile. The calculated free surface motion was then compared with the experimental curve, and the dynamic stress-strain curve was altered, if necessary, to improve the agreement. An example of the final result is shown in Fig. 3.[§] Numerical results are summarized in Table 2.

Two aspects of the foregoing procedure merit further discussion. The first concerns the assumed path for unloading from the maximum compressive stress produced in the target. In this analysis, the stress-strain curve is taken to be anti-symmetric with respect to the strain axis. If a Bauschinger effect is absent,¹⁶ unloading is completely elastic except for the highest stress states of the Rc15, Rc32, and Rc54 steel. Consequently, there is a minimum of work-hardening during the release of the compressive stress. There is no simple way currently available for predicting the change in flow stress with strain after the reverse yield stress is reached. The error introduced by neglecting this, as well as a Bauschinger effect, is estimated to be small. This assertion is based on a series of calculations with the forementioned program in which small perturbations in the unloading path, such as

Table 2 Dynamic stress-strain coordinates for the stress-strain curves of 4340 steel^a

Hardness	Shot	Stress-kbar/strain			
Rc15	21	19.1	37.4	49.5	57.4
		0.0069	0.0165	0.0239	0.0295
	26	16.8	23.2	34.2	40.8
		0.0062	0.0095	0.0161	0.0211
Rc32	13	19.6	24.7	43.2	56.7
		0.0076	0.0100	0.0205	0.0293
	22	20.3	28.4	54.9	58.8
		0.0073	0.0112	0.0259	0.0287
	25	15.8	21.6	33.5	38.2
		0.0059	0.0085	0.0150	0.0182
	27	13.6
		0.0051
Rc54	12	24.0	35.7	44.7	...
		0.0089	0.0137	0.0180	...
	15	14.3	36.3	47.3	57.0
		0.0055	0.0142	0.0190	0.0237
	16	21.4
		0.008
	17	27.3	27.7
		0.0104	0.0107
	18	26.7	31.8
		0.0100	0.0122
	19	31.0	52.9	61.9	...
		0.0119	0.0214	0.0264	...

^a The stress-strain curve is approximated by connecting the coordinates by straight lines.

might be expected due to these effects, were assumed and the free surface motion calculated. No significant change in the free surface motion was observed.

The second observation is that an error in the measurement of the final surface velocity, when converted to material velocity, causes data points to move along the dynamic stress-strain curve rather than parallel to the stress axis. This is fortuitous since the free surface velocity cannot be measured with the precision of the other measurements. It is most significant that, at high stress levels where changes in stress and strain due to error are greatest, the slope of the stress-strain curve varies slowly. This means that a large error in particle velocity is reflected as a much smaller error in the determination of the stress-strain curve.

In order to compare the experimentally determined curves with those predicted from the quasi-static properties of the material, the state of stress of the material in one-dimensional strain must be specified. This has been developed in general form elsewhere,^{8, 15, 16} so only the simplest approach will be reviewed. The principal assumptions in the theory are that 1) there is no volume change due to plastic flow, 2) the flow stress is dependent only on the amount of plastic work done, and 3) a yield criterion of

$$\sigma_x - \sigma_y = Y(W_p) \quad (1)$$

is used.[¶]

To obtain the functional relation between stress and strain in one-dimensional strain, the strain is first separated into elastic and plastic components:

$$\epsilon_x = \epsilon_x^e + \epsilon_y^p \quad (2)$$

$$\epsilon_y = \epsilon_z = 0 \quad \epsilon_y^e = -\epsilon_y^p$$

The elastic strains in the principle stress orientation ($\sigma_y = \sigma_z$) are then given by

$$\epsilon_x^e = (\sigma_x/E) - 2\nu(\sigma_y/E) \quad (3)$$

$$\epsilon_y^e = (\sigma_y/E)(1 - \nu) - \nu(\sigma_x/E)$$

[¶] Both the Von Mises and Tresca yield criteria take this form for the one-dimensional strain experiments described here.

[§] The experimental data are discrete points that were taken from the continuous voltage trace of the slant wire and then corrected for tilt and transformed to distance-time coordinates by computer.

where E is Young's modulus and ν is Poisson's ratio. At the yield point defined by Eq. (1), plastic deformation begins. The assumption that there is no volume change due to plastic flow requires that

$$\epsilon_x^p + 2\epsilon_y^p = 0 \quad (4)$$

so that combining Eqs. (1-4), the relation between stress and strain above the elastic limit (yield point) is determined to be

$$\sigma_x = \sigma + \frac{2}{3}Y(W_p) \quad (5)$$

where

$$\sigma = K\epsilon_x \quad (6)$$

In these equations, σ is the spherical or hydrostatic stress component,** K is the bulk modulus, and the deviatoric stress component $\frac{2}{3}Y(W_p)$ indicates that the flow stress is a function of the plastic work.

In order to apply Eq. (5) to a specific problem, $Y(W_p)$ must be determined. This is most easily accomplished by a one-dimensional stress compression test that must then be related to the one-dimensional strain state through the plastic work.

In one-dimensional stress, the amount of plastic work associated with a change in plastic strain $d\alpha_x^p$ is

$$dW_p = Y d\alpha_x^p \quad (7)$$

For one-dimensional strain the plastic work is given by

$$dW_p = \sigma_x d\epsilon_x^p + 2\sigma_y d\epsilon_y^p \quad (8)$$

which, using Eqs. (1) and (2), reduces to

$$dW_p = Y d\epsilon_x^p \quad (9)$$

The transformation between one-dimensional stress and one-dimensional strain is therefore determined by equating equal amounts of plastic work:

$$d\alpha_x^p = d\epsilon_x^p \quad (10)$$

which may be written in slightly more useful form by integrating both sides and then expressing the result in terms of the total strains:

$$\epsilon_x = \frac{2}{3}\alpha_x - (Y/6K) \quad (11)$$

The last term is due to the elastic strain components that must be subtracted from the total strain to give the plastic strain.

A general procedure for calculating the dynamic stress-strain curve in one-dimensional strain from a quasi-static one-dimensional stress curve (or from a dynamic one-dimensional stress curve if it is available) is to first choose a point (Y, α_x) on the latter. Using these, σ_x and ϵ_x may be calculated from the equations and specification of K . This process is then repeated until the dynamic stress-strain curve is sufficiently defined. The state of one-dimensional strain may be interpreted to be a one-dimensional stress test under a varying hydrostatic stress condition sufficient to assure no change in lateral dimensions of the specimen.

Since both the compression curve and the compressibility are obtained under conditions of nearly constant temperature, they must be corrected to the thermodynamic conditions of the dynamic stress-strain curve, or conversely. If the energy associated with plastic deformation may be neglected (that is, the material is essentially under hydrostatic pressure), the correction is easily made.^{1, 2} However,

** Under the one-dimensional strain condition, $d\epsilon_x = dV/V = dl/l$, where V is the volume of an element and l is its length in the direction of propagation. The strains observed in these experiments were so small that finite strain analysis is unnecessary; natural strain was suitably approximated by nominal or engineering strain.

the flow stresses of the materials under investigation are large, and this approximation cannot be used. Instead, the close proximity of the dynamic stress-strain curve to an adiabat justifies correcting the static data to adiabatic conditions.⁹ This significantly changes the compressibility, but the change in the elastic modulus is negligible.

Bridgman's hydrostatic data for fully hardened steel containing 1.1% carbon¹⁸ were used in calculating dynamic stress-strain curves (one-dimensional strain) for all three hardnesses of 4340. Although Bridgman's steel was undoubtedly somewhat harder than fully hardened 4340, its compressibility should be more representative than that for softer steels with only small amounts of impurities. For comparison, the compressibility of 1.1% carbon steel is greater by about 2% than the compressibility of American Ingot iron, single crystal iron, and stainless-steel H26, and less than that of stainless-steel H29 by about 2%. This, along with the small effect composition and hardness has on the elastic moduli of steels, suggests that the error in using 1.1% carbon steel values for Rc15- and Rc32-4340 steel cannot be great. Since Bridgman's data are only to 30 kbar, his compressibility function was used to extrapolate to higher pressures. It is expected, therefore, that the error in calculating the highest stress states will be greater than for the lower states.

Discussion

The results of computer calculations for experiments on Rc54-4340 steel using the present experimental technique are shown in Fig. 4. These results represent what is believed to be the present optimum in experimentation and are therefore considered most accurate. Since each experiment yields a complete stress-strain curve, these curves would be expected to fall on top of one another if the approximation that stress is a function of strain only is valid. This would result in the existence of a single unique composite curve defining the relation of stress to strain at all stress levels. Within the limits of experimental error and the errors inherent in the analysis, this is observed for Rc54 steel.

The stress-strain curve calculated from quasi-static compression data has been superimposed on the Rc54 experimental curves in Fig. 4. Again, the difference between predicted and measured results may well be due to the approximations of the analysis and is therefore not considered significant. The close agreement suggests that the dynamic stress-strain curve can be predicted with considerable ac-

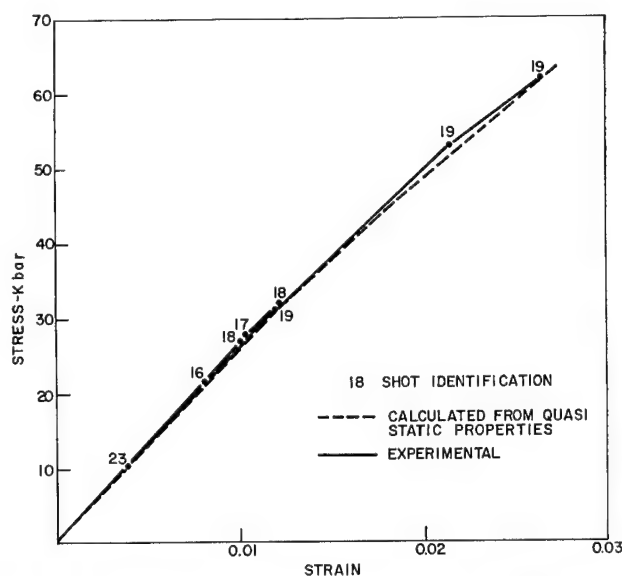


Fig. 4 Dynamic stress-strain curves of Rc54 4340 steel.

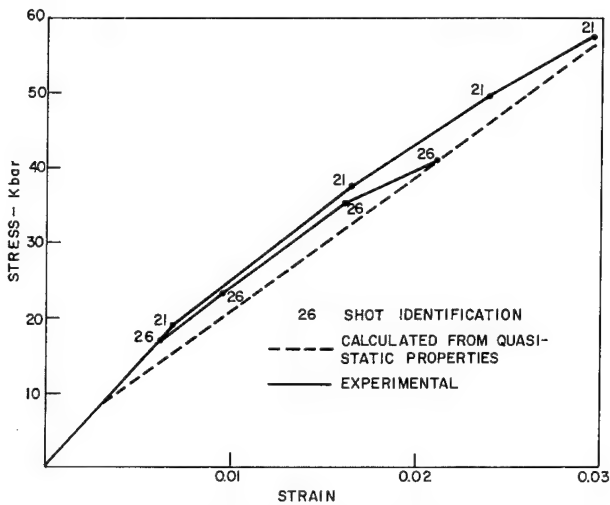


Fig. 5 Dynamic stress-strain curves of Rc15 4340 steel.

curacy from the static properties of this fully hardened 4340 steel.

The results of computer calculations for experiments on Rc15-4340 steel using the present experimental technique are shown in Fig. 5. These differ significantly from the Rc54 curves in that a different curve is observed for each terminal stress state, $\dagger\dagger$ and each curve lies significantly above the curve calculated from quasi-static results. This is, of course, further evidence of the well-known increase in initial flow stress with increase in strain rate observed in steels by Jones, et al.¹⁹ and Taylor and Rice.⁷ In addition, however, the offset ($\frac{3}{4}\%$) shows that this increase in flow stress is not confined to the initial portion of the stress front preceding the yield point but is observed in all parts of the stress wave where the strain rate is high. The experimental technique here was not precise enough to observe the dynamic upper yield point of this steel.

The dynamic stress-strain curves in Fig. 5 for Rc15-4340 were obtained using strain-rate-independent elastic-plastic theory. Each portion of the curves therefore represents some

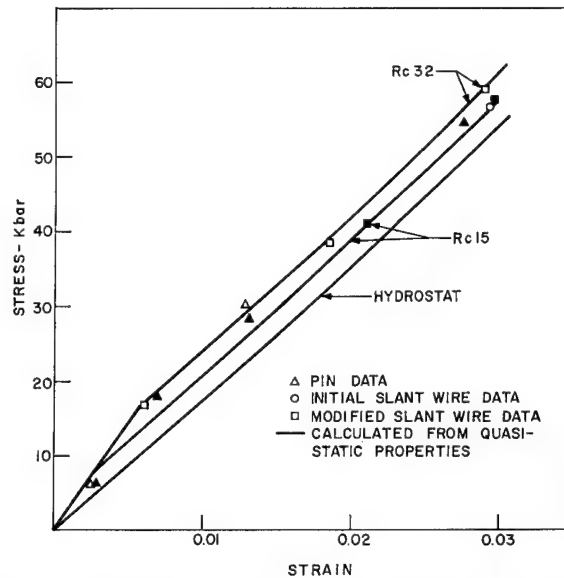


Fig. 7 A comparison of the terminal stress states of Rc32- and Rc15-4340 steel.

average strain rate which is representative of the part of the wave front associated with it. This average reflects the range of strain rates which a given stress increment produces in the material as it propagates through the target and consequently will change as the target thickness is changed. If the dynamic behavior can be represented by a family of curves of constant strain rate,²⁰⁻²² where the effect of increase in strain rate is to increase the stress supported by the material for a given value of strain, then the Rc15 experimental curves may be interpreted as follows. Since a steeper wave front is associated with higher strain rates, curves calculated from higher projectile velocity shots must lie further above the hydrostat than those for low velocity shots. The upper parts of all curves, however, will bend back toward the hydrostat through lower strain rates as the peak stress is approached. The last point on the curve, the terminal stress state, represents the condition in the material of almost constant stress and presumably low strain rate. Therefore, it lies in close proximity to the curve calculated from quasi-static data. Unfortunately, the actual stress-strain path to reach this point cannot yet be determined because analysis techniques incorporating strain-rate effects are not available.

An interesting feature of this result is that, if the quasi-static curve is taken for the equation of state of the impacted target, i.e., the projectile velocity remains the same but the target is loaded slowly, the calculated terminal stress is approximately the same as that of the experimentally determined curves. This implies that the terminal stress state is independent of the loading history within the accuracy of the analysis. However, recent electron microscope examinations of shock-loaded metals reveal microstructures that differ considerably from those of specimens loaded slowly to the same final equivalent strain.²³⁻²⁵ One reason for the close agreement here may be because the effects of microstructural differences may not be sensitively reflected in the one-dimensional strain curves. This is because of the large spherical component of stress present. For example, $\frac{1}{2}\%$ error in stress of the final state of shot 26 could represent a difference of 9% in the flow stress of Rc15 if the hydrostatic stress is known exactly. $\dagger\dagger$ Since $\frac{1}{2}\%$ is the order of the experimental error of this investigation, such a flow

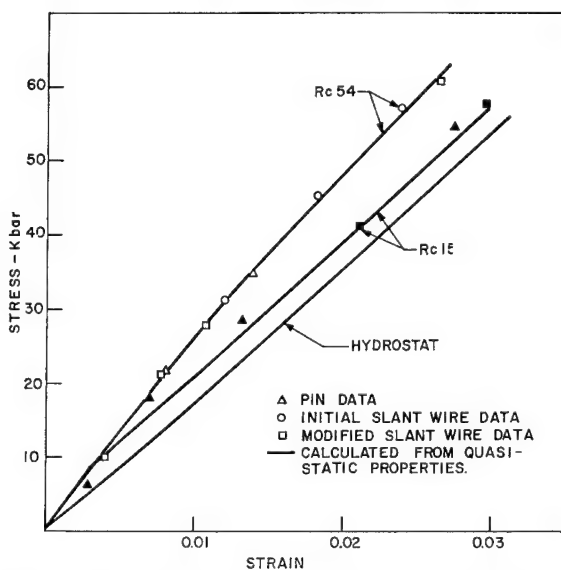


Fig. 6 A comparison of the terminal stress state of Rc54- and Rc15-4340 steel.

$\dagger\dagger$ The terminal stress state is defined as the steady-state stress supported in a region of the material after the wave front has passed through it.

$\dagger\dagger$ For equivalent conditions, this would represent an error of only $2\frac{1}{2}\%$ in Rc54 because of its much greater flow stress.

stress difference would remain undetected. It is evident, however, that the very large increases in flow stress indicated by the large offsets from the quasi-static curve do not persist after the wave front has passed.

The results for Rc32-4340 steel are similar to the Rc15 data with the exception that the maximum offsets from the curve calculated from quasi-static data were only about half the Rc15 curve offsets.

Further details of the differences between the stress-strain curves of Rc15 and Rc54 are in Fig. 6. The work-hardening of the Rc54 steel is reflected by the increasingly large offset from the hydrostat with increasing strain. In contrast, the terminal stress states of Rc15 and Rc32 as plotted in Fig. 7 show that, as the quasi-static tests predict, the only difference is in the larger offset of Rc32-4340 from the hydrostat.

Of secondary interest in these comparisons is the way in which refinements in technique have resulted in better agreement between theory and experiment. The pin shots represent rather gross experimental measurements coupled with an overly simplified analysis, as reflected by the data scatter. The initial slant wire studies were not much better, experimentally, although they did present the opportunity for more exact analysis of the data. The principal difficulty here seems to have been in the way the projectile velocity and tilt were measured. The present experimental technique is accurate enough to give results that are limited by the strain-rate independent condition imposed on the data analysis. There may be many materials, however, such as fully hardened 4340 steel, for which strain-rate effects are small, so that for many applications strain-rate-independent theory adequately describes the propagation of stress waves.

Conclusions

The principal conclusion of this investigation is that the experimentally observed dynamic work-hardening of fully hard 4340 steel is in agreement with its static work-hardening properties. This agreement, along with the observation that strain-rate effects are not large in this steel, suggests that the dynamic stress-strain curve of a material known to be strain-rate insensitive can be accurately predicted from static properties.

A secondary conclusion is that the large increase in flow stress with increase in the strain rate of Rc15- and Rc32-4340 steels is not limited to stress levels around the yield point but persists as long as the strain rate is high. The increase in flow stress is transitory, however, in that, once the wave front is passed and, presumably, the strain rate becomes small, the state of stress in the steel is in agreement with strain-rate-independent theory within experimental error. The validity of this, however, cannot be definitely established until computational techniques incorporating the complicated strain-rate behavior of these materials can be developed.

References

- ¹ Walsh, J. M. and Christian, R. H., "Equation of state of metals from shock wave measurements," *Phys. Rev.* **97**, 1544-1556 (1955).
- ² Rice, M. H., McQueen, R. G., and Walsh, J. M., "Compression of solids by strong shock waves," *Solid State Physics*, edited by F. Seitz and D. Turnbull (Academic Press Inc., New York, 1958), Vol. 6, pp. 1-63.
- ³ Duvall, G. E., "Properties and applications of shock waves," *Response of Metals to High Velocity Deformation*, edited by P. G. Shewmon and V. F. Zackay (Interscience Publishers, Inc., New York, 1960), pp. 165-203.
- ⁴ Al'tshuler, L. V., Bakonova, A. A., and Trunin, R. F., "Shock adiabats and zero isotherms of seven metals at high pressure," *Zh. Eksperim. i Teor. Fiz.* **42**, 91-104 (1961); transl. in *Soviet Phys.* **15**, 65-74 (1962).
- ⁵ Katz, S., Doran, D. G., and Curran, D. R., "Hugoniot equation of state of aluminum and steel from oblique shock measurement," *J. Appl. Phys.* **30**, 568-576 (1959).
- ⁶ Hughes, D. S., Gourley, L. E., and Gourley, M. F., "Shock wave compression of iron and bismuth," *J. Appl. Phys.* **32**, 624-629 (1961).
- ⁷ Taylor, J. W. and Rice, M. H., "Elastic plastic properties of iron," *J. Appl. Phys.* **34**, 364-371 (1963).
- ⁸ Fowles, G. R., "Shock wave compression of hardened and annealed 2024 aluminum," *J. Appl. Phys.* **32**, 1475-1487 (1961).
- ⁹ Lundergan, C. D. and Herrmann, W., "Equation of state of 6061-T6 aluminum at low pressures," *J. Appl. Phys.* **34**, 2046-2053 (1963).
- ¹⁰ Bancroft, D., Peterson, E. L., and Minshall, S., "Polymorphism of iron at high pressure," *J. Appl. Phys.* **27**, 291-298 (1956).
- ¹¹ Curran, D. R., "Nonhydrodynamic attenuation of shock waves in aluminum," *J. Appl. Phys.* **34**, 2677-2685 (1963).
- ¹² Wilkins, M. L., "Calculation of elastic-plastic flow," *Lawrence Radiation Lab. Rept. UCRL-7322*, Univ. of California (April 1963).
- ¹³ Barker, L. M., Lundergan, C. D., and Herrmann, W., "Dynamic response of aluminum," *J. Appl. Phys.* **35**, 1203-1212 (1964).
- ¹⁴ Barker, L. M. and Hollenbach, R. E., "A system for measuring the dynamic properties of materials," *Rev. Sci. Instr.* **35**, 742-746 (1964).
- ¹⁵ Wood, D. S., "On longitudinal plane waves of elastic-plastic strain in solids," *J. Appl. Mech.* **19**, 521-525 (1952).
- ¹⁶ Morland, L. W., "The propagation of plane irrotational waves through an elasticoplastic medium," *Phil. Trans. Roy. Soc. London* **A251**, 341-383 (1959).
- ¹⁷ Barker, L. M., "SWAP-A computer program for shock wave analysis," *Sandia Corp. Research Rept. SC-4796(RR)* (October 1963).
- ¹⁸ Bridgman, P. W., "Linear compressions to 30,000 kg/cm² including relatively incompressible substances," *Proc. Am. Acad. Arts Sci.* **77**, 187-233 (1949).
- ¹⁹ Jones, O. E., Neilson, F. W., and Benedick, W. B., "Dynamic yield behavior of explosively loaded metals determined by a quartz transducer technique," *J. Appl. Phys.* **33**, 3224-3232 (1962).
- ²⁰ Hauser, F. E., Simmons, J. A., and Dorn, J. E., "Strain rate effects in plastic wave propagation," *Response of Metals to High Velocity Deformation*, edited by P. G. Shewmon and V. F. Zackay (Interscience Publishers, Inc., New York, 1960), pp. 93-114.
- ²¹ Karnes, C. H., "Strain-rate effects in cold-worked high purity aluminum," *Doctoral Dissertation*, Univ. of Texas (1964).
- ²² Kolsky, H. and Douch, L. S., "Experimental studies in plastic wave propagation," *J. Mech. Phys. Solids* **10**, 195-223 (1962).
- ²³ Leslie, W. C., Hornbogen, E., and Dieter, G. E., "Structure of shock hardened iron," *J. Iron Steel Inst. (London)* **200**, 622-633 (1962).
- ²⁴ Johari, O. M. and Thomas, G., "Substructures in plastically deformed copper," *Lawrence Radiation Lab. Rept. UCRL-10932 Rev.*, Univ. of California (October 1963).
- ²⁵ Estill, W. B. and Mullendore, A. W., private communication, Sandia Corp. (1963).

Close Analogy between Radiative and Conductive Heat Flux in a Finite Slab

MAX A. HEASLET* AND BARRETT BALDWIN†
Ames Research Center, Moffett Field, Calif.

A parallelism is established between the theoretical analyses of energy transport due to conduction and thermal radiation in a unidimensional configuration. The boundary conditions assumed correspond to two parallel walls of given temperatures separated by a finite slab of gas. A gray-gas theory of radiation is employed in which the coefficients of emission and absorption are independent of frequency; the theory of conduction is based on the Bhatnagar-Gross-Krook model of the Boltzmann equation. Under simplifying assumptions, the half-range form of the equations is modified through the use of relations drawn from continuum theory. Heat flux is predicted for all values of optical thickness or inverse Knudsen number. Comparisons with available numerical calculations based on less restrictive assumptions indicate the fluxes are given with a maximum error of a few percent, yet are expressible analogously in algebraic form. The correspondence between wall accommodation and emission coefficients is exhibited. In the concluding section, generalization to other configurations yields explicit formulas for heat flux between coaxial cylinders and concentric spheres.

Nomenclature

- a = constant introduced in B-G-K model [Eq. (16)]
- f = distribution function
- F = Maxwellian distribution [Eq. (17)]
- h = heat flux [Eqs. (5) and (29)]
- I = specific intensity of radiation [Eq. (1)]
- j = particle flux [Eq. (18b)]
- k = Boltzmann constant
- K = heat conduction coefficient
- L = distance between plates
- m = particle mass
- n = particle number density
- p_{xx} = xx component of pressure tensor
- T = temperature
- v = particle velocity
- v_x = x component of particle velocity
- x = coordinate measured normal to wall
- β = emission function [Eqs. (2) and (30)]
- ϵ = wall emission or accommodation coefficient
- θ = angle relative to x axis
- λ = particle or photon mean free path
- $\mu = \cos\theta$
- $\xi = \int_0^x \frac{dx}{\lambda}$
- $\xi_L = \int_0^L \frac{dx}{\lambda}$
- σ = Stefan-Boltzmann constant

Subscripts

- 1 = value in gas at $x = \xi = 0$
- 2 = value in gas at $x = L$, $\xi = \xi_L$
- M = Maxwellian value
- KN = Knudsen value
- w_1 = value at left wall
- w_2 = value at right wall

Superscripts

- $+$ = half-range value, $0 < \mu \leq 1$ for radiation, $0 < v_x$ for conduction
- $-$ = half-range value, $-1 \leq \mu < 0$ for radiation, $v_x < 0$ for conduction

Introduction

THE theoretical prediction of the rate of transfer of thermal energy through a gaseous medium contained between parallel walls of different temperatures and specified physical properties is a fundamental problem in the study of heat exchange. In the theory of heat conduction in a monatomic gas, one may try to determine the dependence of energy flux on the two wall temperatures, their distance apart, the mean free path length of the gas particles, and the accommodation coefficients of the walls. Similarly, in radiative transfer through an absorbing and emitting gray gas, the energy flux depends again on the wall temperatures, distance apart, the radiation (or photon) mean free path length, and on the coefficients of emission of the walls. A discussion of the similarity in the basic formulation of the two problems has been given by Eckert.¹ The present paper shows how, under simplifying assumptions, the flux in both cases can be predicted to a rather remarkable degree of accuracy while, at the same time, preserving formal similarities between the principal equations for conduction and thermal radiation.

Insofar as gray-gas radiation is concerned, the basic equations are well defined; the main contribution here is the demonstration of an effective use of the assumption of small mean free path length in the half-range form of the equations. Predictions of flux are then shown to possess reasonable merit for all optical thicknesses, even though a portion of the analysis is limited to simplification inherent in the continuum or Rosseland regime.

The exact description of heat conduction for a gas with arbitrary mean free path length relies on some formulation of the Boltzmann equation. The analogy to be developed results from the use of the B-G-K model (Bhatnagar, Gross, and Krook²), and half-range representations of the distribution function are employed. Once the similarity between the two problems is established, one is led naturally to the consideration of proper use of the continuum form of the conduction equations. The stratagem used in the radiation analysis, that is, proper employment of continuum theory, indicates the procedure, and comparisons with more accurate calculations show that the predictions remain good for rarefied gases, that is, in the Knudsen regime of large mean free path length.

It is important to stress that the close analogy achieved holds principally when attention is concentrated on flux.

Received March 9, 1964; revision received September 8, 1964.

* Chief, Theoretical Branch, Thermo- and Gas-Dynamics Division.

† Research Scientist, Thermo- and Gas-Dynamics Division. Member AIAA.

Temperature distributions, for example, are not the same in the two problems. Also, the distributions predicted by the approximate analysis are in both cases increasingly inaccurate as the walls are approached. It appears that flux is the grossest of the physical quantities of interest and is insensitive to approximations. More localized phenomena, such as temperature "slip" at the walls, react much more sharply to imposed approximations. Qualitatively, however, the predictions provide the proper trends and extensions of the method become apparent.

Analysis

Assume, as in Fig. 1, two walls with temperatures T_{w1} and T_{w2} at a distance apart L . In this schematic representation of the problem, conduction and radiation can be indicated simultaneously and, since algebraic similarity is to be featured, the same symbols will be used in the two cases. Thus, the parameters ϵ_1 and ϵ_2 represent either the wall accommodation coefficients of heat conduction, or the wall emission coefficients for radiation. The gaseous medium between the walls has for photon or particle mean free path the local value λ . We assume also that the walls emit and reflect the incident energy diffusely.

Radiative Transport

Consider first the transport of thermal radiation between the walls. Distance x is measured normal to and from the left wall. Now introduce the specific intensity function that denotes the energy transmitted through a unit area (normal to the axis) in a unit time and in a unit solid angle that is inclined at an angle θ to the positive x direction. We distinguish the half-ranges $(-\pi/2 \leq \theta \leq \pi/2, -\pi/2 \leq \pi - \theta \leq \pi/2)$ of the specific intensity by the notation

$$I^+(\mu, \xi) \quad 0 < \mu \leq 1 \quad I^-(\mu, \xi) \\ -1 \leq \mu < 0 \quad (1)$$

where $\mu = \cos\theta$ and $d\xi = dx/\lambda(x)$. The basic transfer equations are (Ref. 3, p. 25 et seq.)

$$\mu(dI^\pm/d\xi) = -I^\pm(\mu, \xi) + [\beta(\xi)/\pi] \quad (2)$$

The function $\beta(\xi)/\pi$ is the so-called source (or emission) function. In the absence of scattering and under the assumption that the index of refraction of the gas is unity, the condition of local thermodynamic equilibrium yields the relation $\beta(\xi) = \sigma T^4(\xi)$, where σ is the Stefan-Boltzmann constant.

Approximation in the method of solution is introduced at this point. First, one notes that the source function, as well as the boundary conditions developed later, are independent of μ when the walls emit and reflect diffusely. As a consequence, the dependence of $I^\pm(\mu, \xi)$ on μ is suppressed by means of an appropriate averaging. The original idea for such an approximation is due to Eddington.⁴ Various numerical values of the averaged quantity $\bar{\mu}$, or its equivalent, can be used depending on particular requirements of the problem at hand.^{5, 6} One rational way in which this averaging can be achieved involves taking first moments with respect to μ in the half-ranges. It suffices here, however, to assume some such operation has been carried out and to rewrite Eq. (2) in the form

$$\pm \bar{\mu}(dI^\pm/d\xi) = -I^\pm(\xi) + [\beta(\xi)/\pi] \quad (3)$$

where the average value $\bar{\mu}$ is yet to be determined.

The quantities $h^+(\xi)$ and $h^-(\xi)$ are now introduced to denote the half-range energy fluxes associated with the motion of photons in the positive and negative x (or ξ) directions, respectively. Then

$$h^+(\xi) = 2\pi \int_0^1 \mu I^+ d\mu = \pi I^+(\xi) \quad (4a)$$

$$h^-(\xi) = 2\pi \int_{-1}^0 \mu I^- d\mu = -\pi I^-(\xi) \quad (4b)$$

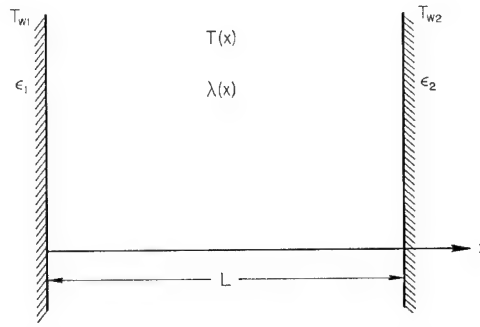


Fig. 1 Sketch showing parallel walls separated by gaseous medium.

Total flux, so defined that it is positive when the net flow of energy in the x direction is positive, is $h(\xi)$, where

$$h(\xi) = h^+(\xi) + h^-(\xi) \quad (5)$$

From Eqs. (3) and (4) one derives the relations

$$\bar{\mu}(dh^+/d\xi) = \beta(\xi) - h^+(\xi) \quad (6a)$$

$$\bar{\mu}(dh^-/d\xi) = \beta(\xi) + h^-(\xi) \quad (6b)$$

Addition and subtraction of Eqs. (6) together with the definition introduced in Eq. (5) yields

$$\bar{\mu}(dh/d\xi) = 2\beta(\xi) - [h^+(\xi) - h^-(\xi)] \quad (7a)$$

$$\bar{\mu}[d(h^+ - h^-)/d\xi] = -h(\xi) \quad (7b)$$

For the problem being considered, conservation of energy requires that flux be a constant. From Eq. (7a), therefore

$$\beta(\xi) = [h^+(\xi) - h^-(\xi)]/2 \quad (8)$$

and the fundamental equations are

$$dh(\xi)/d\xi = 0 \quad (9a)$$

$$d\beta(\xi)/d\xi = -h(\xi)/2\bar{\mu} \quad (9b)$$

Equation (9a) is independent of the approximation we have employed, and the arbitrariness in the choice of $\bar{\mu}$ appears only in the second relation. The decision as to what value to assign to $\bar{\mu}$ is now resolved by insisting that Eq. (9b) must agree with the expression for flux in the limiting regime of an optically thick medium. This final assumption fixes the value $2\bar{\mu} = \frac{4}{3}$ since independent study (e.g., Kourganoff³) of radiative transfer for $\lambda \ll L$ leads to the condition $d\beta/d\xi = -3h/4$ at any point ξ sufficiently distant from an imposed wall or boundary condition. Since the approximate analysis is based on the use of isotropic specific intensity, that is, no dependence of $I^\pm(\mu, \xi)$ on μ , we retain a certain logical consistency by adjusting the arbitrary constant to conform with a regime in which the isotropic condition does apply. Very accurate numerical solutions are available for special values of the physical parameters, and an a posteriori check of the results for these cases will be given later.

The boundary conditions express the equality of outwardly directed flux at each wall to the sum of the wall emission and the reflected portion of the inwardly directed flux at the wall. Since the reflectivity coefficient of an opaque wall is 1 minus the absorption (or emission) coefficient, one has

$$h_1^+ = \epsilon_1 \beta_{w1} - (1 - \epsilon_1) h_1^- \quad (10a)$$

$$-h_2^- = \epsilon_2 \beta_{w2} + (1 - \epsilon_2) h_2^+ \quad (10b)$$

Here, subscripts 1 and 2 refer to conditions in the medium at $x = 0$ and $x = L$, and subscripts $w1$ and $w2$ refer to wall conditions at the same positions. Combination of these relations leads to

$$h \left(\frac{1}{\epsilon_1} + \frac{1}{\epsilon_2} - 1 \right) = \beta_{w1} - \beta_{w2} + \frac{h_2^+ - h_2^-}{2} - \frac{h_1^+ - h_1^-}{2} \quad (11)$$

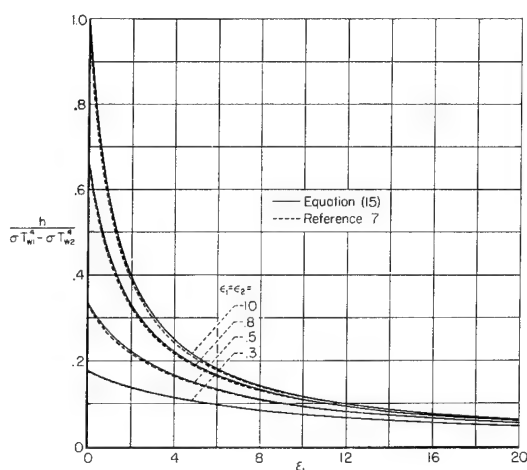


Fig. 2 Dimensionless radiative flux between similar walls as a function of wall emissivity and optical thickness.

Equation (11) retains half-range fluxes, but from Eq. (8) it can be written alternatively as

$$h \left(\frac{1}{\epsilon_1} + \frac{1}{\epsilon_2} - 1 \right) = \beta_{w1} - \beta_{w2} + \beta_2 - \beta_1 \quad (12)$$

The integration of Eqs. (9) subject to the boundary conditions is now a straightforward process. The constant value of flux h is independent of ξ and a function only of the parameters T_{w1} , T_{w2} , ϵ_1 , ϵ_2 , and the optical thickness ξ_L , where

$$\xi_L = \int_0^L \lambda^{-1}(x) dx$$

When $\epsilon_1 = \epsilon_2 = 1$, $\xi_L = 0$, flux is $\sigma T_{w1}^4 - \sigma T_{w2}^4$ and is the heat flux associated with black wall conditions. The end results may be written in the form

$$\beta(\xi) = h \left[b - \frac{3}{4}(\xi - \frac{1}{2}\xi_L) \right] \quad (13)$$

where

$$b = \frac{\sigma T_{w1}^4 \left[(1/\epsilon_2) - \frac{1}{2} + \frac{3}{8}\xi_L \right] + \sigma T_{w2}^4 \left[(1/\epsilon_1) - \frac{1}{2} + \frac{3}{8}\xi_L \right]}{\sigma T_{w1}^4 - \sigma T_{w2}^4} \quad (14)$$

and

$$h = \frac{\sigma T_{w1}^4 - \sigma T_{w2}^4}{[(1/\epsilon_1) + (1/\epsilon_2) - 1] + \frac{3}{4}\xi_L} \quad (15)$$

Equation (13) gives a linear expression for the emission function and represents a rough approximation to the actual distribution of $\sigma T^4(\xi)$. Equation (15) is the principal objective of the analysis. Its accuracy, when compared with available and more exact numerical calculations, is surprisingly good. Figure 2 shows $h/(\sigma T_{w1}^4 - \sigma T_{w2}^4)$ as a function of ξ_L and ϵ for the case of physically similar walls ($\epsilon_1 = \epsilon_2$). Solid lines correspond to the predictions of Eq. (15). The dashed lines were taken from the work of Heaslet and Fuller⁷ where an iterative method was used to solve the basic integral equation of radiation theory for the same boundary conditions. Probstein⁸ has previously noted that for black walls ($\epsilon_1 = \epsilon_2 = 1$) the agreement with an exact numerical analysis carried out by Usiskin and Sparrow⁹ is quite satisfactory. The topmost curve is Probstein's result. Equation (15) has been derived by Adrianov and Polyak¹⁰ and Deissler¹¹ by somewhat different reasoning.

Conductive Transport

Heat conduction between the walls and through a monatomic gas remains to be considered. If Eqs. (8), (9), and the boundary conditions (10) are accepted as fundamental to

the prediction of heat flux, a parallel development is possible. Preliminary to this, the specific forms of the kinetic equations need to be introduced.

The B-G-K² idealization of the Boltzmann equation for the present problem can be expressed as

$$v_z(df/dx) = (a\bar{v}/\lambda)(F - f) \quad (16)$$

where

$$F = n(m/2\pi kT)^{3/2} \exp(-mv^2/2kT) \quad (17)$$

(For a valuable critique of this idealization see Liepmann, Narasimha, and Chahine.¹²) The quantity v_x is the x component of particle velocity v , and \bar{v} is the average particle velocity for the Maxwellian distribution F . The quantity λ is related to the particle mean free path length, also based on F ; and a is a proportionality constant to be determined by requiring the solution for heat flux to be exact at the continuum limit. Thus λ and a may be functions of n and T for arbitrary intermolecular force laws.

The values of n , T and other quantities of interest are given in terms of moments of the distribution function f by the relations:

Number Density

$$n = \int f dv \quad (18a)$$

Flux of Particles

$$j = \int v_x f dv \quad (18b)$$

xx Component of Pressure Tensor

$$p_{xx} = \int mv_x^2 f dv \quad (18c)$$

Internal Energy Density

$$\left(\frac{3}{2}\right)nkT = \int \left(\frac{1}{2}\right)mv^2 f dv \quad (18d)$$

Total Energy Flux

$$h = \int \left(\frac{1}{2}\right)mv_x v^2 f dv \quad (18e)$$

Upon multiplication of Eq. (16) by the appropriate collisional invariant (1 , mv_x , or mv^2) and integration over particle velocities, we get the conservation equations $\partial j / \partial x = 0$, $\partial p_{xx} / \partial x = 0$, $\partial h / \partial x = 0$, or

$$j = 0 \quad (19a)$$

$$p_{xx} = \text{const} = \text{force per unit area on walls} \quad (19b)$$

$$h = \text{const} \quad (19c)$$

The kinetic theory counterpart of the foregoing simplified treatment of radiative transport entails the definition of two half-range distribution functions f^\pm for particles with positive or negative values of v_x , and the two distributions are taken to be Maxwellian, that is,

$$f^\pm = 2n^\pm(m/2\pi kT^\pm)^{3/2} \exp(-mv^2/2kT^\pm) \quad (20)$$

Substitution of this into Eqs. (18a-18d) yields

$$n = n^+ + n^- \quad (21a)$$

$$j = n^+(2kT^+/\pi m)^{1/2} - n^-(2kT^-/\pi m)^{1/2} = 0 \quad (21b)$$

$$p_{xx} = n^+kT^+ + n^-kT^- = \text{const} \quad (21c)$$

$$nkT = n^+kT^+ + n^-kT^- = p_{xx} \quad (21d)$$

The equalities on the right follow from the use of the conservation relations (19a) and (19b) and from combination of (21c) with (21d).

The following simplified treatment of the kinetic theory heat-conduction problem can be cast in a form that is independent of the intermolecular force law. To that end, we choose a definition of λ based on the heat-conduction coefficient and the hard-sphere mean free path, $\lambda_{HS} = (2^{1/2}\pi d^2 n)^{-1}$,

where d is particle diameter. For hard spheres, the heat-conduction coefficient is (Ref. 13, chap. 10)

$$K_{HS} = 1.02513 (75/64d^2)(k^3T/\pi m)^{1/2}$$

Alternatively, an approximate evaluation of the numerical coefficient taken from Jeans¹⁴ leads to

$$K_{HS} = (15/4\pi d^2)(k^3T/\pi m)^{1/2}$$

The difference between the two expressions is less than 1%; we shall adopt the latter because of its more compact form. In a later development, the parameter a , appearing in Eq. (16), will be evaluated by consideration of the form of the equations in the continuum limit corresponding to vanishingly small mean free path. It can be seen that this procedure is independent of the form of the intermolecular force law if an effective mean free path is defined as

$$\lambda = (K/K_{HS})\lambda_{HS} = K/(\frac{1}{4})kn(2kT/\pi m)^{1/2} \quad (22)$$

where K is the continuum heat-conduction coefficient. If momentum transport were considered, a separate effective mean free path would have to be defined for that case, but in the present conduction problem this is not necessary.

It is of interest to compare our effective mean free path for conduction, Eq. (22), with values that have been used in the literature. For Maxwellian molecules, the heat-conduction coefficient is¹³

$$K_M = [5/4\pi A_2(5)](2/m\kappa)^{1/2}k^2T$$

where $A_2(5) = 0.436$ and κ is the constant in the inverse fifth-power force law. In the study of heat flow by Ziering,¹⁵ the solution for Maxwellian molecules is expressed in terms of a mean free path λ_M defined by Maxwell as

$$\lambda_M = 1/[2\pi A_2(5)(\kappa/kT)^{1/2}n]$$

The heat-conduction coefficient can be expressed in terms of this parameter as

$$K_M = (5kn/2)(2kT/m)^{1/2}\lambda_M$$

By substitution in Eq. (22), we find (for Maxwellian molecules)

$$\lambda = (2\pi^{1/2}/3)\lambda_M$$

When expressed in terms of λ , our results are independent of the form of the intermolecular force law. However, for comparison with experiment or other results in the literature, this factor must be considered. For example, Lavin and Haviland¹⁶ define Knudsen numbers for hard spheres and Maxwellian molecules in terms of an average density

$$\bar{p} = \left(\frac{m}{L}\right) \int_0^L n dx \quad (23)$$

It is apparent that \bar{p} is a measure of the amount of gas between the walls which can be inferred from experimentally measurable quantities. The solution to be given later is expressed in terms of the variable ξ , which is related to x and λ by

$$\xi = \int_0^x \frac{dx_1}{\lambda(x_1)} \quad (24a)$$

or

$$d\xi = dx/\lambda \quad (24b)$$

Rearrangement and substitution of Eqs. (22) and (24b) into Eq. (23) yields

$$\bar{p} = \frac{4}{15} \frac{m}{Lk} \int_0^{\xi_L} \frac{K d\xi}{(2kT/\pi m)^{1/2}} \quad (25)$$

The solution to be given later leads to a temperature distribution $T(\xi)$. When the heat-conduction coefficient K is

specified as a function of T , the average density can be evaluated according to Eq. (25).

Through use of Eq. (24b), Eq. (16) becomes

$$v_x(df/d\xi) = a\bar{v}(F - f) \quad (26)$$

which we choose to rewrite in terms of half-range functions ($v_x > 0, v_x < 0$) as

$$(v_x/a\bar{v})(df^\pm/d\xi) = -f^\pm(v, \xi) + F(v, \xi) \quad (27)$$

The half-range energy fluxes are, respectively,

$$h^+(\xi) = 2n^+kT^+(2kT^+/\pi m)^{1/2} \quad (28a)$$

$$h^-(\xi) = -2n^-kT^-(2kT^-/\pi m)^{1/2} \quad (28b)$$

and total flux $h(\xi)$ is

$$h(\xi) = h^+(\xi) + h^-(\xi) \quad (29)$$

Conformity between the present analysis and the approximate theory used previously is preserved if Eq. (27) is rewritten as flux equations with an appropriate averaging in velocity space. Thus, if Eq. (27) is multiplied by $mv_x v^2/2$ and integrations carried out over the half-range particle velocities,

$$(\overline{v_x/a\bar{v}})(dh^+/d\xi) = \beta(\xi) - h^+(\xi) \quad (30a)$$

$$(\overline{v_x/a\bar{v}})(dh^-/d\xi) = \beta(\xi) + h^-(\xi) \quad (30b)$$

where $\beta(\xi) = nkT(2kT/\pi m)^{1/2}$ and the coefficients in the left members of the differential equations are yet to be fixed. The direct analogy with Eqs. (6) is obvious and, as in Eqs. (7), combination of the flux equations yields

$$(\overline{v_x/a\bar{v}})(dh/d\xi) = 2\beta(\xi) - [h^+(\xi) - h^-(\xi)] \quad (31a)$$

$$(\overline{v_x/a\bar{v}})[d(h^+ - h^-)/d\xi] = -h(\xi) \quad (31b)$$

As noted in Eq. (19c), total flux is constant, so

$$\beta(\xi) = [h^+(\xi) - h^-(\xi)]/2 \quad (32)$$

and the fundamental equations become

$$dh(\xi)/d\xi = 0 \quad (33)$$

$$d\beta(\xi)/d\xi = -h(\xi)/2(\overline{v_x/a\bar{v}}) \quad (34)$$

Precision in the statement of the latter relation now appears if, as previously, one expresses it in conformity with the dictates of continuum theory and small mean free path length. With the aid of Eqs. (21c) and (21d), β can be expressed as

$$\beta(\xi) = nkT(2kT/\pi m)^{1/2} = p_{xx}(2kT/\pi m)^{1/2} \quad (35)$$

where p_{xx} is constant. Differentiation and rearrangement leads to

$$d\beta/d\xi = (nk/2)(2kT/\pi m)^{1/2}(dT/d\xi)$$

The quantity $dT/d\xi$ can be eliminated in favor of h by use of the continuum relation $h = -K(dT/dx)$. By substitution of Eq. (22) to remove K , and use of Eq. (24b), we get

$$h = -(\frac{1}{4})nk(2kT/\pi m)^{1/2}(dT/d\xi)$$

Combination of this with the foregoing expression for $d\beta/d\xi$ yields

$$d\beta(\xi)/d\xi = -2h/15 \quad (36)$$

where $\beta(\xi)$ is given explicitly in Eq. (35). In the approximate analysis, $T^+(\xi)$ is a linear function for radiative transport and $T^{1/2}(\xi)$ is a linear function for conductive transport.

It remains to introduce the boundary conditions. More detailed consideration is required than was used earlier in Eqs. (10). We write these conditions as

$$f_1^+(v_x, v) = \epsilon_1 F_{v1} + (1 - \epsilon_1)f_1^-(-v_x, v) \quad v_x > 0 \quad (37a)$$

$$f_2^-(v_x, v) = \epsilon_2 F_{v2} + (1 - \epsilon_2)f_2^+(-v_x, v) \quad v_x < 0 \quad (37b)$$

Here, f_1^\pm and f_2^\pm are the half-range distribution functions in the gas evaluated, respectively, at the wall positions. The distribution functions associated with diffuse emission at the walls are

$$F_{w1} = A_1(m/2\pi kT_{w1})^{3/2} \exp(-mv^2/2kT_{w1}) \quad (38a)$$

$$F_{w2} = A_2(m/2\pi kT_{w2})^{3/2} \exp(-mv^2/2kT_{w2}) \quad (38b)$$

where T_{w1} and T_{w2} are the two wall temperatures. The values of A_1 and A_2 are yet to be determined; the parameters ϵ_1 and ϵ_2 are the wall accommodation coefficients.

The counterparts of Eqs. (10) are

$$h_1^+ = \epsilon_1 k A_1 T_{w1} (2kT_{w1}/\pi m)^{1/2} - (1 - \epsilon_1) h_1^- \quad (39a)$$

$$-h_2^- = \epsilon_2 k A_2 T_{w2} (2kT_{w2}/\pi m)^{1/2} + (1 - \epsilon_2) h_2^+ \quad (39b)$$

Through the use of Eq. (32), one has

$$h \left(\frac{1}{\epsilon_1} + \frac{1}{\epsilon_2} - 1 \right) = \left(\frac{2k^3}{\pi m} \right)^{1/2} \times \frac{(A_1 T_{w1}^{3/2} - A_2 T_{w2}^{3/2}) + \beta_2 - \beta_1}{(A_1 T_{w1}^{3/2} - A_2 T_{w2}^{3/2})} \quad (40)$$

The solution of the differential Eq. (36) is expressible as

$$\beta(\xi) = h[b - (\frac{2}{15})(\xi - \xi_L/2)] \quad (41)$$

$$b = \frac{\{A_1 T_{w1}^{3/2}[(1/\epsilon_2) - \frac{1}{2} + (\xi_L/15)] + A_2 T_{w2}^{3/2}[(1/\epsilon_1) - \frac{1}{2} + (\xi_L/15)]\}}{(A_1 T_{w1}^{3/2} - A_2 T_{w2}^{3/2})} \quad (42)$$

From the boundary conditions one gets

$$h = \frac{(2k^3/\pi m)^{1/2}(A_1 T_{w1}^{3/2} - A_2 T_{w2}^{3/2})}{[(1/\epsilon_1) + (1/\epsilon_2) - 1] + (2\xi_L/15)} \quad (43)$$

The final relation gives flux in terms of the wall emission characteristics, but a difference exists here between conduction and radiation. In the latter case the emission from the walls is purely a function of wall temperature. One distinguishing difference is associated with the fact that photons need not be conserved in absorption and emission at the walls. Thus, a more detailed balancing of conditions is necessary for the gas particles, and the parameters A_1 and A_2 are constrained by known relations. The additional calculations are most easily carried out if a perturbation analysis is used in which the percentage change in temperature is not excessive. To this end we introduce $\Delta T = (T_{w1} - T_{w2})/2$ and assume $2\Delta T/[(\frac{1}{2})(T_{w1} + T_{w2})] \leq 1$.

From Eqs. (21a) and (21b)

$$n^+(\xi) = \frac{n(\xi)[T^-(\xi)]^{1/2}}{[T^+(\xi)]^{1/2} + [T^-(\xi)]^{1/2}} \quad (44)$$

$$n^-(\xi) = \frac{n(\xi)[T^+(\xi)]^{1/2}}{[T^+(\xi)]^{1/2} + [T^-(\xi)]^{1/2}}$$

and from Eq. (21d)

$$T(\xi) = [T^+(\xi)T^-(\xi)]^{1/2}$$

Temperature is, therefore, equal to the geometric mean of the half-range temperatures. If the deviations in the temperatures are small enough that the geometric and arithmetic means can, to a first order, be equated, one has

$$2T(\xi) \approx [T^+(\xi)T^-(\xi)]^{1/2} + [T^+(\xi) + T^-(\xi)]/2 \quad (45)$$

$$2[T(\xi)]^{1/2} \approx [T^+(\xi)]^{1/2} + [T^-(\xi)]^{1/2}$$

Multiplication by v_x and integration of Eqs. (37a) and (37b) over the half-range velocity spaces leads to

$$A_1(T_{w1})^{1/2} = 2n^+(0)[T^+(0)]^{1/2} \\ = 2n(0)T(0)/\{[T^+(0)]^{1/2} + [T^-(0)]^{1/2}\} \approx n(0)[T(0)]^{1/2} \quad (46a)$$

$$A_2(T_{w2})^{1/2} = 2n^-(\xi_L)[T^-(\xi_L)]^{1/2} \\ = 2n(\xi_L)T(\xi_L)/\{[T^+(\xi_L)]^{1/2} + [T^-(\xi_L)]^{1/2}\} \approx n(\xi_L)[T(\xi_L)]^{1/2} \quad (46b)$$

Equation (43) is then rewritten as

$$h = \frac{(2k^3/\pi m)^{1/2}\{n(0)[T(0)]^{1/2}T_{w1} - n(\xi_L)[T(\xi_L)]^{1/2}T_{w2}\}}{[(1/\epsilon_1) + (1/\epsilon_2) - 1] + (2\xi_L/15)} \quad (47)$$

Further reduction is possible through use of the relations

$$p_{xx} = kn(0)T(0) = kn(\xi_L)T(\xi_L) = \text{const}$$

$$p_{xx}[2kT(\xi)/\pi m]^{1/2} = p_{xx}[2kT(\xi_L/2)/\pi m]^{1/2} - (2h/15)(\xi - \xi_L/2)$$

the latter expression being merely a re-expression of Eqs. (41) and (35). Equation (47) then becomes

$$h = \frac{p_{xx}(2k/\pi m)^{1/2}}{[(1/\epsilon_1) + (1/\epsilon_2) - 1] + 2\xi_L/15} \times \left\{ \frac{T_{w1}}{[T(\xi_L/2)]^{1/2} + (h\xi_L/15p_{xx})(\pi m/2k)^{1/2}} - \frac{T_{w2}}{[T(\xi_L/2)]^{1/2} - (h\xi_L/15p_{xx})(\pi m/2k)^{1/2}} \right\} \quad (48)$$

It is convenient at this point to introduce the Knudsen flux h_{KN} , which applies at $\epsilon_1 = \epsilon_2 = 1$, $\xi_L = 0$. Under these conditions $T^+(\xi) = T_{w1}$, $T^-(\xi) = T_{w2}$, and direct calculation yields

$$h_{KN} = \frac{4p_{xx}}{(T_{w1}^{1/2} + T_{w2}^{1/2})} \left(\frac{2k}{\pi m} \right)^{1/2} \Delta T \quad (49a)$$

or, using Eq. (45),

$$h_{KN} = 2p_{xx} \left[\frac{2k}{\pi m(T_{w1}T_{w2})^{1/2}} \right]^{1/2} \Delta T \quad (49b)$$

To the order of accuracy of the present analysis, these results are indistinguishable, but we shall use the first in view of its more straightforward derivation. It may be remarked that to the same order of accuracy Eqs. (49) agree with results given by Kennard¹⁷ (p. 317). This can be seen after noting from Eq. (21d) that $p_{xx} = R\rho'T' + O(\Delta T)$, where ρ' and T' are averaged values of the density and temperature in the gas as defined by Kennard.

Algebraic manipulation of Eq. (48) now leads to the result

$$h \left(\frac{1}{\epsilon_1} + \frac{1}{\epsilon_2} - 1 + \frac{2\xi_L}{15} \right) = \frac{h_{KN} \left\{ \frac{(T_{w1})^{1/2} + (T_{w2})^{1/2}}{2[T(\xi_L/2)]^{1/2}} \right\}}{1 - \frac{2h\xi_L}{15h_{KN}} \left\{ \frac{2[T(\xi_L/2)]^{1/2}}{(T_{w1})^{1/2} + (T_{w2})^{1/2}} \right\} \left[\frac{T_{w1} + T_{w2}}{2T(\xi_L/2)} \right]} \times \left\{ \frac{2(\Delta T)^{1/2}}{(T_{w1})^{1/2} + (T_{w2})^{1/2}} \right\}^4 \quad (50)$$

Two formulas of interest follow from this relation. First, we note that, since $[T(\xi)]^{1/2}$ is a linear function, the bracketed terms are, respectively,

$$\frac{(T_{w1})^{1/2} + (T_{w2})^{1/2}}{[T(0)]^{1/2} + [T(\xi_L)]^{1/2}} \quad \frac{2(T_{w1} + T_{w2})}{\{[T(0)]^{1/2} + [T(\xi_L)]^{1/2}\}^2}$$

When $\epsilon_1 = \epsilon_2 = \epsilon$, it may be conjectured that the ratios of

the averaged wall temperatures and the averaged gas temperatures at the wall are nearly 1. In this case, one gets

$$\frac{h}{h_{KN}} \left(\frac{2}{\epsilon} - 1 + \frac{2\xi_L}{15} \right) = \frac{1 - 2(\xi_L h / 15 h_{KN})}{1 - (2\xi_L h / 15 h_{KN})^2 \{ 2(\Delta T)^{1/2} / [(T_{w1})^{1/2} + (T_{w2})^{1/2}] \}^4} \quad (51)$$

Second, more rigorously, we can restrict the analysis to a first-order theory involving the small parameter $2\Delta T / (T_{w1} + T_{w2})$. Equation (50) then reduces to

$$h = \frac{h_{KN}}{[(1/\epsilon_1) + (1/\epsilon_2) - 1] + (4\xi_L/15)} \quad (52)$$

This latter expression is precisely analogous to radiation flux given in Eq. (15). The role of h_{KN} , which is h evaluated at $\epsilon_1 = \epsilon_2 = 1$, $\xi_L = 0$, is the same as that of blackbody flux $\sigma T_{w1}^4 - \sigma T_{w2}^4$; the difference in the coefficients of ξ_L is attributable to the coefficients appearing in the continuum forms of the transport equations. Figure 3 shows a comparison between this result and detailed calculations of Gross and Ziering¹⁸ for $\epsilon_1 = \epsilon_2 = 1$. The degree of excellence is not as good as that shown in Fig. 2, and, in view of the added simplifications used to achieve this expression, the difference is not surprising. In particular, the starting slope of the approximate curve fails to conform with the more nearly exact calculations. The usefulness of the result in predicting the magnitude of flux is, however, apparent.

Figure 4 shows a comparison between predictions of slip temperature T_s . By definition, when $\epsilon_1 = \epsilon_2 = \epsilon$,

$$T_s / \Delta T = 1 + [T(\xi_L) - T(0)] / 2\Delta T \quad (53)$$

and in the present approximate theory one has

$$\frac{T_s}{\Delta T} = \frac{[(2/\epsilon) - 1]}{[(2/\epsilon) - 1] + (4\xi_L/15)} \quad (54)$$

The comparisons were made to correspond to the results of Gross and Ziering¹⁸ and necessarily were applied at $\epsilon = 1$.

Concluding Remarks

The preceding analysis has shown that heat flux may be calculated approximately through a simplified analysis in which differential equations from continuum theory are solved subject to boundary conditions involving temperature discontinuities at the walls. It is also possible to characterize the final results in another way. To this end we limit attention to fixed values of mean free path λ . Then one notes that the predicted heat flux has the form

$$\frac{h}{h_{\epsilon_1 = \epsilon_2 = 1, \lambda = \infty}} = \frac{1}{A + (B/\lambda)} \quad (55)$$

where A and B are associated, respectively, with the extreme conditions $\lambda \gg 1$ and $\lambda \ll 1$. If this restatement of the end result is given a definitive status, generalizations to other cases become possible so long as A is provided by a free-

Radiation

$$h_1 = \frac{\sigma(T_{w1}^4 - T_{w2}^4)}{(1/\epsilon_1) + (R_1^2/R_2^2)[(1/\epsilon_2) - 1] + \frac{3}{4}(R_1/R_2)[(R_2 - R_1)/\lambda]} \quad (57a)$$

Conduction

$$h_1 = \frac{h_{KN}}{(1/\epsilon_1) + (R_1^2/R_2^2)[(1/\epsilon_2) - 1] + \frac{4}{15}(R_1/R_2)[(R_2 - R_1)/\lambda]} \quad (57b)$$

molecule or optically-thin analysis and B can be calculated from continuum theory. The asymptotic behavior of Eq. (55) is correct for $1/\lambda$ large, and the magnitude of h is exact at $1/\lambda \approx 0$. The one-dimensional analysis and Figs. 2 and 3 indicate that the region of least accuracy will appear

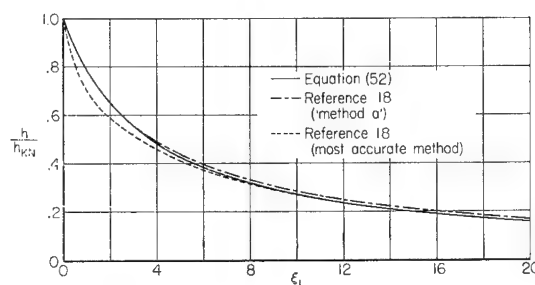


Fig. 3 Dimensionless conductive flux as a function of inverse Knudsen number, $\epsilon_1 = \epsilon_2 = 1$.

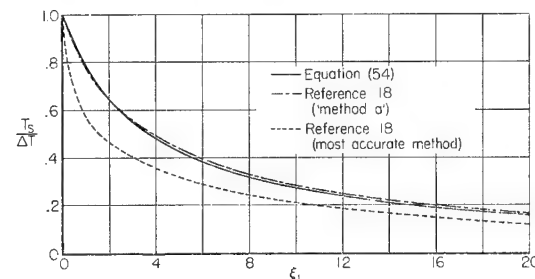


Fig. 4 Dimensionless temperature slip as a function of inverse Knudsen number, $\epsilon_1 = \epsilon_2 = 1$.

at moderately small values of mean free path length where distance is, of course, measured in terms of a characteristic geometric length.

Two additional results follow immediately. Consider, first, two coaxial cylinders with radii R_1 , R_2 ($R_1 < R_2$), temperatures T_{w1} , T_{w2} , and accommodation coefficients or emissivities ϵ_1 , ϵ_2 . If h_1 is heat flux at the inner cylinder, one has

$$h_1 = \frac{\sigma(T_{w1}^4 - T_{w2}^4)}{(1/\epsilon_1) + (R_1/R_2)[(1/\epsilon_2) - 1] + \frac{3}{4}(R_1/\lambda) \ln(R_2/R_1)} \quad (56a)$$

Conduction

$$h_1 = \frac{h_{KN}}{(1/\epsilon_1) + (R_1/R_2)[(1/\epsilon_2) - 1] + \frac{4}{15}(R_1/\lambda) \ln(R_2/R_1)} \quad (56b)$$

In Eq. (56a) the value at $\lambda = \infty$ is provided by Christiansen's formula (as discussed, for example, by Jakob,¹⁹ p. 5, or by Jensen²⁰). A derivation of the corresponding term in Eq. (56b) can be found, for example, in Kennard.¹⁷ The logarithmic terms arise from the fact that the continuum equations in cylindrical geometry require flux h to vary inversely with radius.

Consider, next, two concentric spheres with radii R_1 , R_2 , and, again, let h_1 be heat flux at the inner surface. Equation (55) then yields

Radiation

$$h_1 = \frac{\sigma(T_{w1}^4 - T_{w2}^4)}{(1/\epsilon_1) + (R_1^2/R_2^2)[(1/\epsilon_2) - 1] + \frac{3}{4}(R_1/R_2)[(R_2 - R_1)/\lambda]} \quad (57a)$$

Christiansen's formula again provides the appropriate relation in Eq. (57a). For spherical geometry the continuum theory requires h to vary inversely as radius squared.

It is to be noted that, when $R_2 - R_1 = L$ and R_2 increases indefinitely, the foregoing results reduce to the formulas de-

rived previously for the case of parallel walls. For the radiation problem, the approximate method of Deissler¹¹ yields the same expression for heat flux between parallel walls as Eq. (15), but for the cylindrical geometry, leads to a result that differs from Eq. (56a). Deissler's latter result is, however, not accurate at $\lambda = 0$. When $\epsilon_1 = \epsilon_2 = 1$, Eq. (56b) reduces to a form derived by Lees and Liu.²¹ Equations (56a) and (57a) are also given by Adrianov²² but with a factor 1 in place of $\frac{3}{4}$. In that case, the formulas would not be accurate for large λ . So far as the authors are aware no exact or approximate calculations corresponding to Eq. (57b) have appeared in the literature. A further specialization of interest also follows from Eqs. (57), namely, the case of a single sphere conducting or radiating to an infinite gaseous medium. Here the external radius R_2 becomes arbitrarily large while R_1 is held fixed. A finite, nonzero value of flux is predicted. In the idealized case of the cylindrical geometry or in the purely one-dimensional configuration, the theory predicts zero flux for finite values of T_{w1} and T_{w2} when the distance between the walls becomes infinite. This anomalous behavior stems from the change in the steady-state continuum equations as the dimensionality of the configuration changes. The differences between the single sphere and the other cases are closely analogous mathematically to contrasting results that arise in attempting to predict the drag of the same geometric shapes in a Stokes flow analysis. The latter analysis, however, is based on additional idealizations of the basic physical equations.

In a direct derivation of Eqs. (56) and (57) by the methods of this paper, the recasting of the differential operators in the governing equations offers no difficulty. The boundary conditions require more detailed investigation, however, and the initial study of the finite slab shows that the kinetic theory analysis is the more difficult to carry through and should be limited to small temperature differences. The approach adopted here is essentially one of demanding that the boundary conditions must be exact for limiting values of λ . Equation (55) is thus an interpolation formula with known end conditions. Further improvement would involve increased accuracy in the prediction of the gradient $dh/d\lambda^{-1}$ at $\lambda^{-1} = 0$.

The attainment of an acceptable analogy without great loss in accuracy of predictions has been the theme of this paper and was the motivation for the investigation. It is important, also, to stress that the first-order predictions of temperature distribution are of considerable value as starting points for more exact iterative calculations. It is not possible to maintain a continuing analogy, since differences appear in the character of the influence functions in the integral-equation formulations, for example, but this does not detract from the utility of the first-order results. Two recent investigations may be mentioned in which predictions from a continuum-oriented theory are used to calculate more exact results. The first of these is the work of Heaslet and Fuller⁷; radiative transport and temperature distributions between parallel plates are determined iteratively, starting with the approximation of the emission function given in Eq. (13). In the work of Liepmann, Narasimha, and Chahine,¹² the structure of a plane shock layer is studied by means of the B-G-K model. Success in carrying out an iterative calculation was attributed in part to the use of the Navier-Stokes equations to get a starting solution. This approach is consistent with the type of approximation we have advocated here.

The methods used in the derivation of the present approximate solutions can be generalized in other directions. For example, it may be possible, by slight modifications, to include complicating factors such as simultaneous transport by radiation and conduction in gas mixtures including polyatomic molecules.

References

- ¹ Eckert, E. R. G., "Similarities between energy transport in rarefied gases and by thermal radiation," *Modern Developments in Heat Transfer*, edited by W. E. Ibele (Academic Press, New York, 1963).
- ² Bhatnagar, P. L., Gross, E. P., and Krook, M., "A model for collision processes in gases. I. Small amplitude processes in charged and neutral one-component systems," *Phys. Rev.* **94**, 511-525 (1954).
- ³ Kourganoff, V., *Basic Methods in Transfer Problems* (Clarendon Press, Oxford, England, 1952).
- ⁴ Eddington, A. S., *The Internal Constitution of the Stars* (Cambridge University Press, Cambridge, England, 1926; also Dover Publications, New York, 1959).
- ⁵ Sobolev, V. V., *A Treatise on Radiative Transfer* (D. Van Nostrand Co., Princeton, N. J., 1963).
- ⁶ Vincenti, W. G. and Baldwin, B. S., "Effect of thermal radiation on the propagation of plane acoustic waves," *J. Fluid Mech.* **12**, 449-447 (1962).
- ⁷ Heaslet, M. A. and Fuller, F. B., "Approximate predictions of the transport of thermal radiation through an absorbing plane layer," NASA TN D-2515 (1963).
- ⁸ Probst, R. F., "Radiation slip," *AIAA J.* **1**, 1202-1204 (1963).
- ⁹ Usiskin, C. M. and Sparrow, E. M., "Thermal radiation between parallel plates separated by an absorbing-emitting non-isothermal gas," *Intern. J. Heat Mass Transfer* **1**, 28-36 (1960).
- ¹⁰ Adrianov, V. N. and Polyak, G. L., "Differential methods for studying heat transfer," *Intern. J. Heat Mass Transfer* **6**, 355-362 (1963).
- ¹¹ Deissler, R. G., "Diffusion approximation for thermal radiation in gases with jump boundary conditions," *J. Heat Transfer* **86**, 240-246 (1964).
- ¹² Liepmann, H. W., Narasimha, R., and Chahine, M. T., "Structure of a plane shock layer," *Phys. Fluids* **5**, 1313-1324 (1962).
- ¹³ Chapman, S. and Cowling, T. G., *The Mathematical Theory of Non-Uniform Gases* (Cambridge University Press, Cambridge, England, 1960).
- ¹⁴ Jeans, J., *An Introduction to the Kinetic Theory of Gases* (Cambridge University Press, London, 1960).
- ¹⁵ Ziering, S., "Shear and heat flow for Maxwellian molecules," *Phys. Fluids* **3**, 503-509 (1960).
- ¹⁶ Lavin, M. L. and Haviland, J. K., "Application of a moment method to heat transfer in rarefied gases," *Phys. Fluids*, **5**, 274-279 (1962).
- ¹⁷ Kennard, E. H., *Kinetic Theory of Gases* (McGraw-Hill Book Company, Inc., New York, 1938).
- ¹⁸ Gross, E. P. and Ziering, S., "Heat flow between parallel plates," *Phys. Fluids* **2**, 701-712 (1959).
- ¹⁹ Jakob, M., *Heat Transfer* (John Wiley and Sons, New York, 1957), Vol. II.
- ²⁰ Jensen, H. H., "Some notes on heat-transfer by radiation," *Det. Kgl. Danske Vid. Selskab, Mat-Fys. Med.* **XXIV**, 3-26 (1948).
- ²¹ Lees, L. and Liu, C. Y., "Kinetic-theory description of conductive heat transfer from a fine wire," *Phys. Fluids* **5**, 1137-1148 (1962).
- ²² Adrianov, V. N., "Nekatorye zadachi teorii luchistovo teplotnogo v odnornnykh," *Teploenerg.* **7**, 63-66 (1963).

Interplanetary Trajectories in the Restricted Three-Body Problem

LAWRENCE M. PERKO*

Lockheed Missiles and Space Company, Palo Alto, Calif.

The purpose of this paper is to present an approximate analytic solution to the restricted three-body problem valid for those initial conditions typical of interplanetary trajectories. The planar motion of a particle of negligible mass acted on by the gravitational attractions of two point masses m_0 and m_1 as the particle moves in the plane of motion of m_0 and m_1 to a small neighborhood of m_1 is studied in the framework of the restricted three-body problem for $\mu = m_1/m_0$ much less than one. A boundary-layer type of analysis is applied in order to obtain an approximate analytic solution to this problem. This type of analysis was first applied to this problem by P. A. Lagerstrom and J. Kevorkian. They first considered the two fixed centers problem and then the restricted three-body problem for a special class of initial conditions typical of certain Earth to moon trajectories, namely, those for which the initial angular momentum of the particle with respect to m_0 is $O(\mu^{1/2})$. This paper treats the problem using different independent variables in order to obtain a solution valid for a class of initial conditions typical of interplanetary trajectories; that is, those trajectories for which the initial angular momentum of the particle with respect to m_0 is $O(1)$.

Nomenclature

G	= universal gravitational constant
m_0	= mass of the largest body
m_1	= mass of the secondary body
m_2	= mass of the particle
μ	= m_1/m_0 = mass ratio
\mathbf{r}	= vector from m_0 to m_2
\mathbf{r}_1	= vector from m_0 to m_1
\mathbf{r}_2	= vector from m_1 to m_2
r	= $ \mathbf{r} $ = magnitude of \mathbf{r}
β	= angle between \mathbf{r}_1 and \mathbf{r}
θ	= central angle of m_2 in m_0 -centered nonrotating coordinates
ψ	= angle between \mathbf{r}_1 and \mathbf{r}_2
t	= time = central angle of m_1 in m_0 -centered coordinates
t_0	= initial time
u	= $1/r$
h_0	= initial angular momentum of m_2 relative to m_0
e_0	= initial eccentricity of the instantaneous ellipse
a_0	= initial semimajor axis of the instantaneous ellipse
ω_0	= initial argument of pericenter of the instantaneous ellipse
θ_1	= zero-order angle of arrival
V_∞	= speed at infinity on the m_1 -centered hyperbola
h_2	= angular momentum of the hyperbola
ω_2	= argument of pericenter of the hyperbola
e_2	= eccentricity of the hyperbola
θ_2	= central angle of m_2 in m_1 -centered coordinates
Δ	= distance to the asymptote of the m_1 -centered hyperbola
t_p	= time of pericenter passage on the m_1 -centered hyperbola
(ξ, η)	= m_1 -centered nonrotating coordinates
(\cdot)	= derivative of quantity with respect to time

IN this analysis it will be assumed that m_1 is in a circular orbit about m_0 , although this is not necessary for the success of the method. The equations of motion of the particle with respect to m_0 are then given by

$$\ddot{\mathbf{r}} = -(\mathbf{r}/r^3) - \mu[\mathbf{r}_2/r_2^3 + \mathbf{r}_1] \quad (1)$$

where

$$\mathbf{r}_2 = \mathbf{r} - \mathbf{r}_1$$

and where the coordinates have been normalized by dividing distances by the constant m_0 to m_1 distance d and by dividing time by the constant $(d^3/Gm_0)^{1/2}$. As was mentioned in the abstract, it is assumed that the mass ratio $\mu = m_1/m_0$ is much less than one. The foregoing equations have the form of a singular perturbation problem. The perturbation term has a singularity when $r_2(t) = 0$. The problem will be treated as two ordinary perturbation problems: 1) when the particle is outside a small neighborhood of m_1 , i. e., when $r_2(t) \geq O(\mu^{1/2})$; and 2) when the particle is inside a small neighborhood of m_1 , i. e., when $r_2(t) \leq O(\mu^{1/2})$. The asymptotic expansions of the two perturbation solutions thus obtained are then matched in the boundary layer common to these two regions, i. e., when $r_2(t) = O(\mu^{1/2})$. The perturbation solution for the particle outside a small neighborhood of m_1 is developed in a m_0 -centered nonrotating coordinate system taking the true anomaly θ as the independent variable and effecting the matching in an m_1 -centered nonrotating coordinate system with one axis parallel to the hyperbolic excess velocity. The analysis, therefore, differs considerably from the work of Lagerstrom and Kevorkian¹⁻³ in which the perturbation solution and matching can be carried out in a single rotating coordinate system using the distance along the m_0 m_1 line of centers as the independent variable. The basic ideas and results are, however, the same.

The perturbation solution for the particle outside a small neighborhood of m_1 and its asymptotic expansion will first be derived. The foregoing equations of motion (1) can be written in component form noting that the vectors

$$\mathbf{r}_1 = e_r \cos \beta - e_\theta \sin \beta$$

$$\mathbf{r}_2 = r\mathbf{e}_r - \mathbf{r}_1$$

where $\beta = \theta - t$ is the angle between \mathbf{r}_1 and \mathbf{r} , and θ is measured in a m_0 -centered nonrotating reference frame (Fig. 1). The differential equations become

$$\ddot{r} - r\dot{\theta}^2 = -\frac{1}{r^2} - \mu \left(\cos \beta + \frac{r - \cos \beta}{r_2^3} \right) \quad (2)$$

$$\frac{1}{r} \frac{d}{dt} (r^2 \dot{\theta}) = \mu \left(\sin \beta - \frac{\sin \beta}{r_2^3} \right)$$

The second equation implies that the angular momentum is a constant h_0 , the initial value, plus a perturbation term

$$r^2 \dot{\theta} = h_0 + \mu \int_{t_0}^t r \left(\sin \beta - \frac{\sin \beta}{r_2^3} \right) dt \quad (3)$$

Presented as Preprint 64-52 at the AIAA Aerospace Sciences Meeting, New York, January 20-22, 1964; revision received June 3, 1964. The author wishes to gratefully acknowledge the guidance of J. V. Breakwell and the many helpful suggestions that he contributed to this work.

* Senior Research Engineer.

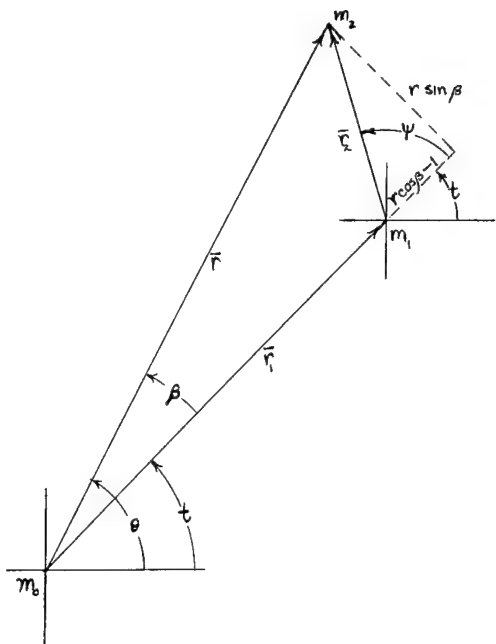


Fig. 1 Coordinate systems.

This equation can be used to write (2) in terms of θ as the independent variable. The dependent variables will be taken as t and $u = 1/r$. The foregoing equations become

$$\left. \begin{aligned} \frac{d^2 u}{d\theta^2} + u &= \frac{1}{h_0^2} + \frac{\mu}{h_0^2} \left\{ r^2 \left(\cos\beta + \frac{r - \cos\beta}{r_2^3} \right) + \right. \\ &\quad \left. r \frac{dr}{d\theta} \left(\sin\beta - \frac{\sin\beta}{r_2^3} \right) - \frac{2}{h_0^2} \int_{\theta_0}^{\theta} r^3 \times \right. \\ &\quad \left. \left(\sin\beta - \frac{\sin\beta}{r_2^3} \right) d\theta \right\} + O(\mu^2) \\ \frac{dt}{d\theta} &= \frac{r^2}{h_0} - \mu \frac{r^2}{h_0^3} \int_{\theta_0}^{\theta} r^3 \left(\sin\beta - \frac{\sin\beta}{r_2^3} \right) d\theta + O(\mu^2) \end{aligned} \right\} \quad (4)$$

where Eq. (3) has been used to write the integrals with respect to t as integrals with respect to θ to $O(\mu)$.

The solution to these equations can be written as an expansion in the small parameter μ :

$$u(\theta) = u_0(\theta) + \mu u_1(\theta) + \mu^2 u_2(\theta) + \dots$$

$$t(\theta) = t_0(\theta) + \mu t_1(\theta) + \mu^2 t_2(\theta) + \dots$$

The well-known zero-order solution to these equations for $e_0 < 1$ is (Ref. 4, p. 90)

$$r_0(\theta) = \frac{1}{u_0(\theta)} = \frac{h_0^2}{1 + e_0 \cos(\theta - \omega_0)}$$

$$t_0(\theta) = t_0 + a_0^{3/2} \left[\sin^{-1} \left(\frac{(1 - e_0^2)^{1/2} \sin(\theta - \omega_0)}{1 + e_0 \cos(\theta - \omega_0)} \right) - \frac{e_0(1 - e_0^2)^{1/2} \sin(\theta - \omega_0)}{1 + e_0 \cos(\theta - \omega_0)} \right]_{\theta_0}^{\theta}$$

Similar equations hold for $e_0 \geq 1$ (Ref. 4, p. 91). Define

$$\beta_0(\theta) = \theta - t_0(\theta)$$

$$r_{20}(\theta) = [1 - 2r_0(\theta) \cos\beta_0(\theta) + r_0^2(\theta)]^{1/2}$$

Then substituting the expansions for $u(\theta)$ and $t(\theta)$ into the differential equations (4) and equating the coefficients of like

powers of μ determines the linear differential equations for $u_1(\theta)$ and $t_1(\theta)$, i. e.,

$$\left. \begin{aligned} \frac{d^2 u_1}{d\theta^2} + u_1 &= \frac{1}{h_0^2} \left[r_0^2(\theta) \left(\cos\beta_0(\theta) + \frac{r_0(\theta) - \cos\beta_0(\theta)}{r_{20}^3(\theta)} \right) + \right. \\ &\quad \left. r_0(\theta) r_0'(\theta) \left(\sin\beta_0(\theta) - \frac{\sin\beta_0(\theta)}{r_{20}^3(\theta)} \right) - \right. \\ &\quad \left. \frac{2}{h_0^2} \int_{\theta_0}^{\theta} r_0^3(\theta) \left(\sin\beta_0(\theta) - \frac{\sin\beta_0(\theta)}{r_{20}^3(\theta)} \right) d\theta \right] \\ \frac{dt_1}{d\theta} &= - \frac{r_0^2(\theta)}{h_0^3} \int_{\theta_0}^{\theta} r_0^3(\theta) \left(\sin\beta_0(\theta) - \frac{\sin\beta_0(\theta)}{r_{20}^3(\theta)} \right) d\theta - \\ &\quad \frac{2}{h_0} r_0^3(\theta) u_1(\theta) \end{aligned} \right\} \quad (5)$$

The initial conditions are chosen so that the particle reaches a small neighborhood of m_1 . In fact, they are specified such that the unperturbed trajectory intersects m_1 at $\theta = \theta_1$, i. e., $r_0(\theta_1) = 1$ and $t_0(\theta_1) = \theta_1$. Small variations in these initial conditions can then be studied by standard error propagation techniques.

In order to determine the singular behavior of the first-order solution, i. e., of $u_1(\theta)$ and $t_1(\theta)$, as θ approaches θ_1 , the singular terms appearing in (5) will be expanded about $\theta = \theta_1$. This is accomplished using the following expansions that are used throughout the paper:

$$\left. \begin{aligned} r_0(\theta) &= 1 - a \left(\frac{1 - h_0}{h_0} \right) (\theta_1 - \theta) + (a^2 - b) \times \\ &\quad \left(\frac{1 - h_0}{h_0} \right)^2 (\theta_1 - \theta)^2 + O(\theta_1 - \theta)^3 \\ t_0(\theta) &= \theta_1 - \frac{1}{h_0} (\theta_1 - \theta) + \\ &\quad \frac{a}{h_0^2} (1 - h_0) (\theta_1 - \theta)^2 + O(\theta_1 - \theta)^3 \\ \beta_0(\theta) &= \left(\frac{1 - h_0}{h_0} \right) (\theta_1 - \theta) \left[1 - \frac{a}{h_0} (\theta_1 - \theta) \right] + \\ &\quad O(\theta_1 - \theta)^3 \end{aligned} \right\} \quad (6)$$

where

$$\begin{aligned} a &= \left[\frac{e_0 \sin(\theta_1 - \omega_0)}{1 + e_0 \cos(\theta_1 - \omega_0)} \right] \left(\frac{h_0}{1 - h_0} \right) = \frac{e_0 \sin(\theta_1 - \omega_0)}{h_0(1 - h_0)} \\ b &= - \frac{1}{2} \left[\frac{e_0 \cos(\theta_1 - \omega_0)}{1 + e_0 \cos(\theta_1 - \omega_0)} \right] \left(\frac{h_0}{1 - h_0} \right)^2 = \\ &\quad - \frac{e_0 \cos(\theta_1 - \omega_0)}{2(1 - h_0)^2} \end{aligned}$$

since

$$1 = r_0(\theta_1) = \frac{h_0^2}{1 + e_0 \cos(\theta_1 - \omega_0)}$$

The other constants appearing in these equations are defined in the Nomenclature. Using these expansions, the behavior of the singular terms in (5) can be described

$$\begin{aligned} \frac{\sin\beta_0(\theta)}{r_{20}^3(\theta)} &= \frac{K_0}{(\theta_1 - \theta)^2} + \frac{K_1}{(\theta_1 - \theta)} + \Psi(\theta) \\ \frac{r_0(\theta) - \cos\beta_0(\theta)}{r_{20}^3(\theta)} &= \frac{-aK_0}{(\theta_1 - \theta)^2} + \frac{K_2}{(\theta_1 - \theta)} + \Phi(\theta) \end{aligned}$$

where the constants

$$K_0 = \frac{h_0^2(1 - h_0)}{(1 + a^2)^{3/2} |1 - h_0|^3}$$

$$K_1 = \frac{aK_0}{h_0} (2 - 3h_0)$$

$$K_2 = -K_0 \left[1 + \left(\frac{1-h_0}{h_0} \right) 2a^2 \right]$$

and the functions

$$\Psi(\theta) = \frac{\sin\beta_0(\theta)}{r_{20}^3(\theta)} - \frac{K_0}{(\theta_1 - \theta)^2} - \frac{K_1}{(\theta_1 - \theta)}$$

$$\Phi(\theta) = \frac{r_0(\theta) - \cos\beta_0(\theta)}{r_{20}^3(\theta)} + \frac{aK_0}{(\theta_1 - \theta)^2} - \frac{K_2}{(\theta_1 - \theta)}$$

remain bounded as θ approaches θ_1 . The behavior of the singular and bounded parts of $\sin\beta_0(\theta)/r_{20}^3(\theta)$ for $\theta_1 = \pi$ is shown graphically in Fig. 2.

The integrals necessary to solve the system (5) will now be written as a singular part plus the integral of a bounded function. Only elementary operations and the concept of adding and subtracting the singular part of a function in order to write it as an integrable function plus a bounded function were used in deriving these integrals:

$$\int_{\theta_0}^{\theta} r_0^3(\theta) \left[\sin\beta_0(\theta) - \frac{\sin\beta_0(\theta)}{r_{20}^3(\theta)} \right] d\theta =$$

$$\frac{-K_0}{(\theta_1 - \theta)} - \frac{aK_0}{h_0} \ln(\theta_1 - \theta) + G_1(\theta)$$

where the function

$$G_1(\theta) = \frac{K_0}{(\theta_1 - \theta_0)} + \frac{aK_0}{h_0} \ln(\theta_1 - \theta_0) + \int_{\theta_0}^{\theta} \Psi_1(\theta) d\theta$$

$$\Psi_1(\theta) = -r_0^3(\theta) [\Psi(\theta) + \sin\beta_0(\theta)] +$$

$$K_0 \left[\frac{1 - r_0^3(\theta) - 3a[(1-h_0)/h_0](\theta_1 - \theta)}{(\theta_1 - \theta)^2} \right] +$$

$$K_1 \left[\frac{1 - r_0^3(\theta)}{(\theta_1 - \theta)} \right]$$

is bounded as θ approaches θ_1 .

Using vector notation to minimize the writing,

$$\int_{\theta_0}^{\theta} r_0(\theta) r_0'(\theta) \left[\sin\beta_0(\theta) - \frac{\sin\beta_0(\theta)}{r_{20}^3(\theta)} \right] \times$$

$$\begin{pmatrix} \cos(\theta - \theta_0) \\ \sin(\theta - \theta_0) \end{pmatrix} d\theta = \int_{\theta_0}^{\theta} \Psi_2(\theta) \begin{pmatrix} \cos(\theta - \theta_0) \\ \sin(\theta - \theta_0) \end{pmatrix} d\theta -$$

$$\frac{aK_0(1-h_0)}{h_0(\theta_1 - \theta)} \begin{pmatrix} \cos(\theta - \theta_0) \\ \sin(\theta - \theta_0) \end{pmatrix} + \frac{aK_0(1-h_0)}{h_0(\theta_1 - \theta_0)} \begin{pmatrix} 1 \\ 0 \end{pmatrix} -$$

$$M_0 \begin{pmatrix} Ci(\theta_1 - \theta) - Ci(\theta_1 - \theta_0) \\ Si(\theta_1 - \theta) - Si(\theta_1 - \theta_0) \end{pmatrix}$$

where

$$Ci(x) = - \int_x^{\infty} \frac{\cos x'}{x'} dx' \quad Si(x) = \int_0^x \frac{\sin x'}{x'} dx'$$

are the cosine-integral and sine-integral functions, respectively. As x approaches zero, $Ci(x)$ behaves like $\ln(x) + \gamma$, where γ is Euler's constant and $Si(x)$ approaches zero. The function

$$\Psi_2(\theta) = r_0(\theta) r_0'(\theta) [\sin\beta_0(\theta) - \Psi(\theta)] - K_1 \left[\frac{r_0(\theta) r_0'(\theta) - a[(1-h_0)/h_0]}{(\theta_1 - \theta)} \right] -$$

$$K_0 \left[\frac{[r_0(\theta) r_0'(\theta) - a[(1-h_0)/h_0] - (2b - 3a^2)[(1-h_0/h_0)^2(\theta_1 - \theta)]}{(\theta_1 - \theta)^2} \right]$$

is bounded as θ approaches θ_1 . Finally,

$$M_0 = aK_0 \left(\frac{1-h_0}{h_0} \right) \begin{bmatrix} -\sin(\theta_1 - \theta_0) \cos(\theta_1 - \theta_0) \\ \cos(\theta_1 - \theta_0) \sin(\theta_1 - \theta_0) \end{bmatrix} -$$

$$K_0 \left(\frac{1-h_0}{h_0} \right)^2 \begin{bmatrix} 2b - \frac{a^2}{1-h_0} \begin{bmatrix} \cos(\theta_1 - \theta_0) \sin(\theta_1 - \theta_0) \\ \sin(\theta_1 - \theta_0) - \cos(\theta_1 - \theta_0) \end{bmatrix} \end{bmatrix}$$

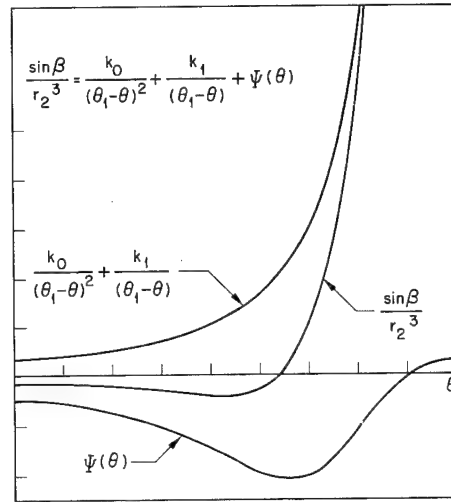


Fig. 2 Singular perturbation.

Similarly,

$$\int_{\theta_0}^{\theta} r_0^2(\theta) \left[\cos\beta_0(\theta) + \frac{r_0(\theta) - \cos\beta_0(\theta)}{r_{20}^3(\theta)} \right] \begin{pmatrix} \cos(\theta - \theta_0) \\ \sin(\theta - \theta_0) \end{pmatrix} d\theta =$$

$$\int_{\theta_0}^{\theta} \Phi_1(\theta) \begin{pmatrix} \cos(\theta - \theta_0) \\ \sin(\theta - \theta_0) \end{pmatrix} d\theta - \frac{aK_0}{(\theta_1 - \theta)} \begin{pmatrix} \cos(\theta - \theta_0) \\ \sin(\theta - \theta_0) \end{pmatrix} +$$

$$\frac{aK_0}{(\theta_1 - \theta_0)} \begin{pmatrix} 1 \\ 0 \end{pmatrix} - M_1 \begin{pmatrix} Ci(\theta_1 - \theta) - Ci(\theta_1 - \theta_0) \\ Si(\theta_1 - \theta) - Si(\theta_1 - \theta_0) \end{pmatrix}$$

where the function

$$\Phi_1(\theta) = r_0^2(\theta) [\cos\beta_0(\theta) + \Phi(\theta)] +$$

$$aK_0 \left[\frac{1 - r_0^2(\theta) - 2a[(1-h_0)/h_0](\theta_1 - \theta)}{(\theta_1 - \theta)^2} \right] +$$

$$K_2 \left[\frac{r_0^2(\theta) - 1}{(\theta_1 - \theta)} \right]$$

is bounded as θ approaches θ_1 ; furthermore,

$$M_1 = aK_0 \begin{bmatrix} -\sin(\theta_1 - \theta_0) \cos(\theta_1 - \theta_0) \\ \cos(\theta_1 - \theta_0) \sin(\theta_1 - \theta_0) \end{bmatrix} -$$

$$K_0 \begin{bmatrix} \cos(\theta_1 - \theta_0) \sin(\theta_1 - \theta_0) \\ \sin(\theta_1 - \theta_0) - \cos(\theta_1 - \theta_0) \end{bmatrix}$$

The last integral that is needed to solve the u_1 equation is

$$\int_{\theta_0}^{\theta} \int_{\theta_0}^{\theta'} r_0^3(\theta') \left[\sin\beta_0(\theta') - \frac{\sin\beta_0(\theta')}{r_{20}^3(\theta')} \right] d\theta' \begin{pmatrix} \cos(\theta - \theta_0) \\ \sin(\theta - \theta_0) \end{pmatrix} d\theta =$$

$$\int_{\theta_0}^{\theta} \left\{ G_1(\theta) \begin{pmatrix} \cos(\theta - \theta_0) \\ \sin(\theta - \theta_0) \end{pmatrix} + \frac{aK_0}{h_0} [\ln(\theta_1 - \theta) - 1] \times \right.$$

$$\left. (\theta_1 - \theta) \begin{pmatrix} \sin(\theta - \theta_0) \\ -\cos(\theta - \theta_0) \end{pmatrix} \right\} d\theta +$$

$$\frac{aK_0}{h_0} (\theta_1 - \theta) [\ln(\theta_1 - \theta) - 1] \begin{pmatrix} \cos(\theta - \theta_0) \\ \sin(\theta - \theta_0) \end{pmatrix} -$$

$$\frac{aK_0}{h_0} (\theta_1 - \theta_0) [\ln(\theta_1 - \theta_0) - 1] \begin{pmatrix} 1 \\ 0 \end{pmatrix} +$$

$$M_3 \begin{pmatrix} Ci(\theta_1 - \theta) - Ci(\theta_1 - \theta_0) \\ Si(\theta_1 - \theta) - Si(\theta_1 - \theta_0) \end{pmatrix}$$

with the constant matrix

$$M_3 = K_0 \begin{bmatrix} \cos(\theta_1 - \theta_0) \sin(\theta_1 - \theta_0) \\ \sin(\theta_1 - \theta_0) - \cos(\theta_1 - \theta_0) \end{bmatrix}$$

These integrals together with the fact that the differential equation

$$(d^2u_1/d\theta^2) + u_1 = F(\theta)$$

with the initial conditions

$$u_1(\theta_0) = u_1'(\theta_0) = 0$$

has the solution

$$u_1(\theta) = \sin(\theta - \theta_0) \int_{\theta_0}^{\theta} F(\theta) \cos(\theta - \theta_0) d\theta - \cos(\theta - \theta_0) \int_{\theta_0}^{\theta} F(\theta) \sin(\theta - \theta_0) d\theta$$

determine the solution of the first equation in (5), i.e.,

$$u_1(\theta) = \sin(\theta - \theta_0)[c_0 + G_3(\theta)] - \cos(\theta - \theta_0)G_2(\theta) + \sin(\theta_1 - \theta)[-A_1 + A_0Ci(\theta_1 - \theta) + B_0Si(\theta_1 - \theta)] + \cos(\theta_1 - \theta)[B_1 + B_0Ci(\theta_1 - \theta) - A_0Si(\theta_1 - \theta)]$$

where the functions

$$\begin{aligned} \left(\frac{G_2(\theta)}{G_3(\theta)} \right) &= \frac{1}{h_0^2} \int_{\theta_0}^{\theta} \left\{ \left[\Phi_1(\theta) + \Psi_2(\theta) - \frac{2}{h_0^2} G_1(\theta) \right] \times \right. \\ &\quad \left(\frac{\sin(\theta - \theta_0)}{\cos(\theta - \theta_0)} \right) + \frac{2aK_0}{h_0^5} (\theta_1 - \theta) [\ln(\theta_1 - \theta) - 1] \times \\ &\quad \left. \left(\frac{\cos(\theta - \theta_0)}{-\sin(\theta - \theta_0)} \right) \right\} d\theta \end{aligned}$$

and the constants

$$\begin{aligned} c_0 &= \frac{aK_0}{h_0^3(\theta_1 - \theta_0)} + \frac{2aK_0}{h_0^5} (\theta_1 - \theta_0) [\ln(\theta_1 - \theta_0) - 1] \\ A_0 &= (K_0/h_0^4) [1 + a^2(1 - h_0)] \\ B_0 &= aK_0/h_0^3 \\ A_1 &= A_0Ci(\theta_1 - \theta_0) + B_0Si(\theta_1 - \theta_0) \\ B_1 &= A_0Si(\theta_1 - \theta_0) - B_0Ci(\theta_1 - \theta_0) \end{aligned}$$

The important thing to note in this equation for $u_1(\theta)$ is that the $1/(\theta_1 - \theta)$ terms have canceled one another and that the $Ci(\theta_1 - \theta)$ terms, which behave like $\ln(\theta_1 - \theta) + \gamma$ as θ approaches θ_1 , therefore determine the singular behavior of $u_1(\theta)$. The first-order solution for the radial distance as a function of θ can then be written as

$$r(\theta) = r_0(\theta) - \mu r_0^2(\theta) u_1(\theta) \quad (7)$$

The equation for $t_1(\theta)$ from (5) can be written as

$$t_1(\theta) = \frac{-2}{h_0} \int_{\theta_0}^{\theta} r_0^3(\theta) u_1(\theta) d\theta + \frac{1}{h_0^3} \int_{\theta_0}^{\theta} r_0^2(\theta) \left[\frac{K_0}{(\theta_1 - \theta)} + \frac{aK_0}{h_0} \ln(\theta_1 - \theta) - G_1(\theta) \right] d\theta$$

Integrating out the singular parts of these functions determines the first-order solution for the time as a function of θ :

$$t(\theta) = t_0(\theta) - \mu \left\{ \frac{K_0}{h_0^3} \ln(\theta_1 - \theta) - G_4(\theta) - \frac{aK_0}{h_0^4} (\theta_1 - \theta) [\ln(\theta_1 - \theta) - 1] \right\} \quad (8)$$

where the function

$$\begin{aligned} G_4(\theta) &= c_1 + \int_{\theta_0}^{\theta} \Phi_2(\theta) d\theta \\ \Phi_2(\theta) &= \frac{1}{h_0^3} \left\{ \frac{K_0[r_0^2(\theta) - 1]}{(\theta_1 - \theta)} + \frac{aK_0}{h_0} [r_0^2(\theta) - 1] \ln(\theta_1 - \theta) - r_0^2(\theta) G_1(\theta) \right\} \end{aligned}$$

is bounded as θ approaches θ_1 ; furthermore

$$c_1 = \frac{K_0}{h_0^3} \ln(\theta_1 - \theta_0) - \frac{aK_0}{h_0^4} [\ln(\theta_1 - \theta_0) - 1](\theta_1 - \theta_0)$$

It will be assumed in these equations that $h_0 \gg \mu^{1/2}$ and that $|1 - h_0| \gg \mu^{1/2}$.

It can be shown that the dominant second-order terms have the form $\mu^2 \ln(\theta_1 - \theta)/(\theta_1 - \theta)$, and that the perturbation solution and the asymptotic expansions to follow are correct to $O(\mu^{3/2})$ for $\theta_1 - \theta = O(\mu^{1/2})$.

The asymptotic expansions of Eqs. (7) and (8) describing the m_0 -centered perturbed conic will now be determined. Let $\theta_1 - \theta = \mu^{1/2}\varphi$ define the angle φ . Then the following asymptotic behavior of the perturbed conic for $\varphi = O(1)$ is determined by expanding Eqs. (7) and (8) about $\theta = \theta_1$:

$$\left. \begin{aligned} r(\theta) &= 1 - \mu^{1/2}a \left(\frac{1 - h_0}{h_0} \right) \varphi + \mu(a^2 - b) \times \\ &\quad \left(\frac{1 - h_0}{h_0} \right)^2 \varphi^2 - \mu[B_0 \ln(\mu^{1/2}\varphi) + G_5(\theta_1)] + O(\mu^{3/2}) \\ t(\theta) &= \theta_1 - \frac{\mu^{1/2}\varphi}{h_0} + \mu \frac{a(1 - h_0)}{h_0^2} \varphi^2 - \\ &\quad \mu \left[\frac{K_0}{h_0^3} \ln(\mu^{1/2}\varphi) - G_4(\theta_1) \right] + O(\mu^{3/2}) \\ \beta(\theta) &= \mu^{1/2} \left(\frac{1 - h_0}{h_0} \right) \varphi - \mu \frac{a(1 - h_0)}{h_0^2} \varphi^2 + \\ &\quad \mu \left[\frac{K_0}{h_0^3} \ln(\mu^{1/2}\varphi) - G_4(\theta_1) \right] + O(\mu^{3/2}) \end{aligned} \right\} \quad (9)$$

where the constant

$$G_5(\theta_1) = \sin(\theta_1 - \theta_0)[c_0 + G_3(\theta_1)] - \cos(\theta_1 - \theta_0)G_2(\theta_1) + B_1 + \gamma B_0$$

The fact that

$$Ci(x) = \gamma + \ln(x) - \frac{x^2}{2 \cdot 2!} + \dots$$

and that

$$Si(x) = x - \frac{x^3}{3 \cdot 3!} + \dots$$

has been used in carrying out these expansions.

These equations are next related to a suitably oriented m_1 -centered, nonrotating coordinate system in which the matching is easily performed.[†] The angle between \mathbf{r}_1 and \mathbf{r}_2 (Fig. 1) is

$$\psi = \tan^{-1} \left(\frac{r \sin \beta}{r \cos \beta - 1} \right)$$

The angle $\varphi_2 = \psi + t - \theta_1$ is then the central angle of \mathbf{r}_2 measured in a nonrotating, m_1 -centered coordinate system. If this system is rotated through the constant angle $\alpha = \tan^{-1}(1/a)$, chosen in the first quadrant for $h_0 \leq 1$ and in the third quadrant for $h_0 > 1$, the components of \mathbf{r}_2 in the resulting m_1 -centered nonrotating coordinate system will be

$$\begin{aligned} \xi &= r_2 \cos(\varphi_2 + \alpha) = \pm r_2 \left(\frac{\sin \varphi_2 - a \cos \varphi_2}{(1 + a^2)^{1/2}} \right) \\ \eta &= r_2 \sin(\varphi_2 + \alpha) = \pm r_2 \left(\frac{a \sin \varphi_2 + \cos \varphi_2}{(1 + a^2)^{1/2}} \right) \end{aligned}$$

the plus sign corresponding to $h_0 \leq 1$ and the minus sign to $h_0 > 1$. From the definition of φ_2 and the fact that by Eq. (9)

$$t - \theta_1 = -\frac{\mu^{1/2}\varphi}{h_0} + O(\mu)$$

$$r_2 = [1 - r \cos \beta + r^2]^{1/2} = O(\mu^{1/2})$$

[†] This approach is due to J. V. Breakwell.

for $\varphi \leq 0(1)$, it follows that

$$\begin{aligned} r_2 \sin \varphi_2 &= r_2 \sin \psi - \frac{\mu^{1/2} \varphi}{h_0} r_2 \cos \psi + 0(\mu^{3/2}) \\ r_2 \cos \varphi_2 &= r_2 \cos \psi + \frac{\mu^{1/2} \varphi}{h_0} r_2 \sin \psi + 0(\mu^{3/2}) \end{aligned}$$

for $\varphi \leq 0(1)$. Finally, since (see Fig. 1)

$$r_2 \sin \psi = r \sin \beta \quad r_2 \cos \psi = r \cos \beta - 1$$

and since the asymptotic behavior of r and β is given by Eq. (9), the asymptotic behavior of ξ and η can be determined using the foregoing equations, i. e.,

$$\left. \begin{aligned} \xi &= \mu^{1/2} \frac{|1 - h_0|(1 + a^2)^{1/2}}{h_0} \varphi + \\ &\mu \left[\frac{|K_0|}{h_0^3} (1 + a^2)^{1/2} \ln(\mu^{1/2} \varphi) + \frac{aG_5(\theta_1) - G_4(\theta_1)}{(1 + a^2)^{1/2}} - \right. \\ &\quad \left. a(1 + a^2)^{1/2} \left(\frac{1 - h_0}{h_0} \right)^2 \varphi^2 \right] + 0(\mu^{3/2}) \\ \eta &= \frac{\mp \mu [aG_4(\theta_1) + G_5(\theta_1)]}{(1 + a^2)^{1/2}} + 0(\mu^{3/2}) \end{aligned} \right\} \quad (10)$$

To see that the φ^2 terms drop out in the η equation, it is necessary to use the fact that $b = 1/(1 - h_0)^{-1/2}$, which follows from the definition of the constant b .

As might be expected, these equations together with the time equation in (9) will be shown to be the same as the asymptotic expansions of a m_1 -centered hyperbola with the asymptote of the hyperbola parallel to the ξ axis. To facilitate this matching, the first equation in (10) is used to eliminate φ in the t and η equations in (9) and (10), respectively. For instance, t and η are written as functions of ξ for $\varphi \leq 0(1)$ or $\xi \leq 0(\mu^{1/2})$ to order $\mu^{3/2}$:

$$\left. \begin{aligned} t &= t_0(\theta_1) - \frac{\xi}{|1 - h_0|(1 + a^2)^{1/2}} + \mu \left[\frac{|K_0|}{h_0^2 |1 - h_0|} \times \right. \\ &\quad \left. \ln \left(\frac{h_0 \xi}{|1 - h_0|(1 + a^2)^{1/2}} \right) + G_6(\theta_1) \right] + 0(\mu^{3/2}) \\ \eta &= \frac{\pm \mu G_7(\theta_1)}{(1 + a^2)^{1/2}} + 0(\mu^{3/2}) \end{aligned} \right\} \quad (11)$$

Note that from the definition of K_0

$$\frac{|K_0|}{h_0^2 |1 - h_0|} = \frac{1}{(1 + a^2)^{3/2} |1 - h_0|^3}$$

in these equations. And the constants

$$\begin{aligned} G_6(\theta_1) &= \frac{aG_5(\theta_1) - G_4(\theta_1)}{(1 + a^2)^{1/2} |1 - h_0|} + G_4(\theta_1) \\ G_7(\theta_1) &= -[aG_4(\theta_1) + G_5(\theta_1)] \end{aligned}$$

are definite integrals of bounded functions from θ_0 to θ_1 .

Next the perturbation solution for the particle inside a small neighborhood of m_1 and its asymptotic expansion will be derived. The differential equation of motion (1) can be written as

$$\ddot{\mathbf{r}}_2 = -\mu \frac{\mathbf{r}_2}{r_2^3} - \left(\frac{\mathbf{r}}{r^3} - \mathbf{r}_1 \right)$$

since $\mathbf{r}_2 = \mathbf{r} - \mathbf{r}_1$ and $\ddot{\mathbf{r}}_1 = (1 + \mu)\mathbf{r}_1$. The unperturbed solution satisfying the equation

$$\ddot{\mathbf{r}}_2 = -\mu(\mathbf{r}_2/r_2^3)$$

has the form of a hyperbolic motion (for positive energy), which can be described (Ref. 5, p. 178) in terms of the variable

$$F = 2 \tanh^{-1} \left[\left(\frac{e_2 - 1}{e_2 + 1} \right)^{1/2} \tan \left(\frac{\theta_2 - \omega_2}{2} \right) \right] \quad (12a)$$

by the equations

$$\begin{aligned} t_p - t &= \frac{\mu h_2^3}{(e_2^2 - 1)^{3/2}} (e_2 \sinh |F| - |F|) \\ r_2 &= \frac{\mu h_2^2}{(e_2^2 - 1)} (e_2 \cosh F - 1) \quad F \leq 0 \end{aligned} \quad (12b)$$

The asymptotic behavior of these equations for $r_2 \geq 0(\mu^{1/2})$ will now be determined. This amounts to determining the behavior far out on the hyperbola [since $\mu^{1/2} \gg \mu$ and the pericenter distance is $0(\mu)$]. Let the auxiliary variable $z = \mu e^{|F|}$. Equations (12) in terms of this variable become

$$\left. \begin{aligned} \theta_2 &= \omega_2 - 2 \tan^{-1} \left[\left(\frac{e_2 + 1}{e_2 - 1} \right)^{1/2} \left(\frac{z - \mu}{z + \mu} \right) \right] \\ t_p - t &= \frac{\mu h_2^3}{(e_2^2 - 1)^{3/2}} \left[\frac{e_2}{2} \left(\frac{z}{\mu} - \frac{\mu}{z} \right) - \ln \frac{z}{\mu} \right] \\ r_2 &= \frac{\mu h_2^2}{(e_2^2 - 1)} \left[\frac{e_2}{2} \left(\frac{z}{\mu} + \frac{\mu}{z} \right) - 1 \right] \end{aligned} \right\} \quad (13)$$

Choosing the argument of pericenter as

$$\omega_2 = 2 \tan^{-1} \left[\left(\frac{e_2 + 1}{e_2 - 1} \right)^{1/2} \right]$$

and measuring θ_2 from the ξ axis orients the hyperbola with its asymptote parallel to the ξ axis. This follows since, with this choice of ω_2 ,

$$\theta_2 = 2 \tan^{-1} \left[\frac{\mu(e_2^2 - 1)^{1/2}}{e_2 z - \mu} \right]$$

and θ_2 approaches zero as z increases without bound, i. e., as r_2 increases without bound. The asymptotic expansions describing the behavior of the hyperbola for $z \geq 0(\mu^{1/2})$, i. e., for $r_2 \geq 0(\mu^{1/2})$, can then be written in component form as

$$\left. \begin{aligned} \xi &= r_2 \cos \theta_2 = \frac{\mu h_2^2}{e_2^2 - 1} \left(\frac{e_2 z}{2\mu} - 1 \right) + 0 \left(\frac{\mu^2}{z} \right) \\ \eta &= r_2 \sin \theta_2 = \frac{\mu h_2^2}{(e_2^2 - 1)^{1/2}} + 0 \left(\frac{\mu^2}{z} \right) \\ t_p - t &= \frac{\mu h_2^3}{(e_2^2 - 1)^{3/2}} \left(\frac{e_2 z}{2\mu} - \ln \frac{z}{\mu} \right) + 0 \left(\frac{\mu^2}{z} \right) \end{aligned} \right\} \quad (14)$$

Then using the first equation in the foregoing to eliminate the auxiliary variable z , these equations can be written in terms of ξ as the independent variable for $\xi \geq 0(\mu^{1/2})$:

$$\begin{aligned} t_p - t &= \frac{\xi}{V_\infty} + \frac{\mu}{V_\infty^3} \left[1 - \ln \left(\frac{2V_\infty^2 \xi}{\mu e_2} \right) \right] + 0(\mu^{3/2}) \\ \eta &= \frac{\mu h_2}{V_\infty} + 0(\mu^{3/2}) \end{aligned} \quad (15)$$

where

$$V_\infty = (e_2^2 - 1)^{1/2} / h_2$$

It can also be shown that the perturbation terms due to m_0 are $0(\mu^{3/2})$ for $r_2 \leq 0(\mu^{1/2})$. This then completes the description of the asymptotic behavior of the m_1 -centered hyperbola.

The matching is now performed, i. e., the constants of the m_1 -centered hyperbola are determined by comparing the asymptotic expansions of the perturbed conic about m_0 as given by (11) and the hyperbola about m_1 as given by (15). The two expansions are identical provided the constants of the m_1 -centered hyperbola are chosen as

$$V_\infty = |1 - h_0|(1 + a^2)^{1/2}$$

$$h_2 = (1 - h_0)G_7(\theta_1)$$

$$t_p = t_0(\theta_1) + \frac{\mu}{V_\infty^3} \left[1 + \ln \left(\frac{\mu h_0 e_2}{2V_\infty^3} \right) \right] + \mu G_6(\theta_1)$$

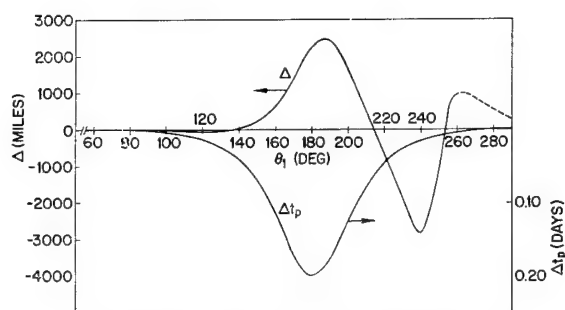


Fig. 3 Effect of Mar's perturbation on certain Earth-Mars trajectories.

where

$$e_2 = (1 + V_\infty^2 h_2^2)^{1/2}$$

Recall that the orientation of the m_1 -centered coordinates is determined by a rotation through the angle

$$\alpha = \tan^{-1}(1/a)$$

chosen in the first quadrant if $h_0 \leq 1$ and in the third quadrant if $h_0 > 1$. This then completes the matching and specifies the constants of the m_1 -centered hyperbola.

Since the inner and outer solutions are written in terms of different independent variables that are not related in any elementary fashion, a composite solution cannot be obtained. However, a uniformly valid asymptotic approximation correct to $O(\mu^{3/2})$ is given by Eqs. (7, 8, and 13), provided they are restricted to the appropriate regions. This follows from the fact that their asymptotic expansions (10) [with the time equation given in (9)] and (14), which are correct to $O(\mu^{3/2})$ for $\varphi \leq O(1)$ and $z \geq O(\mu^{1/2})$, match [when they are both written in terms of ξ for $\xi = O(\mu^{1/2})$ i.e., $\varphi = O(1)$, i.e., $z = O(\mu^{1/2})$] in the boundary layer common to the two regions. Moreover, once the constants of the m_1 -centered hyperbola have been determined in terms of the given initial

conditions and certain definite integrals of bounded functions, the effect of m_1 on trajectories that reach a small neighborhood of m_1 can be studied. For example, the perturbation by Mars on a class of Earth-Mars trajectories leaving a massless Earth at perihelion, with initial conditions such that the unperturbed heliocentric conic intersects Mars, was studied. The definite integrals were evaluated numerically, and the results are plotted as a function of transfer angle θ_1 in Fig. 3. It can be seen that the perturbation by Mars causes the particle to arrive earlier by an amount $\Delta t_p = t_p - t_0(\theta_1)$ and causes the asymptote to be deflected by an amount

$$\Delta = \frac{\mu h_2^2}{(e_2^2 - 1)^{1/2}} = \frac{\mu |G_7(\theta_1)|}{(1 + a^2)^{1/2}}$$

the deflection being away from the sun for transfers less than approximately 214° and toward the sun for larger transfer angles.

In Fig. 3, corresponding to the condition $|1 - h_0| \gg \mu^{1/2}$, there is a small interval about $\theta_1 = \pi/2$ for which no points on the curves were obtained. The curves were continued smoothly across this interval of a few degrees to obtain the curves as shown in Fig. 3.

References

- ¹ Lagerstrom, P. A. and Kevorkian, J., "Matched conic approximations to the two fixed force center problems," *Astron. J.* **68** (March 1963).
- ² Lagerstrom, P. A. and Kevorkian, J., "Earth-to-moon trajectories in the restricted three body problems," *J. Mekan.* **2** (June 1963).
- ³ Lagerstrom, P. A. and Kevorkian, J., "Some numerical aspects of earth-to-moon trajectories in the restricted three body problem," AIAA Preprint 63-3891 (August 1963).
- ⁴ Whittaker, K. T., *A Treatise on the Analytical Dynamics of Particles and Rigid Bodies* (Dover Publications, Inc., New York, 1944).
- ⁵ Moulton, F. R., *An Introduction to Celestial Mechanics* (The Macmillan Co., New York, 1914).

Solar Radio Emission as a Criterion for Solar Proton Event Warning

J. D. FLETCHER*

North American Aviation, Inc., Downey, Calif.

The use of solar radio emission as an indication of impending proton arrival from a solar flare is discussed. Specific characteristics of solar radio emission on fixed frequencies have been found to be associated with solar flares that are proton emitters. These signal characteristics are distinguishable from nonproton emitting flares. Fixed frequencies between 1000 and 3750 Mc tend to show recognizable signal characteristics that will give a warning time from a minimum of 30 min to an average of 2 hr before the arrival of protons near the earth. The correlation between solar radio emission and solar flares and between solar flares and solar cosmic ray or proton events has been known for quite some time and has been well established. If the knowledge were available that a particular solar flare was capable of producing protons, and that, within a relatively short period of time, the protons would be observed in the vicinity of the earth, the warning time gained would be used effectively in many ways.

BOISCHOT¹ described a particular type of radio emission whose characteristics showed a burst that lasted for tens of minutes and whose source did not remain fixed in the solar atmosphere. The source appeared to move outward with speeds up to 1000 km/sec. It followed that any continuum radiation (i.e., radiation showing smooth, even characteristics over a broad band of frequencies) would be called type IV, which originally pertained to a specific characteristic in the meter wavelengths. The definition was later extended to include any long-period continuum emission in any part of the radio spectrum that follows a flare (Boischot and Pick⁷). These definitions of type IV, however precise, were not adequate for solar proton event warning.

Many solar investigators—Boischot,¹ Thompson and Maxwell,² Pick-Gutmann,³ Kundu,⁴ Wild,⁵ and Bell⁶—have found that a significant relation exists between the occurrence of a spectral type IV solar radio outburst in association with a flare and an impending bombardment of protons in the vicinity of the earth. The very high correlation between solar proton events and type IV radio emission appeared to be very encouraging as a means of developing a solar proton event warning system.

It appears from the preceding definitions that a type IV event can be recognized by the use of spectral solar radio receiving equipment. The use of solar radio spectrum analyzers, however, would entail the use of equipment whose complexity would not allow simple analytical procedures. It was necessary to investigate the development of a simplified technique of reception and analysis of the solar radio emission. It was also realized that, if the radio signal associated with a proton emitting flare could be recognized at a single frequency, a system might be developed which would be compact enough for use onboard spacecraft or for widespread terrestrial observations.

The literature was nearly void of cases where investigators had sought for the relationship between the characteristics associated with a fixed frequency solar radio signal and the existence of associated protons. One exception was

Kundu and Haddock.⁸ While comparing centimeter-wave solar bursts with centimeter-wave solar outbursts, they stated that a microwave outburst in the centimeter wavelengths, described as a simple burst with a postburst increase (Covington⁹) with a typical duration of from 10 to 20 min and a rise time of 1 to 3 min, may have solar cosmic rays as associated phenomena. A simple burst, as defined by Covington, is a burst with an intensity greater than 7.5×10^{-22} w - m⁻² (cm/sec)⁻¹ and of relatively short duration. A postburst increase is described as a case in which the flux level remaining after a simple burst is higher than the flux level prior to the occurrence of the simple burst. The realization that a fixed frequency might display characteristics recognizable as being associated with a proton event prompted further investigation.

The initial investigation entailed the use of basic data published in the International Astronomical Union Quarterly Bulletin (IAU) and supplemented by data published by the Central Radio Propagation Laboratory (CRPL) for the period 1956–1961. The purpose of the initial study was to determine the feasibility of the use of a single frequency in the establishment of a solar proton warning system. The time of occurrence of solar radio emission data used in the analysis was compared with proton events selected from a list compiled by Malitson and Webber.¹⁰ If the time of the associated radio emission was not available from this list, a careful study was made of all available observations (IAU, CRPL, or from original records) for a period up to 24 hr prior to the proton arrival time as given by the same list prepared by Malitson and Webber. The 23 solar cosmic ray events used in the analysis were those whose total integrated fluxes were $\geq 1 \times 10^7$ protons-cm⁻² greater than 30 Mev as reported by Malitson and Webber. There is no absolute assurance that every solar radio event investigated was the actual one that was associated with the proton emission, but the possibility of nonassociation is minimal.

Reproductions of original records of fixed frequency solar rf bursts associated with outstanding proton events were studied for signal characteristics indicative of these proton events prior to the actual formal analysis. After studying these records, it was noticed that each of the associated signals had several general characteristics that preceded the arrival of the protons at the surface of the earth, these characteristics being specifically different for each received frequency.

It may be observed from Fig. 1 that the characteristics of the solar radio signal have obvious differences from one frequency to the next. The top trace represents the arrival time of the solar cosmic rays. The other plots represent the

Presented as Preprint 64-64 at the AIAA Aerospace Sciences Meeting, New York, January 20–22, 1964; revision received September 8, 1964. The author is indebted to A. Covington for original records and valuable comments used in the preparation of this paper. The author is also indebted to Alex Shlanta for his able and enthusiastic participation in the data analysis, interpretation, and calculations required for the completion of this paper.

* Research Specialist, Space and Information Systems Division.

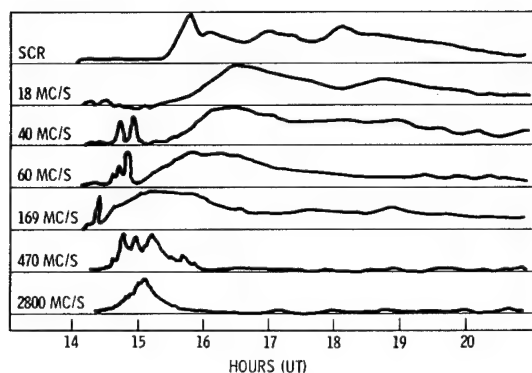


Fig. 1 Typical proton event and solar radio relationship (from Boischot and Warwick¹¹).

radio flux changes with respect to time. The characteristics of the rf signal at the higher frequencies differ somewhat from those at lower frequencies, and the associated causes are not generally agreed upon (Boischot and Warwick¹¹). But the fact remains that rf signal is available for analysis at these higher frequencies prior to the arrival of the solar protons. In particular, it became evident that the characteristics of signal duration and maximum flux density of the associated rf bursts were related to the subsequent proton events, with the actual numerical values for these characteristics being different for each frequency.

It was decided that signal duration and maximum flux density would be worthwhile signal characteristics to study in more detail for proton event warning.

A statistical analysis was made on data taken primarily from the IAU Quarterly Bulletin for the determination of optimum frequencies and resultant signal characteristics that might be used for proton event warning. The initial characteristics used were signal duration (in minutes) and signal maximum flux density [$10^{-22} \text{ w} \cdot \text{m}^{-2} (\text{cm} / \text{sec})^{-1}$]. The object of the statistical analysis was to determine the optimum frequencies and associated signal characteristics that would give the highest probability of warning success (PWS) and the lowest false alarm ratio (FAR).

Probability of warning success (PWS) is defined as

$$\text{PWS} = \frac{\text{rf successes}}{\text{rf successes} + \text{rf failures}}$$

where an rf success is defined as a case in which the signal, received at a solar radio observatory at a particular frequency, is associated with a prescribed proton event and meets the signal characteristics specified. An rf failure is

defined as a case in which a signal associated with a prescribed proton event did not meet the specified signal characteristics. Thus, PWS is the probability that, if a proton event of a particular size did occur, a warning would be given with respect to certain signal characteristics.

False alarm ratio (FAR) is defined as

$$\text{FAR} = \frac{\text{total signals with specific characteristic requirements}}{\text{total signals with characteristic requirements for which proton events followed}}$$

or

$$\text{FAR} = \frac{\text{false alarm signals} + \text{proton event rf signals}}{\text{proton event rf signals}}$$

where a false alarm is a case where a characteristic signal is received and no ensuing proton event follows. Thus, FAR is the inverse of the probability that, if a specific solar rf signal characteristic is received, it will be followed by proton events of a particular size.

Two basic approaches were made to this initial analysis: a restrictive approach and a nonrestrictive approach. In the restrictive approach, the results are restricted in that the rf failure cases for the calculation of the PWS include stations that were in a geographical position to have observed associated rf, for a specific proton event, but did not report any signal observation, or else data were not available. If the observing station did not report any data, it was assumed that the station was in operation at the time of the rf event but did not receive any signal that met the signal characteristics requirements. The assumption that the observatory did receive a signal but that it did not meet the signal characteristics requirements may not be a valid one. Examination of original records from solar observatories have shown radio events for certain proton flares in which the signal characteristics were actually met but the rf data were not published in the IAU Quarterly Bulletin. The assumption that the station was actually in operation because it was in a geographical position to have observed the solar rf may be invalid also. The station may have been inoperative for many reasons, such as equipment failure, power failure, etc.

A nonrestrictive approach is defined as one in which the solar radio data for proton events included in the analysis were those that had associated radio data available for study with no assumptions or restrictions. Optimum frequencies were then determined by choosing the frequency or frequencies that would give the highest PWS and the lowest FAR for associated signal characteristics. The initial signal characteristics chosen were signal duration of 10 min or greater, and a maximum flux density of at least 150 flux units. It may

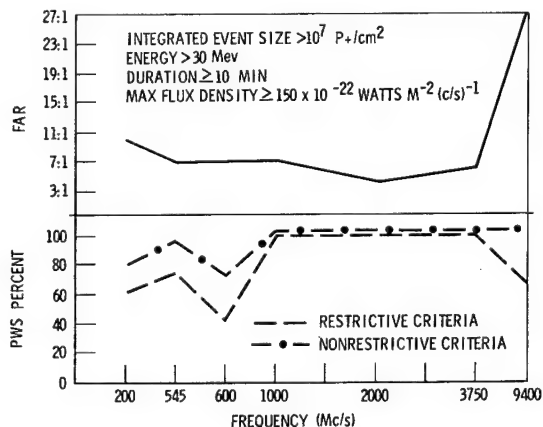


Fig. 2 Optimum frequency and false alarm calculations using IAU data.

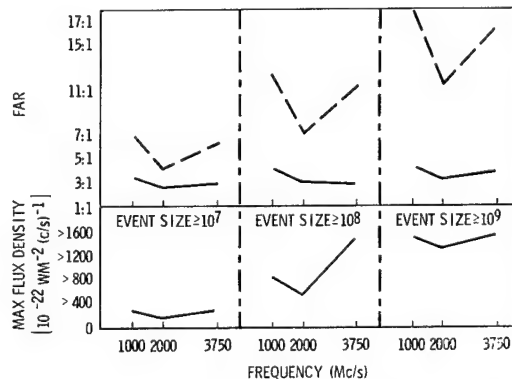
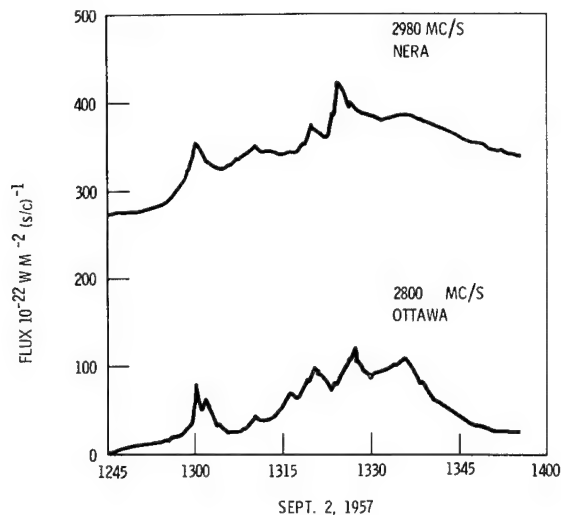


Fig. 3 The top shows false alarm ratios by event size and frequency for varied signal characteristics. The bottom indicates signal characteristic variations while maintaining 100% PWS.



IAU QUARTERLY BULLETIN DATA

	ST. TIME	MAX TIME	MFD	DURATION
2980	1257	-	429	45
2800	1247	1350	120	250

Fig. 4 Example of data normalization problems for simultaneous observations.

be seen in Fig. 2 that the optimum frequencies appear to lie in the range of 1000 to 3750 Mc/sec. It is also apparent that the lowest false alarm ratios are for frequencies near 2000 Mc/sec.

These results tend to agree with those presented by Das Gupta and Basu.¹² They show that large flares whose radio emission occurs near the time of the flare within the frequency range between 1000 to 3750 Mc/sec show the highest correlation of association with major flares.

Individual frequencies in the optimum range of 1000 to 3750 Mc/sec were studied further to see if the FAR could be lowered while still maintaining a 100% PWS. It was found that if an increased signal duration were considered and the maximum flux density varied so that a 100% PWS was maintained for each proton event size, the FAR could be further reduced. Figure 3 depicts the lowering of the false alarm ratio by frequency for event sizes of $\geq 10^7$, $\geq 10^8$, and $\geq 10^9$ protons-cm⁻². Also shown in Fig. 3 is the change in maximum flux density as the proton event size increases while still maintaining a 100% probability of warning success. It is also obvious from Fig. 3 that there is a direct relationship between the maximum flux density and proton event size. The fact that the maximum flux density tends to increase with event size might lead one to believe that the prediction of the size of the impending proton event might be achieved.

Even though relatively low FAR had been shown, especially for larger and more important events when the radiation problem is considered, the fact that the analysis had been based on such a small data sample made us consider the possibility of expanding the analysis. The results shown in Fig. 3 were based on the data from Nagoya, Japan, observing on frequencies of 1000, 2000, 3750, and 9400 Mc/sec. Since a single station is capable of taking solar observation for a maximum 12-hr period each day, flares occurring during the other 12-hr period were not included in the analysis. It appeared that, if a frequency within this range from the other hemisphere could be incorporated into the analysis, 2800 Mc/sec (Ottawa, Canada) or 2980 Mc/sec (Nera, Netherlands), for example, our data sample could be essentially doubled. It was found that this could not be done satisfactorily. Figure 4 shows some examples of the data normalization problems when many original records are

considered. Figure 4 shows that the data reporting procedures may vary from station to station. Ottawa subtracts the mean daily flux prior to reporting observed data for publication, whereas Nera, on the other hand, did not. Both traces shown in Fig. 4 are for the same event at the same time and are both taken from original records obtained from each respective observatory. The table on the same plot shows the data as reported in the IAU Quarterly Bulletin. It is obvious that the results obtained by comparing the maximum flux densities from two or more different stations could not be used with a high degree of reliability but that the consistency of the signal characteristics shown in a single station did provide consistent data. Covington,¹³ Ottawa (2800 Mc/sec), and Tanaka,¹⁴ Nagoya (1000, 2000, 3750, 9400 Mc/sec), have stated that absolute fluxes reported are within $\pm 10\%$ of the actual value. Since more data were readily available at 2800 Mc/sec and since this frequency was within the range that proved to be the most rep-

Table 1 Proton events recognized by Malitson and Webber or D. K. Bailey with total flux $\geq 10^6$ protons-cm⁻² with energies > 30 Mev

No.	Date of event	Flux > 30 Mev	Source
1	Feb. 23, 1956	1.6×10^9	M & W
2	Aug. 31, 1956	3.0×10^7	M & W
3	Nov. 13, 1956	1.0×10^8	Bailey
4	Jan. 20, 1957	3.0×10^8	M & W
5	April 3, 1957	5.0×10^7	Bailey
6	June 21, 1957	1.5×10^8	Bailey
7	July 3, 1957	1.0×10^7	M & W
8	July 24, 1957	7.5×10^6	Bailey
9	Aug. 29, 1957	1.5×10^8	Bailey
10	Aug. 31, 1957	8.0×10^7	Bailey
11	Sept. 2, 1957	5.0×10^7	Bailey
12	Sept. 12, 1957	6.0×10^6	Bailey
13	Sept. 21, 1957	1.15×10^8	Bailey
14	Oct. 20, 1957	1.0×10^7	M & W
15	Feb. 9, 1958	5.0×10^6	M & W
16	March 23, 1958	4.0×10^8	M & W
17	March 25, 1958	6.0×10^8	Bailey
18	April 10, 1958	5.0×10^7	Bailey
19	July 7, 1958	5.0×10^8	M & W
20	July 29, 1958	8.5×10^6	Bailey
21	Aug. 16, 1958	2.0×10^7	M & W
22	Aug. 22, 1958	5.0×10^7	M & W
23	Aug. 26, 1958	5.3×10^7	M & W
24	Sept. 22, 1958	8.5×10^7	Bailey
25	May 10, 1959	1.2×10^9	M & W
26	July 10, 1959	8.0×10^8	M & W
27	July 14, 1959	2.0×10^9	M & W
28	July 16, 1959	3.0×10^9	M & W
29	Sept. 2, 1959	1.15×10^7	Bailey
30	Jan. 12, 1960	6.0×10^6	Bailey
31	March 29, 1960	6.0×10^6	Bailey
32	March 30, 1960	6.0×10^6	Bailey
33	April 1, 1960	2.7×10^6	M & W
34	April 5, 1960	2.0×10^6	M & W
35	April 28, 1960	2.5×10^7	M & W
36	April 29, 1960	1.75×10^8	Bailey
37	May 4, 1960	7.0×10^6	M & W
38	May 6, 1960	5.0×10^6	M & W
39	May 13, 1960	5.0×10^7	Bailey
40	Sept. 3, 1960	4.0×10^7	M & W
41	Nov. 12, 1960	2.7×10^9	M & W
42	Nov. 15, 1960	2.0×10^9	M & W
43	Nov. 20, 1960	6.0×10^7	M & W
44	July 11, 1961	2.0×10^6	M & W
45	July 12, 1961	1.0×10^7	M & W
46	July 15, 1961	1.25×10^7	Bailey
47	July 18, 1961	1.25×10^8	Bailey
48	July 20, 1961	9.0×10^6	M & W
49	July 28, 1961	4.4×10^6	Bailey
50	Sept. 8, 1961	3.0×10^6	Bailey
51	Sept. 10, 1961	3.75×10^7	Bailey
52	Nov. 10, 1961	8.0×10^6	Bailey

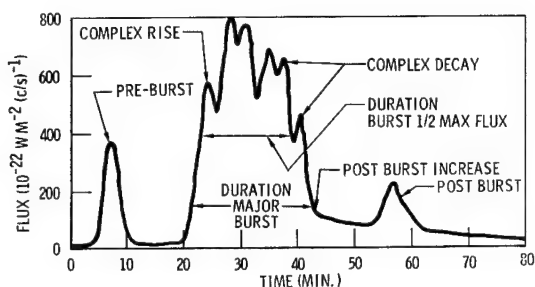


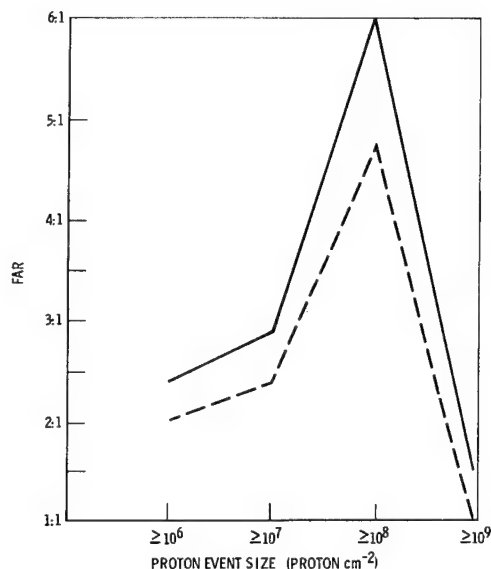
Fig. 5 Model fixed frequency centimeter-wave associated with solar proton event.

representative in the initial analysis, it was selected for more detailed study.

Although the proton event list published by Malitson and Webber is thought to contain all of the proton events whose total fluxes are equal to or greater than 1×10^6 protons- cm^{-2} greater than 30 Mev, there were a number of events recognized by Bailey¹⁵ to be of an equal magnitude in this range. A new proton list was therefore compiled which incorporated these events¹⁶ as shown in Table 1. This list shows normalized values (from 20 to 30 Mev) for Bailey's events.

The original records of all of the outstanding solar radio events were obtained from Covington¹³ at the National Research Council, Ottawa, Canada, observing on 2800 Mc/sec. Ottawa has been observing at this frequency since 1947. Only the records from 1956 to 1961 were used in the analysis because reliable observations of proton events have been made only during this period. The objective was the same as in the initial analysis. We wanted to find some characteristic of the solar radio emission associated with a proton emitting flare that was not recognizable when associated with a flare that was not an observable proton emitter.

The analysis of the original records obtained for 2800 Mc/sec has resulted in a model that is felt to be representative of the radio signal occurring at the time of a proton flare.



CRITERIA					ADDITIONAL CRITERIA	
EVENT SIZE	MFD	DUR	POST INC	POST DUR	EVENT SIZE	DURATION MAJOR BURST DURATION 1/2 MFD
10^6	160	15	15	20	10^6	3.46
10^7	160	15	15	25	10^7	3.46
10^8	300	15	15	25	10^8	3.24
10^9	2500	40	>100	>100	10^9	3.24

Fig. 6 False alarm ratios for combined Malitson and Webber and normalized Bailey proton event list using 2800 Mc/sec data and maintaining 100% PWS.

MALITSON & WEBBER & BAILEY EVENTS
OMITTING 11-13-56, 9-2-57, 7-15-61
PWS 84 PERCENT

SIZE	MFD	DUR	POST FLUX	POST DUR	DUR BUR DUR 1/2 (MFD)	RR
10^6	340	15	15	20	3.75	24
10^7	340	15	15	25	3.75	24
10^8	360	15	15	25	3.75	31
10^9	2500	40	44	>100	3.24	51

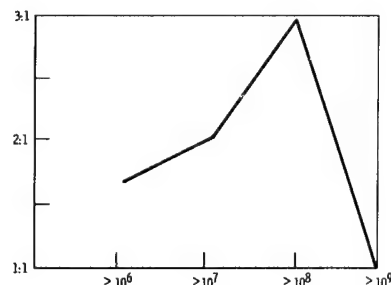


Fig. 7 False alarm ratios for 2800 Mc/sec data using Malitson and Webber and normalized Bailey events.

Figure 5 shows this representation. All of the characteristics shown in the model are not observable for every proton event. Most characteristics, however, are present.

The nomenclature of Fig. 5 is based primarily on the terminology developed by Dodson and Covington.¹⁷ The features that were found to be important included those already found in the initial analysis, such as duration of major burst and maximum flux of the major burst. In addition, all proton events were found to have either a preburst, a complex rise, a complex decay, or any combination thereof. The most outstanding feature found, however, was the post-burst increase. The postburst increase is sometimes accompanied by a postburst. It was noted that every proton

MALITSON & WEBBER EVENTS ONLY
PWS 100 PERCENT

SIZE	MFD	DUR	POST FLUX	POST DUR	DUR BUR DUR 1/2 (MFD)	RR
10^6	340	33	40	20	3.46	24
10^7	340	33	40	90	3.46	24
10^8	360	40	80	240	3.24	51
10^9	2500	50	>100	>100	3.24	51

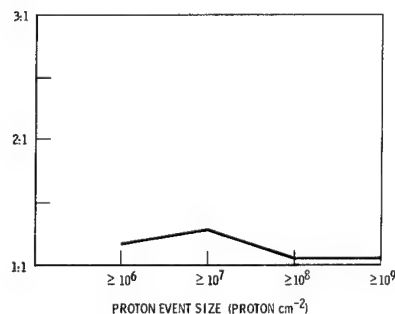


Fig. 8 False alarm ratios for 2800 Mc/sec using Malitson and Webber events alone with varied criteria in each case.

event, according to the combined list of both Malitson and Webber¹⁰ and Bailey,¹⁵ had the postburst increase as an observable feature. This observation agrees with the comment that was mentioned earlier, made by Kundu and Haddock,⁸ that microwave bursts classified as simple by Covington, followed by a postburst increase, have solar cosmic rays as associated phenomena.

Additional salient features found while trying to establish proton event signal characteristics were 1) the rate of rise of the signal from the start of the major burst to the peak flux, in units of flux increase per minute; and 2) the ratio of the duration of the major burst to the duration of the major burst at one-half maximum flux density, with these times taken as shown in Fig. 5.

Figures 6 and 7 show how the reduction in the false alarm ratio as additional signal characteristics were added to the calculations. FAR's were calculated for the event sizes of $\geq 10^6$, $\geq 10^7$, $\geq 10^8$, and $\geq 10^9$ protons-cm⁻² by using a maximum flux density, a duration of major burst, a postburst increase flux, and a postburst duration that was observable in every proton event whose accompanying flare occurred during the normal observational hours at Ottawa. The additional criteria of the ratio of the duration of the major burst to the duration of the major burst at one-half maximum flux density is shown to lower the FAR in every case for every event size.

After further examination of the solar radio data, it was felt that, if three of the proton events from the Bailey list could be considered as having total integrated fluxes that were smaller than stated, the analysis could be improved. These three Bailey events were then omitted from the list, and a recalculation of the FAR ratio was made. By omitting these events, the probability of warning success was lowered from 100 to 84%, but the FAR was lowered a very significant amount by adding the additional criteria, the rate of rise to signal maximum. These results are shown in Fig. 7.

Since the initial analysis used only the proton events as recognized by Malitson and Webber, we applied the same criteria to this list alone and calculated the FAR ratios as shown in Fig. 8. It was found that we are able to recognize every proton event equal to or greater than 10^6 protons-cm⁻² total flux correctly, and that we would not have been falsely alerted in any case for events $\geq 10^8$ protons-cm⁻².

An investigation of this type has limitations because of the small sample size and the subjectivity of the analysis of the original records. Any final conclusions drawn from these results

should be used with some caution. It is felt that the study has shown some significant characteristics that should be looked for when data is available during the forthcoming solar cycle. It is also felt that the data presented at this time show enough merit to justify the building of a system that would give warning of an impending solar proton event.

References

- ¹ Boischot, A., "Étude du rayonnement radioélectrique solaire sur 169 MHz, à l'aide d'un grand interféromètre à réseau," *Ann. Astrophys.* **21**, 273-344 (1958).
- ² Thompson, A. R., "Type IV (continuum) radio bursts from the sun," *J. Phys. Soc. Japan* **17**, 198-202 (1962).
- ³ Pick-Gutmann, M., "Evolution des émissions radioélectriques solaires de type IV et leur relation avec d'autres phénomènes solaires et géophysiques," *Ann. Astrophys.* **24**, 183-210 (1961).
- ⁴ Kundu, M. R., "Nature of type IV solar radio bursts," *J. Phys. Soc. Japan* **17**, 215-219 (1962).
- ⁵ Wild, J. P., "The radio emission from solar flares," *J. Phys. Soc. Japan* **17**, 249-258 (1962).
- ⁶ Bell, B., "Solar radio bursts of spectral types II and IV: their relations to optical phenomena and to geomagnetic activity," *Smithsonian Contrib. Astrophys.* **15**, 239-257 (1963).
- ⁷ Boischot, A. and Pick-Gutmann, M., "Structure of the type IV radio burst and its relation with solar cosmic rays," *J. Phys. Soc. Japan* **17**, 203-206 (1962).
- ⁸ Kundu, M. R. and Haddock, F. T., "Centimeter-wave solar bursts and associated effects," *Inst. Radio Engrs. Trans. Antennas Propagation* **AP-9**, 82-88 (1961).
- ⁹ Covington, A., "Solar emission at 10-cm wavelength," *Paris Symp. Radio Astron.*, 159-165 (1959).
- ¹⁰ Malitson, H. H. and Webber, W. R., "General characteristics of solar cosmic ray events," *NASA TR-169*, pp. 1-17 (1963).
- ¹¹ Boischot, A. and Warwick, C., "Radio emission following the flare of August 22, 1958," *J. Geophys. Res.* **64**, 683-684 (1959).
- ¹² Das Gupta, M. K. and Basu, D., "Solar radio bursts in relation to flare importance," *Astrophys. J.* **137**, 997-999 (1963).
- ¹³ Covington, A., private communication (1963).
- ¹⁴ Tanaka, H., private communication (1963).
- ¹⁵ Bailey, D. K., "The study and detection of solar cosmic rays by radio techniques," *J. Phys. Soc. Japan* **17**, 106-116 (1962).
- ¹⁶ Modisette, J., NASA Manned Spacecraft Center, private communication (1963).
- ¹⁷ Dodson, H. W., Hedeman, R. E., and Covington, A. E., "Solar flares and associated 2800 mc/sec (10.7 cm) radiation," *Astrophys. J.* **133**, 541-563 (1954).

Mass and Magnetic Dipole Shielding against Electrons of the Artificial Radiation Belt

A. BHATTACHARJIE* AND I. MICHAEL†

Northrop Space Laboratories, Hawthorne, Calif.

Computations of magnetic shielding system masses required for protection against electrons of various energies have been performed. We have also obtained a comparison of the required shielding masses for a space vehicle traversing circular orbits through the anomaly in the artificial radiation belt (ARB) at altitudes of 200, 400, 600, and 800 km and inclined at 30° to the earth's equatorial plane: first with a magnetic superconducting solenoidal shielding system approximated by a point dipole and then with a two-layer composite material shielding system consisting of an outer layer of aluminum and an inner layer of lead. The aluminum thickness equaled the practical range of 10-Mev electrons, and the lead was used to attenuate the bremsstrahlung to specified skin dose rates. The averaged electron flux in ARB, used in estimating dose, was computed to be sufficiently accurate for missions not shorter than 100 hr and more accurate for longer missions. The material shielding mass, primarily designed for protection when appreciable bremsstrahlung occur, was at best (no lead) an order of magnitude larger than that of the magnetic shielding system. The mass of the cryogenic system was neglected, being a fraction of the combined mass of the solenoid and support structure.

Nomenclature

l	= solenoid length
r	= solenoid radius
m_w	= solenoid mass
N	= number of turns of the superconducting wire
ρ_w	= density of the superconducting wire
d_w	= diameter of the superconducting wire
I	= current in the wire
H	= magnetic field at the center of the solenoid
M	= magnetic dipole moment
V	= inner forbidden volume
R_p	= practical range of electrons of 10 Mev
m_{st}'	= mass of the containment shell
ρ_{st}/S_y	= density-to-yield strength ratio of the containment shell
M_t	= material shielding mass
R	= dimensionless parameter
L	= dimensionless parameter
M_{st}'	= dimensionless parameter

Introduction

A COMPARISON is made of the relative masses required for an aluminum-lead shield vs a superconducting solenoidal shield for specific cases where the manned space vehicle is in any one of four practical circular orbits passing through the high electron flux region of the artificial radiation belt. The toroidally shaped totally forbidden volume of the dipole is compared with one of equal magnitude enclosed by a spherical shell of material. For the purposes of the calculations that follow, we assume that the electrons of the artificial radiation belt can be characterized by an omnidirectional flux of electrons with an energy distribution given by the fission-energy spectrum of Carter et al.¹

Received March 9, 1964; revision received August 13, 1964. The authors wish to express their appreciation to Robert E. Fortney and Mac R. Morrison for valuable discussions and the permission to use the results of their dose computations and the trajectory analysis in the radiation belt.

* Member of the Research Staff, Nuclear Sciences Division.

† Member of the Research Staff, Nuclear Sciences Division; now at Air Force Cambridge Research Laboratories, Bedford, Mass. Member AIAA.

Magnetic Shielding Mass

Here we will obtain the masses of superconducting magnetic solenoid systems required for protection against electrons of energies up to 10 Mev for a range of shielded volumes utilizing the point-dipole analysis for the inner forbidden volume. For this analysis to be valid, the shielded volume should engulf the solenoid and its supporting masses. Otherwise, one would have to account for the x rays produced by the electrons within the system. We shall utilize an optimizing procedure to calculate the minimum mass for the containment shell. It will be shown that with proper choice of units the relationship between the mass for the containment shell and the dimensions of the superconducting solenoid can be made independent of the magnetic field parameters. Furthermore, this relationship defines a minimum value for the mass. We start by adopting the following model for the superconducting system.²

1) The solenoid is a right circular cylinder of radius r , length l , and mass m_w , comprising N turns of superconducting niobium-tin alloy wire of density $\rho_w = 8 \text{ g/cm}^3$, and diameter $d_w = 0.015 \text{ cm}$.

2) A cylindrical containment shell of mass m_{st}' made of a titanium alloy (Ti-6Al-4V ELI) fits closely about the windings and is utilized to prevent explosive expansion of the energized solenoid. The shell is assumed to have the same radius and length as the solenoid and has a high density-to-yield-strength ratio at 4°K of $\rho_{st}/S_y = 2.46 \times 10^{-10} \text{ g/erg}$.

3) Kash and Tooper^{2,3} show that, for larger shielded volumes, the mass of the thermal insulation and cryogenic systems will be small as compared to the combined mass of the windings and containment structure. Hence, we feel it reasonable to neglect the mass of thermal insulation and also to make no allowance for changes in structural configuration that would be required for coolant ducts in the solenoid. We further neglect the mass of the cryogenic equipment necessary to produce the low temperatures and compensate for heat leaks into the system. Finally, we neglect the possibility of reducing the magnitude of the structural mass by integrating it with the walls of the space vehicle.

Where compressive stresses are taken into account, the mass of the structural containment shell given by Refs. 3 and 4 is

$$m_{st}' = \frac{4M^2\rho_{st}(1 + \beta + \beta^2)^{1/2}k}{\pi r^3 S_y(1 - k^2)} [E(k) - k] \quad (1)$$

$$\beta = \frac{1}{3k^2} \left[2k^2 - (1 - k^2) \frac{K(k) - E(k)}{E(k) - k} \right] \quad (2)$$

Here, $K(k)$ and $E(k)$ are complete elliptic integrals of the first and second kind, where the modulus k is given by

$$k^2 = 4r^2/(l^2 + 4r^2) \quad (3)$$

Equation (1) can be written as

$$m_{st}' = \frac{4M^2\rho_{st}}{\pi S_y} \frac{1}{r^3} f_1 \left(\frac{l}{r} \right) \quad (4)$$

The magnetic field at the center of the solenoid is denoted by H

$$H = 4M/r^2(l^2 + 4r^2)^{1/2} \quad (5)$$

where

$$M = \pi r^2 NI \quad (6)$$

and NI is the number of ampere turns. To prevent the superconducting wire from transforming to the "normal" state, the current I was chosen so that the magnetic field at the windings is less than the critical field. This poses a constraint on H , the field at the center of the solenoid. For our calculations we assume $H = 50,000$ gauss, and the magnetic dipole moment will be given in units of gauss-cubic centimeters.

By making proper choice of units, the equations defining mass and solenoidal dimensions, viz. (4-6), can be made independent of the magnetic field parameters (H , M). Now, m_{st}' can be expressed in units of λ , and r and l in units of R_0 , where

$$\lambda = 2MH\rho_{st}/\pi S_y = 7.830 \times 10^{-6} M \text{ g} \quad (7a)$$

$$R_0 = 2M/H = 3.420 \times 10^{-2} M^{1/3} \text{ cm}$$

Here

$$M = \frac{cp}{e} \left[\frac{4\pi}{3} f(\bar{\tau}) \right]^{-2/3} V^{2/3} = 1.291 \times 10^9 V^{2/3} \text{ gauss-cm}^3 \quad (7b)$$

where V is measured in cubic meters. The expression for M as given previously is derived in Ref. 5 for the case where $\bar{\tau} = 1$, where V represents the volume of the inner forbidden region for an ideal magnetic dipole. When the mass of the structural containment shell is given in units of λ , we shall designate it by the symbol M_{st}' rather than m_{st}' ; likewise when r and l are expressed in units of R_0 , they are referred to as R and L , respectively. Thus, in units of λ and R_0 , Eq. (4) becomes

$$M_{st}' = (1/R^3) f_1(L/R) \quad (8)$$

where now

$$L = 2R[(1/R^6) - 1]^{1/2} \quad (9)$$

This procedure enables us to make an optimum choice of the dimensions of the superconducting coil in the following manner: Plots of M_{st}' vs R and L vs R based on these equations are shown in Fig. 1. Observe that M_{st}' has a minimum at 1.608λ , corresponding to $R = 0.880 R_0$ and $L = 1.08 R_0$, and that from (7) we recall that λ and R_0 are functions of M alone. It is important to emphasize that the minimum value of M_{st}' obtained by this analysis is independent of (H , M) and is therefore true for all values of H and M .

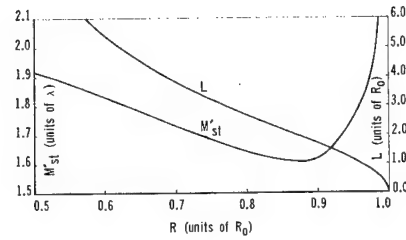


Fig. 1 Curves for optimizing the mass of the containment structure of the superconducting solenoid in terms of the dimensions of the solenoid.

Our optimization procedure consists of first selecting the magnitude of the volume to be shielded for a given maximum electron energy and then finding the corresponding magnetic moment for constant values of H . This determines λ and R_0 and thus $[M_{st}']_{\min}$; hence, $[m_{st}']_{\min}$ is determined. A plot of magnetic moment vs shielded volume for a maximum electron energy of 10 Mev appropriate for calculations pertaining to shielding against electrons of the artificial radiation belt is shown in Fig. 2. Here, the toroidally shaped forbidden volume of the superconducting solenoid (approximated by a point dipole) is compared with one of equal magnitude enclosed by a two-layer composite spherical shell of material. The outer layer consists of aluminum sufficiently thick to stop 10-Mev electrons, and the inner layer is lead of thickness specified so as to yield a given skin dose rate for a given incident electron flux. Note the curve \mathcal{D}_{\max} , maximum skin dose rate, which gives the mass of material shielding for zero thickness of lead. This curve lies a full order-of-magnitude higher than the corresponding magnetic shielding mass curve. A curve showing the forbidden volume as a function of the dipole moment (M) of the solenoid is also shown for reference.

Finally, the containment structure can be modified leading to an appreciable reduction in mass.⁴ A cylindrical shell at the windings counteracts the axial compression, and a series of disks inside the cylinder supports the radial forces. A correction factor is to be applied to our previous mass calculation to obtain the mass $[m_{st}]_{\min}$ for the new configuration. We have

$$[m_{st}]_{\min} = \frac{1 + 2(S_L/S_t)}{2(S_y/S_t)} [m_{st}']_{\min} \quad (10)$$

which is, in our case,

$$[m_{st}]_{\min} = 0.706 [m_{st}']_{\min} \quad (11)$$

The mass of the wire is

$$m_w = 8.883 \times 10^{-6} Nr \text{ kg} \quad (12)$$

where r is given in centimeters and N is determined from Eqs. (5) and (6).

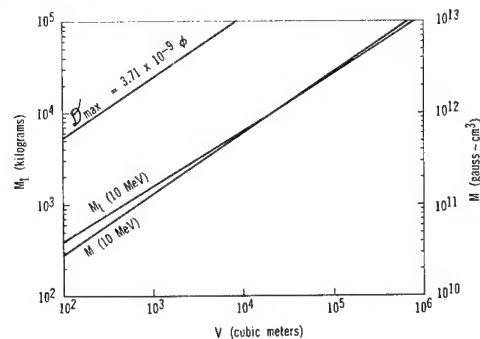


Fig. 2 Relative shielding masses M_i required to protect equal volumes of space V from electrons of the artificial radiation belt: first by magnetic dipole shielding and then by material shielding.

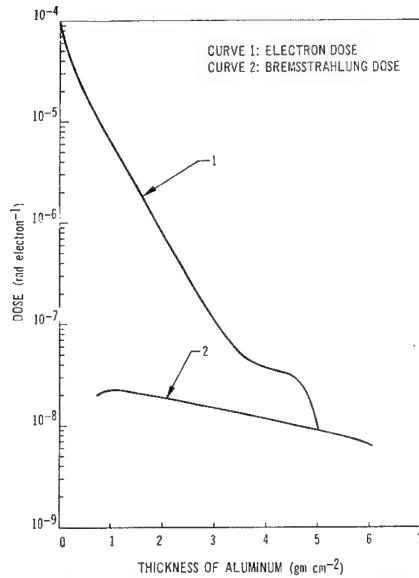


Fig. 3 Relative doses for electrons stopping in aluminum and for their attendant bremsstrahlung production, as a function of aluminum thickness, where 1 g-cm⁻² of aluminum corresponds to 1.924×10^{-2} m.

The over-all mass of the containment structure and the windings is then given by

$$M_t = [m_{st}]_{\min} + m_w \quad (13)$$

A graph of shielded volume V as a function of over-all magnetic system mass M_t is given in Fig. 2 and will be referred to later in order to make a comparison with material shielding.

Material Shielding Mass

The bremsstrahlung skin dose rate on tissue will be the criterion utilized for calculating the mass of material shielding required for protection against electrons of the artificial radiation belt. In our model, a small sphere of tissue is placed at the center of a spherical volume protected by a two-layer composite shielding wall. The outer layer consists of low- Z material of thickness equal to the practical range of the most energetic fission-spectrum electrons (R_p); the inner layer consists of a high- Z material to attenuate the bremsstrahlung produced in the outer layer. The thickness of the inner layer is chosen so as to allow a given dose-rate for a specified average electron flux impinging on the vehicle. In our calculations we have selected aluminum for the outer layer, lead for the inner layer, and we assume that 10 Mev is the cutoff energy for electrons of the fission spectrum (14). Figure 3 illustrates the importance of completely

stopping the electrons in the aluminum. The data for this graph was kindly provided by Fortney⁶ and is based on the assumption of isotropic bremsstrahlung production and a specified transmission factor.⁸ Observe that at given thicknesses of aluminum the electron dose is much larger than the bremsstrahlung dose. This indicates the importance of stopping the electrons completely.

We present pertinent formulas whereby a large class of shielding problems can be solved with relative ease. These results can be applied wherever the following two assumptions are satisfied:

- 1) The electron spectrum is given by Ref. 1:

$$y_0(E) = 3.88 \exp[-0.575E - 0.055E^2], E \text{ in Mev} \quad (14)$$

- 2) The omnidirectional electron flux encountered by the vehicle for any single trajectory is the same at all points along the trajectory within the anomaly of the artificial radiation belt. Outside this anomaly, the vehicle is in a radiation-free environment.

Implicit in our calculations is the assumption that the electron flux encountered by the vehicle is large enough to produce a significant bremsstrahlung dose rate at the surface of the tissue receiver. Our model will not give optimum shielding when this dose rate is very small.

The normalized bremsstrahlung dose from electrons of the artificial radiation belt is given by

$$D_0(T, E_0) = \int_0^{E_0} dE E \gamma(E) \int_0^{t_m} \gamma(E_0, E, t + T + R_p) \times e^{-\sigma(E)t} dt \quad (15)$$

where

$\gamma(E_0, E, t + T + R_p)$	= the number of photons with energies in the interval E to $E + dE$ at a point on the inner surface
E_γ	= the dose conversion factor
$\sigma(E)$	= the absorption coefficient in tissue
E_0	= the maximum energy of the fission spectrum which we take as 10 Mev
T	= the thickness of the lead layer
t_m	= 4.76×10^{-3} m

Since we are dealing with an omnidirectional flux, $D_0/4\pi$ is the flux per steradian and $D = 2\pi(D_0/4\pi)$ is the corresponding skin dose. That is,

$$D = D_0/2 \quad (16)$$

Equation (16) has been evaluated for a number of T -values. The results are shown graphically in Fig. 4 and can be expressed analytically to a good approximation by

$$D = a_0 e^{-\sigma_0 T} \quad T > 3.0 \times 10^{-2} \text{ m} \quad (17)$$

where

$$\log_{10} a_0 = -8.70043 \quad (18)$$

$$1/\sigma_0 = 43.29 \quad (19)$$

Now, if ϕ is the flux per hour of mission time encountered by the vehicle, and \mathfrak{D} is the dose per hour for the model shield of lead thickness T , then we have

$$T = -0.3318 + 0.0381 \log_{10}(\phi/\mathfrak{D}) \text{ m} \quad (20)$$

We may now compute the total mass of material shielding as a function of shielded volume ($V > 10^{0.6} \text{ m}^3$), where

$$M_t = M_t' + a_1 T + a_2 T^2 + a_3 T^3 \text{ kg} \quad (21)$$

and the parameters M_t' , a_1 , a_2 , and a_3 are defined below. Numerical values correspond to our choice of lead and

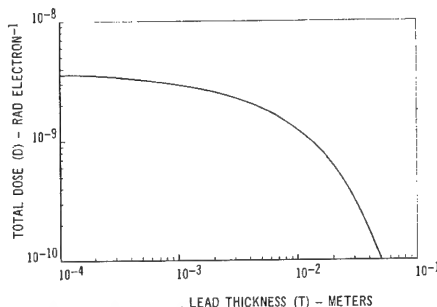


Fig. 4 Skin dose from bremsstrahlung produced by a normalized fission spectrum of electrons in aluminum and attenuated by different thicknesses of lead, where 1 g-cm⁻² of lead is equivalent to 8.81×10^{-4} m.

aluminum and an R_p value for 10-Mev electrons in aluminum of 0.01927 m (see Ref. 7):

$$\begin{aligned} M_t' &= (4\pi/3)[(R_p + R)^3 - R^3]\rho_{Al} = 10^{2.444}V^{0.6557} \\ a_1 &= 4\pi[R_p(R_p + 2R)\rho_{Al} + R^2\rho_{Pb}] = 10^{4.7627}V^{0.6619} \\ a_2 &= 4\pi[R_p\rho_{Al} + R\rho_{Pb}] = 10^{4.9611}V^{1/3} \\ a_3 &= (4\pi/3)\rho_{Pb} = 7.6 \times 10^7 \end{aligned} \quad (21a)$$

From (20-21a) we obtain

$$\log_{10}[M_t - C_1(\phi/\mathcal{D})] = C_2(\phi/\mathcal{D}) + 0.6619 \log_{10} V \quad (22)$$

where

$$\begin{aligned} C_1(\phi/\mathcal{D}) &= 4.203 \times 10^3[-8.7 + \log_{10}(\phi/\mathcal{D})]^3 \\ C_2(\phi/\mathcal{D}) &= 2.1818 + \log_{10}[-8.7 + \log_{10}(\phi/\mathcal{D})] \end{aligned} \quad (22a)$$

The maximum dose rate corresponds to the case $T = 0$, that is,

$$\mathcal{D}_{\max} = 3.71 \times 10^{-9} \phi \text{ rad/hr}$$

In Fig. 2 we have plotted M_t vs V for $\mathcal{D} = \mathcal{D}_{\max}$ in order to compare with magnetic shielding. Observe that the magnetic mass is lower than the material mass by an order of magnitude even for this extreme case.

Material Shielding Examples

In Table 1 we list the values of the constants C_2 and $\log_{10} C_1$, of (22a) for four representative electron fluxes for each of three representative bremsstrahlung skin dose rates; then from Eq. (22) we can calculate masses of shielding required for a given shielded volume. The electron fluxes ϕ_i ($i = 1-4$) listed below correspond, respectively, to computer calculated average flux values for practical satellite orbits of 200, 400, 600, and 800 km alt inclined at 30° to the earth's equator.^{8, 9} These flux value averages are good for mission times equal to or greater than 100 hr and become even more accurate for longer missions.

The dose rates were obtained by taking the NASA-specified skin doses¹⁰ listed below:

$$\begin{aligned} G_1 &= 125 \text{ rad (short mission maximum allowable skin dose)} \\ G_2 &= 233 \text{ rad (maximum allowable skin dose for a mission of 1 yr)} \\ G_3 &= 2282 \text{ rad (maximum allowable skin dose for a mission of 5 yr)} \end{aligned}$$

and performing the prescribed operations:

$$\begin{aligned} \mathcal{D}_1 &= G_1/(125 \text{ hr}) = 1 \text{ (rad/hr)} \\ \mathcal{D}_2 &= G_2/(8760 \text{ hr}) = \frac{1}{35} \text{ rad/hr} \\ \mathcal{D}_3 &= G_3/(43,800 \text{ hr}) = \frac{1}{20} \text{ (rad/hr)} \end{aligned}$$

The corresponding masses of material shielding are given by substituting these values of C_1 , C_2 in Eq. (22).

Concluding Remarks

We have used calculations pertaining to an ideal dipole to approximate the shielding effects of a superconducting solenoid against electrons of the artificial radiation belt. Our method for optimizing the mass of the superconducting solenoid and its containment shell permits us to avoid analyzing all possible systems with different r and l values. This in turn has allowed great simplification of the mathematical form in which the results are expressed. To estimate ma-

Table 1^a Values of C_2 and $\log_{10} C_1$

	$\phi_1 =$ 9.3×10^8	$\phi_2 =$ 1.1×10^{10}	$\phi_3 =$ 5.3×10^{10}	$\phi_4 =$ 1.1×10^{10}
$D_1 = 1$	1.6905 (1.5375) ^b	4.0056 (2.3092)	4.5420 (2.4880)	4.7310 (2.5510)
$D_2 = \frac{1}{35}$	4.3986 (2.4402)	5.0040 (2.6420)	5.2806 (2.7342)	5.3916 (2.7712)
$D_3 = \frac{1}{20}$	4.2111 (2.3777)	4.8891 (2.6037)	5.1888 (2.7036)	5.3073 (2.7431)

^a The constants C_2 and $\log_{10} C_1$ are given in the body of the table for given paired values of \mathcal{D} and ϕ . Here, \mathcal{D} is measured in units of (rad-hr⁻¹) and ϕ in units of (electrons-cm⁻²-hr⁻¹).

^b Numbers in parenthesis are values of C_2 .

terial shielding requirements against bremsstrahlung, care was taken to properly account for ionization, bremsstrahlung, and Compton scattering (using a transmission factor)¹¹ by electrons in aluminum. However, only skin doses on a small sphere of tissue were considered to be within the scope of the present work. The combination of aluminum and lead was considered as not only practical but also as having superior shielding characteristics. Lastly, a significant reduction in the magnetic shielding mass seems possible by integrating the containment shell with the walls of the space vehicle.

Our results indicate a significantly lower mass for the magnetic shield. However, against low electron fluxes, where bremsstrahlung shielding may not be required and the electrons need only be partly stopped, the advantage may be with material shielding. The greater reliability of material shielding will also count in its favor.

References

- Carter, R. E., Reines, F., Wagner, J. J., and Wyman, M. E., "Anti-neutrino absorption cross section II. Expected cross section from measurements of fission fragment electron spectrum," *Phys. Rev.* **113**, 280-286 (1959).
- Kash, S. W. and Tooper, R. F., "Active shielding for manned spacecraft," *Astronautics* **7**, no. 9, 68-75 (1962).
- Kash, S. W. and Tooper, R. F., "Correction on active shielding for manned spacecraft," *Astronautics* **8**, no. 1, 43 (1963).
- Tooper, R. F., "Electromagnetic shielding feasibility study," Aeronautical Systems Div. ASD-TDR-63-194, Chap. 5, pp. 117-128 (May 1963); available from Armed Services Technical Information Agency and from Office of Technical Services, Washington, D. C.
- Bhattacharjee, A. and Michael, I., "Forbidden zones in magnetic fields with various symmetries" *AIAA J.* (submitted for publication).
- Fortney, R. E., private communication, Northrop Space Labs., Hawthorne, Calif. (1963).
- Katz, L. and Penfold, A. S., "Range-energy relations for electrons and the determination of beta-ray end-point energies by absorption," *Rev. Mod. Phys.* **24**, 28-44 (1952).
- Hess, W. N., "The artificial radiation belt made on July 9, 1962," *J. Geophys. Res.* **68**, 667-684 (1963). See the electron flux map contours of his Fig. 7 for computer program Morrison, 1963, to obtain averaged electron fluxes at given altitudes for 30° orbits.
- Morrison, M. R., private communication, Northrop Space Labs., Hawthorne, Calif. (1963). The average electron flux per revolution through the artificial radiation belt was obtained with the aid of TRIGO, a computer program to integrate trapped radiation along geocentric orbits. This program, developed by Northrop Space Labs. (NSL) and described in NSL 63-259, utilizes the E2-grid data of W. N. Hess of NASA Goddard.
- Gill, W. L., private communication, NASA Langley Air Force Base, Va. (1962).
- Perkins, J. F., "Monte Carlo calculations of transport of fast electrons," *Phys. Rev.* **125**, 1781-1784 (1962).

Technical Notes

Identification of Two Types of Separation

J. W. PAULL*

Caulfield Technical College, Caulfield, Australia

Introduction

THE prediction of turbulent boundary-layer separation has remained an order of magnitude less accurate than that of laminar boundary-layer separation, and the accuracy attained in the prediction of the separation of turbulent flow in diverging channels has been so poor as to give the impression that a fundamental difference might exist between this and other forms of separation. A possible distinction between the separation of turbulent flow in a two-dimensional diffuser and laminar boundary-layer separation will be described which, if significant, could explain some of the inaccuracies that have occurred.

Laminar Boundary-Layer Separation

The physical picture of laminar boundary-layer separation has been given by Prandtl¹: the particles in the boundary layer lose energy in overcoming frictional stress and do not retain sufficient energy to completely overcome the adverse pressure gradient; they are brought to rest and then separate from the surface. Beyond this point, flow at the boundary is in a reverse direction to that outside the boundary-layer region. This is shown diagrammatically in Fig. 1.

Turbulent Separation in a Diffuser

Turbulent separation in a diffuser, and possibly also on external surfaces, appears to be somewhat different. This can be shown in the case of flow in a two-dimensional, plane-walled diverging channel. Flow in long diffusers of this type is made up of an initial transition region and a region of self-preserving flow. If the half-angle of the expansion exceeds about 5° , separation occurs. Figure 2 shows the velocity profiles that have been found to exist in the region of self-preserving flow for various degrees of expansion (after Nikuradse¹).

It seems unlikely that it is an accident that these profiles successively approach a profile of a flow that has had the maximum possible momentum loss of those that could symmetrically occupy the full width of the section. This curve

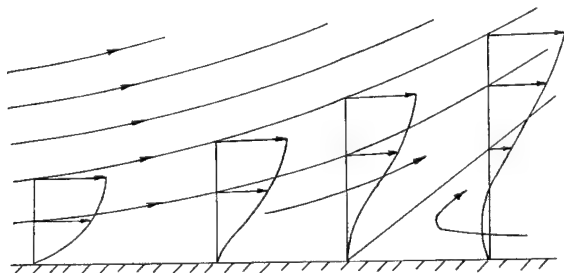


Fig. 1 Laminar boundary-layer separation.

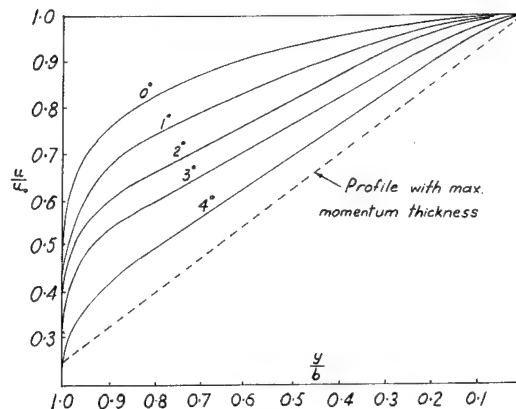


Fig. 2 Velocity profiles in diverging channels (after Nikuradse).

is also shown in Fig. 2. It has been obtained as the solution of the equation

$$I = \int_0^{1.0} \frac{u}{u_0} \left(1 - \frac{u}{u_0}\right) d\left(\frac{y}{b}\right) = \text{a max}$$

where

- u = mean velocity in the x direction at a distance y from the centerline
- u_0 = mean velocity on the centerline
- b = half-width of channel

A discontinuous linear curve of the type shown was first assumed, and a maximum solution was obtained. The calculus of variations showed that this solution was the absolute maximum. It would appear to approximate a profile corresponding to a 5° half-angle divergence.

There would be several reasons why a limit curve of exactly this shape could not be obtained in practice. These are associated with the discontinuities that were assumed possible in the profile. Examination of the variation in wall shear stress in the self-preserving flow region with increasing angles of divergence indicates that, at approximately a 5° angle, the shear stress at the wall would be zero. This would mean that

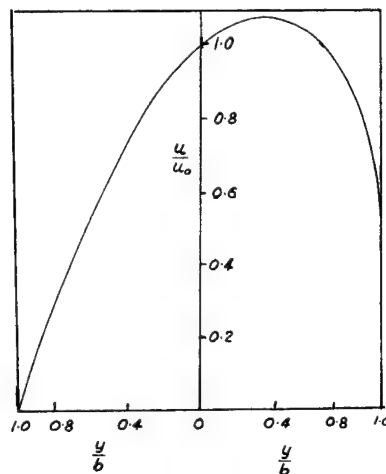


Fig. 3 Critical separation condition.

the gradient of the velocity component u normal to the wall would be zero, and this conflicts with the shape of the limit curve. The discontinuities at $u/u_0 = 0.25$ and $u/u_0 = 1.00$ would also be appreciably smoothed out by viscosity effects.

If there is a limit curve of this shape, then some explanation would be necessary of how the flow changes to one with a profile showing back-flow at a boundary. Nikuradse found that the profile becomes unsymmetrical, and, for larger angles of divergence, reverse flow takes place along one wall. The unsymmetrical, unseparated flow, called by Nikuradse the "critical separation condition," occurred with angles of divergence between 4.8° and 5.1° . This profile is shown in Fig. 3.

Conclusions

1) The velocity profiles that occur for turbulent flow in two-dimensional, plane-walled diffusers successively approach the profile of a flow that has had the maximum possible momentum loss for a flow symmetrically occupying the full width of the section.

2) It seems probable that this is not accidental.

3) If there is a limit profile for turbulent flow in this case, it would indicate that this mechanism of separation was different from that which occurs in the case of laminar boundary layers, and a distinction between them would have theoretical advantages.

References

¹ Nikuradse, J., "Untersuchungen über die Strömung des Wassers in konvergenten und divergenten Kanälen," Ver. Deut. Ing. (Forschungsarb.) 289, 19, 20 (1929).

² Prandtl, L. and Tietjens, O. G., *Applied Hydro- and Aeromechanics* (Dover Publication, Inc., New York, 1957), p. 64.

Sonic Line of Magnetohydrodynamic Nozzle Flow

TATSUO YAMANAKA*

National Aerospace Laboratory, Tokyo, Japan

Nomenclature

A	= Alfvén number
M	= Mach number
R	= curvature
U	= speed of main stream
c	= sound velocity
u, v	= small-perturbation velocity component
k	= specific heat ratio
ϕ	= small-perturbation potential function

Subscript

* = critical condition

Introduction

IT has been well known that a nozzle flow of infinitely conducting inviscid gas, with a magnetic field everywhere parallel to the velocity, has four kinds of transitions.¹⁻³ Among these transitions, the transonic and the transonic-Alfvénic transition are the most interesting regimes for super-sonic plasma nozzle design.

Kogan¹ dealt with the transonic transition; however, his solution is incorrect. This paper presents approximate but general rules for the shape of the sonic line for the plane and axisymmetrical nozzle flow of an infinitely conducting inviscid gas with a magnetic field everywhere parallel to the flow velocity.

The author realized later that Seebass³ has pointed out Kogan's failure in this regime and has derived the correct solution, however, Seebass does not depict the characteristics of his constant "c".

The procedure used is essentially the same as that of Sauer.⁴

Basic Differential Equations

From the momentum equation, according to the assumptions, Resler^{5,6} derived the following differential equations, and later Imai⁷ developed them into three-dimensional flow:

$$\frac{(1-M^2)(1-A^2)}{1-A^2-M^2} \frac{\partial^2 \phi}{\partial x^2} + \frac{\partial^2 \phi}{\partial y^2} = 0 \quad (1)$$

$$u = \frac{1-A^2}{1-A^2-M^2} \frac{\partial \phi}{\partial x} \quad (2a)$$

$$v = \partial \phi / \partial y \quad (2b)$$

From the continuity equation, near critical sound velocity, we have

$$-(k+1) u \frac{\partial u}{\partial x} + \frac{\partial v}{\partial y} = 0 \quad (3)$$

It is assumed that the velocity components u and v may be expressed as power series in y , with the coefficients of the series depending upon x . Since the flow is symmetrical about the x axis, the series for u must contain only even powers of y , whereas that for v must contain only odd powers. Following the preceding thought, the perturbation potential corresponding to the disturbance velocity u and v is now written in the form

$$\phi = f_0(x) + y^2 f_2(x) + y^4 f_4(x) + \dots \quad (4)$$

By differentiation, the velocities are then found to be

$$U_x = U \left(1 + \frac{1-A^2}{1-A^2-M^2} \frac{\partial \phi}{\partial x} \right) = a_0 + \frac{1}{2!} a_2 y^2 + \frac{1}{4!} a_4 y^4 + \dots \quad (5a)$$

$$U_y = U \frac{\partial \phi}{\partial y} = b_1 y + \frac{1}{3!} b_3 y^3 + \frac{1}{5!} b_5 y^5 + \dots \quad (5b)$$

since Eq. (4) is found reasonable.

Substituting Eq. (4) into Eqs. (2), we have

$$u = \frac{1-A^2}{1-M^2-A^2} \frac{\partial \phi}{\partial x} = \frac{1-A^2}{1-A^2-M^2} \times (f_0' + y^2 f_2' + y^4 f_4' + \dots) \quad (6a)$$

$$v = \frac{\partial \phi}{\partial y} = 2y f_2 + 4y^3 f_4 + \dots \quad (6b)$$

Taking the derivatives $\partial u / \partial x$ and $\partial v / \partial y$ in Eqs. (6), substituting these into Eq. (3), and equating coefficients of like powers of y , we obtain the following relations among the coefficients:

$$f_2 = \frac{k+1}{2} \left(\frac{1-A^2}{1-A^2-M^2} \right)^2 f_0' f_0'' \quad (7a)$$

$$f_4 = \frac{k+1}{12} \left(\frac{1-A^2}{1-A^2-M^2} \right)^2 (f_0' f_2'' + f_2' f_0'') \quad (7b)$$

Transonic Transition

In this paper, only transonic transition regime is dealt with, i.e., $M = M^* = 1$, $A = A^* \neq 1$. Now f_0 represents, according to Eq. (6a), the velocity distribution on the x axis.

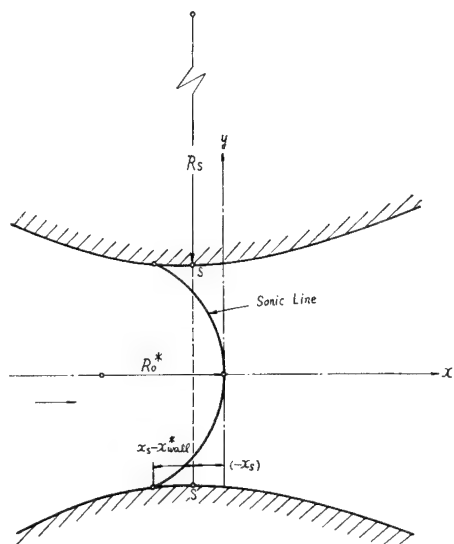


Fig. 1 Sonic line and nomenclature.

For a short distance along the axis, the velocity on the axis may be approximated by a straight line. Restricting our considerations to the neighborhood of the sonic line, and setting $x = 0$ where the sonic line crosses x axis (Fig. 1), we write accordingly

$$f_0' = \frac{A^2}{A^2 - 1} [u]_{y=0} \cong \frac{A^2}{A^2 - 1} \left(\frac{du}{dx} \right)_{y=0} x \quad (8)$$

where $(du/dx)_0$ denotes the velocity gradient on the axis near $x = 0$. Then, from Eqs. (7) and (8), we may rewrite the remaining coefficients as

$$f_2 = \frac{k+1}{2} \left(\frac{du}{dx} \right)_0^2 x \quad f_4 = \frac{(k+1)^2}{24} \frac{A^2 - 1}{A^2} \left(\frac{du}{dx} \right)_0^3 \quad (9)$$

The velocity distribution [Eqs. (6)] may now be expressed as

$$u = \left(\frac{du}{dx} \right)_0 x + \frac{k+1}{2} \left(\frac{du}{dx} \right)_0^2 \frac{A^2 - 1}{A^2} y^2 + \dots \quad (10a)$$

$$v = (k+1) \left(\frac{du}{dx} \right)_0^2 xy + \frac{(k+1)^2}{6} \left(\frac{du}{dx} \right)_0^3 \frac{A^2 - 1}{A^2} y^3 + \dots \quad (10b)$$

From the condition of sonic line, $(1+u)^2 + v^2 = 1$, this may be approximated by $u \cong 0$, and we get, from Eq. (10a),

$$x^* = -\frac{k+1}{2} \frac{A^2 - 1}{A^2} \left(\frac{du}{dx} \right)_0 y^{*2} \quad (11)$$

The sonic curve is, therefore, a parabola containing a parameter of Alfvén number A , and its curvature on the x axis may be shown to be given by

$$\frac{1}{R_0^*} = \frac{d^2 x^*/dy^{*2}}{\{1 + (dx^*/dy^*)^2\}^{1/2}} = (k+1) \frac{A^2 - 1}{A^2} \left(\frac{du}{dx} \right)_0 \quad (12)$$

The location of the sonic curve to the throat section of the nozzle, signified by point s on the wall, is found from Eq. (10b):

$$-x_s = \frac{k+1}{6} \left(\frac{du}{dx} \right)_0 \frac{A^2 - 1}{A^2} y_s^2 \quad (13)$$

and $(-x_s)$ is the maximum distance of the sonic line downstream of the throat. Setting $y^* \cong y_s$, we may find where the sound speed is first reached on the wall.

Equations (11) and (13) may be combined to yield

$$x_s - x_{wall}^* = \frac{A^2 - 1}{A^2} \frac{k+1}{3} \left(\frac{du}{dx} \right)_0 y_s^2 = 2(-x_s) \quad (14)$$

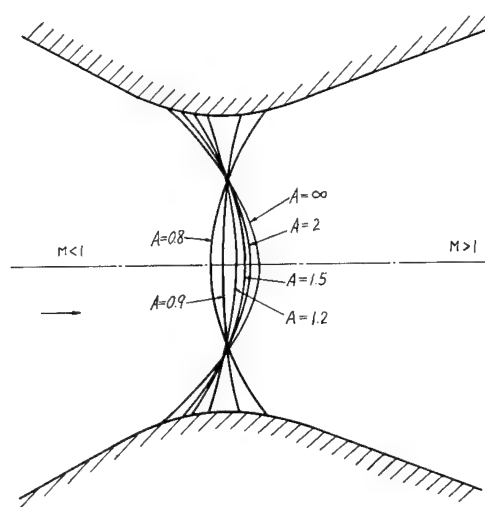


Fig. 2 Shape of sonic line.

The wall curvature near the throat is evaluated as

$$1/R_s \cong \partial u / \partial x$$

then, using Eq. (10b), we have

$$\frac{1}{R_s} = (k+1) \left(\frac{du}{dx} \right)_0^2 y_s = \frac{A^2}{A^2 - 1} \frac{y_s}{R_0^*} \left(\frac{du}{dx} \right)_0 \quad (15)$$

The velocity distribution $(du/dx)_0$ may be defined by y_s and R_s , if we regard the nozzle shape near the throat. Equations (11-15) may be inverted to give the following sonic line parameters in terms of nozzle shape:

$$y_s \left(\frac{du}{dx} \right)_0 = \left\{ \frac{y_s}{(k+1)R_s} \right\}^{1/2} \quad (16)$$

$$R_0^* = \frac{A^2}{A^2 - 1} y_s \left\{ \frac{R_s}{(k+1)y_s} \right\}^{1/2} \quad (17a)$$

$$x_s - x_{wall}^* = 2(-x_s) = \frac{A^2 - 1}{A^2} y_s \left\{ \frac{(k+1)}{9} \frac{y_s}{R_s} \right\}^{1/2} \quad (17b)$$

Similar considerations for axisymmetric nozzle lead to the following results:

$$R_0^* = \frac{A^2}{A^2 - 1} y_s \left\{ \frac{2}{(k+1)} \frac{R_s}{y_s} \right\}^{1/2} \quad (18a)$$

$$x_s - x_{wall}^* = (-x_s) = \frac{A^2 - 1}{A^2} y_s \left\{ \frac{(k+1)}{32} \frac{y_s}{R_s} \right\}^{1/2} \quad (18b)$$

Conclusion

As was seen previously, it has been found that the shape of the sonic line for the plane and axisymmetric nozzle flow of an infinitely conducting inviscid gas with a magnetic field everywhere parallel to the flow velocity is affected by a magnetic field intensity. As we can see from Eqs. (17) and (18), if the Alfvén number is approaching infinity, i.e., a magnetic field intensity approaching zero, the shape of sonic line becomes the same shape of an ordinary nonconducting gas by Sauer,⁴ and if the Alfvén number is less than 1, the right-hand side of Eqs. (17) and (18) change their signs. This means that a parabola convex toward downstream changes into concave toward downstream (see Fig. 2).

These results should be useful for the design of supersonic plasma nozzle exhaust contour.

References

- 1 Kogan, M. N., "On magnetohydrodynamic flows of mixed type," *Prikl. Mat. Mekh.* **25**, 132 (1961).

² Chu, C. K., "Magnetohydrodynamic nozzle flow with three transitions," *Phys. Fluids*, **5**, 550-559 (1962).

³ Seebass, R., "Mixed flows in magnetogasdynamics," *Symposium Transonicum; Proceedings Aachen, 3-7 September, 1962*, edited by K. Osmatitsch, Julius Springer-Verlag, (Berlin/Vienna, 1964), pp. 471-490.

⁴ Sauer, R., "General characteristics of the flow through nozzles at near critical speeds," NACA TM 1147 (1947).

⁵ Resler, E. L. and McCune, J. E., *The Magnetodynamics of Conducting Fluids*, edited by D. Bershader (Stanford University Press, Stanford, Calif., 1959), p. 120.

⁶ Sears, W. R., *Proceedings of the 8th Japan National Congress for Applied Mechanics 1958* (Japan National Committee for Theoretical and Applied Mechanics Science Council of Japan, Tokyo, Japan, 1959), p. 1.

⁷ Imai, I., "On flows of conducting fluids past bodies," *Rev. Mod. Phys.* **32**, 992 (1960).

Similar Solutions for Three-Dimensional Laminar Compressible Boundary Layers

MICHAEL C. FONG*

North American Aviation, Inc., Columbus, Ohio

Nomenclature

e_1, e_2	= metric coefficients
f, g	= similar functions
h	= enthalpy
H	= stagnation enthalpy, $h + \frac{1}{2}(u^2 + w^2)$
K_1	= curvature parameter, $(2\xi/e_1)(\partial e_1/\partial \xi)$
K_2	= dilatation parameter, $(2\xi/e_2)(\partial e_2/\partial \xi)$
K^*	= $(\partial/\partial \xi^*)(\beta^*/rZ)$
M	= Mach number
m	= $[(\gamma - 1)/2]M_\infty^2$
\hat{m}	= $1 + [(\gamma - 1)/2]M_\infty^2$
N	= $\rho\mu/\rho_0\mu_0$
p	= pressure
P_r	= Prandtl number
r	= body radius
T	= temperature
u, v, w	= velocity components
x, y, z	= curvilinear orthogonal coordinates
α	= $2\xi(dZ/d\xi)$
β	= pressure gradient parameter, $(2\xi/u_e)(\partial u_e/\partial \xi)\hat{m}$
β^*	= $-(2\xi/\rho_e u_e^2)(\partial p/\partial \xi)$
ξ, η, ζ	= transformed coordinates
ψ, ϕ	= stream functions
ρ	= density
μ	= dynamic viscosity
θ	= total enthalpy ratio, H/He
ω	= spinning rate

Subscripts

0	= reference state
∞	= freestream condition
e	= outer-edge condition

Superscript

()'	= derivative with respect to η
------	-------------------------------------

THE three-dimensional boundary layer is characterized by crossflow generation and streamline deviation within the boundary layer. An adequate mathematical description of these phenomena entails the consideration of several additional nonlinear terms in the governing equations which are absent in the corresponding two-dimensional or axisymmetric equations. One approach to this problem is to invoke the

concept of the streamline coordinate system for which one of the coordinates is set to be coincident with the local outer-edge streamline projected in the tangent plane. By so doing, the perturbation technique in treating the crossflow effect can be justified for a wide variety of practical applications, and because of the presence of only one external flow component, the construction of a single similarity parameter can be achieved without introducing any restrictive assumptions. The purpose of this note is to discuss a certain class of similar solutions for three-dimensional laminar compressible boundary-layer flows on the basis of the streamline coordinate system and by employing a set of simple transformation variables. Neglected herein are the real gas effects associated with hypersonic flight, flow separation, and laminar-to-turbulent transition phenomena, and the analytical procedures for the determination of surface streamlines in accordance with the theory of differential geometry.

Similar to the consideration by Beckwith,¹ we select a three-dimensional orthogonal streamline coordinate system (x, y, z) with corresponding velocity components u tangent to the external streamline, v normal to the body surface, and w , the crossflow velocity component, normal to u in the tangent plane. The length elements are

$$ds = e_1(x, z)dx \quad dy = dy \quad dn = e_2(x, z)dz \quad (1)$$

and at the outer edge of the boundary layer, $u = u_e$ and $w = w_e = 0$. The governing equations for a three-dimensional laminar compressible boundary layer may then be written as:

Continuity

$$\frac{1}{e_1} \frac{\partial}{\partial x} (\rho u e_2) + \frac{\partial}{\partial y} (\rho v e_2) + \frac{1}{e_1} \frac{\partial}{\partial z} (\rho w e_1) = 0 \quad (2)$$

x Momentum

$$\frac{\rho u}{e_1} \frac{\partial u}{\partial x} + \rho v \frac{\partial u}{\partial y} + \frac{\rho w}{e_2} \frac{\partial u}{\partial z} + \frac{\rho u w}{e_1 e_2} \frac{\partial e_1}{\partial z} - \frac{\rho w^2}{e_1 e_2} \frac{\partial e_2}{\partial x} = -\frac{1}{e_1} \frac{\partial p}{\partial x} + \frac{\partial}{\partial y} \left(\mu \frac{\partial u}{\partial y} \right) \quad (3)$$

y Momentum

$$\partial p / \partial y = 0 \quad (4)$$

z Momentum

$$\frac{\rho u}{e_1} \frac{\partial w}{\partial x} + \rho v \frac{\partial w}{\partial y} + \frac{\rho w}{e_2} \frac{\partial w}{\partial z} + \frac{\rho u w}{e_1 e_2} \frac{\partial e_2}{\partial x} - \frac{\rho u^2}{e_1 e_2} \frac{\partial e_1}{\partial z} = -\frac{1}{e_2} \frac{\partial p}{\partial z} + \frac{\partial}{\partial y} \left(\mu \frac{\partial w}{\partial y} \right) \quad (5)$$

Energy

$$\frac{\rho u}{e_1} \frac{\partial H}{\partial x} + \rho v \frac{\partial H}{\partial y} + \frac{\rho w}{e_2} \frac{\partial H}{\partial z} = \frac{\partial}{\partial y} \left[\mu \left(\frac{\partial H}{\partial y} + \frac{1 - P_r}{P_r} \frac{\partial h}{\partial y} \right) \right] \quad (6)$$

From the continuity equation, we define two stream functions ψ and ϕ as follows:

$$\rho u e_2 = \frac{\partial \psi}{\partial y} \quad \rho v e_2 = \left(-\frac{\partial \psi}{\partial x} - \frac{\partial \phi}{\partial z} \right) \frac{1}{e_1} \quad \rho w e_1 = \frac{\partial \phi}{\partial y} \quad (7)$$

We now introduce the transformation variables

$$\begin{aligned} \xi &= \int_0^x \rho_0 \mu_0 e_1 dx = \int_0^s \rho_0 \mu_0 ds \\ \eta &= \left(\frac{u_e}{2\xi} \right)^{1/2} \int_0^y \rho dy \\ \zeta &= \int_0^z \rho_0 \mu_0 e_2 dz = \int_0^n \rho_0 \mu_0 dn \end{aligned} \quad (8)$$

Received July 6, 1964.

* Research Specialist, Fluid Dynamics and Thermodynamics Group, Columbus Division. Member AIAA.

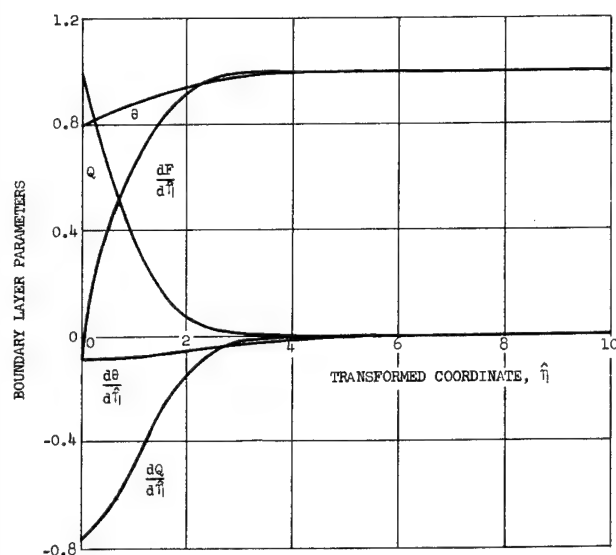


Fig. 1 Boundary-layer parameters vs transformed coordinate η for spin parameter $\omega^2\lambda = 0.005$.

and define related functions $f(\xi, \eta, \zeta)$ and $g(\xi, \eta, \zeta)$ as follows:

$$\psi = (2\xi u_e)^{1/2} e_2 f(\xi, \eta, \zeta) \quad \phi = (2\xi u_e)^{1/2} e_1 g(\xi, \eta, \zeta) \quad (9)$$

from which we obtain

$$u = u_e(\partial f / \partial \eta) \quad w = u_e(\partial g / \partial \eta) \quad (10)$$

Substituting these transformation variables into Eqs. (3-6) and noting that at the outer edge of the boundary layer

$$\frac{\rho_e u_e}{e_1} \frac{\partial u_e}{\partial x} = -\frac{1}{e_1} \frac{\partial p}{\partial x} \quad (11)$$

$$\frac{1}{e_1} \frac{\partial e_1}{\partial z} = -\frac{1}{u_e} \frac{\partial u_e}{\partial z} = \frac{1}{\rho_e u_e^2} \frac{\partial p}{\partial z}$$

and across the boundary layer

$$\frac{\rho_e}{\rho} = \frac{T}{T_e} = \theta \hat{m} - m \left[\left(\frac{\partial f}{\partial \eta} \right)^2 + \left(\frac{\partial g}{\partial \eta} \right)^2 \right] \quad (12)$$

the following equations are obtained:

$$\begin{aligned} \frac{\partial}{\partial \eta} \left(N \frac{\partial^2 f}{\partial \eta^2} \right) + \left(1 + \frac{\beta}{2\hat{m}} + K_2 \right) f \frac{\partial^2 f}{\partial \eta^2} + \beta \left[\theta - \left(\frac{\partial f}{\partial \eta} \right)^2 \right] + \\ \left(K_2 - \beta \frac{m}{\hat{m}} \right) \left(\frac{\partial g}{\partial \eta} \right)^2 + \frac{K_1}{2} g \frac{\partial^2 f}{\partial \eta^2} + 2\xi \left(\frac{\partial f}{\partial \xi} \frac{\partial^2 f}{\partial \eta^2} - \right. \\ \left. \frac{\partial f}{\partial \eta} \frac{\partial^2 f}{\partial \xi \partial \eta} \right) + 2\xi \left(\frac{\partial g}{\partial \xi} \frac{\partial^2 f}{\partial \eta^2} - \frac{\partial g}{\partial \eta} \frac{\partial^2 f}{\partial \xi \partial \eta} \right) = 0 \quad (13) \end{aligned}$$

$$\begin{aligned} \frac{\partial}{\partial \eta} \left(N \frac{\partial^2 g}{\partial \eta^2} \right) + \left(1 + \frac{\beta}{2\hat{m}} + K_2 \right) g \frac{\partial^2 g}{\partial \eta^2} + \\ K_1 \left[\left(\frac{\partial f}{\partial \eta} \right)^2 + \left(\frac{\partial g}{\partial \eta} \right)^2 + \frac{g}{2} \frac{\partial^2 g}{\partial \eta^2} \right] + \\ \beta^* \left(\frac{\rho_e}{\rho} \right) - \left(K_2 + \frac{\beta}{\hat{m}} \right) \left(\frac{\partial f}{\partial \eta} \frac{\partial g}{\partial \eta} \right) + 2\xi \left(\frac{\partial f}{\partial \xi} \frac{\partial^2 g}{\partial \eta^2} - \right. \\ \left. \frac{\partial f}{\partial \eta} \frac{\partial^2 g}{\partial \xi \partial \eta} \right) + 2\xi \left(\frac{\partial g}{\partial \xi} \frac{\partial^2 g}{\partial \eta^2} - \frac{\partial g}{\partial \eta} \frac{\partial^2 g}{\partial \xi \partial \eta} \right) = 0 \quad (14) \end{aligned}$$

$$\begin{aligned} \frac{1}{P_r} \frac{\partial}{\partial \eta} \left(N \frac{\partial \theta}{\partial \eta} \right) - \frac{1 - P_r}{P_r} \frac{m}{\hat{m}} \frac{\partial}{\partial \eta} \left\{ N \frac{\partial}{\partial \eta} \left[\left(\frac{\partial f}{\partial \eta} \right)^2 + \right. \right. \\ \left. \left. \left(\frac{\partial g}{\partial \eta} \right)^2 \right] \right\} + \left(1 + \frac{\beta}{2\hat{m}} + K_2 \right) f \frac{\partial \theta}{\partial \eta} + \frac{K_1}{2} g \frac{\partial \theta}{\partial \eta} + \\ 2\xi \left(\frac{\partial f}{\partial \xi} \frac{\partial \theta}{\partial \eta} - \frac{\partial f}{\partial \eta} \frac{\partial \theta}{\partial \xi} \right) + 2\xi \left(\frac{\partial g}{\partial \xi} \frac{\partial \theta}{\partial \eta} - \frac{\partial g}{\partial \eta} \frac{\partial \theta}{\partial \xi} \right) = 0 \quad (15) \end{aligned}$$

where appropriate boundary conditions must be prescribed for a given problem. It should be remarked that the parameter β^* , which is equal to $-K_1$, is purposely retained in Eq. (14) since, for certain special three-dimensional viscous flow problems, the crossflow effect can best be demonstrated by first taking termwise differentiation of Eq. (5) with respect to ζ , in which case $\partial \beta^* / \partial \zeta$ may be different from $-\partial K_1 / \partial \zeta$.

We are at present concerned with a class of similar solutions wherein $g(\xi, \eta, \zeta) = Z(\zeta) \hat{g}(\xi, \eta)$, with Z and $\partial Z / \partial \zeta$ being known values along any given streamline under consideration. In accordance with the usual requirements for similar (or locally similar) flows, we assume that f , \hat{g} , and θ are primarily dependent on η . Then, Eqs. (11-13) become

$$\begin{aligned} f''' + \left(1 + \frac{\beta}{2\hat{m}} + K_2 \right) f f'' + \beta(\theta - f'^2) + \\ Z^2 \left(K_2 - \beta \frac{m}{\hat{m}} \right) \hat{g}'^2 + \left(\alpha + \frac{1}{2} K_1 Z \right) \hat{g} f'' = 0 \quad (16) \end{aligned}$$

$$\begin{aligned} \hat{g}''' + \left(1 + \frac{\beta}{2\hat{m}} + K_2 \right) f \hat{g}'' + \frac{K_1 \hat{m}}{Z} \left[f'^2 - \theta + Z^2 \times \right. \\ \left. \left(\hat{g}'^2 + \frac{\hat{g} \hat{g}''}{2\hat{m}} \right) \right] - \left(K_2 + \frac{\beta}{\hat{m}} \right) f \hat{g}' + \alpha(\hat{g} \hat{g}'' - \hat{g}'^2) = 0 \quad (17) \end{aligned}$$

$$\begin{aligned} \frac{1}{P_r} \theta'' - \frac{1 - P_r}{P_r} \frac{m}{\hat{m}} (f'^2 + Z^2 \hat{g}'^2)' + \\ \left(1 + \frac{\beta}{2\hat{m}} + K_2 \right) f \theta' + \left(\alpha + \frac{1}{2} K_1 Z \right) \hat{g} \theta' = 0 \quad (18) \end{aligned}$$

where $N = 1$, and α , β , m , \hat{m} , P_r , K_1 , K_2 , and Z are assumed to be constant, at least within the region in which the flow can be regarded as locally similar. Although the foregoing high-order, nonlinear generalized equations for similar flows are still difficult to solve, they are amenable to numerical treatments with the aid of a high-speed digital computer. Flow characteristics for a large number of viscous flow problems can then be determined if proper values are assigned to the constants and appropriate boundary conditions are prescribed. A few interesting special cases are exemplified below.

For the laminar flows in the stagnation region of a spinning axisymmetric blunt-nosed body at zero yaw,²⁻⁴ the following values are assigned to the constants: $e_1 = 1$, $e_2 = r(x)$, $K_1 = 0$, $K_2 = 2$, $\alpha = 0$, $\beta = 2$, $m = 0$, and $\hat{m} = 1$. Furthermore, we may assume $Z \hat{g}' = 2\lambda^{1/2} \omega Q(\eta)$, where ω is the spinning rate and $\lambda = \frac{1}{2}(r/u_e)^2$, $f = \frac{1}{2}F$ and $(\quad)' = 2(d/d\hat{\eta})(\quad)$. Then, Eqs. (16-18) have the form

$$\frac{d^3 F}{d\hat{\eta}^3} + F \frac{d^2 F}{d\hat{\eta}^2} + \frac{1}{2} \left[\theta - \left(\frac{dF}{d\hat{\eta}} \right)^2 \right] + \omega^2 \lambda Q^2 = 0 \quad (19)$$

$$\frac{d^2 Q}{d\hat{\eta}^2} + F \frac{dQ}{d\hat{\eta}} - \frac{dF}{d\hat{\eta}} Q = 0 \quad (20)$$

$$\frac{1}{P_r} \frac{d^2 \theta}{d\hat{\eta}^2} + F \frac{d\theta}{d\hat{\eta}} = 0 \quad (21)$$

with boundary conditions

$$F(0) = \frac{dF(0)}{d\hat{\eta}} = Q(\infty) = 0$$

$$\frac{dF(\infty)}{d\hat{\eta}} = Q(0) = \theta(\infty) = 1 \quad \theta(0) = \frac{h_w}{H_e}$$

These equations are identical with the zero-order equations for the spinning-body problem obtained from employing the usual Mangler and Lees-Dorodnitsyn transformations.⁴ For $\theta(0) = 0.8$, $P_r = 0.722$, $M_\infty = 5$, and $\lambda \omega^2 = 0.005$, which approximately corresponds to a spinning rate of $\omega = 1700$ rpm, the Runge-Kutta scheme was utilized to solve the foregoing differential equations. The calculated results

of various functions are depicted in Fig. 1, and the heat-transfer ratio is found to be

$$\dot{q}_w/(\dot{q}_w)_{\omega=0} = 0.08025/0.08027 \approx 1$$

which indicates negligible spinning effect on convective heat transfer for flows in the stagnation-point region under hypersonic flight conditions. This result was predicted by Scala and Workman,³ and experimentally verified by Whitesel.⁵

Another interesting case is that concerning small but finite crossflow for which the higher-order terms in \hat{g} , α , K_1 , and their lateral derivative $\partial/\partial\zeta$ are neglected. Then, Eqs. (16-18) become (for $P_r = 1$)

$$f''' + \left(1 + \frac{\beta}{2\hat{m}} + K_2\right)f'' + \beta(\theta - f'^2) = 0 \quad (22)$$

$$\hat{g}''' + \left(1 + \frac{\beta}{2\hat{m}} + K_2\right)\hat{g}'' + K_1\hat{m}(f'^2 - \theta) - \left(K_2 + \frac{\beta}{\hat{m}}\right)f'g' = 0 \quad (23)$$

$$\theta'' + \left(1 + \frac{\beta}{2\hat{m}} + K_2\right)\theta' = 0 \quad (24)$$

If we multiply Eq. (23) by e_2 and substitute $(e_2\hat{g})' = V(\eta)G(\xi)$ therein, we obtain

$$V'' + \left(1 + \frac{\beta}{2\hat{m}} + K_2\right)fV' - \left(\frac{\beta}{\hat{m}} + \frac{2\xi}{G} \frac{dG}{d\xi}\right)f'V = \frac{\hat{m}K_1e_2}{G}(\theta - f'^2) \quad (25)$$

It is noted that Eqs. (22, 24, and 25) are essentially those obtained by Beckwith¹ except for the coefficient constants.

Finally, for the case of similar flows in the plane of symmetry of an inclined axisymmetric body with zero streamwise pressure gradient and insulated walls, the following conditions prevail: $e_1 = 1$, $e_2 = r(x)$, $K_1 = 0$, $\beta = 0$, and $\partial g/\partial\eta = 0$. In order to transform the resulting equations into a familiar form, we first differentiate Eq. (14) with respect to ζ^* , which is defined as $r\zeta^* = \zeta$. Then, with the aid of the following definitions:

$$\hat{F} = (1 + K_2)f \quad \hat{G} = \frac{\partial g}{\partial\zeta^*} \quad K^* = \frac{\partial}{\partial\zeta^*} \left(\frac{\beta^*}{rZ}\right)$$

$$C_1 = \frac{2\xi}{r} \quad C_2 = \frac{2\xi}{r} (1 + K_2)^{-1}$$

we obtain

$$\hat{F}'''' + (\hat{F} + C_1\hat{G})\hat{F}'' = 0 \quad (26)$$

$$\hat{G}'''' + (\hat{F} + C_1\hat{G})\hat{G}'' + K^*(\rho_c/\rho) - C_1\hat{G}'^2 - C_2\hat{F}\hat{G}' = 0 \quad (27)$$

which are the governing equations for supersonic flows in the plane of symmetry of a yawed cone with insulated surface.⁶

References

- Beckwith, I. E., "Similarity solutions for small cross flows in laminar compressible boundary layers," NASA TR R-107 (1961).
- Tifford, A. N. and Chu, S. T., "The compressible laminar boundary layer on a rotating body of revolution," J. Aeronaut. Sci. **21**, 345-346 (1954).
- Scala, S. M. and Workman, J. B., "The stagnation point boundary layer on a rotating hypersonic body," J. Aerospace Sci. **26**, 183 (1959).
- Fong, M. C., "Laminar heat transfer over spinning blunt-nosed bodies of revolution in axial hypersonic flows," North American Aviation Rept. FSTN 62-10 (1962).
- Whitesel, F., "Shock tube investigation of the effects of rotation on heat transfer to a hemisphere-cylinder," North American Aviation TN (to be published).
- Moore, F. K., "Laminar boundary layer on cone in supersonic flow at large angle of attack," NACA Rept. 1132 (1953).

Large Amplitude Vibration of Buckled Beams and Rectangular Plates

J. G. EISLEY*

University of Michigan, Ann Arbor, Mich.

Nomenclature

a, b, h	= plate width, length, and thickness (x, y, z directions), respectively
r	= a/b , plate aspect ratio
t	= time
u, v, w	= displacements in the x, y, z directions, respectively
D	= plate flexural rigidity, $Eh^3/12(1 - \nu^2)$
EI	= beam flexural rigidity
F	= stress function
ρ	= mass density
ν	= Poisson's ratio

Introduction

IN recent years, a number of investigations of the large amplitude vibration of beams¹⁻⁴ and flat rectangular plates⁵⁻⁸ have been reported in which the ends of the beams and the edges of the plates have been assumed to remain a fixed distance apart during vibration. In particular, Burgreen² has considered the free vibration of a simply supported beam that has been given an initial end displacement, and the author⁸ has considered free and forced vibration of simply supported and clamped beams and rectangular plates for which initial end and edge displacements have been prescribed. In both reports, a one-degree-of-freedom representation of the equations of motion is used. Results are obtained for edge displacements in the postbuckling as well as the prebuckling region. In the case of forced motion, however, the results were restricted to symmetrical motion about the flat position of the beam or plate. For the buckled beam or plate, it is also possible to have vibration about the static buckled position. This has been discussed for free vibration in the forementioned reports, and it is the purpose of the following remarks to extend the discussion to a case of forced motion.

Equations of Motion

The differential equation of motion for a beam of unit width is

$$\rho h w_{,tt} + (EI w_{,yy})_{,yy} - \frac{Eh}{b} \left[v_0 + \frac{1}{2} \int_0^b (w_{,y})^2 dy \right] w_{,yy} = P(y, t) \quad (1)$$

where v_0 represents an initial axial displacement measured from the unstressed state. For a plate, the dynamic von Kármán equations are

$$\begin{aligned} \nabla^4 F &= E(w_{,xy}^2 - w_{,xx}w_{,yy}) \\ D\nabla^4 w &- h(F_{,yy}w_{,xx} + F_{,xx}w_{,yy} - 2F_{,xy}w_{,xy}) + \rho h w_{,tt} = P(x, y, t) \end{aligned} \quad (2)$$

where

$$\sigma_x = F_{,yy} \quad \sigma_y = F_{,xx} \quad \tau_{xy} = -F_{,xy}$$

are the membrane stresses. When a single mode is assumed and Galerkin's method is applied, the problem reduces to the solution of a single ordinary differential equation in time.

Received July 8, 1964. The research reported in this note was sponsored by NASA under Grant No. NSG-132-61.

* Associate Professor, Department of Aeronautical and Astronautical Engineering. Member AIAA.

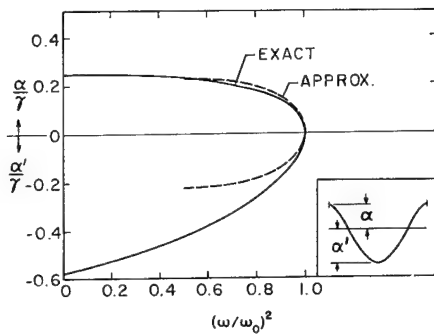


Fig. 1 Free vibration.

In the case of a simply supported beam, for example, we assume

$$w(y, t) = b\xi(t) \sin(\pi y/b) \quad (3)$$

and obtain the following equation in nondimensional form:

$$\xi_{,\tau\tau} + p\xi + q\xi^3 = f(\tau) \quad (4)$$

where

$$p = \frac{\pi^4}{12} \gamma^2 (1 - \lambda) \quad q = \frac{\pi^4}{4} \\ \tau = \left(\frac{E}{\rho}\right)^{1/2} \frac{t}{b} \quad \gamma = \frac{h}{b}$$

The parameter λ is a measure of the initial axial displacement and is defined as

$$\lambda = v_0/v_{0cr} \quad (5)$$

where v_{0cr} is the axial displacement that produces the buckling load. Thus $\lambda > 1$ refers to the postbuckling region. An equation of the same form is obtained for other beam boundary conditions and for plates as well. The coefficients p and q for simply supported and clamped beams and rectangular plates are given in Ref. 8. The remarks that follow apply to these cases as well as others that may be defined.

To study the motion about the static buckled position, it is convenient to change to the variable

$$\delta = \xi - \xi_1 \quad (6)$$

where ξ_1 is the static buckle amplitude and δ is the variation from that position. If Eq. (6) is substituted into Eq. (4), it follows that for harmonic forcing

$$\delta_{,\tau\tau} + \omega_0^2 \delta + c_2 \delta^2 + c_3 \delta^3 = \bar{f} \cos \omega \tau \quad (7)$$

where

$$\omega_0^2 = p + 3q\xi_1^2 \quad c_2 = 3q\xi_1 \quad c_3 = q$$

Note that ω_0 is the linear vibration frequency about the buckled position. The problem of small amplitude vibration of a buckled plate has been more fully discussed elsewhere.^{9, 10}

This equation is of similar form to an equation derived for the vibration of initially curved plates and shells.¹¹⁻¹³ The Linstedt-Duffing perturbation technique^{11,13} used in two of the preceding reports may be applied here. Let

$$\delta = \delta_0 + \alpha \delta_1 + \alpha^2 \delta_2 + \alpha^3 \delta_3 + \dots \\ \omega^2 = \omega_0^2 + \alpha \omega_1^2 + \alpha^2 \omega_2^2 + \alpha^3 \omega_3^2 + \dots \\ \bar{f} = \bar{f}_0 + \alpha \bar{f}_1 + \alpha^2 \bar{f}_2 + \alpha^3 \bar{f}_3 + \dots \quad (8)$$

where the initial conditions on Eq. (7) are taken to be

$$\delta(0) = \alpha \quad \delta_{,\tau}(0) = 0 \quad (9)$$

from which it follows that

$$\delta_1(0) = 1 \quad \delta_0(0) = \delta_2(0) = \delta_3(0) = \dots = 0 \quad (10)$$

It is convenient to introduce the forcing function as follows: let

$$\bar{f}_0 = \bar{f}_1 = \bar{f}_2 = 0 \quad (11)$$

so that

$$\bar{f} = \alpha^3 \bar{f}_3 \quad (12)$$

Then it follows that when Eqs. (8) are substituted into Eq. (7) and terms are collected according to the power of α , a series of equations are obtained. The first is

$$\alpha^0: \delta_{0,\tau\tau} + \omega_0^2 \delta_0 + c_2 \delta_0^2 + c_3 \delta_0^3 = 0 \quad (13)$$

which has as its solution, in view of Eqs. (10),

$$\delta_0(\tau) = 0 \quad (14)$$

and next

$$\alpha^1: \delta_{1,\tau\tau} + \omega_0^2 \delta_1 = 0 \quad (15)$$

which has as its solution

$$\delta_1(\tau) = \cos \omega \tau \quad (16)$$

Continuing, we obtain

$$\alpha^2: \delta_{2,\tau\tau} + \omega_0^2 \delta_2 = -(c_2/2) + \omega_1^2 \cos \omega \tau - (c_2/2) \cos 2\omega \tau \quad (17)$$

To insure a periodic solution, it is necessary that

$$\omega_1^2 = 0 \quad (18)$$

thus the solution to Eq. (17) becomes

$$\delta_2(\tau) = (c_2/6\omega^2)(-3 + 2 \cos \omega \tau + \cos 2\omega \tau) \quad (19)$$

Finally,

$$\alpha^3: \delta_{3,\tau\tau} + \omega_0^2 \delta_3 = -\frac{c_2^2}{3\omega^2} + \left(\omega_2^2 + \frac{5}{6} \frac{c_2^2}{\omega^2} - \frac{3}{4} c_3 + \bar{f}_3\right) \cos \omega \tau - \frac{c_2^2}{3\omega^2} \cos 2\omega \tau - \left(\frac{c_2^2}{3\omega^2} + \frac{c_3}{4}\right) \cos 3\omega \tau \quad (20)$$

Once again, to insure a periodic solution, it is necessary that

$$\omega_2^2 = -\frac{5}{6} \frac{c_2^2}{\omega^2} + \frac{3c_3}{4} - \bar{f}_3 \quad (21)$$

which, from Eqs. (8) and (12), may be written

$$\omega^2 = \omega_0^2 + \alpha^2 \left(\frac{3c_3}{4} - \frac{5}{6} \frac{c_2^2}{\omega^2} - \frac{\bar{f}}{\alpha} \right) \quad (22)$$

It is worth noting that the Ritz-Galerkin and related methods as they are commonly applied are inadequate for obtaining an approximate solution to Eq. (7). It is common practice to use the solution of the corresponding linear equation as an assumed solution of the nonlinear equation. The frequency-amplitude relation is obtained by means of a certain time integration over a cycle of the motion which minimizes the error introduced by this assumption. Unfortunately the restriction imposed by the assumed solution is such that all contributions of the term $c_2 \delta^2$ are lost in the integration, regardless of its actual influence. If, however, more care is used in the selection of an assumed function, this difficulty may be overcome.

In our case, let

$$\delta(\tau) = A + B \cos \omega \tau + C \cos 2\omega \tau \quad (23)$$

and proceed with the Ritz-Galerkin method as described, for example, in Ref. 14. We then obtain four algebraic equations in the four unknowns ω^2 , A , B , and C , but because of the complexity of the equations, no general algebraic solution is possible. If, in addition, we let

$$\omega^2 = \omega_0^2 + \alpha \omega_1^2 + \alpha^2 \omega_2^2 + \dots \\ A = \alpha A_1 + \alpha^2 A_2 + \alpha^3 A_3 + \dots \\ B = \alpha B_1 + \alpha^2 B_2 + \alpha^3 B_3 + \dots \\ C = \alpha C_1 + \alpha^2 C_2 + \alpha^3 C_3 + \dots \quad (24)$$

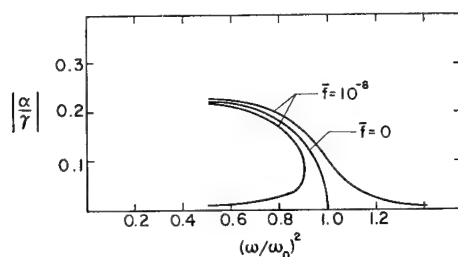


Fig. 2 Forced vibration.

and solve the resulting equations, we arrive at the identical frequency-amplitude relation given by Eq. (22).†

Free Vibration

The relation for free vibration may be obtained by setting $\gamma = 0$ in Eq. (22). An exact solution for free vibration is also possible in this case in terms of elliptic functions. It is

$$\delta(\tau) = (\alpha + \mu)dn(\omega\tau, k) - \mu \quad (25)$$

where

$$\mu = \frac{c_2}{3c_3} \quad \bar{\omega}^2 = \frac{c_3(\alpha + \mu)^2}{2} \quad k^2 = \frac{(\omega_0^2 - c_2\mu)}{\bar{\omega}^2} + 2$$

The initial conditions are

$$\delta(0) = \alpha \quad \delta_{,\tau}(0) = 0 \quad (26)$$

where α is positive and subject to the condition

$$-2 < \frac{(\omega_0^2 - c_2\mu)}{c_3(\alpha + \mu)^2} < -1 \quad (27)$$

Physically this restricts consideration to motion about the buckled position on one side of the flat position. The period of the motion is given by the elliptic integral

$$T = \frac{2K}{\bar{\omega}} = \frac{2}{\bar{\omega}} \int_0^{\pi/2} \frac{d\phi}{1 - k^2 \sin^2 \phi} \quad (28)$$

It should be noted that Eq. (25) is not a general solution to Eq. (7) for arbitrary values of the coefficients ω_0^2 , c_2 , and c_3 but only for free motion when the relation

$$9\omega_0^2 c_3 - 2c_2^2 = 0 \quad (29)$$

holds. This condition is satisfied in this case because Eq. (7) was obtained from Eq. (4). An exact solution in terms of elliptic functions is still possible, however, as described in Ref. 12, for example.

Numerical Results

Numerical results have been obtained from Eqs. (22) and (28) for the special case of a buckled beam with $\lambda = 2$ and $\gamma = 0.005$ and are presented in Fig. 1 for free motion. In this figure, the amplitude is given in terms of the number of beam thicknesses and the frequency in terms of the square of the ratio of the nonlinear to the linear frequency. Since for the exact solution the motion is not symmetrical about the undeflected position, the curve for a negative initial condition differs from that for a positive initial condition. A typical deflection curve for a cycle of the motion is shown in the lower right of the figure. The negative amplitude α' is related to α by

$$\alpha' = (\alpha + \mu)(1 - k^2)^{1/2} - \mu \quad (30)$$

In Fig. 2, the dynamic response of the same beam to harmonic forcing is shown as obtained from Eq. (22).

References

- Woinowsky-Krieger, S., "The effect of an axial force on the vibration of hinged bars," *J. Appl. Mech.* **17**, 35-36 (1950).

† This was pointed out to the author by E. F. Masur.

- Burgreen, D., "Free vibrations of a pin ended column with constant distance between ends," *J. Appl. Mech.* **18**, 135-139 (1951).

- Mettler, E., "Zum Problem der Stabilität erzwingender Schwingungen elastischer Körper," *Z. Angew. Math. Mech.* **31**, 263-264 (1951).

- McDonald, P. H., "Nonlinear dynamic coupling in a beam vibration," *J. Appl. Mech.* **22**, 573-578 (1955).

- Chu, H. N. and Herrmann, G., "Influence of large amplitudes of free flexural vibrations of rectangular elastic plates," *J. Appl. Mech.* **23**, 532-540 (1956).

- Yamaki, N., "Influence of large amplitudes on flexural vibrations of elastic plates," *Z. Angew. Math. Mech.* **41**, 501-510 (1961).

- Lin, Y. K., "Response of a nonlinear flat panel to periodic and randomly-varying loadings," *J. Aerospace Sci.* **29**, 1029-1033, 1066 (1962).

- Eisley, J. G., "Nonlinear vibration of beams and rectangular plates," *Z. Angew. Math. Phys.* **15**, 167-174 (1964).

- Bisplinghoff, R. L. and Pian, T. H. H., "On the vibration of thermally buckled bars and plates," *Proc. IX Congr. Intern. Mech. Appl.* **7**, 307 (1957).

- Herzog, B. and Masur, E. F., "Frequencies and modes of vibration of buckled circular plates," NASA TN D-2245 (February 1964).

- Reissner, E., "Nonlinear effects in vibration of cylindrical shells," Space Technology Labs. Rept. AM-5-6 (September 30, 1955).

- Yu, Y.-Y., "Application of variational equation of motion to the nonlinear vibration analysis of homogeneous and layered plates and shells," *J. Appl. Mech.* **30**, 79-86 (1963).

- Cummings, B. E., "Large-amplitude vibration and response of curved panels," *AIAA J.* **2**, 709-716 (1964).

- Cunningham, W. J., *Introduction to Nonlinear Analysis* (McGraw-Hill Book Co., Inc., New York, 1958), Chap. 6.

Approximate Absorption Coefficients for Vibrational Electronic Band Systems

EDWARD P. FRENCH*

North American Aviation, Downey, Calif.

Introduction

IT is frequently necessary to calculate both spectral and total gas radiation arising from the shock layers, boundary layers, wakes, or exhaust plumes associated with hypersonic vehicles. Such calculations may be required in order to assess radiant heat transfer to vehicle surfaces, interference with onboard optical devices, or detection by remotely located instruments. In addition, gas radiation emission may be used as a diagnostic device in hypervelocity testing.

There are a number of sources of detailed spectral absorption or emission data for the major constituents of equilibrium air.¹⁻³ Similar information about other gas compositions such as air-ablation product mixtures, rocket exhausts, and extraterrestrial atmospheres is not so readily available, however. It is the purpose of this note to describe an approximate method by which spectral radiation can be estimated rapidly for an important class of radiators, namely, vibrational-electronic band systems of diatomic molecules.

Detailed Spectral Absorption Estimates

Meyerott et al.² present the radiative contributions from individual band systems in terms of average spectral absorption coefficients from which spectral emission may be

Received July 13, 1964. The writer wishes to thank Edgar Thompson and Lloyd LeBlanc for their assistance in making the detailed spectral absorption coefficient calculations referred to in this note.

* Senior Technical Specialist, Space Sciences Laboratory, Space and Information Systems Division. Member AIAA.

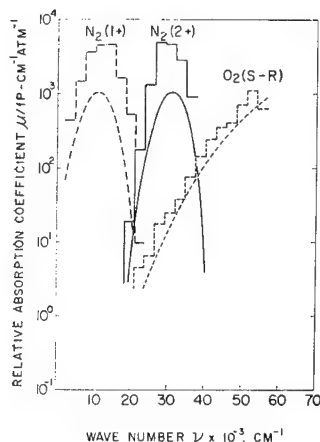


Fig. 1 Approximate and detailed absorption coefficients for N_2 (1+), N_2 (2+), and O_2 (Schumann-Runge) at 6000° K.

obtained directly for cases where the radiating gas is optically thin and local thermodynamic equilibrium exists. The absorption coefficient for a given wave-number interval is taken to be the average of the integrated absorptions from all bands falling within the interval. The integrated absorption from a particular band, characterized by lower vibrational quantum number n and upper vibrational quantum number m , is

$$\int \mu d\nu = \pi r_0 N_n f q_{nm} \quad (1)$$

Here r_0 is the classical electron radius and the integration is over wave number. The concentration N_n is the product of the total concentration of the absorbing species N_t and the relative population of the n th vibration level, which is simply calculated, provided the vibrational levels approximate a Boltzmann distribution. In this case,

$$N_n = L_0 P \exp(-hcE_n/kT)/Q \quad (2)$$

where L_0 is the Loschmidt number, P is the species concentration in standard atmospheres, and E_n is the vibrational energy of the absorbing molecules, measured from the ground state. The oscillator strength f , which is a measure of the electronic transition probability, is assumed to be a constant for the entire band system as an approximation. In general, f must be empirically determined. The Franck-Condon factors q_{nm} represent the nuclear contribution to the transition probability and may be computed for each transition provided the vibrational wave functions are known.

Approximation Based on the Franck-Condon Principle

It is well known that bands having large transition probabilities tend to lie along the Franck-Condon parabola, the locus of upper and lower states for which internuclear separations at the classical turning points are equal.⁴ Bands falling on or near the parabola have Franck-Condon factors

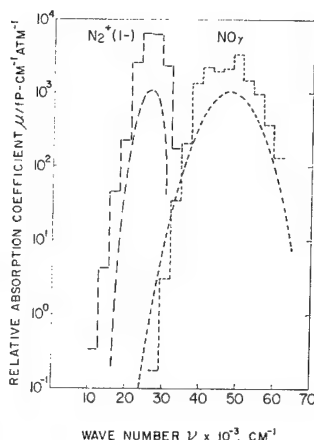


Fig. 2 Approximate and detailed absorption coefficients for N_2^+ (1-) and $NO\gamma$ at 6000° K.

of the order of 0.1, whereas other bands are generally much weaker. This fact suggests that the main features of the spectral absorption curve can be derived by considering only strong bands along the parabola.

The energy of a diatomic molecule can be represented fairly simply by means of the Morse potential⁵

$$V = D[\exp\{-a(r - r_e)\} - 1]^2 \quad (3)$$

where r is the internuclear distance and r_e is its value at equilibrium. This yields the quadratic expression

$$V_n = \omega_e(n + \frac{1}{2}) - \omega_e x_e(n + \frac{1}{2})^2 \quad (4)$$

for the allowed vibrational energy levels.

The dissociation energy D and the constant a in Eq. (3) are related to the coefficients of Eq. (4) as follows:

$$D = \omega_e^2/4\omega_e x_e \quad (5)$$

$$a = (8\pi^2 m_r c \omega_e x_e / h)^{1/2} \quad (6)$$

where m_r is the nuclear reduced mass.

Equation (4) can be solved for the vibrational quantum number so that, when the relations in Eqs. (3) and (5) are substituted, the result is

$$n = \frac{1}{2} \omega_e / \omega_e x_e [1 - \{1 - [\exp\{-a(r - r_e)\} - 1]^2\}^{1/2}] - \frac{1}{2} \quad (7)$$

Equation (7), which holds for either the upper or lower state, provides a relationship between vibrational quantum number and internuclear distance at the turning point. For a particular value of r , therefore, Eq. (7) identifies one pair of quantum numbers on the Franck-Condon parabola. The corresponding transition wave number is

$$\nu = \nu_{00} + \omega_{e1}m - \omega_{e2}n - (\omega_{e2})_1(m^2 + m) + (\omega_{e2})_2(n^2 + n) \quad (8)$$

where ν_{00} is the energy of transition between ground states in wave numbers and the subscripts 1 and 2 denote upper and lower states, respectively.

For each of a series of internuclear spacings, upper and lower vibrational quantum numbers are computed from Eq. (7). Here m and n are treated as continuous variables running from $-\frac{1}{2}$ to $\frac{1}{2}(\omega_e/\omega_{e2} - \frac{1}{2})$. For each value of r , a transition wave number is calculated from Eq. (8).

The average spectral absorption coefficient is computed as though due to a single strong band with q_{nm} equal to 0.1, centered at the transition wave number and extending over an interval $\Delta\nu = 0.5(\omega_{e1} + \omega_{e2})$, the average interval corresponding to unit change in vibrational quantum number.

The final expression for the absorption coefficient is obtained from Eqs. (1) and (2). In the latter,

$$E_n = (\omega_e - \omega_{e2})n - (\omega_{e2})_2 n^2 \quad (9)$$

and the vibrational partition function is approximated by the harmonic oscillator form

$$Q = [1 - \exp(-hc\omega_{e2}/kT)]^{-1} \quad (10)$$

The absorption coefficient can now be expressed as a function of the quantum number n :

$$\mu = \frac{4.759 \times 10^6 P f \exp(-1.439 E_n / T) [1 - \exp(-1.439 \omega_{e2} / T)]}{\omega_{e1} + \omega_{e2}} \quad (11)$$

Results

In order to evaluate the usefulness of the approximate method, it was applied to seven band systems of importance in high-temperature air, namely the O_2 Schumann-Runge, NO beta and gamma, N_2 first positive, second positive and Worley, and N_2^+ first negative systems. The constants

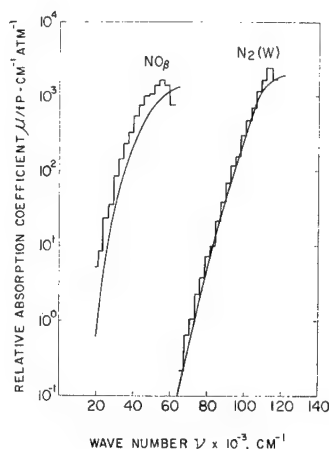


Fig. 3 Approximate and detailed absorption coefficients for NO β and N $_2$ (Worley) at 6000°K.

ω_e , $\omega_e x_e$, ν_{00} , m_r , and r_e were all taken from Table 39 of Ref. 5, except that r_e for the upper state of the NO beta system was taken to be 1.415 Å in accordance with the recommendation of Kivel, et al.⁶ In all cases, transitions involving quantum numbers higher than 20 in either state were arbitrarily rejected, based upon the realization that potential functions fitted to lower vibrational states become increasingly unreliable at higher levels.

The results of the approximate method are compared in Figs. 1–3 with those obtained by digital computer in the manner described in Ref. 2. All bands having finite q_{nm} were considered, and average absorption coefficients over fixed intervals of 2750 cm⁻¹ were computed by summing integrated band absorptions as calculated by Eq. (1). The Franck-Condon factors employed were those tabulated or cited in Ref. 2, supplemented by additional values for the O $_2$ Schumann-Runge system and for the N $_2$ Worley system that were computed directly from Morse wave functions. Absorption coefficients obtained both by the approximate and detailed methods have been expressed per unit f number and per standard atmosphere of absorbing constituent.

The agreement between the approximate (smooth curves) and detailed calculations is surprisingly good. The best results are obtained for systems such as O $_2$ Schumann-Runge, NO beta, and N $_2$ Worley for which the upper and lower electronic states have appreciably different internuclear spacings. In all cases, the approximate method correctly locates the wave number for peak absorption and reproduces the general shape and magnitude of the spectral absorption curve.

On the basis of the demonstrated agreement for the seven band systems considered, it seems justified to regard the method as a reliable means of estimating spectral absorption coefficients for any band system. For those systems for which f numbers and species concentrations are known or can be estimated, absolute absorption coefficients can be calculated. For the much larger number of systems for which little or no intensity information is available, relative spectral absorption coefficients can be estimated if the necessary spectroscopic constants are available.

References

- Kivel, B. and Bailey, K., "Tables of radiation from high temperature air," Avco Research Lab. Rept. 21 (December 1957).
- Meyerott, R. E., Sokoloff, J., and Nicholls, R. W., "Absorption coefficients of air," Geophysical Research Papers 68, Geophysics Research Directorate, U. S. Air Force, Bedford, Mass. (July 1960).
- Nardone, M., Breene, R. G., Zeldine, S., and Riethof, T. R., "Radiance of species in high temperature air," General Electric Co., Rept. R6351D3 (June 1963).
- Herzberg, C., *Molecular Spectra and Molecular Structure I. Spectra of Diatomic Molecules* (D. Van Nostrand, Inc., Princeton, N. J., 1956), pp. 194–198.

- Morse, P. M., "Diatomic molecules according to the wave mechanics. II. Vibrational levels," Phys. Rev. **34**, 58 (1929).
- Kivel, B., Mayer, H., and Bethe, H., "Radiation from hot air Part I. Theory of nitric oxide absorption," Ann. Phys. **2**, 64 (1957).

Significance of the Cross Correlation between the Modes of a Structure on Its Response

GHASSAN R. KHABBAZ*

Lockheed Missiles and Space Company,
Sunnyvale, Calif.

Nomenclature

A	= cross-sectional area of beam
D	= mean square pressure $\times 4 \lambda \theta$
E	= modulus of elasticity
h	= depth of beam
I	= moment of inertia of beam
L	= total length of beam
$W_p(x, x_1, \omega)$	= cross spectrum between the pressure at point x and x_1
x	= nondimensional distance along length of the beam
$y(x)$	= response of beam
$Y_n(\omega)$	= reciprocal of transfer function of n th mode
$\phi_n(x)$	= mode shape of n th mode
ρ	= density of the material of beam
ξ	= ratio of damping to critical damping
τ	= difference in time at which events occurred
λ	= axial correlation length of the pressure field
θ	= correlation lifetime of the pressure field
ω_n	= natural frequency associated with the n th mode
$\langle \dots \rangle$	= ensemble average operation
$\bar{Y}_n(\omega)$	= complex conjugate of $Y_n(\omega)$

Subscripts

a, d, s = acceleration, displacement, and stress, respectively

Introduction

WE represent the dynamic response of a continuous structure in terms of the orthogonal modes $\phi_n(x)$ of free vibration of the undamped system as

$$y(x, t) = \sum_n q_n(t) \phi_n(x) \quad (1)$$

If the pressure acting on the system is a stochastic process, then $q_n(t)$ is a random function. The cross correlation of the response can be represented as

$$\langle y(x, t) y(x_1, t + \tau) \rangle = \sum_m \sum_n \phi_m(x) \phi_n(x_1) \langle q_m(t) q_n(t + \tau) \rangle \quad (2)$$

If the pressure field is stationary in time, then

$$\langle q_m(t) q_n(t + \tau) \rangle = R_{mn}(\tau) \quad (3)$$

The mean square response of the structure at point x reduces to

$$\langle y^2(x, t) \rangle = \sum_m \sum_n \phi_m(x) \phi_n(x) R_{mn}(0) \quad (4)$$

Received July 8, 1964; revision received July 31, 1964. The author wishes to express his indebtedness to R. Herzberg for his helpful suggestions and discussions and to K. Redlack for carrying on the programming.

* Associate Research Scientist. Member AIAA.

Table 1 First mode contribution and model correlation of the response vs damping, space, and time correlation lengths

$\theta\omega_1$	λ	$\xi = 0.01$		$\xi = 0.05$		Q_s
		Q_a	G_a	Q_a	G_a	
10^{-3}	0	0.036	1.00	0.073	1.00	0.645
	1	0.270	0.496	0.287	0.443	0.940
1	0	0.486	1.00	0.495	1.00	0.957
	1	0.893	1.00	0.895	0.999	0.985

From Powell's work,¹ as well as others, it can be shown that

$$R_{mn}(0) = \int_{-\infty}^{\infty} \frac{1}{Y_m(\omega)Y_n(\omega)} \int_0^1 \int_0^1 W_p(x, x_1, \omega) \phi_n \times \\ (x) \phi_m(x_1) dx dx_1 d\omega \quad (5)$$

Usually, the cross spectrum of the pressure extends over a wide band of frequency and hence over a large number of modes. The computation in (4) can be reduced tremendously if one can reduce the double summation to single summation. This means $R_{mn}(0)$ should be zero except when m is equal to n . If the pressure field is spatially uncorrelated, i.e.,

$$W_p(x, x_1, \omega) = S_p(\omega) \delta(x - x_1) \quad (6)$$

then the double summation can be reduced to a single summation because of the orthogonality of the modes.

The uncorrelated pressure field is an idealization of the physical situation. In this note we shall investigate the error introduced in reducing the double summation to a single sum for a correlated pressure field on the following three responses: 1) displacement, 2) stress, and 3) acceleration. Moreover, we shall investigate the effect of damping on the forementioned error.

Modal Analysis of System

For ease of mathematical analysis we shall take the continuous structure as a uniform, simply supported beam. Then²

$$\phi_n(x) = \sin(n\pi x) \quad (7)$$

$$\omega_n = n^2 \left[\frac{EI}{A\rho} \left(\frac{\pi^4}{L^4} \right) \right]^{1/2} \quad (8)$$

$$Y_{nd} = \frac{1}{2} [\omega_n^2 - \omega^2 + 2i\xi\omega\omega_n] \quad (9a)$$

$$Y_{na} = Y_{nd}/\omega^2 \quad (9b)$$

The maximum bending stress at any cross section associated with the n th mode $\phi_n(x)$ is given as

$$S_n = -\frac{h}{2} E \frac{d^2 \phi_n(x)}{dx^2} = \frac{h}{2} E (n\pi)^2 \phi_n(x) \quad (10)$$

Modal Correlation

As was pointed out in the Introduction, for a spatially uncorrelated pressure field, the modes are uncorrelated. We shall investigate in the following section the effect of the spatial correlation of the pressure field on the correlation of the modes. We shall assume that the pressure field is stationary in space and time and that the correlation function of the pressure field can be reduced to a product of two functions, space and time, as follows:

$$W_d(x, x_1, \tau) = DX(x - x_1)T(\tau) \quad (11)$$

We shall choose a spatial correlation function that, in the limit, approaches a delta function and study its effect on the correlation of the modes. Let

$$X(x - x_1) = \frac{1}{2\lambda} e^{-|x - x_1|/\lambda} \quad (12)$$

as

$$\lambda \rightarrow 0 \quad X(x - x_1) \rightarrow \delta(x - x_1)$$

We may add that we shall choose the same function for the time correlation:

$$T(\tau) = (1/2\theta) e^{-|\tau|/\theta} \quad (13)$$

The correlation function given in (13) is that of a Markovian process.³ Substituting (11-13, and 7) into (5) yields

$$R_{mn}(0) = D \int_{-\infty}^{\infty} C_{mn} F_{mn}(\omega) d\omega \quad (14)$$

where

$$C_{mna} = C_{mnd} = \int_0^1 \int_0^1 X(x x_1) \phi_m(x) \phi_n(x_1) dx dx_1 = \\ \frac{\lambda^3 (m\pi)(n\pi)}{2[1 + (n\pi\lambda)^2][1 + (m\pi\lambda)^2]} \{1 + (-1)^{n+m} - e^{-1/\lambda} [(-1)^m + \\ (-1)^n]\} + \frac{1}{2} \frac{\delta_{mn}}{1 + (n\pi\lambda)^2} \quad (15a)$$

$$C_{mns} = (hE/2)^2 (m\pi)^2 (n\pi)^2 C_{mna} \quad (15b)$$

$$F_{mnd}(\omega) = F_{mns}(\omega) = \\ \frac{\int_{-\infty}^{\infty} T(\tau) e^{-i\omega\tau} d\tau}{Y_n(\omega) \bar{Y}_n(\omega)} = \frac{1}{(1 + \theta^2 \omega^2) Y_n(\omega) \bar{Y}_n(\omega)} \quad (16a)$$

$$F_{mna}(\omega) = \omega^4 F_{mnd} \quad (16b)$$

where

$$\delta_{mn} = 1 \text{ if } n = m \quad \delta_{mn} = 0 \text{ if } m \neq n$$

It is interesting to observe that (15) indicates that the even and odd modes are uncorrelated. Moreover, (15) shows that, in the limit as $\lambda \rightarrow 0$, the modes become uncorrelated.

Results

Instead of presenting the results $R_{mn}(0)$ as an $(m \times n)$ matrix, we chose to present them in terms of the following two functions:

$$Q = \frac{R_{11}(0)}{\sum_m \sum_n R_{mn}(0)} \quad (17)$$

$$G = \frac{\sum_n R_{nn}(0)}{\sum_m \sum_n R_{mn}(0)} \quad (18)$$

The ratio Q is a measure of the contribution of the first mode to the mean square response. The ratio G is a measure of the modal correlation. In the limit when the modes become uncorrelated the ratio G should approach unity.

We calculated the ratio Q and G for various parameters ξ , λ and θ : $\xi = 0.01$ to 0.10 ; $\theta\omega_1 = 10^{-3}$ to 10^2 ; and $\lambda = 0$ to 10 .

Conclusion and Discussion

The values for Q_d were always near unity. Thus, for the calculation of the displacement response, one needs to take into consideration the first mode only.

In calculating the stress response one can assume that the modes are uncorrelated since G_s is always near unity (within 9%). When the pressure field has a weak spatial and time correlations, Q_s is only (0.6456), indicating that one needs to consider more than the first mode in calculating the stress response.

There was a large variation in Q_a and G_a over the range of parameters investigated. For small λ , i.e., narrow spatial correlation, G_a is large because the modes are uncorrelated. From Table 1, one observes that G_a decreases with an increase in λ because as λ increases the correlation between the

modes increases. On the other hand, the contribution of the first mode to the total response is small when λ is small and increases with λ . This indicates that as λ increases the contribution of the lower modes increases, i.e., C_{mn} decreases with λ by a smaller amount for m and n small than for m and n large. As θ increases, the power spectral density of the forcing pressure shifts to the lower frequencies. Thus, the contribution of the first mode to the total response increases with an increase in θ . One also observes that G_a increases with θ , indicating that the modes become uncorrelated with an increase in θ .

Knowing the correlation of the pressure field, now one has a basis for neglecting the cross correlation between the modes or considering the first mode only in calculating the response of a structure.

The foregoing conclusions are valid only for the correlation functions that were assigned in Eqs. (10-12). These correlation functions encompass a wide range of physical cases. The discussion does not apply for convective pressure fields. In the latter situations, coincidence might play a significant role and change the picture.

References

- 1 Powell, A., "On the response of structures to random pressures and to jet noise in particular," *Random Vibration*, edited by S. H. Crandall (M.I.T. Press, Cambridge, Mass., 1958), Chap. 8.
- 2 Timoshenko, S. and Young, D. H., *Vibration Problems in Engineering* (D. Van Nostrand Co., Inc., Princeton, N. J., 1955), 3rd ed., p. 332.
- 3 Wang, M. C. and Uhlenbeck, G. E., "On the theory of Brownian motion II," *Selected Papers on Noise and Stochastic Processes*, edited by N. Wax (Dover Publications Inc., New York, 1954); Rev. Mod. Phys. 17, 323-342 (1954).

Time-Dilatation Dilemma and Scale Variation

M. Z. v. KRZYWOBLOCKI*

Michigan State University, East Lansing, Mich.

1. Transformation Equations

WE assume the special theory of relativity in the sense of Einstein. Let us assume two inertial coordinate systems, S and S^* . S^* moves relatively to S at the constant rate v along the X axis. At the S time $t = 0$, the points of origin of S and S^* coincide. The X^* axis coincides with the X axis. The transformation equations are

$$\begin{aligned} x^* &= (x - vt)(1 - v^2/c^2)^{-1/2} \\ y^* &= y \quad z^* = z \end{aligned} \quad (1.1)$$

$$t^* = (t - vx/c^2)(1 - v^2/c^2)^{-1/2} \quad (1.2)$$

The inverse transformation equations are

$$\begin{aligned} x &= (x^* + vt^*)(1 - v^2/c^2)^{-1/2} \\ y &= y^* \quad z = z^* \end{aligned} \quad (1.3)$$

$$t = (t^* + vx^*/c^2)(1 - v^2/c^2)^{-1/2} \quad (1.4)$$

2. Usual Formulation of Time-Dilatation Dilemma

At the present time there exist various forms of the interpretation of the time dilatation (the same refers to the length contraction). Let us consider a clock that is rigidly connected with the starred frame of reference and stationed at some point (x_0^*, y_0^*, z_0^*) . Let us compare the time indi-

cated by that clock with the time t measured in the unstarred system. An S time interval, $(t_2 - t_1)$, is therefore related to the readings t_2^* and t_1^* as follows:

$$t_2 - t_1 = (t_2^* - t_1^*)(1 - v^2/c^2)^{-1/2} \quad (2.1)$$

In a similar way we obtain

$$t_2^* - t_1^* = (t_2 - t_1)(1 - v^2/c^2)^{-1/2} \quad (2.2)$$

and the Lorentz contractions referring to lengths. The rules governing these phenomena are given by Bergmann¹ in the following forms:

Every clock appears to go at its fastest rate when it is at rest relatively to the observer. If it moves relatively to the observer with the velocity v , its rate appears slowed down by the factor $(1 - v^2/c^2)^{-1/2}$. Every rigid body appears to be the longest when at rest relatively to the observer. When it is not at rest, it appears to be contracted in the direction of its relative motion by the factor $(1 - v^2/c^2)^{-1/2}$, while its dimensions perpendicular to the direction of motion are unaffected.¹

Tolman¹⁴ concludes that the time interval between two events (which occur at the same point in S^*), which has the duration dt^* when measured with a given clock in system S^* , will have the longer duration of $dt^* (1 - v^2/c^2)^{-1/2}$ when measured by the clocks in system S . Similarly, the time interval between two events occurring at the same point in S , which has duration dt when measured with a given clock in the system S , has the longer duration of $dt(1 - v^2/c^2)^{-1/2}$ when measured with the clocks in the system S^* . One may refer to the recent controversy on the subject of time dilatation and to the works and notes of Born,² Dingle,³⁻⁶ Palacios,⁹⁻¹¹ Pilgeram,¹² and others. From the more interesting suggestions one should mention the proposition of Schlegel¹³ concerning a distinction between the macroscopic thermodynamic processes, called Claius processes, which are time invariant and independent of the relativistic transformations, and the Lorentz processes, which are subject to the relativistic transformations. Pilgeram¹² introduces the concept of the biological time, independent of the consequences of Einstein's theory of relativity, in his discussion of the Hoerner paper⁷ in which Hoerner concluded that 60 years for a crew member aboard a rocket attempting an interstellar trip will be equivalent to a life span of 5×10^6 years on earth.

It is obvious that any statement in the sense that a uniform motion of a clock will exert some influence upon the internal mechanism of the clock, so that it will slow down or accelerate, is a misleading one. The phenomenon of slowing down or accelerating a clock is a dynamic phenomenon that must involve the action of some sort of forces. The special theory of relativity can obviously refer only to the "kinematic" effects with no action of forces caused by the relative motion. The same refers to the length contraction.

3. Scale Variation in the Time-Dilatation Dilemma

We accept the validity of the Schlegel hypothesis; consequently, the discussion given below refers to phenomena that depend upon the space-time relativistic transformations. Moreover, we assume that, in order to preserve the validity of the fundamental concepts of the special theory of relativity, we allow for the change of the scale (i.e., of a unit) in the systems in question. This is nothing new, since, in various other fields of mathematical physics, the problem of the variation of scale of coordinates is a well known and popular one.[†] Assume two clocks, one in system S and another one in S^* . We would like to synchronize these two clocks so

[†] In gasdynamics there are widely used the so-called similarity rules (by Prandtl-Glauert, Kármán-Tsien and others), where there appears a factor $(1 - v^2/a^2)^{-1/2}$, a = velocity of sound, similar to the relativistic factor. To comply with the physical reality, the scale in one of the two systems in question must be appropriately changed.

that one of them would indicate to us the time on another clock at a given moment. We assume that the only possible communication correlation (correspondence) between these two clocks located in S and S^* is by means of light signals (Lorentz systems). Assume the clock in S^* system located at $x_0^* = 0$. From Eq. (1.1) it is seen that this corresponds to the magnitude $x = vt$ in S system. Inserting this value of x into Eq. (1.2) gives the result

$$t^* = t(1 - v^2/c^2)^{1/2} \quad (3.1)$$

$$t_2 - t_1 = (t_2^* - t_1^*)(1 - v^2/c^2)^{-1/2}$$

For $v^2 = 0$, one has $t_2^* - t_1^* = t_2 - t_1$, which is correct. In order to synchronize both clocks we reason in the following way: Assume that the time interval $(t_2 - t_1)$ on the clock in S system is equal to a chosen unit of time (second, minute, hour). In order that the clock located in S^* be synchronized with the clock in S , i.e., in order that the clock in S^* would show us precisely what time there is on the clock C in S at a given moment from the relativistic standpoint, the unit time-interval $(t_2^* - t_1^*)$ of the clock in S^* must be equal to $(1 - v^2/c^2)^{1/2}$, i.e., must be smaller than $(t_2 - t_1)$, which is equal to a unit. It is assumed that the internal mechanisms of clocks do not belong to a Lorentz family of systems; they belong to a Clausius family of systems in Schlegel's sense. This means that the light signals do not effect the action or the rate of action of the mechanisms of clocks in both S and S^* . Then this implies that for our space trips with very large velocities we have to construct clocks having scales different from scales of the clocks used ordinarily on the earth, i.e., for a synchronization of both clocks in S and S^* we have to have

$$\text{unit of time of a clock in the spaceship} = (1 - v^2/c^2)^{1/2} \quad (3.2)$$

We conclude: Under the assumption that the fundamental principles of the classical special theory of relativity are valid, if a clock C^* , whose internal mechanism belongs to a Clausius family of systems, moves relatively to a clock C located on the earth (C belongs to a Clausius system) with a velocity v , and which is in some sort of a synchronization with C by means of only light signals, which do not affect the action or the rate of action of both clocks, C and C^* , then the (relativistic) unit of time of the clock C^* must be equal to the factor $(1 - v^2/c^2)^{1/2}$ to be in a permanent synchronization with the clock C . The internal mechanism of the clock C^* must be correspondingly designed and constructed to indicate the time synchronized with the time of the clock C so that the time scale of the clock C^* be different from the time scale of the clock C (on the earth).

The foregoing reasoning can be illustrated briefly by the following example: Suppose the spaceship leaves the earth at 3:00 p.m. and both clocks, C and C^* , indicate precisely 3:00 p.m. Suppose that the factor $(1 - v^2/c^2)^{1/2}$ is equal to $\frac{1}{2}$. The unit time of the clock C^* is equal to one-half of the unit time of the clock C , i.e., the clock C^* runs faster than the clock C . Suppose that at 4:00 p.m. on the clock C^* we send a signal to C that it is 4:00 p.m. Actually, at this moment (from the absolute point of view) it is only 3:30 p.m. on the clock C . But the light signal from C^* will reach the observer on the earth and the clock C precisely at 4:00 p.m. In this example the receiving clock C has the same scale as all the other clocks in the S system (on the earth), and the signal-sending clock C^* has the scale changed.

Let us now discuss the inverse case. Assume a clock D located in S system of coordinates at $x = 0$. From Eq. (1.3) we have the corresponding magnitude of x^* equal to $x^* = -vt^*$, which, when inserted into Eq. (1.4), furnishes

$$t = t^*(1 - v^2/c^2)^{1/2} \quad (3.3)$$

$$(t_2^* - t_1^*) = (t_2 - t_1)(1 - v^2/c^2)^{-1/2}$$

We apply the following reasoning: Assume that the time interval $(t_2^* - t_1^*)$ on the clock D^* in S^* system is equal to a unit of time on D^* (second, minute, hour). In order that the clock located in S be synchronized with the clock in S^* , i.e., in order that the clock D in S would show us precisely what time there is on the clock D^* in S^* at a given moment from the relativistic standpoint, the unit time-interval $(t_2 - t_1)$ of the clock D must be equal to $(1 - v^2/c^2)^{1/2}$, i.e., must be smaller than $(t_2^* - t_1^*)$, which is equal to a unit. As in the foregoing, it is assumed that the clock interval mechanisms belong to a Clausius family of systems. We conclude: Under the assumption that the fundamental principles of the classical special theory of relativity are valid, if a clock D^* , whose internal mechanism belongs to a Clausius family of systems, moves relatively to a clock D located on the earth with a velocity v and which is in some sort of a synchronization with D by means of only light signals, which do not affect the action or the rate of action of both clocks D and D^* , then the (relativistic) unit of time of the clock D must be equal to the factor $(1 - v^2/c^2)^{1/2}$ to be in a permanent synchronization with the clock D^* .

The following example may be quoted. Suppose, the spaceship leaves the earth at 3:00 p.m., and both clocks D and D^* indicate precisely 3:00 p.m. With the factor $(1 - v^2/c^2)^{1/2}$ equal to $\frac{1}{2}$, the unit of time of D is equal to one-half of the unit time of all the other clocks on the earth and of the clock D^* , i.e., the clock D runs faster than all the other clocks on the earth. Suppose that at 4:00 p.m. on D we send a signal to D^* that it is 4:00 p.m. Actually, at this moment it is only 3:30 p.m. on all of the other clocks on the earth and on the clock D^* . But the light signal from D will reach the observer in the spaceship and the clock D^* precisely at 4:00 p.m. In this example the signal-sending clock D has the scale changed, whereas the receiving clock D^* has the same scale as all the other clocks on the earth. Hence, a distinction must be made between the signal-sending clocks C^* and D , and the signal-receiving clocks, C and D^* .

The foregoing proposition of the various time scales of the signal-sending and signal-receiving clocks seems to explain the so-called clock paradox. The dilemma of the length contraction is treated in another paper by the author.

References

- ¹ Bergmann, P. G., *Introduction To The Theory of Relativity* (Prentice-Hall, Inc., Englewood Cliffs, N. J., 1942).
- ² Born, M., "Special theory of relativity," *Nature* **197**, 1287 (1963).
- ³ Dingle, H., "A proposed astronomical test of the 'ballistic' theory of light emission," *Monthly Notices Roy. Astron. Soc.* **119**, 67-71 (1959).
- ⁴ Dingle, H., "Relativity and electromagnetism: An epistemological appraisal," *Phil. Sci.* **27**, 233-253 (July 1960).
- ⁵ Dingle, H., *The Special Theory of Relativity* (Methuen and Co. Ltd., London, 1960).
- ⁶ Dingle, H., "Special theory of relativity," *Nature* **197**, 1248 (1963).
- ⁷ Hoerner, v. S., "Time dilatation," *Science* **138**, 1180-1181 (1962).
- ⁸ Palacios, J., *Relatividad* (Espasa-Calpe, Madrid, 1960).
- ⁹ Palacios, J., "A reappraisal of the principle of relativity as applied to moving interferometers," *Rev. Real Acad. Cienc. Exact. Fis. Nat. Madrid* **LV** 3-14 (1961); also **55**, 191 (1961); also **54**, 497 (1960).
- ¹⁰ Palacios, J., "The relativistic behavior of clocks," *Rev. Real Acad. Cienc. Exact. Fis. Nat. Madrid* **LVI**, 287-306 (1962).
- ¹¹ Palacios, J., "The inner inconsistency of Einstein's theory," *Rev. Real Acad. Cienc. Exact. Fis. Nat. Madrid* **LVII**, 585-593 (1963).
- ¹² Pilgeram, L. O., "Time dilatation," *Science* **138**, 1180 (1962).
- ¹³ Schlegel, R., *Time and Physical World* (Michigan State University Press, East Lansing, Mich., 1961), p. 211.
- ¹⁴ Tolman, R. C., *Relativity, Thermodynamics and Cosmology* (Clarendon Press, Oxford, England, 1934), p. 24.

Effect of Fluid Motion on Free Surface Shape under Reduced Gravity

JIN H. CHIN* AND L. W. GALLAGHER†
Lockheed Missiles and Space Company,
Sunnyvale, Calif.

UNDER reduced gravity conditions, the free-surface shape of a liquid propellant in a tank may be highly curved. Under static conditions, the free-surface shape is determined by the balance between surface tension forces and gravity forces. When fluid motion exists, whether caused by effects of buoyant forces or by surface-tension gradient, the free surface may change from its static shape. Since the energy transfer across the free surface and between the propellant and tank wall depends upon the free-surface shape and the wetted area, it is of both theoretical and practical interest to examine the fluid-motion effects on free-surface shape under reduced gravity conditions.

The fluid motion under the conditions of interest is governed by the usual conservation equations in fluid dynamics. The main difference is in the boundary conditions at the free surface. However, the system of equations with the boundary conditions is complex and highly "coupled"; its solution is difficult without many simplifications and approximations. In this study, the fluid motion effects will be examined qualitatively by solving an "uncoupled" problem; that is, the free-surface shape will be calculated by assuming that the free surface is an axisymmetric stream surface with given axisymmetric velocity distributions.

The conditions along a stream surface may be described by Bernoulli's equation:

$$p + (\rho g y / g_c) + (\rho u^2 / 2g_c) = p_0 \quad (1)$$

where on the left-hand side are the pressure, gravity, and velocity heads, respectively, for a point on the liquid side of the free surface at radial distance r ; p_0 is the pressure head at the origin. From a symmetry consideration, the stream velocity at the origin vanishes. The g field is assumed to be in the negative $-y$ or axial direction.

Because of the free-surface curvature, a difference exists between the liquid pressure p and the ullage pressure p_0 :

$$p_0 - p = \frac{\sigma}{r} \left[\frac{r y_r}{(1 + y_r^2)^{1/2}} \right], \quad (2)$$

where σ is the liquid surface tension, and the subscript r means differentiation with respect to r . Equation (2) reduces to the Laplace equation when the free-surface shape is spherical. Since the ullage pressure is uniform, Eqs. (1) and (2) may be combined to yield

$$\frac{\sigma}{r} \left[\frac{r y_r}{(1 + y_r^2)^{1/2}} \right]_r - \frac{\rho g y}{g_c} - \frac{\rho u^2}{2g_c} - 2\sigma y_{rr}(0) = 0 \quad (3)$$

where the last term is obtained by evaluating the first term at $r = 0$, with the condition of symmetry $y_r(0) = 0$ and using the L'Hospital rule. Now Eq. (3) may be nondimensionalized by introducing $F = y/a$, $R = r/a$, and $V = u/u_m$, where a is the tank radius and u_m the maximum free-surface velocity; that is,

$$\frac{1}{R} \left[\frac{R F_R}{(1 + F_R^2)^{1/2}} \right]_R - BF - \frac{W}{2} V^2 - 2F_{RR}(0) = 0 \quad (4)$$

where $B = \rho g a^2 / \sigma g_c =$ Bond number, and $W = \rho a u_m^2 / \sigma g_c =$ Weber number. Equation (4) is a second-order, nonlinear, ordinary differential equation with the following boundary conditions: $F_R(0) = 0$, condition of symmetry; $F_R(1) = \cot \theta$, condition of satisfaction of contact angle. Before solution $F_{RR}(0)$ is not known; its value must be such to satisfy the two boundary conditions and the datum condition $F(0) = 0$. Without solving the "coupled" problem, the selection of the velocity distribution is somewhat arbitrary. In addition to the symmetry condition $V(0) = 0$ already mentioned, the no-slip condition $V(1) = 0$ may be used. From the consideration of liquid stratification in a tank, the flow near the free-surface center may be similar to an "inverted" axisymmetric stagnation flow with a tangential velocity proportional to the radial distance. The flow near the side wall is more complicated and is likely to be "separated" near the "corner" region. If separation does not occur, then the flow near the side wall may be similar to one-half of an "inverted," oblique, two-dimensional impinging jet. As a first approximation, the "approach" velocity toward the wall along the stagnation streamline in the jet is proportional to the distance from the wall. One of the simplest velocity distributions that satisfies the preceding behaviors is a double-sine distribution given by

$$V = \begin{cases} \sin \frac{\pi}{2} \left(\frac{R}{R_m} \right) & 0 \leq R \leq R_m \\ \sin \frac{\pi}{2} \left(\frac{1-R}{1-R_m} \right) & R_m \leq R \leq 1 \end{cases} \quad (5)$$

where R_m is the radial location of u_m . This velocity distribution will be used for the numerical calculations.

The magnitude of the Bond number depends on the liquid properties, tank radius, and the g level. For instance, $B = 2$ for liquid hydrogen, $a = 10$ ft, and $g/g_0 = 10^{-6}$. The magnitude of the Weber number is more difficult to determine. From order-of-magnitude considerations of the effects of side-wall free convection and surface-tension gradient, Chin¹ shows that, at low g levels, the Weber number can be very large. For instance, $W \sim 10$ for liquid hydrogen, $a = 10$ ft, $g/g_0 = 10^{-6}$, side-wall heat flux = 1 Btu/ft²-hr, and propellant height = 10 ft. However, with the mathematical model used, and for a given Bond number, contact angle, and velocity distribution, there exists a limiting Weber number above which numerical solutions cannot be obtained ($F_R = \infty$ for $R < 1$). Thus, the range of the Weber number of interest is not unlimited.

For small values of B , Eq. (4) may be solved numerically by the method of integral and successive approximations. After each term of Eq. (4) is multiplied by RdR and then integrated from $R = 0$ to $R = R$, the following equation is obtained:

$$\frac{R F_R}{(1 + F_R^2)^{1/2}} = F_{RR}(0)R^2 + \frac{W}{2} \int_0^R V^2 R dR + B \int_0^R F R dR \quad (6)$$

The factor $F_{RR}(0)$ may be eliminated by applying the boundary condition at $R = 1$ to Eq. (6). After manipulations, there results

$$R F_R / (1 + F_R^2)^{1/2} = E(R) \quad (7)$$

where

$$E(R) = R^2 \cos \theta + \frac{W}{2} \left(\int_0^R V^2 R dR - R^2 \int_0^1 V^2 R dR \right) + B \left(\int_0^R F R dR - R^2 \int_0^1 F R dR \right)$$

Received July 13, 1964. This work was sponsored by NASA under Contract NAS 8-11525.

* Member of Flight Technology, Research and Development Division. Member AIAA.

† Member of Flight Technology, Research and Development Division.

Equation (7) may be solved for F_R and then integrated to yield

$$F = \int_0^R \frac{E(R) dR}{[R^2 - E^2(R)]^{1/2}} \quad (8)$$

Equation (8) is an integral equation for F and may be solved by the method of successive approximations. For $B = 0$, no successive approximation is required. For small values of Bond numbers and Weber numbers ($B < 10$, $W < 5$), experience indicates that the convergence in the computer

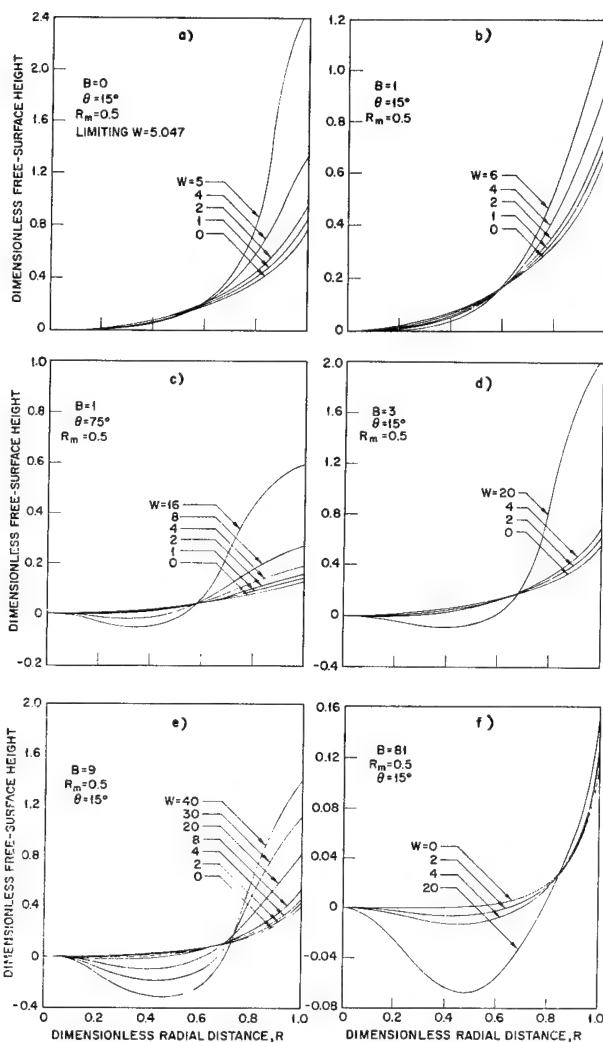


Fig. 1 Dimensionless distribution of free-surface height.

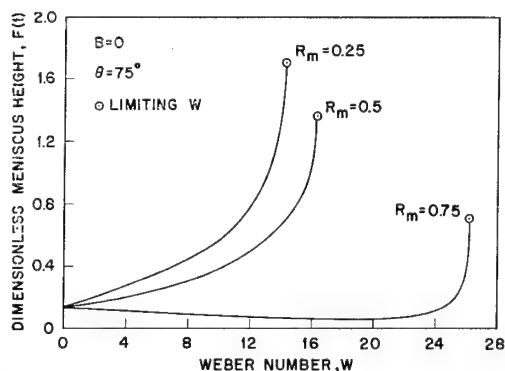


Fig. 2 Effects of Weber number and location of velocity maximum on dimensionless meniscus height.

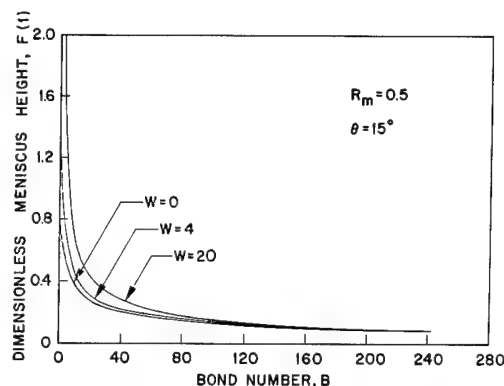


Fig. 3 Effects of Bond number and Weber number on dimensionless meniscus height.

calculation is very rapid. For large values of B and W , instability is encountered during consecutive approximations; therefore, an alternate numerical method is more appropriate for these cases.

The fact that a limiting Weber number exists in the numerical solution may be easily observed from Eq. (8) for $B = 0$; it corresponds to the smallest value of W to make $R \pm E(R) = 0$.

Expressions for some limiting cases may be obtained from Eq. (8). For instance, when $B = W = 0$, Eq. (8) yields

$$F = (1/\cos\theta) [1 - (1 - R^2 \cos^2\theta)^{1/2}] \quad (9)$$

which is an equation for a circle. For $B \ll 1$ and $W = 0$, Eqs. (8) and (9) may be used to yield a first-order approximation for F :

$$F \approx \frac{1}{\cos\theta} [1 - (1 - R^2 \cos^2\theta)^{1/2}] - \frac{B}{3 \cos^3\theta} \left\{ \ln \frac{2}{[1 + (1 - R^2 \cos^2\theta)^{1/2}]} + \frac{R^2 \cos^2\theta - \left(\frac{1 + \sin\theta + \sin^2\theta}{1 + \sin\theta} \right) [1 - (1 - R^2 \cos^2\theta)^{1/2}]}{2} \right\} \quad (10)$$

An alternate numerical method using the Runge-Kutta technique of solving Eq. (4) is used, involving the iteration of the values of $F_{RR}(0)$ to satisfy the correct value of θ . One nonlinear characteristic of Eq. (4) is that F_R may change from a small number to a very large number in one integration step, if the initially assumed $F_{RR}(0)$ is not near the correct value. To prevent computer overflow, the integration process is stopped whenever $|F_R| > 10^7$ and the iteration cycle is continued with a more appropriate value of $F_{RR}(0)$. The convergence of the numerical solution is rapid for all Bond numbers, provided that the Weber number is less than the limiting value.

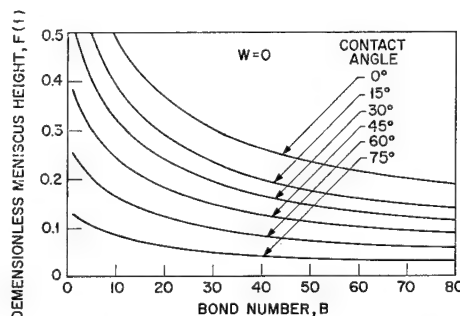


Fig. 4 Effects of Bond number and contact angle on dimensionless meniscus height.

Figures 1a-1f show the dimensionless distribution of free-surface height for $R_m = 0.5$ and different values of B . The effects of the contact angle θ may be seen by comparison of Figs. 1b and 1c. The effects of Weber number on the dimensionless meniscus height $F(1)$ are shown in Fig. 2 for different values of R_m ; the limiting Weber numbers are also indicated. Figure 3 shows the effects of Bond numbers on the meniscus height for $\theta = 15^\circ$, $R_m = 0.5$, and different values of W . The meniscus heights for the static case are given in Fig. 4.

The following conclusions may be drawn from Figs. 1-4: 1) surface velocities have strong effects on liquid free-surface shape and meniscus height; 2) the relative effect of Weber number on the meniscus height decreases as the Bond number increases; and 3) for the velocity distributions selected, the meniscus height increases for most cases as the Weber number is increased (there are exceptions, e.g., for the case with $B = 0$, $\theta = 75^\circ$, and $R_m = 0.75$).

Reference

¹ Chin, J. H., et al., "Theoretical and experimental studies of zero-g heat transfer modes," Lockheed Missiles and Space Co., Monthly Progr. Rept., NASA Contract NAS 8-11525 (November-December 1963).

Influence of Magnetic Fields upon Separation

WILLIAM H. HEISER*

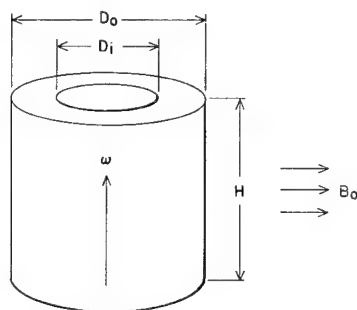
Massachusetts Institute of Technology,
Cambridge, Mass.

IT is well known that rotational motion of a conductor is resisted by induced currents if a magnetic field not parallel to the axis of rotation is applied. For example, a solid cylindrical shell of arbitrary thickness and diameter set spinning initially with angular velocity ω_0 in the presence of a transverse magnetic field B_0 (Fig. 1) can be shown to slow down in accordance with the equation

$$\omega(t) = \omega_0 \exp\{-(\sigma B_0^2/2\rho)t\}$$

provided that ρ and σ are constant throughout the material, $D_0 \ll H$, and $\mu_0 \sigma \omega_0 D_0^2$ (the magnetic Reynolds number) $\ll 1$. The striking magnitude of this effect is indicated by the

Fig. 1 Solid cylindrical shell spinning in transverse magnetic field.



Received July 16, 1964. These experiments were performed for the film "Magnetohydrodynamics" by J. A. Shercliff, produced by Educational Services Inc. for the National Committee for Fluid Mechanics Films, with the financial support of the National Science Foundation.

* Assistant Professor of Mechanical Engineering.

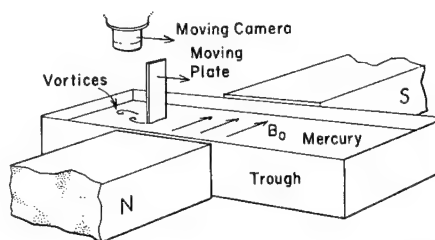


Fig. 2 Schematic representation of the experiment.

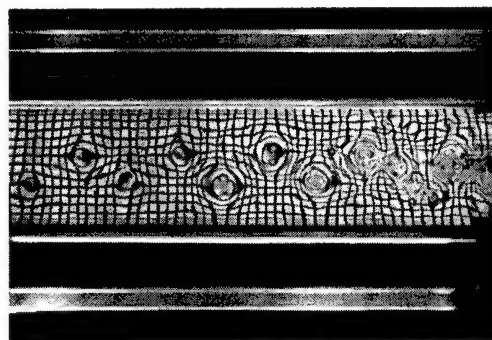


Fig. 3 Vortex street generated in the magnetic field-free region at the start of the run.

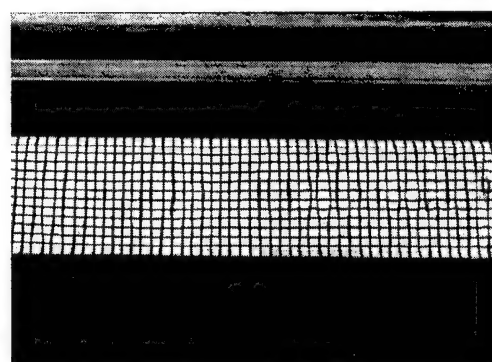


Fig. 4 No vortex street can be observed within the region of transverse magnetic field.

result that the time required for a copper shell to slow to $\frac{1}{10}$ of its initial rotational speed ($4.6\rho/\sigma B_0^2$) in the presence of a transverse field of 1 w/m^2 is only $\sim 10^{-3}$ sec. The resistance to radial current flow causes the decay time to increase as D_0/H increases.

Experiments were conducted to demonstrate this effect upon the Kármán vortex street generated by a flat plate moving with constant velocity through still mercury (Fig. 2) at the studios of Educational Services Inc., Watertown, Mass. The experiments were photographed from above as a grid, with an apparent spacing approximately the diameter of the individual vortices, was reflected from the mercury surface. This technique made the small surface dimples caused by the rotating mercury quite visible as distortions of the regular grid pattern.

Figures 3-5 are three consecutive photographs of the reflected grid pattern taken during a single constant velocity run from left to right, the flat plate being at the extreme right in each photograph. Figure 3 shows clearly the vortex street generated outside the region of transverse magnetic field. Figure 4 gives no indication that vortices are ever generated within the region of magnetic field. Figure 5 shows the resumption of the vortex street in the region where the magnetic field fringes. For the experiment shown in

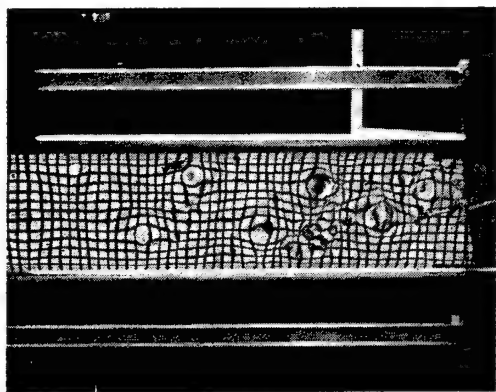


Fig. 5 The vortex street resumes in the magnetic field-free region at the end of the run.

these photographs, Reynolds number (based upon flat-plate width) $\sim 10^4$, magnetic Reynolds number (based upon flat-plate width) $\sim 10^{-3}$, vortex decay time $(4.6\rho/\sigma B_0^2) \sim 1$ sec, and vortex $D_0/H \sim 1$.

Despite the fact that the vortex decay time was long enough to allow observation of the persisting vortices, none can be seen in the magnetic field region of this experiment.

Vortices could only be observed within the magnetic field region when the vortex decay time was increased to ~ 5 sec. In accordance with the notion that the transverse magnetic field suppresses the rotation of existing vortices, the vortices observed within the magnetic field in this case did die out much more rapidly than those found outside the magnetic field.

These observations indicate that the stronger transverse magnetic field did more than merely suppress the vortices created by the flat plate, but that the magnetic field altered the separation characteristics of the boundary layer to prevent the formation of the vortex street. Although a complete solution of the problem is difficult, the Kármán-Pohlhausen technique can be used to determine whether magneto-hydrodynamic effects are large enough to possibly influence separation.¹

Since the still mercury can impress the condition of zero electric field upon the thin boundary layer, the current density at the wall of the moving flat plate must be nearly $\sigma_0 U_0 B_0$, where U_0 is the plate velocity. Consequently, the momentum equation at the plate wall becomes approximately

$$\nu \left(\frac{\partial^2 u}{\partial y^2} \right)_0 = -U_0 \frac{dU}{dx} - \frac{\sigma U_0 B_0^2}{\rho}$$

and the resulting shape factor Λ' is, therefore, related to the conventional shape factor $\Lambda = (\delta^2/\nu)(dU/dx)$ through the expression

$$\Lambda' = \Lambda \{ 1 + \sigma B_0^2 / \rho (dU/dx) \}$$

Note that $\Lambda' \geq \Lambda$ because the induced currents tend to fill out the velocity profile and that separation still occurs when $\Lambda' = -12$. For the experiment just described, $\sigma B_0^2 / [\rho(dU/dx)] \sim -1$, indicating that the effect of the induced currents in the boundary layer upon separation cannot be neglected for this case. Furthermore, the Hartmann number (based upon flat-plate width) for this experiment was approximately 100, which means that the magnetohydrodynamic forces will tend to decrease the absolute value of Λ' by reducing δ .

The results of these experiments, therefore, appear to be quantitatively in accord with boundary-layer theory, and they demonstrate that magnetic fields can exert a strong influence upon boundary-layer separation. It was also experimentally demonstrated that a magnetic field transverse to the axis of a two-dimensional, wide-angle diffuser could prevent boundary-layer separation.

Reference

- ¹ Schlichting, H., *Boundary Layer Theory* (McGraw-Hill Book Co., Inc., New York, 1960), 4th ed., Chap. 12, p. 243.

Three-Dimensional Symmetric Vortex Flow

AJIT KUMAR RAY*

Department of Transport, Government of Canada,
Ottawa, Canada

MANY problems of interest in missile or aircraft aerodynamics require a detailed knowledge of the vortex flow due to bodies of revolution or lifting surfaces, and in the following the behavior of symmetrical vortex pattern in the presence of a semicircular section in the crossflow plane has been explored with the help of a simplified model in which the vorticity is moving along the feeding sheets into the cores at all times.

Symmetric vortex separation is exactly identified in the two-dimensional picture of the wake development behind a circular cylinder. The boundary layer separates from the surface of the cylinder at the rearward stagnation point, and the two separation points move symmetrically away from this point around the cylinder. When these boundary-layer separation points reach a certain angular distance from the rearward point, the two regions of vorticity break away from the boundary layer and proceed downstream, forming the wake. Depending upon the Reynolds number, the flow behind the cylinder in the wake is identified as the Stokes flow (without the wake formation), symmetric vortex shedding and anti symmetric vortex formation with rapid transgress into turbulent motion in the wake.

In the three-dimensional flow, the forementioned vortex separation is observed on the leeward side of the slender bodies of revolution at a comparatively large angle of attack in the subsonic to supersonic range. If we imagine a fixed plane in the fluid perpendicular to the axis of the body of revolution, then the body pierces the plane with a velocity $U \sin \alpha$, α being the local body angle of attack and U the velocity. Now, considering the case in which the expanding circle, as the nose pierces the plane, changes slowly with x , x being taken in the direction of the body axis, the flow in the crossflow plane can be looked upon as the two-dimensional one. Such a procedure will not be invalid in view of the conical flow assumption in the slender body theory.

In the present problem of flow past a half cone, the flow in the crossflow plane can be solved by choosing a suitable transformational function that will map the flow plane conformally past the semicircle section into the flow in the crossflow plane past a circular section.¹ Designating the physical plane (i.e., the semicircle plane) by the Z plane and the transformed plane (i.e., the circle plane) by the τ plane, the appropriate transformation mapping the flow conformally between the two planes is given by

$$\left(\frac{Z - 3(3)^{1/2}a/4}{Z + 3(3)^{1/2}a/4} \right) = \left(\frac{\tau - ae^{-i\pi/6}}{\tau + ae^{i\pi/6}} \right)^{3/2} \quad (1)$$

where C , the center of the circle, has been taken as the origin in the τ plane, and infinity has been preserved during the transformation in both planes.¹

Received July 16, 1964.

* Employee. Member AIAA.

The flow in the circle plane (i.e., τ plane) has been studied² by writing down the complex potential function in the following way:

$$F(\tau) = \phi + i\psi \\ = -iU\alpha(\tau - a^2/\tau) - i\Gamma/2\pi \log[(\tau - \tau_0) \times (\tau + \alpha^2/\tau_0)/(\tau + \bar{\tau}_0)(\tau - \alpha^2/\bar{\tau}_0)] \quad (2)$$

ϕ and ψ being the potential and stream functions of the flow in the crossflow plane, $(\tau_0, -\bar{\tau}_0)$ the coordinates of the centers of the vortex cores, α the local body angle of attack (α being assumed small), and Γ the strength of the vortex.

Then considering the points $T(= ae^{-i\pi/6})$ and $L(= -ae^{i\pi/6})$,¹ as the stagnation points of the flow, we finally get, after some algebraic simplification, the following relation:

$$\frac{\Gamma/2\pi a U \epsilon_0}{(\alpha/\epsilon_0)} = \frac{(ae^{-i\pi/6} - \tau_0)(ae^{-i\pi/6} + \bar{\tau}_0)(ae^{i\pi/6} - \tau_0)(ae^{i\pi/6} + \bar{\tau}_0)}{a(\tau_0 + \bar{\tau}_0)(\tau_0\bar{\tau}_0 - a^2)} \quad (3)$$

where ϵ_0 is the semivertical angle of the cone in the circle plane. Another boundary condition is needed for the determination of the flow that, for the present simplified model of the actual flow, is the condition of zero net force on the feeding vortex sheet, because the assumed vortex system (the feeding vortex sheet and the concentrated vortex)³ must have a zero net force acting on it since only the conical surface and not the fluid can sustain the forces. Application of this idea to the model then requires that the forces on the feeding vortex sheet be canceled by equal and opposite forces on the concentrated vortex, and mathematically this leads to the following relation:

$$-i(\alpha/\epsilon_0)(1 + a^2/\tau_0^2) - i\Gamma/2\pi a U \epsilon_0 \{ [a\tau_0/(\tau_0^2 + a^2)] - [a/\tau_0 + \bar{\tau}_0] - [a\bar{\tau}_0/(\tau_0\bar{\tau}_0 - a^2)] \} = (2\bar{\tau}_0/a - e^{i\pi/6}) \quad (4)$$

Now the relations (3) and (4) will determine τ_0 (i.e., the coordinate of the vortex center) as a function of (α/ϵ_0) , (α/ϵ_0) being the dimensionless body angle of attack, and thus the locus of the vortex center, and further, the functional relationship between $\Gamma/2\pi a U \epsilon_0$ and (α/ϵ_0) , which are needed for the complete evaluation of the problem. From the knowledge of the flow in the circle plane (i.e., τ plane), the flow in the physical plane (i.e., Z plane) can be determined by the help of the transformation given in Eq. (1).

The lift function in the present case can be calculated with the help of the momentum consideration,^{3,4} i.e.,

$$L = -\rho U \operatorname{Re} \left[\int_{C_1} F(Z) dZ \right] \quad (5)$$

where Re stands for the real part of the expression under the sign of integration and C_1 is the contour just containing the wake, or

$$L = -\rho U \operatorname{Re} \left[\int_C F(\tau) \frac{dZ}{d\tau} d\tau \right] \quad (6)$$

where the integration is being carried out at a large distance from the wake in the circle plane; by the usual complex integration technique, it follows that

$$C_L/\epsilon_1^2 = 6.213(\alpha/\epsilon_1) + 4.734(\alpha/\epsilon_1)F(\alpha/\epsilon_1)$$

where C_L is the lift coefficient defined by the relation $C_L = L/(\rho U^2 S/2)$, S being the area of the curved surface of the semicone, ϵ_1 the semiaperture of the half-cone in the physical plane ($\epsilon_1 \cong 1.30\epsilon_0$ approximately), and

$$F\left(\frac{\alpha}{\epsilon_1}\right) = \frac{(ae^{-i\pi/6} - \tau_0)(ae^{-i\pi/6} + \bar{\tau}_0)(ae^{i\pi/6} - \tau_0)(ae^{i\pi/6} + \bar{\tau}_0)}{a^2\tau_0\bar{\tau}_0}$$

to which the right-hand expression can be reduced.

Since (α/ϵ_1) is a function of the space coordinates, $F(\alpha/\epsilon_1)$ is assumed to be analytic in the ring region bounded by the two concentric circles (the inner one being the circle of radius a forming the conical surface in the τ plane and the outer one being a large circle in the wake in the τ plane), and it may be expressed as

$$F(\alpha/\epsilon_1) = [(A_{-1})/(\alpha/\epsilon_1) + A_0 + A_1(\alpha/\epsilon_1) + \dots]$$

[an expansion similar to Laurent's series stopping at the left at $1/(\alpha/\epsilon_1)$, since the lift coefficient can not be infinite as $(\alpha/\epsilon_1) \rightarrow 0$] so that

$$C_L/\epsilon_1^2 = 4.734 A_{-1} + (\alpha/\epsilon_1)[6.213 + 4.74A_0 \dots] \quad (7)$$

so that when $(\alpha/\epsilon_1) \rightarrow 0$, (C_L/ϵ_1^2) becomes equal to $4.734 A_{-1}$ where A_{-1} may be either positive or negative. However, one may attempt to evaluate the case of $(\alpha/\epsilon_1) \rightarrow 0$, i.e., for zero angle of attack, directly.

The equation to the conical surface (namely the half-cone)⁴ can be written as

$$Z_+ \equiv f(x, y) = (K^2 x^2 - y^2)^{1/2} \quad (8)$$

where $K = \tan \epsilon_1$, ϵ_1 being the semivertical angle of the semicone, and the orientation of the coordinates is the following: the x axis is parallel to the direction of the main flow, the y axis points toward the starboard, and the z axis points upward.

The proper boundary condition (of the three-dimensional flow) to be satisfied at any point on the conical surface is given by⁵

$$w - U(\partial f/\partial x) = 0$$

i.e.,

$$w/U = (\partial f/\partial x) = K^2 x/(K^2 x^2 - y^2)^{1/2} \quad (9)$$

where w is the induced velocity of the flow in the Z direction, and U is the mainstream flow in the x direction.

If Γ is the circulation around any section of the half-cone, the normal induced velocity at any point y_1 of the span is determined by the relation

$$w(y_1) = \frac{1}{4\pi} \int_{-s}^{+s} \frac{d\Gamma/dy}{y_1 - y} dy$$

where $s = Kx$ in the present case.¹ Putting $y = -s \cos \theta$ where θ varies from 0 to π across the span of the semicircle, the circulation Γ may be expressed in a Fourier's series:

$$\Gamma = 4sU \sum_1^\infty A_n \sin n\theta$$

the values of the coefficients A_n must be determined in accordance with the two equations connecting Γ and w . The normal induced velocity at the point y_1 or θ_1 of the semicircle becomes

$$w(\theta_1) = \frac{U}{\pi} \int_0^\pi \frac{\sum n A_n \cos n\theta}{(\cos \theta - \cos \theta_1)} d\theta = U \sum_1^\infty n A_n \frac{\sin n\theta_1}{\sin \theta_1}$$

and therefore,

$$\frac{w(\theta)}{U} = \sum_1^\infty u A_n \left(\frac{\sin n\theta}{\sin \theta} \right) \\ = (\partial f/\partial x) \text{ [from condition (9)]}$$

from which we find that

$$A_n(1 - \cos n\pi) = \Gamma/\pi/2$$

The lift function

$$L = \int_{-s}^{+s} \rho U \Gamma dy$$

and therefore, the lift coefficient is given by

$$C_L/\epsilon_1^2 = (\pi/0.845)(a_1/a)^2$$

where $a_1 = Kx = s$; in the present case, it is the radius of the semicircle in the physical plane, and a is the radius in the transformed plane.

Remarks

It may be remarked here in this connection that, in the Brown and Michael work,³ the condition of zero net force configuration has been satisfied in the physical plane (i.e., the delta-wing plane). The transformed plane, i.e., θ plane, has been brought in the picture to facilitate the formulation of the potential flow corresponding to the physical plane. However, in the present problem, the flow investigation has been carried out in the transformed plane because the condition of zero net force configuration of the vortex sheet and the concentrated vortex can be satisfied in the transformed plane, since, in this plane also, the flow separates from the surface, and the vortex sheet is formed from the feeding points on either side of the body. It is true that, depending upon the geometrical shape of the body in the crossflow plane, the geometrical shape of the locus of the vortex center will also change; this is being reflected in some of the analytical derivations in the transformed as well as in the physical plane. One can easily write down the analytical relations in the physical plane in the following way. In place of Eq. (1), we start with the equation

$$\left(\frac{\tau - ae^{-i\pi/6}}{\tau + ae^{2i\pi/6}} \right) = \left(\frac{Z - [3(3)^{1/2}/4]a}{Z + [3(3)^{1/2}/2]a} \right)^{2/3} \quad (10)$$

from which we put

$$\tau/a = f(Z/a) \quad (11)$$

where

$$f\left(\frac{Z}{a}\right) = \frac{(3)^{1/2}}{2} \times \frac{\{1 + [3(3)^{1/2}/4](a/Z)\}^{2/3} + \{1 - [3(3)^{1/2}/4](a/Z)\}^{2/3}}{\{1 + [3(3)^{1/2}/4](a/Z)\}^{2/3} - \{1 - [3(3)^{1/2}/4](a/Z)\}^{2/3}} \quad (12)$$

The equation corresponding to Eq. (2) can be written as

$$F(Z/a) = -iU\alpha a(f - 1/f) - i\Gamma/2\pi \log(f - f_0) - i\Gamma/2\lambda \log(f + 1/f_0) + i\Gamma/2\lambda \log(f + \bar{f}_0) + i\Gamma/2\lambda \log(f - 1/\bar{f}_0) \quad (13)$$

The lift function can be written down in the following way:

$L(x)$ = the sectional lift in the crossflow plane

$$= -\rho U Re \left[\int_C F(Z) dZ \right] = 21 \pi \rho U^2 a^2 \alpha + \rho U \Gamma a \frac{(f_0 + \bar{f}_0)(f_0 \bar{f}_0 - 1)}{f_0 \bar{f}_0}$$

or, expressing the lift coefficient C_L as defined earlier, we find that

$$C_L = 6.23 \left(\frac{\alpha}{\epsilon_1} \right) + 4.741 \frac{\Gamma}{2\pi a U \epsilon_1} \frac{(f_0 + \bar{f}_0)(f_0 \bar{f}_0 - 1)}{f_0 \bar{f}_0}$$

However, the stagnation-point consideration in the physical plane (cf., Eq. 3) leads to the following equation:

$$\frac{\Gamma/2\pi a U \epsilon_1}{(\alpha/\epsilon_1)} = \frac{(f_1 - f_0)(f_1 + \bar{f}_0)(f_0 + \bar{f}_1)(\bar{f}_1 - \bar{f}_0)}{(f_0 + \bar{f}_0)(f_0 \bar{f}_0 - 1)} \quad (14)$$

and therefore,

$$\frac{C_L}{\epsilon_1^2} = 6.23 \left(\frac{\alpha}{\epsilon_1} \right) + 4.741 \left(\frac{\alpha}{\epsilon_1} \right) \times \frac{(f_1 - f_0)(f_1 + \bar{f}_0)(f_0 + \bar{f}_1)(\bar{f}_1 - \bar{f}_0)}{f_0 \bar{f}_0} \quad (15)$$

The condition of zero net force configuration in the physical plane now becomes

$$\left[-iU\alpha a \left(1 + \frac{1}{f_0^2} \right) - \frac{i\Gamma}{2\pi} \frac{1}{[f_0 + (1/f_0)]} + \frac{i\Gamma}{2\pi} \frac{1}{f_0 - (1/f_0)} + \frac{i\Gamma}{2\pi} \frac{1}{f_0 + \bar{f}_0} \right] - \frac{i\Gamma}{4\pi} \frac{f_0''}{(f_0')^2} = U \epsilon_1 \left(2 \frac{Z_0}{a_1} - 1 \right) \frac{1}{(df/dZ)_0} \quad (16)$$

In case $f''(Z/a)$ can be neglected (which is possible only when the vortex center is very close to the feeding point) Eq. (16) becomes equivalent to Eq. (4) if we can interpret $(df/dZ)_0$ as the magnification of the scale of transformation between the physical plane and the transformed plane.

References

- 1 Durand, W. F., *Aerodynamic Theory* (Dover Publications Inc., New York, 1963), Sec. 19, p. 77, Fig. 37; Chap. EIV, Secs. 2 and 3.
- 2 Bryson, A. E., "Symmetric vortex separation on circular cylinders and cones," American Society of Mechanical Engineers, Paper 59-APM-13 (1959).
- 3 Brown, C. E. and Michael, W. H., Jr., "On the slender delta wings with leading edge separation," NACA TN 3430 (1953).
- 4 Smith, J. H. B., "The theory of a thin slender conical wing with the wing boundary condition applied at its surface," Royal Aircraft Establishment Rept. 2602 (1960).
- 5 Robinson, A. and Lauermaun, J. A., "Aerofoil theory for steady flow in three dimensions," *Wing-Theory* (Oxford University Press, Oxford, England, 1953).

Torque on a Satellite Due to Gravity Gradient and Centrifugal Force

PHILIP S. CARROLL*

The Bendix Corporation, Ann Arbor, Mich.

IN order to analyze the rotational dynamics of earth-orbiting satellites during the preliminary design of their attitude control systems, it is customary and usually necessary to determine the approximate values of gravity-gradient torques on the satellites. Very often these values are based strictly on the gradient in gravitational force across the distributed mass of the satellite. For the case of a symmetric satellite in a circular orbit, such values might typically be calculated using the expression given by Nidey.¹ When this expression [Eq. (18) of Ref. 1] is written in scalar form, the result is

$$T_g = \left(\frac{3}{2} \right) \omega_0^2 (I_s - I_t) \sin 2\beta' \quad (1)$$

where

T_g = magnitude of the instantaneous gravity-gradient torque vector, ft-lb

ω_0 = orbital revolution rate, rad/sec

I_s = moment of inertia about the axis of symmetry, slugs-ft²

I_t = transverse moment of inertia, slugs-ft²

β' = angle from the symmetry axis to local vertical (when $I_s < I_t$) or the horizontal plane (when $I_s > I_t$), rad

The torque acts about the transverse body axis that lies instantaneously in the horizontal plane, and the torque direction is such as to decrease β' . There are several examples in the literature wherein expressions equivalent to Eq. (1) are used to derive values of gravity-gradient torques.²⁻⁵ These results imply erroneously that their results give a

Received July 17, 1964.

* Supervisor, Control and Stabilization Section, Bendix Systems Division. Member AIAA.

complete indication of the torque that tends to orient a satellite axis of minimum moment of inertia along the local vertical.

Actually, there is another external torque due to the natural space environment, of the same form as Eq. (1), which also tends to orient an axis of minimum moment of inertia along local vertical. This torque is due to the gradient in centrifugal force on particles of the satellite caused by minute differences in the radial distances to the particles from the center of curvature of the orbital path. As given by Davis,⁶ the value of the centrifugal-force-gradient torque is

$$T_c = (\frac{1}{2})\omega_0^2(I_s - I_t) \sin 2\beta'' \quad (2)$$

where β'' is the angle from the symmetry axis to either the plane of the orbit (when $I_s < I_t$) or a normal to the plane of the orbit (when $I_s > I_t$) in radians. The torque acts about the transverse body axis that lies instantaneously in the orbit plane, and the torque direction is such as to decrease β'' . Some references include this torque as part of the total "gravity-gradient" torque.^{7, 8}

The vector sum of the gravity-gradient torque and the torque due to centrifugal-force gradient is a total torque vector that also tends to decrease β' and β'' . Both the magnitude and direction of the total torque vector vary as either β' or β'' varies, and the general expressions for the component magnitudes of the total torque are quite complex. Therefore, the succeeding derivations are limited to special cases and average values.

When the total torque vector is horizontal and in the orbit plane, its magnitude is

$$T_h = (\frac{4}{3})\omega_0^2(I_s - I_t) \sin 2\beta \quad (3)$$

where β is the angle from the symmetry axis to the orbit plane for either $I_s > I_t$ or $I_s < I_t$. This case occurs when the symmetry axis is in a vertical plane normal to the orbit plane, and it illustrates the direct addition of the gravity-gradient and centrifugal-force-gradient contributions. The result is the maximum possible torque for a given value of β . When the total torque vector is vertical, its magnitude is

$$T_v = (\frac{1}{2})\omega_0^2(I_s - I_t) \sin 2\beta \quad (4)$$

This occurs when the symmetry axis is horizontal, and it illustrates the case when only the centrifugal torque is effective. The result is the minimum possible torque for a given value of β . Between these two extremes, the total torque vector varies sinusoidally in magnitude as a function of symmetry-axis orientation.

To determine the average total torque value per orbit, for a fixed orientation of the symmetry axis, the two contributions are considered separately. The average gravity-gradient torque is given in Ref. 1 as

$$T_{g,av} = (\frac{3}{4})\omega_0^2(I_s - I_t) \sin 2\beta \quad (5)$$

where β' can be replaced by β because of the averaging. The instantaneous torque components normal to the orbit plane all cancel out over one orbit, and the resulting average torque vector is in the orbit plane. The average centrifugal-force-gradient torque is

$$T_{c,av} = (\frac{1}{2})\omega_0^2(I_s - I_t) \sin 2\beta \quad (6)$$

where β'' of Eq. (2) can be replaced here by β because of the averaging. The directions of the two average torque contributions of Eqs. (5) and (6) are the same, and thus they are added directly. Therefore, the average torque due to gravity gradient and centrifugal force is

$$T_{av} = (\frac{5}{4})\omega_0^2(I_s - I_t) \sin 2\beta \quad (7)$$

When $I_s < I_t$, the torque direction is such as to decrease β to zero; when $I_s > I_t$, its direction is such as to increase β to 90°. Thus, Eq. (7) represents exactly the same type of moment as Eq. (5) [Eq. (23) of Ref. 1]. However, an im-

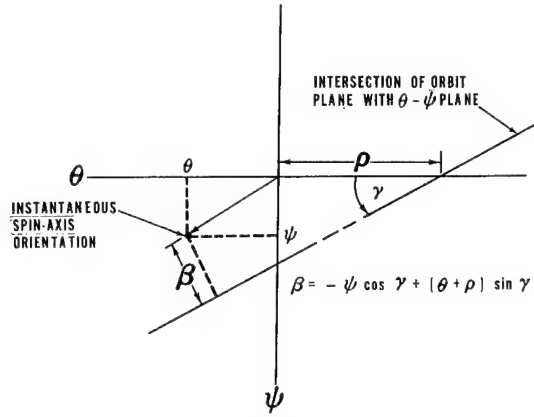


Fig. 1 Orientation of spin axis in θ - ψ plane and its angle β from orbit plane.

provement has been made by the increase in magnitude due to the centrifugal-force gradient. Therefore, Eq. (7) should be used for the determination of average "gravity-gradient" torques in preference to other expressions that do not account for the gradient in centrifugal force.

Probably the most useful application of average values of gravity-gradient and centrifugal-force-gradient torques is in the dynamic analysis of spinning satellites. Since the spin axis maintains a relatively fixed orientation in inertial space, the value of β in Eq. (7) is constant over the time period of one orbit for which the average value is taken. Therefore, if the torque of Eq. (7) can be resolved into torque components acting about the satellite body axes, the equations of motion for precession due to gravity-gradient and centrifugal force can be written.

For this purpose, it is first assumed that the spin axis does not drift far from the orbit plane, so that β is small. Thus $\sin 2\beta = 2\beta$, and Eq. (7) is linearized. Next, β is expressed in terms of the Euler angles of the spin axis from its initial orientation in inertial space. This can be done by observing the spin-axis orientation in the θ - ψ plane relative to the orbit plane. The angles θ and ψ are the Euler angles representing the deviation of the spin axis from its initial orientation. In Fig. 1 the orbit plane is shown as its intersection with the θ - ψ plane, which is normal to the initial spin axis orientation, and the angles ρ and γ represent the orbit-plane orientation. By a geometrical construction in Fig. 1, it can be shown that

$$\beta = -\psi \cos \gamma + (\theta + \rho) \sin \gamma \quad (8)$$

Thus, by substitution into Eq. (7), the total torque on a spinning satellite due to gravity-gradient and centrifugal force is given as

$$T = (\frac{5}{2})\omega_0^2(I_s - I_t)[- \psi \cos \gamma + (\theta + \rho) \sin \gamma] \quad (9)$$

The torque vector is in the orbit plane, and it can be resolved into satellite transverse body axes by a simple transformation through the rapidly changing Euler angle ϕ . Since $\phi = \omega_s t$, the body-axis torques vary sinusoidally at the spin rate. Thus,

$$T_y = -(\frac{5}{2})\omega_0^2(I_s - I_t)[- \psi \cos \gamma + (\theta + \rho) \sin \gamma] \times \sin(\gamma - \omega_s t) \quad (10)$$

$$T_z = (\frac{5}{2})\omega_0^2(I_s - I_t)[- \psi \cos \gamma + (\theta + \rho) \sin \gamma] \cos(\gamma - \omega_s t) \quad (11)$$

References

- 1 Nidey, R. A., "Gravitational torque on a satellite of arbitrary shape," *ARS J.* **30**, 203-204 (1960).
- 2 Roberson, R. E., "Gravitational torque on a satellite vehicle," *J. Franklin Inst.* **265**, 13-22 (January 1958).

³ Wiggins, L. E., "Relative magnitudes of the space-environment torques on a satellite," AIAA J. 2, 770-771 (1964).

⁴ Nesbit, R. A., "Gravity gradient torques," Aerospace Corp., A-61-1732.2-18 (May 1961).

⁵ Frick, R. H. and Garber, T. B., "General equations of motion of a satellite in a gravitational gradient field," The Rand Corp., RM-2527 (December 1959).

⁶ Davis, W. R., "Determination of a unique attitude for an earth satellite," Lockheed Aircraft Corp., LMSD 2132A (AD 264958) (1957).

⁷ Michelson, I., "Coupling effects of gravity-gradient satellite motions," ARS J. 32, 1735 (1962).

⁸ Fischell, R. E. and Mobley, F. F., "A system for passive gravity-gradient stabilization of earth satellites," The Johns Hopkins Univ., Applied Physics Lab., TG 514 (August 1963).

Modification of the Hydrazine-Nitrogen Tetroxide Ignition Delay

HAROLD G. WEISS*

Dynamic Science Corporation, South Pasadena, Calif.

BRUCE JOHNSON†

Jet Propulsion Laboratory,

California Institute of Technology, Pasadena, Calif.

AND

H. DWIGHT FISHER* AND MELVIN GERSTEIN‡

Dynamic Science Corporation, South Pasadena, Calif.

IGNITION delay measurements were made on the system hydrazine-nitrogen tetroxide, and the effect of additives on the ignition delay time was determined. The apparatus used was of the type developed by Kilpatrick and Baker,¹ but was modified as described below. Delay times were both shortened and lengthened by additives, but the majority of the compounds tested tended to shorten the ignition time.

Vapor-phase studies of the hydrazine-nitrogen tetroxide system have been reported in the literature,² and a thermal rather than free radical reaction mechanism has been proposed for the reaction. Studies of liquid phase interactions of hydrazine and nitrogen tetroxide have been concerned primarily with explosion hazards,³ hence, ignition delay times were not reported. The purpose of the experiments reported here was to determine the effect of additives on the ignition delay time for liquid nitrogen tetroxide and hydrazine. Additives were selected with the hope that a clue to the reaction mechanism could be obtained from the delay data. For example, thermal moderators, free radical traps, free radical sources, and surface active agents were used. The latter agents were used because of suspected immiscibility of the two reactants. The fact that nitrogen tetroxide and hydrazine are immiscible was subsequently proved by photographing⁴ the dropwise addition of N_2O_4 to N_2H_4 .

Apparatus and Experimental Procedures

The apparatus for the measurement of ignition delay times consisted of a reaction chamber of approximately 450-cm³ volume, two injection pistons of 0.515- and 0.466-in. diam and

0.375-in. stroke, and a driving piston that, when acted upon by compressed gas, drove the two small pistons simultaneously. The drive gas was contained in an accumulator bottle of about 1-ft³ volume at 1500 psig and was released by a quick acting solenoid valve (90% open in 2 msec).

Hydrazine was contained behind the larger of the two injection pistons; thus, all measurements were made at a volume ratio $N_2H_4/N_2O_4 = 1.22$. Valves located in the casing surrounding the small pistons facilitated refilling between runs. An overflow was incorporated into the fill system to insure the absence of gas bubbles. The propellant storage spaces were sealed from the reaction chamber by 5-mil teflon disks, which were held in place by washers and lock bolts. Each of the lock bolts was drilled with a 0.060-in hole that constituted the injection orifice. The two streams were injected at 90° to each other in a swirl chamber, resulting in tangential mixing. The reaction chamber was cleaned after each run and was flushed with nitrogen for 20 min prior to each measurement.

Delay time was measured by photographing an oscilloscope trace that recorded both light emission and pressure. The photocell pickup was located in the end of the reactor to insure the maximum view of the reaction chamber. The photocell amplifier was operated at maximum gain to insure the detection of the initial light release. The pressure sensor was mounted flush with the inner wall of the reactor and was located 3 in. from the injection ports.

In initial runs, a 1-mil teflon seal was used between propellants and reaction chamber. It was observed in these runs that light was emitted coincident with a small pressure rise and that the more rapid pressure rise conventionally associated with ignition occurred later. It was also difficult to obtain reproducible results in these experiments. This initial small pressure rise was identified as ignition by N_2O_4 vapor, which had prematurely leaked by the teflon disk and

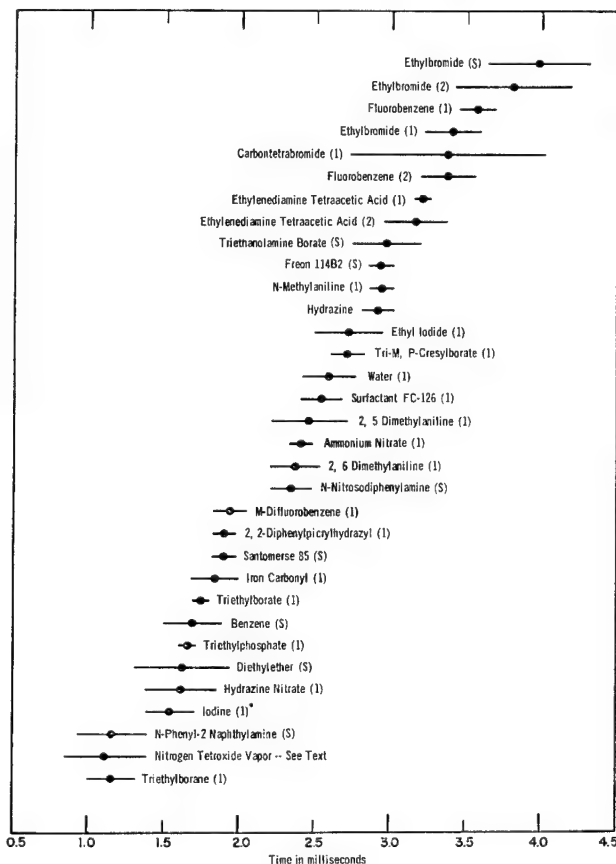


Fig. 1 Ignition delay data where an asterisk indicates that the substance is added to N_2O_4 .

Received July 20, 1964. This work was performed at the Dynamic Science Laboratories for the Jet Propulsion Laboratory, California Institute of Technology, sponsored by NASA under Contract NAS7-100. The authors wish to thank J. F. Ditter for conducting the miscibility experiments and James Herr and Harold Thomas for assisting with the ignition delay experiments.

* Senior Chemist.

† Development Engineer.

‡ President. Member AIAA.

was eliminated by substitution of the 5-mil teflon. In succeeding experiments, the light emission and sharp pressure rise occurred nearly simultaneously, the light preceding the pressure rise on the average of 0.1 msec. Since the light deflection values can be read more accurately from the phototrace, it is these values that are reported here.

Olin Mathieson technical grade anhydrous hydrazine density 1.004, which was certified by the manufacturer to contain 1.4% water and 0.005% insoluble matter, was used without further purification. Nitrogen tetroxide, having a reported minimum purity of 99.5%, was obtained from the Mathieson Company and was also used directly as supplied.

Results

A summary of the ignition delay data for the hydrazine-nitrogen tetroxide system, both with and without additives, is shown graphically in Fig. 1. The values given in Fig. 1 were obtained by normalizing on an average delay time value for hydrazine. This was necessary because slight differences in delay times were observed for pure hydrazine during the course of the experimental program when it became necessary to change to a new lot. In the graph, the dots represent the average delay times and the horizontal lines the average errors for each set of determinations. In most cases, the delay time was obtained as the average of three separate measurements. The error limits are small enough to establish that the additives are effecting real changes in the delay times. The large spread of values obtained in the runs with carbon-tetrabromide is attributed to chemical reaction with the hydrazine, since a pressure build-up in the hydrazine storage indicated a slow reaction with carbontetrabromide.

With the exception of iodine, which was added to the nitrogen tetroxide, all additives were dissolved in the hydrazine. The numbers in parenthesis in Fig. 1 indicate the concentration of additive in weight percent. In a few cases, indicated by (s) in Fig. 1, the additive was only partially soluble in the hydrazine. In these cases, 1% of additive was placed in the hydrazine, the liquid was agitated until no more additive appeared to be dissolving, and the resulting saturated hydrazine solution was then decanted from the remaining undissolved additive.

The fact that delay times were shortened with surfactant FC-126 and Santomerse 85, two surface active agents, indicates that solubility of the two reactants is a factor in the delay times. Two possible intermediates in the reaction, hydrazine nitrate and ammonium nitrate, also reduced the ignition time.

In one set of experiments the reactor was flushed with N_2O_4 instead of nitrogen, and the delay time for $N_2H_4-N_2O_4$ without additives was measured. As expected, a significant decrease in the ignition delay time was observed. These results are in agreement with those observed for the triethylamine-nitric acid reaction,⁵ where the delay times became shorter when the initial gas-phase oxidant concentration (O_2 or N_2O_4) was increased. It is reported,⁵ in fact, that shortest delay times were obtained when nitrogen tetroxide was substituted for air in the bomb reactor. Acceleration by gas-phase oxidant, coupled with the fact that most gas-phase reactions involve free radical mechanisms, makes us believe that the hydrazine-nitrogen tetroxide reaction proceeds by a free radical mechanism, although the delay reported here does not conclusively support this view.

References

- ¹ Kilpatrick, M. and Baker, L. L., Jr., *Fifth Symposium on Combustion* (Reinhold Publishing Corp., New York, 1955), Paper 11, p. 196.
- ² Skinner, G. B., Hedley, W. H., and Snyder, A. D., "Mechanism and chemical inhibition of the hydrazine-nitrogen tetroxide reaction," Monsanto Research Corp., Dayton, Ohio, Tech. Doc. Rept. Aeronautical Systems Div., TDR-62-1041 (December 1962).

³ Friedman, R., Barnes, W. P., Jr., and Markels, M., Jr., "A study of explosions induced by contact of hydrazine-type fuels with nitrogen tetroxide," Atlantic Research Corp., Alexandria, Va., Tech. Doc. Rept. Aeronautical Systems Div., TDR-62-685 (September 1962).

⁴ Weiss, H. G. and Klusmann, E. B., "Determination of miscibility characteristics of highly reactive liquids," J. Am. Chem. Soc. **84**, 4993 (1962).

⁵ Schalla, R. L. and Fletcher, E. A., *Sixth Symposium on Combustion* (Reinhold Publishing Corp., New York, 1957), Paper 123, p. 911.

Payload Scaling Laws for Boost Rockets

DONALD VAN ZELM WADSWORTH*

Bell Telephone Laboratories, Inc., Whippany, N. J.

Explanatory

FOR a given change in payload weight, we wish to determine what compensatory changes (i.e., scaling) must be made in other rocket parameters (such as thrust and initial stage weights) in order that the final burnout position, velocity, and time be unaffected. This is a problem of interest in preliminary design studies when numerical data generated for one payload are to be applied to other payloads. In this article, we determine the scaling laws that leave a boost rocket trajectory invariant to payload weight changes. These laws are different from the usual "payload exchange ratios" used in mission design where only the characteristic velocity is held invariant.

Derivation of Scaling Laws

The rocket parameters appearing explicitly in the differential equations of motion must be invariant to changes in payload weight if the trajectory is to be unaltered. The invariant parameters can be found by examining the equations of motion:

$$\mathbf{a} = (F/m)\mathbf{r} - (D/m)\mathbf{r} - \mathbf{g}$$

where \mathbf{a} is the acceleration, \mathbf{r} a unit vector parallel to the rocket's longitudinal axis, \mathbf{g} the acceleration of gravity, m the mass, F the thrust, and D the drag force. We assume thrust and drag act parallel to the longitudinal axis. We neglect lift for the present discussion, since angles of attack are small during the gravity turn. This will not affect the generality of the scaling laws. Boldface characters denote vector quantities.

The thrust¹ consists of a momentum thrust F_m and a pressure thrust F_p :

$$F_m = p_e r^{-1} a f(\gamma, r)$$

$$F_p = a(p_e - p)$$

where p_e is the design chamber pressure of the rocket motor, p_e the pressure at the exit of the nozzle, p the ambient pressure (a function of altitude), γ the ratio of the specific heats of the exhaust gases, r the ratio of the nozzle area at the exit to the area at the throat, a the cross-sectional area of the nozzle exit, and $f(\)$ denotes "function of." For scaling, we shall assume that the parameters γ , p_e , p_e , r are invariant. It turns out that vacuum specific impulse (a property of the propellant) must be an invariant, so that it is reasonable to assume γ to be invariant. The only thrust parameter to be scaled is a .

The drag force is given by

$$D = \frac{1}{2} \rho V^2 A C_D$$

Received July 20, 1964.

* Member of Technical Staff. Member AIAA.

where ρ is atmospheric density, V the speed relative to the atmosphere, A the effective cross-sectional area of the rocket, and C_D the coefficient of drag (which depends on Mach number primarily). We shall assume that C_D is invariant to scaling so that the only drag parameter to be scaled is A .

If we let μ be the ratio of the final to initial weight of a single stage rocket, t the burning time, and s the time from initiation of burning, then mass m is given by

$$m = h(t - s + \mu s)(1 - \mu)^{-1}$$

where h is the mass burning rate (assumed independent of s). Reference to the equations of motion shows that they will be invariant to payload changes if the parameters t , μ , a/h , and A/h are kept invariant (in addition to those specified previously). Under these conditions, it is evident that for any given value of p the function $Fh^{-1}g^{-1} = I =$ specific impulse will be invariant as stated previously (g is the mass-to-weight conversion factor). From the preceding definitions, we have $gh = t^{-1}W(1 - \mu)$, where W is the initial weight. Then the invariants a/h and A/h can be replaced by the invariants a/W and A/W .

For an n stage rocket, let W_L denote payload weight, w_i the initial weight of the i th stage (without any upper stages), W_i the initial weight of the i th rocket (weight of i th stage plus all upper stages and payload), I_i the specific impulse of the i th stage, σ_i the final to initial weight ratio of the i th stage, and μ_i the final to initial weight ratio of the i th rocket.

By definition,

$$\mu_i = \frac{W_{i+1} + \sigma_i w_i}{W_i} = 1 - (1 - \sigma_i) \frac{w_i}{W_i}$$

$$W_i = w_i + w_{i+1} + \dots + w_n + W_L$$

If Δ denotes a change in a quantity, we obtain from the preceding the following scaling laws:

$$(1 - \mu_i)\Delta W_i = \Delta w_i - \Delta(\sigma_i w_i)$$

$$\Delta a_i = (a_i/W_i)\Delta W_i \quad \Delta A_i = (A_i/W_i)\Delta W_i$$

$$\Delta F_i = (F_i/a_i)\Delta a_i$$

In general, the stage weight at burnout can be expressed as

$$\sigma_i w_i = \omega_{xi} + \alpha_i w_i + \beta_i F_i$$

which states that the burnout weight contains a portion ω_{xi} independent of stage weight and thrust, a portion $\alpha_i w_i$ dependent upon the stage weight (fuel tanks and structure), and a portion $\beta_i F_i$ dependent upon the thrust level (the rocket motor and pumps). Consequently, if we assume ω_{xi} , α_i , and β_i are not to be scaled, $\Delta(\sigma_i w_i) = \alpha_i \Delta w_i + \beta_i \Delta F_i$. For a wide variety of rockets, it can be assumed that $\alpha_i \approx 0.1$ and $\beta_i \approx 0.01$.

Scaling Laws for a Two-Stage Rocket

Using the preceding scaling laws and the invariance of t_i , μ_i , ω_{xi} , α_i , and β_i , we obtain for a two-stage rocket (in which one stage is in the atmosphere)

$$\Delta I_1 = \Delta I_2 = 0$$

$$\Delta F_1 = (F_1/W_1)\Delta W_1 \quad \Delta A_1 = (A_1/W_1)\Delta W_1$$

$$\Delta a_1 = (a_1/W_1)\Delta W_1$$

$$\Delta F_2 = (F_2/W_2)\Delta W_2 \quad \Delta a_2 = (a_2/W_2)\Delta W_2$$

$$\Delta W_1 = \Delta w_1 + \Delta W_2 \quad \Delta W_2 = \Delta w_2 + \Delta W_L$$

$$\Delta w_1 = \left(1 - \mu_1 + \frac{\beta_1 F_1}{W_1}\right) \left(\mu_1 - \alpha_1 - \frac{\beta_1 F_1}{W_1}\right)^{-1} \times (\Delta w_2 + \Delta W_L)$$

$$\Delta w_2 = \left(1 - \mu_2 + \frac{\beta_2 F_2}{W_2}\right) \left(\mu_2 - \alpha_2 - \frac{\beta_2 F_2}{W_2}\right)^{-1} \Delta W_L$$

Using $-\dot{w}$ to denote weight rate of propellant consumption (\dot{w} is a negative quantity), we also have

$$\Delta(-\dot{w}_1) = (1 - \mu_1)t_1^{-1}\Delta W_1$$

$$\Delta(-\dot{w}_2) = (1 - \mu_2)t_2^{-1}\Delta W_2$$

If the \dot{w}_i are the design parameters rather than the σ_i , it is convenient to calculate μ_i from $\mu_i = 1 + \dot{w}_i t_i / W_i$.

Example

The preceding scaling laws were applied to a typical two-stage ICBM using a realistic physical model of the rocket and its environment, including a rotating oblate earth with a standard atmosphere and variation of the coefficients of lift and drag with Mach number. A nominal booster power flight trajectory for a 4500-lb payload was simulated on the digital computer. Then the payload was reduced by 700 lb and the scaling laws used to determine the following changes in the booster parameters:

$\Delta F_1 = -32,750$ lb	$\Delta F_2 = -6706$ lb
$\Delta A_1 = -8.6$ ft ²	$\Delta a_1 = -334$ in. ²
$\Delta \dot{w}_1 = 131$ lb/sec	$\Delta \dot{w}_2 = 21$ lb/sec
$\Delta W_1 = -24,472$ lb	$\Delta W_2 = -4167$ lb
$\Delta w_1 = -20,304$ lb	$\Delta w_2 = -3493$ lb

With the new payload, the "scaled" booster trajectory was simulated and, as expected, was identical with the nominal trajectory. For this example we took $\mu_1 = \mu_2 = 0.26$.

Reference

¹ Koelle, H. H., *Handbook of Astronautical Engineering* (McGraw-Hill Book Co., Inc., New York, 1961), pp. 20-1-20-9.

Unsteady Flow Past Junctions in Ducts

A. G. HAMMITT* AND H. J. CARPENTER†
TRW Space Technology Laboratories,
Redondo Beach, Calif.

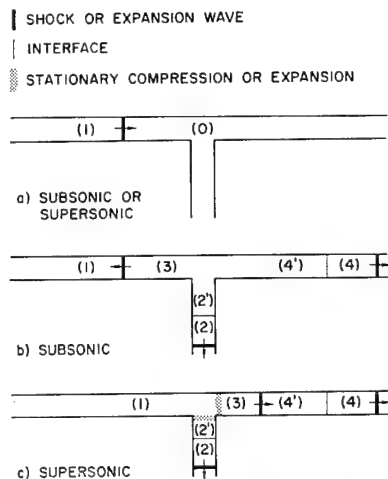
THE problem of shock waves in ducts is one that is important to bomb shelter installations that use some sort of ventilation or other piping system connecting to the atmosphere. Although these systems are relatively simple from a plumbing point of view, they are generally beyond the state of the art of standard one-dimensional flow analysis. In particular, they usually contain L and T junctions for which standard one-dimensional flow analyses are not available.

The purpose of this note is to set up the boundary conditions to be applied at such discontinuities to fit into a one-dimensional unsteady flow analysis. The detailed, non-one-dimensional flow pattern near the junction will be ignored, but the effect a few diameters away, where the flow has become one-dimensional again, will be described. The viscous and shock losses that occur near the junctions will be summed up by (over-all) loss coefficients. These loss coefficients can be obtained from steady flow data and used to predict the losses for the unsteady cases. Although the treatment of the flow at the junctions is empirical with regard to these loss coefficients, it is the best that can be expected within the framework of one-dimensional inviscid theory. A true de-

Received July 21, 1964.

* Manager, Aerosciences Laboratory Research Staff. Member AIAA.

† Member of Technical Staff. Member AIAA.

Fig. 1 Wave motion in T juncture.

scription of the flow cannot be obtained without considering both three-dimensional and viscous effects, which is beyond present technology.

To demonstrate the analysis, the case of a T juncture will be considered. Figure 1 shows the situation both before and after the shock wave reaches the T . Two cases must be considered; these are when flow velocities behind the initial shock wave are subsonic (Figs. 1a and 1b) and supersonic (Figs. 1a and 1c). In either case, there are a limited number of disturbances that can exist in the flow. In Fig. 1a, a shock wave is shown moving down the duct toward the T . There is no flow ahead of this shock (0) and subsonic flow behind (1). Figure 1b shows the situation that must exist after the flow has

passed through the T juncture. There are transmitted shocks passing down the two legs of the T with conditions (2) and (2') and (4) and (4') behind them, the primed and unprimed quantities being those on separate sides of the entropy discontinuity. There can be steady-state phenomena standing in each leg of the T at the T and a reflected wave moving upstream with condition (3) behind it.

Figure 1a is also the initial picture for the supersonic case, and Fig. 1c gives the situation after the shock has passed through the T , the difference being that the upstream propagating wave is now swept down the straight leg of the T since the velocity here is supersonic. For the case illustrated, the perpendicular leg of the T is not supersonic, and so no upstream propagating wave can be swept down it, but the case where it is supersonic could easily be considered.

In the present analysis, the steady phenomena at the juncture will have loss coefficients assigned to them. These loss coefficients will be picked from incompressible steady-state results, the only ones available, and then the predicted results checked against shock-tube experiments.

The method of solution is best illustrated on a pressure-velocity (p - u) diagram. Figures 2a and 2b show these diagrams for both subsonic and supersonic cases. These two diagrams are self-explanatory when studied with reference to Fig. 1. The loss coefficients for the flow that turns into the vertical leg has been taken as one dynamic head based on the flow velocity ahead of the T and one-half the dynamic head

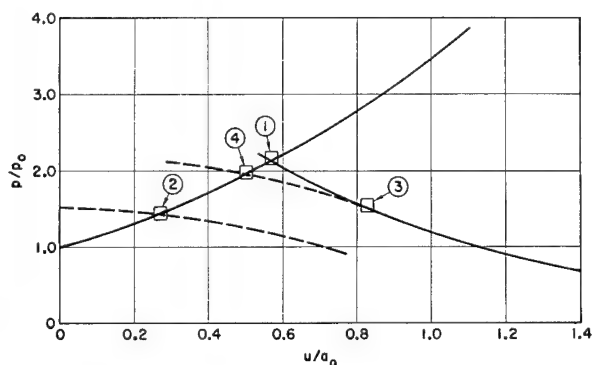


Fig. 2a Pressure-velocity curves for subsonic case.

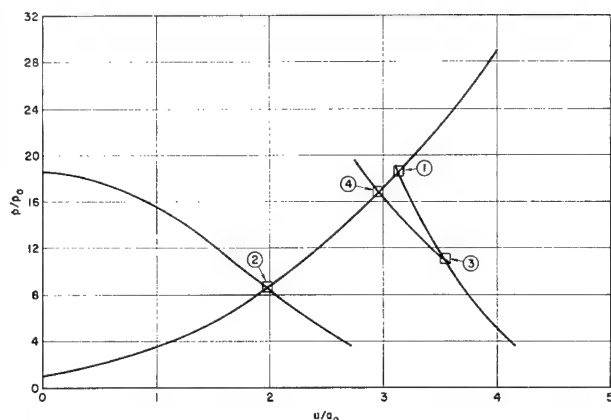
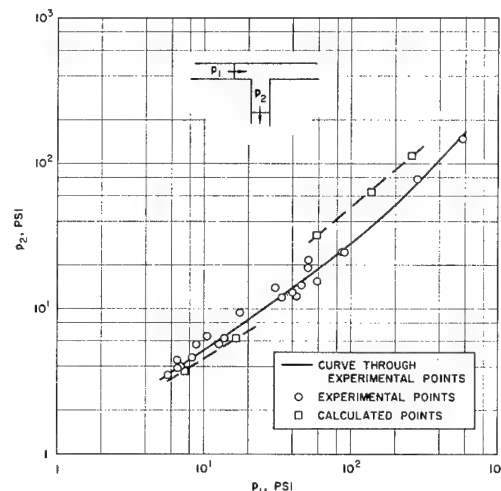
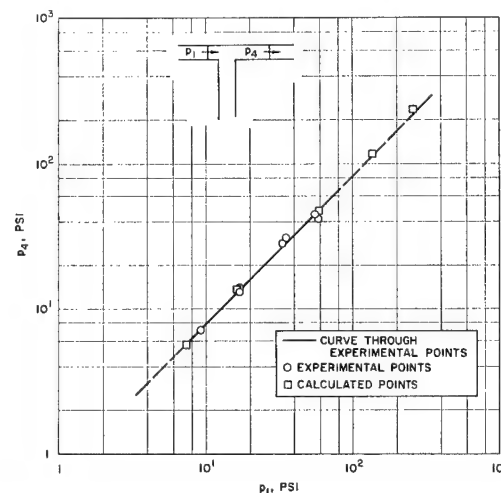


Fig. 2b Pressure-velocity curves for supersonic case.

Fig. 3a Incident vs transmitted overpressure in the perpendicular leg of T .Fig. 3b Incident vs transmitted overpressure past T .

based on the flow velocity in the vertical leg. This loss is shown on Fig. 2 by starting the p - u curve for the flow entering the vertical leg from zero velocity instead of from the actual velocity that exists and constructing the curve to show a loss of one-half the dynamic head. The losses specified in this way are consistent with the two limiting cases of no flow into the vertical leg, where static pressure should exist, and flow from zero velocity in the straight tube, where the loss based on the inflow dynamic head is taken because of the poor inlet configuration.

The solutions can now be carried out by assuming different shock strengths and then using the continuity relation at the T juncture to determine the relative area ratios appropriate to the conditions assumed. If a particular area ratio is desired, different conditions can be assumed until the required area ratio is obtained. The conditions shown correspond to equal areas in all legs of the T .

Calculations for a T configuration with equal area legs have been made for various shock strengths and the losses as assumed previously (Fig. 3). Compared with experimental measurements made in the reference, the agreement is reasonable for both subsonic and supersonic cases. Other values of the loss coefficients, particularly higher values of the loss coefficient based on the inflow dynamic head for the supersonic cases, would give better results. Measurement of these losses by steady-state experiments would be useful. For initial shock strengths that give Mach numbers near 1 ($P_s \sim 56$ psi), no solution is possible using the loss coefficients selected, indicating that they are not correct for these Mach numbers. The extension of this model to L junctures and other configurations is obvious and will not be considered here.

One use of this model is to correlate the experimental data, such as in Ref. 1, in terms of a few loss coefficients and to provide a tool for extrapolating to other values of initial shock strength. Its more important use is to provide a boundary condition at the juncture to use in unsteady flow calculations by the method of characteristics. Empirical data will probably never be available to provide the detailed information of what happens as waves of different types (such as multiple reflections due to the downstream configuration of the two legs) impinge upon the T and some analytic model such as this one is required to provide a self consistent boundary condition.

Reference

¹ "Information summary of blast patterns in tunnels and chambers," Ballistic Research Labs. Memo. Rept. 1390, 2nd ed. Defense Atomic Support Agency Rept. 1273 (March 1962).

Model Law for Parachute Opening Shock

KENNETH E. FRENCH*

Lockheed Missiles and Space Company,
Sunnyvale, Calif.

Nomenclature

- C_D = drag coefficient, dimensionless
 D_0 = canopy constructed diameter, ft
 F = net force on system, lb
 F_p = peak opening shock, lb
 f_j = functional relationship ($j = 1, 2$)
 g = acceleration of gravity, ft/sec²
 k = coefficient of proportionality, dimensionless
 l_s = parachute suspension-line length, ft
 M = mass of chute plus mass of attached load, slug

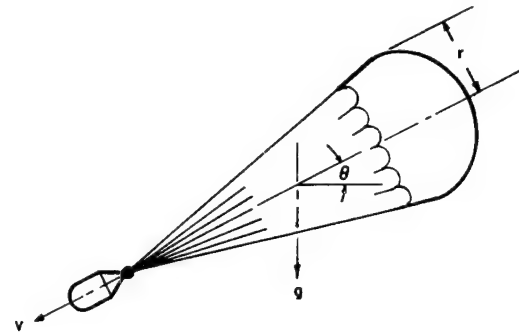


Fig. 1 Diagram of system.

- m_{air} = mass of air within and associated with inflating chute, slug
 q = instantaneous dynamic pressure, lb/ft²
 q_0 = dynamic pressure at beginning of inflation, lb/ft²
 R = maximum projected radius of fully inflated chute, ft
 r = instantaneous value for chute maximum projected radius, ft
 r_0 = chute maximum projected radius at beginning of inflation, ft
 S = πr^2 = chute reference drag area, ft²
 S_0 = $\pi D_0^2/4$ = chute reference drag area based on canopy cloth area, ft²
 v = instantaneous value of velocity, fps
 v_0 = velocity at beginning of inflation, fps
 θ = angle of inclination to the horizontal, deg or rad
 π = a pure number = 3.14...
 ρ = atmospheric mass density, slug/ft³

Introduction

PARACHUTE opening shock, the maximum force developed during inflation of a parachute, has been the subject of several theoretical investigations (for additional references on opening shock see Ref. 1, pp. 272-274). Of these, Pounder's excellent work² appears to provide the most rational and thorough analysis. In view of the date of Pounder's work (1956), it is somewhat surprising that no model law for parachute opening shock is currently regarded as acceptable.³ The lack of application of Pounder's work is apparently due to its mathematical complexity and its requirement for rather good test data on the inflation sequence for a particular type of parachute. Because of these obstacles to rapid, practical application of Pounder's theory, it is desirable to develop simple, approximate scaling laws for parachute opening shock. Such a development and its correlation with test data are the subjects of this paper.

Dimensional Analysis

Consider the problem of dynamical similarity in determining peak opening shock in the testing of a parachute. For simplicity, assume that the parachute inflates along a flight path of constant inclination and that the suspended load has

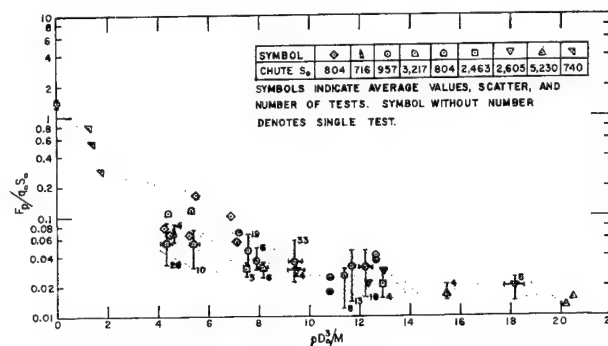


Fig. 2 Euler number vs mass ratio.

Received July 20, 1964.

* Research Specialist. Member AIAA.

Table 1 Summary of data on extended skirt-type parachutes^a

Parachute configuration				Range of test parameters ^b						
Skirt extension, %	S_0 , ft ²	l_s/D_0	N/D_0 , ft ⁻¹	Mg/S_0 , lb/ft ²	v_0 , fps	q_0 , lb/ft ²	Reynolds number, $\times 10^{-6}$	Mach number	Froude number	Number of tests
10.0	804	1.00	0.63	0.67	262	79	52	0.23	67	6
				0.42	193	42	38	0.17	36	
10.0	716	0.75	0.93	0.23	150	25	280	0.13	24	4
10.0	957	0.73	0.86	0.23	504	190	86	0.47	227	102
					185	25	31	0.17	30	
10.0	3217	0.74	0.53	0.73	231	59	89	0.20	26	6
				0.49	194	43	77	0.17	18	
12.5	804	1.00	0.75	0.71	337	127	66	0.29	110	40
			0.50	0.54	196	44	30	0.17	37	
12.5	2463	0.70	0.57	0.68	263	76	93	0.23	38	7
				0.39	228	57	80	0.20	29	
12.5	2605	0.71	0.94	0.64	336	147	119	0.32	61	12
				0.33	224	63	79	0.21	26	
14.3	5230	0.99	1.00	0.48	447	226	223	0.39	77	6
				0.35	279	87	138	0.24	30	
15.0	452	1.00	0.67	0.28	240	14	10	0.25	74	3
					180	6	5	0.19	42	

^a Data from Ref. 5, except: data for 15% extended skirt ($S_0 = 452$) parachute from Ref. 6, and data for $\rho D_0^3/M = 0$ in Fig. 2 from Ref. 1.

^b Where two numbers are given, the top denotes maximum and the bottom denotes minimum.

^c N is the number of gores in parachute canopy.

negligible drag area relative to that of the inflating chute. With the use of these assumptions and for the system shown in Fig. 1, the force-balance equation is

$$F = mg \sin \theta - \frac{1}{2} \rho v^2 C_D \pi r^2 \quad (1)$$

where

$$m = \text{total mass of system} = M + m_{\text{air}} \quad (2)$$

Following the custom of dimensional analysis,⁴ assume that the volume of air within, and associated with, the canopy may be taken as proportional to a characteristic canopy dimension cubed. This assumption gives

$$m_{\text{air}} = k \rho r^3 \quad (3)$$

And, hence

$$m = M + k \rho r^3 \quad (4)$$

Substituting Eq. (4) back into Eq. (1) and rearranging,

$$\begin{aligned} (\pi/2) \{ (\rho r^3/M) / [1 + (k \rho r^3/M)] \} (1/\frac{1}{2} \rho v^2) (1/\pi r^2) F = \\ (\sin \theta g r / v^2) - (C_D \pi / 2) \times \\ \{ (\rho r^3/M) / [1 + (k \rho r^3/M)] \} \end{aligned} \quad (5)$$

In Eq. (5), $\frac{1}{2} \rho v^2$ is the instantaneous dynamic pressure, πr^2 is the instantaneous canopy reference area, and k and C_D are characteristic of a given class or type of parachute.[†] For a given type or class of parachute, Eq. (5) therefore may be written in the form

$$F/q_0 S = f_1[(g r \sin \theta / v^2), (\rho r^3/M)] \quad (6)$$

Or, replacing the variable radius r with the constructed canopy diameter D_0 , the variable velocity v with the velocity at beginning of inflation v_0 , and the variable net force F with the peak opening shock F_p :

$$F_p/q_0 S_0 = f_2[(g D_0 \sin \theta / v_0^2), (\rho D_0^3/M)] \quad (7)$$

which is the required model law. Note that, in Eq. (7), $F_p/q_0 S_0$ and $g D_0 \sin \theta / v_0^2$ are variants of the Euler and Froude numbers,⁴ respectively, whereas $\rho D_0^3/M$ is a dimensionless "mass ratio" resulting from the analysis.

[†] As discussed later, C_D may also be a function of the Reynolds number.

Test Data

If the relationship shown in Eq. (7) is valid, it should be possible to plot $F_p/q_0 S_0$ vs $\rho D_0^3/M$ (or $g D_0 \sin \theta / v_0^2$) at $g D_0 \sin \theta / v_0^2 = \text{const}$ (or at $\rho D_0^3/M = \text{const}$) for geometrically similar parachutes and thus to determine the nature of the function f_2 . Unfortunately, however, available parachute test data are too limited both in range and adequate reporting of test conditions to permit a comprehensive coverage of the independent variables. This writer, therefore, has taken data available on extended skirt-type parachutes^{1,5,6} and plotted Euler number vs mass ratio in Fig. 2 without any consideration of the Froude-number-related variable $g D_0 \sin \theta / v_0^2$. Details on parachute configurations and the range of test variables covered by the data of Fig. 2 are shown in Table 1.

Figure 2, which covers slightly more than two decades of Euler numbers, is surprisingly well correlated in view of the facts that one of the independent variables ($g D_0 \sin \theta / v_0^2$) has been neglected and that the test data are for parachutes that, though generally similar, differ in important details (e.g., N/D_0 ratio). The data must also be viewed in the knowledge that even repeated tests of the same parachute system under the same release conditions show standard deviations in $F_p/q_0 S_0$ values of up to $\pm 26\%$.⁷

In an effort to determine the significance of the $g D_0 \sin \theta / v_0^2$ parameter, Euler number has been plotted vs Froude number at about constant mass ratio in Fig. 3 for the only parachute configuration with sufficient test data available to do this. Figure 3 shows that the test data spread of Fig. 2 is further reduced by taking into account Froude-number variations.

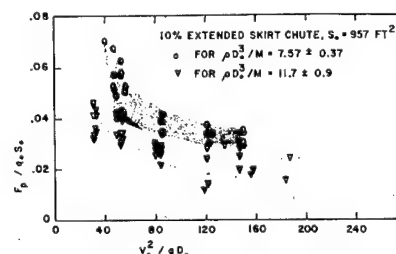


Fig. 3 Euler number vs Froude number at constant mass ratio.

Discussion

Considering that Figs. 2 and 3 are based primarily on test data that give launch speed rather than v_0 † and that offer no clue as to variations of the angle θ in the Froude-number-related parameter $gD_0 \sin\theta/v_0^2$, the data of the figures are sufficiently well correlated to indicate the general validity of the model law set forth in Eq. (7).

Since the test data used (cf. Table 1) are for cases well below Mach 1, compressibility effects do not enter into any of the scatter observed in Figs. 2 and 3. However, in the derivation of Eq. (7) it was assumed that C_D could be treated solely as a characteristic of the parachute, which may not be the case. That is, although the relatively high Reynolds numbers of Table 1 appear to justify neglect of viscous effects, the Reynolds numbers of the table are based on parachute diameter D_0 , which does not appear to be the best choice of a characteristic length for flow of air through the canopy. A better choice would be a Reynolds number based on some characteristic dimension of the canopy material, and the resulting (lower) Reynolds numbers might well be significant with respect to opening shock.

Equation (7) indicates that both $\rho D_0^3/M$ and $gD_0 \sin\theta/v_0^2$ must be held constant for dynamical similarity in free-flight testing of parachute opening shock. It is, in fact, physically possible to maintain simultaneously both of these parameters at their correct values. The model law and data presented herein also indicate that proper adjustment of the test variables may be used to test opening shock at low altitude on a parachute system intended for use at high altitude, to extrapolate opening shock test data on scale models to full scale, and to test in the earth's atmosphere parachute systems intended for use in other planetary atmospheres. However, it is obvious that more and better test data are required to verify completely any model law for incompressible flow parachute opening shock, with data particularly required at $\rho D_0^3/M$ numbers from 0 to, say, 5.

References

- 1 "Performance of and design criteria for deployable aerodynamic decelerators," Aeronautical Systems Div., ASD-TR-61-579, Wright-Patterson Air Force Base, pp. 149-164, 272-274 (December 1963).
- 2 Pounder, E., "Parachute inflation process wind tunnel study," Wright Air Development Center, TR 56-391, Wright-Patterson Air Force Base (September 1956).
- 3 Shepardson, W. P., "Progress in aerodynamic decelerator research and development," Proceedings of Retardation and Recovery Symposium, Tech. Doc. Rept. Aeronautical Systems Div. ASD-TDR-63-239, Wright-Patterson Air Force Base, pp. 6-12 (May 1963).
- 4 Bennett, C. O. and Myers, J. E., *Momentum, Heat, and Mass Transfer* (McGraw-Hill Book Co., Inc., New York, 1962), Chap. 14, pp. 147-163.
- 5 Walcott, W. B., "Study of parachute scale effects," Tech. Doc. Rept. Aeronautical Systems Div., ASD-TDR-62-1023, Wright-Patterson Air Force Base, pp. 57-62 (January 1963).
- 6 "Discoverer parachute improvement program," Lockheed Missiles and Space Co., Rept. LMSD-447720 (January 20, 1961).
- 7 Heinrich, H. G. and Scipio, L. A., "Performance characteristics of extended skirt parachutes," Wright Air Development Center TR 59-562, Wright-Patterson Air Force Base (October 1959).

† It is difficult to obtain a value for v_0 corresponding to a definite radius r_0 for the chute in an early stage of inflation, whereas it is a trivial matter to report the airspeed at which a packed parachute is launched from an aircraft or test vehicle. The result is, unfortunately, that only the launch speed is usually reported.

Capillary Stability in an Inverted Rectangular Channel for Free Surfaces with Curvature of Changing Sign

PAUL CONCUS*

University of California, Berkeley, Calif.

Nomenclature

B	= Bond number
F	= equilibrium interface
x, y	= nondimensional Cartesian coordinates
Δ	= \pm curvature
ϵ	= variational parameter
η	= perturbation to F
θ	= contact angle
λ	= undetermined parameter
ψ	= angle between tangent to F and horizontal
$()'$	= differentiation with respect to x

Introduction

IN a previous paper,¹ an investigation of the stability of an incompressible inviscid fluid contained in an inverted rectangular channel was performed mathematically with the effects of surface tension taken into account. The purpose was to determine the effect of contact angle and Bond number on the stability of such a fluid configuration in a low-gravity environment. The investigation was restricted to those fluid-gas equilibrium interfaces for which the curvature does not change sign. The analysis is extended in this report to include equilibrium interfaces for which the curvature does change sign. The omission of such interfaces in the original analysis is shown to be justified because they are all dynamically unstable. In addition, the details omitted in Ref. 1 of the calculation of the critical Bond number for equilibrium interfaces for which the curvature does not change sign are also presented.

Formulation

The differential equation for an equilibrium free surface $y = F(x)$ (see Fig. 1) is given by Eq. (3) of Ref. 1 as

$$\{F'/[(1 + F'^2)^{1/2}]\}' + BF - \lambda = 0 \quad -1 < x < 1 \quad (1)$$

The boundary conditions are given by Eq. (4) of Ref. 1 and are

$$F'(1) = -F'(-1) = \cot\theta \quad (2)$$

where θ is the contact angle between the fluid and the wall. Only values of θ for which $0 < \theta < \pi/2$ (wetting fluid) will be considered, since, as was shown in Ref. 1, the problem for $\pi/2 < \theta < \pi$ (nonwetting fluid) can be formulated in terms of an equivalent problem for $0 < \theta < \pi/2$.

Equation (1) can be solved in terms of the parameter

$$\psi = \tan^{-1}F' \quad (2a)$$

the slope of the surface, to yield

$$B(F^2/2) - \lambda F = \cos\psi - C$$

where F is now a function of ψ . The boundary conditions, Eq. (2), become $\psi = \pm(\pi/2 - \theta)$ at $x = \pm 1$, respectively. The constant of integration C may be conveniently evaluated by choosing the origin of coordinates properly. The coordinates shown in Fig. 1 of Ref. 1 were chosen so that the origin would lie on the fluid-vapor interface, halfway between the walls. It is more convenient here to choose the x axis to

Received July 21, 1964. This work was carried out mainly under the Independent Research Program of the Lockheed Missiles and Space Company and secondarily under the auspices of the U. S. Atomic Energy Commission.

* Mathematician, Lawrence Radiation Laboratory.

intersect the interface when $\psi = 0$ rather than when $x = 0$. That is, $F = 0$ when $\psi = 0$ and $x = x_0$ is not necessarily 0, see Fig. 1). The boundary conditions require that $\psi = 0$ at least once by continuity, but ψ may equal zero more than once, in which case any particular point where $\psi = 0$ and the curvature is positive (concave downward) may be singled out to define where $F = 0$. With this choice of coordinates, the constant of integration C is one, so that

$$(BF^2/2) - \lambda F = \cos \psi - 1$$

or

$$F = (\lambda \pm \Delta/B) \quad (3)$$

where

$$\Delta = [\lambda^2 + 2B(\cos \psi - 1)]^{1/2} \quad (4)$$

Substitution into Eq. (1) shows that $\mp \Delta$ is the curvature. Notice that the value of $C = 1$ is not only compatible with $F = 0$ at $\psi = 0$, but also with $F = 2\lambda/B$ at $\psi = 0$, depending on whether one takes the lower or upper sign for the square root.

The corresponding solution for x passing through $x = x_0$ when $\psi = 0$ is obtained from Eqs. (2a) and (3). It is

$$x = x_0 \mp \int_0^\psi \frac{\cos \psi \, d\psi}{\Delta} \quad (5)$$

The value of x_0 can be determined from the boundary conditions once a choice is made concerning the sign.

In Ref. 1 (as in the first reference of Ref. 1), only the solution taking the lower sign is considered, since it is the one passing through the required value $F = \psi = 0$. The solution taking the upper sign is not considered on the grounds that it does not pass through $F = \psi = 0$. The ensuing analysis in Ref. 1 then determines that $x_0 = 0$, and, on this basis, the critical Bond number is found. Notice, however, that for values of ψ equal to $\pm\psi_0$ where the curvature vanishes,

$$\psi_0 = \cos^{-1}[1 - (\lambda^2/2B)] \quad 0 \leq \psi_0 < \pi \quad (6)$$

it is possible to join continuously the two branches of the solution, one having the upper sign and the other the lower sign in Eq. (3). Since the curvature vanishes at these points, the derivatives up to the second would also join continuously. Equation (6) shows that joining can take place (for real values of ψ) only if $B \geq \lambda^2/4$. In this paper, values of $B \geq \lambda^2/4$ are considered, and equilibrium solutions made up of joined branches are allowed. The purpose is to examine the stability of such joined solutions.

Stability Analysis for Joined Interfaces

The stability of the equilibrium interfaces consisting of joined solutions can be investigated by considering the second variation in the same manner described in Ref. 1 for unjoined solutions. The second variation for trial functions of the form $y = F(x) + \epsilon \eta(x)$, where $F(x)$ is the equilibrium solution, ϵ is a parameter, and $\eta(x)$ is the perturbing function, is given by Eqs. (5) and (6) of Ref. 1. Equation (7) of Ref. 1 is the Jacobi equation, which must be satisfied by $\eta(x)$ to make the second variation vanish. It can be written in the form

$$[\eta'/(1 + F'^2)^{3/2}]' + B\eta = 0 \quad (7)$$

In the present case, care must be taken to use the appropriate signs in each of the branches of F .

No matter which sign is chosen for F and x , however, the relationship

$$dF/dx = \tan \psi \quad (8)$$

still holds, and Eq. (7) becomes

$$(d/dx)[\cos^3 \psi (d\eta/dx)] + B\eta = 0$$

upon substitution of Eq. (8).

This equation, when rewritten in terms of derivatives with respect to ψ , yields

$$\frac{(d/d\psi)[\cos^3 \psi (d\eta/d\psi)]}{(dx/d\psi)^2} - \frac{(d^2x/d\psi^2) \cdot [\cos^3 \psi (d\eta/d\psi)]}{(dx/d\psi)^3} + B\eta = 0 \quad (9)$$

Substitution of Eq. (5) into Eq. (9) shows that Eq. (9) is independent of whether the upper or lower sign is used in the solution for x . Thus, Jacobi's equation is unchanged when joined solutions, as well as nonjoined solutions, are considered. Hence, the least eigenvalue, which is the critical Bond number, is also unchanged. Therefore, the stability criterion for the critical Bond number is unaltered from that given in Ref. 1.

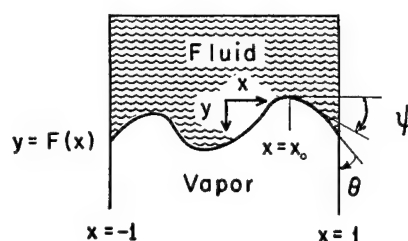


Fig. 1 Geometric configuration.

It is now shown that, for Bond numbers less than the critical one, only the simple unjoined interfaces discussed in Ref. 1 can be stable; the joined interfaces are always unstable. To do this, it is sufficient to show that for joined interfaces a conjugate point to one of the end points $x = \pm 1$ lies within the interval $-1 < x < 1$; or, in other words, if the general solution of Eq. (7) is made to satisfy nontrivially one of the boundary conditions Eq. (2) in Ref. 1 [that $d\eta/dx = 0$ at $x = -1$ or $x = +1$] then $d\eta/dx$ will also vanish for some x in this interval. Such a property makes it possible to choose a function that makes the second variation negative.

For Δ to be real, ψ must lie within the limits $-\psi_0 \leq \psi \leq \psi_0$. Thus, if F is to be an equilibrium interface satisfying the boundary conditions, Eq. (2), then $\pi/2 - \theta \leq \psi_0$. If, in addition, there is an interior joining point, then $\psi = \pm\psi_0$ for some point in $-1 < x < 1$. Then continuity in ψ requires that ψ must take on at least one of the values $-(\pi/2 - \theta)$ or $(\pi/2 - \theta)$ in the interior. That is, in order for there to be a joining point, ψ must assume one of its boundary values at least once in the interior. However, this means that a solution of Eq. (7), for which $d\eta/dx$ vanishes at a boundary point, also has $d\eta/dx$ vanish at an interior point because, by use of $d\psi/dx$ as calculated from Eq. (5), it follows that

$$(d\eta/dx) = \mp (\Delta/\cos \psi)(d\eta/d\psi)$$

a function of ψ alone. Thus, joined interfaces cannot provide an extremal solution, and hence they cannot be stable.

Conclusion

The foregoing analysis shows that equilibrium interfaces possessing a curvature that changes sign are always unstable and that the only possible stable interfaces are those with a curvature that does not change sign. Thus, the stability criteria for the critical Bond number derived in Ref. 1 by consideration of only those interfaces possessing curvature of constant sign are valid in general.

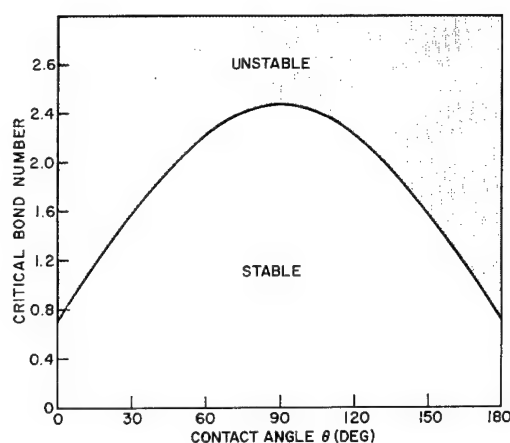


Fig. 2 Critical Bond number as a function of contact angle.

Appendix: Calculation of the Critical Bond Number for the Stability of Equilibrium Interfaces

The critical Bond number can be calculated by first finding the general solution of Eq. (9) for η as a function of ψ . Substitution of $d\psi/dx$, as calculated from Eq. (5), into Eq. (9) yields

$$\frac{d}{d\psi} \left(\cos^3 \psi \frac{d\eta}{d\psi} \right) + \sin \psi \cos^2 \psi \left(1 - B \frac{\cos \psi}{\Delta^2} \right) \frac{d\eta}{d\psi} + B \eta \frac{\cos^2 \psi}{\Delta^2} = 0$$

The general solution is

$$\eta = C \tan \psi + D[(\lambda/B\Delta) + \tan \psi \cdot I(\psi)]$$

where

$$I(\psi) = - \int_0^\psi \frac{\lambda^2 \cos \psi}{\Delta^3} d\psi$$

It is always required that $-\psi_0 \leq \psi \leq \psi_0$ in order that Δ be real. The derivative of η with respect to ψ is given by $d\eta/d\psi = \sec^2 \psi [C + DI(\psi)]$, so that the derivative with respect to x is

$$\frac{d\eta}{dx} = \frac{d\eta}{d\psi} \frac{d\psi}{dx} = \mp \Delta \sec^3 \psi \cdot [C + DI(\psi)]$$

Application of the boundary conditions at $x = \pm 1$ yields

$$\Delta_1 \sec^3 \psi_1 [C - DI(\psi_1)] = 0$$

$$\Delta_1 \sec^3 \psi_1 [C + DI(\psi_1)] = 0$$

where $\psi_1 = \pi/2 - \theta$, and Δ_1 is the value of Δ when ψ equals ψ_1 . Since for $0 < \psi_1 < \pi/2$ neither $\sec^3 \psi_1$ nor $I(\psi_1)$ can vanish, the equations can be satisfied only if $\Delta_1 = 0$, and the product $\Delta_1 I(\psi_1)$ may, in general, be nonzero so that D must also be chosen zero. The requirement that $\Delta_1 = 0$ implies that

$$\lambda^2 = 2B(1 - \cos \psi_1) = 2B(1 - \sin \theta)$$

When this relationship is used in Eq. (5) and the boundary conditions that $\psi = \pm(\pi/2 - \theta)$ at $x = \pm 1$, respectively, are applied, it follows that $x_0 = 0$, and that the critical Bond number relationship is

$$\frac{1}{2} \left\{ \int_0^{(\pi/2 - \theta)} \frac{\cos \psi d\psi}{(\cos \psi - \sin \theta)^{1/2}} \right\}^2 = B$$

which is Eq. (19) of Ref. 1. Figure 2 of Ref. 1 is reproduced here which is a graph of the foregoing relationship giving the critical Bond number as a function of contact angle.

Reference

- Concus, P., "Capillary stability in an inverted rectangular tank," *Advances in the Astronautical Sciences* (Western Periodicals Co., North Hollywood, Calif., 1963), Vol. 14, pp. 21-37.

Technical Comments

Errata: "Computer Analysis of Asymmetrical Deformation of Orthotropic Shells of Revolution"

GERALD A. COHEN*

Philco Corporation, Newport Beach, Calif.

[AIAA J. 2, 932-934 (1964)]

IN the above article replace 1) $C_1^{(1)}$ by $C_1^{(2)}$ in the third equation of Eqs. (1); 2) R by R_2 in the first equation of Eqs. (5); 3) Z_{10}^{-1} by Z_{11}^{-1} in the first and second equations of Eqs. (17); and 4) Ω_i by Ω_i in the fourth equation of Eqs. (17).

Received June 1, 1964.

* Staff Member, Aeronutronic Division. Member AIAA.

Comment on Non-Newtonian Flow

B. STEVERDING*

U. S. Army Missile Command, Redstone Arsenal, Ala.

ABLATION materials of greatest practical interest, organic and inorganic glasses, have a strong tendency to non-Newtonian flow behavior. The occurrence of gas bubbles, caused by boiling, degassing, or decomposition of the substrate promotes also non-Newtonian flow properties. Non-Newtonian behavior is related to flow-induced structural changes within the liquid, caused by the orientation or degree of entanglement of very large molecules. In Ref. 1 the Ostwald-de Waele power-law was chosen:

$$\tau = a(du/dy)^n \quad (1)$$

to describe the non-Newtonian properties of the fluid. This law is valid for isothermal conditions, but it is a fact that the zero shear viscosity of practically all substances with non-Newtonian flow behavior is a strong function of the temperature. In all cases where temperature gradients occur throughout the liquid layer, as in ablation, the Ostwald-de Waele power-law will give wrong results. In order to treat the problem of non-Newtonian, nonisothermal flow of liquids, the laws of the temperature and shear rate dependency of liquids must be combined, and the boundary-layer equations must be integrated with this expression for the viscosity. The generally accepted relationship for the temperature dependency of the viscosity is

$$\mu = \exp(A/T - B) \quad (2)$$

This dependency is also true for non-Newtonian liquids as long as the zero shear viscosity is under consideration. The zero shear viscosity will, in the following, be expressed by μ . Eyring² and Bueche³ developed expressions for the shear dependency of non-Newtonian liquids. For not too large deviations from Newtonian flow, they arrive at the following equation:

$$1/\mu_\tau = (1/\mu)(1 + k\tau^2) \quad (3)$$

where μ_τ is the viscosity at the shear stress τ , and k is a constant, determining the degree of deviation from Newtonian flow properties. If k is negative, the fluid is rheopex, and with a positive k the fluid is thixotropic. By writing Eq. (2) in the form

$$\mu/\mu_i = (T/T_i)^{-n} \quad (4)$$

where μ_i is the zero shear viscosity at interface temperature and the power factor for n is defined by $n = A/T$, the expression for the shear and temperature dependencies of the viscosity can be combined to the following expression, which may be handled easily in the subsequent integration process:

$$\frac{1}{\mu_\tau} = \frac{1}{\mu_i} \left(\frac{T}{T_i} \right)^n (1 + k\tau^2) \quad (5)$$

By neglecting the inertia terms, which is always justified for non-Newtonian liquids, the liquid-layer equations near the stagnation point have the form

$$(\partial/\partial x)(ru) + (\partial/\partial y)(rv) = 0 \quad (6a)$$

$$\frac{\partial p}{\partial x} = \frac{\partial}{\partial y} \left\{ \mu_i \left(\frac{T}{T_i} \right)^{-n} \frac{1}{1 + k\tau^2} \frac{\partial u}{\partial y} \right\} \quad (6b)$$

$$u \frac{\partial T}{\partial x} + v \frac{\partial T}{\partial y} = \alpha \frac{\partial^2 T}{\partial y^2} \quad (6c)$$

The only deviation from the well familiar liquid-layer equations appears in Eq. (6b) where the viscosity coefficient is replaced by a viscosity function $\mu(\tau, T)$. The integration of Eqs. (6a-6c) for the vicinity of the stagnation point, where not only the shear stress but also the pressure gradient contribute to non-Newtonian behavior, is straightforward and leads to the following result:

$$\mu_i v_w^4 (v_w - v_i) = \frac{2a\alpha^2}{n^2} v_w^2 - \frac{4b\alpha^3}{n^3} v_w + x^2 k \left\{ \frac{4a^3\alpha^2}{n^2} v_w^2 - \frac{24a^2b\alpha^3}{n^3} v_w + \frac{72ab^2\alpha^4}{n^4} \right\} \quad (7)$$

v_w is the total ablation velocity, v_i the ablation velocity by evaporation, $a = \partial\tau/\partial\dot{\gamma}$, $b = \partial^2\tau/\partial\dot{\gamma}^2$, and α is the thermal diffusivity of liquid. For $k = 0$ the result is equivalent to that obtained by Bethe and Adams.⁴ Equation (7) shows that for $x = 0$, that is, at the stagnation point, there is no modification of the flow by non-Newtonian behavior, but deviations increase with x^2 in the vicinity of the stagnation point. The value for k changes over several orders of magnitude for various substances from zero to 10^{-2} . In order to treat the ablation behavior of non-Newtonian liquids, the heat-transfer conditions have to be known in addition to Eq. (7). In case the flow of liquids containing gas bubbles has to be treated, k does not, of course, express structural changes within the liquid, but an experimentally determined proforma value for k may be used.

More comprehensive calculations about the ablation of non-Newtonian liquids are now being carried out and will be reported.

References

- Wells, C. S., "Unsteady boundary-layer flow of a non-Newtonian fluid on a flat plate," AIAA J. 2, 951-952 (1964).
- Eyring, H., "Viscosity, plasticity, and diffusion as examples of absolute reaction rates," J. Chem. Phys. 4, 283 (1936).

Received June 12, 1964.

* Scientific Advisor, Physical Sciences Laboratory; also Instructor at the University of Alabama, Huntsville, Ala. Member AIAA.

³ Bueche, J., "Influence of rate of shear on the apparent viscosity of A-dilute polymer solutions, and B-bulk polymers," J. Chem. Phys. **22**, 1570 (1954).

⁴ Bethe, H. A. and Adams, M. C., "A theory for the ablation of glassy materials," Avco Research Rept. 38 (November 1958).

Reply by Author to B. Steverding

C. SINCLAIR WELLS JR.*

Ling-Temco-Vought, Inc., Dallas, Texas

THE author is grateful for the opportunity to exchange views on the flow of non-Newtonian fluids with B. Steverding. The paper¹ to which the preceding comments refer contains the solution to a simple problem of two-dimensional, unsteady, isothermal, purely viscous, non-Newtonian boundary-layer flow. The solution was found through a technique for establishing the conditions for similarity (velocity profiles that transform linearly in y). The situation that Steverding is investigating is very interesting and is basically a different problem since the flow is nonisothermal and steady.

The interesting comparison between the two analyses, as the comment points out, is that of the different expressions used to describe the non-Newtonian effect of shear rate. There is, of course, no need to defend the use of the Ostwald-de Waele (power-law) expression, which is phenomenological in nature, as opposed to the Eyring-Bueche expression, which is based on macromolecular considerations. The lack of a theoretical basis for the power-law is conceded initially, and the justification for its use is only in its form, which allows it to be solved explicitly for shear rate. It would seem that the primary consideration in choosing a formulation of the viscous properties for a boundary-layer problem is the accuracy of the formulation in describing the shear rate dependence over the applicable range of flow conditions. In other words, any formulation that describes the measured fluid properties with a prescribed accuracy (and satisfies the mathematical conditions) is appropriate for use in solving a fluid mechanics problem.

As for the temperature dependence of the viscous properties, it is not obvious to the author that the power-law will give wrong results per se for nonisothermal flow, since the coefficient and exponent could be experimentally determined as a function of temperature. The formulations given by Steverding for the temperature-dependence would be particularly interesting, however, if the constants could be predicted theoretically for non-Newtonian fluids, or if the number of empirically determined constants could be reduced.

One question concerning the comment may be worth mentioning for the sake of non-Newtonian fluid nomenclature. The Eyring-Bueche expression is said to provide for rheopectic or thixotropic behavior of viscosity. Thixotropy (or rheopecty) is generally used to describe time-dependent flow effects.^{2, 3} Neither the power-law nor the Eyring-Bueche expressions provide for time-dependence. Rather, it appears that (for $k\tau^2 < 1$) the sign of k determines whether the fluid is shear thinning or shear thickening.

It may be of interest to note that the two-dimensional stagnation boundary layer of a power-law non-Newtonian fluid under conditions of steady isothermal flow (considering the convective terms, but not the inertia terms) does give similar solutions.⁴ The boundary-layer thickness δ is given by

$$\delta = \eta_0 \left[\frac{(n+1)(\bar{x})^{n-1}}{2 R_{0n} \alpha^2 - n} \right]^{1/(n+1)}$$

where the symbols are those defined in Ref. 1. δ is seen to be directly proportional to $(\bar{x})^{(n-1)/(n+1)}$ and inversely proportional to $R_{0n}^{1/(n+1)}$. This is compared with δ for stagnation flow of a Newtonian fluid which is not a function of x and is inversely proportional to $R_{0n}^{1/2}$.

References

- ¹ Wells, C. S., "Unsteady boundary-layer flow of a non-Newtonian fluid on a flat plate," AIAA J., **2**, 951-952 (1964).
- ² Van Wazer, J. R., Lyons, J. W., Kim, K. W., and Colwell, R. E., *Viscosity and Flow Measurement* (Interscience Publishers, New York, 1963), pp. 12-22.
- ³ Hahn, J. H., Ree, T., and Eyring, H., "Flow mechanism of thixotropic substances," Ind. Eng. Chem. **51**, 856 (1959).
- ⁴ Wells, C. S., "Similar solutions of the boundary layer equations for purely viscous non-Newtonian fluids," NASA TN-D-2262 (1964).

Comment on "Conical Shock-Wave Angle"

MARY F. ROMIG*

The Rand Corporation, Santa Monica, Calif.

SEVERAL approximation formulas for conical shock-wave angles have recently appeared in this Journal.^{1, 2} It is the purpose of this note to point out two other equations, both based on the hypersonic similarity rule, which are useful at high values of the hypersonic similarity parameter $M_1 \sin \theta_*$.

Linnell and Bailey³ first applied the hypersonic similarity law to the Kopal tables⁴ and obtained the following formula for the shock-wave half angle θ_w :

$$M_1 \sin \theta_w = 1 - \cos \theta_* + \{1 + [(\gamma + 1)/2] M_1^2 \sin^2 \theta_*\}^{1/2} \quad (1)$$

where M_1 is the freestream Mach number, θ_* the cone semi-vertex angle, and γ the ratio of specific heats. For $M_1 \geq 6$ and $\theta_* < 50^\circ$, Eq. (1) agrees to within 5% with the data of Ref. 4. Notice that, for large values of M_1 and small values of $\cos \theta_*$, Eq. (1) approaches Eq. (2) of Ref. 1. However, under these conditions, say for $M_1 \lesssim 10$ and $\theta_* \lesssim 40^\circ$, the air behind the shock-wave will become dissociated and these equations will no longer describe the shock geometry correctly. Instead, a second approximation equation derived from the numerical solutions of Ref. 5 can be used.

When the conical flow solutions of Ref. 5 for dissociated air were obtained, it was pleasantly surprising to find that the results correlated extremely well with the hypersonic similarity parameter $M_1 \sin \theta_*$, even more so than for the case of a perfect gas. As a result, the following estimation formula has been useful in predicting values for the shock-wave angle for cases when the air behind the shock is expected to be in dissociation equilibrium and where tabulated values are not available:

$$M_1 \sin \theta_w = (0.39 - 0.01 \log p_1) + (1.03 + 0.005 \log p_1) M_1 \sin \theta_* \quad (2)$$

where p_1 is the ambient pressure in atmospheres.

Equation (2) agrees with the exact numerical calculations of Ref. 5 to within $\pm 1\%$, for $M_1 \sin \theta_* \geq 6$.

Received July 27, 1964. Any views expressed in this comment are those of the author. They should not be interpreted as reflecting the views of The Rand Corporation or the official opinion or policy of any of its governmental or private research sponsors.

* Physical Scientist, Aero-Astronautics Department. Associate Fellow Member AIAA.

Received July 16, 1964.

* Research Scientist, LTV Research Center. Member AIAA.

References

- ¹ Hord, R. A., "Conical shock-wave angle," *AIAA J.* **2**, 1359-1360 (1964).
- ² Zumwalt, G. W. and Tang, H. H., "Mach number independence of conical shock pressure coefficient," *AIAA J.* **1**, 2389-2391 (1963).
- ³ Linnell, R. D. and Bailey, J. Z., "Similarity-rule estimation methods for cones and parabolic noses," *J. Aeronaut. Sci.* **23**, 796-797 (1956).
- ⁴ Kopal, Z. (director), "Tables of supersonic flow around cones," TR 1, Staff of the Computing Section, Center of Analysis, Massachusetts Institute of Technology (1947).
- ⁵ Romig, M. F., "Application of the hypersonic similarity rule to conical flow of dissociated air," *Aero/Space Eng.* **18**, 56-59, 75 (1959).

Comments on "Iterative and Power Series Solutions for the Large Deflection of an Annular Membrane"

JAMES G. SIMMONDS*

Massachusetts Institute of Technology, Cambridge, Mass.

Introduction

IN a recent technical note,¹ Pifko and Goldberg applied the Föppl-Hencky large deflection membrane equations to a uniformly loaded annular membrane, fixed at the outer boundary and supported at the inner boundary, and reduced the governing equations to the following nonlinear differential equation and boundary conditions:

$$f^2(d^2f/d\xi^2) = -\frac{1}{32}(\lambda^2 - \xi)^2 \quad (1)$$

$$2df/d\xi - (1 + \nu)f = 0 \text{ at } \xi = 1 \quad (2)$$

$$f = 0 \text{ at } \xi = \lambda^2 \quad (3)$$

where f is a nondimensional stress function defined in Ref. 1, $\xi^{1/2}$ the nondimensional radial distance, λ the nondimensional inner boundary radius, and ν is Poisson's ratio.

These authors constructed a power series solution of Eq. (1) about the point $\xi = \lambda^2$, satisfying Eq. (3), of the form

$$f(\xi) = (a_1^4/4)[1 - \Phi - \frac{2}{3}\Phi^2 - \frac{1}{18}\Phi^3 - \frac{1}{18}\Phi^4 - \frac{3}{27}\Phi^4 - \frac{1}{567}\Phi^5 \dots] \quad (4)$$

where

$$\Phi = (\xi - \lambda^2)/a_1^3 \quad (5)$$

They also provided a table of values of a_1 for various values of λ for $\nu = 0.3$ which make Eq. (4) satisfy Eq. (2).

The purpose of this note is first to point out that Eqs. (1-5) are a limiting form of a set of equations obtained by the writer in Ref. 2 and that the series in brackets in Eq. (4), including one additional term, can be readily obtained from Eqs. (29) and (31) of Ref. 2, and second to show how, by a simple calculation, a table of a_1 vs λ for any value of ν may be constructed from Table 1 of Ref. 1.

Derivation of Results

We first note that the series in brackets must be a universal function since its coefficients are independent of the parameters λ and ν , which enter into the boundary conditions given by Eqs. (2) and (3). Indeed, if we take Φ as a new independent variable,

$$g = (4/a_1^4)f \quad (6)$$

as a new dependent variable, and set

$$a_1 = 4df/d\xi \text{ at } \xi = \lambda^2 \quad (7)$$

then Eqs. (1-3) go over into the following parameter-free initial value problem:

$$g^2(d^2g/d\Phi^2) + 2\Phi^2 = 0 \quad (8)$$

$$g = 0, dg/d\Phi = 1 \text{ at } \Phi = 0 \quad (9)$$

Equation (2) now reads

$$dg/d\Phi - 2a_1^3(1 + \nu)g = 0 \text{ at } \Phi = (1 - \lambda^2)/a_1^3 \quad (10)$$

and the method by which this equation is to be satisfied will be discussed presently.

In Ref. 2, the equations governing the large deflections of a normally loaded, spinning, elastic membrane were reduced to the following differential equation and initial conditions:

$$y^2(d^2y/dx^2) + kx^2 + 2y^2 = 0 \quad (11)$$

$$y = 0, dy/dx = 1 \text{ at } x = 0 \quad (12)$$

If the following change of variable is introduced,

$$x = 2\Phi/k \quad y = 2g/k \quad (13)$$

then Eqs. (11) and (12) read

$$g^2(d^2g/d\Phi^2) + 2\Phi^2 + (4/k)g^2 = 0 \quad (14)$$

$$g = 0, dg/d\Phi = 1 \text{ at } \Phi = 0 \quad (15)$$

In the limit as $k \rightarrow \infty$, Eqs. (14) and (15) become identical to Eqs. (8) and (9).

A power series solution of Eq. (11), subject to Eqs. (12), is given by Eqs. (27, 29, and 30) of Ref. 2, where the first seven coefficients of this series are explicitly calculated. If the transformations given by Eqs. (13) are introduced into this power series solution and the limit taken as $k \rightarrow \infty$, we obtain terms identical to those in brackets in Eq. (4) plus the one additional explicit term

$$-(219241/63504)\Phi^7 \quad (16)$$

Returning to Eq. (10), we must, in order to satisfy this equation, pick an arbitrary value of Φ , say Φ_0 , calculate the corresponding value of $(dg/d\Phi)_0$ and g_0 , solve for the value of a_1^3 for which Eq. (10) is satisfied, and then see what λ turns out to be from the condition

$$\Phi_0 = (1 - \lambda^2)/a_1^3 \quad (17)$$

The foregoing analysis indicates how a table of a_1 vs λ for any value of Poisson's ratio ν may be constructed once a table for a particular value of ν has been constructed. Specifically, if we let λ and a_1 correspond to $\nu = 0.3$ and Λ and A_1 correspond to arbitrary values of ν , then for any value of Φ_0 , the following two relations must hold:

$$1.3a_1^3 = (1 + \nu)A_1^3(1 - \lambda^2)/a_1^3 = (1 - \Lambda^2)/A_1^3 \quad (18)$$

or

$$A_1 = \left(\frac{1.3}{1 + \nu} \right)^{1/3} a_1, \quad \Lambda = \left[1 - \frac{1.3}{1 + \nu}(1 - \lambda^2) \right]^{1/2} \quad (19)$$

From Eqs. (19), a table of A_1 vs Λ for any ν can be constructed with a_1 vs λ given by Table 1 of Ref. 1.

References

- ¹ Pifko, A. B. and Goldberg, M. A., "Iterative and power series solutions for the large deflection of an annular membrane," *AIAA J.* **2**, 1340-1342 (1964).
- ² Simmonds, J. G., "The finite deflection of a normally loaded, spinning elastic membrane," *J. Aerospace Sci.* **29**, 1180-1189 (1962).

Received August 5, 1964.

* Research Assistant, Department of Mathematics.

Reply by Authors to J. G. Simmonds

ALLAN B. PIFKO* AND MARTIN A. GOLDBERG†
*Grumman Aircraft Engineering Corporation,
 Bethpage, N. Y.*

ADDITIONAL evidence of the accuracy and convergence associated with a recently developed iterative technique^{1,2} was presented in Ref. 3. This was accomplished by comparing the iterative solution for a uniformly loaded annular membrane, fixed at the outer boundary and free of tractions and support at the inner boundary with a power series solution.

In the preceding comment Simmonds draws attention to that portion of the paper dealing with the power series solution. The alternate procedure employed by Simmonds leads precisely to the solution obtained by the authors. Indeed, making use of the transformation

$$\Phi = (1 - \lambda^2)/a_1^3 \quad (1)$$

$$\eta = 2 - (1 + \nu)(1 - \lambda^2)$$

in the controlling algebraic equation for a_1 , λ , and ν [Eqs.

(24b), Ref. 4] leads directly to the relations

$$1.3a_1^3 = (1 + \nu)A_1^3 \quad (2)$$

$$(1 - \lambda^2)/a_1^3 = (1 - \Lambda^2)/A_1^3$$

given by Simmonds. Conversely, the governing equation for Φ [Eq. (10) of the preceding comment] can be recast to permit a direct solution for a priori specified values of ν and λ .

Invariant relations such as Eqs. (2) increase the usefulness of the available numerical results with a minimal amount of additional calculations. However, Simmonds remarks are somewhat optimistic. The results presented in Table 1 of Ref. 3 are insufficient to provide a complete spectrum of coefficients. To take full advantage of the invariant relations requires a complete table of results based on $\nu = 0.5$. Therefore, to augment the results given in Ref. 3, a more complete Table 1 (for $\nu = 0.5$) is given. The necessary equations to be used in conjunction with this table are

$$\Lambda = \left[1 - \frac{1.5}{1 + \nu} (1 - \lambda^2) \right]^{1/2} \quad (3)$$

$$A_1 = \left(\frac{1.5}{1 + \nu} \right)^{1/3} a_1$$

which replace Eqs. (19) of the preceding note.

Table 1 Coefficients a_1 for $\nu = 0.5$ and various values of λ

λ	a_1	λ	a_1
0	1.845	0.36	1.649
0.01	1.845	0.37	1.639
0.02	1.844	0.38	1.630
0.03	1.844	0.39	1.620
0.04	1.842	0.40	1.610
0.05	1.841	0.41	1.600
0.06	1.839	0.42	1.590
0.07	1.836	0.43	1.580
0.08	1.834	0.44	1.570
0.09	1.831	0.45	1.559
0.10	1.827	0.46	1.548
0.11	1.824	0.47	1.538
0.12	1.820	0.48	1.527
0.13	1.816	0.49	1.516
0.14	1.811	0.50	1.505
0.15	1.806	0.51	1.494
0.16	1.801	0.52	1.483
0.17	1.795	0.53	1.471
0.18	1.790	0.54	1.460
0.19	1.784	0.55	1.448
0.20	1.777	0.56	1.436
0.21	1.771	0.57	1.424
0.22	1.764	0.58	1.412
0.23	1.757	0.59	1.400
0.24	1.750	0.60	1.388
0.25	1.743	0.61	1.375
0.26	1.735	0.62	1.362
0.27	1.727	0.63	1.350
0.28	1.719	0.64	1.336
0.29	1.711	0.65	1.323
0.30	1.703	0.66	1.310
0.31	1.694	0.67	1.296
0.32	1.685	0.68	1.282
0.33	1.676	0.69	1.268
0.34	1.667	0.70	1.254
0.35	1.658		

References

- Goldberg, M. A., "A modified large deflection theory of plates," *Proceedings of the Fourth U. S. National Congress of Applied Mechanics* (American Society of Mechanical Engineers, New York, 1962), pp. 611-618.
- Goldberg, M. A. and Pifko, A. B., "Large deflection analysis of uniformly loaded annular membranes," *AIAA J.* **1**, 2111-2115 (1963).
- Pifko, A. B. and Goldberg, M. A., "Iterative and power series solutions for the large deflection of an annular membrane," *AIAA J.* **2**, 1340-1342 (July 1964).
- Pifko, A. B. and Goldberg, M. A., "Comments on an iteration procedure for the large deflection analysis of initially flat membranes," Grumman Research Dept. Publ. RM-232 (June 1964).

Distribution of Nearly Circular Orbits

DAVID A. CONRAD*

Hughes Aircraft Company, El Segundo, Calif.

1. Introduction

IN a recent paper¹ the theory of errors was employed to assess the precision of a guidance system designed to place a payload in a prescribed circular orbit. The essence of the analysis consists in determining the distribution of the square of the orbital eccentricity

$$e^2 = f(\beta, r, v) = \sin^2 \beta + [(rv/gR^2) - 1]^2 \cos^2 \beta \quad (1)$$

based on assumed normal distributions of the orbital parameters β , r , v at burnout. The distance r is measured from the center of the earth, v is the velocity, β is the heading angle measured outward from the normal to the radius vector, and g and R are the gravitational constant and earth radius.

In the referenced paper, the solution is obtained, approximately, first in terms of the gamma distribution and then,

Received June 24, 1964.

* Senior Staff Engineer, Surveyor System Analysis Laboratory, Space Systems Division. Member AIAA.

Received September 17, 1964.

* Research Engineer, Research Department. Associate Member AIAA.

† Formerly Head of Applied Mechanics, Research Department; now Associate Professor, Aerospace Engineering and Applied Mechanics Department, Polytechnic Institute of Brooklyn, Brooklyn, N. Y.

even more approximately, in terms of the normal distribution. It is the purpose of this comment to point out that Monte-Carlo methods can be easily used to compute directly the distribution to any desired degree of accuracy. The advantage of such an approach is in requiring a minimum of statistical theory to produce a precise result in an extremely short time.

2. Error Sources

As in the reference, it will be assumed that the parameters β, r, v are normally distributed with covariance matrix Σ . This matrix is obtained by a straightforward linear transformation of the covariance matrix of the fundamental error sources. Although it is convenient if this matrix is diagonal (independent error sources), this is by no means essential.

In the Monte-Carlo procedure it is necessary to generate (on a digital computer) random samples of β, r, v according to the desired normal distribution. This can be done either by generating a random vector of the fundamental error sources (possibly correlated) and then applying the linear transformation, or by directly generating the correlated samples of β, r, v . In both cases it is necessary to generate samples of correlated, normally distributed random variables.

3. Generation of Samples of Correlated Gaussian Variables†

There are well established computer methods for the generation of a vector x of independent Gaussian variables with zero mean and unit variance. It is desired to obtain the vector y with covariance matrix Σ_y by a linear transformation C on x :

$$y = Cx + \bar{y} \quad (2)$$

where \bar{y} is the mean of y and

$$\Sigma_y = E[(y - \bar{y})(y - \bar{y})^T] = CC^T \quad (3)$$

where T indicates the transpose. If C is chosen as a lower triangular matrix, the elements c_{ij} ($j \leq i$) may be computed sequentially from the relations

$$\sum_{k=1}^j c_{ik}c_{jk} = \sigma_{ij} \quad k \leq j \leq i \quad (4)$$

for $j = 1$, Eqs. (4) have only one term yielding

$$c_{11} = \sigma_{11}^{1/2} \quad c_{k1} = \sigma_{k1}/c_{11} \quad (5)$$

For $j = 2$, there are two terms, but only one new unknown element is involved. Hence,

$$c_{22} = (\sigma_{22} - c_{21}^2)^{1/2} \quad c_{k2} = (\sigma_{k2} - c_{k1}c_{21})/c_{22} \quad (6)$$

The pattern continues for higher j , with only one new element appearing in each equation.

With the elements of C known, the correlated components of the random vector y are computed directly in terms of the independent components of x from (2).

4. The Monte-Carlo Simulation

The calculation, then, consists in generating samples of the normally distributed independent components of x (in this case a three-vector), computing the components β, r, v of y from (2), and then computing e^2 from (1).

The time required for such a computation on an IBM 7090 would be less than 1 min for 10,000 runs, including the sorting of the results necessary to produce the complete distribution. An experienced programmer should be able to write and check out such a program in about one week.

In comparison, the method proposed by Beckwith¹ requires the computation of the eigenvalues of a large ($n = 20$ to 30) matrix, or else the assumption that e^2 is normal. In

both cases the accuracy of the approximations is difficult to evaluate and requires considerably more statistical sophistication than the direct approach afforded by the Monte-Carlo method.

It should be noted that Skidmore and Braham² have presented an alternate approach to the same problem, namely numerical integration of the trivariate Gaussian distribution of β, r, v over the region in β, r, v space bounded by a particular value of e^2 . This procedure is not difficult to apply in the event that a multivariate Gaussian integration program is available. This latter reference also contains a relatively complete description of the general problem of statistical analysis of satellite trajectories

References

- ¹ Beckwith, R. E., "Approximate distribution of nearly circular orbits," AIAA J. 2, 913-916 (1964).
- ² Braham, H. S. and Skidmore, L. J., "Guidance error analysis of satellite trajectories," J. Aerospace Sci. 29, 1091-1101 (1962).

Reply by Author to D. A. Conrad

R. E. BECKWITH*

University of Southern California, Los Angeles, Calif.

1. Introduction

THE preceding comment advocates the superiority of Monte Carlo methods over the methods presented in Ref. 1 for answering certain questions pertaining to the precision of "nearly circular" orbits. Without agreeing or disagreeing with D. A. Conrad, the present note seeks to place the issue in clearer perspective.

2. Monte Carlo Method

A rich, if diffuse, literature exists in *model sampling* or *Monte Carlo method*, as the technique is now more popularly known. Principal applications have been made in the areas of nuclear studies, logistics, heuristic problem solving, and evaluation of complicated integrals. Whether the original problem is deterministic or stochastic, the Monte Carlo method consists of building and "playing" an appropriate game of chance in which stochastic convergence of relevant sample statistics to basic system parameters is assured under very general conditions by the strong law of large numbers and the central limit theorem and in which distribution laws of arbitrary statistics can be determined to any desired degree of accuracy by appropriate techniques, such as that due to Kolmogorov-Smirnov.

The efficient use of Monte Carlo techniques depends heavily upon one's ability to transform one game of chance into another one, in which the expected values of the important system statistics remain unchanged, but for which the statistics in the transformed game have smaller sampling variances than those of the original game.

The writer, who has used the Monte Carlo method to treat a great variety of problems which posed particular analytic difficulty, has no quarrel with others who would employ it for the same reason.† He would point out, however, that many questions that can be answered by a straightforward sensitivity analysis of an analytic model become costly exercises

Received July 21, 1964.

* Associate Professor, Graduate School of Business Administration.

† Today's rather widespread practice of usage of Monte Carlo or gaming techniques by persons who are unprepared either to recognize analytically solvable problems or treat them by analytic methods, or to comprehend the intricacies to modern statistical theory, a commentary not relevant to this reply to the preceding note, is to be deplored, however.

† The methods of this section were pointed out to the author by L. J. Skidmore.

when approached by sampling methods. On the other hand, and in all fairness, it should be admitted that the problem of determining the distribution of general orbits (a topic of importance in assessing the probability of "hitting" a specific "window" in position-velocity space) probably can be handled best by Monte Carlo methods. A good rule to follow is to allow the intrinsic characteristics of the particular problem to dictate the method of treatment to be employed.†

3. Some Points of Confusion

Contrary to a statement in the preceding comment, it is not assumed in Ref. 1 that β , r , and v are normally distributed with covariance matrix Σ ; but it can be inferred, from assumptions made regarding the fundamental guidance parameters, that these quantities possess, approximately, a trivariate normal distribution, with covariance matrix $A\Sigma_x A'$, where the prime denotes the transpose of a matrix. Here, $A = (a_{ij})$ is the $3 \times n$ matrix associated with Eqs. (3) and (4) of Ref. 1, and Σ_x is the covariance matrix of the "errors" associated with the n fundamental guidance parameters.

The x of the preceding note is a random vector of three components, which are distributed independently and identically according to the standard normal law; it is not to be confused with the x of Ref. 1.

4. Monte Carlo vs Analytic Treatment

Two ways of employing the Monte Carlo method in this situation suggest themselves. One is to generate the random n -tuple (X_1, \dots, X_n) of "errors" in the fundamental guidance parameters, and through Eqs. (3), or equivalently, through Eqs. (6) and (5) of Ref. 1 to simulate (1), the square of the orbital eccentricity. [In this connection the writer is grieved to call attention to the absence of a sign of equality between the f term and the \sin^2 term in formula (1) of Ref. 1.] The other method, favored in the preceding note and possibly more efficient from the sampling viewpoint, is to draw random triples from the trivariate normal population with means zero and covariance matrix $A\Sigma_x A'$.

Either method necessitates the computation of the elements of A and Σ_x , which is possibly the most formidable task in the exercise.

The analytic procedure proposed in Ref. 1 was not represented as being superior to any other legitimate method. The computation of the eigenvalues of matrix $(c_{ij}\sigma_i\sigma_j)$, as advocated in Ref. 1, may not be a particularly difficult task, however. The issue depends on the rank of this matrix; if it is $r < n$, then it is well known that $n - r$ of the eigenvalues are zero. Numerical methods for computing the eigenvalues of a real, symmetric matrix are well known and generally available (cf. Ref. 2). Routines for calculating the eigenvalues of a positive-definite (or positive-semidefinite) matrix according to decreasing numerical magnitude are in common use in factor analysis studies; they would appear to be especially suitable in the present application where eigenvalues smaller than a preassigned positive constant could be ignored, thus simplifying the analytic treatment by a certain amount.

5. Generation of Random Numbers

The validity of Monte Carlo applications, in a precise mathematical sense, depends on the intrinsic quality of the "random" number sequences employed. The sequences with which we are compelled, for reasons of economy, to work are not random, but "pseudo-random," in the sense that they possess at least some of the properties of random sequences. The particular properties demanded in different applications vary.

A fundamental and commonly required property, moreover, one which is essential in the application recommended in

the preceding note, is that the sequence of numbers be *equidistributed*, as defined in Ref. 3. The currently favored mixed congruential methods for generating pseudo-random sequences⁴ are the computer implementation of what, in full-precision arithmetic, are called *multiply sequences* in Ref. 3.

Theorem 20 in Ref. 3 establishes that r -dimensional derived sequences (obtained from a multiply sequence) cannot be equidistributed in the r -dimensional unit cube, for any $r > 1$. This result, valid for full-precision arithmetic, casts grave doubts on the implicit postulate that computer-generated sequences possess this desirable property, without which random ordered r -tuples cannot be produced.

The effect of the foregoing is that computed quantities that depend on these r -tuples, such as orbital eccentricity or its square, cannot be considered to be random observations. Consequently, one really has little a priori grounds for believing in the validity of standard statistical procedures when applied to Monte Carlo experiments and no obvious direct method for testing for such validity. As an example, presumed 90% confidence limits for an important system parameter may in fact have an associated true confidence coefficient considerably smaller than 0.9.

References

- Beckwith, R. E., "Approximate distribution of nearly circular orbits," AIAA J. 2, 913-916 (1964).
- Cooley, W. W. and P. R. Lohnes, *Multivariate Procedures for the Behavioral Sciences* (John Wiley & Sons, Inc., New York, 1962), Chaps. 8 and 9.
- Franklin, J. N., "Deterministic simulation of random processes," Math. Computation 17, 28-59 (1963).
- Hull, T. E. and Dobell, A. R., "Random number generators," SIAM Rev. 4, 230-254 (1962).

Errata: "Optimal Variable-Thrust Transfer of a Power-Limited Rocket between Neighboring Circular Orbits"

FRANK W. GOBETZ*

United Aircraft Corporation, East Hartford, Conn.

[AIAA J. 2, 339-343 (1964)]

IN the above article, the equations for the out-of-plane motion are incorrect and should be replaced by the following:

$$\frac{C_5}{C_3} = \frac{\tan \tau_f + (w_f/z_f)}{1 - (w_f/z_f) \tan \tau_f} \quad (31)$$

$$C_3 = \frac{(\sin \tau_f + \tau_f \cos \tau_f) z_f - (\tau_f \sin \tau_f) w_f}{\tau_f^2 - \sin^2 \tau_f} \quad (40)$$

$$A_z = 2C_3 \left\{ \left[\frac{\tan \tau_f + (w_f/z_f)}{1 - (w_f/z_f) \tan \tau_f} \right] \cos \tau - \sin \tau \right\} \quad (44)$$

$$\frac{J}{w_0^3 r_0^2} = \frac{(y_f/r_0)^2 (5\tau_f + 3 \sin \tau_f)}{8[\tau_f (5\tau_f + 3 \sin \tau_f) - 16(1 - \cos \tau_f)]} + \frac{i^2}{\tau_f + |\sin \tau_f|} \quad (45)$$

$$\frac{z_f}{r_0 i} = \left(\frac{1 \pm \cos \tau_f}{2} \right)^{1/2} \quad (49)$$

Received June 22, 1964.

* Analytical Research Engineer, Research Laboratories. Member AIAA.

† The writer, in fact, advocated and employed the Monte Carlo method in treating the original version of the problem of Ref. 1, but did not consider the application worthy of publication.

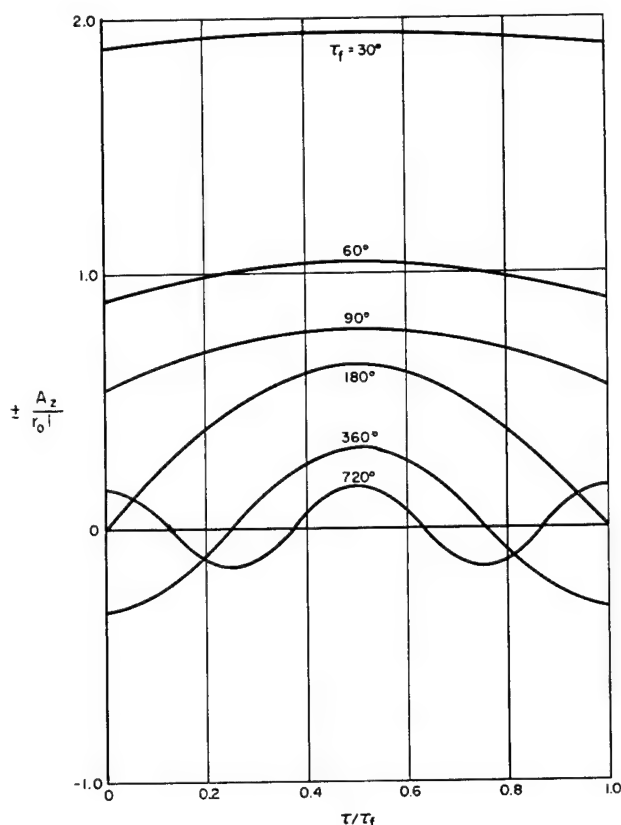


Fig. 5 Normal component of acceleration.

$$\frac{J_2}{i^2} = \frac{1}{\tau_f + |\sin \tau_f|} \quad (51)$$

These changes result in a slightly different graphical form of the optimal out-of-plane component of thrust acceleration $A_z/r_0 \dot{\theta}$ shown in Fig. 5. It is noted that Eq. (49) is double-valued, leading to a double-valued steering program $\pm A_z/r_0 \dot{\theta}$ in Fig. 5. The resultant change in the payoff J is imperceptible for the scale chosen in Fig. 6 of the article.

Longitudinal Mode Instability

J. R. OSBORN*

Purdue University, Lafayette, Ind.

IN recent years, the problems associated with the occurrence of the longitudinal mode of combustion pressure oscillations in liquid rocket motors have been considered solved.¹⁻³ The solution that has been regarded as being the most complete is that published in Refs. 1 and 3. That solution is based upon the concept of a sensitive time lag.³ The definitions and discussions of the sensitive time lag are described in detail^{1, 3, 4} and will not be discussed herein, but the phase relationships will be briefly reviewed.

By considering a disturbance passing through the combustion zone, it is evident that the sensitive time lag is at a minimum when the pressure is at a maximum for the assumed relationship between them.⁴ Thus, for an oscillating pressure, the sensitive time lag will also oscillate and be out of phase.

Furthermore, this oscillation in the sensitive time lag can be related to the oscillation in the burning rate, which in turn can be related to an oscillation in the effect of the burning rate. Therefore, if the oscillation in the effect of the burning rate is in phase with the oscillating combustion pressure, the system tends to be unstable. Conversely, for an out-of-phase relationship the system tends to be stable.

By the proper use of these phase relationships for different length combustion chambers,¹ it can be shown that there exists (theoretically) the so-called lower critical length, below which oscillations are damped, as well as the so-called upper critical length, above which the oscillations are also damped. Both of these lengths are predicted by the time lag theory,³ and it is correctly stated in the conclusions³ that this upper limit cannot be explained by any other mechanism advanced to date. It is further stated⁵ that the results of Ref. 3 show that it is not true that only a lower critical length exists, but that for each mode of longitudinal oscillation there exists a range of lengths outside which the operation is stable, whereas inside it is unstable. In essence then, the validity of the preceding time lag theory¹ is based upon the physical existence of the so-called upper critical length, and the comparison of experiment to theory¹ requires that both lengths exist (see, for example, Figs. 10 and 13 of Ref. 1).

More recent experimental work,⁶ however, agrees with earlier experimental work^{2, 7} in that no upper critical length was found. In addition, the results of a theory recently completed⁸ indicate that no upper critical length should exist. That theory is based upon assuming an Arrhenius-type rate function for the combustion zone dynamics as contrasted with the time lag assumption.⁴

On the basis of the preceding experimental work^{2, 6, 7} as well as the preceding theoretical work,⁸ there is a serious question concerning the validity of the time lag theory⁴ for describing combustion pressure oscillations of the longitudinal mode. It would seem that the necessary existence of the upper critical length clearly invalidates the time lag theory, particularly in those situations where the chemical kinetics predominate, as they do in the case of the premixed gas rocket.² That is, the time lag theory is invalid for those situations in which no upper critical length can be found experimentally. In those situations where an upper critical length was found, its existence may possibly be explained by the dissipative effects assumed negligible by the time lag theory.⁷ Dissipative effects are also neglected in Ref. 8.

Furthermore, the validity of the time lag theory for describing the transverse mode can also be questioned, at least in those cases for which the chemical kinetics again predominate, that is, at least for the premixed gas motor.⁹

It can be concluded that the solution to the problem of combustion instability does not exist at the present time, but that new theories based upon more realistic assumptions,⁸ which agree more closely with the experimental work,^{2, 6, 10} make the problems less formidable.

References

- 1 Crocco, L., Grey, J., and Harrie, D. T., "Theory of liquid propellant rocket combustion instability and its experimental verification," *ARS J.* **30**, 159-168 (1960).
- 2 Zucrow, M. J. and Osborn, J. R., "An experimental study of high-frequency combustion pressure oscillations," *Jet Propulsion* **28**, 654-659 (1958).
- 3 Crocco, L., Grey, J., and Harrie, D. T., "On the importance of the sensitive time lag in longitudinal high-frequency rocket combustion instability," *Jet Propulsion* **28**, 841-843 (1958).
- 4 Crocco, L. and Cheng, S. I., *Theory of Combustion Instability in Liquid Propellant Rocket Motors* (Butterworths Scientific Publications, Ltd., London, 1956), pp. 3, 12, 13-15, 19-24.
- 5 Crocco, L., "Comments on the Zucrow-Osborn paper on combustion oscillations," *Jet Propulsion* **28**, 843-844 (1958).
- 6 Sirignano, W. A. and Crocco, L., "A shock wave model of unstable rocket combustors," *AIAA J.* **2**, 1285-1296 (1964).
- 7 Zucrow, M. J. and Osborn, J. R., "Reply to Crocco's criticism of the Zucrow-Osborn paper," *ARS J.* **29**, 221-222 (1959).

Received August 3, 1964.

* Professor, School of Mechanical Engineering. Associate Fellow Member AIAA.

⁸ Srinath, S. K., "A theoretical investigation of longitudinal high-frequency pressure oscillations," unpublished Master's Thesis, Purdue Univ. (January 1965).

⁹ Zucrow, M. J., Osborn, J. R., Murthy, S. N. B., and Bonnell, J. M., "Limiting conditions for the onset of combustion pressure oscillations (transverse mode) in gaseous propellant rocket motors," AIAA Paper 64-370 (June 1964).

¹⁰ Derr, R. L., "An experimental investigation of longitudinal combustion pressure oscillations," unpublished Master's Thesis, Purdue Univ. (August 1962).

Reply by Author to J. R. Osborn

L. CROCCO*

Princeton University, Princeton, N. J.

WHEN dealing with combustion instability in rockets, one must carefully avoid confusion between liquid propellant rockets and premixed gas rockets.[†] The behavior of the two is generally quite different. Liquid propellant rockets do exhibit, almost invariably, the so-called "time-lag behavior." For a variable-length rocket operating at an assigned mixture ratio,¹⁻³ the "time-lag behavior" is characterized by the fact that any given longitudinal mode of oscillation appears to be unstable only between two critical motor lengths and stable out of this length range. Experimentally, this characterization has been found to be true using different propellants and different types of injectors¹⁻³ (doublet and triplet designs using unlike propellants and showerhead types), although, for another type of injector (like-on-like), the range of spontaneous longitudinal instability appears less sharply defined. Difficulties in finding two stability limits have arisen with certain injectors only because the magnitudes of the sensitive time lag were such that the lengths required were beyond the range of the variable-length rocket used. Variable-sector angle rocket tests⁴ have proved that the pressure-sensitive time-lag concept holds for transverse as well as longitudinal modes.

In fact, it was clearly established by experiments conducted at Princeton on a carefully controlled gas rocket⁵ as well as by the experiments of Purdue, that, under appropriate mixture ratio conditions, the operation of this type of rocket is always unstable (above a certain critical length) and hence does not exhibit the time-lag behavior described previously. Actually, from the point of view of unstable operation, gas rockets appear to be more representative of solid propellant rather than to liquid propellant rockets. This similarity, in addition to scientific curiosity, stimulate theoretical investigations within the Princeton group to obtain a better understanding of the mechanism of gas rocket instability. After eliminating the process of heat exchange with the walls from the role of driving force^{6,7} (which is reputed to play an important role in solid propellants) attention turned to chemical kinetics. Culick^{8,9} already had shown that, if the rate at which chemical energy is being liberated within the gases is represented by an Arrhenius-type rate function depending only on density and temperature (as if the variations of the concentrations did not play any role), the instability that may result does not present the time-lag behavior. Although Culick's disregard of the concentrations seems to result in a substantial overestimate of the driving force due to chemical kinetics, the same simple assumption was used for the gas rocket,^{10,11} and the analysis by Sirignano was broadened so as to include the presence of shock waves. These theoretical

studies not only confirmed Culick's results, but also provided a certain number of positive indications that this may indeed be the correct mechanism of gas rocket instability. It appears now that similar theoretical results have been obtained by the Purdue group.¹²

If the role of chemical kinetics in gas rocket instability is confirmed by more precise experimental and theoretical analyses, one can wonder indeed what can be its importance (assumed negligible in existing theories) in the instability of solid propellants or even in liquid propellant rockets.[‡] However, independent of the final answer to this question, for most liquid propellant rockets, the observed time-lag behavior makes it necessary to rely on other driving mechanisms. The right question to ask is not if the sensitive time-lag theory does correctly represent the observed behavior (which it certainly does), but why it does so, and what the physical interpretation of the existence of a characteristic time must be.

The identification of the characteristic time with a diffusion time was attempted by Strahle based on a convective, collapsed flame model of droplet burning.¹⁴⁻¹⁶ A well-defined result of this theory is that the unsteady behavior of the flame in front of the droplet cannot justify the observed time-lag behavior. On the other hand, evidence indicates that the unsteady behavior of the flame in the wake region behind the droplet may provide the necessary driving mechanism.

Additional details on the various questions mentioned here can be found either in the previously cited references, or in Ref. 17.

References

- Crocco, L., Grey, J., and Harrie, D. T., "Theory of liquid propellant rocket combustion instability and its experimental verification," *ARS J.* **30**, 159-168 (1960).
- Crocco, L., Grey, J., and Harrie, D. T., "On the importance of the sensitive time lag in longitudinal high frequency rocket combustion instability," *Jet Propulsion* **28**, 841-843 (1958).
- Crocco, L., Harrie, D. T., and Reardon, F. H., "Combustion instability in liquid propellant rocket motors," Princeton Univ. Aeronautical Engineering Rept. 216-bb (July 15, 1959); confidential.
- Crocco, L., Harrie, D. T., and Reardon, F. H., "Transverse combustion instability in liquid propellant rocket motors," *ARS J.* **32**, 366 (1962).
- Schob, W. J., Glassman, I., and Webb, M. J., "An experimental investigation of heat transfer and pressure effects on longitudinal combustion instability in a rocket motor using premixed gaseous propellants," Princeton Univ. Aeronautical Engineering Rept. 649 (June 1963).
- Bortzmeyer, H. G. and Crocco, L., "Analysis of longitudinal high frequency combustion instability in a gas fueled rocket motor," Princeton Univ. Aeronautical Engineering Rept. 587 (December 5, 1961).
- Bertrand, J., Crocco, L., and Glassman, I., "Theoretical and experimental investigations of longitudinal high-frequency combustion in a gas fueled rocket motor," Princeton Univ. Aeronautical Engineering Rept. 624 (September 1962).
- Culick, F. E. C., "Stability of high frequency pressure oscillations in gas and liquid rocket combustion chambers," Massachusetts Institute of Technology Aerophysics Lab. TR 480 (June 1961).
- Culick, F. E. C., "Stability of high frequency pressure oscillations in rocket combustion chambers," *AIAA J.* **1**, 1097-1104 (1963).
- Sirignano, W. A. and Crocco, L., "A shock wave model of unstable rocket combustors," *AIAA J.* **2**, 1285, 1296 (1964).
- Sirignano, W. A., "A theoretical study of nonlinear combustion instability: longitudinal mode," Dept. of Aerospace and Mechanical Sciences, Princeton Univ. TR 677 (March 1964).
- Srinath, S. K., "A theoretical investigation of longitudinal high frequency pressure oscillations," unpublished Master's Thesis, Purdue Univ. (August 1964).

[‡] This question was raised and discussed¹³ by the Princeton group at the Air Force Office of Scientific Research Contractors' Meeting on Combustion Instability in Rocket Motors held in 1963 at Nantucket, Mass.

Received September 14, 1964.

* Robert H. Goddard Professor, Department of Aerospace and Mechanical Sciences. Fellow Member AIAA.

[†] Although the first type is extremely important for its practical applications, the second has mainly a scientific interest, and its practical utility has not been shown as yet.

¹³ Crocco, L., Glassman, I., and Webb, M. J., "Combustion processes in rocket motors," abstracts of papers, 16th Air Force Office of Scientific Research Contractors' Meeting on Liquid Rocket Combustion Research (June 25-28, 1963).

¹⁴ Strahle, W. C. and Crocco, L., "Analytical investigation of several mechanisms of combustion instability," Bulletin of the Fifth Liquid Propulsion Symposium, Chemical Propulsion Information Agency (November 13-15, 1963).

¹⁵ Strahle, W. C., "A theoretical study of unsteady droplet burning: transients and periodic solutions," Princeton Univ., Ph.D. Thesis, Aeronautical Engineering Lab. Rept. 671 (December 1963).

¹⁶ Strahle, W. C., "Periodic solutions to a convective droplet burning problem: the stagnation point," International Combustion Symposium, Cambridge, England (August 1964).

¹⁷ Crocco, L., "Theoretical studies on liquid propellant rocket instability," International Combustion Symposium, Cambridge, England (August 1964).

Comment on "An Alternate Interpretation of Newton's Second Law"

V. W. SNYDER*

Kitt Peak National Observatory,† Tucson, Ariz.

THE object of this note is to extend the work of Bottaccini¹ to the angular momentum theorem and to clarify the methodology used. Bottaccini has shown¹ that the motion of a variable mass system can be written in the classical Newtonian form

$$\Sigma \mathbf{F} = d\mathbf{G}/dt \quad (1)$$

where the momentum of the system is represented by the Stieltjes integral

$$\mathbf{G} = \int \mathbf{U} dm \quad (2)$$

in which the integral is taken over all the mass in the system. In classical mechanics, this would be referred to as a "material" or "Lagrangian" description of the system.

Bottaccini has also shown² that, for piecewise continuous masses, Eq. (1) becomes

$$\Sigma \mathbf{F} = \frac{d}{dt} \int_{\sigma} \rho \mathbf{U} d\tau \quad (3)$$

where σ is the volume of the mass in the system. Using Leibnitz's theorem for differentiating a volume integral, Eq. (3) can be expanded to

$$\Sigma \mathbf{F} = \int_{\sigma} \frac{\partial(\rho \mathbf{U})}{\partial t} d\tau + \int_{\mu} \rho \mathbf{U} \mathbf{U} \cdot \mathbf{n} dS \quad (4)$$

where μ is the boundary surface of the material volume. This boundary surface has to move with the velocity of the mass to be consistent with a material description of the system.

The evaluation of the volume integral in Eq. (4) is difficult as the result of the material description of the system; for computational purposes, it would be advantageous to use a spatial description, that is, an arbitrary control volume that contains the identified mass at a given time. Equation (4) represents an instantaneous condition, and thus the integral evaluated on the spatial and material volumes must have the

same value at a given instant of time. A moment later, the two integrals will have different values, but this presents no difficulty. Now using Leibnitz's theorem again, except that this time the boundary is moving with the arbitrary velocity \mathbf{V} of the control volume, Eq. (4) can be expressed as

$$\Sigma \mathbf{F} = \frac{d}{dt} \int_{\tau} \rho \mathbf{U} d\tau + \int_s \rho \mathbf{U} (\mathbf{U} - \mathbf{V}) \cdot \mathbf{n} ds \quad (5)$$

where s is the boundary of the spatial volume. As Bottaccini² points out, this equation has been developed by Thorpe³ and is much more convenient for computational purposes.

A similar methodology can be used to show that the moment equation can be written in classical form

$$\Sigma \mathbf{M} = d\mathbf{H}/dt \quad (6)$$

where \mathbf{H} is the angular momentum of the system. The angular momentum is represented for a piecewise continuous mass by the integral

$$\mathbf{H} = \int_{\sigma} (\mathbf{r} \times \rho \mathbf{U}) d\tau \quad (7)$$

in which the integration is over all the mass of the system. This material description of the system can be transformed to a spatial description by the use of Leibnitz's theorem. Thus, after the transformation, Eq. (6) will become

$$\Sigma \mathbf{M} = \frac{d}{dt} \int_{\sigma} (\mathbf{r} \times \rho \mathbf{U}) d\tau + \int_s (\mathbf{r} \times \rho \mathbf{U}) (\mathbf{U} - \mathbf{V}) \cdot \mathbf{n} ds \quad (8)$$

for piecewise continuous mass.

Equation (8) gives the moment on a spatial control volume in terms of the angular momentum of the control volume and expelling gases with respect to an inertial frame of reference. The first term offers some difficulty in computing. Dynamicists have found that this difficulty can be eliminated by selecting an accelerating origin in the body. For a rigid body, it has been shown⁴ that the moments about the moving origin at a will be

$$\mathbf{M}_a = (d/dt)(I\boldsymbol{\Omega}) - \mathbf{R}' \times d^2\mathbf{r}_a/dt^2 \quad (9)$$

where I is the inertia tensor, $\boldsymbol{\Omega}$ the angular velocity of the body, \mathbf{R}' the position vector of the center of mass measured from the a , and $d^2\mathbf{r}_a/dt^2$ is the acceleration of the origin.

Using Eqs. (5) and (8), the moment about a for a variable mass system can be written

$$\begin{aligned} \mathbf{M}_a &= \Sigma \mathbf{M} - \mathbf{r}_a \times \mathbf{F} \\ &= \frac{d}{dt} \int_{\tau} \mathbf{r} \times \rho \mathbf{U} d\tau - \mathbf{r}_a \times \frac{d}{dt} \int_{\tau} \rho \mathbf{U} d\tau + \\ &\quad \int_s [(\mathbf{r} - \mathbf{r}_a) \times \rho \mathbf{U}] (\mathbf{U} - \mathbf{V}) \cdot \mathbf{n} ds \end{aligned} \quad (10)$$

Equation (10) can be rewritten as

$$\begin{aligned} \mathbf{M}_a &= \frac{d}{dt} \int_{\tau} (\mathbf{r} - \mathbf{r}_a) \times \rho \mathbf{U} d\tau + \\ &\quad \int_s [(\mathbf{r} - \mathbf{r}_a) \times \rho \mathbf{U}] (\mathbf{U} - \mathbf{V}) \cdot \mathbf{n} ds + \\ &\quad \frac{d\mathbf{r}_a}{dt} \times \int_{\tau} \rho \mathbf{U} d\tau \end{aligned} \quad (11)$$

From the concept of the mass center, the last integral in Eq. (11) can be replaced by⁵

$$\int_{\tau} \rho \mathbf{U} d\tau = m \frac{d\mathbf{R}}{dt} + \int_s \rho (\mathbf{r} - \mathbf{R}) (\mathbf{U} - \mathbf{V}) \cdot \mathbf{n} ds$$

Received August 27, 1964.

* Graduate Assistant, Space Division; also Graduate Student, University of Arizona, Tucson, Ariz. Student Member AIAA.

† Operated by the Association of Universities for Research in Astronomy, Inc. under contract with the National Science Foundation.

where m is the total mass in control volume, and \mathbf{R} is the velocity of the mass center. Thus, Eq. (11) becomes

$$\begin{aligned} \mathbf{M}_a = & \frac{d}{dt} \int_V (\mathbf{r} - \mathbf{r}_a) \times \rho \mathbf{U} d\tau + \\ & \int_s [(\mathbf{r} - \mathbf{r}_a) \times \rho \mathbf{U}][\mathbf{U} - \mathbf{V}] \cdot \mathbf{n} ds + \\ & \frac{d\mathbf{r}_a}{dt} \times \frac{d\mathbf{R}}{dt} + \frac{d\mathbf{r}_a}{dt} \times \int_s \rho (\mathbf{r} - \mathbf{R})(\mathbf{U} - \mathbf{V}) \cdot \mathbf{n} ds \quad (12) \end{aligned}$$

where $d\mathbf{r}_a/dt$ is the velocity of the moving origin at a . Equation (11) has been developed by Bowen⁵ using a different approach to the problem. Equation (12) still presents some difficulties in computing the moment which can only be eliminated by additional assumptions of the system. Rankin⁶ has developed the equation of motion for a rocket from a

slightly different approach than was shown previously. It can be shown that Eq. (12) would be reduced to the equation given by Rankin⁶ if his assumptions were used.

References

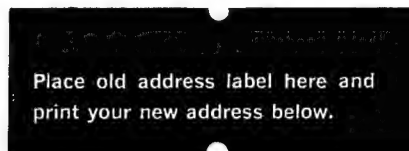
- ¹ Bottaccini, M., "An alternate interpretation of Newton's second law," AIAA J. 1, 927-928 (1963).
- ² Bottaccini, M., "Addendum: 'An alternate interpretation of Newton's second law,'" AIAA J. 2, 1164-1165 (1964).
- ³ Thorpe, J. F., "On the momentum theorem for a continuous system of variable mass," Am. J. Phys. 30, 637-640 (1962).
- ⁴ Nara, H. R. (ed.), *Vector Mechanics for Engineers, Part II, Dynamics* (John Wiley and Sons, Inc., New York, 1962), p. 226.
- ⁵ Bowen, R. M., "Integral and local statements of the balance equation of continuum mechanics for variable mass regions," Air Force Institute of Technology TR 64-1 (January 1964).
- ⁶ Rankin, R. A., "The mathematical theory of the motion of rotated and unrotated rockets," Phil. Trans. Roy. Soc. London A241, 457-585 (March 1949).



The post office WILL NOT forward this publication unless you pay additional postage. SO PLEASE . . . at least 30 days before you move, send us your new address, including the postal zone or ZIP code. Your old address label will assist the Institute in correcting your stencil and insuring that you will receive future copies of this publication.

RETURN TO:

AIAA—1290 Avenue of the Americas
New York, N. Y. 10019



Name.....

Address.....

City..... Zone.....

State.....

Table of Contents reprinted from

Journal of Spacecraft and Rockets

VOLUME 1 NUMBER 6

NOVEMBER-DECEMBER 1964

SURVEY PAPER

Inertial Guidance, Navigation, and Control Systems.....R. C. Duncan and A. S. Gunnerson Jr. 577

CONTRIBUTED PAPERS

Spinning Vehicle Nutation Damper.....	K. H. Wadleigh, A. J. Galloway, P. N. Mathur	588
Simply Mechanized Attitude Control for Spinning Vehicles.....	G. W. LeCompte and J. G. Bland	593
Missile Attitude Stabilization by Lyapunov's Second Method.....	A. W. Merz	598
Velocity Requirements and Re-Entry Flight Mechanics for Manned Mars Missions.....	E. B. Pritchard	605
Economy of Large Launch Vehicles Including Orbital Labor Cost.....	K. A. Ehrlicke	611
Orbital Burden Rates for Manned Space Missions.....	H. H. Koelle	620
Preliminary Study of Air Augmentation of Rocket Thrust.....	L. L. Perini, W. E. Wilson, R. E. Walker, G. L. Dugger	626
Failure Mechanisms in Dense Tungsten Alloy Rocket Nozzles.....	E. L. Olcott and J. D. Batchelor	635
Analysis of Self-Cooling with Infiltrated Porous Tungsten Composites.....	F. B. Gessner, J. D. Seader, R. J. Ingram, T. A. Coultas	643
Design of a Separating High-Altitude Probe.....	M. Sevik, L. L. Mitchum, D. R. Barnes	649
Effects of Various Re-Entry Vehicle Parameters on Radio Frequency Attenuation.....	F. A. Vicente	653
Solar Energy Thermionic Electrical Power Supplies.....	W. R. Menetrey and A. Smith	659
Stratified Layer Flow Model: A Numerical Approach to Liquid Temperature Stratification.....	G. C. Vliet, J. J. Brogan, T. S. Sheppard, F. H. Morse, F. L. Hines	666

ENGINEERING NOTES

Experimental Evaluation of Solid Propellant Rocket Motors under Acceleration Loads.....	J. G. Horton II	673
Approximation of Time of Ballistic Entry.....	T. T. Kumagai	675
Correlation for Maximum Pressure of "Hi-Lo" Igniter.....	R. L. Beauregard and C. F. Sharn	676
Heat Transfer in the Vicinity of Two-Dimensional Protuberances.....	A. Datis, B. G. Broach, H. H. Yen	678
Effect of Rocket Engine Vibration on an Air-Core Superconducting Magnet.....	L. J. Krzycki, W. M. Byrne Jr., J. B. Lee	680
Nutational Stability of an Axisymmetric Body Containing a Rotor.....	V. D. Landon and B. Stewart	682
Alouette Topside Sounder Satellite: Experiments, Data, and Results.....	J. H. Chapman	684
Application of Biot's Variational Method to Convective Heating of a Slab.....	H. N. Chu	686
Shock Reflection and Interaction at Hypersonic Speeds.....	S. Molder and E. J. Szpiro	688
Inertia-Compensated Balance for Wind-Tunnel Buffet Measurements.....	C. V. Stahle, C. G. Stouffer, W. Silver	690
Ignition Transient Control through Inhibiting of Propellant Grain.....	H. Gibby	692

TECHNICAL COMMENTS

Further Comments on "Cost Minimization of a Space System by Multiple Launchings".....	D. J. Zigrang	694
---	---------------	-----

REPRINTED TABLES OF CONTENTS

September-October 1964 Journal of Aircraft.....	695
September 1964 AIAA Journal.....	696, 697
October 1964 AIAA Journal.....	698, 699

1964 JOURNAL OF SPACECRAFT AND ROCKETS INDEX

Author Index.....	700
Subject Index.....	702

Index of Papers Published in AIAA Journal

Volume 2—January through December 1964

Issue	Pages	Issue	Pages
January	1-224	July	1169-1360
February	225-416	August	1361-1520
March	417-592	September	1521-1680
April	593-784	October	1681-1872
May	785-976	November	1873-2064
June	977-1168	December	2065-2256

TN, TC, and SA indicate Technical Note, Technical Comment, and Survey Article, respectively; RS indicates supplement of translated Russian articles

AUTHORS

- Abbadi, Beshir A. and Tankin, Richard S. Effect of radiation on upper limits of inflammability (TN)..... 758
- Acker, T., Henley, E., McAlevy, R. F., III, and Odian, G. Effect of radiation on ammonium perchlorate propellants (TC)..... 1165
- Acton, Russell U. (see Houghton, Arthur V.)
- Addy, A. L. (see Chow, W. L.)
- Agosta, Vito D. (see Hammer, Sanford S.)
- Albini, Frank A. Approximate evaluation of slender radome performance in hypersonic flight..... 476
- Scattering and absorption of plane waves by cylindrically symmetrical underdense zones..... 524
- Album, Hyman H. Flow inclination measurements in hypersonic tunnels (TN)..... 104
- Allegre, J. (see Charwat, A. F.)
- Almroth, B. O. Postbuckling behavior of orthotropic cylinders under axial compression..... 1795
- Alpinieri, Louis J. Turbulent mixing of coaxial jets..... 1560
- Alwan, A. M. Large deflection of sandwich plates with orthotropic cores (TN)..... 1820
- Andersen, W. H. Comments on "Gas-film effects in the linear pyrolysis of solids" (TC)..... 404
- Anderson, John D. Reply by author to H. R. Westerman (TC)..... 1869
- Anderson, Ralph, Brown, Robert S., and Shannon, Larry J. Heterogeneous reactions in ignition and combustion of solid propellants (TN)..... 179
- Anderson, Thomas P. Comment on "A class of linear magneto-hydrodynamic flows" (TC)..... 588
- Angelino, Gianfranco. Approximate method for plug nozzle design (TN)..... 1834
- Angelus, T. A. (see Yount, R. A.)
- Appleton, J. P. Aerodynamic pitching derivatives of a wedge in hypersonic flow (TN)..... 2034
- Aris, R. and Denn, M. M. N-segment least-squares approximation (TC)..... 1516
- Armenakas, Anthony E. Influence of initial stress on the vibrations of simply supported circular cylindrical shells..... 1607
- Aroesty, J. Slip flow and hypersonic boundary layers (TC)..... 189
- Aronowitz, Leonard and Coe, Warren. Delays in initiation of discharges in pulsed plasma accelerators (TN)..... 2019
- Auelmann, Richard R. Trajectories with constant normal force starting from a circular orbit (TN)..... 561
- Bachynski, M. P. Simulation of geophysical phenomena in the laboratory (SA)..... 1873
- Bagchi, Keshab Chandra. Flow of viscoelastic Maxwell fluid (TN)..... 759
- Bailey, Allan B. (see Potter, J. Leith)
- Baker, Edward H. Analysis of a symmetrically loaded sandwich cylinder (TN)..... 108
- Stability of circumferentially corrugated sandwich cylinders under combined loads..... 2142
- Baker, Jerome M. Approximate solution to flux concentration by hydromagnetic flow (TN)..... 112
- Baker, Robert M. L., Jr. Extension of f and g series to non-two-body forces (TN)..... 1337
- Baldwin, Barrett (see Heaslet, Max. A.)
- Baldwin, Lionel V. (see Kuo, Yung-Huang)
- (see Sandborn, V. A.)
- Ball, Robert E. (see Schjelderup, H. C.)
- Barakauskas, Edward J. Sudden expansion of a bounded jet at a high pressure ratio (TN)..... 1644
- Barker, L. M. (see Butcher, Barry M.)
- Barlow, John (see Irons, Bruce)
- Baron, J. R. (see Shih, W. C. L.)
- Baronti, Paolo O. (see Libby, Paul A.)
- Barreto, E. (see Marks, A.)
- Bartlett, Eugene P. Effective heat of ablation of graphite (TN)..... 171
- Bauer, Helmut F. Liquid sloshing in a 45° sector compartmented cylindrical tank (TN)..... 768
- Baum, Eric. Initial development of the laminar separated shear layer (TN)..... 128
- , King, Hartley H., and Denison, M. Richard. Recent studies of the laminar base-flow region..... 1527
- Bazeley, G. (see Draper, Keith J.)
- Beckwith, R. E. Approximate distribution of nearly circular orbits —Reply by author to D. A. Conrad (TC)..... 2234
- Bell, P. O. Orbit determination by angular measurements (TN)..... 1862
- Benton, Edward R. Supersonic magnus effect on a finned missile (TN)..... 153
- and Platou, Anders, S. Comments on "Wing-tail interference as a cause of 'magnus' effects on a finned missile" (TC)..... 410
- Zonal flow inside an impulsively started rotating sphere (TN)..... 1840
- Berge, G. K. (see Blair, D. W.)
- Bernett, E. C., Scott, Ronald F., Jaffe, L. D., Frink, E. P., and Martens, H. E. Bearing capacity of simulated lunar surfaces in vacuum Bernhart, W. D. (see Cook, E. L.)
- Best, G. C. Comment on "Derivation of element stiffness matrices" (TC)..... 1515
- Bhattacharjee, M. (see Bhattacharya, R. N.)
- Bhattacharjee, A. and Michael, I. Mass and magnetic dipole shielding against electrons of the artificial radiation belt..... 2198
- Bhattacharya, R. N. and Bhattacharjee, M. Modification of Weierstrass-Erdmann corner conditions in space navigations (TN)..... 1145
- Bieniek, M. P. and Shinozuka, M. Finite plane deformation of a thick-walled cylinder (TN)..... 568
- Billik, B. H. Some optimal low-acceleration rendezvous maneuvers Bird, J. F. (see Hart, R. W.)
- Bird, G. A. and Wetherall, C. J. Lift contribution to the sonic boom (TN)..... 582
- Bizjak, Frank and Stai, Donald F. Temperature-entropy diagram of monomethylhydrazine (TN)..... 954
- Black, Harold D. A passive system for determining the attitude of a satellite (TN)..... 1350
- Blair, D. W., Eriksen, E., and Berge, G. K. Acoustic absorption coefficients of combustion gases (TN)..... 392
- Bleich, Gary D. (see Zeiberg, Seymour L.)
- Bleick, W. E. and Faulkner, F. D. Orbital transfer with minimum fuel (TN)..... 113
- Blick, E. F. (see High, M. D.)
- Blitzer, Leon. Nodal period of an earth satellite (TN)..... 1459
- Bloom, A. M. (see Yuan, S. W.)
- Bloom, Martin H. and Steiger, Martin H. Reply by authors to Y.-H. Kuo and L. V. Baldwin (TC)..... 1164
- (see Steiger, Martin H.)
- Blottner, F. G. Chemical nonequilibrium boundary layer..... 232
- Nonequilibrium laminar boundary-layer flow of ionized air..... 1921
- Boedeker, Laurence R. (see Covert, Eugene E.)
- Bogan, Alexander (see Oman, Richard A.)
- Bollinger, Loren E. Experimental detonation velocities and induction distances in hydrogen-air mixtures (TN)..... 131
- Bonomo, Phillip J. (see Schlegel, Leo B.)
- Bottacini, M. Addendum: "An alternate interpretation of Newton's second law" (TC)..... 1164
- Boynton, Frederick P. Chemical kinetic analysis of rocket exhaust temperature measurements (TN)..... 577
- Brady, J. J. (see Lyons, W. C., Jr.)
- Brandmaier, H. E., Durand, J. L., Gouridine, M. C., and Rubel, A. An investigation of Hall propulsor characteristics..... 674
- Bray, K. N. C. Comment on "Thermal ionization behind strong shock waves" (TC)..... 1161
- Briggs, Joel L. Comment on calculation of oblique shock waves (TC)..... 974
- Brook, J. E. Compact formal analysis of beam columns (TN)..... 1824
- Brogan, T. R. (see Louis, J. F.)
- Broglio, Luigi. A general theory on space and re-entry similar trajectories..... 1774
- Brong, E. A. and Leigh, D. C. Method of Belotserkovskii for asymmetric blunt-body flows (TN)..... 1852
- Brooke, Darrell and Thomas, Richard E. Effect of transverse enthalpy gradient on blunt body pressure distributions in hypersonic flow (TN)..... 1829
- Brown, Robert S. (see Anderson, Ralph)
- Browning, S. C. (see Davidson, O. C.)
- Brownlee, W. G. Nonlinear axial combustion instability in solid propellant motors..... 275
- Bryson, Arthur E., Jr. (see Denham, Walter F.)
- Buckey, C. R. (see Hyman, J., Jr.)
- Buckmaster, J. D. An investigation of cylindrical starting flows (TN)..... 1649
- (see Gibson, Walter E.)
- Budiansky, Bernard and Radkowski, Peter P. Reply by authors to G. A. Greenbaum (TC)..... 592
- Bungay, Richard W. (see Herrmann, George)
- Burggraf, Odus R. (see Schuerch, Hans U.)

- Burstein, Samuel Z. Numerical methods in multidimensional shocked flows..... 2111
- Bush, John E. Flow of combustion gases through a perforation in a solid propellant grain (TN)..... 2022
- Bush, William B. Local similarity expansions of the boundary-layer equations (TN)..... 1857
- Bushnell, David and Hoff, Nicholas J. Influence coefficients of a circular cylindrical shell with rapidly varying parabolic wall thickness..... 2167
- Buss, Harvey (see Kubota, Toshi)
- Butcher, Barry M., Barker, L. M., Munson, D. E., and Lundergan, C. D. Influence of stress history on time-dependent spall in metals (SA)..... 977
- and Canon, Jack R. Influence of work-hardening on the dynamic stress-strain curves of 4340 steel..... 2174
- Bynum, D. J., Rastrelli, L. U., and DeHart, R. C. Surface strains in case-bonded models of rocket motors..... 343
- Byrne, W. J., Jr. and Raynor, S. An analysis of the yawing motion of a rocket with a varying mass (TN)..... 962
- Cable, A. J. Experimental measurement of pitot pressure in the boundary layer on a model in a hypersonic gun tunnel (TN)..... 944
- Cann, Gordon L. and Marlotte, Gary L. Hall current plasma accelerator..... 1234
- Canon, Jack R. (see Butcher, Barry M.)
- Cantrell, R. H. Reply by author to W. H. Andersen (TC)..... 406
- , Hart, R. W., and McClure, F. T. Linear acoustic gains and losses in solid propellant rocket motors..... 1100
- (see Hart, R. W.)
- Cappelli, A. P. Reply by author to R. E. Lavender (TC)..... 412
- Carlson, Donald J. and Hoglund, Richard F. Particle drag and heat transfer in rocket nozzles..... 1980
- (see Lewis, Clarke H., Jr.)
- Carpenter, H. J. (see Hammit, A. G.)
- Carroll, Philip S. Equations of motion for spin stabilization analysis in terms of Euler angles (TN)..... 1483
- Torque on a satellite due to gravity gradient and centrifugal force (TN)..... 2220
- Carson, Ralph S. (see Hendricks, Charles D., Jr.)
- (see Hogan, J. J.)
- Casaccio, Anthony. Similar solutions for the laminar mixing of reactive gases..... 1403
- Chamay, A. (see Migdal, David)
- Chapel, R. E. (see Cook, E. L.)
- Chapin, S. G. and Rumpel, W. F. Measurement of uniform flow duration in a chambered, buffered shock tube (TN)..... 1499
- Chapman, Gary T. (see Davy, William C.)
- Chao, C. C. (see Pao, Yih-Hsing)
- Charwat, A. F. Boundary of underexpanded axisymmetric jets issuing into still air (TN)..... 161
- and Allegre, J. Interaction of a supersonic stream and a transverse supersonic jet..... 1965
- Chebotaev, G. A. Motion of an artificial earth satellite in an orbit of small eccentricity (RS)..... 203
- Cheng, Ping. Two-dimensional radiating gas flow by a moment method (TN)..... 1662
- Childs, M. E. (see Miller, D. S.)
- Chin, Jin H. and Hearne, L. F. Shock-layer radiation for sphere-cones with radiative decay (TN)..... 1345
- and Gallagher, L. W. Effect of fluid motion on free surface shape under reduced gravity (TN)..... 2215
- Cho, A. Y. and Shelton, H. Cesium neutral and ion emission from carburized and oxygenated porous tungsten..... 2135
- Chopra, Kuldeep P. Some dimensional considerations of studies in space-flight simulation (TN)..... 2047
- Chow, W. L. and Addy, A. L. Interaction between primary and secondary streams of supersonic ejector systems and their performance characteristics..... 686
- Chu, C. K. (see Marks, A.)
- Chu, Chong-Wei. A simple derivation of three-dimensional characteristic relations (TN)..... 1336
- Equivalence of nonequilibrium flows behind normal and oblique shock waves (TN)..... 1833
- Chu, Wen-Hwa. Fuel sloshing in a spherical tank filled to an arbitrary depth..... 1972
- Citron, S. J., Dunin, S. E., and Meissinger, H. F. A terminal guidance technique for lunar landing..... 503
- Clancy, Thomas F. and Mitchell, Thomas P. Effects of radiation forces on the attitude of an artificial earth satellite..... 517
- Clarke, Victor C., Jr. Earth radius/kilometer conversion factor for the lunar ephemeris (TN)..... 363
- Clary, Robert R. (see Watkins, Jerry D.)
- Clingman, Bruce E. Dynamics loads due to wind shear..... 76
- Coates, Ralph L., Horton, M. D., and Ryan, N. W. T-burner method of determining the acoustic admittance of burning propellants..... 1119
- (see Ryan, Norman W.)
- Coe, Warren (see Aronowitz, Leonard)
- Cohen, Gerald A. Computer analysis of asymmetrical deformation of orthotropic shells of revolution (TN)..... 932
- Errata: "Computer analysis of asymmetrical deformation of orthotropic shells of revolution" (TC)..... 2231
- Colburn, D. S., Harker, K. J., and Kino, G. S. A synthesis method of electrostatic gun design..... 322
- Colgate, Stirling A. Vortex gas accelerator..... 2138
- Collins, D. J. and Spiegel, J. M. Effect of gage material on convective heat transfer (TN)..... 777
- and Horton, T. E. Experimental convective heat-transfer measurements (TN)..... 2046
- Compton, Dale L. (see Davy, William C.)
- Concus, Paul. Capillary stability in an inverted rectangular channel for free surfaces with curvature of changing sign (TN)..... 2228
- Conly, John F. (see Skalak, Richard)
- Connor, Laurence N. and Erickson, Wayne D. Entropy production in vibrational-nonequilibrium nozzle flow (TN)..... 397
- Conrad, David A. Distribution of nearly circular orbits (TC)..... 2234
- Conti, Raul J. Stagnation equilibrium layer in nonequilibrium blunt-body flows (TN)..... 2044
- Cook, E. L., Chapel, R. E., and Bernhart, W. D. Comment on "Basis for derivation of matrices for the direct stiffness method" (TC)..... 1161
- Cool, T. A. (see Zukoski, Edward E.)
- Cooney, J. A. (see Sheer, C.)
- Cooper, John A. Effects of interface combustion and mixing on shock-tunnel conditions (TN)..... 1669
- Cosens, G. L. (see Ragland, K. W.)
- Cost, Thomas L. Approximate Laplace transform inversions in viscoelastic stress analysis..... 2157
- Council, F. E., Jr. Conversion of coordinates: latitude-longitude to cislunar (TN)..... 551
- Covert, Eugene E., Boedeker, Laurence R., and Haldeman, Charles W. Recent results of studies of the traveling wave pump..... 1040
- Craig, Roger A. (see Davy, William C.)
- Cresci, Robert J. (see Librizzi, Joseph)
- Crocco, L. Reply by author to J. R. Osborn (TC)..... 2237
- (see Reardon, F. H.)
- (see Sirignano, W. A.)
- Crumpp, J. E. and Price, E. W. Effect of acoustic environment on the burning rate of solid propellants..... 1274
- Cullen, R. E. (see Ragland, K. W.)
- Cummings, Benjamin E. Large-amplitude vibration and response of curved panels..... 709
- Danby, J. M. A. Matrix methods in the calculation and analysis of orbits..... 13
- The matrixization of Keplerian motion..... 16
- Davidson, O. C. and Browning, S. C. An axially compressed, cylindrical shell with a viscoelastic core (TN)..... 2015
- Davy, William C., Craig, Roger A., Chapman, Gary T., and Compton, Dale L. Ablation-products radiation from cones..... 1583
- Dawson, V. C. D. (see Piacesi, R.)
- Decher, R. (see Louis, J. F.)
- Deerwester, Jerry M. Plane-change requirements associated with rendezvous in a lunar satellite orbit..... 890
- DeHart, R. C. (see Bynum, D. J.)
- Delaney, Lawrence J., Eagleton, Lee C., and Jones, Walter H. A semiquantitative prediction of the erosion of graphite nozzle inserts..... 1428
- Demetriades, Anthony. Hot-wire measurements in the hypersonic wakes of slender bodies..... 245
- Electron fluctuations in an equilibrium turbulent plasma (TN)..... 1347
- Denham, Walter F. and Bryson, Arthur E., Jr. Optimal programming problems with inequality constraints II: solution by steepest-ascent..... 25
- and Speyer, Jason L. Optimal measurement and velocity correction programs for midcourse guidance..... 896
- Denison, M. Richard (see Baum, Eric)
- Denn, M. M. (see Aris, R.)
- Dennon, Jack D. Potential flow past a parabolic leading edge (TN)..... 934
- Deskins, H. Eugene. Correlation of flat-plate pressures using the rarefaction parameter $M \propto C \propto 1/2 / Re_x \propto 1/2$ (TN)..... 573
- (see Griffith, B. J.)
- Devan, Leroy and Oberai, Madan Mohan. Approximate solution of second-order boundary-layer equations (TN)..... 1838
- Dewey, C. Forbes, Jr. (see Kubota, Toshi)
- Dewhirst, Donald L. A load-sinkage equation for lunar soils (TN)..... 761
- Didriksson, Theodor (see Penzien, Joseph)
- Diesel, John W. A new approach to gravitational gradient determination of the vertical..... 1189
- Divoky, D. (see Mayer, E.)
- Dix, Donald M. Energy transfer processes in a partially ionized, two-temperature gas..... 2081
- Dixon, R. J. (see Page, R. H.)
- Dobbins, Richard A. and Temkin, S. Measurements of particulate acoustic attenuation..... 1106
- Dowell, Earl. Flutter of multibay panels at high supersonic speeds..... 1805
- (see Voss, H. M.)
- Dragos, Lazar. Theory of thin airfoils in magnetoaerodynamics..... 1223
- Draper, Keith J., Irons, B., and Bazeley, G. Comment on "Vibration of a 45° right triangular cantilever plate by a gridwork method" (TC)..... 1870
- (see Irons, Bruce)
- Dresser, D. L., Laurita, W. G., Dunlop, J. D., II, Huber, H., and LeBihan, R. Theory and experiment of a capillary-type emitter..... 52
- Ducati, Adriano C., Giannini, Gabriel M., and Muehlberger, Erich. Experimental results in high-specific-impulse thermo-ionic acceleration (TN)..... 1452
- Dunin, S. E. (see Citron, S. J.)
- Dunlop, J. D., II (see Dresser, D. L.)
- Dunn, Michael G. Correlation of boost phase turbulent heating flight data (TN)..... 122
- Durand, J. L. (see Brandmaier, H. E.)
- Durham, S. C. (see Horton, W. H.)
- Dusek, Hermann M. Error propagation in astro-inertial guidance systems for low-thrust missions..... 879
- Dwork, M. J. Reply by author to R. O. Wilke (TC)..... 1358
- Dykema, O. W. (see Iwanicki, L. R.)
- Eagleton, Lee C. (see Delaney, Lawrence J.)
- Eastman, Donald W. (see Radtke, Leonard P.)
- Eaton, C. F. A transient solution of the Fokker-Planck equation (TN)..... 2033
- Eckerman, Jerome (see Pallone, Adrian J.)
- Eckert, E. R. G. (see Sparrow, E. M.)
- Eckhardt, W. O. (see Hyman, J., Jr.)
- Edelbaum, Theodore N. Comment on "Application of dynamic programming to optimizing the orbital control process of a 24-hour communications satellite" (TC)..... 974
- Optimum low-thrust rendezvous and station keeping..... 1196

- Edelman, Raymond and Rosenbaum, Harold. Viscous multicomponent-multiphase flow with application to axisymmetric jets of hydrogen..... 2104
- Edquist, C. T. Effect of shock curvature on turbulent heating of sphere-cones (TN)..... 1486
- Edwards, D. K. and Tellep, D. M. Reply by authors to N. H. Kemp (TC)..... 1865
- Ehlers, F. Edward. Linearized analysis of the pressure waves in a tank undergoing an acceleration (TN)..... 110
- Eisel, J. L., Horton, M. D., Price, E. W., and Rice, D. W. Preferred frequency oscillatory combustion of solid propellants..... 1319
- Eisley, J. G. Large amplitude vibration of buckled beams and rectangular plates (TN)..... 2207
- Eisner, W. and Goodman, A. F. Determination of dominant error sources in an inertial navigation system by iterative weighted least squares..... 722
- El-Saden, M. R. Reply by author to T. P. Anderson (TC)..... 590
- Emery, Ashley F. Temperature distributions downstream of a moving heat sink (TN)..... 779
- Engler, John F. and Nachbar, William. Experiments with a solid-propellant acoustic oscillator..... 1279
- Enkenhus, K. R. Effect of variable Lewis number on heat transfer in a binary gas (TN)..... 747
- Erdos, John I. and Gold, Harris. Comments on "Transition correlations for hypersonic wakes" (TC)..... 1675
- (see Pallone, Adrian J.)
- Erickson, Wayne D. (see Connor, Laurence N.)
- Eriksen, E. (see Blair, D. W.)
- Escobar, P. R. Calculation of the surface range of a ballistic missile (TN)..... 571
- Etkin, B. Dynamics of gravity-oriented orbiting systems with application to passive stabilization..... 1008
- Evans, John E. (see Meyerott, Roland E.)
- Fairbairn, A. R. Spectrum of shock-heated gases simulating the Venus atmosphere..... 1004
- Fan, L. T., Hwang, C. L., and Hwang, W. S. Convective model of Hartmann flow (TN)..... 1859
- Fanucci, J. B. (see Ness, N.)
- Fay, James A., Moffatt, W. Craig, and Probstein, Ronald F. An analytical study of meteor entry..... 845
- Faulkner, F. D. (see Bleick, W. E.)
- Fernandez, F. L. and Levinsky, E. S. Air ionization in the hypersonic laminar wake of sharp cones (TN)..... 1829
- (see Levinsky, E. S.)
- Filler, W. S. Comment on "Solid propellant driven shock tube" (TC)..... 592
- Fisher, H. Dwight (see Weiss, Harold G.)
- Fitzgerald, Robert J. Comment on "Optimal measurement and velocity correction programs for midcourse guidance" (TC)..... 968
- Fixler, Sol Zalel. Umbra and penumbra eclipse factors for satellite orbits (TN)..... 1455
- Flandro, G. A. Roll torque and normal force generation in acoustically unstable rocket motors..... 1303
- Fleming, D. P. (see Sparrow, E. M.)
- Fleming, R. O., Jr. and Fleming, R. W. Determination of propellant properties by the arc image furnace technique (TN)..... 117
- Fleming, R. W. (see Fleming, R. O., Jr.)
- Fletcher, J. D. Solar radio emission as criterion for solar proton event warning..... 2193
- Foner, S. N., Hudson, R. L., and Nall, B. H. Admittance measurements of solid propellants by an acoustic oscillator technique..... 1123
- Fong, Michael C. Similar solutions for three-dimensional laminar compressible boundary layers (TN)..... 2205
- Fontijn, A. (see Rosner, Daniel E.)
- Forray, M. and Newman, M. Analogy between three-dimensionally heated plates and generalized plane stress (TN)..... 165
- Forrette, R. E. Comment on "Relative variation of rocket vehicle specific impulse and structural weight fraction for constant burnout velocity" (TC)..... 188
- Forsberg, Kevin. Influence of boundary conditions on the modal characteristics of thin cylindrical shells..... 2150
- Forward, Robert L. Zero thrust velocity vector control for interstellar probes: Lorentz force navigation and circling..... 885
- Fox, M. G. (see McKeown, D.)
- Fraser, M. D. (see Mickle, H. S.)
- French, Edward P. Approximate absorption coefficients for vibrational electronic band systems (TN)..... 2209
- French, Kenneth E. Model law for parachute opening shock (TN)..... 2226
- Friichtenicht, J. F. (see Slattery, J. C.)
- Frink, E. P. (see Burnett, E. C.)
- Fromme, Joseph A. Least-squares approach to unsteady kernel function aerodynamics (TN)..... 1349
- Frueh, Frank J. A flutter design parameter to supplement the Regier number (TN)..... 1343
- Fuhs, Allen E. An instrument to measure velocity/electrical conductivity of arc plasma jets..... 667
- and Gibb, O. L. Plasma sheath transducer for axisymmetric reentry vehicles (TN)..... 773
- and Kelly, J. A. Zero angle-of-attack sensor (TN)..... 1492
- Gallagher, L. W. (see Chin, Jin H.)
- Gallagher, R. H. (see Gellatly, Ronald A.)
- Garvine, Richard W. Hypersonic viscous flow near a sharp leading edge (TN)..... 1660
- Gellatly, Ronald A. and Gallagher, R. H. Sandwich cylinder instability under nonuniform axial stress (TN)..... 398
- Comment on "Effective shear modulus of honeycomb cellular structures" (TC)..... 1518
- Genin, Joseph. Phase shift in a massless vibrating beam (TN)..... 118
- and Peloubet, R. P. Flutter characteristics of titanium alloys (TN)..... 1482
- Gerard, George (see Lakshminathan, C.)
- Gerstein, Melvin (see Weiss, Harold G.)
- Gersten, Robert H. and Schwarzbein, Z. E. Preliminary orbit determination from self-contained data (TN)..... 751
- Geyling, F. T. Drag displacements and decay of near-circular satellite orbits..... 1174
- Ghoshal, S. Temperature and velocity profiles along a vertical hot plate in a compressible fluid considering the effect of buoyancy (TN)..... 364
- One-dimensional flow considering buoyancy forces (TN)..... 2016
- Giannini, Gabriel M. (see Ducati, Adriano C.)
- Gibb, O. L. (see Fuhs, Allen E.)
- Gibbings, J. C. Flow in contracting ducts (TC)..... 191
- Gibbons, Edward F. (see Miller, David B.)
- Gibson, E. G. (see Zukoski, Edward E.)
- Gibson, Walter E. and Buckmaster, John D. Effects of species diffusion and heat conduction on nonequilibrium flows behind strong shocks..... 1681
- Giedt, W. H. (see Tong, Henry)
- Gierasch, P. J. (see Levy, Richard H.)
- Giere, A. C. Some energy and momentum considerations in the perforation of plates (TN)..... 1471
- Glassman, I., Sawyer, R. F., and Mellor, A. M. Propellant potential of vaporized metals in temperature-limited rocket systems (TN)..... 2049
- Gobet, Frank W. Optimal variable-thrust transfer of a power-limited rocket between neighboring circular orbits..... 339
- Errata: "Optimal variable-thrust transfer of a power-limited rocket between neighboring circular orbits" (TC)..... 2236
- Godunov, S. K. Estimate of errors for approximate solutions of the simplest equations of gasdynamics (RS)..... 208
- Gold, Harris. Laminar wake with arbitrary initial profiles (TN)..... 948
- (see Erdos, John I.)
- Gold, Richard R. (see Mirels, Harold)
- Goldberg, Gary (see Mark, Herman)
- Goldberg, Martin A. (see Pifko, Allan B.)
- Goldford, Arnold (see Migdal, David)
- Goldburg, A. (see Washburn, W. K.)
- Goodman, A. F. (see Eisner, W.)
- Goulard, Robert. Preliminary estimates of radiative transfer effects on detached shock layers..... 494
- Gourdin, M. C. (see Brandmaier, H. E.)
- (see Kahn, Bernard)
- Greenbaum, Gilbert A. Comments on "Numerical analysis of unsymmetrical bending of shells of revolution" (TC)..... 590
- Greenberg, Michael D. An improved Glauert series for certain airfoil problems (TN)..... 1666
- Grey, Jerry and Jacobs, Paul F. Experiments on turbulent mixing in a partially ionized gas..... 433
- Gribben, R. J. Three-dimensional boundary layers with a normal wall velocity (TN)..... 164
- Griffith, B. J. and Lewis, Clark H. Laminar heat transfer to spherically blunted cones at hypersonic conditions..... 438
- , Deskins, H. Eugene, and Little, H. R. Condensation studies in hotshot tunnels (TN)..... 1645
- (see Whitfield, Jack D.)
- Gross, Joseph F. (see Li, Ting-Yi)
- Gross, R. A. and Kessey, K. O. Magnetohydrodynamic species separation in a gaseous nuclear rocket..... 295
- (see Kessey, Kwadwo O.)
- Grubin, Carl. Docking dynamics for rigid-body spacecraft..... 5
- Gruszczynski, J. S. and Warren, W. R., Jr. Experimental heat-transfer of hypervelocity flight in planetary atmospheres..... 1542
- Guman, William J. and Truglio, William. Surface effects in a pulsed plasma accelerator (TN)..... 1342
- Hailey, W. C. (see Warga, J.)
- Hains, F. D. Additional modes of instability for poiseuille flow over flexible walls (TN)..... 1147
- Haldeman, Charles W. (see Covert, Eugene E.)
- Hale, Francis J. and Kerrebrock, Jack L. Insulator boundary layers in magnetohydrodynamic channels..... 461
- Hall, David F., Kemp, Robert F., and Sellen, J. M., Jr. Plasma-vehicle interaction in a plasma stream..... 1032
- Hall, Gordon R. Thrust effectiveness of oxidizer injection in a convergent-divergent nozzle..... 1434
- Hamel, Bernard B. A model for the transition regime in hypersonic rarefied gasdynamics..... 1047
- Erratum: "A model for the transition regime in hypersonic rarefied gasdynamics" (TC)..... 1679
- Harmesh, B. (see Slattery, J. C.)
- Hammer, Sanford S. and Agosta, Vito D. Longitudinal wave propagation in liquid propellant rocket motors (TN)..... 2042
- (see Peschke, William T.)
- Hammitt, A. G. Comments on "Radiation slip" (TC)..... 975
- and Carpenter, H. J. Unsteady flow past junctures in ducts (TN)..... 2224
- Hansen, C. Frederick. A radiation model for nonequilibrium molecular gases..... 611
- Harker, K. J. (see Colburn, D. S.)
- Harrison, Edwin F. Intermolecular-force effects on the thermodynamic properties of helium with application (TN)..... 1854
- Harrie, D. T. (see Reardon, F. H.)
- Hart, R. W., Bird, J. F., Cantrell, R. H., and McClure, F. T. Non-linear effects in instability of solid-propellant rocket motors..... 1270
- (see Cantrell, R. H.)
- Hassan, H. A. Exact solutions of gas-particle nozzle flows (TN)..... 395
- Hayes, J. E. (see Lin, S. C.)
- Heard, Donald E. (see Jaroudi, Riad)
- Hearne, L. F. (see Chin, Jin H.)
- Heaslet, Max A. and Baldwin, Barrett. Close analogy between radiative and conductive heat flux in a finite slab..... 2180
- Heiser, William H. Influence of magnetic fields upon separation (TN)..... 2180
- Henderson, D. B. (see Levy, Richard H.)
- Henderson, L. F. Maximum total pressure recovery across a system of n shock waves (TN)..... 1138

- Hendricks, Charles D., Jr., Carson, Ralph S., Hogan, James J., and Schneider, John M. Photomicrography of electrically sprayed heavy particles. 733
 —(see Hogan, J. J.)
- Henley, E. (see Acker, T.)
- Herrington, L. E. Correlation of motor and strand composite propellant burning rate (TN). 1671
- Herrmann, L. R. Stress functions for the axisymmetric, orthotropic, elasticity equations (TN). 1822
- Herrmann, George and Bungay, Richard W. Shell buckling and nonconservative forces (TC). 1165
- Herzl, G. G. General solution of the rigid body impact problem (TN). 959
- Hester, J. Charles and Sewell, Kenneth G. Thermodynamic properties of high-temperature helium (TN). 1329
- High, M. D. and Blick, E. F. Cone pressure distribution at large and small angles of attack (TN). 2054
- Hijman, R. (see Miller, D. S.)
- Hoelmer, W. and Saarlus, M. Weak interacting hypersonic flow over cones (TN). 1846
- Hoff, Nicholas J. (see Bushnell, David)
- Hoffman, Myron A. (see Kerrebrock, Jack L.)
- Hogan, J. J., Carson, R. S., Schneider, J. M., and Hendricks, C. D. Factors influencing electrically sprayed liquids (TN). 1460
 —(see Hendricks, Charles D., Jr.)
- Hoglund, Richard F. (see Carlson, Donald J.)
- Hollister, Donald D. A technique for the experimental determination of the electrical conductivity of plasmas. 1568
- Holloway, Paul F. (see Sterrett, James R.)
- Hopkins, Edward J. Some effects of planform modification on the skin friction drag (TC). 413
- Hopper, D. (see McKeown, D.)
- Hord, Richard A. Conical shock-wave angle (TC). 1359
- Horgan, J. J. (see Migdal, David)
- Horton, M. D. Use of the one-dimensional T-burner to study oscillatory combustion. 1112
 —(see Coates, Ralph L.)
 —(see Eisel, J. L.)
- Horton, T. E. (see Collins, D. J.)
 —(see Wolf, F.)
- Horton, W. H. and Durham, S. C. Variation in buckle shape in cylindrical shells under external pressure and axial load (TN). 943
- Houghton, Arthur V. and Acton, Russell U. Optical-acoustic effects in solid films (TN). 120
- Hoyt, Frank C. Stationary earth orbits (TN). 1470
- Hrach, Frank J. Proton fluxes along low-acceleration trajectories through the Van Allen belt (TN). 762
- Hsia, Henry Tao-Sze (see Karamcheti, Krishnamurty)
- Hsu, Pao-Tan (see Strickland, James A.)
- Hubbatt, James E. Integral solution for compressible laminar mixing (TN). 1657
- Huber, H. (see Dresser, D. L.)
- Hudson, R. L. (see Foner, S. N.)
- Hunt, James L. (see Jones, Robert A.)
- Hunziker, Raul R. Estimation of the autocorrelation functions of radio tracking errors (TN). 1135
 —Comparison of Markov and least-squares missile position and velocity estimates (TN). 2024
- Huston, Ronald L. Wave propagation in rotating elastic media (TN). 575
- Hwang, C. L. (see Fan, L. T.)
- Hwang, W. S. (see Fan, L. T.)
- Hyman, J., Jr., Eckhardt, W. O., Knechtli, R. C., and Buckley, C. R. Formation of ion beams from plasma sources: Part I. 1739
- Imber, Murray (see Rubin, Irving)
- Inami, Y. H. and Shanfield, H. Nonacoustic combustion pulsations of ammonium perchlorate containing aluminum. 1314
- Inger, George R. Nonequilibrium hypersonic flat-plate boundary-layer flow with a strong induced pressure field. 452
- Inman, Robert M. Approximation of the eigenvalues for heat transfer in laminar tube slip flow (TN). 373
- Irons, Bruce and Barlow, John. Comment on "Matrices for the direct stiffness method" (TC). 403
 —and Draper, Keith. Comment on "Derivation of element stiffness matrices" (TC). 1677
 —(see Draper, Keith J.)
- Iwanicki, L. R. and Dykema, O. W. Effect of a cavitating venturi on wave propagation in a duct (TN). 753
- Jacobs, Paul F. (see Grey, Jerry)
- Jaffe, L. D. (see Burnett, E. C.)
- Jagadeesan, K. Heat transfer due to hydromagnetic channel flow with conducting walls (TN). 756
- Jahn, Robert G. and von Jaskowsky, Woldemar. Current distributions in large-radius pinch discharges. 1749
- Jain, M. K. and Srinivasan, J. Hydromagnetic heat transfer in the thermal entrance region of a channel with electrically conducting walls. 1886
- James, Carlton S. Experimental study of radiative transport from hot gases simulating in composition the atmospheres of Mars and Venus. 470
- Janes, G. Sargent (see Levy, Richard H.)
- Janowitz, Gerald S. and Libby, Paul A. Eigenvalues for the equation of species conservation with heterogeneous reaction (TN). 1849
- Jaroudi, Riad and Heard, Donald E. Optimum geometric factors for semicircular fins in radiation-cooled nozzles (TN). 146
 —and Heard, Donald E. Errata: "Optimum geometric factors for semicircular fins in radiation-cooled nozzles" (TC). 1168
 —and McDonald, Allan J. Injection thrust termination and modulation in solid rockets (TN). 2036
- Jazwinski, Andrew H. Optimal trajectories and linear control of nonlinear systems. 1371
- Johns, D. J. Reduction of torsional stiffness due to thermal stress in thin, solid wings (TN). 1850
- Johns, Robert H. Mismatch stresses in pressure vessels (TN). 1827
- Johnson, Bruce (see Weiss, Harold G.)
- Johnston, George S. Postbuckling behavior of heated skin panels (TN). 141
- Jones, Robert A. and Hunt, James L. Use of temperature-sensitive coatings for obtaining quantitative aerodynamic heat-transfer data (TN). 1354
- Jones, Robert E. A generalization of the direct-stiffness method of structural analysis. 821
- Jones, Walter H. (see Delaney, Lawrence J.)
- Kahn, Bernard and Gourdin, Meredith C. Electrogasdynamics power generation. 1423
- Kalensher, B. E. (see Toms, Ronald S. H.)
- Kane, J. J. Nonequilibrium sodium ionization in alminar boundary layers (TN). 1651
- Kane, Thomas R. and Likins, Peter W. Comment on "Equilibrium orientations of gravity-gradient satellites" (TC). 1357
 —and Likins, Peter W. Erratum: "Comment on 'Equilibrium orientations of gravity-gradient satellites'" (TC). 1866
- Kang, Garfield and Kenehan, Martin F. Longitude positioning and orbit control of the 24-hour equatorial satellite. 991
- Kao, Hsiao C. Hypersonic viscous flow near the stagnation streamline of a blunt body: I. A test of local similarity. 1892
 —Hypersonic viscous flow near the stagnation streamline of a blunt body: II. Third-order boundary-layer theory and comparison with other methods. 1898
- Karamcheti, Krishnamurty and Hsia, Henry Tao-Sze. Reply by authors to W. Simon (TC). 1359
- Kass, Sheldon. Maximum rendezvous launch window characteristics (TN). 580
- Kaul, C. N. Anisotropic gas flow (TN). 1145
- Keefe, R. E. Natural frequencies of meridional vibration in thin conical shells (TN). 1825
- Kelley, Henry J. A second variation test for singular extremals. 1380
- Kelly, J. A. (see Fuhs, Allan E.)
- Kemp, Nelson H. Heat transfer at zero Prandtl number in flows with variable thermal properties (TN). 1864
 —Prandtl number dependence of heat transfer in Falkner-Skan flow (TC). 2062
- Kemp, Robert F. (see Hall, David F.)
- Kempner, Joseph (see Sheng, James)
 —(see Vafakos, William P.)
- Kenehan, Martin F. (see Kang, Garfield)
- Kennedy, Ernest D. Wake-like solutions of the laminar boundary-layer equations. 225
- Kenneth, Paul (see McGill, Robert)
- Kerrebrock, Jack L. Nonequilibrium ionization due to electron heating: I. Theory. 1072
 —and Hoffman, Myron A. Nonequilibrium ionization due to electron heating: II. Experiments. 1080
 —(see Hale, Francis J.)
- Kessey, Kwadwo O. Rotating electrically conducting fluids in a long cylinder. 864
 —and Gross, R. A. Gaseous nuclear rocket with MHD vortex fuel containment (TN). 1461
 —(see Gross, R. A.)
- Khazzab, Ghassan R. Significance of the Cross Correlation between the Modes of a Structure on Its Response (TN). 2211
- Kiernan, T. J. (see Krenzke, M. A.)
- King, Hartley H. and Talbot, Lawrence. Effect of mass injection on the drag of a slender cone in hypersonic flow. 836
 —(see Baum, Eric)
- Kino, G. S. (see Colburn, D. S.)
- Kirchhoff, Robert H. Calorimetric heating-rate probe for maximum-response-time interval (TN). 966
- Klaimon, Jerold H. Re-entry wake in an earth-fixed coordinate system (TN). 745
 —Hypersonic flow field around a hemisphere in a CO₂-N₂-A gas mixture (TN). 953
- Klosner, Jerome M. (see Roth, Robert S.)
- Knechtel, Earl D. and Pitts, William C. Experimental investigation of electric drag on satellites (TN). 1148
- Knechtli, R. C. (see Hyman, J., Jr.)
- Knystaustas, R. Growth of the turbulent inner wake behind 3-in.-diam spheres (TN). 1485
- Kochi, K. C. Exact first-order navigation-guidance mechanization and error propagation equations for two-body reference orbits (TN). 365
 —Exact two-body error sensitivity coefficients (TN). 1502
- Korbacher, G. K. Jet flap characteristics for high-aspect-ratio wings. 64
- Kordig, James W. Backside temperatures of an internal insulator in a solid-propellant motor (TN). 1475
- Kornecki, Aleksander. Asymptotic solution of a toroidal shell subjected to nonsymmetric loads (TN). 2020
- Koskela, Paul E. Determination of the preliminary orbits of artificial lunar and planetary satellites. 917
- Kosson, Robert L. Reply by author to R. M. Terrill (TC). 588
- Krause, Egon (see Zakkay, Victor)
- Krenzke, M. A. and Kiernan, T. J. Erratum: "Elastic stability of near-perfect shallow spherical shells" (TC). 784
- Krzywoblocki, M. Z. v. Time-dilation dilemma and scale variation (TN). 2213
- Kubota, Toshi and Dewey, C. Forbes, Jr. Momentum integral methods for the laminar free shear layer. 625
 —Reeves, Barry L., and Buss, Harvey. A family of similar solutions for axisymmetric incompressible wakes (TN). 1493
 —(see McCarthy, John F., Jr.)
- Kumagai, Tom T. Range and angle prediction tracking of objects with definable trajectories (TN). 557

- Kuo, Ta-Jin (see Zakkay, Victor)
- Kuo, Yung-Huang and Baldwin, Lionel V. Comments on "Three-dimensional effects in viscous wakes" (TC)..... 1163
- Kurzus, S. C. (see Rosner, Daniel E.)
- Kuskevics, Guntis and Thompson, Barry L. Comparison of commercial, spherical powder, and wire bundle tungsten ionizers..... 284
- Kyser, James B. Tracer-spark technique for velocity mapping of hypersonic flow fields (TN)..... 393
- Reply by author to G. Rudinger (TC)..... 1517
- Lacy, L. (see Shelton, R. D.)
- Laitone, E. V. Chaplygin's transformation applied to magnetogasdynamics (TN)..... 1856
- Lakshmikantham, C. and Gerard, George. Plastic stability of spherical plates..... 1999
- Lakshminarayana, B. Extension of lifting-line theory to a cascade of split aerofoils (TN)..... 938
- A simple device for the qualitative measurement of the vortices (TN)..... 1353
- Lam, S. H. A general theory for the flow of weakly ionized gases..... 256
- and Leigh, D. C. Inner-outer expansion method for couple-stress effects (TN)..... 1511
- Lange, Benjamin. The drag-free satellite..... 1590
- Larson, Carl A. Space station design parameter effects on artificial g field (TN)..... 1454
- Lary, E. C. (see Pinsley, E. A.)
- Laurita, W. G. (see Dresser, D. L.)
- Laurmann, J. A. Structure of the boundary layer at the leading edge of a flat plate in hypersonic slip flow (TN)..... 1655
- Lawrence, Robert LeRoy. Velocity profiles from compressible wall jets (TN)..... 574
- LeBihan, R. (see Dresser, D. L.)
- Lee, Gentry. An analysis of two-impulse orbital transfer..... 1767
- Lee, Richard S. A unified analysis of supersonic nonequilibrium flow over a wedge: I. Vibrational nonequilibrium..... 637
- Lees, Lester. Hypersonic wakes and trails..... 417
- Interaction between the solar plasma wind and the geomagnetic cavity..... 1576
- and Reeves, Barry L. Supersonic separated and reattaching laminar flows: I. General theory and application to adiabatic boundary-layer/shock-wave interactions..... 1907
- Leigh, D. C. (see Brong, E. A.)
- (see Lam, S. H.)
- Levensteins, Z. J. (see Lyons, W. C., Jr.)
- Levinson, E. S. and Fernandez, F. L. Approximate nonequilibrium air ionization in hypersonic flows over sharp cones (TN)..... 565
- (see Fernandez, F. L.)
- Levy, Richard H., Petschek, H. E., and Siscoe, G. L. Aerodynamic aspects of the magnetospheric flow (SA)..... 2065
- , Gierasch, P. J., and Henderson, D. B. Hypersonic magnetohydrodynamics with or without a blunt body..... 2091
- and Jones, G. Sargent. Plasma radiation shielding (TN)..... 1835
- Lewallen, J. M. (see Tapley, B. D.)
- Lewellen, W. S. (see Rosenzweig, M. L.)
- Lewis, Clark H. and Neel, C. A. Thermodynamic properties for imperfect air and nitrogen to 15,000°K (TN)..... 1847
- (see Griffith, B. J.)
- Lewis, Clarke H., Jr. and Carlson, Donald J. Normal shock location in underexpanded gas and gas-particle jets (TN)..... 776
- Li, Chou H. (see Oman, Richard A.)
- Li, Ting-Yi and Gross, Joseph F. Transverse curvature effects in axisymmetric hypersonic boundary layers (TC)..... 1868
- Lianis, G. (see Valanis, K. C.)
- Libby, Paul A., Baronti, Paolo O., and Napolitano, Luigi. Study of the incompressible turbulent boundary layer with pressure gradient..... 445
- and Pierucci, Mauro. Laminar boundary layer with hydrogen injection including multicomponent diffusion..... 2118
- (see Janowitz, Gerald S.)
- Librizzi, Joseph and Cresci, Robert J. Transpiration cooling of a turbulent boundary layer in an axisymmetric nozzle..... 617
- Likins, Peter W. (see Kane, Thomas R.)
- Lin, S. C. and Hayes, J. E. A quasi-one-dimensional treatment of chemical reactions in turbulent wakes of hypersonic objects..... 1214
- Lin, Y. K. Random vibration of a Myklestad beam..... 1448
- Little, H. R. (see Griffith, B. J.)
- Loeffler, A. L., Jr. (see Maciulaitis, A.)
- Louis, J. F., Decher, R., and Brogan, T. R. Production of intense radiation heat pulses (TN)..... 156
- Lubow, Anthony G. Optimal functional approximation using dynamic programming (TN)..... 376
- Luidens, Roger W. Mars nonstop round-trip trajectories (TN)..... 368
- Lundergan, C. D. (see Butcher, Barry M.)
- Lykoudis, Paul S. Length of the laminar hypersonic wake during ballistic re-entry (TN)..... 155
- Laminar compressible mixing behind finite bases (TN)..... 391
- Lyon, Richard H. and Maidanik, Gideon. Statistical methods in vibration analysis..... 1015
- Lyons, W. C., Jr., Brady, J. J., Levensteins, Z. J. Hypersonic drag, stability, and wake data for cones and spheres..... 1948
- Lysen, John C. Variable-mesh difference equation for the stream function in axially symmetric flow (TN)..... 163
- Errata: "Variable-mesh difference equation for the stream function in axially symmetric flow" (TC)..... 1359
- Maciulaitis, A. and Loeffler, A. L., Jr. A theoretical investigation of MHD channel entrance flows..... 2100
- Maddox, A. R. Laminar boundary layer with fluid injection (TN)..... 133
- Maddox, Arnold W. Heat transfer on power law bodies (TN)..... 1474
- Maidanik, Gideon (see Lyon, Richard H.)
- Maiden, C. J. and McMillan, A. R. An investigation of the protection afforded a spacecraft by a thin shield..... 1992
- Malmuth, Norman D. Three-dimensional perturbations on hypersonic wedge flow..... 1383
- Mandl, Paul. A theoretical study of the inviscid hypersonic flow about a conical flat-top wing-body combination..... 1956
- Mark, Herman, Goldberg, Gary, and Mirtich, Michael J. Determination of cratering energy densities for metal targets by means of reflectivity measurements (TN)..... 965
- Mark, Robert. A simple geometric method for analyzing polarization states in photoelasticity (TN)..... 150
- Marks, A., Barreto, E. and Chu, C. K. Charged aerosol energy converter Markson, Edward E. N th order solutions to certain thrust integrals (TN)..... 381
- Marlotte, Gary L. (see Cann, Gordon L.)
- Martellucci, Anthony. Boundary-layer transition on a slender cone in hypersonic flow (TN)..... 771
- Martens, H. E. (see Burnett, E. C.)
- Maslen, S. H. Inviscid hypersonic flow past smooth symmetric bodies..... 1055
- Mathieu, Richard D. Mechanical spallation of charring ablators in hyperthermal environments..... 1621
- Maus, James R. and Snyder, William T. Effect of boundary-layer removal on high velocity flame stabilization (TN)..... 2030
- Mayer, E. and Divoky, D. Transpiration and film cooling combined with external cooling (TN)..... 578
- McAlevy, R. F., III (see Acker, T.)
- McCarthy, John F., Jr. and Kubota, Toshi. A study of wakes behind a circular cylinder at $M = 5.7$ 629
- McChesney, Malcolm. One-dimensional Rayleigh flow of a partially ionized gas (TC)..... 1866
- McClure, F. T. (see Cantrell, R. H.)
- (see Hart, R. W.)
- McCue, Gary A. Optimization and visualization of functions (TN)..... 99
- McDonald, Allan J. (see Jaroudi, Riad)
- McElman, John A. Flutter of two parallel flat plates connected by an elastic medium (TN)..... 377
- McGill, Robert and Kenneth, Paul. Solution of variational problems by means of a generalized Newton-Raphson operator..... 1761
- McKeown, D., Fox, M. G., Schmidt, J. J., and Hopper, D. Sputtering in the upper atmosphere (TN)..... 400
- , Fox, M. G., Schmidt, J. J., and Hopper, D. Reply by authors to R. V. Stuart (TC)..... 1678
- McMillan, A. R. (see Maiden, C. J.)
- Meissinger, H. F. (see Citron, S. J.)
- Melcher, B. W., II (see Taylor, R. L.)
- (see Washburn, W. K.)
- Mellor, A. M. (see Glassman, I.)
- Mellor, G. L. Equilibrium turbulent boundary layers (TN)..... 1650
- Menkes, J. Scattering of radar waves by an underdense turbulent plasma (TN)..... 1154
- Mercer, R. J. Calculation of gravitational force components (TC)..... 1166
- Meyerand, R. G., Jr. (see Pinsley, E. A.)
- Meyerott, Roland E. and Evans, John E. Auroral measurements and upper atmospheric physics..... 1169
- Michael, I. (see Bhattacharjee, A.)
- Michelson, Irving. Reply by author to T. R. Kane and P. W. Likins (TC)..... 1357
- Euler angles for libration analysis (TN)..... 1469
- Mickle, H. S., Smith, K. A., and Fraser, M. D. Velocity defect law for a transpired turbulent boundary layer (TN)..... 173
- and Smith, K. A. Reply by authors to H. Tennekes (TC)..... 415
- Migdal, David, Horgan, J. J., and Chamay, A. An experimental evaluation of plug cluster nozzles (TN)..... 1325
- and Goldford, Arnold. Exact kinetic and approximate nozzle recombination losses (TN)..... 1457
- Miles, John B. Heat diffusion from line source into mixing region of two parallel streams (TN)..... 2038
- Miller, David B. and Gibbons, Edward F. Experiments with an electron cyclotron resonance plasma accelerator..... 35
- Miller, D. S., Hijman, R., and Childs, M. E. Mach 8 to 22 studies of flow separations due to deflected control surfaces..... 312
- Miller, R. H. Rotor blade harmonic air loading..... 1254
- Milligan, Mancil W. Nozzle characteristics in the transition regime between continuum and free molecular flow..... 1088
- Millikan, Roger C. (see White, Donald R.)
- Milstead, Andrew H. Location of catch-up point in a ΔV perturbed circular orbit (TN)..... 940
- Minkowycz, W. J. (see Sparrow, E. M.)
- Mirels, Harold. Shock tube test time limitation due to turbulent-wall boundary layer..... 84
- Analytical solution for constant enthalpy MHD accelerator (TN)..... 145
- , Gold, Richard R., and Mullen, James F. Minimum-length MHD accelerator with constant enthalpy and magnetic field (TN)..... 1141
- Mirtich, Michael J. (see Mark, Herman)
- Mitchell, Thomas P. (see Clancy, Thomas F.)
- Moffatt, W. Craig. Analysis of MHD channel entrance flows using the momentum integral method (TN)..... 1495
- (see Fay, James A.)
- Moore, Jeffrey A. (see Pallone, Adrian J.)
- Moran, John P. Addendum: "The vertical water-exit and -entry of slender symmetric bodies" (TN)..... 1480
- Moreland, William J. Comment on "Mathematical analysis of corotating nose-gear shimmy phenomenon" (TC)..... 415
- Morkovin, Mark V. Aerodynamic loads on bluff bodies at low speeds (TC)..... 2058
- Morizumi, S. J. Analytical determination of shape factors from a surface element to an axisymmetric surface (TN)..... 2028
- Muehlberger, Erich (see Ducati, Adriano C.)
- Muhuri, P. K. Hydromagnetic flow between two rotating cylinders (TN)..... 1328
- Mullen, James F. (see Mirels, Harold)

- Munson, D. E. (see Butcher, Barry M.)
- Nachbar, William (see Engler, John F.)
- Nall, B. H. (see Foner, S. N.)
- Napier, D. H., Nettleton, M., Simonson, J. R., and Thackeray, D. P. C. Temperature measurement in a chemical shock tube by sodium-line reversal and C_2 reversal methods (TN) 1136
- Napolitano, Luigi (see Libby, Paul A.)
- Nardo, S. V. Ablation of a cylindrical cavity in an infinite medium (TN) 936
- Nedderman, R. M. Comment on "Method for the determination of velocity distribution in a thin liquid film" (TC) 1865
- Neel, C. A. (see Lewis, Clark H.)
- Nelson, Edward O. Angle of attack from body-fixed rate gyros (TN) 1324
- Nerem, Robert M. and Stickford, George H. Radiative and convective heating during hypervelocity re-entry (TN) 1156
- and Stickford, George H. A thin-film radiative heat-transfer gage (TN) 1647
- Ness, N. and Fanucci, J. B. Pressure gradient effects on nonequilibrium far wakes (TN) 1514
- Nettleton, M. (see Napier, D. H.)
- Neuringer, Joseph L. Induced forces in annular magneto-fluid dynamic traveling wave devices 267
- and Turner, James H. Small magnetofluid-dynamic peristaltic motions inside an annular circular cylindrical induction compressor 2076
- Newman, M. (see Forray, M.)
- Newton, Robert R. Damping of a gravitationally stabilized satellite 20
- Nicoll, Kenneth M. A study of laminar hypersonic cavity flows 1535
- Niedenfuhr, F. W. Reply by author to G. Herrmann and R. W. Bungay (TC) 1166
- Nissel, Neil (see Vafakos, William P.)
- Noble, L. M. (see Scarf, F. L.)
- Nowinski, J. L. Large-amplitude oscillations of oblique panels with an initial curvature 1025
- Oberai, Madan Mohan (see Devan, Leroy)
- Odian, G. (see Acker, T.)
- Olfe, D. B. Radiation-perturbed flow fields of normal and oblique shock waves 1928
- Oman, Richard A., Bogan, Alexander, Weiser, Calvin H., and Li, Chou H. Interactions of gas molecules with an ideal crystal surface 1722
- Orlik-Rückemann, Kazimierz J. Quadratic effects of frequency on aerodynamic derivatives (TN) 1507
- Osborn, J. R. Longitudinal mode instability (TC) 2237
- Page, R. H. and Dixon, R. J. A transformation for wake analyses (TN) 1464
- Pallone, Adrian J., Erdos, John I., and Eckerman, Jerome. Hypersonic laminar wakes and transition studies 855
- , Moore, Jeffrey A., and Erdos, John I. Nonequilibrium, non-similar solutions of the laminar boundary-layer equations 1706
- (see Wood, Albert D.)
- Pao, Yih-Ho. Statistical behavior of a turbulent multicomponent mixture with first-order reactions 1550
- Pao, Yih-Hsing and Chao, C. C. Diffractions of flexural waves by a cavity in an elastic plate 2004
- Park, Chul. Heat transfer from nonequilibrium ionized argon gas (TN) 169
- Dissociative relaxation in viscous hypersonic shock layers 1202
- Parr, O. Flow in the three-dimensional boundary layer on a spinning body of revolution (TN) 361
- Paul B. Shadows produced by spin-stabilized communication satellites 924
- Pauli, J. W. Identification of two types of separation (TN) 2202
- Paynter, Howard L. Time for a totally wetting liquid to deform from a gravity-dominated to a null-gravity equilibrium state 1627
- Peloubet, R. P. (see Geinin, Joseph)
- Penner, S. S. and Thomas, M. Approximate theoretical calculation of continuum opacities 1572
- Evaporation coefficients from exposure of a solid to laser radiation (TN) 1664
- Penzien, Joseph and Didriksson, Theodor. Effective shear modulus of honeycomb cellular structure 531
- and Didriksson, Theodor. Reply by authors to R. A. Gellatly (TC) 1519
- Perko, Lawrence M. Interplanetary trajectories in the restricted three-body problem 2187
- Persson, S. Lennart. Method for determination of velocity distribution in a thin liquid film (TN) 372
- Reply by author to R. M. Nedderman (TC) 1866
- Peschke, William T. and Hammer, Sanford S. Pressure gradients in a liquid propellant rocket motor (TN) 1467
- Peskin, Richard L. and Raco, Roland J. Drop size from a liquid jet in a longitudinal electric field (TN) 781
- Petersen, Eugene E. (see Shannon, Larry J.)
- Petschek, H. E. (see Levy, Richard H.)
- Phinney, Ralph. Nondimensional solutions of flows with vibrational relaxation 240
- Piacesi, R., Waser, R. H., and Dawson, V. C. D. Temperature yield strength correlation in hypervelocity impact (TN) 2040
- Pian, Theodore H. H. Derivation of element stiffness matrices (TN) 576
- Derivation of element stiffness matrices by assumed stress distributions (TN) 1333
- (see Stricklin, James A.)
- Pierucci, Mauro (see Libby, Paul A.)
- Pifko, Allan B. and Goldberg, Martin A. Iterative and power series solutions for the large deflection of an annular membrane (TN) 1340
- and Goldberg, Martin A. Reply by authors to J. G. Simmonds (TC) 2234
- Pigache, D. A semitoroidal reflex discharge as a propulsion device (TN) 1332
- Pines, Samuel. Constants of the motion for optimum thrust trajectories in a central force field 2010
- Pinsley, E. A., Lary, E. C., and Meyerand, R. G., Jr. Comment on "Propulsion application of the modified penning arc plasma ejector" (TC) 401
- Pisacane, Vincent L. Particle motion in the equatorial plane 1361
- Pitts, William C. (see Knechtel, Earl D.)
- Platou, Anders S. (see Benton, Edward R.)
- Pohle, Frederick V. A dynamical model for Kordylewski cloud satellites (TN) 1818
- Potter, J. Leith and Whitfield, Jack D. Comment on "Effects of controlled roughness on boundary-layer transition at a Mach number of 6.0" (TC) 407
- and Bailey, Allan B. Pressures in the stagnation regions of blunt bodies in rarefied flow (TN) 743
- Potter, R. A. (see Shelton, R. D.)
- Pottsepp, Lembit (see Rott, Nicholas)
- Povinelli, Louis A. and Rosenstein, Robert A. Alumina size distributions from high-pressure composite solid-propellant combustion 1754
- Powers, Sidney A. Drag minimization using exact methods (TN) 941
- Pozi, A. Viscous jets from nonnarrow orifices (TN) 949
- Price, E. W. (see Crump, J. E.)
- (see Eisel, J. L.)
- Pringle, Ralph, Jr. Bounds on the librations of a symmetrical satellite 908
- Probstein, Ronald F. Reply by author to A. G. Hammitt (TC) 976
- (see Fay, James A.)
- Progelhof, R. C. Determination of the mass of gas in a rapidly discharging vessel (TN) 137
- Pressure variation in a tank undergoing an acceleration (TN) 1505
- Przemieniecki, J. S. Tetrahedron elements in the matrix force method of structural analysis (TN) 1152
- Punga, Valdemars. Euler's moment equations for a variable-mass unsymmetrical top (TN) 937
- Motion of the center of gravity of a variable-mass body (TN) 1482
- Raat, Jan. Skin friction of slender cones in hypersonic flow (TN) 755
- Raco, Roland J. (see Peskin, Richard L.)
- Radbill, John R. Application of quasilinearization to boundary-layer equations (TN) 1860
- Radkowski, Peter P. (see Budiansky, Bernard)
- Radtke, Leonard P. and Eastman, Donald W. Reply by authors to L. Roberts and J. C. South Jr. (TC) 973
- Ragland, K. W., Cosens, G. L., and Cullen, R. E. Detonation of hydrogen-oxygen at low temperature and high pressure (TN) 142
- Rastrelli, L. U. (see Bynum, D. J.)
- Ray, Ajit Kumar. Three-dimensional symmetric vortex flow (TN) 2218
- Raynor, S. (see Byrne, W. J., Jr.)
- Reardon, F. H., Crocco, L., and Harje, D. T. Velocity effects in transverse mode liquid propellant rocket combustion instability 1631
- Rebrov, A. K. Free molecular heat transfer near a wall (RS) 215
- Reeves, Barry L. (see Kubota, Toshi)
- (see Lees, Lester)
- Resler, E. L., Jr. and Rosensweig, R. E. Magnetocaloric power 1418
- Rice, D. W. Effect of oxidizer concentration on combustion instability of a solid propellant (TN) 1654
- (see Eisel, J. L.)
- Rigdon, W. S. (see Thomas, M.)
- Rittenhouse, L. E. (see Tempelmeier, K. E.)
- Roberts, J. H. and Webb, M. J. Measurement of droplet size for wide range particle distributions (TN) 583
- Roberts, Leonard and South, Jerry C., Jr. Comments on exhaust flow field and surface impingement (TC) 971
- Robertson, Richard L. Comment on "Design analysis of earth-lunar trajectories: launch and transfer characteristics" (TC) 969
- Rodden, William P. Flutter of multibay panels at supersonic speeds (TN) 1476
- Rom, Josef and Segner, Arnan. Laminar heat transfer to a two-dimensional backward facing step from the high-enthalpy supersonic flow in the shock tube 251
- Romagnoli, Robert J. Optimization of window-type filters for silicon solar cells (TN) 101
- Romero, Jacob B. Fuel containment in the gaseous-core nuclear rocket by MHD-driven vortices 1092
- Romig, Mary F. Comment on "Conical shock-wave angle" (TC) 2232
- Rosebrock, T. L., Clingman, D. L., and Gubbins, D. G. Pulsed electromagnetic acceleration of metal plasmas 328
- Rosen, B. Walter. Tensile failure of fibrous composites 1985
- Rosenbaum, Harold (see Edelman, Raymond)
- Rosenstein, Robert A. (see Povinelli, Louis A.)
- Rosenzweig, M. L., Lewellen, W. S., and Ross, D. H. Confined vortex flows with boundary-layer interaction 2127
- Rosenweig, R. E. (see Resler, E. L., Jr.)
- Roshko, Anatol and Smith, Jerome A. Measurements of test time in the GALTIT 17-inch shock tube (TN) 186
- Rosler, Richard S. Rapid estimation of the far-field in an axisymmetric compressible jet (TN) 1489
- Rosner, Daniel E. Convective diffusion as an intruder in kinetic studies of surface catalyzed reactions (SA) 593
- , Fontijn, A., and Kurzius, S. C. Chemical scavenger probes in nonequilibrium gasdynamics (TN) 779
- Analysis of air arc-tunnel heat-transfer data (TN) 945
- Ross, D. H. (see Rosenzweig, M. L.)
- Roth, Robert S. and Klosner, Jerome M. Nonlinear response of cylindrical shells subjected to dynamic axial loads 1788
- Rothacker, D. L. (see Sheer, C.)
- Rott, Nicholas and Pottsepp, Lembit. Simplified calculation of the jet-damping effects (TN) 764
- Rubel, A. (see Brandmaier, H. E.)
- Rubin, Irving and Imber, Murray. Optimization study of space radiators 353
- Ruder, Joseph M. Stratification in a pressurized container with sidewall heating (TN) 135

- Rudinger, George. Comments on "Tracer-spark technique for velocity mapping of hypersonic flow fields" (TC)..... 1517
- Ruger, Charles J. Skip-impact criteria of a re-entry trajectory with negative lift (TN)..... 585
- Rumpel, W. F. (see Chapin, S. G.)
- Ryan, Norman W. and Coates, Ralph L. Acoustic instability: influence of and on the solid phase..... 1130
—(see Coates, Ralph L.)
- Saarias, M. Reference temperature method for computing displacement thickness (TN)..... 2056
—(see Hoelmer, W.)
- Safran, Harris. Back-scattering properties of moon and earth at X band (TN)..... 100
- Salomonovich, A. E. Some results obtained with the 22-meter radio telescope (RS)..... 193
- Salzman, P. K. Determination of the maximum transmitted shock at the interface between two condensed media (TN)..... 359
- Sandborn, V. A. and Baldwin, L. V. Hot-wire calorimeter study of ion production and acceleration..... 660
- Sastry, M. S. A note on "Pressure distribution for hypersonic boundary-layer flow" (TN)..... 961
- Sauerwein, Harry and Sussman, Mark. Numerical stability of the three-dimensional method of characteristics (TN)..... 387
- Sawyer, R. F. (see Glassman, I.)
- Scarf, F. L. and Noble, L. M. Dynamics of the solar wind (TN)..... 1158
- Schapery, R. A. Effect of cyclic loading on the temperature in viscoelastic media with variable properties..... 827
- Schechter, Hans B. Dumbbell librations in elliptic orbits..... 1000
- Schjelderup, H. C. and Ball, Robert E. Final shape of a dynamically loaded elastic-plastic redundant structure (TN)..... 958
- Schlegel, Leo B. and Bonomo, Philip J. Improved calculation of vacuum vertical trajectories (TN)..... 1487
- Schmidt, J. J. (see McKeown, D.)
- Schneider, John M. (see Hendricks, Charles D., Jr.)
—(see Hogan, J. J.)
- Schuerch, Hans U. Effect of diameter upon elastic properties in thin fibers (TN)..... 569
—and Burggraf, Odus R. Analytical design for optimum filamentary pressure vessels..... 809
- Schurmann, E. E. H. (see Thyson, N. A.)
- Schwarzbein, Z. E. (see Gersten, Robert H.)
- Scott, Ronald F. (see Burnett, E. C.)
- Seginer, Arnan (see Rom, Josef)
- Sehgal, Robert and Strand, Leon. A theory of low-frequency combustion instability in solid rocket motors..... 696
- Sellen, J. M., Jr. (see Hall, David F.)
- Serpico, Joseph C. Elastic stability of conical shells under axisymmetric pressure band loadings (TN)..... 389
- Sevik, M. Elastic stability of castellated plates (TN)..... 174
—Lift on an oscillating body of revolution..... 302
—Lift on an oscillating ellipsoid of revolution..... 646
- Sewell, Kenneth G. (see Hester, J. Charles)
- Shaffer, Bernard W. Stress-strain relations of reinforced plastics parallel and normal to their internal filaments..... 348
- Shaffer, Francis B. Probability of meteoroid penetration..... 738
- Shair, F. H. Interaction of an oscillating magnetic field with fluid in Couette flow (TN)..... 1510
—Theoretical performance comparison of working fluids in a nonequilibrium MHD generator..... 1883
—A compatibility equation for nonequilibrium ionization (TN)..... 2026
- Shane, Edward D. Equilibrium electron density on Mars (TN)..... 1497
- Shanfield, H. (see Inami, Y. H.)
- Shannon, Larry J. and Petersen, Eugene E. Deflagration characteristics of ammonium perchlorate strands (TN).....
—(see Anderson, Ralph)
- Sharman, P. W. Reply by author to J. Singer (TC)..... 411
- Sheer, C., Cooney, J. A., and Rothacker, D. L. Fluid transpiration through anodic boundary of an electric arc..... 483
- Shelton, H. (see Cho, A. Y.)
- Shelton, R. D., Potter, R. A., Lacy, L., and Stuhlinger, E. Evaluation and analysis of thrust units for power-limited propulsion systems..... 682
- Sheng, James and Kempner, Joseph. Errata: "Residual analysis for circular cylindrical shells under segmental line-load" (TC)..... 784
- Shih, W. C. L. and Baron, J. R. Nonequilibrium blunt-body flow using the method of integral relations..... 1062
- Shinozuka, M. Stresses in an incompressible viscoelastic-plastic thick-walled cylinder..... 1800
—(see Bieniek, M. P.)
- Sichel, Martin. Integral equations for viscous hypersonic nozzle flow (TN)..... 148
—Effect of the boundary layer upon the flow in a conical hypersonic nozzle (TN)..... 180
- Simmonds, James G. Comments on "Iterative and power series solutions for the large deflection of an annular membrane" (TC)..... 2233
- Simon, Wayne E. Comments on "Mach number independence of the conical shock pressure coefficient" (TC)..... 411
—Comments on "Integral approach to an approximate analysis of thrust vector control by secondary injection" (TC)..... 1358
- Simonson, J. R. (see Napier, D. H.)
- Singer, Josef. Comment on "A theoretical interaction equation for the buckling of circular shells under axial compression and external pressure" (TC)..... 410
- Singh, B. (see Yen, Shee-Mang)
- Singh, M. P. Oscillating sphere in a rotating viscous fluid (TN)..... 1513
- Sirignano, W. A. and Crocco, L. A shock wave model of unstable rocket combustors..... 1285
- Siscoe, G. L. (see Levy, Richard H.)
- Skalak, Richard and Conly, John F. Surface waves on a rotating fluid..... 306
- Slattery, J. C., Frichtenicht, J. F., and Hamermesh, B. Interaction of micrometeorites with gaseous targets..... 543
- Smith, C. Edward, Jr. Intermolecular-force effects on the thermodynamic properties of nitrogen (TN)..... 183
- Smith, Jerome A. (see Roshko, Anatol)
- Smith, K. A. (see Mickley, H. S.)
- Smith, Myron C. and Wu, Ching-Sheng. Magnetohydrodynamic hypersonic viscous flow past a blunt body (TN)..... 963
- Snyder, V. W. Comment on "An alternate interpretation of Newton's second law (TC)..... 2239
- Snyder, William T. (see Maus, James R.)
- Sobel, L. H. Effects of boundary conditions on the stability of cylinders subject to lateral and axial pressures..... 1437
- Sotter, G. (see Swithenbank, J.)
- South, Jerry C., Jr. (see Roberts, Leonard)
- Spauld, Frank W. (see Zukoski, Edward E.)
- Sparrow, E. M. and Fleming, D. P. Temperature recovery factors for flow longitudinal to a circular cylinder (TN)..... 386
—, Minkowycz, W. J., and Eckert, E. R. G. Diffusion-thermo effects in stagnation-point flow of air with injection of gases of various molecular weights into the boundary layer..... 652
- Spence, D. A. Reply by author to N. H. Kemp (TC)..... 2063
- Speyer, Jason L. (see Denham, Walter F.)
- Spiegel, J. M. (see Collins, D. J.)
- Spier, Edward E. (see Wilson, Paul E.)
- Spindler, Fred and Wang, Kenneth. MGD space propulsion system for lunar missions (TN)..... 152
- Springer, George S. and Tsai, Steven W. Effect of thermal accommodation on cylinder and sphere drag in free molecule flow (TN)..... 126
- Springfield, James F. (see Wood, Albert D.)
- Srinivasan, A. V. Buckling load of bars with variable stiffness: a simple numerical method (TN)..... 139
- Srinivasan, J. (see Jain, M. K.)
- Srivastava, A. C. Flow of second-order fluids with heat transfer (TN)..... 749
- Stai, Donald F. (see Bizjak, Frank)
- Stalker, R. J. Area change with a free-piston shock tube (TN)..... 396
- Stancil, R. T. A new approach to steepest-ascent trajectory optimization..... 1365
- Stearman, Ronald. Flutter of a ring of panels..... 1441
- Steele, C. R. Orthotropic pressure vessels with axial constraint..... 703
- Steg, Leo. An introduction and appreciation..... 1
- Steginsky, Bernard. Calculation of cylindrical blast wave propagation with counterpressure (TN)..... 175
- Steiger, Martin H. and Bloom, Martin H. Linearized viscous free mixing with streamwise pressure gradients..... 263
—Similarity in axisymmetric viscous free mixing with streamwise pressure gradient (TN)..... 1509
—(see Bloom, Martin H.)
- Sterrett, James R. and Holloway, Paul F. Reply by authors to J. L. Potter and J. D. Whitfield (TC)..... 408
- Stevenson, T. Neil. Turbulent boundary layers with transpiration (TN)..... 1500
- Steverding, B. Surface activity and preferential ablation (TN)..... 549
—Comment on non-Newtonian flow (TC)..... 2231
- Stewart, Roger B. A calorimeter study of a magnetically stabilized arc-heater (TN)..... 384
- Stewartson, K. Falkner-Skan equations for wakes (TN)..... 1327
- Stickford, George H. (see Nerem, Robert M.)
- Stoker, Joseph H. Use of stress relaxation tests to characterize time dependencies of a composite solid propellant (TN)..... 1816
- Strack, Sainsbury L. Supersonic pitot tube measurements at an angle of attack (TN)..... 778
- Strand, Leon (see Sehgal, Robert)
- Strehlow, Roger A. Detonation initiation (TC)..... 783
- Stricklin, James A., Hsu, Pao-Tan, and Pian, Theodore H. H. Large elastic, plastic, and creep deflections of curved beams and axisymmetric shells..... 1613
- Stuart, R. V. Comments on "Sputtering in the upper atmosphere" (TC)..... 1678
- Stuhlinger, E. (see Shelton, R. D.)
- Sussman, Mark (see Sauerwein, Harry)
- Suzuki, Bob H. (see Tong, Henry)
- Swigart, Rudolph, J. Hypersonic blunt-body flow fields at angle of attack (TN)..... 115
- Swithenbank, J. and Sotter, G. Vortex generation in solid propellant rockets..... 1297
- Switzky, Harold. Deformations and stresses in an axially restrained beam (TN)..... 109
- Tabakoff, Widen (see Tepe, Frank R., Jr.)
- Talbot, Lawrence. Reply by author to J. Aroesty (TC)..... 190
—(see King, Hartley H.)
- Tankin, Richard S. (see Abbadi, Beshir A.)
- Tapley, B. D. and Lewallen, J. M. Solar influence on satellite motion near the stable earth-moon libration points..... 728
- Tasi, James. Effect of mass loss on the transient response of a shallow spherical sandwich shell..... 58
- Taylor, R. L. Creep and relaxation (TN)..... 1659
- , Melcher, B. W., II, and Washburn, W. K. Studies of the luminous hypersonic wake..... 1731
- Tellep, D. M. (see Edwards, D. K.)
- Temkin, S. (see Dobbins, Richard A.)
- Tempelmeyer, K. E. and Rittenhouse, L. E. Vortex flow in arc heaters (TN)..... 766
- Tennekes, H. Comment on "Velocity defect law for a transpired turbulent boundary layer" (TC)..... 414
- Tennyson, R. C. Buckling of circular cylindrical shells in axial compression (TN)..... 1351
- Tepe, Frank R., Jr. and Tabakoff, Widen. Shock interaction in a hypersonic flow (TN)..... 1478
- Terrill, R. M. Comment on "An approximate solution for laminar boundary layer flow" (TC)..... 587
- Thackeray, D. P. C. (see Napier, D. H.)

- Thomas, M. and Rigdon, W. S. A simplified formulation for radiative transfer (TN)..... 2052
 —(see Penner, S. S.)
- Thomas, Richard E. (see Brooke, Darrell)
- Thompson, Barry L. (see Kuskevics, Guntis)
- Thompson, Philip A. Jet-driven resonance tube..... 1230
- Throne, James L. Stability of the hodograph equations in one-dimensional reacting gas flow (TN)..... 360
- Thurman, William E. A flow-separation spike for hypersonic control of a hemisphere-cylinder (TN)..... 159
- Thurston, Gaylen A. Asymmetrical buckling of spherical caps under uniform pressure (TN)..... 1832
- Thyson, N. A. and Schurmann, E. E. H. Reply by authors to T.-Y. Li and J. F. Gross (TC)..... 1869
- Ting, Lu. Effect of shock-induced vorticity on the compressible boundary layer along a flat plate..... 490
- Toba, Kaoru (see Zakkay, Victor)
- Toms, Ronald S. H. and Kalensher, B. E. Control of a synchronous satellite by continuous radial thrust..... 1179
- Tong, Henry and Giedt, W. H. Supersonic stagnation point heat transfer at low Reynolds numbers (TN)..... 185
- and Suzuki, Bob H. Stagnation-point heat transfer to surfaces of arbitrary catalytic (TN)..... 2051
- Touryan, K. J. Transient temperature variation in a thermally orthotropic cylindrical shell (TN)..... 124
- Density distribution over a moving circular plate in free-molecule flow (*U*) (TN)..... 559
- Traugott, S. C. A transonic experiment at hypersonic speed..... 1521
- Truglio, William (see Guman, William J.)
- Truitt, Robert W. Reply by author to K. N. C. Bray (TC)..... 1162
- Tsai, D. H. Flow field in a swirl chamber (TN)..... 1504
- Tsai, Steven W. (see Springer, George S.)
- Tsao, C. H. Strain-displacement relations in large displacement theory of shells (TC)..... 2060
- Tung, Chee. Instability of three-row vortex streets (TN)..... 1143
- Turner, James H. (see Neuringer, Joseph L.)
- Vafakos, William P., Nissel, Neil, and Kempner, Joseph. Energy solution for simply supported oval shells (TN)..... 555
- Valanis, K. C. and Lianis, G. Thermal stresses in a viscoelastic cylinder with temperature dependent properties (TN)..... 1642
- Vinh, N. X. Comment on "Interception of high-speed target by beam rider missile" (TC)..... 409
- A property of cotangential elliptical transfer orbits (TN)..... 1841
- Vogler, Frank Henry. Analysis of an electrostatic shield for space vehicles..... 872
- Vojvodich, Nick S. and Pope, Ronald B. Effect of gas composition on the ablation behavior of a charring material..... 536
- von Jaskowsky, Woldemar (see Jahn, Robert G.)
- Voss, H. M. and Dowell, E. H. Effect of aerodynamic damping on flutter of thin panels (TN)..... 119
- Wadsworth, Donald van Zelm. Payload scaling laws for boost rockets (TN)..... 2223
- Wall, John K. Theoretical penetration of hypervelocity projectiles into massive targets..... 1242
- Wan, Koon Sang. Turbulent wake characteristics with different eddy viscosity coefficients (TN)..... 121
- Wang, Chang-Yi. Contours for stagnation-point mass injection in hypersonic flow (TN)..... 178
- Wang, Kenneth (see Spindler, Fred)
- Warga, J. and Hailey, W. C. Determination of extreme entry angles into a planetary atmosphere..... 335
- Warren, William E. Bending of rhombic plates (TN)..... 166
- Warren, W. R., Jr. (see Gruszczynski, J. S.)
- Waser, R. H. (see Piacetti, R.)
- Washburn, W. K., Goldberg, A., and Melcher, B. W., II. Hypersonic cone wake velocities obtained from streak pictures (TN)..... 1465
- (see Taylor, R. L.)
- Watkins, Jerry D. and Clary, Robert R. Vibrational characteristics of thin-wall conical frustum shells (TN)..... 1815
- Webb, M. J. (see Roberts, J. H.)
- Webb, Wilmot, H. Self-preserving fluctuations and scales for the hypersonic turbulent wake (TN)..... 2031
- Weil, Herschel. Broadside radar echoes from ionized trails..... 429
- Weingarten, V. I. Free vibration of thin cylindrical shells..... 717
- Stability of internally pressurized conical shells under torsion..... 1782
- Weiser, Calvin H. (see Oman, Richard A.)
- Weiss, Harold G., Johnson, Bruce, Fisher, H. Dwight, and Gerstein, Melvin. Modification of the hydrazine-nitrogen tetroxide ignition delay (TN)..... 2223
- Weissenburger, J. T. Integration of discontinuous expressions arising in beam theory (TN)..... 106
- Wells, Curtis Sinclair, Jr. Unsteady boundary-layer flow of a non-Newtonian fluid on a flat plate (TN)..... 951
- Reply by author to B. Steverding (TC)..... 2232
- Wells, William R. Re-entry heat conduction of a finite slab with a nonconstant thermal conductivity (TN)..... 379
- In-plane lunar injection opportunities from an orbiting space station (TN)..... 383
- Wen, Kwan-Sun. Wake transition (TN)..... 956
- Westerman, H. Robert. Comment on "Orbital motion in the theory of general relativity" (TC)..... 1869
- Wetherall, C. J. (see Bird, G. A.)
- Wetzel, Lewis. Far-flow approximations for precursor ionization profiles..... 1208
- White, Donald R. and Millikan, Roger C. Vibrational relaxation in air (TN)..... 1844
- Whitfield, Jack D. and Griffith, B. J. Hypersonic viscous drag effects on blunt slender cones..... 1714
- (see Potter, J. Leith)
- Wiggins, Lyle E. Relative magnitudes of the space-environment torques on a satellite (TN)..... 770
- Wilke, Kenneth A. Numerical study of hydrogen-fluorine kinetics in nozzles (TN)..... 374
- "Equilibrium" gas composition computation with constraints (TC)..... 409
- Wilke, R. O. Comment on "Coning effects caused by separation of spin-stabilized stages" (TC)..... 1358
- Williams, Harry E. A "membrane" solution for axisymmetric heating of dome-shaped shells of revolution (TN)..... 1491
- Williams, M. L. Structural analysis of viscoelastic materials (SA)..... 785
- Wilson, Howard B., Jr. Mathematical determination of stresses and displacements in star-perforated grains..... 1247
- Wilson, Paul E. and Spier, Edward E. Nonlinear pressure coupling in cylindrical shell analysis (TN)..... 370
- Winicur, Daniel H. Electric propulsion characteristics of a pulsed plasma rail accelerator (TN)..... 1673
- Winslow, P. M. Ion engine reliability as affected by corrosion of materials..... 42
- Wolf, F. and Horton T. Effect of argon addition on shock-layer radiance of CO₂-N₂ gas mixtures (TN)..... 1472
- Woo, Stephen D. L. (see Zakkay, Victor)
- Wood, Albert D., Springfield, James F., and Pallone, Adrian J. Chemical and vibrational relaxation of an inviscid hypersonic flow..... 1697
- Wu, Ching-Sheng (see Smith, Myron C.)
- Yamanaka, Tatsuo. Sonic line of magnetohydrodynamic nozzle flow (TN)..... 2203
- Yen, K. T. Effect of microwave radiation on the ionized gas behind a strong normal shock wave..... 71
- Reply by author to M. McChesney (TN)..... 1867
- Yen, Shee-Mang and Singh, B. Laminar boundary-layer development on yawed cone (TN)..... 775
- Yount, R. A. and Angelus, T. A. Chuffing and nonacoustic instability phenomena in solid propellant rockets..... 1307
- Yu, E. Y. Long-term coupling effects between librational and orbital motions of a satellite (TN)..... 553
- Yuan, S. W. and Bloom, A. M. An analytical approach to hypervelocity impact (TN)..... 1667
- Zakkay, Victor, Toba, Kaoru, and Kuo, Ta-Jin. Laminar, transitional, and turbulent heat transfer after a sharp convex corner..... 1389
- Krause, Egon, and Woo, Stephen D. L. Turbulent transport properties for axisymmetric heterogeneous mixing..... 1939
- Zeiberg, Seymour L. Transition correlations for hypersonic wakes (TN)..... 564
- Oxygen-electron attachment in hypersonic wakes (TN)..... 1151
- and Bleich, Gary D. Finite-difference calculation of hypersonic wakes..... 1396
- Reply by author to J. I. Erdos and H. Gold (TC)..... 1677
- Zukoski, Edward E., Cool, T. A. and Gibson, E. G. Experiments concerning nonequilibrium conductivity in a seeded plasma..... 1410
- and Spaid, Frank W. Secondary injection of gases into a supersonic flow..... 1689
- Zumwalt, Glen W. Reply by author to W. E. Simon (TC)..... 411

SUBJECTS

AERODYNAMICS OF BODIES, COMBINATIONS, AND INTERNAL FLOW

- Lift on an oscillating body of revolution. M. Sevik. 302
 Mach 8 to 22 studies of flow separations due to deflected control surfaces. D. S. Miller, R. Hijman, and M. E. Childs. 312
 Approximate evaluation of slender radome performance in hypersonic flight. Frank A. Albini. 476
 Lift on an oscillating ellipsoid of revolution. M. Sevik. 646
 Hypersonic blunt-body flow fields at angle of attack. Rudolph J. Swigart (TN). 115
 Supersonic magnus effect on a finned missile. Edward R. Benton (TN). 153
 Drag minimization using exact methods. Sidney A. Powers (TN). 941
 An analysis of the yawing motion of a rocket with a varying mass. W. J. Byrne Jr. and S. Raynor (TN). 962

AERODYNAMICS OF WINGS, ROTORS, AND CONTROL SURFACES

- Jet flap characteristics for high-aspect-ratio wings. G. K. Korbacher. 64
 Rotor blade harmonic air loading. R. H. Miller. 1254
 Extension of lifting-line theory to a cascade of split aerofoils. B. Lakshminarayana (TN). 938
 Quadratic effects of frequency on aerodynamic derivatives. Kazimierz J. Orlik-Rückemann (TN). 1507
 An improved Glauert series for certain airfoil problems. Michael D. Greenberg (TN). 1666
 Model law for parachute opening shock. Kenneth E. French (TN). 2226
 Comments on "Wing-tail interference as a cause of 'magnus' effects on a finned missile." Edward R. Benton and Anders S. Platou (TC). 410
 Some effects of planform modification on the skin friction drag. Edward J. Hopkins (TC). 413

ASTRONOMY AND ASTROPHYSICS

- Solar influence on satellite motion near the stable earth-moon libration points. B. D. Tapley and J. M. Lewallen. 728
 Drag displacements and decay of near-circular satellite orbits. F. T. Geyling. 1174
 Interplanetary trajectories in the restricted three-body problem. Lawrence M. Perko. 2187
 Some results obtained with the 22-meter radio telescope. A. E. Salomonovich (RS). 193
 Earth radius/kilometer conversion factor for the lunar ephemeris. Victor C. Clarke Jr. (TN). 363
 Mars nonstop round-trip trajectories. Roger W. Luidens (TN). 368
 Extension of f and g series to non-two-body forces. Robert M. L. Baker Jr. (TN). 1337
 Improved calculation of vacuum vertical trajectories. Leo B. Schlegel and Philip J. Bonomo (TN). 1487
 A dynamical model for Kordylewski cloud satellites. Frederick V. Pohle (TN). 1818
 Time-dilation dilemma and scale variation. M. Z. v. Krzywoblocki (TN). 2213
 Comment on "Orbital motion in the theory of general relativity." H. Robert Westerman (TC). 1869
 Reply by author to H. R. Westerman. John D. Anderson (TC). 1869

AUXILIARY SYSTEMS

- Charged aerosol energy converter. A. Marks, E. Barreto, and C. K. Chu. 45
 Comparison of commercial, spherical powder, and wire bundle tungsten ionizers. Guntis Kuskevics and Barry L. Thompson. 284
 Fluid transpiration through anodic boundary of an electric arc. C. Sheer, J. A. Cooney, and D. L. Rothacker. 483
 Optimization of window-type filters for silicon solar cells. Robert J. Romagnoli (TN). 101

COMMUNICATIONS

- Scattering and absorption of plane waves by cylindrically symmetrical underdense zones. F. A. Albini. 524
 Range and angle prediction tracking of objects with definable trajectories. Tom T. Kumagai (TN). 557
 Estimation of the autocorrelation functions of radio tracking errors. Raul R. Hunziker (TN). 1135

ELECTRONICS

- Plasma sheath transducer for axisymmetric re-entry vehicles. Allen E. Fuhs and O. L. Gibb (TN). 773

FACILITIES, RESEARCH, AND SUPPORT

- Jet-driven resonance tube. Philip A. Thompson. 1230
 A calorimeter study of a magnetically stabilized arc-heater. Roger B. Stewart (TN). 384
 Area change with a free-piston shock tube. R. J. Stalker (TN). 396
 Supersonic pitot tube measurements at an angle of attack. Sainsbury L. Strack (TN). 778
 Some dimensional considerations of studies in space-flight simulation. Kuldip P. Chopra (TN). 2047
 Comment on "Solid propellant driven shock tube." W. S. Filler (TC). 592

FLUID DYNAMICS

- Convective diffusion as an intruder in kinetic studies of surface catalyzed reactions. Daniel E. Rosner (SA). 593
 Shock tube test time limitation due to turbulent-wall boundary layer. Harold Mirels. 84
 Wake-like solutions of the laminar boundary-layer equations. Ernest D. Kennedy. 225
 Chemical nonequilibrium boundary layer. F. G. Blottner. 232
 Nondimensional solutions of flows with vibrational relaxation. Ralph Phinney. 240
 Hot-wire measurements in the hypersonic wakes of slender bodies. Anthony Demetriades. 245
 Linearized viscous free mixing with streamwise pressure gradients. Martin H. Steiger and Martin H. Bloom. 263
 Surface waves on a rotating fluid. Richard Skalak and John F. Conly. 306
 Hypersonic wakes and trails. Lester Lees. 417
 Study of the incompressible turbulent boundary layer with pressure gradient. Paul A. Libby, Paolo O. Baronti, and Luigi Napolitano. 445
 Nonequilibrium hypersonic flat-plate boundary-layer flow with a strong induced pressure field. George R. Inger. 452
 Effect of shock-induced vorticity on the compressible boundary layer along a flat plate. Lu Ting. 490
 Momentum integral methods for the laminar free shear layer. Toshi Kubota and C. Forbes Dewey Jr. 625
 A study of wakes behind a circular cylinder at $M = 5.7$. John F. McCarthy Jr. and Toshi Kubota. 629
 A unified analysis of supersonic nonequilibrium flow over a wedge: I. Vibrational nonequilibrium. Richard S. Lee. 637
 Interaction between primary and secondary streams of supersonic ejector systems and their performance characteristics. W. L. Chow and A. L. Addy. 686
 Effect of mass injection on the drag of a slender cone in hypersonic flow. Hartley H. King and Lawrence Talbot. 836
 Hypersonic laminar wakes and transition studies. Adrian Pallone, John Erdos, and Jerome Eckerman. 855
 A model for the transition regime in hypersonic rarefied gasdynamics. Bernard B. Hamel. 1047
 Inviscid hypersonic flow past smooth symmetric bodies. S. H. Maslen. 1055
 Nonequilibrium blunt-body flow using the method of integral relations. W. C. L. Shih and J. R. Baron. 1062
 Nozzle characteristics in the transition regime between continuum and free molecular flow. Mancil W. Milligan. 1088
 Dissociative relaxation in viscous hypersonic shock layers. Chul Park. 1202
 Far-flow approximations for precursor ionization profiles. Lewis Wetzel. 1208
 A quasi-one-dimensional treatment of chemical reactions in turbulent wakes of hypersonic objects. S. C. Lin and J. E. Hayes. 1214
 Theory of thin airfoils in magnetoaerodynamics. Lazar Dragos. 1223
 Three-dimensional perturbations on hypersonic wedge flow. Norman D. Malmuth. 1383
 Finite-difference calculation of hypersonic wakes. Seymour L. Zeiberg and Gary D. Bleich. 1396
 Similar solutions for the laminar mixing of reactive gases. Anthony Casaccio. 1403
 A transonic experiment at hypersonic speed. S. C. Traugott. 1521
 Recent studies of the laminar base-flow region. Eric Baum, Hartley H. King, and M. Richard Denison. 1527
 A study of laminar hypersonic cavity flows. Kenneth M. Nicoll. 1535
 Statistical behavior of a turbulent multicomponent mixture with first-order reactions. Yih-Ho Pao. 1550
 Turbulent mixing of coaxial jets. Louis J. Alpinieri. 1560
 Secondary injection of gases into a supersonic flow. Edward E. Zukoski and Frank W. Spaid. 1689
 Chemical and vibrational relaxation of an inviscid hypersonic flow. Albert D. Wood, James F. Springfield, and Adrian J. Pallone. 1697
 Nonequilibrium, nonsimilar solutions of the laminar boundary-layer equations. Adrian J. Pallone, Jeffrey A. Moore, and John I. Erdos. 1706
 Hypersonic viscous drag effects on blunt slender cones. Jack D. Whitfield and B. J. Griffith. 1714
 Interactions of gas molecules with an ideal crystal surface. Richard A. Oman, Alexander Bogan, Calvin H. Weiser, and Chou H. Li. 1722
 Studies of the luminous hypersonic wake. R. L. Taylor, B. W. Melcher II, and W. K. Washburn. 1731
 Hypersonic viscous flow near the stagnation streamline of a blunt body: I. A test of local similarity. Hsiao C. Kao. 1892
 Hypersonic viscous flow near the stagnation streamline of a blunt body: II. Third-order boundary-layer theory and comparison with other methods. Hsiao C. Kao. 1898
 Supersonic separated and reattaching laminar flows: I. General theory and application to adiabatic boundary-layer shock-wave interactions. Lester Lees and Barry L. Reeves. 1907

- Nonequilibrium laminar boundary-layer flow of ionized air. F. G. Blottner 1921
- Turbulent transport properties for axisymmetric heterogeneous mixing. Victor Zakkay, Egon Krause, and Stephen D. L. Woo 1939
- Hypersonic drag, stability, and wake data for cones and spheres. W. C. Lyons Jr., J. J. Brady, and Z. J. Levensteins 1948
- A theoretical study of the inviscid hypersonic flow about a conical flat-top wing-body combination. Paul Mandl 1956
- Interaction of a supersonic stream and a transverse supersonic jet. A. F. Charwat and J. Allegre 1965
- Viscous multicomponent-multiphase flow with application to axisymmetric jets of hydrogen. Raymond Edelman and Harold Rosenbaum 2104
- Numerical methods in multidimensional shocked flows. Samuel Z. Burstein 2111
- Laminar boundary layer with hydrogen injection including multicomponent diffusion. Paul A. Libby and Mauro Pierucci 2118
- Confined vortex flows with boundary-layer interaction. M. L. Rosenzweig, W. S. Lewellen, and D. H. Ross 2127
- Estimate of errors for approximate solutions of the simplest equations of gasdynamics. S. K. Godunov (RS) 208
- Flow inclination measurements in hypersonic tunnels. Hyman H. Album (TN) 104
- Linearized analysis of the pressure waves in a tank undergoing an acceleration. F. Edward Ehlers (TN) 110
- Approximate solution to flux concentration by hydromagnetic flow. Jerome M. Baker (TN) 112
- Turbulent wake characteristics with different eddy viscosity coefficients. Koon Sang Wan (TN) 121
- Correlation of boost phase turbulent heating flight data. Michael G. Dunn (TN) 122
- Effect of thermal accommodation on cylinder and sphere drag in free molecule flow. George S. Springer and Steven W. Tsai (TN) 126
- Initial development of the laminar separated shear layer. Eric Baum (TN) 128
- Laminar boundary layer with fluid injection. A. R. Maddox (TN) 133
- Determination of the mass of gas in a rapidly discharging vessel. R. C. Progelhof (TN) 137
- Integral equations for viscous hypersonic nozzle flow. M. Siegel (TN) 148
- Length of the laminar hypersonic wake during ballistic re-entry. Paul S. Lykoudis (TN) 155
- A flow-separation spike for hypersonic control of a hemisphere-cylinder. William E. Thurman (TN) 159
- Boundary of underexpanded axisymmetric jets issuing into still air. A. F. Charwat (TN) 161
- Variable-mesh difference equation for the stream function in axially symmetric flow. J. C. Lysen (TN) 163
- Three-dimensional boundary layers with a normal wall velocity. R. J. Gribben (TN) 164
- Velocity defect law for a transpired turbulent boundary layer. H. S. Mickley, K. A. Smith, and M. D. Fraser (TN) 173
- Calculation of cylindrical blast wave propagation with counterpressure. Bernard Steginsky (TN) 175
- Contours for stagnation-point mass injection in hypersonic flow. Chang-Yi Wang (TN) 178
- Effect of the boundary layer upon the flow in a conical hypersonic nozzle. Martin Siegel (TN) 180
- Measurements of test time in the GARCIT 17-inch shock tube. Anatol Roshko and Jerome A. Smith (TN) 186
- Determination of the maximum transmitted shock at the interface between two condensed media. P. K. Salzman (TN) 359
- Stability of the hodograph equations in one-dimensional reacting gas flow. James L. Throne (TN) 360
- Flow in the three-dimensional boundary layer on a spinning body of revolution. O. Parr (TN) 361
- Temperature and velocity profiles along a vertical hot plate in a compressible fluid considering the effect of buoyancy. S. Ghoshal (TN) 364
- Method for determination of velocity distribution in a thin liquid film. S. L. Persson (TN) 372
- Numerical stability of the three-dimensional method of characteristics. Harry Sauerwein and Mark Sussman (TN) 387
- Laminar compressible mixing behind finite bases. Paul S. Lykoudis (TN) 391
- Tracer-spark technique for velocity mapping of hypersonic flow fields. James B. Kyser (TN) 393
- Exact solutions of gas-particle nozzle flows. H. A. Hassan (TN) 395
- Entropy production in vibrational-nonequilibrium nozzle flow. Laurence N. Connor and Wayne D. Erickson (TN) 397
- Density distribution over a moving circular plate in free-molecule flow (U). K. J. Touryan (TN) 559
- Transition correlations for hypersonic wakes. Seymour L. Zeiberg (TN) 564
- Approximate nonequilibrium air ionization in hypersonic flows over sharp cones. E. S. Levinsky and F. L. Fernandez (TN) 565
- Correlation of flat-plate pressures using the rarefaction parameter $M \propto C \propto^{1/2}/Re \propto^{1/2}$. H. Eugene Deskins (TN) 573
- Velocity profiles from compressible wall jets. Robert LeRoy Lawrence (TN) 574
- Pressures in the stagnation regions of blunt bodies in rarefied flow. J. Leith Potter and Allan B. Bailey (TN) 743
- Effect of a cavitating venturi on wave propagation in a duct. L. R. Iwanicki and O. W. Dykema (TN) 753
- Skin friction of slender cones in hypersonic flow. Jan Raat (TN) 755
- Flow of viscoelastic Maxwell fluid. Keshab Chandra Bagchi (TN) 759
- Vortex flow in arc heaters. K. E. Tempelmeyer and L. E. Rittenhouse (TN) 766
- Boundary-layer transition on a slender cone in hypersonic flow. Anthony Martellucci (TN) 771
- Laminar boundary-layer development on yawed cone. Shee-Mang Yen and B. Singh (TN) 775
- Normal shock location in underexpanded gas and gas-particle jets. Clarke H. Lewis Jr. and Donald J. Carlson (TN) 776
- Chemical scavenger probes in nonequilibrium gasdynamics. D. E. Rosner, A. Fontijn, and S. C. Kurzus (TN) 779
- Drop size from a liquid jet in a longitudinal electric field. Richard L. Peskin and Roland J. Raco (TN) 781
- Potential flow past a parabolic leading edge. Jack D. Dennon (TN) 934
- Experimental measurement of pitot pressure in the boundary layer on a model in a hypersonic gun tunnel. A. J. Cable (TN) 944
- Laminar wake with arbitrary initial profiles. Harris Gold (TN) 948
- Viscous jets from nonnarrow orifices. A. Pozzi (TN) 949
- Unsteady boundary-layer flow of a non-Newtonian fluid on a flat plate. Curtis Sinclair Wells Jr. (TN) 951
- Hypersonic flow field around a hemisphere in a $\text{CO}_2\text{-N}_2\text{-A}$ gas mixture. Jerold H. Klaimon (TN) 953
- Wake transition. Kwan-Sun Wen (TN) 956
- A note on "Pressure distribution for hypersonic boundary-layer flow." M. S. Sastry (TN) 961
- Magnetohydrodynamic hypersonic viscous flow past a blunt body. Myron C. Smith and Ching-Sheng Wu (TN) 963
- Maximum total pressure recovery across a system of n shock waves. L. F. Henderson (TN) 1138
- Anisotropic gas flow. C. N. Kaul (TN) 1145
- Additional modes of instability for Poiseuille flow over flexible walls. F. D. Hains (TN) 1147
- Oxygen-electron attachment in hypersonic wakes. Seymour L. Zeiberg (TN) 1151
- Falkner-Skan equation for wakes. K. Stewartson (TN) 1327
- Hydromagnetic flow between two rotating cylinders. P. K. Muhlert (TN) 1328
- A simple derivation of three-dimensional characteristic relations. Chong-Wei Chu (TN) 1336
- A simple device for the qualitative measurement of the vortices. B. Lakshminarayana (TN) 1353
- A transformation for wake analyses. R. H. Page and R. J. Dixon (TN) 1464
- Hypersonic cone wake velocities obtained from streak pictures. W. K. Washburn, A. Goldberg, and B. W. Melcher II (TN) 1465
- Shock interaction in a hypersonic flow. Frank R. Tepe Jr. and Widen Tabakoff (TN) 1478
- Addendum: "The vertical water-exit and -entry of slender symmetric bodies." John P. Moran (TN) 1480
- Growth of the turbulent inner wake behind 3-in.-diam spheres. R. Knystautas (TN) 1485
- Rapid estimation of the far-field in an axisymmetric compressible jet. Richard S. Rosler (TN) 1489
- A family of similar solutions for axisymmetric incompressible wakes. Toshi Kubota, Barry L. Reeves, and Harvey Buss (TN) 1493
- Measurement of uniform flow duration in a chambered, buffered shock tube. S. G. Chapin and W. F. Rumpel (TN) 1499
- Turbulent boundary layers with transpiration. T. Neil Stevenson (TN) 1500
- Flow field in a swirl chamber. D. H. Tsai (TN) 1504
- Pressure variation in a tank undergoing an acceleration. R. C. Progelhof (TN) 1505
- Similarity in axisymmetric viscous free mixing with streamwise pressure gradient. M. H. Steiger (TN) 1509
- Oscillating sphere in a rotating viscous fluid. M. P. Singh (TN) 1513
- Pressure gradient effects on nonequilibrium far wakes. N. Ness and J. B. Fanucci (TN) 1514
- Sudden expansion of a bounded jet at a high pressure ratio. Edward J. Barakauskas (TN) 1644
- Condensation studies in hotshot tunnels. B. J. Griffith, H. Eugene Deskins, and H. R. Little (TN) 1645
- An investigation of cylindrical starting flows. J. D. Buckmaster (TN) 1649
- Equilibrium turbulent boundary layers. G. L. Mellor (TN) 1650
- Nonequilibrium sodium ionization in laminar boundary layers. J. J. Kane (TN) 1651
- Structure of the boundary layer at the leading edge of a flat plate in hypersonic slip flow. J. A. Laurmann (TN) 1655
- Integral solution for compressible laminar mixing. James E. Hubbard (TN) 1657
- Hypersonic viscous flow near a sharp leading edge. Richard W. Garvine (TN) 1660
- Two-dimensional radiating gas flow by a moment method. Ping Cheng (TN) 1662
- Effects of interface combustion and mixing on shock-tunnel conditions. John A. Copper (TN) 1669
- Effect of transverse enthalpy gradient on blunt body pressure distributions in hypersonic flow. Darrell Brooke and Richard E. Thomas (TN) 1829
- Air ionization in the hypersonic laminar wake of sharp cones. F. L. Fernandez and E. S. Levinsky (TN) 1829
- Equivalence of nonequilibrium flows behind normal and oblique shock waves. Chong-Wei Chu (TN) 1833
- Approximate method for plug nozzle design. Gianfranco Angelino (TN) 1834
- Approximate solution of second-order boundary-layer equations. Leroy Devan and Madan Mohan Oberai (TN) 1838
- Zonal flow inside an impulsively started rotating sphere. Edward R. Benton (TN) 1840
- Vibrational relaxation in air. Donald R. White and Roger C. Millikan (TN) 1844
- Weak interacting hypersonic flow over cones. W. Hoelmer and M. Saarlus (TN) 1846
- Eigenvalues for the equation of species conservation with heterogeneous reaction. Gerald S. Janowitz and Paul A. Libby (TN) 1849
- Method of Belotserkovskii for asymmetric blunt-body flows. E. A. Brong and D. C. Leigh (TN) 1852
- Local similarity expansions of the boundary-layer equations. William B. Bush (TN) 1857

- Convective model of Hartmann flow. L. T. Fan, C. L. Hwang, and W. S. Hwang (TN)..... 1859
- Application of quasilinearization to boundary-layer equations. John R. Radbill (TN)..... 1860
- Effect of boundary-layer removal on high velocity flame stabilization. James R. Maus and William T. Snyder (TN)..... 2030
- Self-preserving fluctuations and scales for the hypersonic turbulent wake. Wilnot H. Webb (TN)..... 2031
- A transient solution of the Fokker-Planck equation. C. F. Eaton (TN)..... 2033
- Aerodynamic pitching derivatives of a wedge in hypersonic flow. J. P. Appellon (TN)..... 2034
- Stagnation equilibrium layer in nonequilibrium blunt-body flows. Raul J. Conti (TN)..... 2044
- Cone pressure distribution at large and small angles of attack. M. D. High and E. F. Blick (TN)..... 2054
- Identification of two types of separation. J. W. Paull (TN)..... 2202
- Similar solutions for three-dimensional laminar compressible boundary layers. Michael C. Fong (TN)..... 2205
- Effect of fluid motion on free surface shape under reduced gravity. Jin H. Chin and L. W. Gallagher (TN)..... 2215
- Three-dimensional symmetric vortex flow. Ajit Kumar Ray (TN)..... 2218
- Unsteady flow past junctures in ducts. A. G. Hammitt and H. J. Carpenter (TN)..... 2224
- Capillary stability in an inverted rectangular channel for free surfaces with curvature of changing sign. Paul Concus (TN)..... 2228
- Slip flow and hypersonic boundary layers. J. Aroesty (TC)..... 189
- Reply by author to J. Aroesty. L. Talbot (TC)..... 190
- Flow in contracting ducts. J. C. Gibbings (TC)..... 191
- Comment on "Effects of controlled roughness on boundary-layer transition at a Mach number of 6.0." J. Leith Potter and Jack D. Whitfield (TC)..... 407
- Reply by authors to J. L. Potter and J. D. Whitfield. James R. Sterrett and Paul F. Holloway (TC)..... 408
- Comments on "Mach number independence of the conical shock pressure coefficient." Wayne E. Simon (TC)..... 411
- Reply by author to W. E. Simon. Glen W. Zumwalt (TC)..... 411
- Comment on "Velocity defect law for a transpired turbulent boundary layer." H. Tennekes (TC)..... 414
- Reply by authors to H. Tennekes. H. S. Mickley and K. A. Smith (TC)..... 415
- Comment on "An approximate solution for laminar boundary layer flow." R. M. Terrill (TC)..... 587
- Reply by Author to R. M. Terrill. Robert L. Kosson (TC)..... 588
- Detonation initiation. Roger A. Strehlow (TC)..... 783
- Comments on exhaust flow field and surface impingement. Leonard Roberts and Jerry C. South Jr. (TC)..... 971
- Reply by authors to L. Roberts and J. C. South Jr. Leonard P. Radtke and Donald W. Eastman (TC)..... 973
- Comment on calculation of oblique shock waves. Joel L. Briggs (TC)..... 974
- Comments on "Three-dimensional effects in viscous wakes." Yung-Huang Kuo and Lionel V. Baldwin (TC)..... 1163
- Reply by authors to Y.-H. Kuo and L. V. Baldwin. Martin H. Bloom and Martin H. Steiger (TC)..... 1164
- Conical shock-wave angle. Richard A. Hord (TC)..... 1359
- Reply by authors to W. Simon. Krishnamurthy Karamcheti and Henry Tao-Sze Hsia (TC)..... 1359
- Errata: "Variable-mesh difference equation for the stream function in axially symmetric flow." John C. Lyson (TC)..... 1359
- Comments on "Tracer-spark technique for velocity mapping of hypersonic flow fields." George Rudinger (TC)..... 1517
- Reply by author to G. Rudinger. J. B. Kyser (TC)..... 1517
- Comments on "Transition correlations for hypersonic wakes." John I. Erdos and Harris Gold (TC)..... 1675
- Reply by author to J. I. Erdos and H. Gold. Seymour L. Zeiberg (TC)..... 1677
- Erratum: "A model for the transition regime in hypersonic rarefied gasdynamics." Bernard B. Hamel (TC)..... 1679
- Comment on "Method for the determination of velocity distribution in a thin liquid film." R. M. Nedderman (TC)..... 1865
- Reply by author to R. M. Nedderman. S. Lennart Persson (TC)..... 1866
- One-dimensional Rayleigh flow of a partially ionized gas. Malcolm McChesney (TC)..... 1866
- Reply by author to M. McChesney. K. T. Yen (TC)..... 1867
- Transverse curvature effects in axisymmetric hypersonic boundary layers. Ting-Yi Li and Joseph F. Gross (TC)..... 1868
- Reply by authors to T.-Y. Li and J. F. Gross. N. A. Thyson and E. E. Schurmann (TC)..... 1869
- Comment on "Conical shock-wave angle." Mary F. Romig (TC)..... 2232

GEOPHYSICS

- Simulation of geophysical phenomena in the laboratory. M. P. Bachynski (SA)..... 1873
- Interaction of micrometeorites with gaseous targets. J. C. Slattery, J. F. Friichtenicht, and B. Hamernesh..... 543
- Probability of meteoroidal penetration. Francis B. Shaffer..... 738
- An analytical study of meteor entry. James A. Fay, W. Craig Mofatt, and Ronald F. Probst..... 845
- Auroral measurements and upper atmospheric physics. Roland E. Meyerott and John E. Evans..... 1169
- Interaction between the solar plasma wind and the geomagnetic cavity. Lester Lees..... 1576
- Back-scattering properties of moon and earth at X band. Harris Safran (TN)..... 100
- Sputtering in the upper atmosphere. D. McKeown, M. G. Fox, J. J. Schmidt, and D. Hopper (TN)..... 400
- Proton fluxes along low-acceleration trajectories through the Van Allen belt. Frank J. Hrach (TN)..... 762

- Temperature distributions downstream of a moving heat sink. Ashley F. Emery (TN)..... 779
- Calculation of gravitational force components. R. J. Mercer (TC)..... 1166
- Comments on "Sputtering in the upper atmosphere." R. V. Stuart (TC)..... 1678
- Reply by authors to R. V. Stuart. D. McKeown, M. G. Fox, J. J. Schmidt, and D. Hopper (TC)..... 1678

HEAT TRANSFER AND THERMODYNAMICS

- Laminar heat transfer to a two-dimensional backward facing step from the high-enthalpy supersonic flow in the shock tube. Josef Rom and Arnan Segner..... 251
- Optimization study of space radiators. Irving Rubin and Murray Imber..... 353
- Laminar heat transfer to spherically blunted cones at hypersonic conditions. B. J. Griffith and Clark H. Lewis..... 438
- Effect of gas composition on the ablation behavior of a charring material. Nick S. Vojvodich and Ronald B. Pope..... 536
- A radiation model for nonequilibrium molecular gases. C. Frederick Hansen..... 611
- Transpiration cooling of a turbulent boundary layer in an axisymmetric nozzle. Joseph Librizzi and Robert J. Cresci..... 617
- Diffusion-thermo effects in stagnation-point flow of air with injection of gases of various molecular weights into the boundary layer. E. M. Sparrow, W. J. Minkowycz, and E. R. G. Eckert..... 652
- Laminar, transitional, and turbulent heat transfer after a sharp convex corner. Victor Zakkay, Kaoru Toba, and Ta-Jin Kuo..... 1389
- Experimental heat-transfer studies of hypervelocity flight in planetary atmospheres. J. S. Gruszczynski and W. R. Warren Jr..... 1542
- Ablation-products radiation from cones. William C. Davy, Roger A. Craig, Gary T. Chapman, and Dale L. Compton..... 1583
- Mechanical spallation of charring ablators in hyperthermal environments. Richard D. Mathieu..... 1621
- Effects of species diffusion and heat conduction on nonequilibrium flows behind strong shocks. Walter E. Gibson and John D. Buckmaster..... 1681
- Radiation-perturbed flow fields of normal and oblique shock waves. D. B. Olfe..... 1928
- Energy transfer processes in a partially ionized, two-temperature gas. Donald M. Dix..... 2081
- Close analogy between radiative and conductive heat flux in a finite slab. Max A. Heaslet and Barrett Baldwin..... 2180
- Stratification in a pressurized container with sidewall heating. Free molecular heat transfer near a wall. A. K. Rebrov (RS)..... 215
- Joseph M. Ruder (TN)..... 135
- Optimum geometric factors for semicircular fins in radiation-cooled nozzles. Riad Jaroudi and Donald E. Heard (TN)..... 146
- Production of intense radiation heat pulses. J. F. Louis, R. Decher, and T. R. Brogan (TN)..... 156
- Heat transfer from nonequilibrium ionized argon gas. Chul Park (TN)..... 169
- Intermolecular-force effects on the thermodynamic properties of nitrogen. C. Edward Smith Jr. (TN)..... 183
- Supersonic stagnation point heat transfer at low Reynolds numbers. Henry Tong and W. H. Giedt (TN)..... 185
- Approximation of the eigenvalues for heat transfer in laminar tube slip flow. Robert M. Inman (TN)..... 373
- Re-entry heat conduction of a finite slab with a nonconstant thermal conductivity. William R. Wells (TN)..... 379
- Temperature recovery factors for flow longitudinal to a circular cylinder. E. M. Sparrow and D. P. Fleming (TN)..... 386
- Surface activity and preferential ablation. B. Steverding (TN)..... 549
- Transpiration and film cooling combined with external cooling. E. Mayer and D. Divoky (TN)..... 578
- Effect of variable Lewis number on heat transfer in a binary gas. K. R. Enkenhus (TN)..... 747
- Flow of second-order fluids with heat transfer. A. C. Srivastava (TN)..... 749
- Heat transfer due to hydromagnetic channel flow with conducting walls. K. Jagadeesan (TN)..... 756
- Effect of gage material on convective heat transfer. D. J. Collins and J. M. Spiegel (TN)..... 777
- Ablation of a cylindrical cavity in an infinite medium. S. V. Nardo (TN)..... 936
- Analysis of air arc-tunnel heat-transfer data. Daniel E. Rosner (TN)..... 945
- Calorimetric heating-rate probe for maximum-response-time interval. Robert H. Kirchhoff (TN)..... 966
- Temperature measurement in a chemical shock tube by sodium-line reversal and C₂ reversal methods. D. H. Napier, M. Nettleton, J. R. Simonson, and D. P. C. Thackeray (TN)..... 1136
- Radiative and convective heating during hypervelocity re-entry. Robert M. Nerem and George H. Stickford (TN)..... 1156
- Thermodynamic properties of high-temperature helium. J. Charles Hester and Kenneth G. Sewell (TN)..... 1329
- Use of temperature-sensitive coatings for obtaining quantitative aerodynamic heat-transfer data. Robert A. Jones and James L. Hunt (TN)..... 1354
- Heat transfer on power law bodies. Arnold W. Maddox (TN)..... 1474
- Effect of shock curvature on turbulent heating of sphere-cones. C. T. Edquist (TN)..... 1486
- Thermal stresses in a viscoelastic cylinder with temperature dependent properties. K. C. Valanis and G. Lianis (TN)..... 1642
- Thermodynamic properties for imperfect air and nitrogen to 15,000°K. Clark H. Lewis and C. A. Neel (TN)..... 1847
- Reduction of torsional stiffness due to thermal stress in thin, solid wings. D. J. Johns (TN)..... 1850
- Intermolecular-force effects on the thermodynamic properties of helium with application. Edwin F. Harrison (TN)..... 1854
- One-dimensional flow considering buoyancy forces. S. Ghoshal (TN)..... 2016

Analytical determination of shape factors from a surface element to an axisymmetric surface. S. J. Morizumi (TN).....	2028
Heat diffusion from line source into mixing region of two parallel streams. John B. Miles (TN).....	2038
Experimental convective heat-transfer measurements. D. J. Collins and T. E. Horton (TN).....	2046
Stagnation-point heat transfer to surfaces of arbitrary catalyticity. Henry Tong and Bob H. Suzuki (TN).....	2051
A simplified formulation for radiative transfer. M. Thomas and W. S. Rigdon (TN).....	2052
Reference temperature method for computing displacement thickness. M. Saarlus (TN).....	2056
Approximate absorption coefficients for vibrational electronic band systems. Edward P. French (TN).....	2209
Comments on "Gas-film effects in the linear pyrolysis of solids." W. H. Andersen (TC).....	404
Reply by author to W. H. Andersen. R. H. Cantrell (TC).....	406
"Equilibrium" gas composition computation with constraints. Kenneth A. Wilde (TC).....	409
Comments on "Radiation slip." A. G. Hammit (TC).....	975
Reply by author to A. G. Hammit. Ronald F. Probst (TC).....	976
Comment on "Thermal ionization behind strong shock waves." K. N. C. Bray (TC).....	1161
Reply by author to K. N. C. Bray. Robert W. Truitt (TC).....	1162
Errata: "Optimum geometric factors for semicircular fins in radiation-cooled nozzles." Riad Jaroudi and Donald E. Heard (TC).....	1168
Heat transfer at zero Prandtl number in flows with variable thermal properties. Nelson H. Kemp (TC).....	1864
Reply by authors to N. H. Kemp. D. K. Edwards and D. M. Tellep (TC).....	1865
Prandtl number dependence of heat transfer in Falkner-Skan flow. Nelson H. Kemp (TC).....	2062
Reply by author to N. H. Kemp. D. A. Spence (TC).....	2063
Comment on non-Newtonian flow. B. Steverding (TC).....	2231
Reply by author to B. Steverding. C. Sinclair Wells Jr. (TC).....	2232

INSTRUMENTATION AND PHOTOGRAPHY

Zero angle-of-attack sensor. A. E. Fuhs and J. A. Kelly (TN).....	1492
A thin-film radiative heat-transfer gage. Robert M. Nerem and George H. Stickford (TN).....	1647

MATERIALS, METALLIC

Ion engine reliability as affected by corrosion of materials. P. M. Winslow.....	42
Cesium neutral and ion emission from carburized and oxygenated porous tungsten. A. Y. Cho and H. Shelton.....	2135

MATERIALS, NONMETALLIC

Bearing capacity of simulated lunar surfaces in vacuum. E. C. Burnett, Ronald F. Scott, L. D. Jaffe, E. P. Frink, and H. E. Martens.....	93
A semiquantitative prediction of the erosion of graphite nozzle inserts. Lawrence J. Delaney, Lee C. Eagleton, and Walter H. Jones.....	1428
Tensile failure of fibrous composites. B. Walter Rosen.....	1985
Effective heat of ablation of graphite. Eugene P. Bartlett (TN).....	171
Effect of diameter upon elastic properties in thin fibers. H. Schuerch (TN).....	569

MATHEMATICS

Solution of variational problems by means of a generalized Newton-Raphson operator. Robert McGill and Paul Kenneth.....	1761
Optimization and visualization of functions. Gary A. McCue (TN).....	99
Optimal functional approximation using dynamic programming. Anthony G. Lubowe (TN).....	376
Calculation of the surface range of a ballistic missile. P. R. Escobal (TN).....	571
Euler's moment equations for a variable-mass unsymmetrical top. Valdemars Punga (TN).....	937
Least-squares approach to unsteady kernel function aerodynamics. Joseph A. Fromme (TN).....	1349
Motion of the center of gravity of a variable-mass body. Valdemars Punga (TN).....	1482
Comparison of Markov and least-squares missile position and velocity estimates. Raul R. Hunziker (TN).....	2024
Comment on "Application of dynamic programming to optimizing the orbital control process of a 24-hour communication satellite." Theodore N. Edelbaum (TC).....	974
Addendum: "An alternate interpretation of Newton's second law." M. Bottaccini (TC).....	1164
N-segment least-squares approximation. R. Aris and M. M. Denn (TC).....	1516

METEOROLOGY

Instability of three-row vortex streets. Chee Tung (TN).....	1143
--	------

NAVIGATION AND GUIDANCE

A terminal guidance technique for lunar landing. S. J. Citron, S. E. Dunin, and H. F. Meissinger.....	503
Determination of dominant error sources in an inertial navigation system by iterative weighted least squares. W. Eisner and A. F. Goodman.....	722
Error propagation in astro-inertial guidance systems for low-thrust missions. Hermann M. Dusek.....	879
Zero thrust velocity vector control for interstellar probes: Lorentz force navigation and circling. Robert L. Forward.....	885
Plane-change requirements associated with rendezvous in a lunar satellite orbit. Jerry M. Deerwester.....	890
Optimal measurement and velocity correction programs for mid-course guidance. Walter F. Denham and Jason L. Speyer.....	896
Longitude positioning and orbit control of the 24-hour equatorial satellite. Garfield Kang and Martin F. Kenahan.....	991
Dynamics of gravity-oriented orbiting systems with application to passive stabilization. B. Etkin.....	1008
A new approach to gravitational gradient determination of the vertical. John W. Diesel.....	1189
A general theory on space and re-entry similar trajectories. Luigi Broglio.....	1774
Exact first-order navigation-guidance mechanization and error propagation equations for two-body reference orbits. K. C. Kochi (TN).....	365
Conversion of coordinates: latitude-longitude to cislunar. F. E. Council Jr. (TN).....	551
Long-term coupling effects between librational and orbital motions of a satellite. E. Y. Yu (TN).....	553
Maximum rendezvous launch window characteristics. Sheldon Kass (TN).....	580
Modification of Weierstrass-Erdmann corner conditions in space navigations. R. N. Bhattacharya and M. Bhattacharjee (TN).....	1145
Angle of attack from body-fixed rate gyros. Edward O. Nelson (TN).....	1324
A passive system for determining the attitude of a satellite. Harold D. Black (TN).....	1350
Equations of motion for spin stabilization analysis in terms of Euler angles. Philip S. Carroll (TN).....	1483
Exact two-body error sensitivity coefficients. K. C. Kochi (TN).....	1502
Torque on a satellite due to gravity gradient and centrifugal force. Philip S. Carroll (TN).....	2220
Comment on "Optimal measurement and velocity correction programs for midcourse guidance." Robert J. Fitzgerald (TC).....	968
Comment on "Equilibrium orientations of gravity-gradient satellites." Thomas R. Kane and Peter W. Likins (TC).....	1357
Reply by author to T. R. Kane and P. W. Likins. Irving Michelson (TC).....	1357
Distribution of nearly circular orbits. David A. Conrad (TC).....	2234

PHYSICS, GENERAL

Theoretical penetration of hypervelocity projectiles into massive targets. John K. Wall.....	1242
Time for totally wetting liquid to deform from a gravity-dominated to a null-gravity equilibrium state. Howard L. Paynter.....	1627
Optical-acoustic effects in solid films. Arthur V. Houghton and Russell U. Acton (TN).....	120
Lift contribution to the sonic boom. G. A. Bird and C. J. Wetherall (TN).....	582
Measurement of droplet size for wide range particle distributions. J. H. Roberts and M. J. Webb (TN).....	583
Determination of cratering energy densities for metal targets by means of reflectivity measurements. Herman Mark, Gary Goldberg, and Michael J. Mirtich (TN).....	965
Factors influencing electrically sprayed liquids. J. J. Hogan, R. S. Carson, J. M. Schneider, and C. D. Hendricks (TN).....	1460
An analytical approach to hypervelocity impact. S. W. Yuan and A. M. Bloom (TN).....	1667
Temperature yield strength correlation in hypervelocity impact. R. Piacesi, R. H. Waser, and V. C. D. Dawson (TN).....	2040
Comment on "An alternate interpretation of Newton's second law." V. W. Snyder (TC).....	2239

PHYSICS, PLASMA

Experiments with an electron cyclotron resonance plasma accelerator. David B. Miller and Edward R. Gibbons.....	35
Theory and experiment of a capillary-type emitter. D. L. Dresser, W. G. Laurita, J. D. Dunlop II, H. Huber, and R. LeBihan.....	52
Effect of microwave radiation on the ionized gas behind a strong normal shock wave. K. T. Yen.....	71
A general theory for the flow of weakly ionized gases. S. H. Lam.....	256
Induced forces in annular magneto-fluid dynamic traveling wave devices. Joseph L. Neuringer.....	267
A synthesis method of electrostatic gun design. D. S. Colburn, K. J. Harker, and G. S. Kino.....	322
Pulsed electromagnetic acceleration of metal plasmas. T. L. Rosebrock, D. L. Clingman, and D. G. Gubbins.....	328
Broadside radar echoes from ionized trails. Herschel Weil.....	429
Experiments on turbulent mixing in a partially ionized gas. Jerry Grey and Paul F. Jacobs.....	433
Insulator boundary layers in magnetohydrodynamic channels. Francis J. Hale and Jack L. Kerrebrock.....	461
Hot-wire calorimeter study of ion production and acceleration. V. A. Sandborn and L. V. Baldwin.....	660

- An instrument to measure velocity/electrical conductivity of arc plasmajets. A. E. Fuhs..... 667
- An investigation of Hall propulsor characteristics. H. E. Brandmaier, J. L. Durand, M. C. Gourdine, and A. Rubel..... 674
- Rotating electrically conducting fluids in a long cylinder. Kwadwo O. Kessey..... 864
- Plasma-vehicle interaction in a plasma stream. David F. Hall, Robert F. Kemp, and J. M. Sellen Jr..... 1032
- Recent results of studies of the traveling wave pump. Eugene E. Covert, Laurence R. Boedeker, and Charles W. Haldeman..... 1040
- Nonequilibrium ionization due to electron heating: I. Theory. Jack L. Kerrebrock..... 1072
- Nonequilibrium ionization due to electron heating: II. Experiments. Jack L. Kerrebrock and Myron A. Hoffman..... 1080
- Hall current plasma accelerator. Gordon L. Cann and Gary L. Marlotte..... 1234
- Experiments concerning nonequilibrium conductivity in a seeded plasma. E. E. Zukoski, T. A. Cool, and E. G. Gibson..... 1410
- Magnetocaloric power. E. L. Resler Jr. and R. E. Rosensweig..... 1418
- Electrodynamic power generation. Bernard Kahn and Meredith C. Gourdine..... 1423
- A technique for the experimental determination of the electrical conductivity of plasmas. Donald D. Hollister..... 1568
- Approximate theoretical calculation of continuum opacities. S. S. Penner and M. Thomas..... 1572
- Formation of ion beams from plasma sources: Part I. J. Hyman Jr., W. O. Eckhardt, R. C. Knechtli, and C. R. Buckley..... 1739
- Current distributions in large-radius pinch discharges. Robert G. Jahn and Woldemar von Jaskowsky..... 1749
- Theoretical performance comparison of working fluids in a nonequilibrium MHD generator. F. H. Shair..... 1883
- Hydromagnetic heat transfer in the thermal entrance region of a channel with electrically conducting walls. M. K. Jain and J. Srinivasan..... 1886
- Small magnetofluid-dynamic peristaltic motions inside an annular circular cylindrical induction compressor. Joseph L. Neuringer and James H. Turner..... 2076
- Hyperersonic magnetohydrodynamics with or without a blunt body. R. H. Levy, P. J. Gierasch, and D. B. Henderson..... 2091
- A theoretical investigation of MHD channel entrance flows. A. Maculatis and A. L. Loeffler Jr..... 2100
- Vortex gas accelerator. Stirling A. Colgate..... 2138
- Analytical solution for constant enthalpy MHD accelerator: H. Mirels (TN)..... 145
- Minimum-length MHD accelerator with constant enthalpy and magnetic field. Harold Mirels, Richard R. Gold, and James F. Mullen (TN)..... 1141
- Scattering of radar waves by an underdense turbulent plasma. J. Menkes (TN)..... 1154
- Surface effects in a pulsed plasma accelerator. William J. Guman and William Truglio (TN)..... 1342
- Electron fluctuations in an equilibrium turbulent plasma. Anthony Demetriades (TN)..... 1347
- Experimental results in high-specific-impulse thermo-ionic acceleration. Adriano C. Ducati, Gabriel M. Giannini, and Erich Muehlberger (TN)..... 1452
- Analysis of MHD channel entrance flows using the momentum integral method. W. Craig Moffatt (TN)..... 1495
- Interaction of an oscillating magnetic field with fluid in Couette flow. F. H. Shair (TN)..... 1510
- Electric propulsion characteristics of a pulsed plasma rail accelerator. Daniel H. Winicour (TN)..... 1673
- Chaplygin's transformation applied to magnetogasdynamics. E. V. Laitone (TN)..... 1856
- Delays in initiation of discharges in pulsed plasma accelerators. Leonard Aronowitz and Warren Coe (TN)..... 2019
- A compatibility equation for nonequilibrium ionization. F. H. Shair (TN)..... 2026
- Sonic line of magnetohydrodynamic nozzle flow. Tatsuo Yamanaka (TN)..... 2293
- Influence of magnetic fields upon separation. William H. Heiser (TN)..... 2217
- Comment on "Propulsion application of the modified penning arc plasma ejector." E. A. Pinsley, E. C. Lary, and R. G. Meyer and Jr. (TC)..... 401
- Reply by author to R. M. Terrill. Robert L. Kosson (TC)..... 588
- Comment on "A class of linear magnetohydrodynamic flows." Thomas P. Anderson (TC)..... 588
- Reply by author to T. P. Anderson. M. R. El-Saden (TC)..... 590
- Effect of acoustic environment on the burning rate of solid propellants. J. E. Crump and E. W. Price..... 1274
- Experiments with a solid-propellant acoustic oscillator. John F. Engler and William Nachbar..... 1279
- A shock wave model of unstable rocket combustors. W. A. Sirignano and L. Crocco..... 1285
- Nonacoustic combustion pulsations of ammonium perchlorate containing aluminum. Y. H. Inami and H. Shanfield..... 1314
- Preferred frequency oscillatory combustion of solid propellants. J. L. Eisel, M. D. Horton, E. W. Price, and D. W. Rice..... 1319
- Thrust effectiveness of oxidizer injection in a convergent-divergent nozzle. Gordon R. Hall..... 1434
- Velocity effects in transverse mode liquid propellant rocket combustion instability. F. H. Reardon, L. Crocco, and D. T. Harrie..... 1631
- Alumina size distributions from high-pressure composite solid-propellant combustion. Louis A. Povinelli and Robert A. Rosenstein..... 1754
- Determination of propellant properties by the arc image furnace technique. R. O. Fleming Jr. and R. W. Fleming (TN)..... 117
- Experimental detonation velocities and induction distances in hydrogen-air mixtures. Loren E. Bollinger (TN)..... 131
- Detonation of hydrogen-oxygen at low temperature and high pressure. K. W. Ragland, G. L. Cosens, and R. E. Cullen (TN)..... 142
- Heterogeneous reactions in ignition and combustion of solid propellants. Ralph Anderson, Robert S. Brown, and Larry J. Shannon (TN)..... 179
- Numerical study of hydrogen-fluorine kinetics in nozzles. Kenneth A. Wilde (TN)..... 374
- Acoustic absorption coefficients of combustion gases. D. W. Blair, E. Eriksen, and G. K. Berge (TN)..... 392
- Effect of radiation on upper limits of inflammability. Beshir A. Abbadi and Richard S. Tankin (TN)..... 758
- Liquid sloshing in a 45° sector compartmented cylindrical tank. Helmut F. Bauer (TN)..... 768
- Temperature-entropy diagram of monomethylhydrazine. Frank Bizjak and Donald F. Stai (TN)..... 954
- Correlation of motor and strand composite propellant burning rate. L. E. Herrington (TN)..... 1671
- Flow of combustion gases through a perforation in a solid propellant grain. John E. Bush (TN)..... 2022
- Propellant potential of vaporized metals in temperature-limited rocket systems. I. Glassman, R. F. Sawyer, and A. M. Mellor (TN)..... 2049
- Modification of the hydrazine-nitrogen tetroxide ignition delay. Harold G. Weiss, Bruce Johnson, H. Dwight Fisher, and Melvin Gerstein (TN)..... 2222
- Effect of radiation on ammonium perchlorate propellants. T. Acker, E. Henley, R. F. McAlevy III, and G. Odian (TC)..... 1165
- Longitudinal mode instability. J. R. Osborn (TC)..... 2237
- Reply by author to J. R. Osborn. L. Crocco (TC)..... 2238

PROPULSION

- Nonlinear axial combustion instability in solid propellant motors. W. G. Brownlee..... 275
- Magnetohydrodynamic species separation in a gaseous nuclear rocket. R. A. Gross and K. O. Kessey..... 295
- Evaluation and analysis of thrust units for power-limited propulsion systems. R. D. Shelton, R. A. Potter, L. Laey, and E. Stuhlinger..... 682
- A theory of low-frequency combustion instability in solid rocket motors. Robert Sehgal and Leon Strand..... 696
- Photomicrography of electrically sprayed heavy particles. Charles D. Hendricks Jr., Ralph S. Carson, James J. Hogan, and John M. Schneider..... 733
- Fuel containment in the gaseous-core nuclear rocket by MHD-driven vortices. Jacob B. Romero..... 1092
- Linear acoustic gains and losses in solid propellant rocket motors. R. H. Cantrell, R. W. Hart, and F. T. McClure..... 1100
- Nonlinear effects in instability of solid-propellant rocket motors. R. W. Hart, J. F. Bird, R. H. Cantrell, and F. T. McClure..... 1270
- Vortex generation in solid propellant rockets. J. Swithenbank and G. Sotter..... 1297
- Roll torque and normal force generation in acoustically unstable rocket motors. G. A. Flandro..... 1303
- Chuffing and nonacoustic instability phenomena in solid propellant rockets. R. A. Yount and T. A. Angelus..... 1307
- Particle drag and heat transfer in rocket nozzles. Donald J. Carlson and Richard F. Hoglund..... 1980
- MGD space propulsion system for lunar missions. Fred Spindler and Kenneth Wang (TN)..... 152
- Deflagration characteristics of ammonium perchlorate strands. Larry J. Shannon and Eugene E. Petersen (TN)..... 168
- Chemical kinetic analysis of rocket exhaust temperature measurements. Frederick P. Boynton (TN)..... 577
- Simplified calculation of the jet-damping effects. Nicholas Rott and Lembit Pottsepp (TN)..... 764
- An experimental evaluation of plug cluster nozzles. D. Migdal, J. J. Horgan, and A. Chamay (TN)..... 1325
- A semitoroidal reflex discharge as a propulsion device. D. Pigache (TN)..... 1332
- Exact kinetic and approximate nozzle recombination losses. David Migdal and Arnold Goldford (TN)..... 1457
- Gaseous nuclear rocket with MHD vortex fuel containment. K. O. Kessey and R. A. Gross (TN)..... 1461
- Pressure gradients in a liquid propellant rocket motor. William T. Peschke and Sanford S. Hammer (TN)..... 1467
- Backside temperatures of an internal insulator in a solid-propellant motor. James W. Kordig (TN)..... 1475
- Effect of oxidizer concentration on combustion instability of a solid propellant. D. W. Rice (TN)..... 1654
- Injection thrust termination and modulation in solid rockets. Riad Jaroudi and Allan J. McDonald (TN)..... 2036

PHYSICS, SOLID-STATE

- Evaporation coefficients from exposure of a solid to laser radiation. S. S. Penner (TN)..... 1664

PROPELLANTS AND COMBUSTION

- Measurements of particulate acoustic attenuation. Richard A. Dobbins and S. Temkin..... 1106
- Use of the one-dimensional T-burner to study oscillatory combustion. M. D. Horton..... 1112
- T-burner method of determining the acoustic admittance of burning propellants. R. L. Coates, M. D. Horton, and N. W. Ryan..... 1119
- Admittance measurements of solid propellants by an acoustic oscillator technique. S. N. Foner, R. L. Hudson, and B. H. Nall..... 1123
- Acoustic instability: influence of and on the solid phase. Norman W. Ryan and Ralph L. Coates..... 1130

Longitudinal wave propagation in liquid propellant rocket motors. Sanford S. Hammer and Vito D. Agosta (TN).....	2042
Comment on "Relative variation of rocket vehicle specific impulse and structural weight fraction for constant burnout velocity." R. E. Forrette (TC).....	188
Comments on "Integral approach to an approximate analysis of thrust vector control by secondary injection." Wayne E. Simon (TC).....	1359
Reply by author to W. Simon. Krishnamurthy Karamcheti and Henry Tao-Sze Hsia.....	1359

SPACE RADIATION

Aerodynamic aspects of the magnetospheric flow. R. H. Levy, H. E. Petschek, and G. L. Siscoe(SA).....	2065
Experimental study of radiative transport from hot gases simulating in composition the atmospheres of Mars and Venus. Carlton S. James.....	470
Preliminary estimates of radiative transfer effects on detached shock layers. Robert Goulard.....	494
Effects of radiation forces on the attitude of an artificial earth satellite. Thomas F. Clancy and Thomas P. Mitchell.....	517
Analysis of an electrostatic shield for space vehicles. Frank Henry Vogler.....	872
Spectrum of shock-heated gases simulating the Venus atmosphere... A. R. Fairbairn.....	1004
Particle motion in the equatorial plane. Vincent L. Pisacane.....	1361
Solar radio emission as criteria for solar proton event warning. J. D. Fletcher.....	2193
Mass and magnetic dipole shielding against electrons of artificial radiation belt. A. Bhattacharjee and I. Michael.....	2198
Experimental investigation of electric drag on satellites. Earl D. Knechtel and William C. Pitts (TN).....	1148
Dynamics of the solar wind. F. L. Scarf and L. M. Noble (TN).....	1158
Shock-layer radiation for sphere-cones with radiative decay. Jin H. Chin and L. F. Hearne (TN).....	1345
Effect of argon addition on shock-layer radiance of CO ₂ -N ₂ gas mixtures. F. Wolf and T. Horton (TN).....	1472
Equilibrium electron density of Mars. Edward D. Shane (TN).....	1497
Plasma radiation shielding. Richard H. Levy and G. Sargent James (TN).....	1835

SPACE SCIENCES

Matrix methods in the calculation and analysis of orbits. J. M. A. Danby.....	13
The matriciant of Keplerian motion. J. M. A. Danby.....	16
Determination of extreme entry angles into a planetary atmosphere. J. Warga and W. C. Hailey.....	335
Optimal variable-thrust transfer of a power-limited rocket between neighboring circular orbits. Frank W. Gobetz.....	339
Some optimal low-acceleration rendezvous maneuvers. B. H. Billik.....	510
Bounds on the librations of a symmetrical satellite. Ralph Pringle Jr.....	908
Approximate distribution of nearly circular orbits. R. E. Beckwith.....	913
Determination of the preliminary orbits of artificial lunar and planetary satellites. Paul E. Koskela.....	917
Dumbbell librations in elliptic orbits. Hans B. Schechter.....	1000
Optimum low-thrust rendezvous and station keeping. Theodore N. Edelbaum.....	1196
A new approach to steepest-ascent trajectory optimization. R. T. Stancil.....	1365
Optimal trajectories and linear control of nonlinear systems. Andrew H. Jazwinski.....	1371
A second variation test for singular external. Henry J. Kelly.....	1380
An analysis of two-impulse orbital transfer. Gentry Lee.....	1767
Constants of the motion for optimum thrust trajectories in a central force field. Samuel Pines.....	2010
Nth order solutions to certain thrust integrals. Edward E. Markson (TN).....	381
Trajectories with constant normal force starting from a circular orbit. Richard R. Auelmann (TN).....	561
Preliminary orbit determination from self-contained data. Robert H. Gersten and Z. E. Schwarzbein (TN).....	751
A load-sinkage equation for lunar soils. Donald L. Dewhurst (TN).....	761
Relative magnitudes of the space-environment torques on a satellite. Lyle E. Wiggins (TN).....	770
Location of catch-up point in a ΔV perturbed circular orbit. Andrew H. Milstead (TN).....	940
Umbra and penumbra eclipse factors for satellite orbits. Sol Zale Fixler (TN).....	1455
Nodal period of an earth satellite. Leon Blitzer (TN).....	1459
Euler angles for libration analysis. Irving Michelson (TN).....	1469
Stationary earth orbits. Frank C. Hoyt (TN).....	1470
A property of cotangential elliptical transfer orbits. N. X. Vinh (TN).....	1841
Orbit determination by angular measurements. P. O. Bell (TN).....	1862
Comment on "Design analysis of earth-lunar trajectories: launch and transfer characteristics." Richard L. Robertson (TC).....	969
Reply by author to D. A. Conrad. R. E. Beckwith (TC).....	2235
Errata: "Optimal variable-thrust transfer of a power-limited rocket between neighboring circular orbits." Frank W. Gobetz (TC).....	2236

SPACE VEHICLES

Optimal programming problems with inequality constraints II: solution by steepest-ascent. Walter F. Denham and Arthur E. Bryson Jr.....	25
---	----

Shadows produced by spin-stabilized communication satellites. B. Paul.....	924
Control of a synchronous satellite by continuous radial thrust. Ronald S. H. Toms and B. E. Kalensher.....	1179
Motion of an artificial earth satellite in an orbit of small eccentricity. G. A. Chebotarev (RS).....	203
Skip-impact criteria of a re-entry trajectory with negative lift. Charles J. Ruger (TN).....	585
Re-entry wake in an earth-fixed coordinate system. Jerold H. Klaimon (TN).....	745
Comment on "Interception of high-speed target by beam rider missile." N. X. Vinh (TC).....	409

SPACE VEHICLE (LAUNCH VEHICLES)

Payload scaling laws for boost rockets. Donald van Zelm Wadsworth (TN).....	2223
Comment on "Coning effects caused by separation of spin-stabilized stages." R. O. Wilke (TC).....	1358
Reply by author to R. O. Wilke. M. J. Dwork (TC).....	1358

SPACE VEHICLES (SPACECRAFT)

Docking dynamics for rigid-body spacecraft. Carl Grubin.....	5
Damping of a gravitationally stabilized satellite. Robert R. Newton.....	20
The drag-free satellite. Benjamin Lange.....	1590
Orbital transfer with minimum fuel. W. E. Bleick and F. D. Faulkner (TN).....	113
In-plane lunar injection opportunities from an orbiting space station. William R. Wells (TN).....	383
Space station design parameter effects on artificial g field. Carl A. Larson (TN).....	1454
Reply by author to R. E. Lavender. A. P. Cappelli (TC).....	412
Erratum: "Comment on 'Equilibrium orientations of gravity-gradient satellites.'" Thomas R. Kane and Peter W. Likins (TC).....	1866

STRESSES AND LOADS

Structural analysis of viscoelastic materials. M. L. Williams (SA)...	785
Influence of stress history on time-dependent spall in metals. B. M. Butcher, L. M. Barker, D. E. Munson, and C. D. Lundergan (SA).....	977
Effect of mass loss on the transient response of a shallow spherical sandwich shell. James Tasi.....	58
Dynamic loads due to wind shear. Bruce E. Clingan.....	76
Surface strains in case-bonded models of rocket motors. D. J. Bynum, L. U. Rastrelli, and R. C. DeHart.....	343
Stress-strain relations of reinforced plastics parallel and normal to their internal filaments. Bernard W. Shaffer.....	348
Large-amplitude vibration and response of curved panels. Benjamin E. Cummings.....	709
Free vibration of thin cylindrical shells. V. I. Weingarten.....	717
A generalization of the direct-stiffness method of structural analysis. Robert E. Jones.....	821
Effect of cyclic loading on the temperature in viscoelastic media with variable properties. R. A. Schapery.....	827
Statistical methods in vibration analysis. Richard H. Lyon and Gideon Maidanik.....	1015
Large-amplitude oscillations of oblique panels with an initial curvature. J. L. Nowinski.....	1025
Mathematical determination of stresses and displacements in star-perforated grains. Howard B. Wilson Jr.....	1247
Effects of boundary conditions on the stability of cylinders subject to lateral and axial pressures. L. H. Sobel.....	1437
Flutter of a ring of panels. Ronald Stearman.....	1441
Random vibrations of a Myklestad beam. Y. K. Lin.....	1448
Influence of initial stress on the vibrations of simply supported circular cylindrical shells. Anthony E. Armenakis.....	1607
Large elastic, plastic, and creep deflections of curved beams and axisymmetric shells. James A. Stricklin, Pao-Tan Hsu, and Theodore H. H. Pian.....	1613
Stability of internally pressurized conical shells under torsion. V. I. Weingarten.....	1782
Nonlinear response of cylindrical shells subjected to dynamic axial loads. Robert S. Roth and Jerome M. Klosner.....	1788
Postbuckling behavior of orthotropic cylinders under axial compression. B. O. Almroth.....	1795
Stresses in an incompressible viscoelastic-plastic thick-walled cylinder. M. Shinozuka.....	1800
Flutter of multibay panels at high supersonic speeds. Earl Dowell.....	1805
Fuel sloshing in a spherical tank filled to an arbitrary depth. Wen-Hwa Chu.....	1972
Plastic stability of spherical plates. C. Lakshminathan and George Gerard.....	1999
Diffractions of flexural waves by a cavity in an elastic plate. Yih-Hsing Pao and C. C. Chao.....	2004
Stability of circumferentially corrugated sandwich cylinders under combined loads. Edward H. Baker.....	2142
Influence of boundary conditions on the modal characteristics of thin cylindrical shells. Kevin Forsberg.....	2150
Approximate laplace transform inversions in viscoelastic stress analysis. Thomas L. Cost.....	2157
Influence coefficients of a circular cylindrical shell with rapidly varying parabolic wall thickness. David Bushnell and Nicholas J. Hoff.....	2167

- Influence of work-hardening on the dynamic stress-strain curves of 4340 steel. Barry M. Butcher and Jack R. Canon..... 2174
- Analysis of a symmetrically loaded sandwich cylinder. E. H. Baker (TN)..... 108
- Deformations and stresses in an axially restrained beam. Harold Switzky (TN)..... 109
- Phase shift in a massless vibrating beam. Joseph Genin (TN)..... 118
- Effect of aerodynamic damping on flutter of thin panels. H. M. Voss and E. H. Dowell (TN)..... 119
- Transient temperature variation in a thermally orthotropic cylindrical shell. K. J. Touryan (TN)..... 124
- Buckling load of bars with variable stiffness: A simple numerical method. A. V. Srinivasan (TN)..... 139
- Postbuckling behavior of heated skin panels. George S. Johnston (TN)..... 141
- A simple geometric method for analyzing polarization states in photoelasticity. Robert Mark (TN)..... 150
- Analogy between three-dimensionally heated plates and generalized plane stress. M. Forray and M. Newman (TN)..... 165
- Bending of rhombic plates. William E. Warren (TN)..... 166
- Nonlinear pressure coupling in cylindrical shell analysis. Paul E. Wilson and Edward E. Spier (TN)..... 370
- Flutter of two parallel flat plates connected by an elastic medium. John A. McElman (TN)..... 377
- Elastic stability of conical shells under axisymmetric pressure band loadings. Joseph C. Serpico (TN)..... 389
- Sandwich cylinder instability under nonuniform axial stress. R. A. Gellatly and R. H. Gallagher (TN)..... 398
- Energy solution for simply supported oval shells. William P. Vafakos, Neil Nissel, and Joseph Kempner (TN)..... 555
- Finite plane deformation of a thick-walled cylinder. M. P. Bieniek and M. Shinozuka (TN)..... 568
- Wave propagation in rotating elastic media. Ronald L. Huston (TN)..... 575
- Derivation of element stiffness matrices. Theodore H. H. Pian (TN)..... 576
- Computer analysis of asymmetrical deformation of orthotropic shells of revolution. Gerald A. Cohen (TN)..... 932
- Variation in buckle shape in cylindrical shells under external pressure and axial load. W. H. Horton and S. C. Durham (TN)..... 943
- Final shape of a dynamically loaded elastic-plastic redundant structure. H. C. Schjelderup and Robert E. Ball (TN)..... 958
- General solution of the rigid body impact problem. G. G. Herzl (TN)..... 959
- Derivation of element stiffness matrices by assumed stress distributions. Theodore H. H. Pian (TN)..... 1333
- Iterative and power series solutions for the large deflection of an annular membrane. Allan B. Pifko and Martin A. Goldberg (TN)..... 1340
- A flutter design parameter to supplement the Regier number. Frank J. Frueh (TN)..... 1343
- Buckling of circular cylindrical shells in axial compression. R. C. Tennyson (TN)..... 1351
- Some energy and momentum considerations in the perforation of plates. A. C. Gierle (TN)..... 1471
- Flutter of multibay panels at supersonic speeds. William P. Rodden (TN)..... 1476
- Flutter characteristics of titanium alloys. Joseph Genin and R. P. Peloubet (TN)..... 1482
- A "membrane" solution for axisymmetric heating of dome-shaped shells of revolution. Harry E. Williams (TN)..... 1491
- Inner-outer expansion method for couple-stress effects. S. H. Lam and D. C. Leigh (TN)..... 1511
- Creep and relaxation. R. L. Taylor (TN)..... 1659
- Vibrational characteristics of thin-wall conical frustum shells. Jerry D. Watkins and Robert R. Clary (TN)..... 1815
- Use of stress relaxation tests to characterize time dependencies of a composite solid propellant. Joseph H. Stoker (TN)..... 1816
- Large deflection of sandwich plates with orthotropic cores. A. M. Alwan (TN)..... 1820
- Stress functions for the axisymmetric, orthotropic, elasticity equations. L. R. Herrmann (TN)..... 1822
- Compact formal analysis of beam columns. J. E. Brock (TN)..... 1824
- Natural frequencies of meridional vibration in thin conical shells. R. E. Keffe (TN)..... 1825
- Mismatch stresses in pressure vessels. Robert H. Johns (TN)..... 1827
- Asymmetrical buckling of spherical caps under uniform pressure. Gaylen A. Thurston (TN)..... 1832
- An axially compressed, cylindrical shell with a viscoelastic core. O. C. Davidson and S. C. Browning (TN)..... 2015
- Asymptotic solution of a toroidal shell subjected to nonsymmetric loads. Aleksander Kornecki (TN)..... 2020
- Large amplitude vibration of buckled beams and rectangular plates. J. G. Easley (TN)..... 2207
- Significance of the cross correlation between the modes of a structure on its response. Ghassan R. Khabbaz (TN)..... 2211
- Comment on "A theoretical interaction equation for the buckling of circular shells under axial compression and external pressure." Josef Singer (TC)..... 410
- Reply by author to J. Singer. P. W. Sharman (TC)..... 411
- Comment on "Mathematical analysis of corotating nose-gear shimmy phenomenon." William J. Moreland (TC)..... 415
- Comments on "Numerical analysis of unsymmetrical bending of shells of revolution." Gilbert A. Greenbaum (TC)..... 590
- Reply by authors to G. A. Greenbaum. Bernard Budiansky and Peter P. Radkowski (TC)..... 592
- Errata: "Residual analysis for circular cylindrical shells under segmental line-load." James Sheng and Joseph Kempner (TC)..... 784
- Erratum: "Elastic stability of near-perfect shallow spherical shells." M. A. Krenzke and T. J. Kiernan (TC)..... 784
- Comment on "Basis for derivation of matrices for the direct stiffness Method." E. L. Cook, R. E. Chapel, and W. D. Bernhart (TC)..... 1161
- Shell buckling and nonconservative forces. George Herrmann and Richard W. Bungay (TC)..... 1165
- Reply by author to G. Herrmann and R. W. Bungay. F. W. Niedenfuhr (TC)..... 1166
- Comment on "Derivation of element stiffness matrices." G. C. Best (TC)..... 1515
- Comment on "Effective shear modulus of honeycomb cellular structure." Ronald A. Gellatly (TC)..... 1518
- Reply by authors to R. A. Gellatly. Joseph Penzien and Theodor Didriksson (TC)..... 1519
- Comment on "Vibration of a 45° right triangular cantilever plate by a gridwork method." K. J. Draper, B. Irons, and G. Bazeley (TC)..... 1870
- Aerodynamic loads on bluff bodies at low speeds. Mark V. Morkovin (TC)..... 2058
- Strain-displacement relations in large displacement theory of shells. C. H. Tsao (TC)..... 2060
- Errata: "Computer analysis of asymmetrical deformation of orthotropic shells of revolution." Gerald A. Cohen (TC)..... 2231
- Comments on "Iterative and power series solutions for the large deflection of an annular membrane." James G. Simmonds (TC)..... 2233
- Reply by authors to J. G. Simmonds. Allan B. Pifko and Martin A. Goldberg (TC)..... 2234

STRUCTURAL DESIGN

- Effective shear modulus of honeycomb cellular structure. Joseph Penzien and Theodor Didriksson..... 531
- Orthotropic pressure vessels with axial constraint. C. R. Steele..... 703
- Analytical design for optimum filamentary pressure vessels. Hans U. Schuerch and Odus R. Burggraf..... 809
- An investigation of the protection afforded a spacecraft by a thin shield. C. J. Maiden and A. R. McMillan..... 1992
- Integration of discontinuous expressions arising in beam theory. J. T. Weissenburger (TN)..... 106
- Elastic stability of castellated plates. M. Sevik (TN)..... 174
- Tetrahedron elements in the matrix force method of structural analysis. J. S. Przemieniecki (TN)..... 1152
- Comment on "Matrices for the direct stiffness method." Bruce Irons and John Barlow (TC)..... 403
- Comment on "Derivation of element stiffness matrices." Bruce Irons and Keith Draper (TC)..... 1677

Information for Contributors to Journals of the AIAA

Manuscripts: Send all manuscripts, with covering letter, to the Managing Editor, AIAA Scientific Publications, 1290 Avenue of the Americas, New York, N. Y. 10019. Each manuscript must be accompanied by written assurance as to security clearance in the event the subject matter lies in a classified area or if the paper originates under government sponsorship. Full responsibility rests with the author. Signed assurance must be given that the manuscript or its equivalent *has not been submitted for publication elsewhere*. The AIAA has prior publication rights to any paper presented at its meetings. Preprints will be considered automatically for publication in one of the AIAA's four periodicals. The author will be informed as soon as possible after a meeting as to the particular publication to which his preprint has been assigned. No formal submittal by the author will be necessary in the case of preprints, but the Editors would naturally welcome a statement by the author as to the journal he prefers.

Send 3 copies of each manuscript, typed double spaced on one side of the page only, with wide margins to allow for instructions to the printer. Footnotes, references, and figure captions also should be typed double spaced. Use standard-size ($8\frac{1}{2} \times 11$ -in.) good-quality bond paper. Manuscripts must be submitted in English.

Manuscripts must be as brief as the proper presentation of the ideas will allow. Exclusion of dispensable material and conciseness of expression will influence the Editors' acceptance of a manuscript. In terms of standard-size double-spaced typed pages, a typical maximum length is 22 pages of text (including equations), 1 page of references, 1 page of abstract, and 12 illustrations. Fewer illustrations permit more text, and vice versa. Greater length will be acceptable in exceptional cases, whenever the subject clearly merits expanded space. The Editor may request written justification to defend the extra space.

Short manuscripts, not more than one-quarter of the maximum length stated for full articles, may qualify for publication as Technical Notes or Technical Comments. They may be devoted to new developments requiring prompt disclosure or to comments on previously published papers. They must, in the judgment of the Editors, contribute interesting or significant information. Such manuscripts are published within a few months of the date of receipt.

Titles and Authors' Names. The title should be brief. Lengthy titles will be shortened by the Editor. The author's name should be typed on the line below the title, and it is preferable to use the full name. The company affiliation should follow on the next line, with the author's official title given in a footnote.

Abstract. Each full-length paper must be accompanied by a 100- to 200-word abstract, written as a single paragraph, below the company affiliation. It should be a summary (not an introduction!) and complete in itself (no numerical references). The abstract should indicate the subjects dealt with in the paper and should state the objectives of the investigation. Newly observed facts and conclusions of the experiment or argument discussed in the paper must be stated in summary form. An inadequate abstract will be sufficient cause for delay in publication. For detailed instructions on the preparation of abstracts, see the Style Manual of the American Institute of Physics, page 5.¹

Mathematics. Equations and symbols may be handwritten or typewritten; clarity for the printer is essential. Greek letters and unusual symbols should be identified in the margin. If handwritten, distinguish between capital and lower case letters; between the letter o and zero; ell, the number one, and prime; k and kappa; u and mu; v and nu; n and eta; indicate subscripts and superscripts.

Always use the solidus for fractions in the text and for simple fractions in displayed equations. Avoid the radical sign for indicating square root; use parentheses and fractional superscripts instead. Complicated special symbols should be avoided, such as letters with both a dot and a bar over them. Use angular brackets $\langle \rangle$ rather than a bar over a group of symbols to denote average.

References: References are to be grouped at the end of the manuscript and are to be given as follows:

1) Books: Whittaker, E. T., *Analytical Dynamics* (Dover Publications, Inc., New York, 1937), 4th ed., Chap. IV, p. 91.

2) Journals: Brown, D. C., "Optical refraction with emphasis on corrections for points outside the atmosphere," *ARS J.* **31**, 549-550 (1961).

Use standard abbreviations for Journals as given in the "List of Periodicals" published by Chemical Abstracts. Always give inclusive page numbers for references to journal articles and a page or chapter number for books. Each reference must be cited in the text. Other literature may be listed under a heading "Bibliography."

Illustrations: Line drawings must be clear and sharp to make clear engravings. Use black ink on white paper or tracing cloth. Lettering should be large enough to be legible (at least $\frac{1}{16}$ in. high) after reduction. Plan figures for reduction to column width ($3\frac{1}{4}$ in.). Photographs should be glossy prints, not matte or semi-matte. Each illustration must have a caption; captions should be listed in order on a separate sheet. Write your name and the figure number in the margin of each illustration. Cite each figure in numerical order in the text.

Tables: Tables should be planned to fit the page width of the Journal (7 in.). Tables that must be placed sideways are to be avoided. Use a double rule at the top, a single rule under the column headings, a double rule at the end. Avoid vertical rules, which are expensive to set. Table footnotes should be placed under the final double rule and should be indicated by letters a, b, c, etc. Do not number table footnotes consecutively with text references. Each table must have a caption. Cite each table in numerical order in the text.

Symbols: Use standard symbols whenever possible, preferably those recommended by the American Standards Association. For a list of special symbols available to most printers, see the Style Manual of the American Institute of Physics.¹

Alterations: Take great care that the manuscript is typographically accurate. A limited number of alterations in proof are unavoidable, but the cost of making extensive alterations in proof as a result of an inaccurate or unclear manuscript will be charged to the author. Likewise, the cost of remaking engravings as a result of an incorrect original drawing will be charged to the author.

Check List:

- 1) Letter of submittal with written assurance that article or its equivalent has not been submitted elsewhere
- 2) 3 copies, typed original manuscript, covering letter
- 3) Abstract
- 4) Original line drawings of figures, glossy prints of photographs, preferably not larger than $8\frac{1}{2} \times 11$ in.; include a set of figures with each of the extra copies of the manuscript
- 5) List of figure captions typed on separate page
- 6) Titles of articles and inclusive page numbers for journal references; page or chapter number for book references
- 7) All references, figures, and tables numbered consecutively and cited in numerical order in the text
- 8) Greek letters and unusual symbols identified for printer

¹ Available from American Institute of Physics, 335 East 45th Street, New York, N. Y. 10017. Price: \$1.00.

CONTENTS—Continued

TECHNICAL NOTES

Identification of Two Types of Separation.....	J. W. Paull	2202
Sonic Line of Magnetohydrodynamic Nozzle Flow.....	T. Yamanaka	2203
Similar Solutions for Three-Dimensional Laminar Compressible Boundary Layers.....	M. C. Fong	2205
Large Amplitude Vibration of Buckled Beams and Rectangular Plates.....	J. G. Eisley	2207
Approximate Absorption Coefficients for Vibrational Electronic Band Systems.....	E. P. French	2209
Significance of the Cross Correlation between the Modes of a Structure on Its Response.....	G. R. Khabbaz	2211
Time-Dilatation Dilemma and Scale Variation.....	M. Z. v. Krzywoblocki	2213
Effect of Fluid Motion on Free Surface Shape under Reduced Gravity.....	J. H. Chin and L. W. Gallagher	2215
Influence of Magnetic Fields upon Separation.....	W. H. Heiser	2217
Three-Dimensional Symmetric Vortex Flow.....	A. K. Ray	2218
Torque on a Satellite Due to Gravity Gradient and Centrifugal Force.....	P. S. Carroll	2220
Modification of the Hydrazine-Nitrogen Tetroxide Ignition Delay.....	H. G. Weiss, B. Johnson, H. D. Fisher, M. Gerstein	2222
Payload Scaling Laws for Boost Rockets.....	D. v. Z. Wadsworth	2223
Unsteady Flow Past Junctions in Ducts.....	A. G. Hammitt and H. J. Carpenter	2224
Model Law for Parachute Opening Shock.....	K. E. French	2226
Capillary Stability in an Inverted Rectangular Channel for Free Surfaces with Curvature of Changing Sign.....	P. Concus	2228

TECHNICAL COMMENTS

Errata: "Computer Analysis of Asymmetrical Deformation of Orthotropic Shells of Revolution".....	G. A. Cohen	2231
Comment on Non-Newtonian Flow.....	B. Steverding	2231
Reply by Author to B. Steverding.....	C. S. Wells Jr.	2232
Comment on "Conical Shock-Wave Angle".....	M. F. Romig	2232
Comments on "Iterative and Power Series Solutions for the Large Deflection of an Annular Membrane".....	J. G. Simmonds	2233
Reply by Authors to J. G. Simmonds.....	A. B. Pifko and M. A. Goldberg	2234
Distribution of Nearly Circular Orbits.....	D. A. Conrad	2234
Reply by Author to D. A. Conrad.....	R. E. Beckwith	2235
Errata: "Optimal Variable-Thrust Transfer of a Power-Limited Rocket between Neighboring Circular Orbits".....	F. W. Gobetz	2236
Longitudinal Mode Instability.....	J. R. Osborn	2237
Reply by Author to J. R. Osborn.....	L. Crocco	2238
Comment on "An Alternate Interpretation of Newton's Second Law".....	V. W. Snyder	2239

REPRINTED TABLE OF CONTENTS

November-December 1964 Journal of Spacecraft and Rockets.....	2241
---	------